# APPLICATIONS OF SUPRAMOLECULAR NANOCAPSULES: REGIOSELECTIVE FUNCTIONALIZATION OF FULLERENES AND MOLECULAR RECOGNITION OF ENDOHEDRAL METALLOFULLERENES

**Míriam Pujals Crusat**

DOCTORAL THESIS

# APPLICATIONS OF SUPRAMOLECULAR NANOCAPSULES: REGIOSELECTIVE FUNCTIONALIZATION OF FULLERENES AND MOLECULAR RECOGNITION OF ENDOHEDRAL METALLOFULLERENES

Míriam Pujals Crusat

2024

Doctoral programme in Chemistry

Supervised by: Prof. Xavi Ribas Salamaña

Tutor: Prof. Xavi Ribas Salamaña

Presented to obtain the degree of PhD at the University of Girona

Universitat de Girona

Prof. Xavi Ribas Salamaña from Universitat de Girona,

I DECLARE:

That the thesis entitled “Applications of supramolecular nanocapsules: regioselective functionalization of fullerenes and molecular recognition of endohedral metallofullerenes”, presented by Míriam Pujals Crusat to obtain a doctoral degree, has been completed under my supervision and meets the requirements to opt for an international Doctorate.

For all intents and purposes, I hereby sign this document.

Prof. Xavi Ribas Salamaña

Girona, February 19, 2024

# PUBLICATIONS RESULTING FROM THIS THESIS

Pujals, M; Pèlachs, T.; Fuertes-Espinosa, C.; Parella, T.; Garcia-Borràs, M.; Ribas, X. Regioselective access to orthogonal Diels-Alder $C_{60}$ bis-adducts and tris-heteroadducts via supramolecular mask strategy. *Cell Rep. Phys. Sci*. **2022**, 3, 100992

Pujals, M; Iannace, V.; Ribas, X. Two-fold enhancement of equatorial bis-PCBM-$C_{60}$ adducts using a supramolecular mask. *Supramol. Chem.* **2024**. DOI: 10.1080/10610278.2024.2338141

# PUBLICATIONS NOT INCLUDED IN THIS THESIS

Fuertes-Espinosa, C.; García-Simón, C.; Pujals, M.; Garcia-Borràs, M.; Gómez, L.; Parella, T.; Juanhuix, J.; Imaz, I.; Maspoch, D.; Costas, M.; Ribas, X. Supramolecular Fullerene Sponges as Catalytic Masks for Regioselective Functionalization of $C_{60}$. *Chem*, **2020**, 6, 169–186.

Fuertes-Espinosa, C.; Pujals, M.; Ribas, X. Supramolecular Purification and Regioselective Functionalization of Fullerenes and Endohedral Metallofullerenes. *Chem*, **2020**, 6, 3219–3262.

García-Simón, C.; Colomban, C.; Çetin, Y. A.; Gimeno, A., Pujals, M.; Ubasart, E.; Fuertes-Espinosa, C.; Asad, K.; Chronakis, N.; Costas, M. Jiménez-Barbero, J.; Feixas, F.; Ribas, X. Complete Dynamic Reconstruction of $C_{60}$, $C_{70}$ and $(C_{59}N)_2$ Encapsulation into an Adaptable Supramolecular Nanocapsule. *J. Am. Chem. Soc.*, **2020**, 142, *37*, 16051-16063.

Ubasart, E.; García-Simón, C.; Pujals, M.; Asad, K.; Chronakis, N.; Parella, T.; Ribas, X. Straightforward Supramolecular Purification of $C_{84}$ from a Fullerene Extract. *Org. Chem. Front.*, **2021**, 8, 4101–4105.

Steudel, F. M.; Ubasart, E.; Leanza, L.; Pujals, M.; Parella, T.; Pavan, G. M.; Ribas, X.; von Delius, M. Synthesis of $C_{60}$/[10]CPP-catenanes by Regioselective, Nanocapsule-templated Bingel Bis-addition. *Angew. Chem. Int. Ed.*, **2023**, 62, *42*, e202309393

# LIST OF ABBREVIATIONS

| | |
|---|---|
| γ-CD | γ-cyclodextrin |
| 10[CPP] | [10]cycloparaphenylene |
| 0D | Zero-dimensional |
| 1D | One-dimensional |
| 2D | Two-dimensional |
| 3D | Three-dimensional |
| An | Anthracene |
| BPO | Benzoyl peroxide |
| CPP | Cycloparaphenylene |
| CRY | Cryptophane-111 |
| $Cu^{II}$ | Copper (II) |
| DCM | Dichloromethane |
| DBU | 1,8-diazabicyclo(5.4.0)undec-7-ene |
| DFT | Density Functional Theory |
| e.e. | Enantiomeric excess |
| EMF | Endohedral metallofullerene |
| equiv. | Equivalents |
| ETL | Electron transport layer |
| FMO | Frontier molecular orbitals |
| HIV | Human immunodeficiency virus |
| HOMO | Highest occupied molecular orbital |
| HPLC | High pressure liquid chromatography |
| HR-ESI-MS | High resolution mass spectrometry |
| IPR | Isolated pentagon rule |
| $K_a$ | Association constant |
| DNA | Deoxyribonucleic acid |
| DMF | *N,N*-dimethylformamide |
| $Fe^{II}$ | Iron (II) |
| L | Ligand |
| LUMO | Low unoccupied molecular orbital |
| M | Metal |
| m/z | Mass-to-charge ratio |
| MD | Molecular dynamic |
| MeONa | Sodium methoxide |

|  |  |
|---|---|
| MOF | Metal-organic framework |
| NaAsc | Sodium ascorbate |
| NaBArF | Sodium tetrakis[3,5-bis(trifluoromethyl)phenyl]borate |
| NCF | Metal-nitride cluster fullerenes |
| NIR | Near-infrared |
| NMR | Nuclear magnetic resonance |
| NSC | Neural stem cells |
| *o*-DCB | *o*-dichlorobenzene |
| $PC_{61}BM$ or PCBM | Phenyl-$C_{61}$-butyric acid methyl ester |
| PCE | Power conversion efficiency |
| Pn | Pentacene |
| PrSC | Perovskite solar cell |
| $Pd^{II}$ | Palladium (II) |
| ROS | Reactive oxygen species |
| SMM | Single molecule magnet |
| MeONa | Sodium methoxide |
| TBAP | Tetrabutylammonium perchlorate |
| THF | Tetrahydrofuran |
| TFT | Thin-film transistor |
| TLC | Thin-layer chromatography |
| NBS | *N*-bromosuccinimide |
| $NEt_3$ | Triethylamine |
| UV-vis | Ultraviolet-visible |
| $Zn^{II}$ | Zinc (II) |

# ACKNOWLEDGEMENTS

This work would not have been possible without the following collaborations:

- Serveis Tècnics de Recerca from Universitat de Girona for technical support, with special remark to Dr. Laura Gómez (HR-ESI-MS), Vicenç Oliveras (MALDI-MS) and Lluïsa Matas (NMR).
- Dr. Marc Garcia-Borràs from the Institut de Química Computacional i Catàlisi (Universitat de Girona) for the computational modeling data.
- Dr. Teodor Parella from Universitat Autònoma de Barcelona for the support with the NMR data.
- Prof. Max von Delius, MSc Fabian Steudel and all the members of Delius group for the collaborative project regarding the molecular shuttle and for hosting the scientific visit.
- Prof. Alexey A. Popov for the collaborative project regarding the purification of EMFs.
- Financial support by:
    - Universitat de Girona (IFUdG2019-2021 and MOB2021)
    - MINECO-Spain (PID2019-104498GB-I00)
    - Fundación Areces (Regiosolar)

També vull donar les gràcies en especial a en Xavi per haver confiat en mi, donar-me l'oportunitat de seguir en el món de l'acadèmia i ajudar-me a donar forma a aquesta tesis. També agrair a en Miquel i l'Anna per haver confiat en mi.

Vull donar les gràcies als companys del grup de recerca, amb especial èmfasi a algunes persones:

Gràcies als mentors que vaig tenir quan vaig entrar al lab: a la Cristina, per introduir-me en el món de la supra quan vaig fer el TFG, i a en Carles, per ajudar-me i guiar-me en tot moment durant els primers mesos de doctorat.

Gràcies al "dream team" que vam formar quan vaig entrar a fer el doctorat: Carla, Ernest i Pau. A tu Carla, per la teva bogeria i alegria en tot moment però, alhora, per la teva comprensió i tendresa quan era necessari. Ernest, per ser el meu company colze a colze al laboratori des que vaig entrar fins que vas marxar, per totes les hores invertides al lab, al roco i en festes majors. I a tu Pau, el meu company grup, company de pis i amic. La persona amb qui he passat més hores durant aquests últims 5 anys. La nostra amistat

traspassa les poiates del lab i arriba molt més enllà. Gràcies per totes les hores de converses, consells, rallades, riures i per cuidar-nos quan més ho hem necessitat.

Gràcies també a les “nenes del supra”. Clara, l’última incorporació, espero que ho petis amb la meva herència que et deixo del lab. Gràcies per la paciència que has tingut a les pistes de pàdel amb nosaltres, ets una crack. Tània, la meva primera estudiant i, més tard, companya de Diels-Alder. Gràcies per totes les hores compartides de lab i pàdel. Y a ti, Valentina, gracias por todo. Entraste al lab en plena pandemia y enseguida ya te ganaste mi corazón. En poco tiempo nos hicimos amigas y nunca imaginé que llegarías a ser tan importante para mí. Gracias por ser como eres y hacerme un huequito en tu vida. Gracias por todas las experiencias vividas: deshaucio, Teleco, Orequé?, Islandia, Canet rock, Mallorca, noches en Cucut, Salero y Estadi, comidas con pollo a l’ast… y por mil anécdotas más.

També donar les gràcies a gent del grup que han estat molt presents durant aquests quasi 5 anys: Eric, Adrià, Arnau, Judith, Hugo, Marco, Filippo...

Finalment, agrair als meus amics externs al laboratori per estar sempre al meu costat i donar-me l’energia necessària quan els experiments no sortien i, especialment, a la família, que sempre ha confiat en mi des del moment que van saber que començava un doctorat.

# TABLE OF CONTENTS

# LIST OF FIGURES

# LIST OF TABLES

# SUMMARY

Since the discovery of fullerenes and endohedral metallofullerenes (EMFs), these spheroidal carbon cages have attracted the attention of the scientific community due to their exceptional electronic and physicochemical properties. Bare fullerenes and mono-adducts are applied in many different fields, including material science, solar cell energy conversion and biomedical applications. However, broad use of fullerenes as poly-adducts is hampered by the uncontrolled regioselectivity during their functionalization and by the costly purification methods of fullerenes derivatives and EMFs. Metal-directed self-assembled nanocapsules have been used as supramolecular shadow masks to poly-functionalize fullerenes in an itero-, chemo- and regioselective fashion and, also, as supramolecular platforms to encapsulate selectively EMFs from soots or extracts. In this thesis, the scope of functionalization reactions of fullerenes when using supramolecular nanocapsules as templates has been widely extended and, moreover, new terbium-based endohedral fullerenes have been encapsulated selectively using the same family of nanocapsules.

In Chapter IV, bis-functionalization of fullerene $C_{60}$ has been carried out in a controlled way through Diels-Alder reaction using the supramolecular mask approach. In addition, the regioselectivity of the reaction has been orthogonally switched thanks to the different host-guest interactions of the corresponding mono-adducts with the nanocapsule.

In Chapter V, PCBM-based bis-adducts have been synthesized using the same strategy as the previous chapter. This way, the relative yield of equatorial bis-adducts has been increased from 26 to 57% in comparison to the non-templated reaction. Also, novel heteroadducts have also been explored by combining $PC_{61}BM$ with Bingel and Prato reactions.

In Chapter VI, the synthesis of a molecular shuttle based on a $C_{60}$/[10]CPP [2]catenane has been pursued, featuring two fullerenes as recognition sites for one [10]CPP ring. Different synthetic routes have been studied, starting with a Bingel reaction via supramolecular mask approach to obtain pure-isomer bis-adducts with reactive terminal moieties. Then, different reactions have been employed to close the macrocyclic shuttle, such as the olefin metathesis, the copper(I)-catalysed azide-alkyne cycloaddition or the Bingel-Hirsch reaction.

Finally, in Chapter VII, $Tb_2@C_{80}^-$ has been selectively encapsulated by supramolecular nanocapsules from a fullerene extract, thus separating it from a mixture that also contained $Tb@C_{80}^-$, $Tb@C_{82}^-$ and $Tb_2@C_{78}^-$.

# RESUM

Els ful·lerens i metal·lo-ful·lerens endoèdrics han captat l'atenció de la comunitat científica des del seu descobriment a causa de les seves propietats electròniques i fisicoquímiques excepcionals. Els ful·lerens i mono-adductes es poden aplicar en diferents camps de la química, com ara en ciència dels materials, en el camp de la conversió de l'energia solar o en aplicacions biomèdiques. Tot i així, l'ús extensiu dels ful·lerens com a poli-adductes està obstaculitzat per la falta de control de la regioselectivitat durant el procés de funcionalització dels ful·lerens i per l'alt cost dels mètodes de purificació dels poli-adductes i dels metal·lo-ful·lerens endoèdrics. Les nanocàpsules autoensamblades dirigides per enllaços metall-lligand s'han utilitzat com a motlles supramoleculars per funcionalitzar ful·lerens de manera itero-, quimio- i regioselectiva i, a més, s'han utilitzat com plataformes per encapsular selectivament metal·lo-ful·lerens endoèdrics. En aquesta tesis, el ventall de reaccions de funcionalització de ful·lerens utilitzant nanocàpsules com a motlles s'ha ampliat significativament i, a més, un nou metal·lo-ful·lerè amb àtoms de terbi en el seu interior s'ha encapsulat selectivament utilitzant el mateix tipus de nanocàpsules.

Al Capítol IV, s'ha dut a terme la bis-funcionalització del ful·lerè $C_{60}$ de manera controlada a través de la reacció de Diels-Alder utilitzant motlles supramoleculars. A més a més, la seva regioselectivitat s'ha pogut regular ortogonalment gràcies a les diferents interaccions entre els corresponents mono-adductes amb les nanocàpsules.

Al Capítol V, s'han sintetitzat bis-adductes derivats del $PC_{61}BM$ utilitzant la mateixa estratègia que el capítol anterior. D'aquesta manera, el rendiment relatiu dels bis-adductes equatorials s'ha incrementat del 26 al 57% en comparació amb la síntesi clàssica de bis-adductes. També, s'han obtingut nous heteroadductes combinant el $PC_{61}BM$ amb la reacció de Bingel i de Prato.

Al Capítol VI, s'ha explorat la síntesi d'una llançadora molecular basada en un [2]catenà format per dos ful·lerens com a punts de reconeixement per un anell [10]CPP. Per a la seva síntesi, primer s'han format els bis-adductes isomèricament purs amb grups funcionals terminals reactius a través de la reacció de Bingel. Després, s'han utilitzat diferents reaccions per tancar el macrocicle, com ara la metàtesis d'olefines, la cicloaddició azida-alquí catalitzada per coure(I) o la reacció de Bingel-Hirsch.

Finalment, al Capítol VII, l'anió $Tb_2@C_{80}^-$ s'ha capturat selectivament per les mateixes nanocàpsules, provinent d'un extracte de ful·lerens que contenia una barreja de espècies aniòniques, entre les quals també hi havia $Tb@C_{80}^-$, $Tb@C_{82}^-$ i $Tb_2@C_{78}^-$.

# RESUMEN

Los fulerenos y metalo-fullerenos endoédricos han captado la atención de la comunidad científica desde su descubrimiento gracias a sus propiedades electrónicas y fisicoquímicas excepcionales. Los fullerenos y mono-aductos se pueden aplicar en diferentes campos de la química, como en ciencia de los materiales, en conversión de la energía solar o en aplicaciones biomédicas. Sin embargo, el uso extensivo de los fullerenos como poli-aductos está obstaculizado por la falta de control de la regioselectividad durante la funcionalización de los fullerenos y por el alto coste de la purificación de los poli-aductos y de los metalo-fullerenos endoédricos. Las nanocápsulas autoensambladas dirigidas por enlaces metal-ligando se han utilizado como plantillas supramoleculares para funcionalizar fullerenos de manera itero-, quimio- y regioselectiva y, además, se han utilizado como plataformas para encapsular selectivamente metalo-fullerenos. En esta tesis, el rango de reacciones de funcionalización de fullerenos utilizando las nanocápsulas como plantillas se ha ampliado significativamente y, además, un nuevo metalo-fullereno con átomos de terbio en su interior se ha encapsulado selectivamente utilizando las mismas nanocápsulas.

En el Capítulo IV, se ha llevado a cabo la bis-funcionalización controlada del fullereno $C_{60}$ a través de la reacción de Diels-Alder con plantillas supramoleculares. Además, se ha podido regular ortogonalmente su regioselectividad gracias a las diferentes interacciones entre los correspondientes mono-aductos con las nanocápsulas.

En el Capítulo V, se han sintetizado bis-aductos derivados del $PC_{61}BM$ utilizando la misma estrategia que en el capítulo anterior. De esta forma, el rendimiento relativo de los bis-aductos ecuatoriales se ha incrementado del 26 al 57%, en comparación con la síntesis clásica. También, se han obtenido nuevos aductos combinando el $PC_{61}BM$ con la reacción de Bingel y Prato.

En el Capítulo VI, se ha explorado la síntesis de una lanzadera molecular basada en un [2]catenano formado por dos fullerenos como puntos de reconocimiento para un anillo [10]CPP. Para su síntesis, primero se han formado bis-aductos isoméricamente puros con grupos funcionales terminales a través de la reacción de Bingel. Después, se han utilizado diferentes reacciones para cerrar el macrociclo, como la metátesis de olefinas, la cicloadición azida-alquino catalizada por cobre(I) o la reacción de Bingel-Hirsch.

Finalmente, en el Capítulo VII, el anión $Tb_2@C_{80}^-$ se ha capturado selectivamente por las mismas nanocápsulas, proveniente de un extracto de fulerenos que contenía una mezcla de $Tb@C_{80}^-$, $Tb@C_{82}^-$, $Tb_2@C_{78}^-$ y $Tb_2@C_{80}^-$.

# CHAPTER I. GENERAL INTRODUCTION

## I.1 Supramolecular chemistry

“Chemistry beyond the molecule”: this is one of the first definitions of supramolecular chemistry described by the Nobel laureate Jean-Marie Lehn in 1987. This relatively young area of chemistry is based on molecular entities whose chemical units are held together by weak and reversible interactions, as opposed to conventional molecular chemistry, which focuses its attention on covalent bonds.[1]

The non-covalent interactions that construct supramolecular architectures are hydrogen bonds, electrostatic interactions, van der Waals forces, and π-π and cation-π interactions. Also, metal-ligand coordination is used to drive the assembly of building blocks (more details in *I.1.1 Self-assembly chemistry*). Although all these interactions are weak when compared to covalent bonds, when they occur in a cooperative manner, very stable supramolecular architectures can be formed.[2]

There are two main groups in which supramolecular chemistry can be divided: self-assembly and host-guest chemistry.

### *I.1.1 Self-assembly chemistry*

Self-assembly focuses on the association of two or more molecules through reversible interactions to form larger structures. The advantage of using these labile interactions is the ability to correct mistakes during the synthesis of these supramolecules and to finally form the most thermodynamically stable product, overcoming the need of multistep, time-consuming synthetic procedures of the covalent approach. A relevant example of self-assembly that can be found in nature is the formation of the DNA double helix.[3]

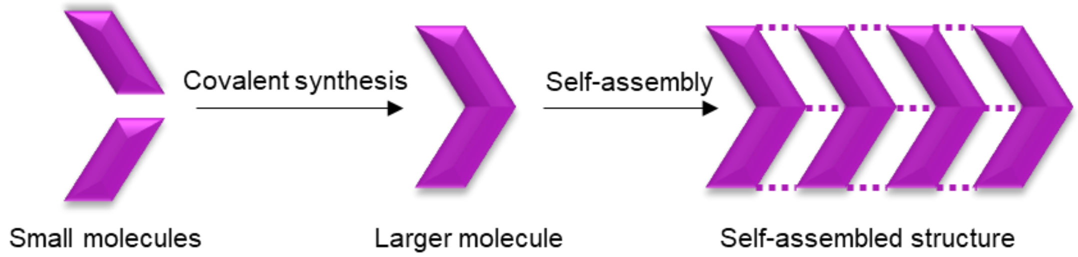

*Figure I.1. Schematic representation of the self-assembly process among different building blocks.*

Although self-assembly is a good tool to generate bigger molecules than using the covalent approach, when the complexity of target supramolecules increases, a lack of directionality of the small molecules appears turning into low yields. Metal-directed coordination is a very useful tool to drive the supramolecular synthesis towards a precise architecture. It presents the following advantages:

- High directionality of the metal-ligand coordinative bonds leading to many predictable coordination geometries.

- Great versatility due to diverse transition-metal complexes (and predictable geometries) and to a broad spectrum of available multidentate ligands.

- Fine-tuning of the kinetic lability of the complexes to different self-assembly conditions.

- Control of the polarity and charge state of the resulting objects via the formation of charged or neutral complexes.[2]

Most of the ligands used for self-assembled architectures remain highly symmetrical to facilitate the self-assembly process and avoid the formation of mixtures of products. If the assembly of unsymmetric ligands can be controlled, lower symmetrical architectures can be accessible, displaying different selective molecular recognition or different catalytic properties.[4]

### I.1.2 Host-guest chemistry

Host-guest chemistry is based on, at least, two molecular structures which interact through non-covalent bonds and one is larger than the other (host), so it can accommodate the smaller one (guest) in its cavity.

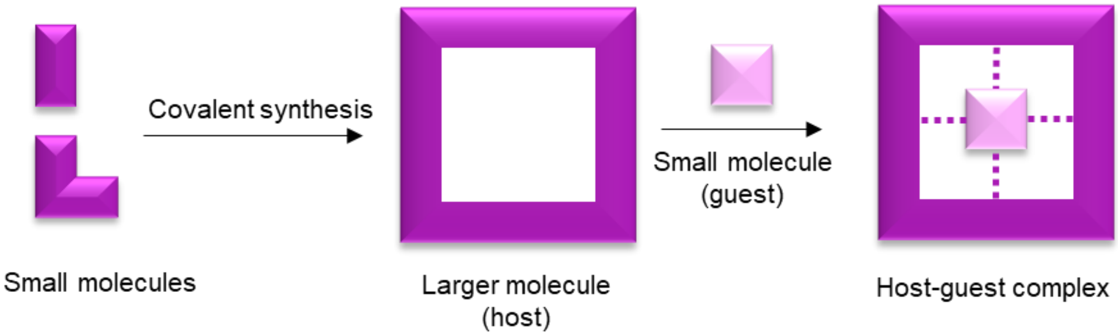

*Figure I.2. Schematic representation of the synthesis of a host molecule and the subsequent encapsulation of a smaller molecule (guest).*

Template-directed or guest-induced synthesis is a method that is often used to synthetize supramolecular architectures in order to pre-organize the building blocks of the host in a certain relative geometry around the guest, giving rise to higher yields or even modifying the selectivity of the outcome structures. [5–7]

### *I.1.3 Self-assembled nanocapsules and applications*

When building blocks has complementary size and shape and reaction conditions are optimal, supramolecular structures can be generated via self-assembly and they are classified according to their dimensionality[8] (Figure I.3):

- Zero-dimensional (0D): include well-defined discrete metal-organic self-assembled molecules (see examples below), dendrimers[9] and metal nanoparticles.[10]
- One-dimensional (1D): fibrous and tubular assemblies[11,12] as well as linear polymers.[13]
- Two-dimensional (2D): nanoscopic sheets.[14,15]
- Three-dimensional (3D): metal-organic frameworks (MOFs).[16]

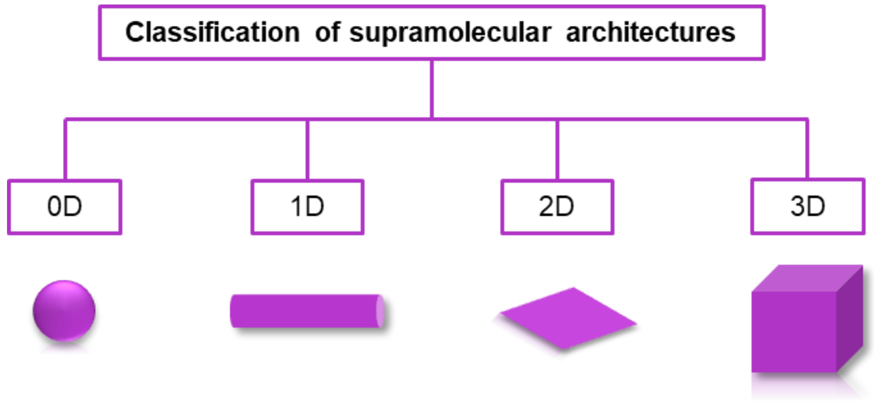

*Figure I.3. Classification of supramolecular architectures according to their dimensionality.*

Nevertheless, well-defined discrete molecules can be divided into two subgroups: 2D metallacycles (triangles,[17] rhomboids,[18] squares,[19] rectangles[20] and higher polygons[21,22]) that adopt planar geometries, and nanocapsules, 3D molecular architectures that feature inner cavities which are ideal to host and stabilize small molecules. One of the pioneers in this field is Prof. Makoto Fujita, whose research group reported in 1995 one of the first guest-induced self-assembled nanocages: a spherical-like nanocapsule formed by two tridentate ligands coordinated by $Pd^{II}$ atoms.[23] A few years after, a new series of spherical-like giant $M_nL_{2n}$ metal-organic self-assembled nanocages was introduced by the same group using ligands with different bend angles, achieving an outer diameter up to 8.2 nm for $M_{30}L_{60}$ compound (Figure I.4).[24–27]

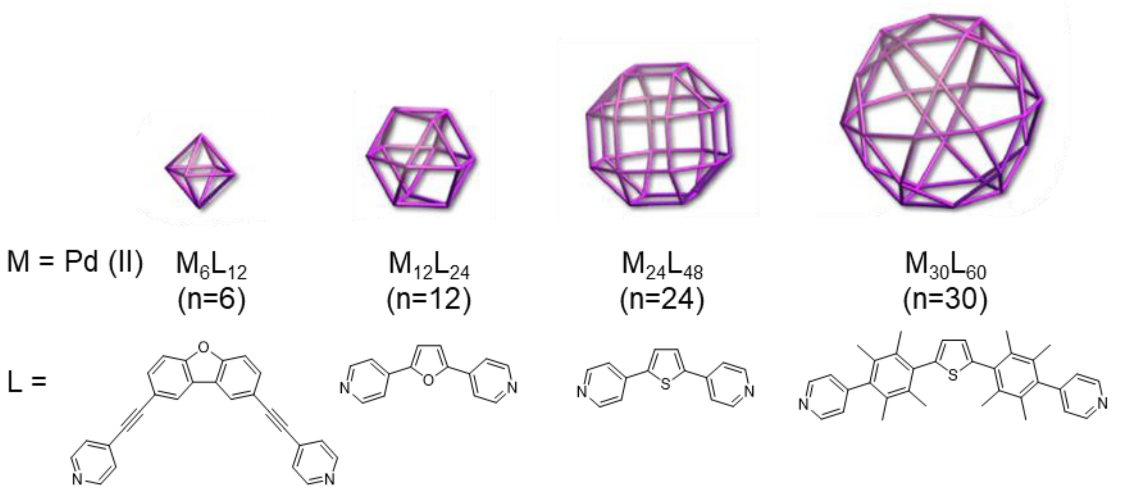

*Figure I.4. The family of $M_nL_{2n}$ polyhedra by Fujita's work. Metals (M) and bridging ligands (L) are mapped onto the vertices and edges of the polyhedral, respectively. Reprinted with permission from Fujita et al.*[27] *Copyright © 2010, The American Association for the Advancement of Science.*

Since their discovery, self-assembled nanocapsules have caught the attention of the scientific community. The increase of structural and functional complexity of self-assembled nanocapsules has led to the development of a wide range of different applications, such as reactivity modulation, molecular separation, catalysis, biological applications or gas storage.

Reactivity modulation using self-assembled nanocages has gained importance during the last years. Thanks to the well-defined voids with specific sizes and shapes, nanocapsules can be used as templates or masks to increase the efficiency or/and selectivity of a wide range of reactions when compared to the same non-templated reactions. Inspired by enzyme's cavities, Takezawa, Fujita and coworkers reported a siteselective electrophilic addition of linear diterpenoids, which were folded into a U-shaped conformation within the cavity of a $Pd^{II}$ metal-organic self-assembled nanocapsule (Figure I.5).[28] Following this trend, Ribas' group reported the synthesis of a $Pd^{II}$ prismatic tetragonal cage which was used as a supramolecular shadow mask to functionalize fullerenes $C_{60}$ in a regioselective manner (Figure I.7, more details in *I.2.2.2 Supramolecular receptors as functionalization platforms for fullerenes*).[29]

Self-assembled metallocages have been also explored as a tool to extract target molecules by selective encapsulation from mixtures of different compounds. Nitschke and coworkers reported the selective anion extraction of $ReO_4^-$ anion in the presence of 10 other common anions ($F^-$, $Cl^-$, $BF_4^-$…) in water using a $Fe^{II}$ tetrahedral cage (Figure I.6). Moreover, the extracted guest could be released by adding a solvent in which the cage disassembles. Also, the nanocapsule could be reused by adding a proper solvent in which the cage is stable.[30] Other examples of selective encapsulation involving larger targets are reported by Ribas' group, who used their aforementioned $Pd^{II}$ nanocapsule type to extract selectively fullerene $C_{84}$ from a mixture of fullerenes, allowing the enrichment of the $C_{84}$ content from 0.7% to 86% (Figure I.7).[31] By changing the metal from $Pd^{II}$ to $Cu^{II}$, a new tetragonal prismatic cage was described by the same group which could selectively encapsulate and extract different scandium- and uranium-based endohedral metallofullerenes (EMFs) following similar protocols (more details in *I.3.2 Molecular recognition of EMFs using supramolecular platforms*).[32–34]

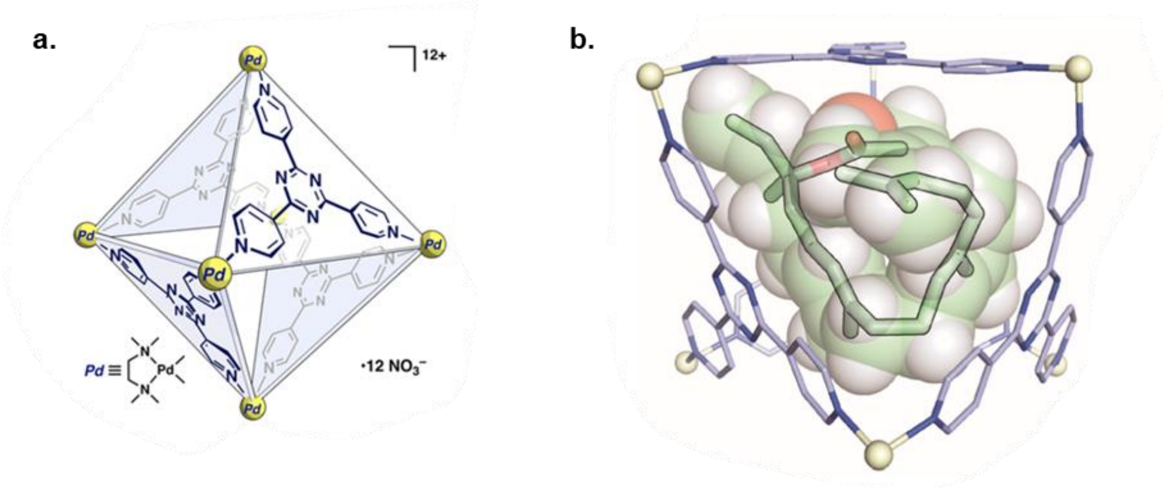

*Figure I.5. a) Metal-organic self-assembled cage from Takezawa's and Fujita's work. b) Inclusion of a linear terpenoid folded into U-shaped conformation within the cavity of the cage. Reprinted with permission from Takezawa, Fujita et al.*[28] *Copyright © 2019 American Chemical Society.*

Self-assembled nanocapsules can be used also as supramolecular nanoreactors for catalysis when catalysts are introduced in their cavities. Therefore, nanocapsules can be considered as a second coordination sphere upon catalyst inclusion within their cavities, modifying and improving the enantioselective levels via steric control. Asymmetric hydroformylation (Figure I.7)[35] or aza-Cope rearrengements[36] have been performed using catalysts confined in nanocapsules, obtaining excellent enantioselectivities when compared with the non-hosted catalyst.

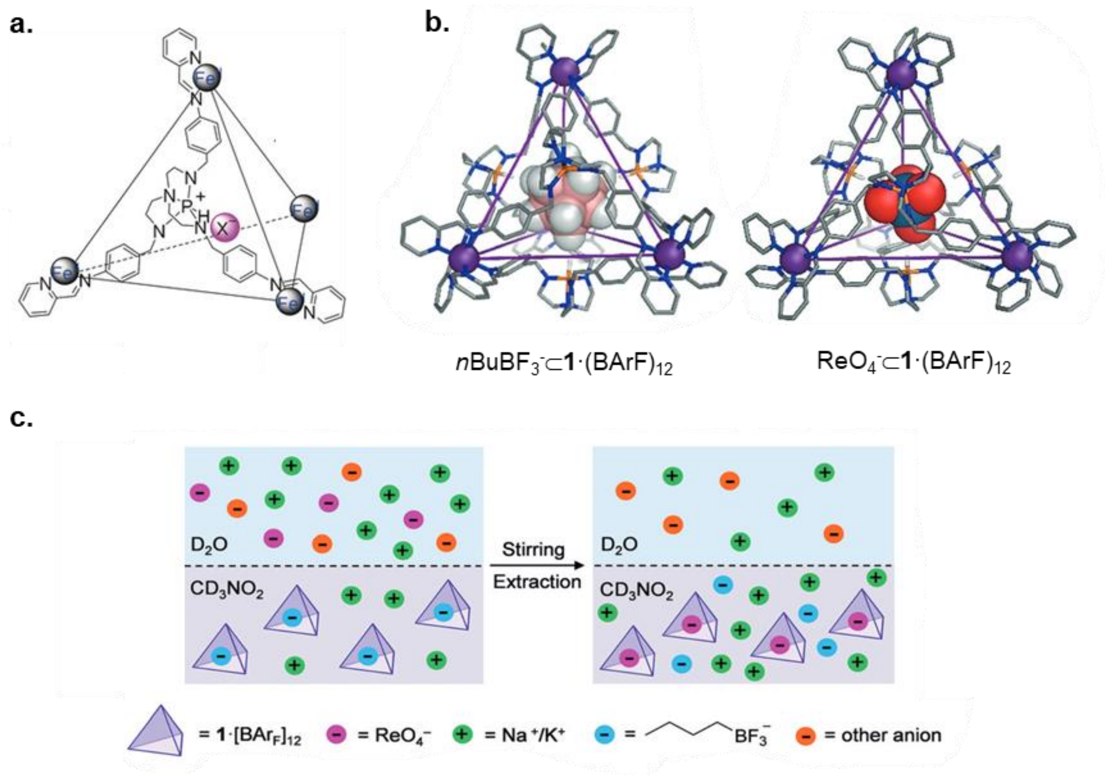

*Figure I.6. a) Metal-organic self-assembled cage from Nitschke's work. b) Inclusion of nBuBF$_3^-$ and ReO$_4^-$ anions within the cavity of the cage. c) Schematic representation of the liquid-liquid selective extraction of ReO$_4^-$ in the presence of other anions. Reprinted with permission from Nitschke et al.*[30] *Copyright © 2018. Published by Wiley-VCH Verlag GmbH & Co. KGaA.*

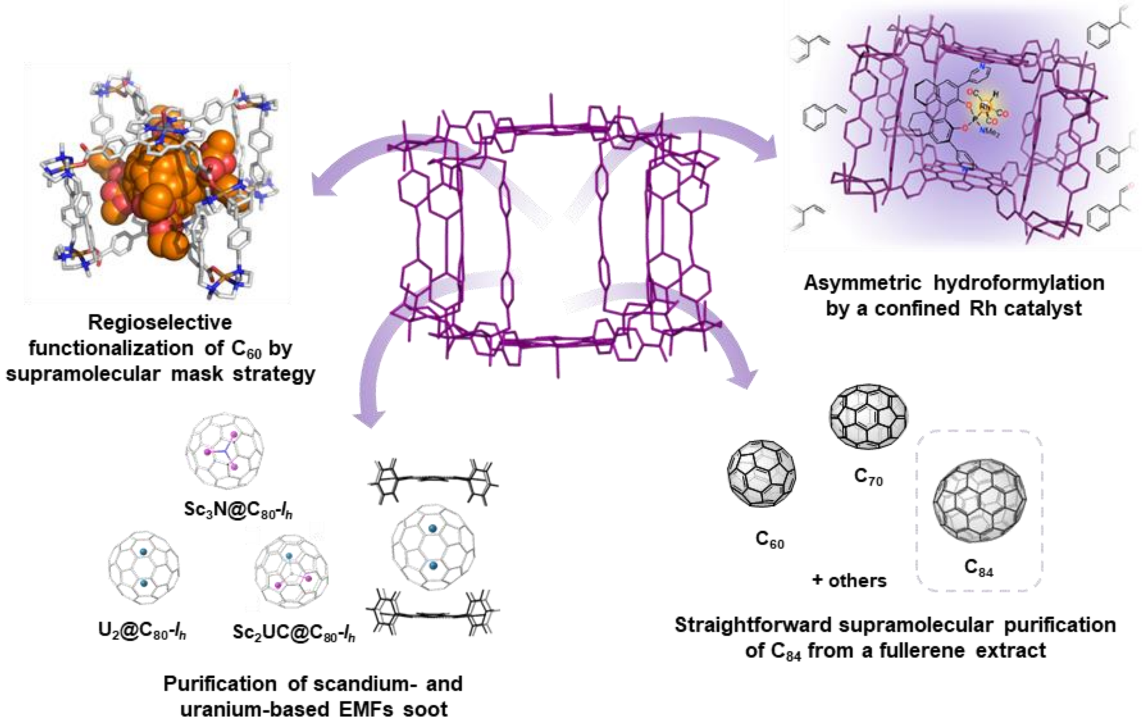

*Figure I.7. Schematic representation of different applications of self-assembled prismatic tetragonal nanocapsules from Ribas' work.*

Regarding to biological applications, self-assembled cages have been used as anticancer agents,[37] drug delivery systems[38] or diagnostic imaging.[39] If the nanocapsule is large enough, proteins can be introduced in their cavities, such as the example of Fujita's group, who described a cuboctahedro-symmetrical cage large enough to host a single-molecule protein (a cutinase-like enzyme formed by 206 amino acids) as depicted in Figure I.8. They demonstrated that the encapsulation of the protein prolonged 1000-fold its half-life when exposed to an organic solvent.[40]

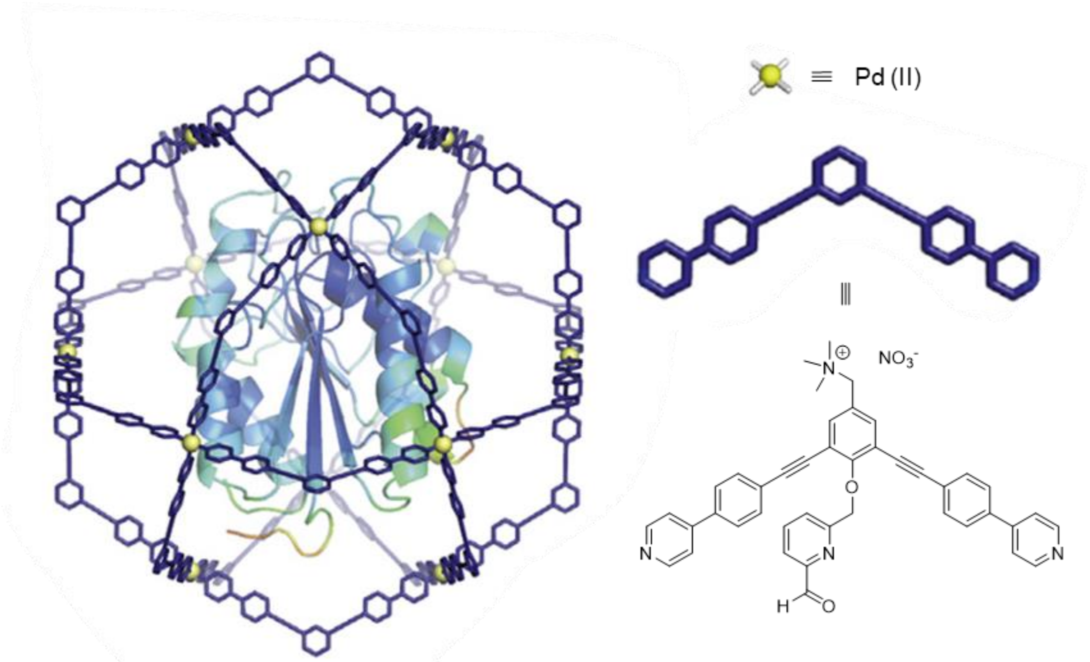

*Figure I.8. Metal-organic self-assembled nanocage hosting a cutinase-like enzyme in its cavity from Fujita's work. Reprinted with permission from D. Fujita, M. Fujita et al.*[40] *Copyright © 2021 Elsevier Inc.*

Finally, there are a few examples of metal-organic self-assembled nanocapsules which are used to storage gas, since they are porous materials.[41–43]

### *I.1.3.1 Molecular Russian dolls*

During the last two decades, new supramolecular complexes comprising a guest inside a host and, at the same time, inside a larger host (*i.e.* 1:1:1 ternary complex) have been reported. However, the investigation in this field is rather scarce. One of the first examples of these "molecular Russian dolls" or "Matryoshka-like complexes" was reported by Kim and coworkers in 2001, who explored the inclusion of a macrocycle wrapping a five-coordinate $Cu^{II}$ center in the cavity of a cucurbit[8]uril (Figure I.9).[44]

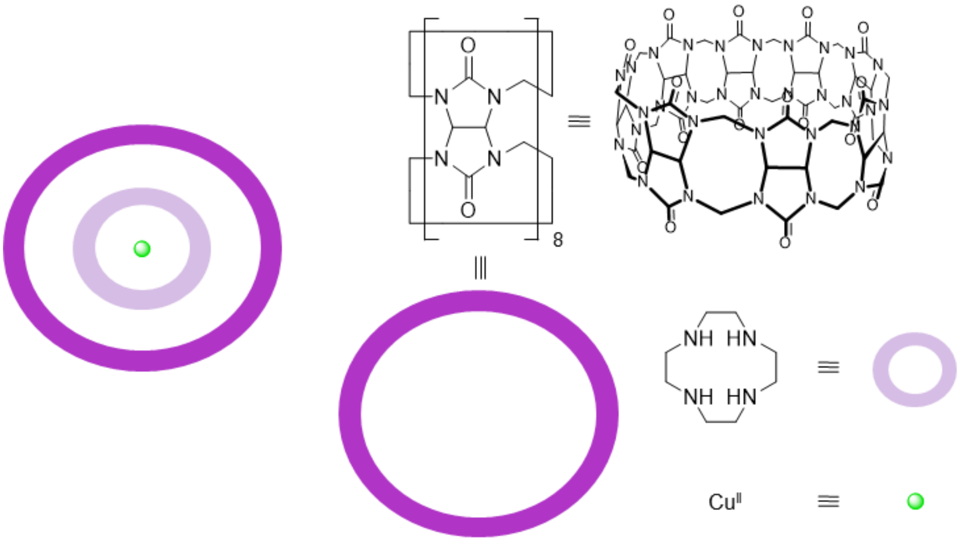

*Figure I.9. Schematic representation of a 1:1:1 ternary complex from Kim's work.*

There are examples of 1:1:1 ternary complexes involving metal-directed self-assembled nanocapsules. As an illustration, Nitschke's group reported the synthesis of a triazatruxene-based $Fe^{II}_4L_4$ nanocapsule which is able to encapsulate a molecule of cryptophane-111 (CRY) in an enantioselective manner. At the same time, CRY can accommodate a caesium cation in its cavity, as depicted in Figure I.10.[45]

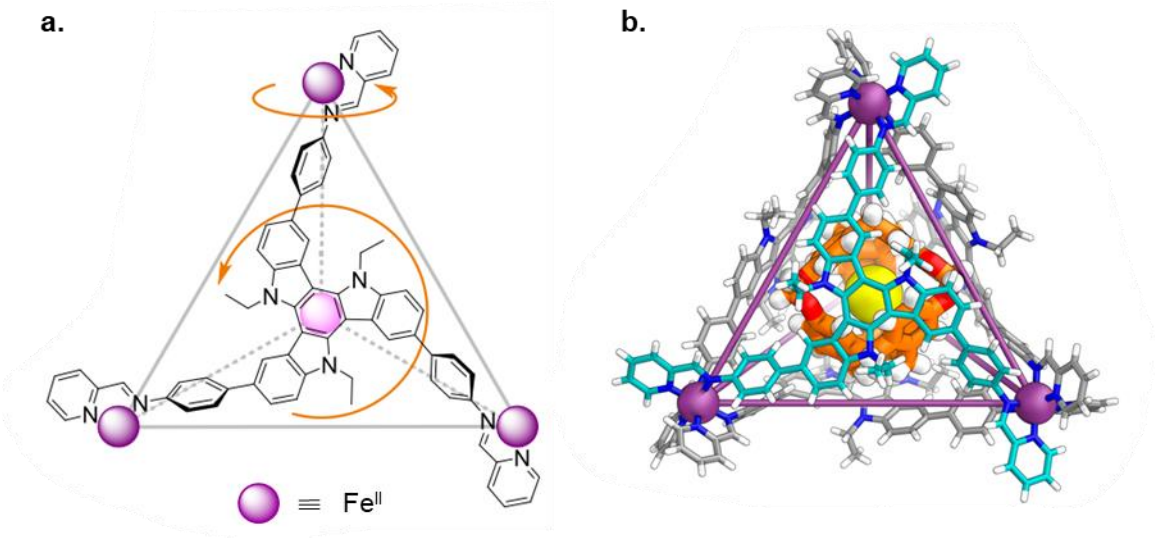

*Figure I.10. Molecular representation of metal-organic self-assembled nanocage from Nitschke's work. Only ΔΔΔΔ enantiomer is shown for clarity. b) Crystal structure of $Cs^+ \subset CRY \subset ΔΔΔΔ$-cage. Reprinted with permission from Nitschke et al.[45] Copyright © 2019 American Chemical Society.*

Also, Delius, Ribas and coworkers described the synthesis of a $Pd^{II}$ prismatic tetragonal complex that can accommodate in its cavity a wrapped fullerene $C_{60}$ by a [10]cycloparaphenylene ([10]CPP), as shown in Figure I.11, which enables the itero-, chemo- and regioselective bis-functionalization of $C_{60}$ through Bingel reaction (more details in *I.2.2.2 Supramolecular receptors as functionalization platforms for fullerenes*).[46]

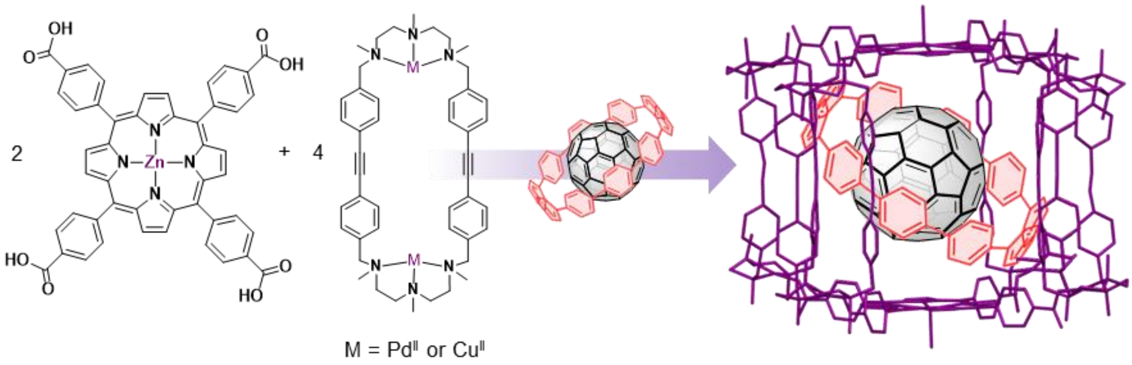

*Figure I.11. Schematic representation of the host-guest synthesis of 1:1:1 ternary complex from Ribas' work.*

## I.2 Fullerenes

Fullerenes are hollow, spheroidal molecules formed by polycyclic systems of 5- and 6-membered rings of $sp^2$ carbons bonded by single and double bonds. Fullerenes were discovered by Kroto, Smalley and Curl in 1985,[47] who reported their production in multiple gram scale. This discovery led them to win the Nobel Prize in 1996.[48]

Fullerenes are formed when vaporised carbon condenses in an atmosphere of inert gas using a plasma induced by an electric arc discharge between metal-oxide/graphite electrodes at extremely high temperatures (>1000ºC). The released carbon atoms are mixed with a stream of helium gas to form clusters of atoms that forms the final fullerene soot.[49]

Fullerenes are denoted by the empirical formula $C_n$, where $n$ is the number of carbon atoms. Fullerenes with the same number of carbon atoms can adopt more than one geometry *(i.e.* each fullerene can present more than one isomer). The most abundant and stable one is the $C_{60}$-$I_h$, also called "buckminsterfullerene", whose carbon atoms are arranged in 20 hexagons and 12 pentagons with a geometry of a truncated icosahedron ($I_h$) cage.[47] The stability of these carbon cages is dictated by the "isolated pentagon rule" (IPR), which states that the most stable fullerenes are those in which each pentagon is surrounded exclusively by hexagons, since the local strain of a bond shared by two 5-membered carbon rings increases, giving rise to less stable carbon cages.[50,51] Nevertheless, some non-IPR fullerenes can be stabilized by endohedral encapsulation or exohedral functionalization.[52]

Larger fullerenes (higher fullerenes) have also been isolated and characterized with different geometries and shapes ($C_{74}$-$D_{3h}$, $C_{78}$-$D_{3h}$, $C_{82}$-$C_{3v}$, $C_{84}$-$D_2$, $C_{88}$-$C_2$, $C_{90}$-$C_{5h}$, $C_{100}$-$D_{5d}$...).[53] Also, even-numbered fullerenes up to $C_{600}$ and even larger fullerenes have been reported in the early stage of fullerene research, and it is now well established that the so-called giant fullerenes exist in great numbers and variety (Figure I.12).[54,55]

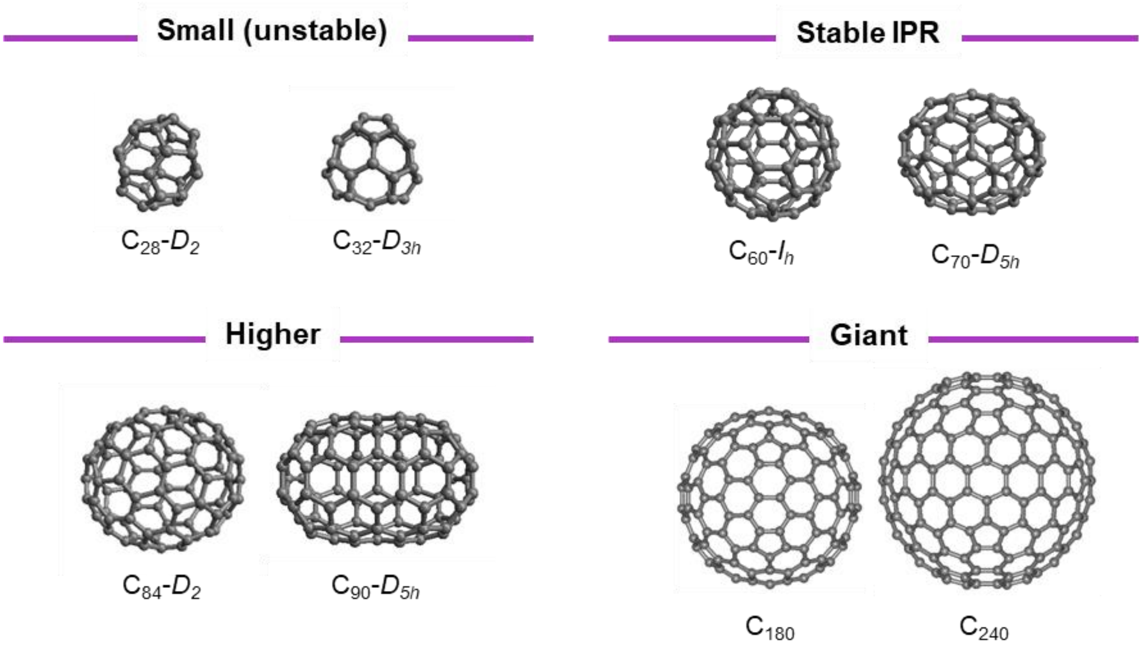

*Figure I.12. Examples of representative fullerenes from four different types (small, stable IPR, higher and giant fullerenes).*

Recently, in 2020, Xie, Stevenson and coworkers reported the isolation and characterization of fullertubes, a new allotropic form of the carbon which has a well-defined and reproducible structure resembling a fullerene-capped, small radius, single-wall carbon nanotube capsule (Figure I.13).[56] These carbon architectures range from $C_{90}$ to $C_{200}$ and, in contrast to nanotubes, they are soluble in organic solvents. The scarcity of fullertube research is attributed to their low abundance in arc-generated soot extract (0.001-0.005%) and the lack of an efficient separation method for fullertube purification. Xie, Stevenson and coworkers reported a chemical separation approach to obtain isomerically pure $C_{100}$-$D_{5d}$, $C_{96}$-$D_{3d}$ and $C_{90}$-$D_{5h}$ fullertubes in two stages: the first stage involves the reaction of primary amines with spheroidal fullerenes, which can be removed from the extract, and the second stage requires only one-step HPLC purification, which is rapid, cost-effective, facile and green.[56]

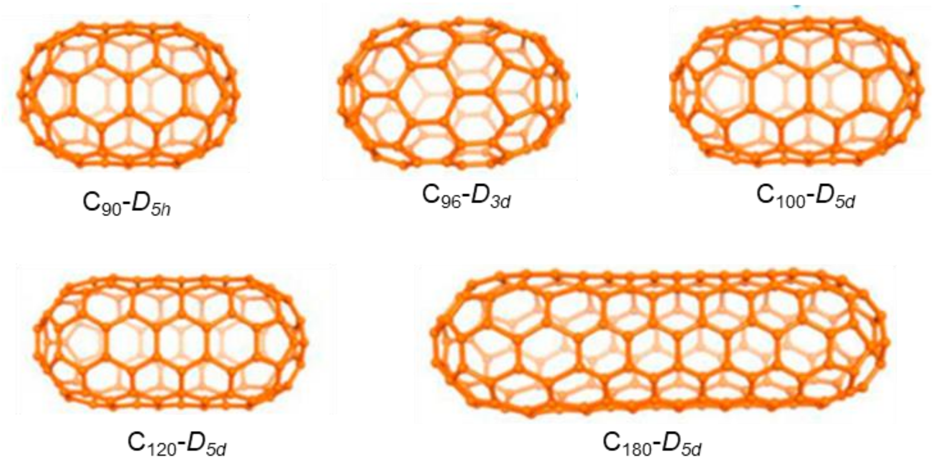

*Figure I.13. Examples of fullertubes. Reprinted with permission from Xie, Stevenson et al.[56] Copyright © 2019 American Chemical Society.*

### *I.2.1 Derivatization of fullerenes*

Although fullerenes can present good levels of stability and excellent electronic properties, they present some drawbacks, such as considerable solubility problems, limited tunability of electron affinities and weak absorption in the visible and near-infrared (NIR). Their functionalization has been developed from the early stages of their discovery in order to overcome these problems.

Despite the extreme conjugation of fullerenes and the presence of a delocalized π-system on their surface, they behave chemically and physically as an electron-deficient polyolefin rather than an electron rich aromatic system.[57] Therefore, fullerenes can be reduced up to six electrons.[58] This high affinity to electrons is due to their triply degenerate low-lying lowest unoccupied molecular orbitals (LUMOs).

X-ray diffraction analysis by Ibers and coworkers demonstrated that fullerene $C_{60}$ present two types of C-C bonds: [6,6] bonds (junction of two hexagons, C-C distance = 1.391 Å) and [5,6] bonds (junction of one pentagon and one hexagon, C-C distance = 1.449 Å).[59] Since [6,6] bonds are shorter, functionalization of fullerenes takes place at these bonds, as they have a formal double-bond character compared to [5,6] bonds.

In this context, a wide variety of functionalization reaction of fullerenes has been reported from the beginning of 1990s, such as halogenations, reactions with organometallic compounds, cycloadditions, nucleophilic additions, arylations… as can be seen in Figure I.14.[60]

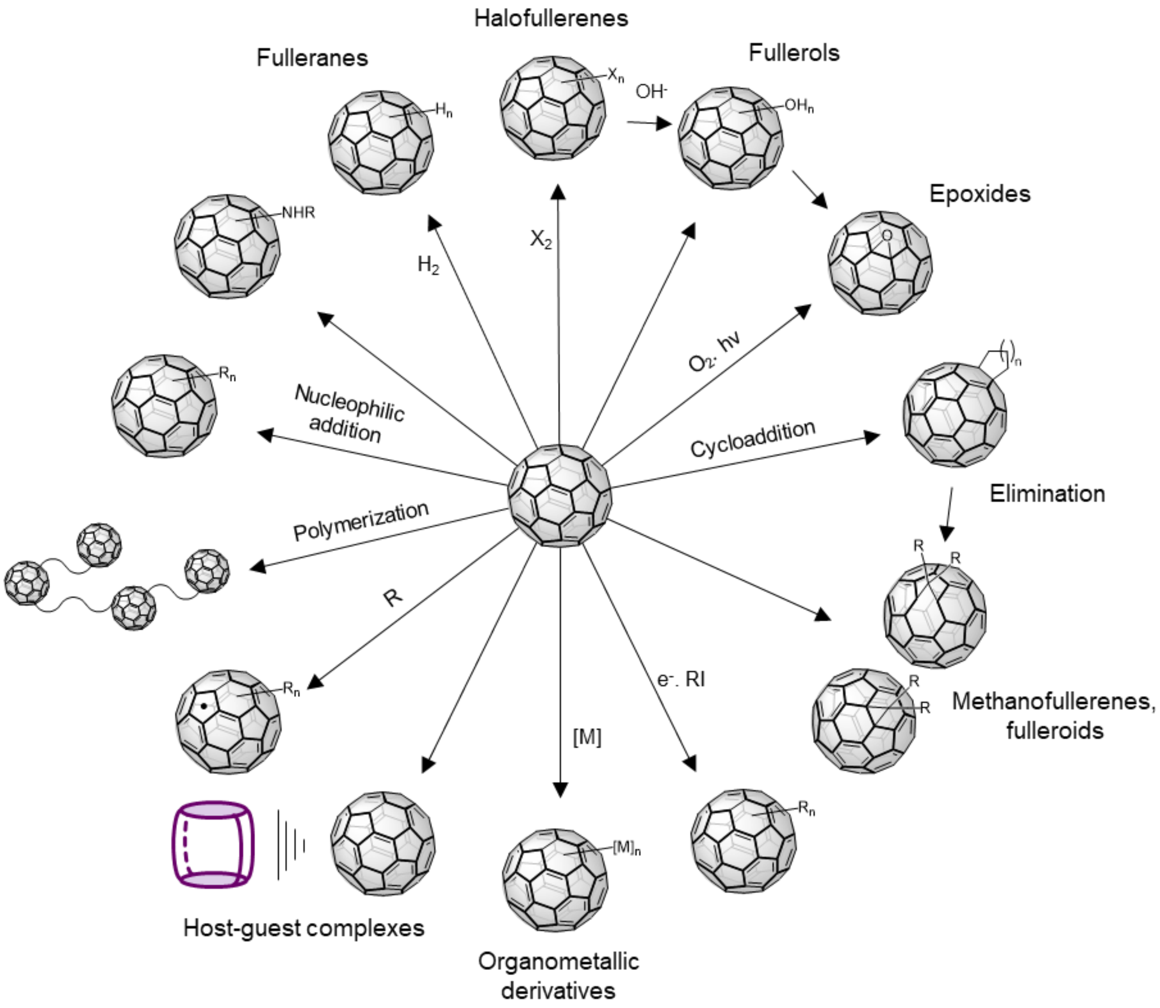

*Figure I.14. Schematic representation of functionalization reactions to derivatize fullerenes.*

These derivatives can be applied in all sorts of applications, from photovoltaic devices to photonic liquid crystals, owing to their electron acceptor properties. In addition, biomedical applications, such as antiviral and anticancer agents, have also been developed.

### *I.2.1.1 Photovoltaics applications*

Photovoltaics cells (or solar cells) are devices that are able to convert sunlight into electrical power. Fullerene-based solar cells have shown great power conversion efficiency (PCE) because of high electron mobility of fullerenes, their 3D character, and their ability to delocalize their LUMOs, which results in a robust charge delocalization. Nevertheless, as mentioned before, pristine fullerenes show a limited tunability of electron affinities and weak absorption in the visible and NIR, resulting in low PCEs values. Phenyl-$C_{61}$-butyric acid methyl ester ($PC_{61}BM$) was one of the first fullerene derivatives that could overcome all these drawbacks, and rapidly it was converted as one of the first reference values of PCE, since it was an easy-accessible and highly soluble mono-adduct.[61] However, a wide variety of fullerene derivatives have been tested in solar cells because of their excellent electronic transport properties and their easy integration into multilayers devices.[53]

In the case of perovskites solar cells (PrSC, solar cells that includes commonly a lead- or tin-halide material as the light-harvesting active layer, Figure I.15), a fullerene-based layer is used as electron transport layer (ETL) to enhance the charge separation promoted by the perovskite and thus avoid charge recombination. Poly-functionalization of fullerenes was demonstrated to improve their photoelectrical properties, since PrSC containing a isomer-pure bis-functionalized analogue of $PC_{61}BM$ (bis-$PC_{61}BM$) as ETL showed higher efficiencies (20.8%) compared to those using $PC_{61}BM$ (19.9%).[62] Interestingly, efficiencies of solar cells containing isomer-pure derivatives were much higher compared to those achieved by bulk heterojunction solar cells (solar cells which contain a blend made of electron donor and electron acceptor molecules as the light-harvesting active layer) made up with a non-purified mixture of different bis-adducts, giving poor PCEs around 2.5%.[63] These low efficiencies are attributed to morphological and energetic disorder in the active layer coming from the mixture of bis-adducts resulting in degrading effect of the device.

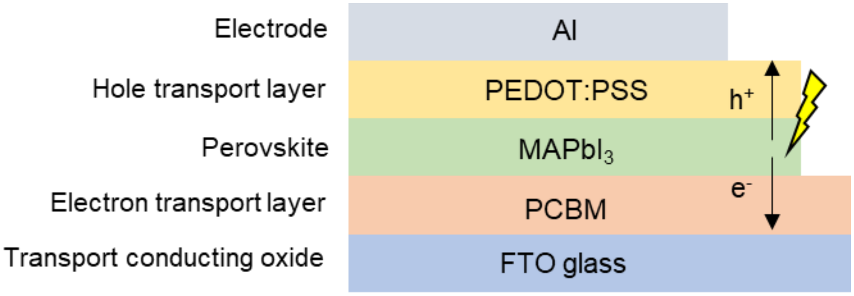

*Figure I.15. Schematic representation of a conventional (n-i-p) planar perovskite solar cell. Al: aluminium. PEDOT:PSS : poly(3,4-ethylenedioxythiophene)-poly(styrenesulfonate). $MAPbI_3$: methylammonium lead iodide. PCBM: phenyl-$C_{61}$-butyric acid methyl ester. FTO: fluorine-doped tin oxide*

### *I.2.1.2 Photonic liquid crystals*

Fullerene-based liquid crystals with highly ordered columnar assemblies of the fullerene units are interesting materials for organic electronics and, especially, photovoltaic applications if oriented at surfaces.[64] During fullerene poly-functionalization, control of the number of additions and their relative positions (*i.e.* itero- and regioselectivity, respectively)[65] is essential to govern the mesogenic orientations and directionalities and, thus, the supramolecular organizations into various mesophases to impact directly into the physical properties of the materials. For instance, several pure-isomer Prato bis-adducts condensed with liquid-crystal promoters were organized into a mono-layered smectic A phase (Figure I.16).[66] This example demonstrates that controlled and judicious poly-additions of mesogenic molecules is a method of choice to control the $C_{60}$ aggregation tendency.

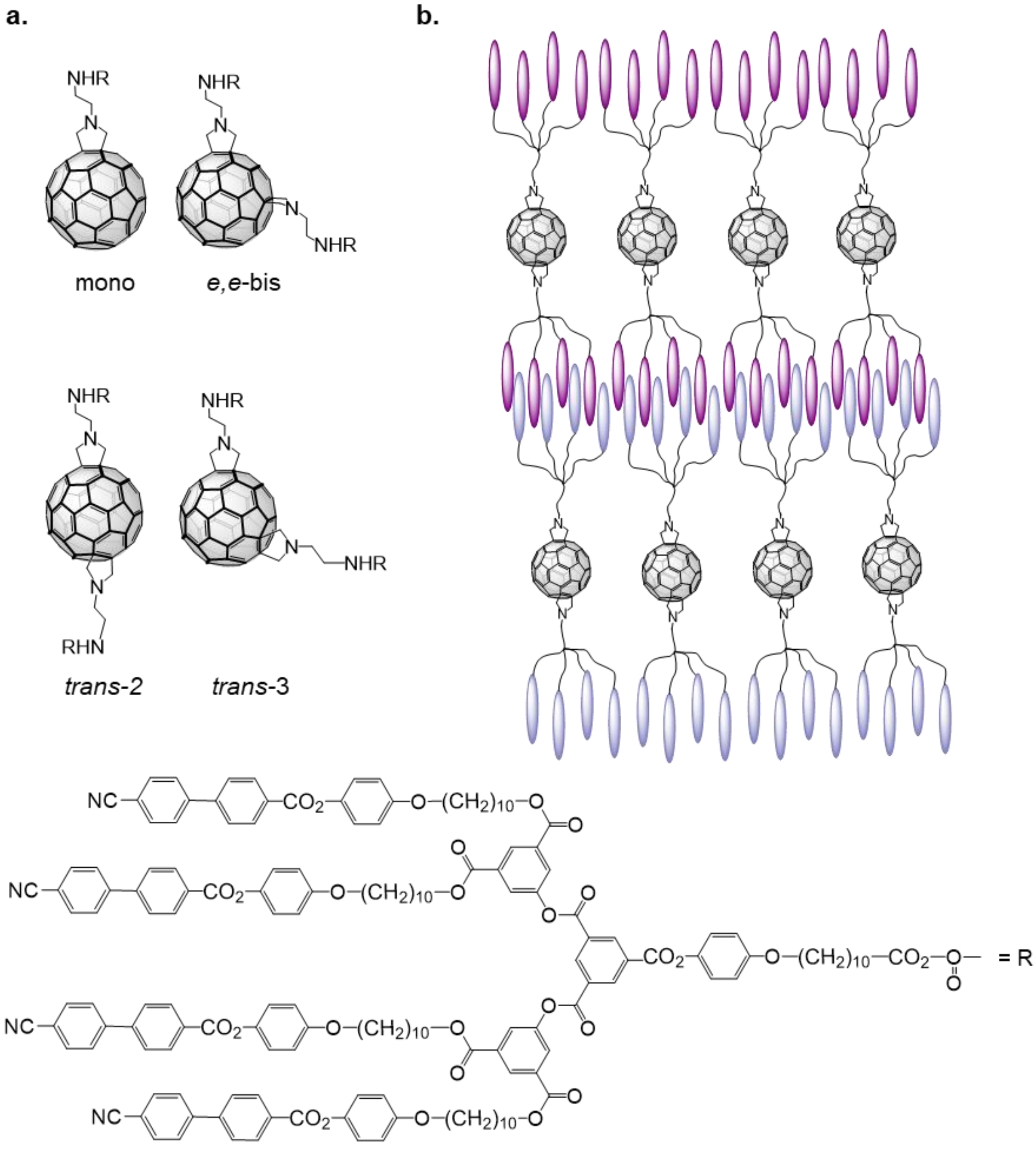

*Figure I.16. a) Molecular structures of fullerene-based liquid crystal from Prato's work. b) Supramolecular organization of bis-adducts within the smectic A phase.*

### *I.2.1.3 Nanoelectronics*

Organic thin-film transistors (TFTs) have attracted much attention because of their application to flexible electronic devices and high mobilities comparable or superior to amorphous silicon TFTs. Fullerene $C_{60}$ is a promising material for organic TFTs, since it is known as an excellent *n*-type semiconductor. Therefore, different devices using $C_{60}$ fullerene with bottom-contact geometry have been reported showing high mobilities of 1.4 – 6.0 $cm^2/(V \cdot s)$.[67–69]

Fullerenes have been also used in the sensor area thanks to their excellent electrical conductivity, charge transport properties and charge separation. They have been used to prepare strain sensors,[70,71] gas sensors,[72,73] and electrochemical sensors for the detection of dopamine, glucose, amino acids, uric acid, $H_2O_2$ and other biomolecules.[74]

### *I.2.1.4 Biomedical applications*

The antiviral activity of fullerenes and their derivatives is based on their steric and electronic interactions and their antioxidant activity. First studies reported in 1993 by Friedman[75] and Sijbesma[76] demonstrated experimentally and theoretically that fullerene derivatives made molecular complexes with human immunodeficiency virus (HIV) proteases, showing a clear effect of virus inhibition. Also, bis-adducts bearing two ammonium groups have been found active against HIV by Da Ros and coworkers.[77] Interestingly, *trans* regioisomers showed a better inhibition effect than *cis* and equatorial ones, demonstrating again the importance of the relative positions of the substituents on the fullerene cage.

Fullerenes can also exhibit anticancer activity since they can be photoexcited by photoirradiation and can transfer their energy from the ground state $^3O_2$ producing the excited state $^1O_2$ (singlet oxygen). During this process, superoxide anion radical $O_2^{-\cdot}$ and hydroxyl radical $HO^\cdot$ also are produced. These species are reactive oxygen species (ROS) which produce oxidative stress, leading to cell death by apoptosis.[78] Therefore, fullerenes are perfect candidates to be used as photosensitizers in photodynamic therapy (PDT). Troshin, Hsu and coworkers reported the synthesis of water-soluble penta-arylated derivatives that promoted neural stem cells (NSC) proliferation and neural repair regulating the mitochondrial activity, but they didn’t prevent from a proliferative effect on glioblastoma (compound 1, Figure I.17). Also, they synthesized penta-aminated derivatives that could kill glioblastoma cells by increasing the generation of ROS in mitochondria without producing a destructive effect on NSC (compound 2, Figure I.17).[79] Therefore, fullerene derivatives with different functional groups act on mitochondria like molecular switches that can either promote or suppress the generation of ROS to achieve neuroprotective or antitumor effects.

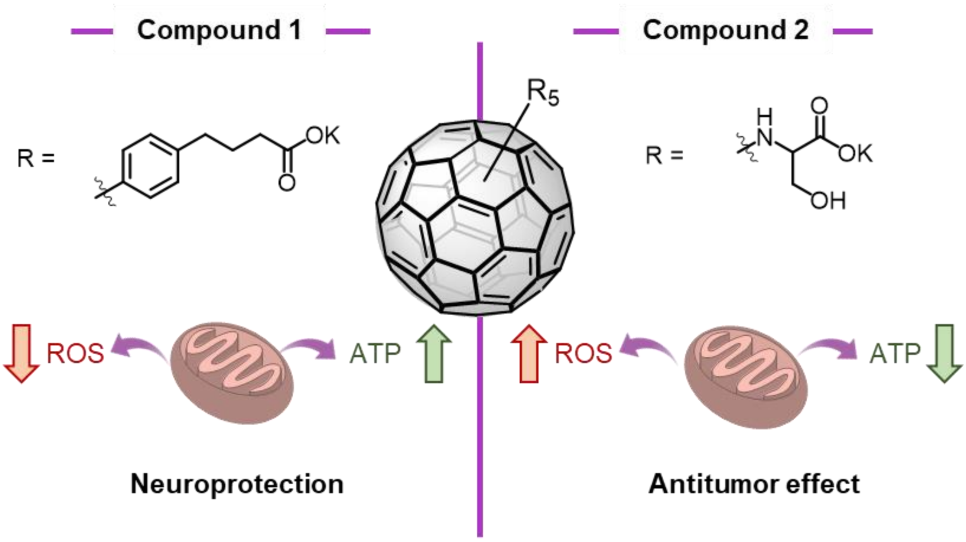

*Figure I.17. Molecular structures of the water-soluble fullerene derivatives and their respective functions on cells from Troshin's and Hsu's work.*

### *I.2.2 Strategies for fullerene regioselective functionalization*

As seen in the previous section, controlling the regioselectivity when fullerenes are poly-functionalized is essential to improve yields and efficiencies of different applications. Nevertheless, due to the high levels of symmetry of fullerenes and, therefore, the presence of multiple bonds with similar reactivity, their functionalization ends up with mixtures of several non-equivalent regioisomers and multiple carbon-based products.

Considering the example of the synthesis of bis-adducts, the addition of a second symmetric substituent to a mono-adduct leads to eight potential regioisomers as shown in Figure I.18 (ordered by increasing distance between substituents: *cis*-1, *cis*-2, *cis*-3, *e*, *trans*-4, *trans*-3, *trans*-2 and *trans*-1). If the substituents are non-symmetric, up to 22 spectroscopically distinguishable isomers can be formed (36 taking into account the respective enantiomers), although only 19 are accessible owing to steric hindrance from *cis*-1 regioisomers.[80,81] When these mixtures of multiple regioisomers are obtained, multistep high performance liquid chromatography (HPLC) separation is required. The chromatographic methods needed to separate these compounds are expensive, tedious and time-consuming and, in the end, they are not practicable. For this reason, there is a need to develop new strategies to poly-functionalize fullerenes in a controlled fashion, increasing the levels of itero-, chemo-, regio- and stereoselectivity and, consequently, decreasing the number of potential isomers.

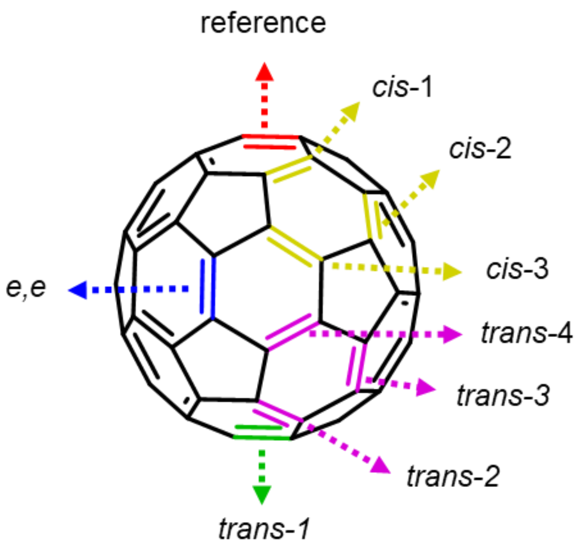

*Figure I.18. Diagram of the second addition to a $C_{2v}$-symmetrical $C_{60}$ mono-adduct (first addend is the reference).*

The strategies to synthetize multiple substituted fullerenes will be divided in two sections: “covalent strategies to poly-functionalize fullerenes” and “supramolecular receptors as functionalization platforms for fullerenes”.

### *I.2.2.1 Covalent strategies to poly-functionalize fullerenes*

One of the first strategies to poly-functionalize fullerenes regioselectively was the tether-directed functionalization approach pioneered by Diederich and coworkers in the 90s.[82,83] Poly-adducts of fullerene $C_{60}$ were prepared in a regioselective manner by tether-directed remote functionalization, achieving exclusively equatorial bis- and tris-adducts by Diels-Alder reaction (Figure I.19.a). Also, tether-directed regioselective functionalization was carried out using Bingel reaction with bis(malonates).[83] This excellent regioselective control is dictated by the length and nature of the tether, which directs the successive additions to specific [6,6] bonds. Nevertheless, the tether moiety is commonly not removable, which compromises the applicability of these derivatives.

Recently, Nierengarten and coworkers described the bis-functionalization of fullerenes in which removable tethers based on di-tert-butylsilylene and tetra-iso-propyldisiloxane subunits were used (Figure I.19.b).[84] By changing the length and rigidity of the spacers, the regioselectivity could be tuned successfully.

Another strategy known as “orthogonal transposition” was designed by Kräutler and coworkers, who presented the first example using removable anthracene addends (Figure I.19.c).[85] This protocol used first the anthracene-based *trans*-1-bis-adduct (synthesized previously through solid-state Diels-Alder reaction[86]) to direct the poly-cyclopropanation along all the equatorial belt of $C_{60}$ by Bingel reaction. Then, anthracene addends were easily removed by retro-Diels-Alder, achieving exclusively the cyclopropanated *e,e,e,e*-tetrakis-adduct.

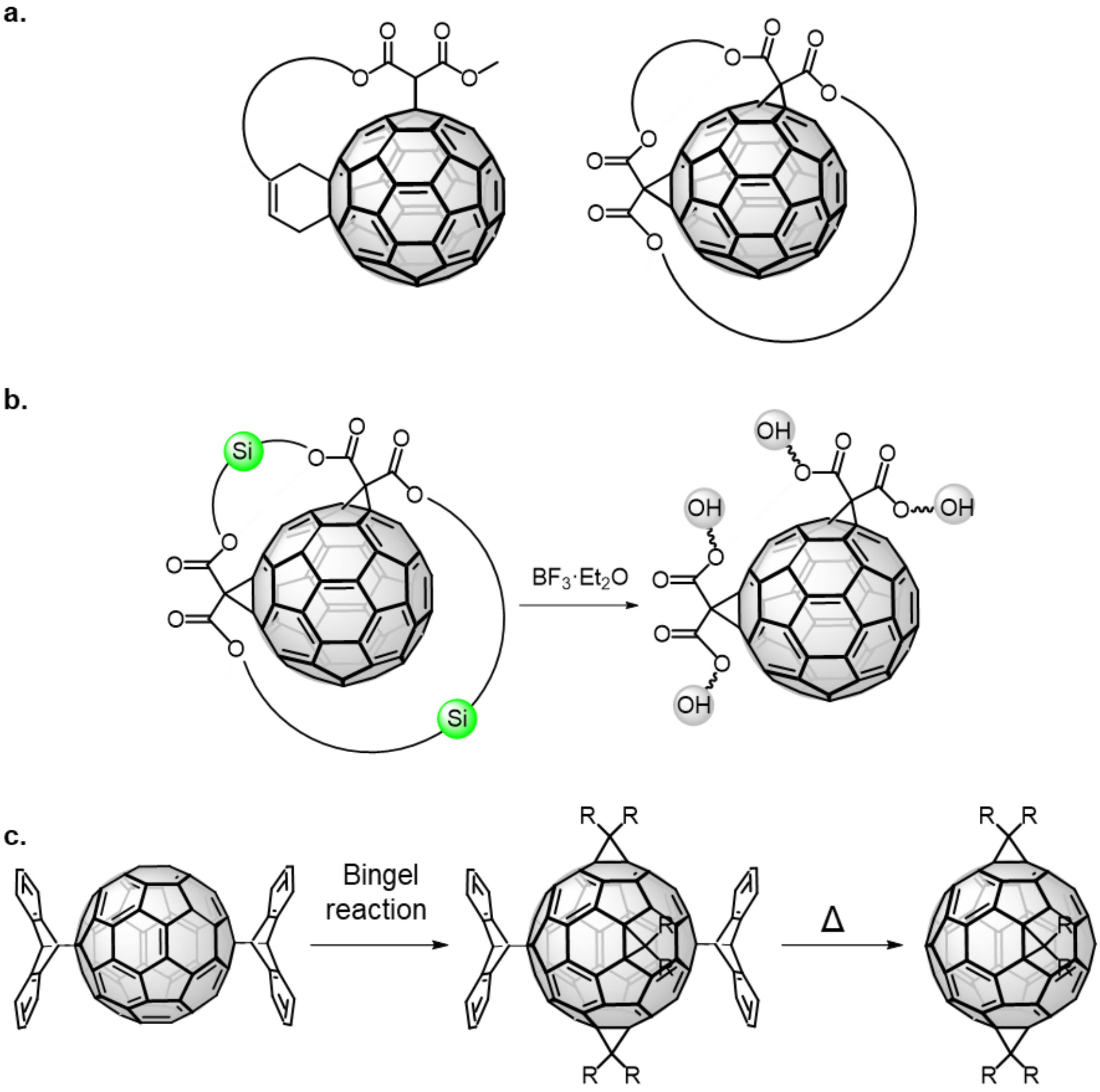

*Figure I.19. Covalent strategies to poly-functionalize fullerenes regioselectively. a) Tethered remote approach from Diederich's work. b) Cleaveable tethers strategy from Nierengarten's work. c) Removable orthogonal templates affording equatorial tetrakis-adducts from Kräutler's work.*

### *I.2.2.2 Supramolecular receptors as functionalization platforms for fullerenes*

One of the first host-guest examples involving fullerenes as guests was reported by Wennerström and co-workers in 1992 (Figure I.20).[87] They employed γ-cyclodextrin (γ-CD) to capture $C_{60}$ forming a 2:1 host-guest complex that was soluble in water. This fact states that solubility is inherited from the host since $C_{60}$ is only soluble in a few organic solvents, such as toluene or *o*-dichlorobenzene (*o*-DCB) while cyclodextrins are soluble in water. Cyclodextrins have a hydrophobic cavity that can hold small molecules thanks to its basket-like shape. Their shape and dimensions create a perfect environment to interact with fullerene $C_{60}$ that give rise to a highly stable host-guest complex. Since their discovery, many efforts have been employed to synthetize more sophisticated fullerene receptors with high binding constants in organic solvents based on extended aromatic panels, such as calixarenes (as the aforementioned example), bowls,[88] porphyrins[89] or carbon-nanohoops.[90]

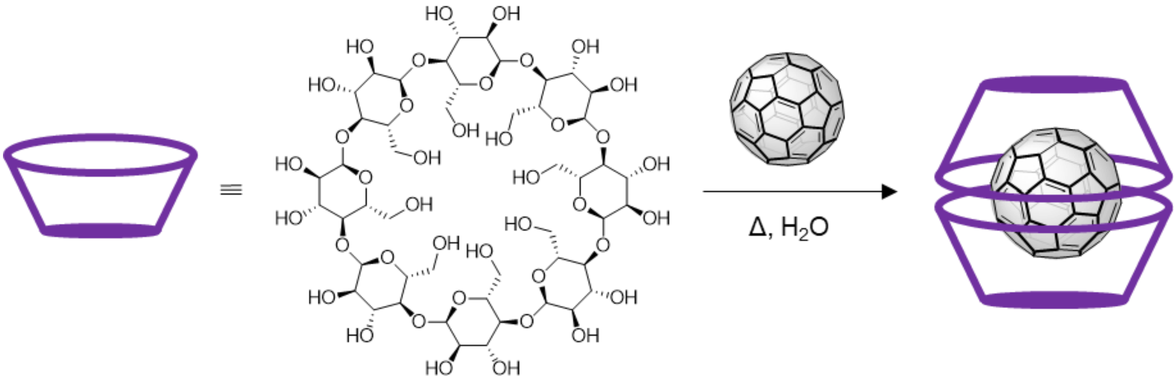

*Figure I.20. Synthesis of 2:1 γ-CD:$C_{60}$ host-guest complex from Wennerström's work.*

A few years after, examples of fullerene-containing hosts turned out to be excellent supramolecular platforms to functionalize fullerenes in a regioselective manner thanks to the partial restriction of the accessible guest surface coming from the steric hindrance of the host. Herein, a few examples of these supramolecular templates are shown.

Clever and coworkers designed a low-molecular-weight fullerene receptor, which was self-assembled using quinoline ligands and a source of palladium (II) (Figure I.21).[88] Owing to the steric demand from these bent ligands, the assembly led to a $[Pd_2L_3(MeCN)_2]^{4+}$ bowl-shaped supramolecular structure. This particular geometry avoided poly-functionalization of $C_{60}$ and allowed only its mono-functionalization by Diels-Alder reaction through the larger cavity window.

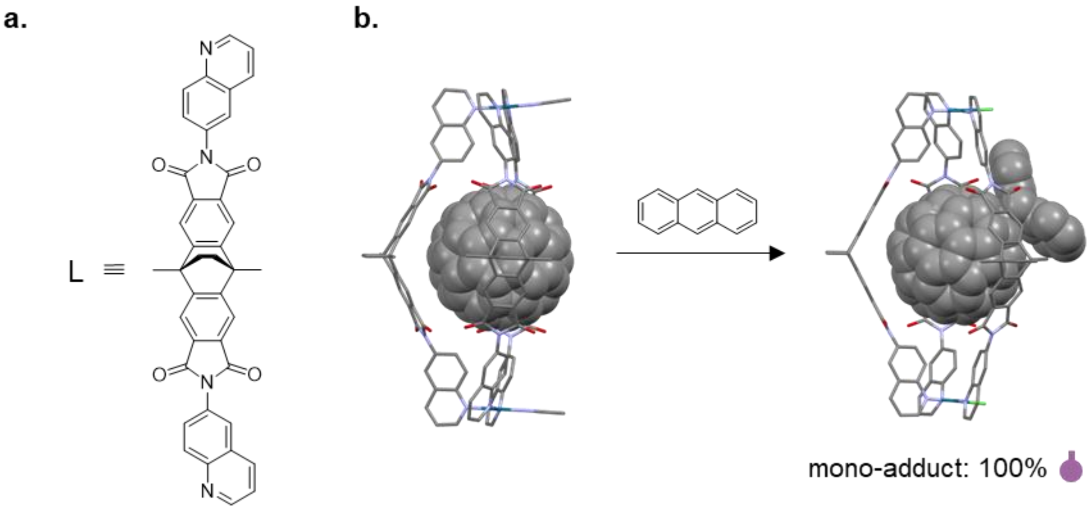

*Figure I.21. a) Quinoline-based ligand used for the synthesis of the metal-organic self-assembled nanocage from Clever's work. b) Mono-functionalization of fullerene $C_{60}$ through Diels-Alder reaction using the bowl-shaped nanocapsule as supramolecular template.*

Tomás Torres, Gema de la Torre and coworkers reported the synthesis of a water-soluble metallo-organic $Pd^{II}$-subphthalocyanine cage that accelerated the Diels-Alder reaction in water media using anthracene (and 9-functionalized anthracenes) and $C_{60}$/$C_{70}$ to give the corresponding mono-adducts thanks to the hydrophobic environment provided by the nanocapsule.[91,92]

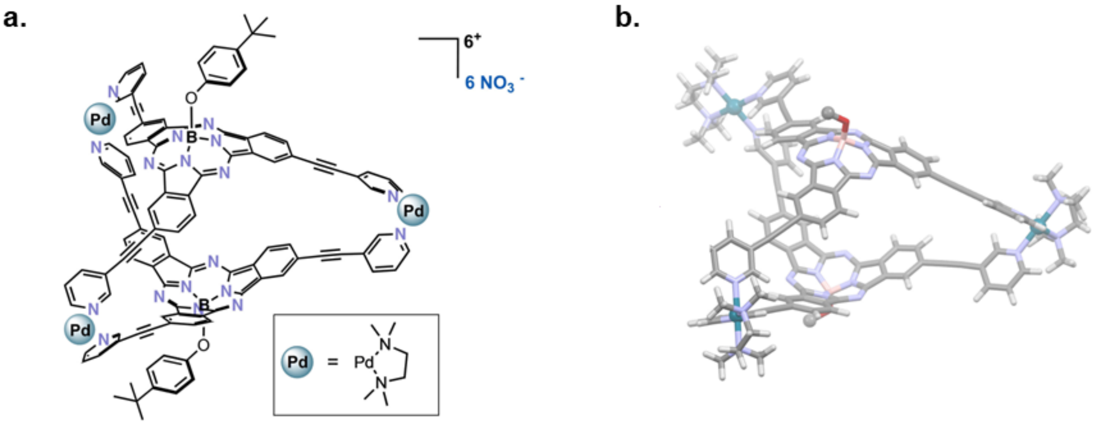

*Figure I.22. a) Molecular representation of the water-soluble metallo-organic $Pd^{II}$-subphthalocyanine cage of Torres, de la Torre and coworkers. b) DFT analysis of the same nanocapsule. Reprinted with permission from Torres, de la Torre et al.[91] Copyright © 2024, Advanced Synthesis & Catalysis published by Wiley-VCH GmbH.*

Metalloporphyrin-based molecular structures are excellent candidates to be used as fullerene receptors, since they present a large π-conjugated system that tend to act as π-donor moieties. As mentioned above, fullerenes behave as π-acceptor molecules. This electronic complementarity favours the π-π interactions between these two systems.[93] In this background, Nitschke's group was one of the pioneers of using cubic nanocapsules to functionalize fullerenes within their inner cavities (Figure I.23).[94] They were able to functionalize $C_{60}$ by Diels-Alder reaction controlling the chemo- and iteroselectivity, leading to the exclusive obtention of bis-adducts. Ribas group went a step further and described a Pd$^{II}$ prismatic tetragonal nanocapsule capable of controlling not only the chemo- and iteroselectivity, but also the regioselectivity of Bingel cyclopropanation on $C_{60}$ (Figure I.24.a). The addition pattern was strictly dictated by the four cross-shaped apertures of the container. Thus, equatorial bis-, tris- and tetrakis-adducts were exclusively obtained in a sequential fashion.[46]

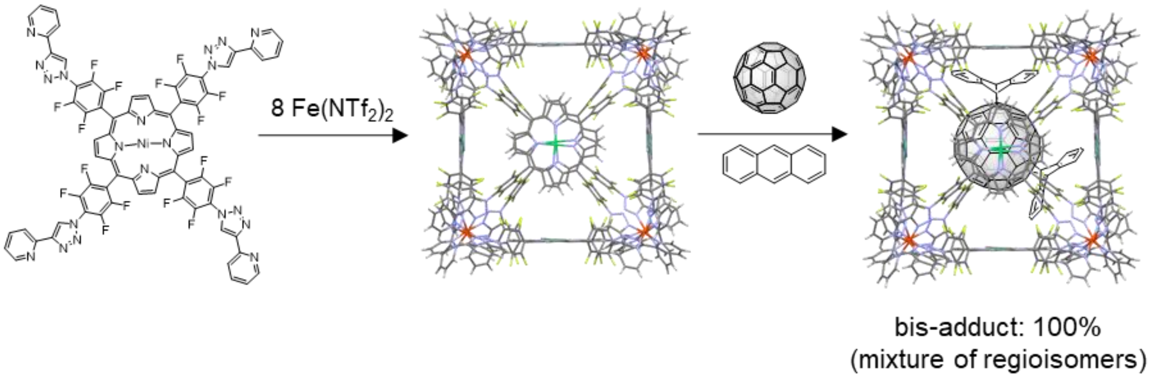

*Figure I.23. Self-assembly of the metal-organic nanocapsule and bis-functionalization of fullerene $C_{60}$ by means of Diels-Alder reaction using the nanocapsule as a templating platform from Nitschke's work.*

Host-guest complexes based on cycloparaphenylenes (CPPs) and fullerenes present high binding constants ($K_a \sim 10^6\ M^{-1}$).[95] These results motivated Delius and coworkers to use these carbon nanohoops as supramolecular directing groups for the regioselective poly-functionalization of fullerenes (Figure I.24.b).[90] When the second addition reaction was performed to a wrapped mono-adduct by [10]CPP, only *trans*-3 and *trans*-2 regioisomers were observed (with traces of *trans*-1). Thus, the presence of the aromatic nanohoop suppresses the formation of equatorial and *cis* regioisomers compared to non-templated Bingel reactions.[96]

A few years after, a collaborative project between Ribas and Delius works was published, putting together their respective previous works. They reported the synthesis of a matryoshka-like complex formed by a Pd$^{II}$ prismatic tetragonal nanocapsule which host a molecule of $C_{60}$ wrapped by the aforementioned aromatic nanoring (Figure I.24.c).[46] This ternary complex enabled the chemo-, itero- and regioselective bis-functionalization of $C_{60}$ by Bingel reaction, giving rise to the symmetry-mismatched *trans*-3-bis-adduct as a single product. Therefore, the presence of the aromatic nanohoop that is tilted (~15°) with respect to the zinc porphyrins of the nanocage in this ternary complex changes completely the addition pattern of Bingel cyclopropanation in comparison with the analogue binary complex.

Recently, the same authors used this matryoshka-like system to obtain a [10]CPP/$C_{60}$-based catenane by functionalizing encapsulated fullerene $C_{60}$ using a bis-bromomalonate-based tether (Figure I.24.d).[97] After disassembly of the cage, 87% selectivity for the formation of a single isomer (*in,out-trans-3*) was achieved by combining three approaches: the use of a bis-bromomalonate (tether approach), the use of the supramolecular complex of $C_{60}$ with [10]CPP macrocycle (template approach) and its incorporation within the tetragonal prismatic nanocapsule (shadow mask approach).

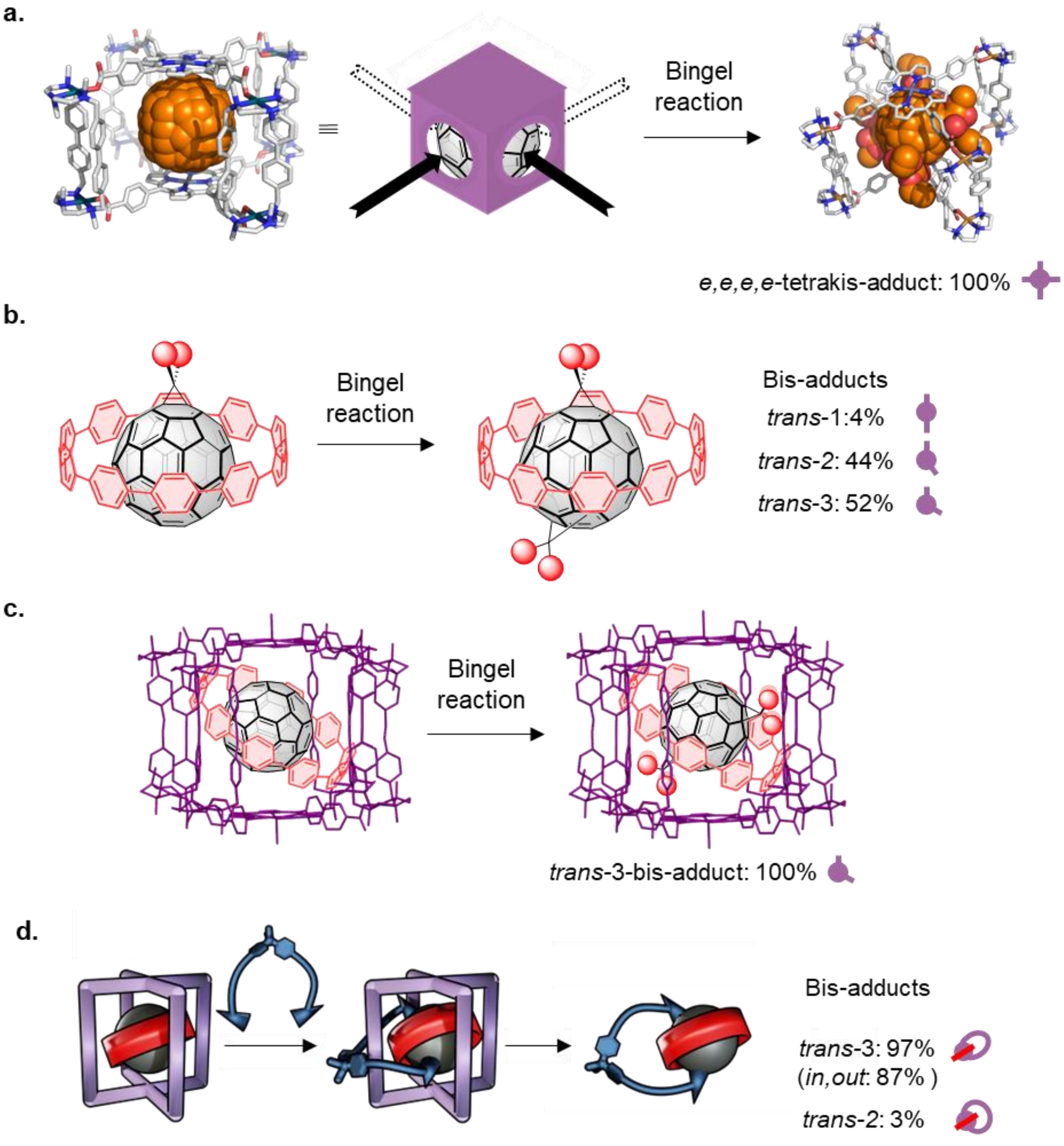

*Figure I.24. a) [10]CPP nanohoop as directing platform from Delius' work. b) Metal-organic self-assembled nanocapsule from Ribas' work as supramolecular shadow mask. c) Matryoshka-like complex as supramolecular mask from Delius' and Ribas' work. d) Synthesis of a [10]CPP/$C_{60}$ catenane by regioselective functionalization of $C_{60}$ combining previous strategies. Relative yields are shown for each example.*

Beuerle's group reported the synthesis of a trigonal bipyramidal covalent organic cage which encapsulated successfully fullerene $C_{60}$ and enabled its itero- and regioselective tris-functionalization by means of Prato reaction (Figure I.25).[98] Remarkably, only four out of the 46 possible regioisomers were formed, with a predominant selectivity for the symmetry-matched *t3,t3,t3*-tris-adduct (tris-adduct with three equidistant addends along the equatorial belt of $C_{60}$ sphere).

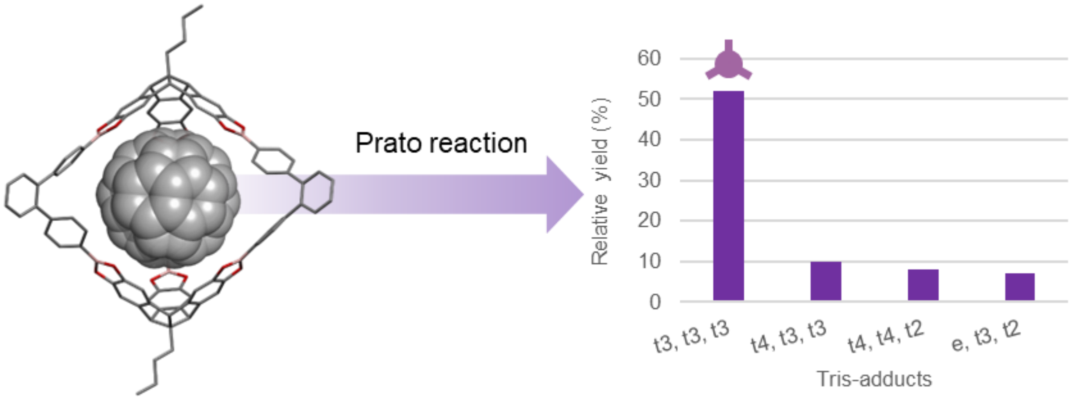

*Figure I.25. Organic nanocapsule from Beuerle's work that enables selective functionalization of fullerene $C_{60}$ through Prato reaction to give t3,t3,t3-tris-adduct majorly.*

Recently, Nitschke's group reported the synthesis of an enantiopure metal-organic cage built with chiral formylpyridines, which served as mask to control the itero-, chemo-, regio- and even the stereoselectivity of $C_{60}$ and $PC_{61}BM$ functionalization through intramolecular Diels-Alder reaction (Figure I.26).[99] The chiral formylpyridine moiety dictated the stereochemistry of chiral fullerene derivatives without being incorporated into them, obtaining a 88% enantiomeric excess (*e.e.*) for *e,e,e*-tris-adduct (starting from $C_{60}$) and a 64% *e.e.* for *trans*-3-bis-adduct (starting from $PC_{61}BM$).

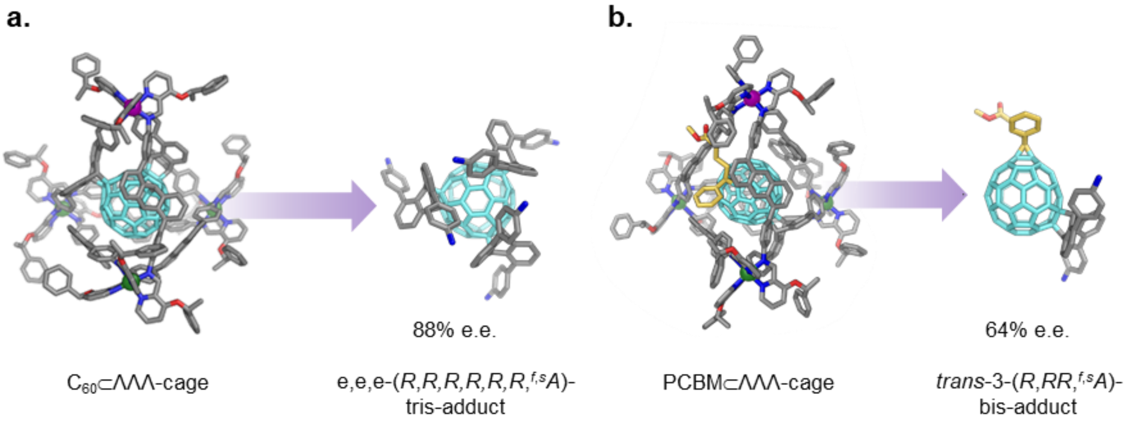

*Figure I.26. Metal-organic self-assembled nanocapsule that controls chemo-, itero-, regio- and enantioselectivity when used as supramolecular mask for the functionalization of a) $C_{60}$ and b) $PC_{61}BM$. Only one enantiomer is shown for clarity. Reprinted with permission from Nitschke et al.[99] Copyright © 2022, under exclusive licence to Springer Nature Limited.*

## I.3 Endohedral metallofullerenes

Fullerenes possess an inner cavity that makes them a robust container for other smaller species. When these spherical-like carbon cages contain metal atoms in their cavities, these species are named “endohedral metallofullerenes” (EMFs). First evidence of EMFs was reported in 1985, when La@$C_{60}$ was detected by mass spectrometry.[100] A few years after, in 1991, the first macroscopic production and isolation of air-stable La@$C_{82}$ was reported.[101] EMFs stand out for their charge transfer from the encapsulated metal atoms to the carbon cage, forming a non-dissociating salt. For example, for La@$C_{82}$, lanthanum has a formal charge of 3+ and $C_{82}$, a formal charge of 3-.

The discovery of lanthanum metallofullerenes was soon followed by the elucidation of a wide variety of EMF. Besides lanthanum, other metals such as scandium, yttrium or gadolinium (among others) or even metal clusters have been demonstrated to perform an intramolecular charge transfer towards fullerenes, which stabilizes carbon cages and/or metal clusters that cannot exist in their empty/isolated form.[102,103]

On the basis of the composition of the internal metallic species, EMFs can be divided in two main categories: classical EMFs and clusterfullerenes. The former include monometallofullerenes and dimetallofullerenes and the latter contain nitride clusterfullerenes, carbide clusterfullerenes, methano-clusterfullerenes, oxide clusterfullerenes, sulfide clusterfullerenes and cyano clusterfullerenes (Figure I.27).[104]

The interplay of carbon cages and encaged species results in new nanomaterials with exciting electronic states and properties. They can be applied in different fields, such as in biomedical applications (as magnetic resonance imaging or X-ray contrast agent,[106,107] radiotracers,[108] radiopharmaceuticals,[109] antitumorals[110] or antimicrobials[111]) and in organic photovoltaics (acceptors in PrSCs,[112] donor-acceptor dyads[113] or photoelectrochemistry cells[114]), but also can be used as single-molecule magnets[115] or even superconductors.[116] Nevertheless, all these applications have not been fully exploited due to the hampered obtention of pure EMFs, since the production of EMFs gives rise to complex mixtures of different hollow fullerenes and EMFs, nanotubes and carbon-based compounds. Their purification via chromatographic techniques is still expensive and long-time consuming due to not only for the wide variety of species in fullerene extracts, but also for the extremely low quantity of EMFs found in those extracts. This drawback can be overcome with the use of different separation protocols that involves electrochemical or precipitation techniques and the use of covalent or supramolecular receptors for molecular recognition of EMFs.

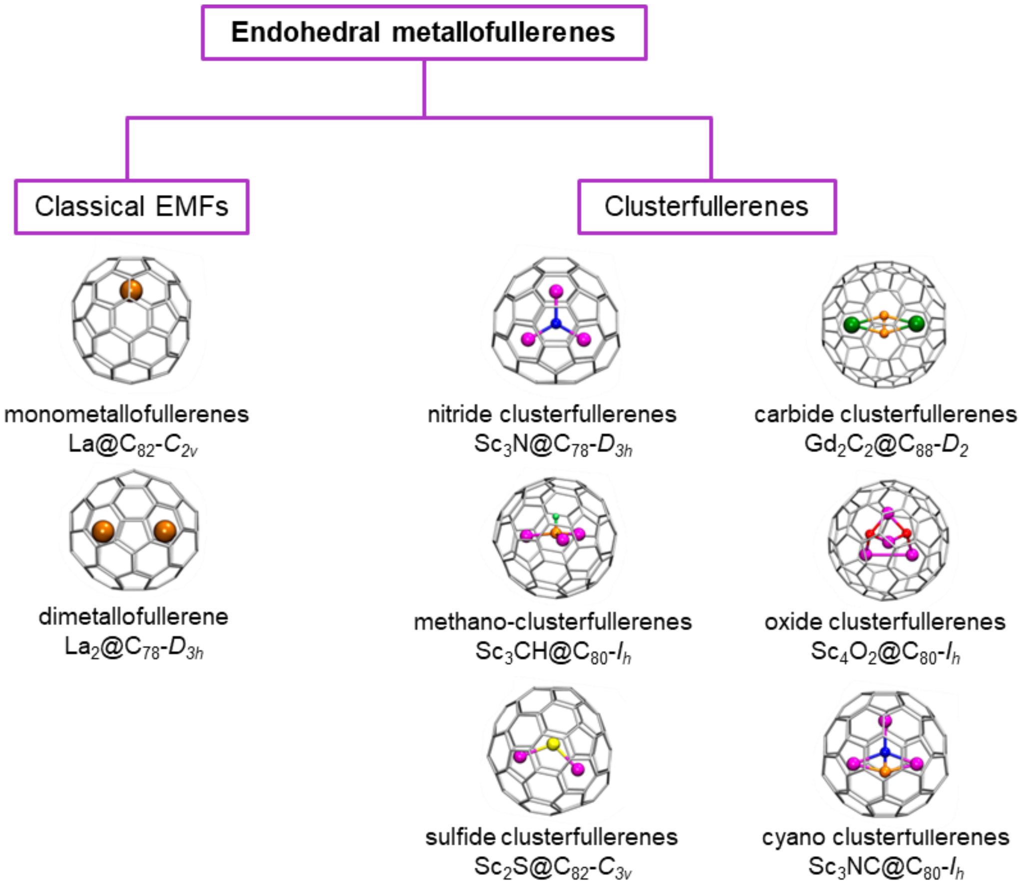

*Figure I.27. Classification of endohedral metallofullerenes with representative examples. Reprinted with permission Popov, Yang and Dunsch.[105] Copyright © 2013. American Chemical Society*

### I.3.1 Purification and separation techniques

Endohedral metallofullerenes possess π-electron-rich surface, so generally they are reactive towards Lewis acid. When EMF are mixed with Lewis acids, complexation may take place, leading to precipitation of EMFs. In 2009, Stevenson and coworkers reported that metallic nitride and oxometallic EMFs exhibit different reactivity towards Lewis acids, such as $AlCl_3$ or $FeCl_3$.[117] The reactivity order found was $Sc_4O_2@C_{80}$-$I_h$ > $Sc_3N@C_{78}$ > $Sc_3N@C_{68}$ > $Sc_3N@C_{80}$-$D_{5h}$ > $Sc_3N@C_{80}$-$I_h$, while hollow fullerenes such as $C_{60}$ or $C_{70}$ are largely unreactive towards Lewis acids (Figure I.28). They also used this technique to isolate the isomerically pure $Sc_3N@C_{80}$-$I_h$.

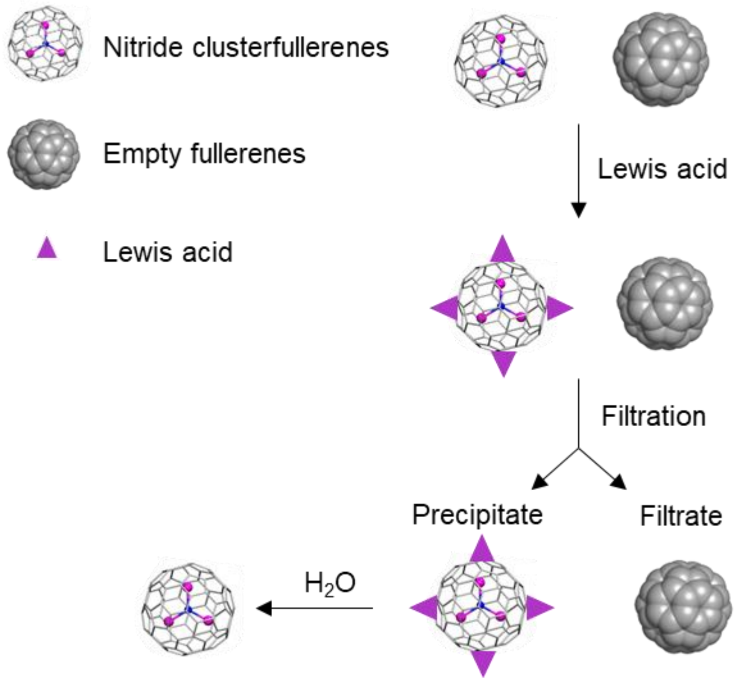

*Figure I.28. Schematic representation of separation and purification of nitride clusterfullerenes on the basis of selective complexation of Lewis acid from Stevenson's work.*

$TiCl_4$ is also used as a Lewis acid agent. Akiyama and Shinohara used $TiCl_4$ to complex monometallofullerenes based on trivalent metal ions ($Y^{3+}$, $La^{3+}$, $Ce^{3+}$, $Er^{3+}$, $Gd^{3+}$, $Lu^{3+}$) and divalent metal ions ($Sm^{2+}$, $Eu^{2+}$, $Tm^{2+}$, $Yb^{2+}$), which easily decomplexed to provide pure metallofullerenes by a simple water treatment.[118] They were successfully separated from empty fullerenes with up >99% purity within 10 minutes.

Exohedral functionalization of fullerenes and EMFs is another strategy to perform efficient separation of these species. Dorn and coworkers reported that metal nitride clusterfullerenes can be separated orthogonally from empty fullerenes and classical EMFs by using a column packed with a cyclopentadienyl-functionalized resin.[119] Empty fullerenes and classical EMFs are bonded to the resin by Diels-Alder reaction, whereas metal nitride clusterfullerenes remain intact and pass through the column (Figure I.29). The bonded empty fullerenes and metallofullerenes can be recovered upon heating in the presence of maleic anhydride.

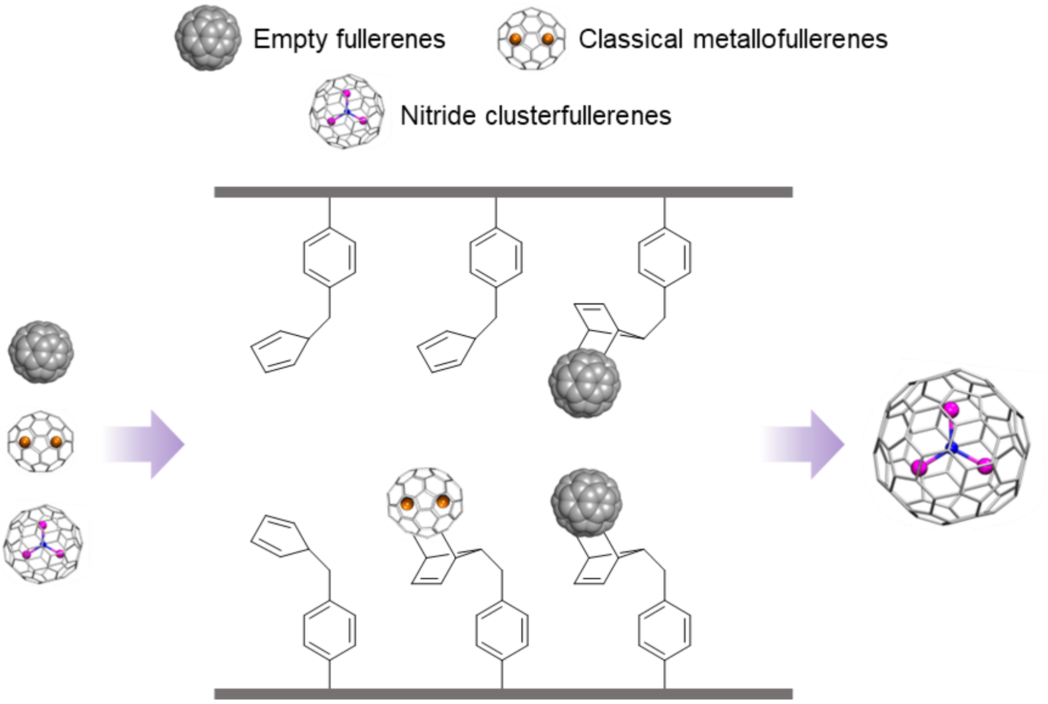

*Figure I.29. Schematic representation of purification process of metal nitride clusterfullerenes using the cyclopentadienyl-functionalized resin method from Dorn's work.*

Following the same trend, Stevenson and coworkers reported the isolation of metal nitride clusterfullerenes through selective reaction with cyclopentadienyl- or amino-functionalized silica, named "Stir and Filter Approach" (SAFA).[120] This approach was used to separate $Sc_3N@C_{80}$-$D_{5h}$ from $Sc_3N@C_{80}$-$I_h$ due to the rapid reactivity of $D_{5h}$ isomer with diamino silica in comparison to $I_h$ isomer.

Another strategy taking advantage of orthogonal reactivities was reported by Gibson, Dorn and coworkers, who used molten 9-methylanthracene to separate empty fullerenes from metal nitride clusterfullerenes in a solvent-free fashion.[121] Hollow fullerenes were converted to 9-methylanthracene adducts, while metal nitride clusterfullerenes remained unreacted. New anthracene-based adducts presented different solubilities in organic solvent as compared to intact EMFs, thus, they could be removed easily with washes of diethyl ether, enriching the extract about 60% the content of $Sc_3N@C_{80}$.

### *I.3.2 Molecular recognition of EMFs using supramolecular platforms*

In 2006, Akasaka and coworkers reported the 1:1 host-guest complexation of lanthanum metallofullerenes from extracts of fullerene soots using different azacrown ethers (Figure I.30).[122] They observed that saturated azacrown ethers complexed $La@C_{82}$ successfully. The facile electron transfer (characteristic of EMFs with low reduction potential) was pointed to be at the basis of the highest affinity of azacrown ether macrocycles towards

La@$C_{82}$ in comparison to $C_{60}$ and $C_{70}$. Also, 1:1 host-guest complexes with unsaturated thiacrown ethers were studied.[123]

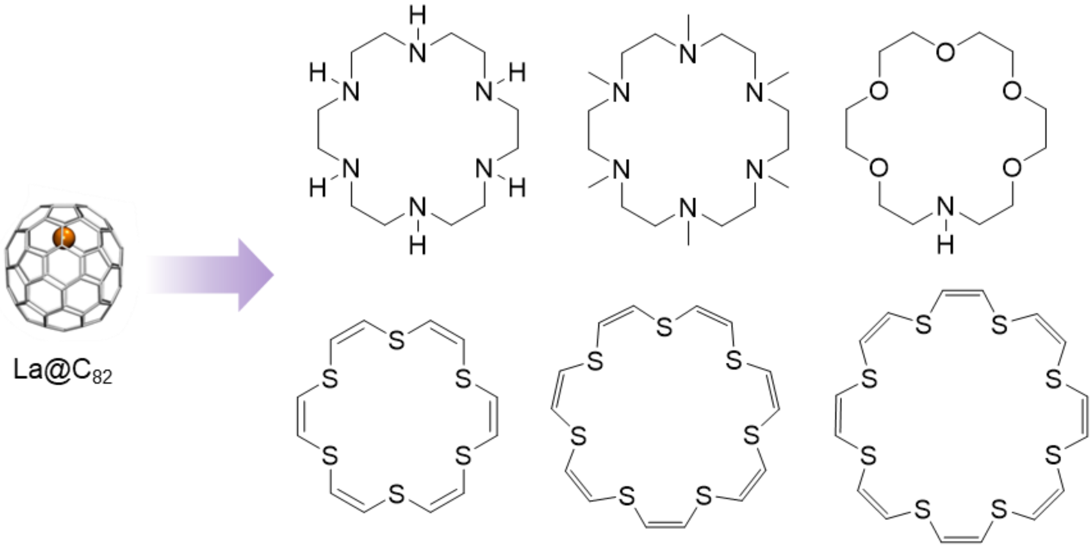

*Figure I.30. Scheme representation of the 1:1 host-guest complexes using different heterocrown ethers to capture La@$C_{82}$ from Akasaka's work.*

Cycloparaphenylenes also have been used as supramolecular platforms for size selective extractions of EMFs, since previous studies showed that CPP interact strongly with hollow fullerenes.[95] Itami, Shinohara and coworkers hypothesized that EMFs which comprise negatively charged fullerene cages with positively charged metal atom(s), interact with π-conjugated molecules more strongly than empty fullerenes. Moreover, they had to find the perfect size/shape complementary between EMFs and π-conjugated nanohoops. Successfully, they managed to selectively encapsulate $M_x$@$C_{82}$-$C_{2v}$ (x=1, 2) using [11]CPP such as Gd@$C_{82}$-$C_{2v}$, Tm@$C_{82}$-$C_{2v}$, and $Lu_2$@$C_{82}$-$C_{2v}$, demonstrating that this technique can be applied to the extraction and enrichment of EMFs from fullerene extracts.[124]

Costas, Echegoyen, Ribas and coworkers designed a $Cu^{II}$-based prismatic tetragonal nanocapsule which enabled the isolation of $Sc_3N$@$C_{80}$ from arc-processed raw soot, just by soaking solid crystals of the cage in a solution of EMFs soot.[125] This strategy allowed the encapsulation of $C_{60}$, $C_{70}$ and scandium-based EMFs with the exception of $Sc_3N$@$C_{80}$ (both $I_h$ and $D_{5h}$ isomers), which remained in solution (Figure I.31.a). Up to 85% recovery of the total amount of $Sc_3N$@$C_{80}$ from the initial mixture was achieved with very high purity (>99%).

The same nanocapsule was also used by Echegoyen, Ribas and coworkers for the selective encapsulation of uranium-based metallofullerenes. The addition of fresh crystals of the same metal-organic nanocapsule to a solution of scandium- and uranium-based EMFs soot allowed the selective encapsulation of $U_2$@$C_{80}$-$I_h$ and $Sc_2CU$@$C_{80}$-$I_h$

in a sequential fashion from an arc-produced soot and they were released applying an easy solvent-washing protocol (Figure I.31.b).[126] This demonstrates that the nanocapsule is capable of discriminating EMFs with the same carbon cage but with different internal metal-cluster. Computational analysis to study how $U_2@C_{80}$-$I_h$ and $Sc_3N@C_{80}$-$I_h$ interact with the nanocapsule revealed that the alignment of the two uranium ions of $U_2@C_{80}$-$I_h$ with both zincs of the porphyrin of the nanocapsule seems to favour the interaction with the nanocapsule by the higher negative charge present on carbon atoms closer to the $U^{3+}$. Therefore, the preferential capture of icosahedral $C_{80}$ when it possesses two encapsulated uranium ions seems to be related to the linear double-conical symmetry of the electron density induced by the presence of the guest ions. For $Sc_3N@C_{80}$-$I_h$, the electron density is averaged over an equatorial belt and thus it interacts less efficiently with the porphyrin units of the nanocage.

Finally, the same cage was used by the same group for the selective recognition of uranium-based $C_{78}$ EMFs species from a soot mixture containing hollow fullerenes and EMFs. They explored the molecular recognition of $U_2@C_{78}$-$D_{3h}$ and $U_2C@C_{78}$-$D_{3h}$ in the presence of a variety of U-based EMFs, such as $U@C_{74}$, $U@C_{82}$ and $U_2@C_{80}$-$I_h$.[127] The addition of crystalline nanocapsule to a solution of EMFs extract resulted in a sequential, clean and selective binding of $U_2@C_{78}$-$D_{3h}$ and $U_2C@C_{78}$-$D_{3h}$ over the rest of the EMFs (Figure I.31.c). The presence of the same metal-cluster in $U_2@C_{78}$ and $U_2@C_{80}$ suggested that the selective molecular recognition is governed by the size/shape relationship between the host and guest rather than the internal metal-cluster. Computational studies demonstrated that flattened $C_{78}$-$D_{3h}$ carbon cage causes an enhanced interaction between the carbon cage and the porphyrins units of the nanocapsule in comparison to the spherical $C_{80}$-$I_h$.

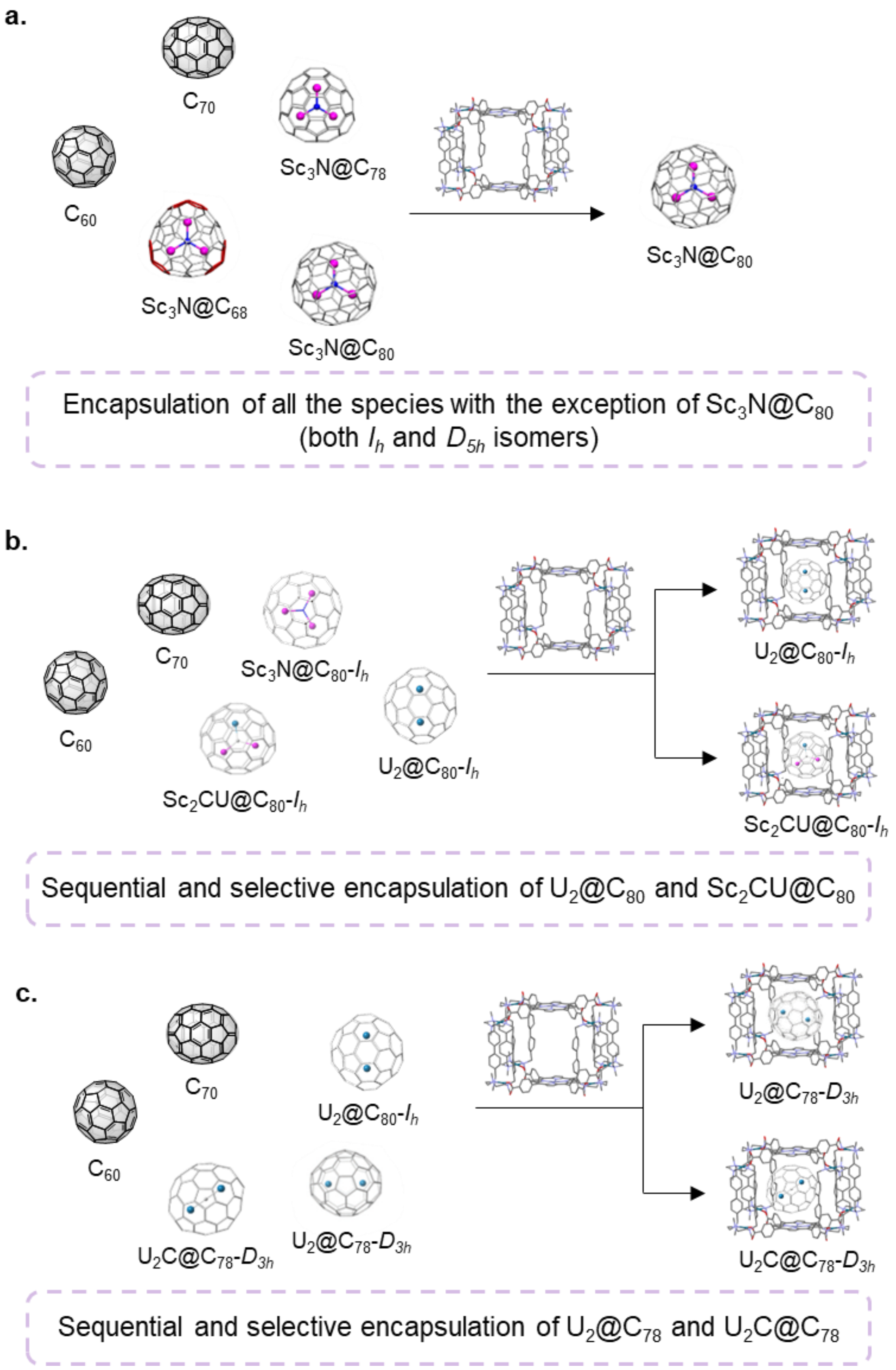

*Figure I.31. Selective encapsulation of scandium- and uranium-based endohedral metallofullerenes by self-assembled metal-organic nanocapsules from Echegoyen's and Ribas' work.*

# CHAPTER II. OBJECTIVES

The use of metal-directed self-assembled nanocapsules bearing extended aromatic panels has turned out an excellent strategy to achieve controlled functionalization of fullerenes and selective isolation of endohedral metallofullerenes, thanks to the accommodation of these spheroidal carbon cages into their inner cavities. Following this approach, the main objectives of this thesis are the itero-, chemo- and regioselective functionalization of fullerene $C_{60}$ through different reactions and, also, the selective molecular recognition of dimetallic terbium-based endohedral fullerenes from a fullerene/EMF extract using the reported $Pd^{II}$- and $Cu^{II}$-based prismatic tetragonal supramolecular nanocapsules by our research group.

### Itero-, chemo- and regioselective functionalization of fullerene $C_{60}$ and synthesis of novel heteroadducts via supramolecular mask strategy (Chapter IV, V and VI)

The objective of this part of the thesis is to extend the scope of fullerene functionalization reactions of the supramolecular mask strategy applied by our research group beyond Bingel reaction.

Functionalization of $C_{60}$ by Diels-Alder reaction will be explored via supramolecular mask approach. Acenes with different lengths will be used to explore the steric limitations of the nanocapsules and, consequently, the orthogonal regioselective outcome. A detailed computational modeling will provide crucial insights to rationalize the regioselective control exerted by the supramolecular mask on the successive additions. (Chapter IV)

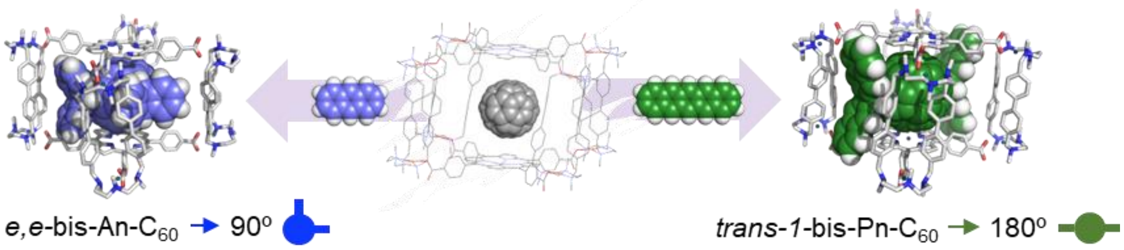

*Figure II.1. Representation of the first objective of this thesis (Chapter IV).*

These self-assembled nanocapsules will be also used for the controlled formation of $PC_{61}BM$-based bis-adducts using semi-stabilized sulfur ylides, which requires safer and milder reaction conditions than classical reagents (diazo compounds). Moreover, novel bis-heteroadducts will be explored through Prato and Bingel reaction in combination with $PC_{61}BM$ via supramolecular mask strategy using nanocapsules of different sizes. (Chapter V)

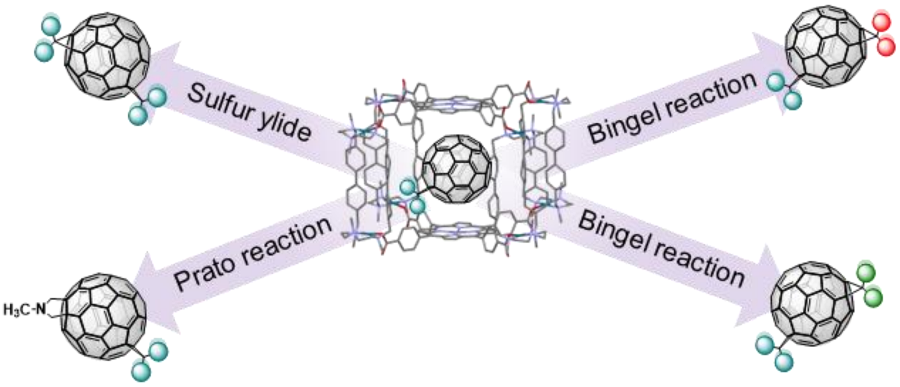

*Figure II.2. Representation of the second objective of this thesis (Chapter V).*

Finally, the synthesis of a molecular shuttle based on a $C_{60}$/[10]CPP-based [2]catenane system will be pursued. The first step will focus on a Bingel reaction using non-symmetrical bromomalonates that feature one reactive terminal moiety. Upon bis-functionalization of $C_{60}$, these terminal moieties might allow the connection of two bis-adducts (one of them wrapped by a [10]CPP ring) to form the desired [2]catenane with two stations for the one [10]CPP ring. This project is in collaboration with Prof. Max von Delius and MSc Fabian Steudel from Ulm University (Germany), who provided all the bromomalonates for Bingel reactions. (Chapter VI)

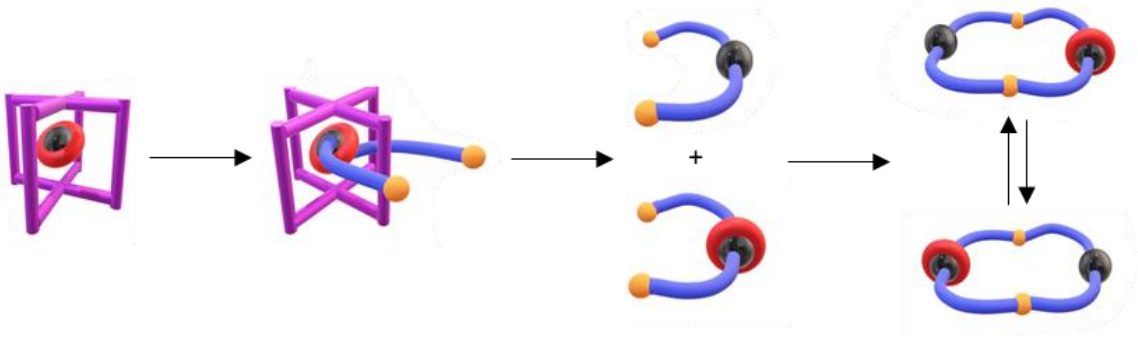

*Figure II.3. Representation of the third objective of this thesis (Chapter VI).*

## Selective encapsulation of bimetallic terbium-based endohedral fullerenes (Chapter VII)

The obtention of pure EMFs is extremely hampered due to the complex mixtures obtained during their production. Prismatic tetragonal nanocapsules will be used to selectively isolate the anionic $Tb_2@C_{80}^-$ species from an endohedral metallofullerene extract including $Tb@C_{80}^-$, $Tb@C_{82}^-$, $Tb_2@C_{78}^-$ and $Tb_2@C_{80}^-$. This project is in collaboration with Alexey A. Popov from the Leibniz Institute for Solid State and Materials Research, in Dresden (Germany), who provided the EMF extracts.

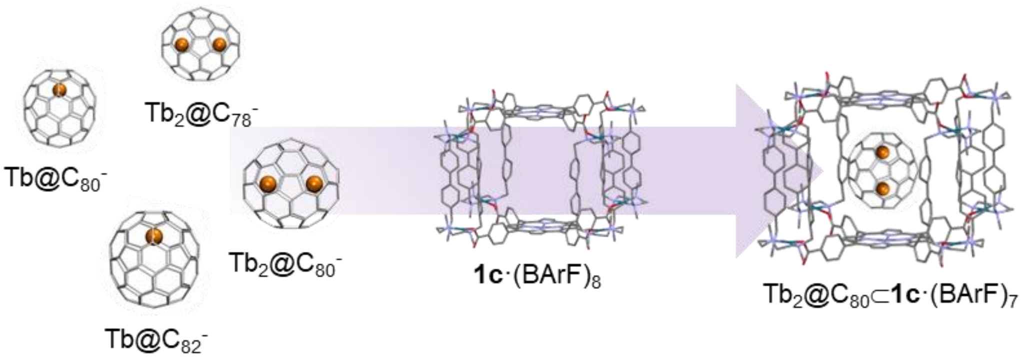

*Figure II.4. Representation of the fourth objective of this thesis (Chapter VII).*

# CHAPTER III. METHODOLOGY

Reagents and solvents used were commercially available reagent quality unless indicated otherwise. Supramolecular nanocapsules **1b**·(BArF)$_8$, **1c**·(BArF)$_8$, **1d**·(BArF)$_8$ and **1f**·(BArF)$_8$ (see Figure IV.1) were synthesized according to published procedures.[31,89,97,125]

Host-guest complexes (fullerenes, derivatives or EMFs encapsulated by **1b**·(BArF)$_8$, **1c**·(BArF)$_8$ and matryoshka systems with **1d**·(BArF)$_8$ and **1f**·(BArF)$_8$) were analysed by HR-ESI-MS and $^1$H-NMR. Derivatives were analysed by NMR, HPLC, UV-vis spectroscopy and MALDI-MS. EMFs were analysed by MALDI-MS.

Computational modeling was performed by Molecular Dynamic simulations in combination with the analysis of molecular orbitals.

**HR-ESI-MS** experiments were collected and analysed on Bruker MicroTOF-Q-II using $CH_3CN$ as mobile phase.

**HPLC** data concerning fullerene adducts identity were collected on Agilent Technologies LC 1200 series instrument equipped with Cosmosil Buckyprep-M and Cosmosil Buckyprep-D columns (4.6 mm I.D. x 250 mm, particle size: 5 µm, Nacalai Tesque, Inc.) and monitored with a UV detector at 320 nm and using toluene as solvent (0.5 ml/min flow).

**MALDI-TOF-MS** analysis were collected on a Autoflex maX Bruker Daltonics with a Bruker Smartbeam II (355 nm wavelength) using a matrix made from a mixture of trans-2-[3-(4-tert-butylphenyl)-2-methyl-2-propenylidene]malononitrile (DCTB) and sodium trifluoroacetate (NaTFA) in tetrahydrofuran.

**NMR experiment details**: All NMR experiments were performed at 298 K on a Bruker AVANCE 400 NMR spectrometer operating at 400.13 MHz and on a Bruker AVANCE 500 NMR spectrometer operating at 500.13 MHz and equipped with a cryoprobe z-gradient inverse probe-head capable of producing gradients in the z direction with a maximum strength of 53.5 G cm$^{-1}$. The description of the $^{13}$C NMR data is solely focused on the ester of the malonate addends and anthracene and pentacene moieties. Homonuclear and heteronuclear 2D NMR experiments (COSY, ROESY, NOESY, HSQC, and HMBC) were recorded under routine conditions. Diffusion NMR experiments were recorded with a stabilized temperature of 298K using the ledbpgs sequence (BRUKER library) that incorporates bipolar gradient pulses and a longitudinal eddy current delay of 5ms. The gradient strength was linearly incremented in 16 steps from 2% up to 95% of the maximum gradient strength. Diffusion times and gradient pulse durations were optimized for each experiment to achieve a 95% decrease in the resonance intensity at the largest gradient amplitude; typically, diffusion times of 150 ms and rectangular gradient pulses of 1.5 ms were employed. Sample rotation at 20Hz were used to avoid unwanted convection effects always presents in $CDCl_3$ solutions. After Fourier transformation followed by the same phase and baseline correction of each 1D dataset, the diffusion dimension of the 2D DOSY spectra was obtained by using the dosy protocol included into the TOPSPIN software package. The diffusion coefficients obtained from the DOSY experiments were used to evaluate the hydrodynamic radius of the fullerene systems for all samples according to the Stokes-Einstein equation.

**Molecular Dynamics (MD) simulations:** Molecular Dynamics (MD) simulations were performed using the GPU code (*pmemd*)[128] of the AMBER 16 package.[129] Parameters for fullerenes and acetonitrile (solvent) were generated within the *antechamber* module using the general AMBER force field (*gaff*),[130] with partial charges set to fit the electrostatic potential generated at the HF/6-31G(d) level by the RESP model.[131] The charges were calculated according to the Merz–Singh–Kollman scheme[132,133] using the Gaussian 09 package.[134] Parameters for supramolecular metallo-cages were generated using the MCPB.py[135] module included in AmberTools16,[29,129] following the same protocols used in our previous work.[29] Each host-guest system was immersed in a pre-equilibrated truncated octahedron box with a 12 Å buffer of acetonitrile molecules using the *leap* module, resulting in the addition of around 750 solvent molecules. The systems were neutralized by addition of explicit counter ions ($Cl^-$). All subsequent calculations were done using the Stony Brook modification of the Amber14 force field (*ff14sb*).[136] A two-stage geometry optimization approach was performed. The first stage minimizes the positions of solvent molecules and ions imposing positional restraints on the solute by a harmonic potential with a force constant of 500 $kcal \cdot mol^{-1} \cdot Å^{-2}$ and the second stage minimizes all the atoms in the simulation cell except those involved in the harmonic distance restraint. The systems were gently heated using six 50 ps steps, incrementing the temperature by 50 K for each step (0–300 K) under constant-volume and periodic-boundary conditions. Long-range electrostatic effects were modelled using the particle-mesh-Ewald method.[137] An 8 Å cutoff was applied to Lennard–Jones and electrostatic interactions. Bonds involving hydrogen were constrained with the SHAKE algorithm. Harmonic restraints of 30 $kcal \cdot mol^{-1}$ were applied to the solute and the Andersen equilibration scheme was used to control and equalize the temperature. The time step was kept at 1 fs during the heating stages, allowing potential inhomogeneities to self-adjust. Each system was then equilibrated for 2 ns with a 2 fs time step in the NPT ensemble. Production trajectories were then run for an additional 1,000 ns (1 µs) under the NVT ensemble and periodic-boundary conditions. A total of 3 different replicas (including independent minimizations, heating and equilibration steps and production runs) for each system were carried out.

**Electronic structure calculations:** All electronic structure calculations were performed using the Gaussian09 software package.[134] Frontier molecular orbitals (FMOs) of isolated molecules (the pristine $C_{60}$, anthracene, pentacene and the corresponding Diels-Alder mono- and bis-adducts) were analysed from optimized structures at the Hartree Fock (HF) level and using the 6-31G(d,p) basis set for all atoms. Frontier Molecular Orbitals (FMO) were analysed form these optimized structures using the HF/6-31G(d,p) wavefunctions. FMOs were visualized and rendered using Chemcraft. All optimized stationary points were characterized as minima using frequency calculations.

Reaction energies were calculated using Density Functional Theory (DFT) calculations, and the Gaussian09 software package.[134] The wB97XD functional[138] together with the 6-31G(d,p) basis set was employed for optimizations, and energies were refined by single point calculations at the ωB97XD/6-311G** level. All optimized stationary points were characterized as minima using frequency calculations, and enthalpies and entropies were calculated for 1 atm and 298.15 K.

FMOs for a model system were analysed, to show that the conclusions drawn from the qualitative analyses of the orbital distribution based on independent fullerene derivatives are consistent.

A truncated model system based on two porphyrins with one mono-anthracene-$C_{60}$ molecule in between equivalent to model systems reported by Ribas et al. was used.[89,126,127] The model system [2xPorph – mono-An-$C_{60}$] was optimized at the wB97XD/6-31G(d,p) level of theory, which includes dispersion corrections that are essential to reproduce the geometries and energetics of non-covalent supramolecular systems involving large carbon structures using DFT. The optimized structures describe the mono-anthracene-$C_{60}$ when interacting with the two porphyrins, in a similar interacting mode as found when encapsulated in the nanocapsule[89]. FMOs were analysed from these optimized structure using the wB97XD/6-31G(d,p) wavefunction.

# CHAPTER IV. REGIOSELECTIVE ACCESS TO ORTHOGONAL DIELS-ALDER $C_{60}$ BIS-ADDUCTS AND TRIS-HETEROADDUCTS VIA SUPRAMOLECULAR MASK STRATEGY

This chapter corresponds to the following publication:

Pujals, M; Pèlachs, T.; Fuertes-Espinosa, C.; Parella, T.; Garcia-Borràs, M.; Ribas, X. *Cell Rep. Phys. Sci*. **2022**, 3, 100992

As discussed in *I.2.2.2 Supramolecular receptors as functionalization platforms for fullerenes*, Ribas and coworkers designed a range of metal-organic prismatic tetragonal nanocapsules which were synthesized through the self-assembly of tetracarboxylated $Zn^{II}$-metalloporphyrins with $Pd^{II}/Cu^{II}$ macrocyclic complexes in a proportion of 2:4, respectively (Figure IV.1). The modification of the M-M distance of these macrocyclic complexes offers nanocapsules with different cavity sizes. Therefore, these nanocapsules can interact with different guests, from anionic planar π-guest molecules[139] to Rh-phosphoramidite-based catalysts,[140] fullerenes[29,31,46,89] or endohedral metallo-fullerenes.[34,125,126] These nanocapsules offer different applications, as discussed in *I.1.3 Self-assembled nanocapsules and applications.* Among them, they are excellent fullerene receptors and are capable of controlling the chemo-, itero- and regioselectivity of their functionalization, which is a very challenging task due to its high spheroidal symmetry.

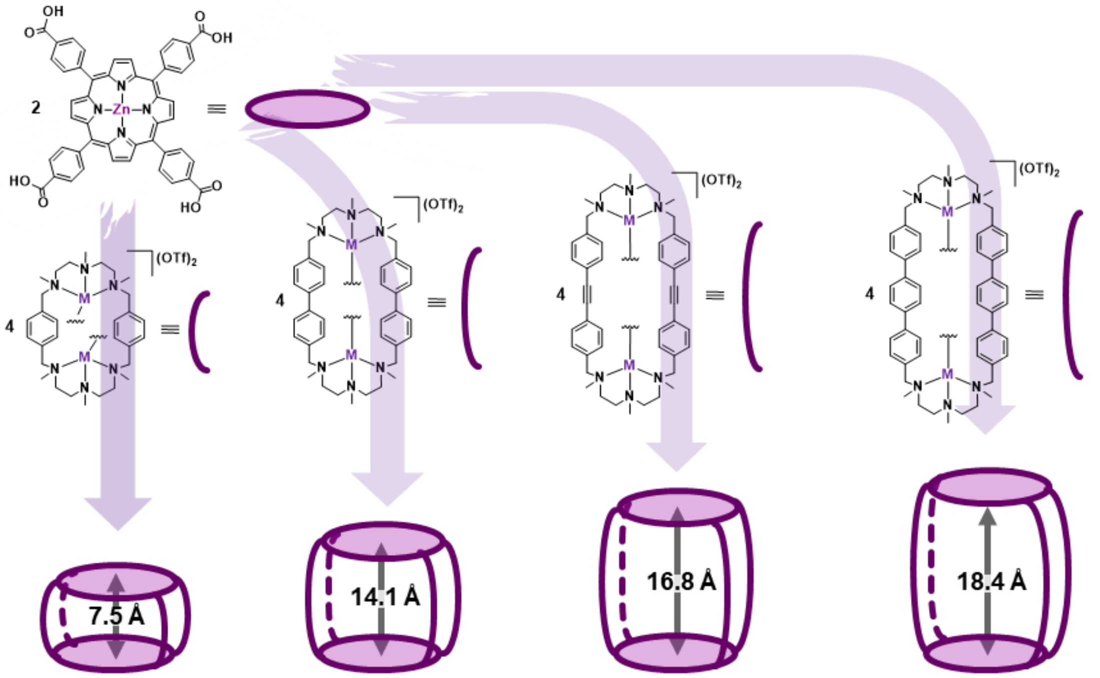

**1a**·(BArF)$_8$ (M = Pd)

**1b**·(BArF)$_8$ (M = Pd)
**1c**·(BArF)$_8$ (M = Cu)

**1d**·(BArF)$_8$ (M = Pd)
**1e**·(BArF)$_8$ (M = Cu)

**1f**·(BArF)$_8$ (M = Pd)
**1g**·(BArF)$_8$ (M = Cu)

*Figure IV.1. Metal-organic self-assembled prismatic tetragonal nanocapsules reported by Ribas and coworkers.*

Particularly, **1b**·(BArF)$_8$ nanocapsule shows an excellent affinity to fullerene $C_{60}$ ($K_a \sim 10^7$ $M^{-1}$ in toluene/acetonitrile (9:1) as solvent), which converts it into an excellent fullerene receptor. This host also presents a remarkable breathing effect, since the zinc-zinc inter-distance between porphyrin subunits of the nanocapsule swings from 14.1 Å when the cavity is empty to 13.1 Å upon $C_{60}$ encapsulation, as observed from X-ray structures and computational modeling.[89] This high adaptability of the nanocapsule enables the successful regioselective functionalization of fullerene $C_{60}$ through Bingel reaction, obtaining exclusively symmetry-matched equatorial bis-, tris- and tetrakis-adducts.[29]

In this chapter, this supramolecular mask strategy will be extended to Diels-Alder functionalization of $C_{60}$. Diels-Alder reaction is a pericyclic, concerted reaction which involves a conjugated diene (two π bonds) and an alkene (known as dienophile, one π bond) to form a new 6-membered ring, and it is classified as a thermally-allowed [4+2] cycloaddition. As mentioned in *I.2 Fullerenes*, fullerenes act as an electron-deficient polyolefin, so they can be considered as the dienophiles of the Diels-Alder reaction system in contrast to acenes (electron-rich polycyclic aromatic hydrocarbons) that are considered as the conjugated dienes of the system. [141–143]

In this work, two different acenes (anthracene (An) versus pentacene (Pn)) will be used to bis-functionalize fullerene $C_{60}$ with the presence of nanocapsules as supramolecular masks in a divergent and regioselective manner. Moreover, the mask strategy will be used to afford novel heteroadducts combining Diels-Alder with Bingel reaction in a regioselective fashion. Finally, computational modeling combining molecular dynamics (MD) simulations and electronic structure analyses will provide a clear understanding of the divergent regioselective control achieved by the nanocapsule.

## IV.1 Regioselective Diels-Alder bis-functionalization of $C_{60}$ using the supramolecular mask strategy

### *IV.1.1 Templated Diels-Alder reaction using anthracene*

Encapsulated $C_{60}$ fullerene by $Pd^{II}$-based nanocapsule **1b**·$(BArF)_8$ ($C_{60}\subset$**1b**·$(BArF)_8$) was submitted to Diels-Alder reaction by the addition of 30 equivalents of anthracene in acetonitrile at 50°C. Solubility of the host-guest complex is dictated by the host (i.e. **1b**·$(BArF)_8$ nanocapsule), which is highly soluble in acetonitrile, in contrast to fullerenes that are soluble in toluene or *o*-DCB. After 48 hours, bis-adducts were afforded as the main product (bis-An-$C_{60}$), with the minor presence of the corresponding mono-adduct (mono-An-$C_{60}$) in a ratio of 1:0.4, as monitored by high resolution mass spectrometry (HR-ESI-MS, Figure IV.2.b). Attempts to increase the ratio toward bis-adducts have been unsuccessful due to the interplay of the retro-Diels-Alder reaction (Annex IV, Table S.1).

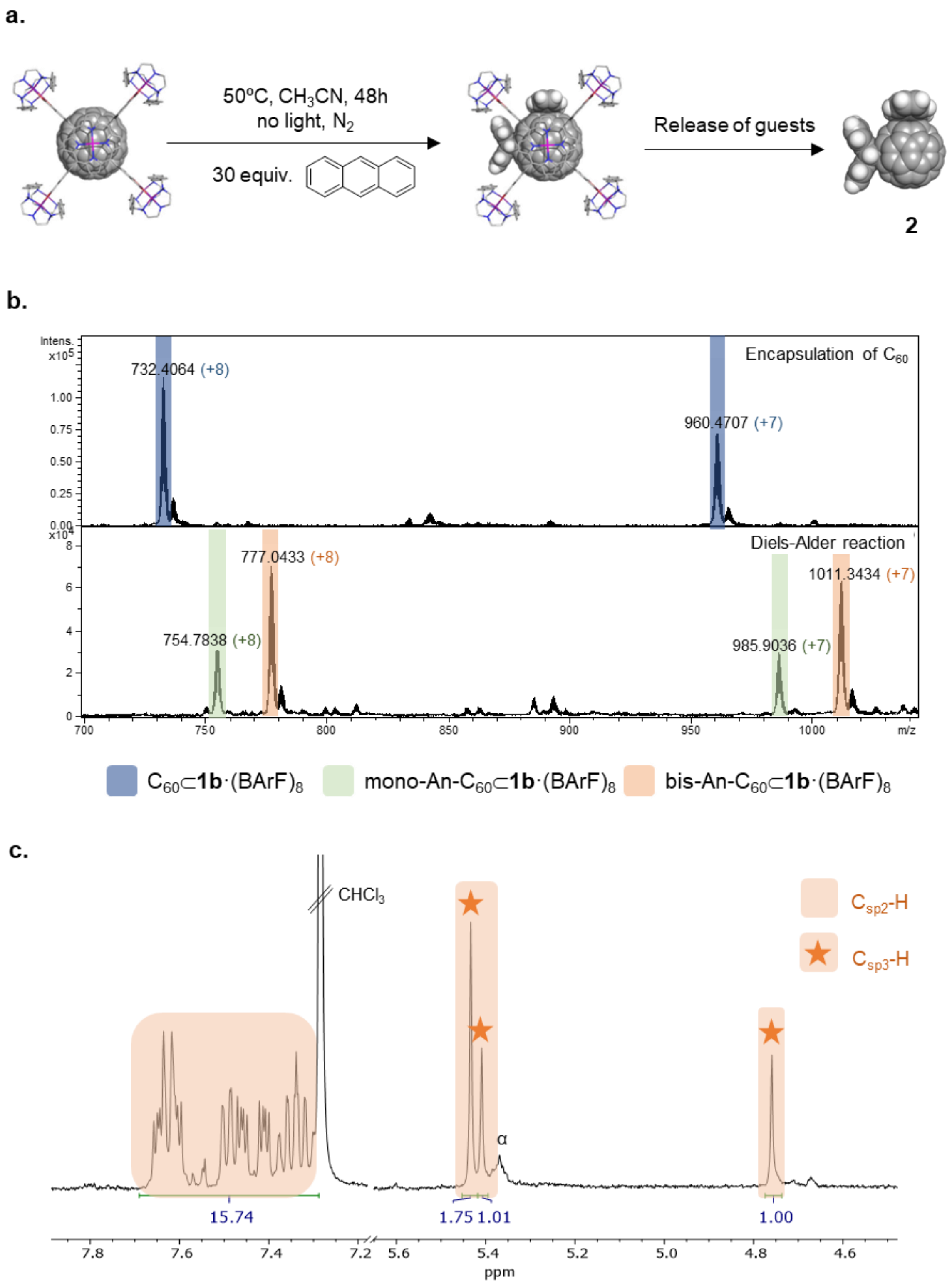

*Figure IV.2. a) Schematic representation of the synthesis of **2** using **1b**·(BArF)$_8$ as a supramolecular mask. b) HR-ESI-MS monitoring of the formation of bis-An-C$_{60}$⊂**1b**·(BArF)$_8$. c) $^1$H-NMR spectrum of e,e-bis-An-C$_{60}$ (**2**). α: TLC-silica impurities. In orange, signals corresponding to protons of anthracene addends (highlighting with a star the cycloadded C$_{sp3}$ protons).*

The functionalized product was easily released from the cage by using an easy solvent-washing protocol with chloroform (Annex IV, Figure S.1) and, remarkably, a single bis-adduct was found as seen in the HPLC chromatogram (Annex IV, Figure S.2 and S.3).

Nuclear magnetic resonance (NMR) characterization (Annex IV, Figure S.4 – S.10) indicated that the isomerically pure equatorial bis-adduct (*e,e*-bis-An-$C_{60}$, **2**) was solely formed, with a distinctive 2:1:1 signal pattern between 4.6 and 5.6 ppm rising from the $C_s$ symmetry of the product (Figure IV.2.c). This distribution of signals corresponds to the cycloadded $C_{sp3}$ protons of the two anthracene-based addends in an equatorial fashion (i.e. addends positioned at a 90º angle). This represents a very remarkable control of the regioselectivity imposed by the nanocapsule, as previous reported functionalization studies of Diels-Alder reaction with anthracene towards bare $C_{60}$ afforded mixtures of five different isomers among bis-adducts (16% *e,e*, 1.3% *trans*-1, 13% *trans*-2, 26% *trans*-3 and 10% *trans*-4).[144,145]

### *IV.1.2 Templated Diels-Alder reaction using pentacene*

$C_{60}$⊂**1b**·$(BArF)_8$ was submitted to Diels-Alder reaction by the addition of 2.1 equivalents of pentacene in a mixture of acetonitrile/dichloromethane (4:1) at 65ºC. After 16 hours, encapsulated bis-adduct (bis-Pn-$C_{60}$⊂**1b**·$(BArF)_8$) was detected as the main product of the crude by HR-ESI-MS monitoring (Figure IV.3.b) alongside traces of encapsulated mono-adduct (mono-Pn-$C_{60}$⊂**1b**·$(BArF)_8$).

In this case, the interplay of retro-Diels-Alder reaction was almost non-existing since only traces of the corresponding mono-adduct were present, in contrast to the formation of bis-An-$C_{60}$⊂**1b**·$(BArF)_8$. In order to understand the differences regarding the equilibrium between the Diels-Alder and the retro-Diels-Alder of both systems, a simple thermodynamic equilibrium analysis was performed between the corresponding mono- and bis-adducts. Structures were calculated using Density Functional Theory (DFT) and optimised using the wB97XD functional and the 6-31(d,p) basis set (see computational details in *Chapter III. Methodology*).

*Table IV.1. Thermodynamic equilibrium between mono- and bis-adducts for Diels-Alder reaction using anthracene and pentacene. Changes in Electronic (E) and Gibbs (G) free energies between corresponding bis-adducts and mono-adducts are shown.*

| System | ΔE (kcal/mol) | ΔG (kcal/mol) |
|---|---|---|
| bis-An-$C_{60}$ | -31.3 | -13.4 |
| bis-Pn-$C_{60}$ | -45.2 | -27.0 |

As can be seen in Table IV.1, the change in Gibbs free energy for the formation of *e,e*-bis-An-$C_{60}$ is -13.4 kcal/mol, while the change in Gibbs free energy for the formation of *trans*-1-bis-Pn-$C_{60}$ is -27.0 kcal/mol, indicating that latter is much more stable than the former and that *e,e*-bis-An-$C_{60}$ is much more prone to suffer a retro-Diels-Alder reaction at higher temperatures, as observed experimentally.

Upon nanocapsule disassembly by the addition of trifluoromethanesulfonic acid, bis-adducts were obtained in 79% relative yield among all the fullerene derivatives (small quantities of tris-adducts were produced during the workup). As can be seen in the HPLC chromatogram after disassembly of the cage, there is a predominant peak (retention time: 7.576 min) which represents 78% of the total bis-adducts (Annex IV, Figure S.14). It was easily purified through a simple preparative thin-layer chromatography (TLC) and analysed by HPLC and ultraviolet-visible (UV-vis) spectroscopy (Annex IV, Figure S.15). Nevertheless, it was isolated in 30% yield due to insolubility issues of this isomer. NMR characterization (Annex IV, Figure S.16 and S.17) confirmed that this predominant bis-adduct was the *trans*-1-bis-Pn-$C_{60}$ (**4**), since there was a unique singlet at 6.32 ppm (Figure IV.3.c) rising from the $D_{2h}$ symmetry of the derivative that corresponds to the cycloadded $C_{sp3}$ protons of the two pentacene-based addends positioned in a *trans*-1 fashion (i.e. addends positioned at a 180º angle).

A high-field shifting of $C_{sp3}$ protons of *e,e*-bis-An-$C_{60}$ can be observed in comparison with $C_{sp3}$ protons of *trans*-1-bis-Pn-$C_{60}$, due to the anisotropic effect induced by the ring currents of adjacent aromatic rings. In the case of *e,e*-bis-An-$C_{60}$, the anthracene-based addends are placed perpendicularly (in a 90º angle) facing each other and the anisotropic effect of the aromatic protons from one addend produces a considerable shielding effect of the cycloadded $C_{sp3}$ protons to the other addend (5.43, 5.41, and 4.76 ppm, Figure IV.2.c).

In the case of *trans*-1-bis-Pn-$C_{60}$, since pentacene-based addends are placed at a 180º angle, this effect is not noticed by $C_{sp3}$ protons and their shifts are higher (6.32 ppm, Figure IV.3.c). The minor peaks at 6.22, 8.44, and 8.62 ppm correspond to the isomerization of both pentacene moieties, giving rise to bis-adducts featuring non-symmetric addends (see Annex IV, Figure S.16), but the regioselectivity of the product remains intact (addends at 180º).

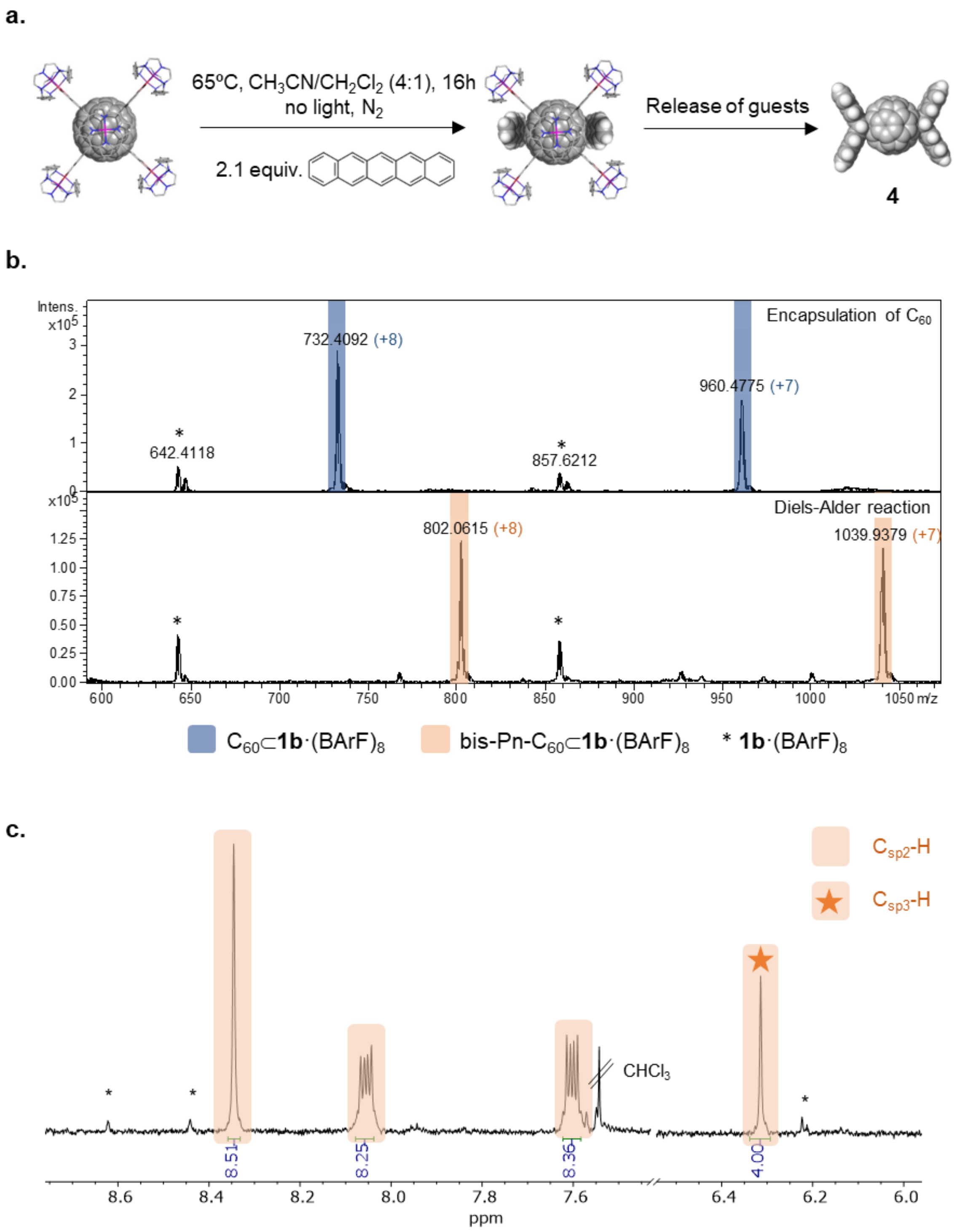

*Figure IV.3. a) Schematic representation of the synthesis of **4** using **1b**·$(BArF)_8$ as a supramolecular mask. b) HR-ESI-MS monitoring of the formation of bis-Pn-$C_{60}$⊂**1b**·$(BArF)_8$. c) $^1$H-NMR spectrum of trans-1-bis-Pn-$C_{60}$ (**4**). In orange, signals corresponding to protons of pentacene addends (highlighting with a star the cycloadded $C_{sp3}$ protons). * Signals corresponding to the minor isomer due to isomerization of pentacene addends, see Annex IV, Figure S.16.*

## IV.2 Computational modeling

Computational modeling was used to rationalize the regioselectivity outcome when different acenes are used (anthracene versus pentacene) to bis-functionalize encapsulated fullerenes by using **1b**·(BArF)$_8$ nanocapsule. Molecular dynamics (MD) simulations and analysis of molecular orbitals were carried out to gain insights into the host-guest equilibria and the regioselectivity achieved of the final products.

### *IV.2.1 Molecular dynamics simulations*

MD simulations were performed (see computational details in *Chapter III. Methodology*). For each system, three replicas of MD trajectories of 1000 ns each (accumulating a total of 3 ms of simulation time) were carried out (Annex IV, Figures S.63 – S.75) using the modelled **1b**·(Cl)$_8$ nanocapsule considering an explicit solvent box of acetonitrile.[29] Also, videos of MD simulations are attached.

MD simulations of mono-An-C$_{60}$⊂**1b**·(Cl)$_8$ revealed that gate-to-gate rotation of the anthracene-based addend can occur. These gate-to-gate rotations take place at the nanosecond-to-microsecond timescale, as different rotations are observed throughout the 1000 ns of simulation time (Figure IV.4.a). Therefore, it is expected that the anthracene moiety can explore the four symmetric gates of the capsule indistinctively, although longer MD trajectories would be required for the anthracene moiety to equally visit all the nanocapsule gates during the simulations. Moreover, the relative orientation of the anthracene moiety of mono-An-C$_{60}$ with respect to the porphyrin units of the nanocapsule was also analysed. MD simulations indicated that the anthracene moiety of the mono-adduct can be oriented in a parallel or in a perpendicular way with respect to the porphyrins of the cage. The interconversion between both orientations along its C$_{2v}$ axis occurs fast and they are indistinctively explored by the anthracene moiety (Figure IV.4.b, see Annex IV, Figures S.63 – S.65 for replicas). In contrast, MD simulations for the *e,e*-bis-An-C$_{60}$⊂**1b**·(Cl)$_8$ revealed that gate-to-gate rotation is totally prohibited and each anthracene moiety is completely fixed to a single gate (i.e. no spinning of the bis-adduct is observed). This indicates that the addition of a second anthracene-based addend restricts the dynamics of the fullerene derivative in the nanocapsule (see Annex IV, Figures S.66 – S.68 for replicas).

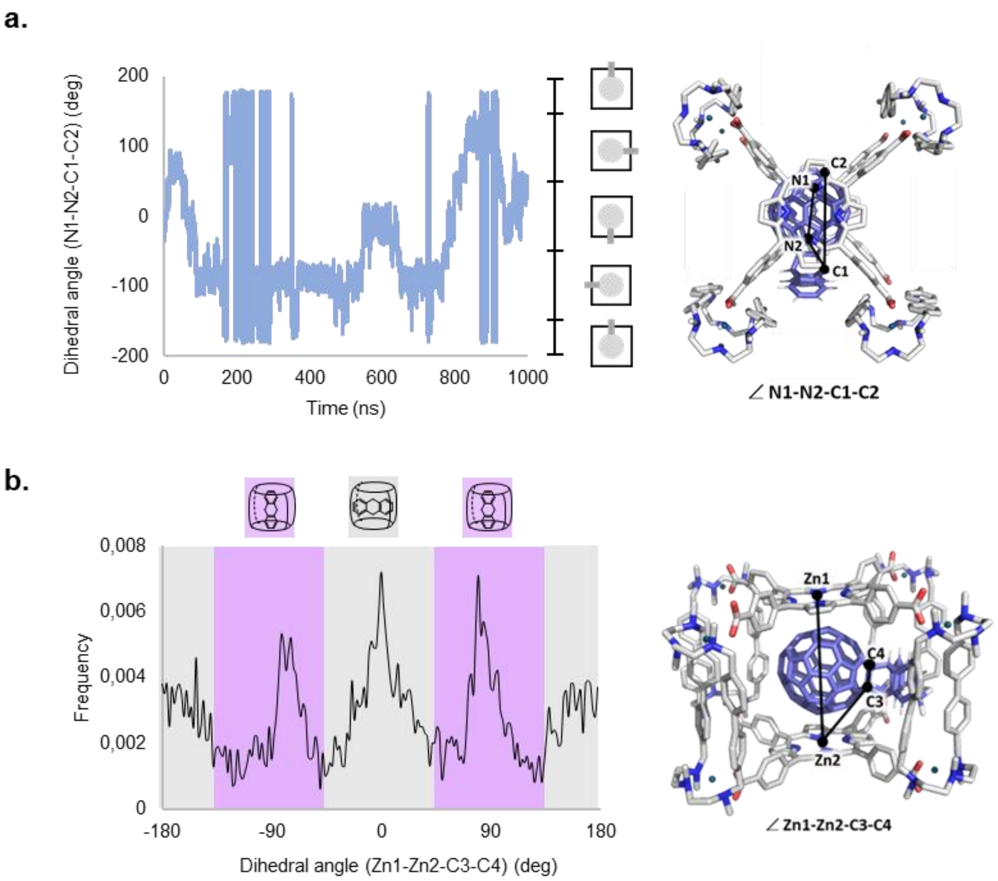

*Figure IV.4. Analysis and characterization of the host-guest equilibria of mono-An-$C_{60}$⊂**1b**·$(Cl)_8$ using MD simulations. a) ∠N1-N2-C1-C2 dihedral angle describes the relative rotation of the encapsulated mono-An-$C_{60}$ with respect to the nanocapsule gates along the MD simulation time. N1 and N2 are atoms from the porphyrin, while C1 and C2 are atoms from the fullerene derivative (see scheme). Different values explored for the ∠N1-N2-C1-C2 dihedral angle along the simulation time describe gate-to-gate rotations of the anthracene addend. b) ∠Zn1-Zn2-C3-C4 dihedral angle describes the relative orientation of the anthracene addend with respect to the nanocapsule porphyrins. Zn1 and Zn2 are atoms from the porphyrins, while C3 and C4 are atoms from the fullerene derivative (see scheme). The presented histogram plot (180 bins of 2 ° each) describes the most visited ∠Zn1-Zn2-C3-C4 dihedral values during the 1000 ns MD trajectory (see Annex IV Figures S.63 – S.65 for additional replicas).*

MD simulations of encapsulated mono-Pn-$C_{60}$ were carried out to gain insights into the differences in regiofunctionalization when the acene used in the templated Diels-Alder reaction is extended. Simulations revealed that the pentacene-based addend is fixed in a single window of the nanocapsule, since no gate-to-gate transitions are observed along the microsecond timescale MD trajectory (Figure IV.5.a). This is in sharp contrast to what was observed for the mono-An-$C_{60}$, in which gate-to-gate rotation are permitted at the same timescale. In addition, MD simulations showed that mono-Pn-$C_{60}$ could be only positioned in a perpendicular way (i.e. the pentacene addend pointing to the porphyrins of the cage) due to the steric hindrance that the molecular macrocyclic complexes of the nanocapsule exert to the bulkier addend (Figure IV.5.b, see Annex IV, Figures S.69 – S.71 for replicas). This is in sharp contrast to the mono-An-$C_{60}$ host-guest system, in which the guest is allowed to adopt both conformations (anthracene addend can be positioned in parallel and in perpendicular respect to the porphyrins). MD simulations of the *trans*-1-bis-Pn-C$_{60}$ host-guest system also showed that the guest is, as expected, fixed in a single orientation: with both addends pointing to the porphyrins of the nanocapsule (Annex IV, Figures S.73 – S.75).

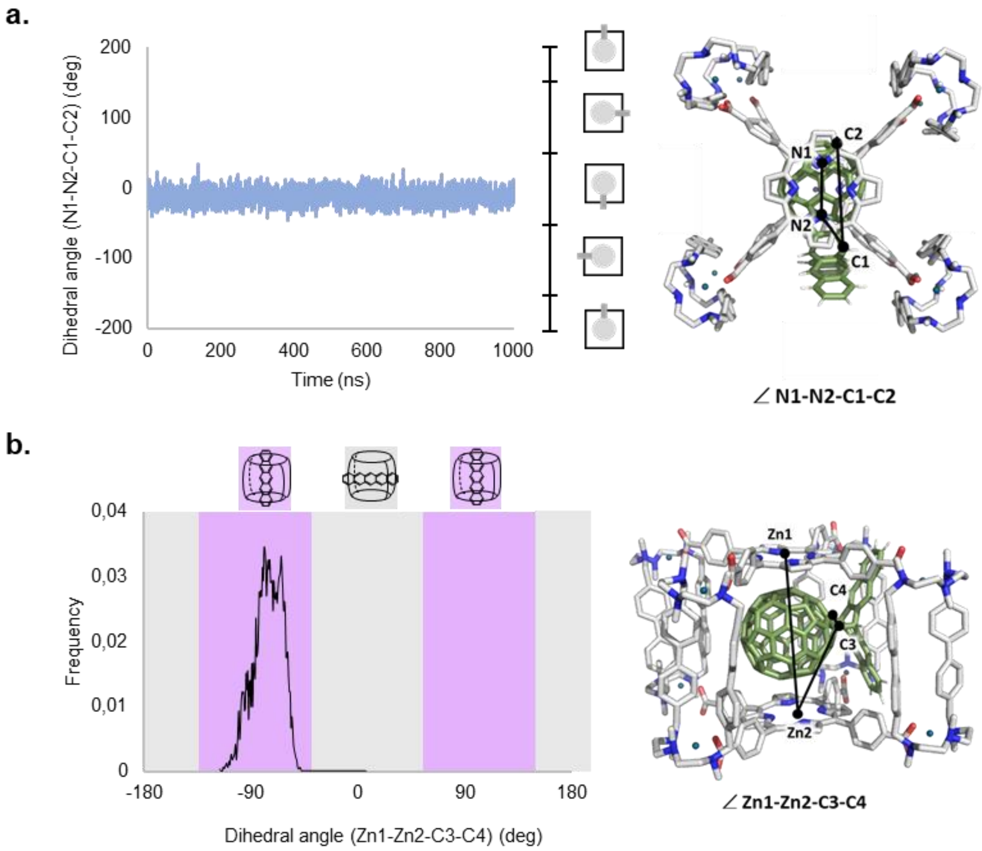

*Figure IV.5. Analysis and characterization of the host-guest equilibria of mono-Pn-C$_{60}$⊂**1b**·(Cl)$_8$ using MD simulations. a) ∠N1-N2-C1-C2 dihedral angle describes the relative rotation of the encapsulated mono-Pn-C$_{60}$ with respect to the nanocapsule gates along the MD simulation time. N1 and N2 are atoms from the porphyrin, while C1 and C2 are atoms from the fullerene derivative (see scheme). Different values explored for the ∠N1-N2-C1-C2 dihedral angle along the simulation time describe gate-to-gate rotations of the pentacene addend. b) ∠Zn1-Zn2-C3-C4 dihedral angle describes the relative orientation of the pentacene addend with respect to the nanocapsule porphyrins. Zn1 and Zn2 are atoms from the porphyrins, while C3 and C4 are atoms from the fullerene derivative (see scheme). The presented histogram plot (180 bins of 2 ° each) describes the most visited ∠Zn1-Zn2-C3-C4 dihedral values during the 1000 ns MD trajectory (see Annex IV Figures S.69 – S.71 for additional replicas).*

### *IV.2.2 Analysis of frontier molecular orbitals*

In order to fully understand the regioselectivity of the final products, careful analysis of the frontier molecular orbitals (FMOs) involved in the Diels-Alder reactions was performed.

In 1965, Woodward and Hoffmann proposed a set of rules to understand the reactivity trends of organic cycloaddition reactions based on the molecular orbital theory.[146] Frontier molecular orbitals are the highest occupied molecular orbital (HOMO) and the lowest unoccupied molecular orbital (LUMO), and for a thermally-allowed cycloaddition reaction, both FMOs of the involved species need to interacts in-phase (constructive overlap)[147]. For a standard or normal electron-demand Diels-Alder reaction, HOMO of the diene overlaps with LUMO of the dienophile (Figure IV.6). As mentioned before in this chapter, acenes (anthracene and pentacene) are considered the dienes of these systems and the corresponding mono-adducts are considered the dienophiles.

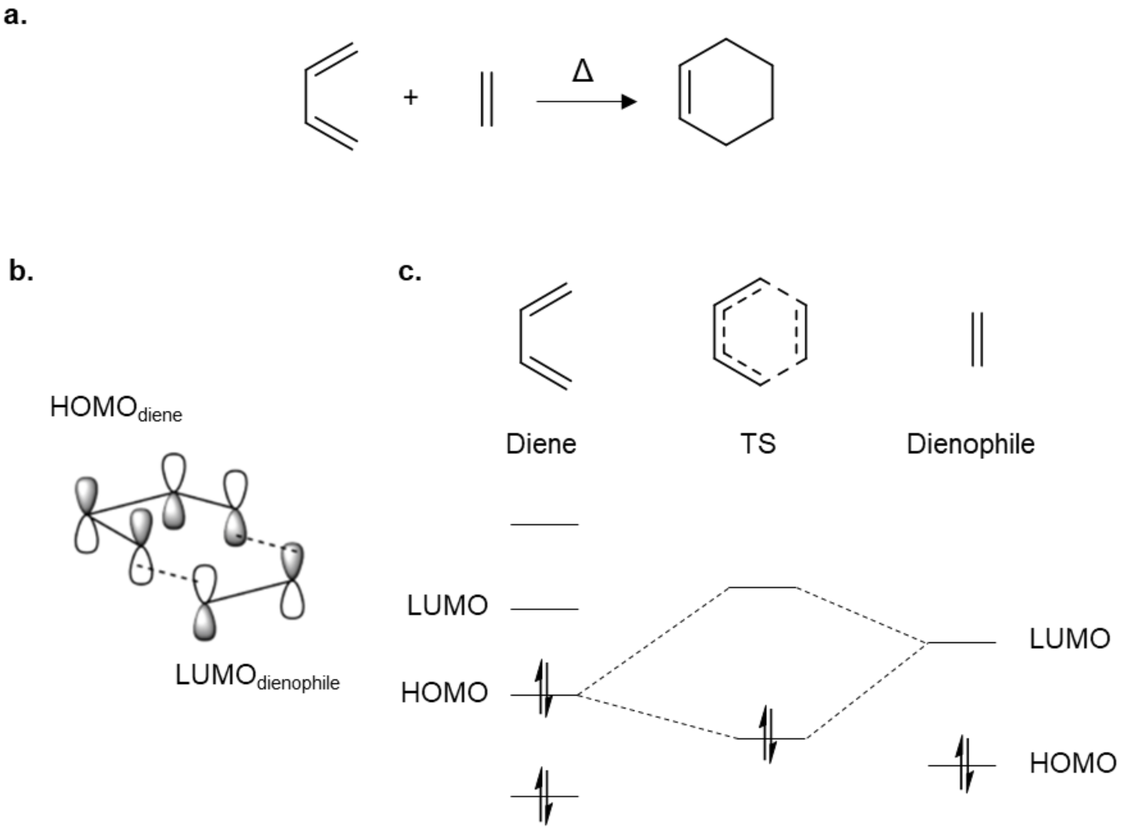

*Figure IV.6. a) A generic Diels-Alder reaction. b) Schematic representation of an effective overlap between $\mathrm{HOMO}_{diene}$ and $\mathrm{LUMO}_{dienophile}$ of a generic normal electron-demand Diels-Alder reaction. c) Generic molecular orbital diagram of a normal electron-demand Diels-Alder reaction. TS: transition state*

LUMOs and HOMOs of anthracene, pentacene, mono-An-$C_{60}$ and mono-Pn-$C_{60}$ were calculated and analysed using the HF/6-31G(d,p) basis set. Reaction energies were calculated using DFT calculations (see computational details in *Chapter III. Methodology*). FMO of mono-An-$C_{60}$ also were calculated with a truncated model system based on two porphyrins with one mono-adduct molecule in between (equivalent model system to the ones used in previous similar systems[34,89,126]) to demonstrate that the distribution of LUMOs of 2xPorph/mono-An-$C_{60}$ complex is totally equivalent to the distribution of the orbital lobes of mono-An-$C_{60}$ molecule (Annex IV, Figure S.77).

In order to understand the regioselectivity outcome of the Diels-Alder reaction when using anthracene, HOMO of the anthracene and LUMOs of mono-An-$C_{60}$ were studied. LUMO of mono-An-$C_{60}$ (-0.090 eV) has the appropriate antibonding orbital contributions on the equatorial bond (*e* bond), while close in energy, LUMO+1 (0.117 eV) has also appropriate antibonding orbital lobes localized on the equatorial-prime bond (*e'* bond) (Figure IV.7). Functionalization of any of these two bonds (*e* and *e'*) from the mono-adduct would lead to the same bis-adduct product by symmetry. Other bonds of the mono-An-$C_{60}$ surface also exhibit appropriate antibonding LUMO or LUMO+1 contributions; however, their functionalization is restricted due to sterics imposed by the nanocapsule (see Annex IV, Figure S.76 for more perspectives of each LUMO).

Since mono-An-$C_{60}$ spins along its $C_{2v}$ axis inside the nanocapsule as seen by MD simulations, both equatorial bonds (*e* and *e'*) are exposed to a gate and accessible to perform a Diels-Alder reaction. On the other hand, the *trans*-1 bond has antibonding orbital contributions in the LUMO+2, and it is accessible from the opposite gate of the nanocapsule. However, the significantly higher energy of this molecular orbital (0.411 eV) with respect to the LUMO and LUMO+1 makes the *trans*-1 bond kinetically much less reactive than the equatorial ones.

Taking all these parameters into account, the kinetically most favourable second Diels-Alder addition is expected to be at one of the equatorial positions (*e* or *e'*) rather than at *trans*-1, leading to the exclusive formation of *e,e*-bis-An-$C_{60}$, which also corresponds to the thermodynamically more stable product (see calculated reaction energies for the formation of the corresponding equatorial and *trans*-1 bis-adducts, Annex IV, Table S.2) and is in good agreement with the experimental section.

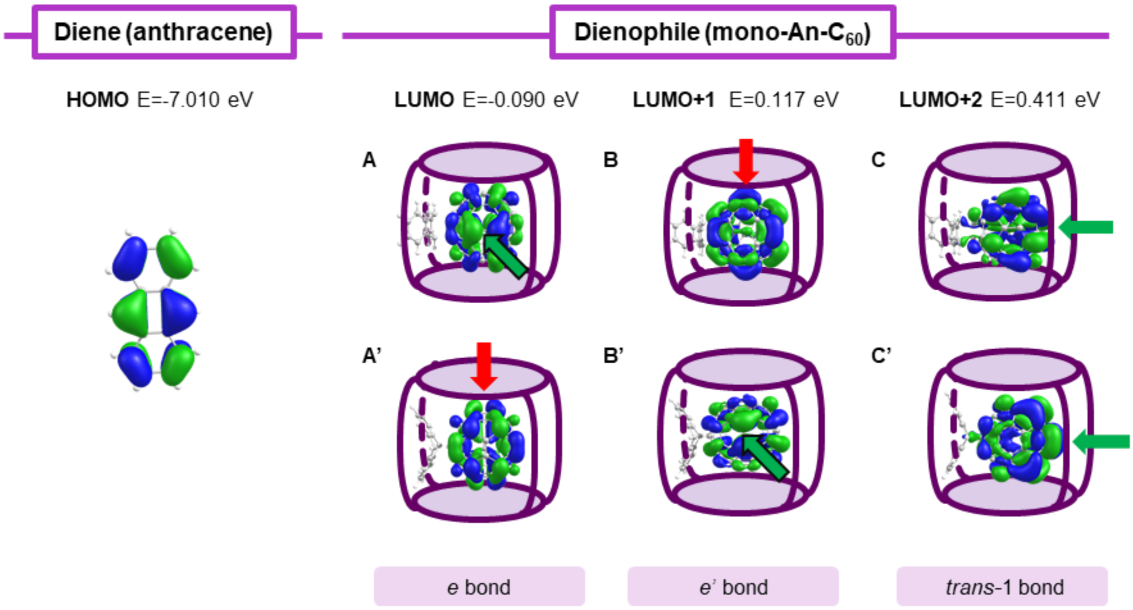

*Figure IV.7. Frontier molecular orbitals involved in the Diels-Alder reaction with anthracene. HOMO of anthracene and LUMO, LUMO+1 and LUMO+2 of mono-An-$C_{60}$ given in eV. A schematic representation of the mono-adducts' LUMOs when encapsulated is shown. Two possible orientations of mono-An-$C_{60}$ are depicted inside the nanocapsule, considering its possible rotation as characterized from MD simulations: anthracene addend oriented in parallel (A, B and C) or perpendicularly (A', B' and C') with respect to the porphyrins.*

The same reasoning was developed to study the regioselectivity outcome of the Diels-Alder reaction when using pentacene considering the same geometrical restrictions imposed by the nanocapsule.

Taking into account the unique permitted orientation of mono-Pn-$C_{60}$ that is formed inside the nanocapsule (pentacene addend pointing towards the porphyrins), the first LUMO orbital (-0.095 eV) does not have antibonding contributions localized on any bond that is easily accessible from the windows of the cage (Figure IV.8). LUMO+1 (0.114 eV) has appropriate antibonding lobes on the *e'* bond that are exposed to a gate. Nevertheless, the *e'* bond is oriented perpendicular to the porphyrins, which implies that the second pentacene moiety would approach parallel to the porphyrins for reaction, and it has been demonstrated by MD simulations that this conformation is not allowed. For this reason, the second addition of a pentacene to mono-Pn-$C_{60}$ reacts through the less reactive LUMO+2 (0.408 eV). Even it is higher in energy, it has appropriate antibonding lobes that are exposed to a gate and is localized on the *trans*-1 bond. This position implies that the second pentacene addend is positioned in a permitted fashion (vertically with respect to the porphyrins) without any steric hindrance, as seen by MD simulations (see Annex IV, Figure S.78 for more perspectives of each LUMO). Therefore, although LUMO+2 is expected to be kinetically less reactive than LUMO or LUMO+1, geometric restrictions imposed by the supramolecular mask favour the regioselective formation of *trans*-1-bis-Pn-$C_{60}\subset$**1b**$\cdot(Cl)_8$, which corresponds to the thermodynamically less stable product in the absence of the nanocapsule (Annex IV, Table S.2).

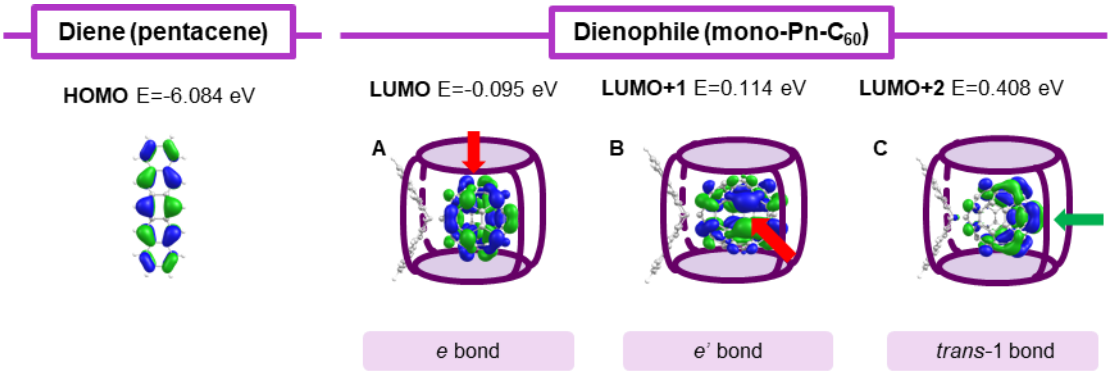

*Figure IV.8. Frontier molecular orbitals involved in the Diels-Alder reaction with pentacene. HOMO of pentacene and LUMO, LUMO+1 and LUMO+2 of mono-Pn-$C_{60}$ given in eV. A schematic representation of the mono-adducts' LUMOs when encapsulated is shown.*

## IV.3 Controlled regioselective synthesis of poly-heteroadducts of $C_{60}$

Synthesis of bis-heteroadducts combining anthracene and pentacene addends was carried out. Mono-An-$C_{60}$ was fully encapsulated within **1b**$\cdot(BArF)_8$ and 1.1 equivalents of pentacene were added. The major product detected by HR-ESI-MS was an encapsulated bis-adduct which contained one anthracene- and one pentacene-based addend (Figure IV.9.b). This bis-adduct was purified and characterized by 1D and 2D NMR in order to know the distribution of the addends (Annex IV, Figure S.18 – S.24). In the $^1$H-NMR spectrum, the diagnostic distribution of signals 1:2:1 between 4.9 and 5.7 ppm that corresponds to the cycloadded $C_{sp3}$ protons confirmed the equatorial nature of the derivative (*e,e*-bis-An-Pn-$C_{60}$, **5**) (Figure IV.9.c), as seen before in the NMR characterization of *e,e*-bis-An-$C_{60}$ (**2**). In the NOESY spectrum, singlets integrating one proton each at 4.98 and 5.62 ppm (cycloadded $C_{sp3}$ protons) correlate to the singlets (7.95 and 8.10 ppm) of the $C_{sp2}$ protons of the pentacene addend (Figure IV.9.d), meaning that $C_{sp3}$ protons of the pentacene addend have different electronic environment and they are not chemically equivalents. Thus, the derivative has been necessarily formed with the pentacene addend in vertical orientation within the mask, as depicted in Figure IV.9.a.

Synthesis of heteroadducts combining Diels-Alder and Bingel reaction (an addition-elimination reaction that adds cyclopropane rings to fullerenes)[148] were performed using encapsulated *e,e*-bis-An-$C_{60}$ and *trans*-1-Pn-$C_{60}$ as starting platforms via supramolecular mask strategy.

*e,e*-bis-An-$C_{60}$ was encapsulated in the more adaptable Cu$^{II}$-based **1c**·(BArF)$_8$, since the encapsulation in the analogous Pd$^{II}$-based nanocapsule (**1b**·(BArF)$_8$) was not efficient due to its rigidity of the gate entrances. Once the *e,e*-bis-An-$C_{60}$⊂**1c**·(BArF)$_8$ host-guest complex was formed, Bingel reaction using diethyl bromomalonate and sodium hydride was performed. After HR-ESI-MS monitoring, a tris-adduct (bis-An-mono-diethylmalonate-$C_{60}$) rising from the addition of one diethyl malonate was detected as the major product (Figure IV.10.b). After releasing it from the nanocapsule with a solvent-washing protocol with $CHCl_3$, careful characterization by NMR, MALDI-MS and UV-vis spectroscopic analyses (Annex IV, Figures S.25 – S.34) revealed that a mixture of only two tris-adducts (i.e. two regioisomers **6**(I) and **6**(II)) was detected in a 1:3.7 ratio. In the $^1$H-NMR spectrum, two sets of singlets with a 1:1:1:1 distribution corresponding to the cycloadded $C_{sp3}$ protons of the anthracene-based addends were found between 4.8 and 5.6 ppm, confirming that there are two regioisomers of tris-adducts: *e,e*-bis-An-*e*-mono-diethylmalonate-$C_{60}$ **6**(I) and **6**(II) (Figure IV.10.c).

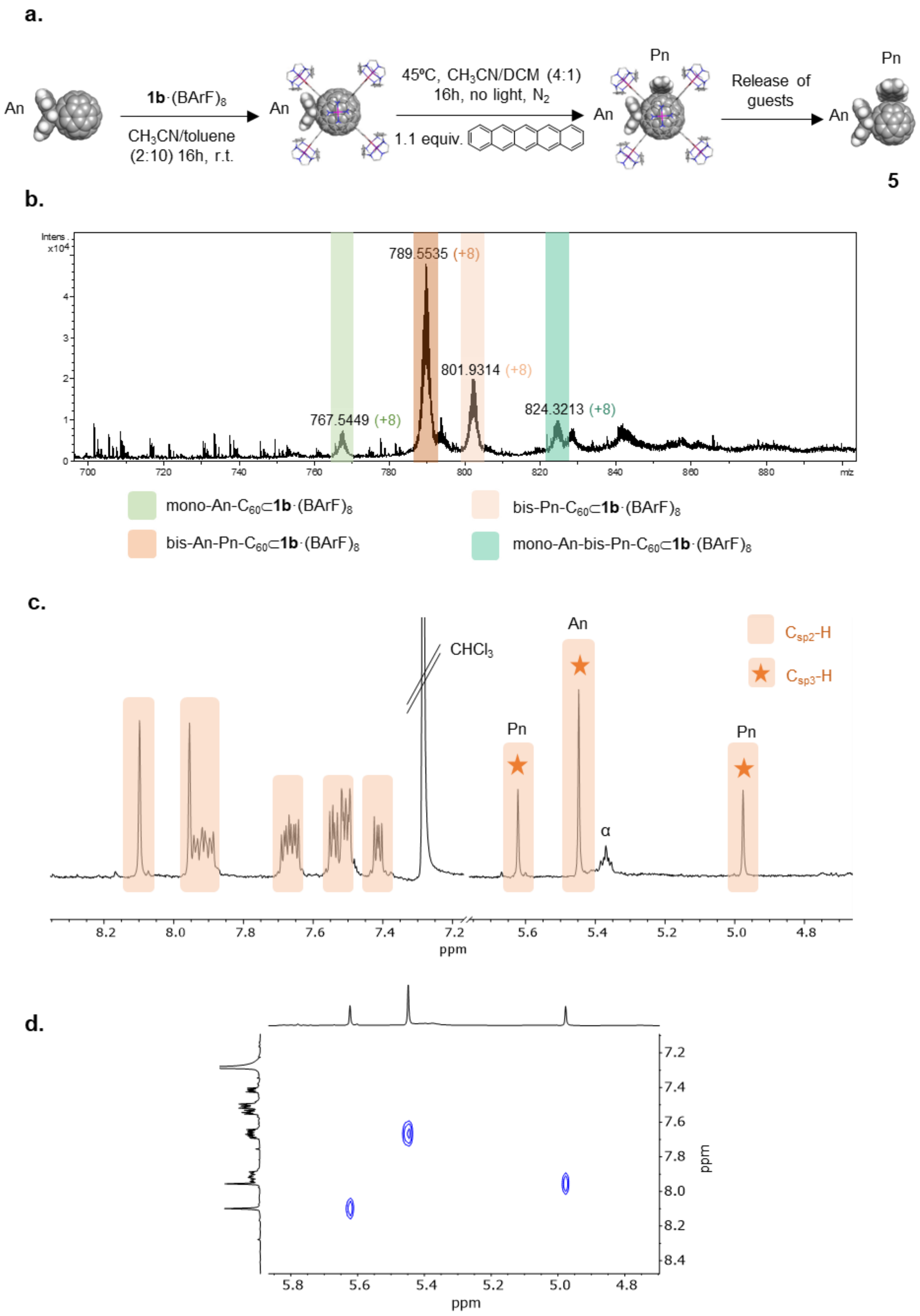

*Figure IV.9. a) Schematic representation of the synthesis of **5** using **1b**·(BArF)$_8$ as a supramolecular mask. b) HR-ESI-MS monitoring of the formation of bis-An-Pn-C$_{60}$⊂**1b**·(BArF)$_8$. c) $^1$H-NMR spectrum of e,e-bis-An-Pn-C$_{60}$ (**5**). α: TLC-silica impurities. In orange, signals corresponding to protons of anthracene and pentacene addends (highlighting with a star the cycloadded C$_{sp3}$ protons). d) NOESY NMR of cycloadded C$_{sp3}$ protons correlating to aromatic C$_{sp2}$ protons.*

Encapsulation of *trans*-1-bis-Pn-$C_{60}$ in order to hetero-functionalize this fullerene derivative was not efficient, even using $Cu^{II}$-based **1c**·(BArF)$_8$ (only minor amounts of this encapsulated bis-adduct were detected by HR-ESI-MS). This was somehow expected from MD analyses that described that pentacene addend of mono-Pn-$C_{60}$ (which is pointing to the porphyrins) stands out from the nanocage (Annex IV, Figure S.72). Therefore, Bingel reaction was performed on mono-Pn-$C_{60}$⊂**1b**·(BArF)$_8$, in which mono-adduct **3** was successfully encapsulated by **1b**·(BArF)$_8$ (Annex IV, Figure S.11 – S.13). The hetero-functionalization gave rise to a tris-adduct as the main product (mono-Pn-bis-diethylmalonate-$C_{60}$) alongside small amounts of the corresponding hetero-tetrakis-adduct (Figure IV.11.b), despite pushing the experimental conditions (heating and larger conditions times). Successfully, a single isomer of the tris-heteroadduct (**7**) was found in a 63% yield after releasing the guests by a solvent-washing protocol with $CHCl_3$ and a complete characterization by NMR, MALDI-MS and UV-vis spectroscopy (Annex IV, Figure S.35 – S.44). The solely singlet at 5.86 ppm of the $^1$H-NMR spectrum (Figure IV.11.c) indicates that cycloadded $C_{sp3}$ protons of pentacene-based addends are positioned in a *trans*-1 fashion.

Hetero-hexakis-adducts were also prepared by taking advantage of the directing ability of the Diels-Alder addends of *e,e*-bis-An-$C_{60}$ and *trans*-1-Pn-$C_{60}$.

*e,e*-bis-An-$C_{60}$ was subjected to Bingel cyclopropanation with a large excess of diethyl bromomalonate and NaH. After 48 hours of reaction, hexakis-heteroadduct was mainly formed with small amounts of pentakis-adducts, as confirmed by MALDI-MS and NMR (Annex IV, Figures S.45 – S.52). The 2:1:1 distribution pattern of signals in the $^1$H-NMR spectrum corresponding to the cycloadded $C_{sp3}$ protons confirmed that the $C_s$ symmetry featured by *e,e*-bis-An-$C_{60}$ (**2**) remained (Figure IV.12.b). Therefore, the octahedral $T_h$-hetero-hexakis-adduct (**8**) was formed as the major product.

Finally, *trans*-1-Pn-$C_{60}$ was also subjected to exhaustive Bingel cyclopropanation following the same conditions as the cyclopropanation of *e,e*-bis-An-$C_{60}$. After 2 days of reaction, hexakis-heteroadduct (**9**) was formed as the unique product as monitored by TLC and HPLC (Annex IV, Figure S.53). After characterization by MALDI-MS and NMR (Annex IV, Figure S.54 – S.61), the only singlet found at 5.43 ppm in the $^1$H-NMR spectrum corresponding to the cycloadded $C_{sp3}$ protons confirmed again that the $D_{2h}$ symmetry of *trans*-1-Pn-$C_{60}$ (**4**) remained intact (Figure IV.12.d). Thus, Bingel reaction took place along all the equatorial belt of the bis-adduct, obtaining the corresponding octahedral heteroadduct as the unique product.

Notably, diffusion coefficients extracted from diffusion-ordered NMR spectroscopy (DOSY-NMR) of all homo- and heteroderivatives were in strong agreement with the increasing bulkiness of the molecules (Annex IV, Figure S.62).

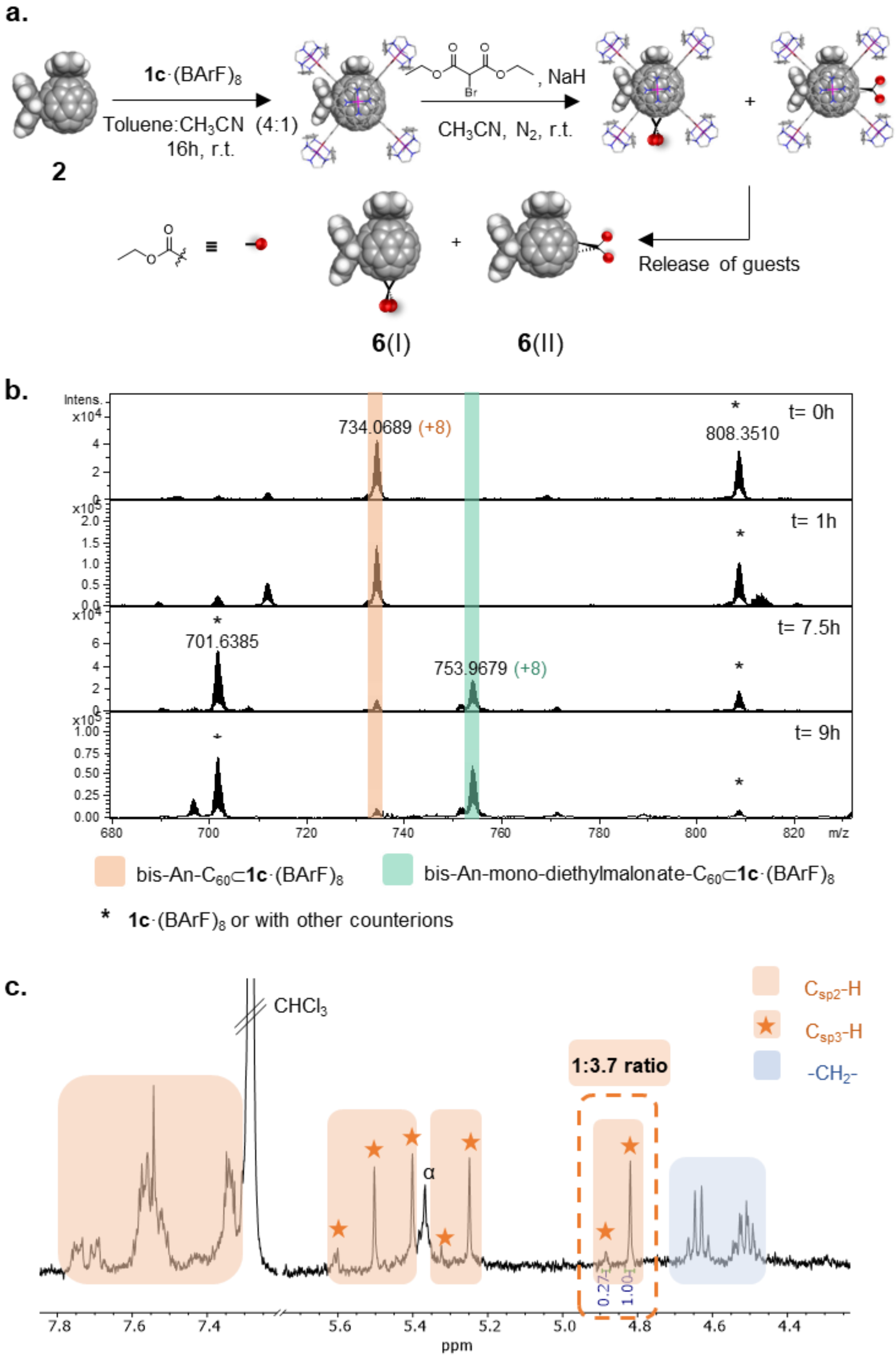

*Figure IV.10. a) Schematic representation of the synthesis of **6** using **1c**·(BArF)$_8$ as a supramolecular mask. b) HR-ESI-MS monitoring of the formation of bis-An-mono-diethylmalonate-C$_{60}$⊂**1c**·(BArF)$_8$ (mixture of isomers **6**(I) and **6**(II)). c) $^1$H-NMR spectrum of e,e-bis-An-e-mono-diethylmalonate-C$_{60}$ **6**(I) and **6**(II). In orange, signals corresponding to protons of anthracene addends (highlighting with a star the cycloadded C$_{sp3}$ protons); in blue, signals corresponding to protons of diethyl malonate addend.*

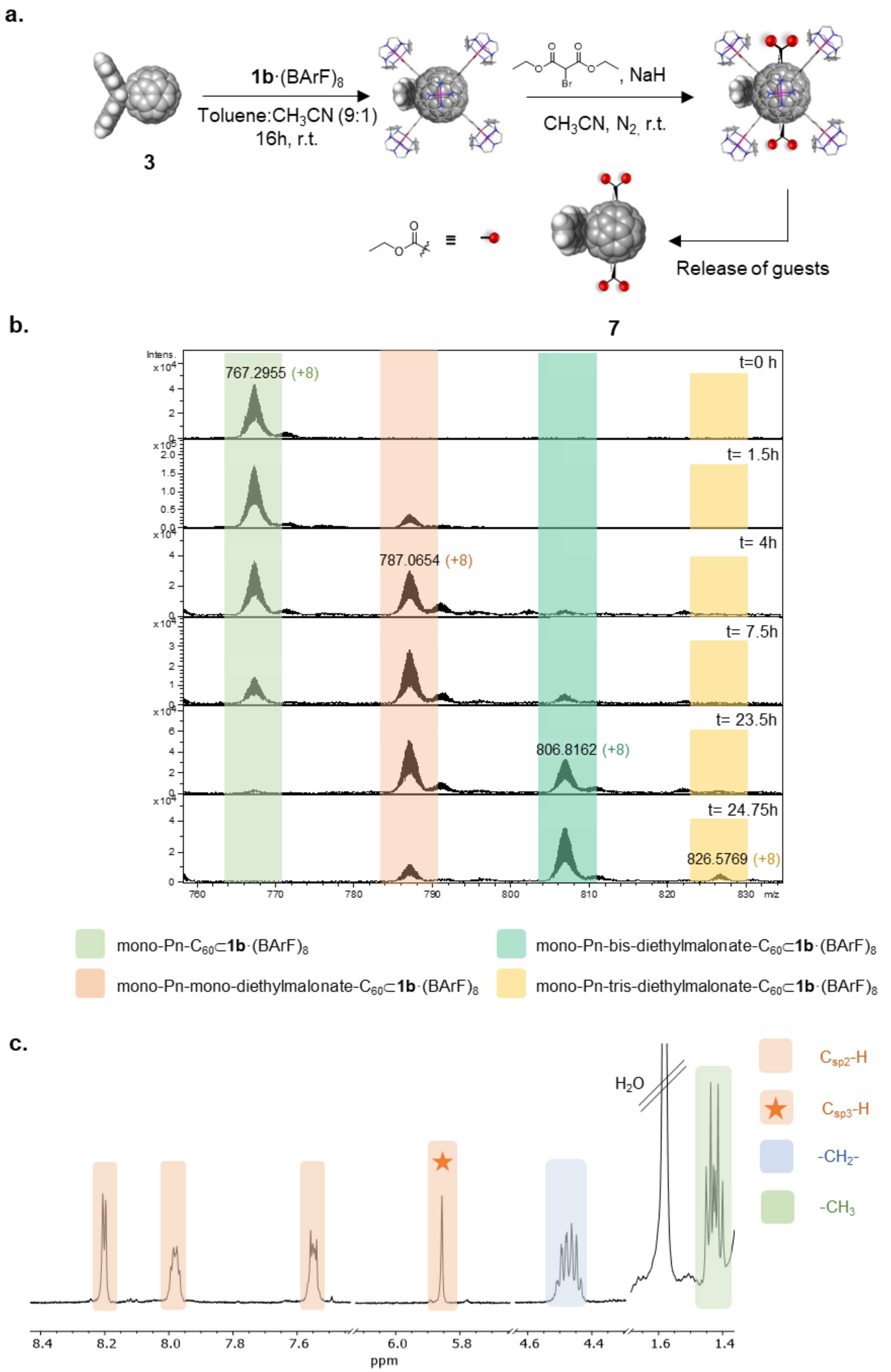

*Figure IV.11. a) Schematic representation of the synthesis of **7** using **1b**·(BArF)$_8$ as a supramolecular mask. b) HR-ESI-MS monitoring of the formation of mono-Pn-bis-diethylmalonate-C$_{60}$⊂**1b**·(BArF)$_8$. c) $^1$H-NMR spectrum of e-mono-Pn-trans-1-bis-diethylmalonate-C$_{60}$ (**7**). In orange, signals corresponding to protons of pentacene addends (highlighting with a star the cycloadded C$_{sp3}$ protons); in blue and green, signals corresponding to protons of diethyl malonate addend.*

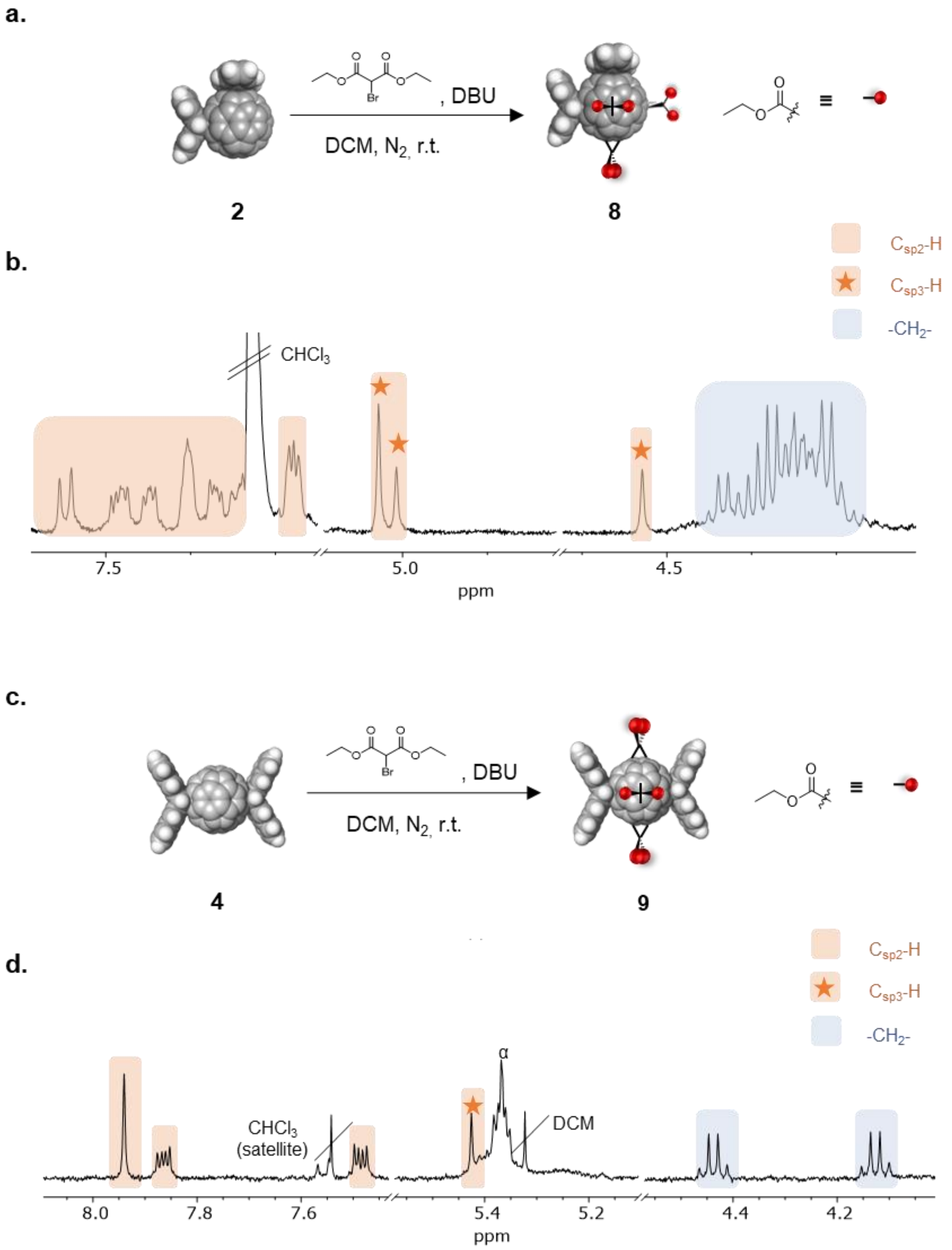

*Figure IV.12. a) Schematic representation of the synthesis of **8**. b) $^1$H-NMR spectrum of e,e-bis-An-based Th-hetero-hexakis-$C_{60}$ (**8**). c) Schematic representation of the synthesis of **9**. d) $^1$H-NMR spectrum of trans-1-bis-Pn-e,e,e,e-tetrakis-diethylmalonate-$C_{60}$ (**9**). In orange, signals corresponding to protons of pentacene addends (highlighting with a star the cycloadded $C_{sp3}$ protons); in blue, signals corresponding to protons of diethyl malonate addend.*

# CHAPTER V. TWO-FOLD ENHANCEMENT OF EQUATORIAL BIS-PCBM-$C_{60}$ ADDUCTS USING A SUPRAMOLECULAR MASK

This chapter corresponds to the following publication:

Pujals, M; Iannace, V.; Ribas, X. *Supramol. Chem.* **2024**.
DOI: 10.1080/10610278.2024.2338141

## V.1 Diazo compounds as precursors for the synthesis of PCBM-based derivatives

[6,6]-phenyl-$C_{61}$-butyric acid methyl ester ($PC_{61}BM$) is the [6,6]-methanofullerene most used as electron acceptor material in bulk heterojunction solar cells and as electron transport layer in perovskite-based solar cells devices because of its easy-accessibility and high solubility in many solvents, as discussed in *I.2.1.1 Photovoltaics applications*. Nevertheless, PCBM preparative methods have been limited to the few classical procedures reported by Hummelen, Wudl and coworkers in mid 90s.[149,150] These methods require the presence of 1-phenyl-1-[3-(methoxycarbonyl)propyl]diazomethane as the active species to perform the cyclopropanation on fullerenes. This diazo compound is formed *in situ* through base-induced decomposition of 4-benzoylbutyrate-*p*-tosylhydrazone, which is synthesized following an easy 2-step synthetic route: commercial 4-benzoylbutyric acid is esterified with the presence of methanol, followed by the inclusion of a tosyl group at the benzylic position.[150] Once the diazo compound is generated, it undergoes a 1,3-dipolar cycloaddition towards $C_{60}$ (Figure V.1). This method gives rise to isomeric intermediates, named [5,6]-fulleroids, which require conversion into the corresponding [6,6]-methanofullerene by thermal or electrochemical processing (heating up to 180°C).

If PCBM-based bis-adducts are targeted, up to 22 spectroscopically-distinguishable regioisomers can be formed in front of the 8 potential regioisomers obtained when symmetrical precursors are used, since the former don't present symmetric substituent groups.[81,96] For this reason, there is an urge to control the regioselectivity of these reactions in order to avoid the formation of mixtures of multiple regioisomers and, thus, to avoid the use of long, expensive and often unsuccessful chromatographic methods.

Following the supramolecular mask approach from Ribas' group,[29] tetragonal prismatic nanocapsules (see Chapter IV, Figure IV.1) were used to explore the regioselective formation of PCBM-like bis-adducts using the abovementioned conditions. The excellent affinity between **1b**·(BArF)$_8$ nanocapsule and $C_{60}$ fullerene ($K_a$ ~ $10^7$ $M^{-1}$)[89] and the stability of this host-guest complex under the Bingel reaction prompted us to test this supramolecular nanocapsule as a mask to synthesize PCBM-based derivatives.

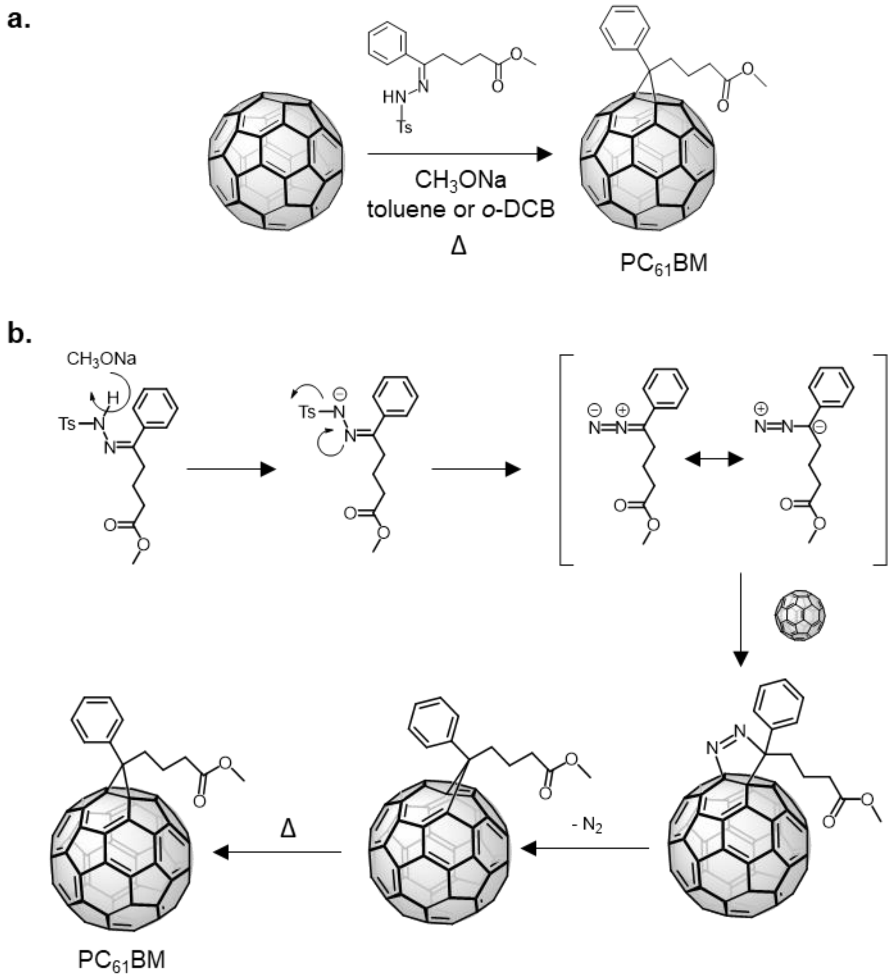

*Figure V.1. a) Formation of PC$_{61}$BM through 1,3-dipolar cycloaddition using diazo compounds. b) Reaction mechanism of 1,3-dipolar cycloaddition for the formation of PC$_{61}$BM.*

First, PC$_{61}$BM was encapsulated within the cavity of **1b**·(BArF)$_8$. The encapsulation was completed with the addition of 1.5 equivalents of guest. Following conditions by Hummelen and Wudl, the 1,3-dipolar cycloaddition was performed using PCBM-C$_{60}$$\subset$**1b**·(BArF)$_8$, 1 equivalent of $CH_3ONa$ and 1 equivalent of 4-benzoylbutyrate-*p*-tosylhydrazone in acetonitrile under inert atmosphere. After 16 hours of stirring at 70°C, encapsulated bis-adduct **11** (bis-PCBM-C$_{60}$$\subset$**1b**·(BArF)$_8$) was the main product of the crude (Figure V.2).

Products were released from **1b**·(BArF)$_8$ by disassembly of the nanocapsule by the addition of trifluoromethanesulfonic acid. Next, they were heated up at 115°C for 24 hours in toluene in order to perform the completed isomerization from open [5,6]-fulleroids to closed [6,6]-methanofullerenes. Unfortunately, broad peaks were observed when the crude was analysed by HPLC (Figure V.3) and an intractable mixture of isomers was formed, indicating that the reaction was not regioselective.

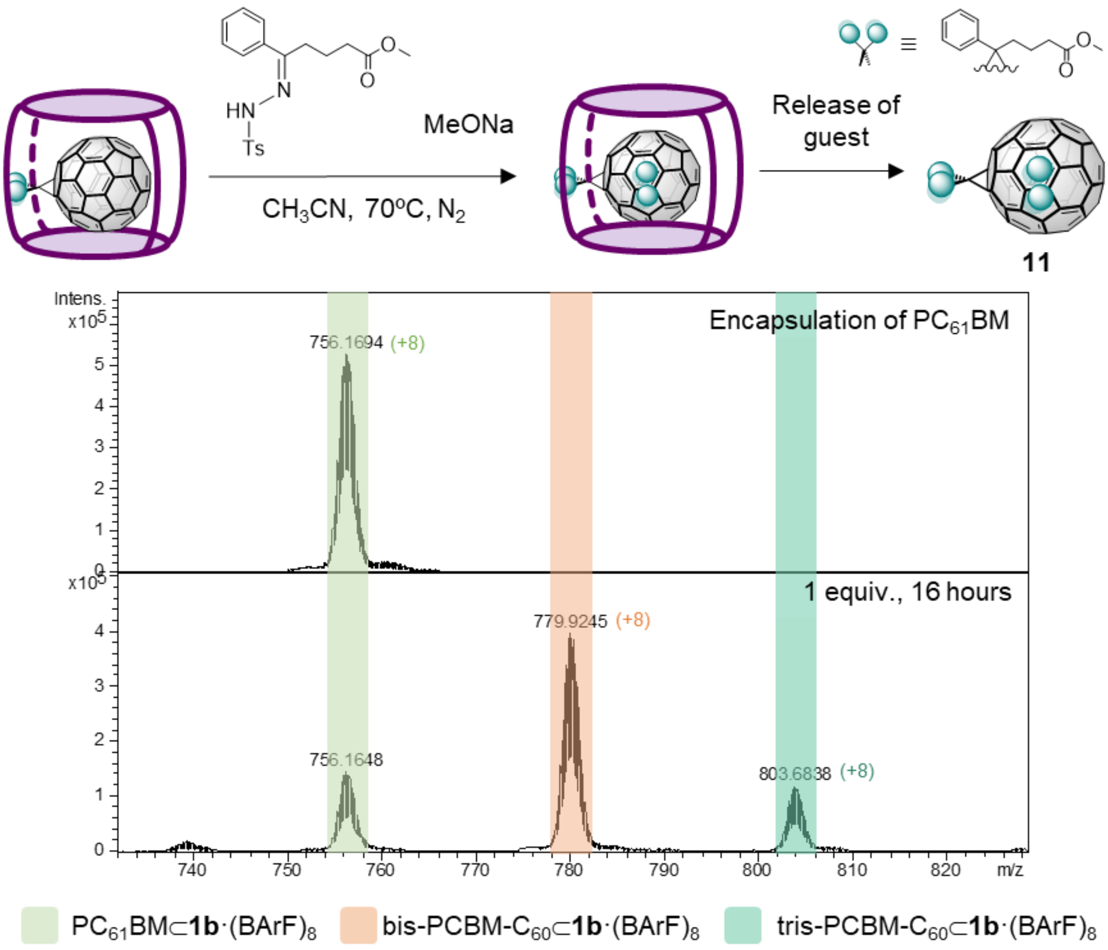

*Figure V.2. HR-ESI-MS monitoring of the formation of bis-PCBM-$C_{60}\subset$**1b**·(BArF)$_8$ via 1,3-dipolar cycloaddition.*

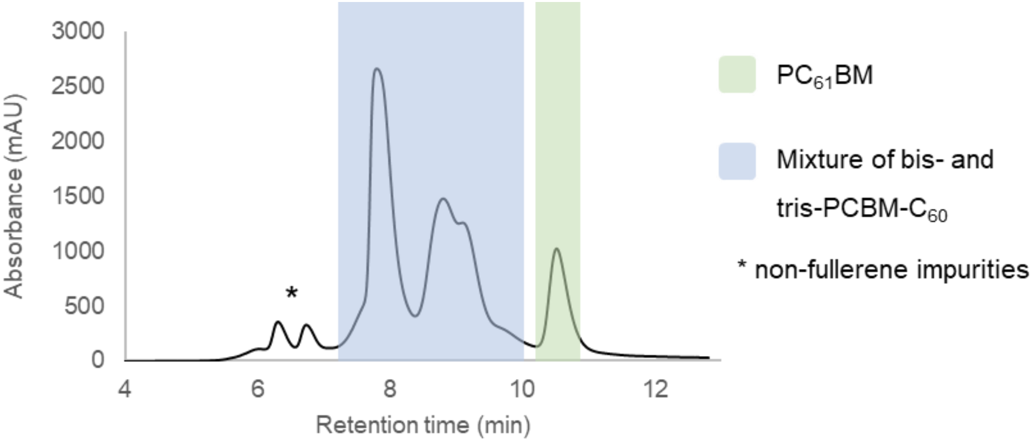

*Figure V.3. HPLC analysis of products after conversion from [5,6]-fulleroids into [6,6]-methanofullerenes without the presence of* ***1b****·(BArF)$_8$. 1,3-dipolar cycloaddition was performed via supramolecular mask strategy.*

Attempts of carrying out the isomerization process with the presence of the cage were also performed (115°C in acetonitrile for 24 hours). Unfortunately, the harsh conditions provoked total decomposition of the cage and the resulting crude could not be analysed.

## V.2 Sulfur ylides as precursors to synthesize PCBM-like derivatives

Since **1b**·(BArF)$_8$ nanocapsule was not stable under classical conditions for the synthesis of PCBM-like derivatives, a milder alternative reaction had to be used.

Among the various synthetic approaches to produce fullerene derivatives, addition-elimination reactions such as Bingel reaction,[148] reactions of stabilized sulfur ylides[151] or reactions of silylated nucleophiles[152] efficiently afford directly closed [6,6]-methanofullerenes. This means that is not necessary to undergo isomerization processes, since [5,6]-open fulleroids are not generated and, thus, these reactions can be carried out under mild conditions. Nevertheless, the resulting cyclopropane rings possess carbonyl groups which limits the preparation of PCBM-based derivatives. Ohno, Ito and coworkers reported in 2013 an alternative to these strategies, which involve a sulfur semi-stabilized ylide (a ylide stabilized with a phenyl group) generated *in situ* from the corresponding sulfonium salt with the presence of a base (such as 1,8-diazabicyclo(5.4.0)undec-7-ene, DBU) (Figure V.4).[153] Since the reaction proceeds via addition-elimination and under simpler, milder conditions (room temperature) than classical methods, the reaction was used to prepare the desired bis-adducts following the supramolecular shadow mask approach.

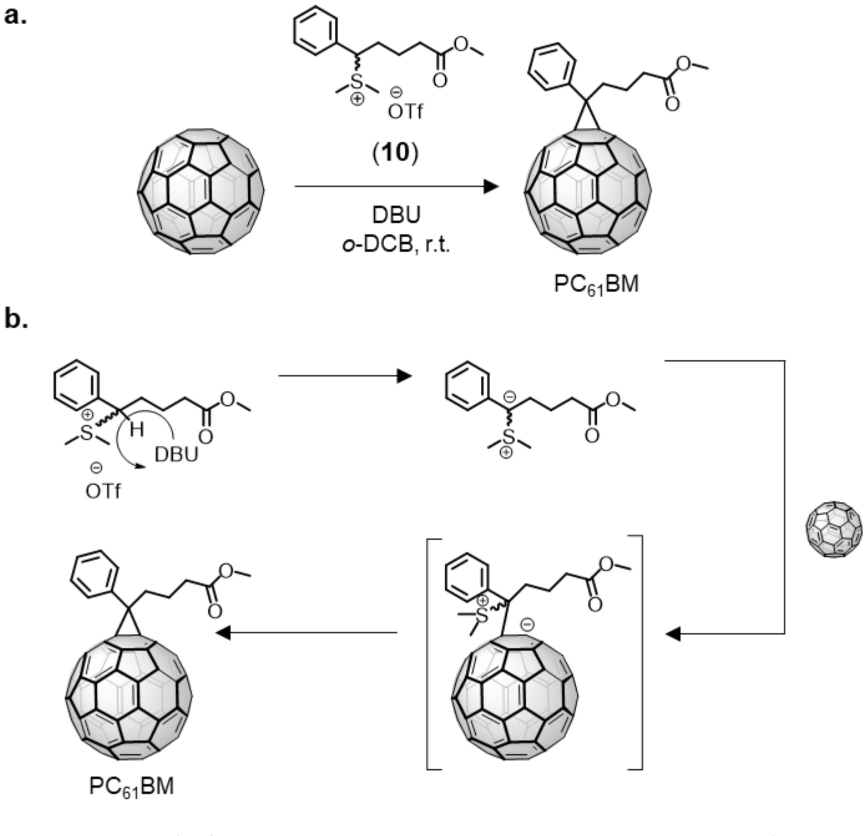

*Figure V.4. a) Formation of PC$_{61}$BM through addition-elimination reaction using sulfur semi-stabilized ylides. b) Reaction mechanism of addition-elimination reaction at the [6,6] bond for the formation of PC$_{61}$BM.*

### *V.2.1 Synthesis of PCBM-based bis-homoadducts*

The corresponding sulfonium salt, dimethyl(5-methoxy-5-oxo-1-phenylpentyl)sulfonium triflate (**10**), was synthetized following a reported 2-step synthetic route. Bromination of methyl-5-phenylpentanoate at the benzyl position followed by a nucleophilic substitution of the bromide with dimethyl sulfide achieved the desired salt (see details in *Annex V.1 Experimental procedures* and $^1$H-NMR characterization in Annex V, Figures S.79 – S.81).[153]

Since **1b**·(BArF)$_8$ nanocapsule is not stable with the presence of DBU, a brief screening of four bases to deprotonate the sulfonium salt was performed. Four equivalents of each base and four equivalents of sulfonium salt were added to four solutions of C$_{60}$⊂**1b**·(BArF)$_8$ in acetonitrile at room temperature under inert atmosphere. The reaction was monitored by HR-ESI-MS (Table V.1).

*Table V.1. Screening of bases to prepare PCBM-based bis-adducts using **1b**·(BArF)$_8$. [a]Ratio calculated by HR-ESI-MS after 3 hours. [b]Nanocapsule could not be detected by HR-ESI-MS since it decomposed.*

| Experiment | Base | Ratio C$_{60}$⊂**1b**·(BArF)$_8$ : PC$_{61}$BM⊂**1b**·(BArF)$_8$ [a] |
|---|---|---|
| 1 | DBU | --- [b] |
| 2 | NaH | 1:0 |
| 3 | NEt$_3$ | |
| 4 | CH$_3$ONa | 1:0.33 |

Apart from DBU, bases such sodium hydride or triethylamine (NEt$_3$) were tested, but the reaction didn't proceed at all. Then, sodium methoxide (MeONa) was used for the formation of PC$_{61}$BM. After 3 hours, a ratio of 1:0.33 encapsulated C$_{60}$:mono-adduct (C$_{60}$⊂**1b**·(BArF)$_8$ and PC$_{61}$BM⊂**1b**·(BArF)$_8$, respectively) was observed, indicating that the 1,3-dipolar cycloaddition took place.

After this brief screening, the optimization of the yield to obtain bis-homoadducts was performed. Starting from PC$_{61}$BM⊂**1b**·(BArF)$_8$ in acetonitrile, 2.5 equivalent of the sulfonium salt **10** and MeONa were added sequentially at room temperature, as can be seen in Figure V.5. After 18.5 hours, encapsulated bis-adduct **11** was the main product (68%, bis-PCBM-C$_{60}$⊂**1b**·(BArF)$_8$) alongside minor quantities of encapsulated mono-adduct (22%, PC$_{61}$BM⊂**1b**·(BArF)$_8$) and tris-adduct (10%, tris-PCBM-C$_{60}$⊂**1b**·(BArF)$_8$).

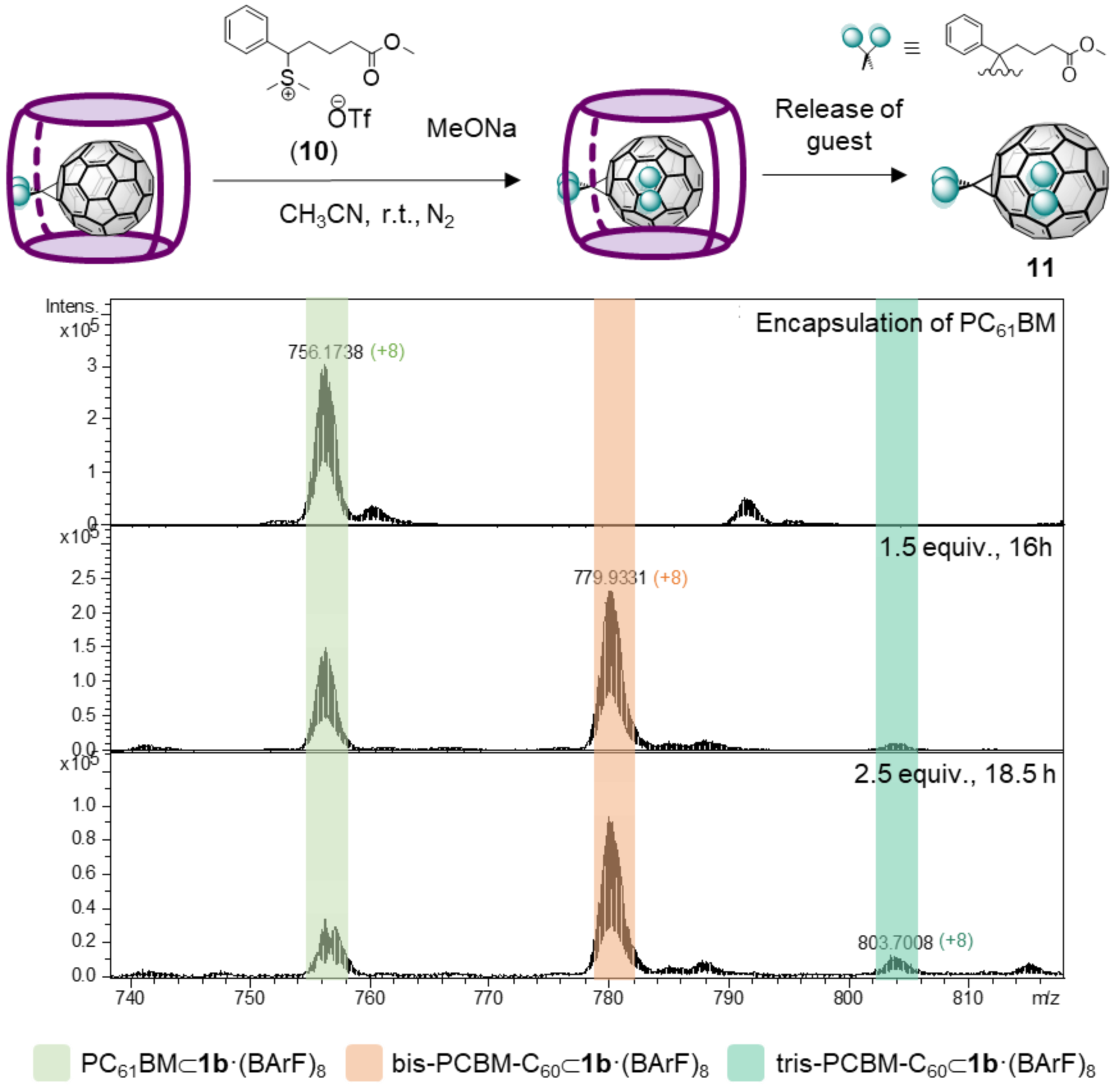

*Figure V.5. HR-ESI-MS monitoring of the formation of bis-PCBM-$C_{60} \subset$**1b**·$(BArF)_8$ via addition-elimination using sulfonium salt **10**.*

Bis-adducts were released from the nanocapsule adding 20 equivalents of trifluoromethanesulfonic acid and stirring it at room temperature for 1 hour to disassemble the nanocapsule. Then, solvent was evaporated under reduced pressure and the released guests were extracted with toluene. They were easily purified by a preparative TLC using toluene:ethyl acetate (95:5) as eluent. Two main fractions were obtained that were characterized by MALDI-MS, confirming that they both are bis-adducts (Figure V.6).

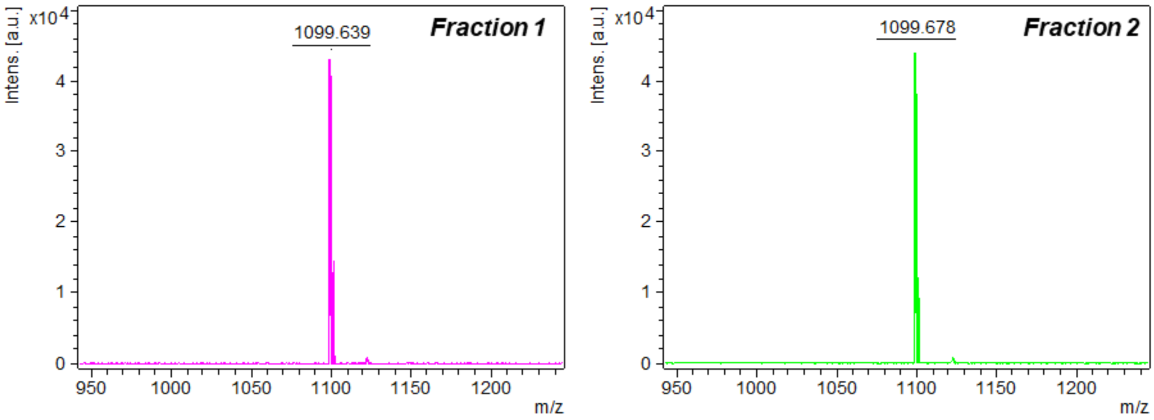

*Figure V.6. MALDI-MS analysis of bis-homoadducts **11** after releasing from **1b**·(BArF)$_8$ nanocapsule.*

HPLC analysis presented four peaks for fraction 1 and one single peak for fraction 2 (Figure V.7.a). UV-vis analysis (Figure V.7.b) allowed to assign the identity of each peak, since each addition pattern to $C_{60}$ present a unique UV-vis spectrum and, therefore, they can be used as a fingerprint for the identification of each regioisomer. The UV-vis spectrum of each peak matched perfectly with previously reported spectra of PCBM-based bis-adducts by using bare $C_{60}$[80,81] and, therefore, it allowed the assignment of the obtained bis-adducts using **1b**·(BArF)$_8$, as can be seen in Figure V.7 and Figure V.8. Unfortunately, they couldn't be characterized by nuclear magnetic resonance (NMR) because of the low quantities obtained of each regioisomer. For this reason, isomers with the same addition pattern couldn't be distinguished among them, although they could be detected (i.e. *trans*-3 (I) / *trans*-3 (II) and *e,e* (I) / *e,e* (II) couldn't be distinguished between them).

The yield was calculated by HPLC using $C_{60}$ as internal standard. Due to the different extinction coefficients of bis-adducts and $C_{60}$, a correction factor was determined by measuring peak area *vs*. concentration plots for bis-adducts and $C_{60}$ (more details in *Annex V.2 Linear calibration for quantitative HPLC analysis*). The total yield of **11** were 36.4% and relative yields of each regioisomer are shown in Figure V.8.a.

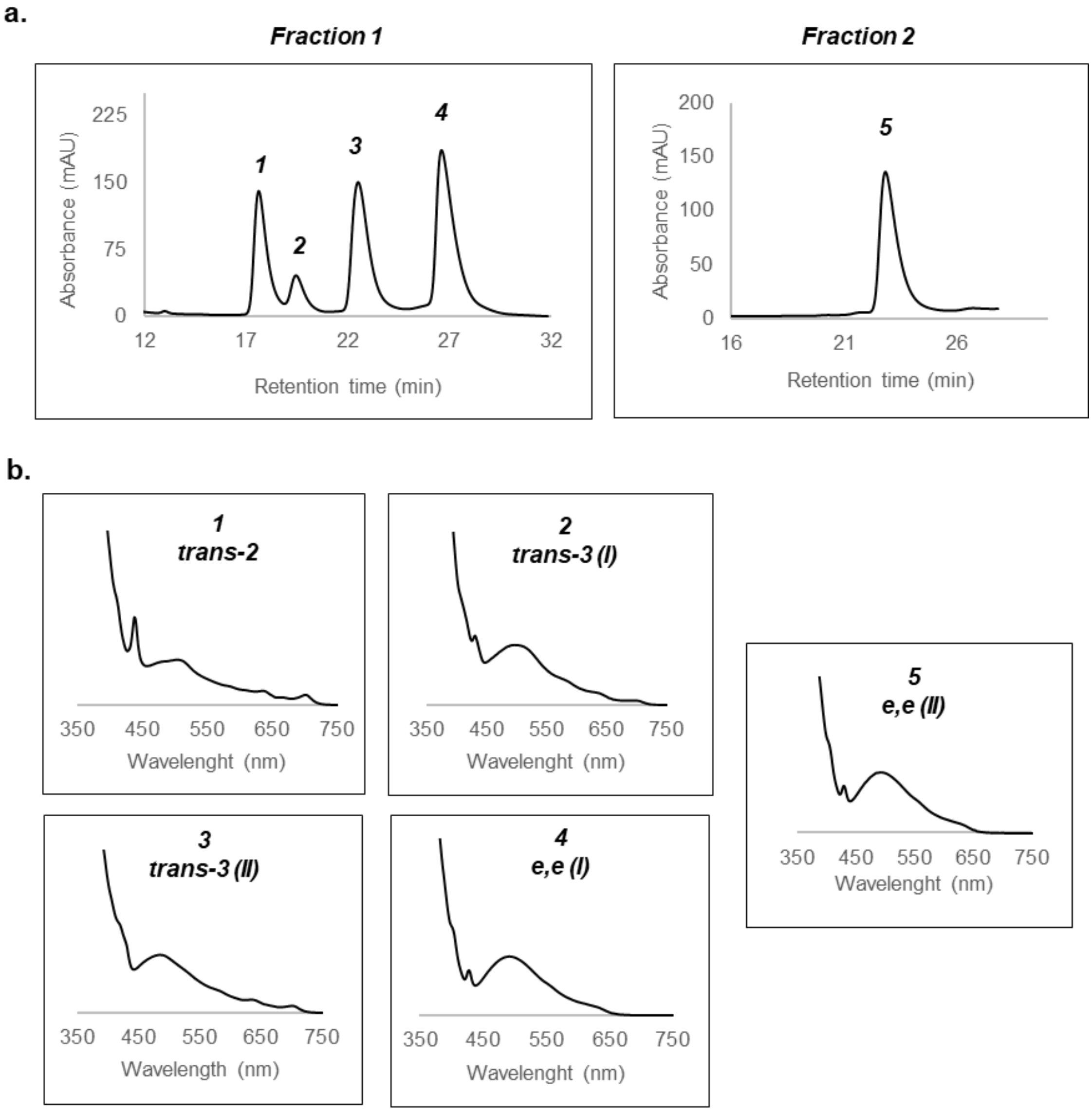

*Figure V.7. a) HPLC analysis of fraction 1 and 2 from the synthesis of bis-homoadducts **11** using supramolecular mask strategy. b) UV-vis spectra of each peak from HPLC analysis of bis-homoadducts **11**.*

**a.**

| Peak | Regioisomer | Quantitative yield (%) | Relative yield (%) |
|---|---|---|---|
| 1 | ***trans*-2** | 6.0 | 16.6 |
| 2 | ***trans*-3 (I)** | 1.5 | 4.2 |
| 3 | ***trans*-3 (II)** | 8.5 | 23.4 |
| 4 | **e,e (I)** | 12.4 | 34.1 |
| 5 | **e,e (II)** | 7.9 | 21.8 |

**b.**

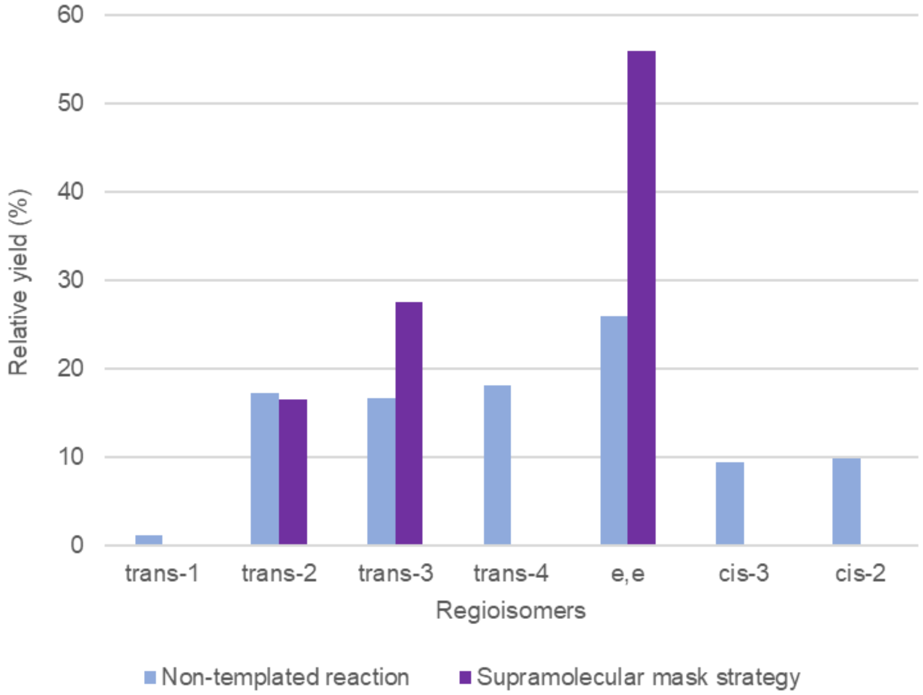

*Figure V.8. a) Quantitative and relative yield of each regioisomer of **11** obtained by supramolecular mask strategy. b) Outcome comparison between using non-templated reaction and supramolecular strategy to synthesize bis-adducts **11**.*

It is worth noting that relative yields of equatorial bis-adducts obtained by this supramolecular approach were considerably increased with respect to those obtained from the non-templated reaction,[80] showing an enrichment from 26.0 to 55.7% (Figure V.8.b). Moreover, this strategy allows their formation by an easy, rapid and straightforward methodology in front of the reported multi-stage and multicolumn HPLC process in peak-recycling mode.

A new approach to further explore the regioselectivity of the addition-elimination of sulfur ylide **10** to $C_{60}$ under the supramolecular mask strategy was replacing **1b**·(BArF)$_8$ by **1d**·(BArF)$_8$ nanocapsule, which presents a slightly larger cavity (distance between zinc porphyrins 14.1 Å vs 16.8 Å, respectively) that can accommodate a $C_{60}\subset$[10]CPP complex.[46] As seen in previous works reported by Ribas' group, the addition pattern of Bingel cyclopropanation changes completely between both systems (from equatorial to *trans*-3 addition) because of the presence of the aromatic nanohoop that is slightly tilted (~15°) with respect to the zinc porphyrins of **1d**·(BArF)$_8$. For this reason, this three-shell complex was also used to explore the cyclopropanation of $C_{60}$ using semi-stabilized sulfur ylides.

Functionalization of $C_{60}$⊂[10]CPP⊂**1d**·(BArF)$_8$ was tested using 10 equivalents of the corresponding sulfonium salt and 10 equivalents of $CH_3ONa$ added sequentially. As can be seen in the HR-ESI-MS monitoring (Annex V, Figure S.82), after two days, $PC_{61}BM$⊂[10]CPP⊂**1d**·(BArF)$_8$ was formed in a ratio of 1:2 (encapsulated $C_{60}$:$PC_{61}BM$, respectively). These results prompted us to repeat the reaction using the same conditions starting from $PC_{61}BM$⊂[10]CPP⊂**1d**·(BArF)$_8$ to achieve the corresponding bis-homoadduct **11**.

The addition of one equivalent of [10]CPP to $PC_{61}BM$ led to the corresponding inclusion complex $PC_{61}BM$⊂[10]CPP. This was confirmed by $^1$H-NMR, since all signals were shifted in comparison to $PC_{61}BM$ (Figure V.9.a). Then, $PC_{61}BM$⊂[10]CPP was completely encapsulated by **1d**·(BArF)$_8$ giving the desired matryoshka-like complex $PC_{61}BM$⊂[10]CPP⊂**1d**·(BArF)$_8$. This also was confirmed by $^1$H-NMR and HR-ESI-MS (Figure V.9 and Annex V, Figure S.83 and S.84).

Functionalization of $PC_{61}BM$⊂[10]CPP⊂**1d**·(BArF)$_8$ was tested using 15 equivalents of the corresponding sulfonium salt and 15 equivalents of $CH_3ONa$ added sequentially in acetonitrile (see HR-ESI-MS monitoring in Annex V, Figure S.85). Unfortunately, the presence of encapsulated **11** was not detected at all and the cage decomposed after the addition of a considerable excess of sulfonium salt **10** and $CH_3ONa$ and 23 hours of stirring. The lack of reactivity might be attributed to steric limitations of the guest, since these non-symmetric substituents are bulkier than those obtained by Bingel reaction when using diethyl bromomalonate.

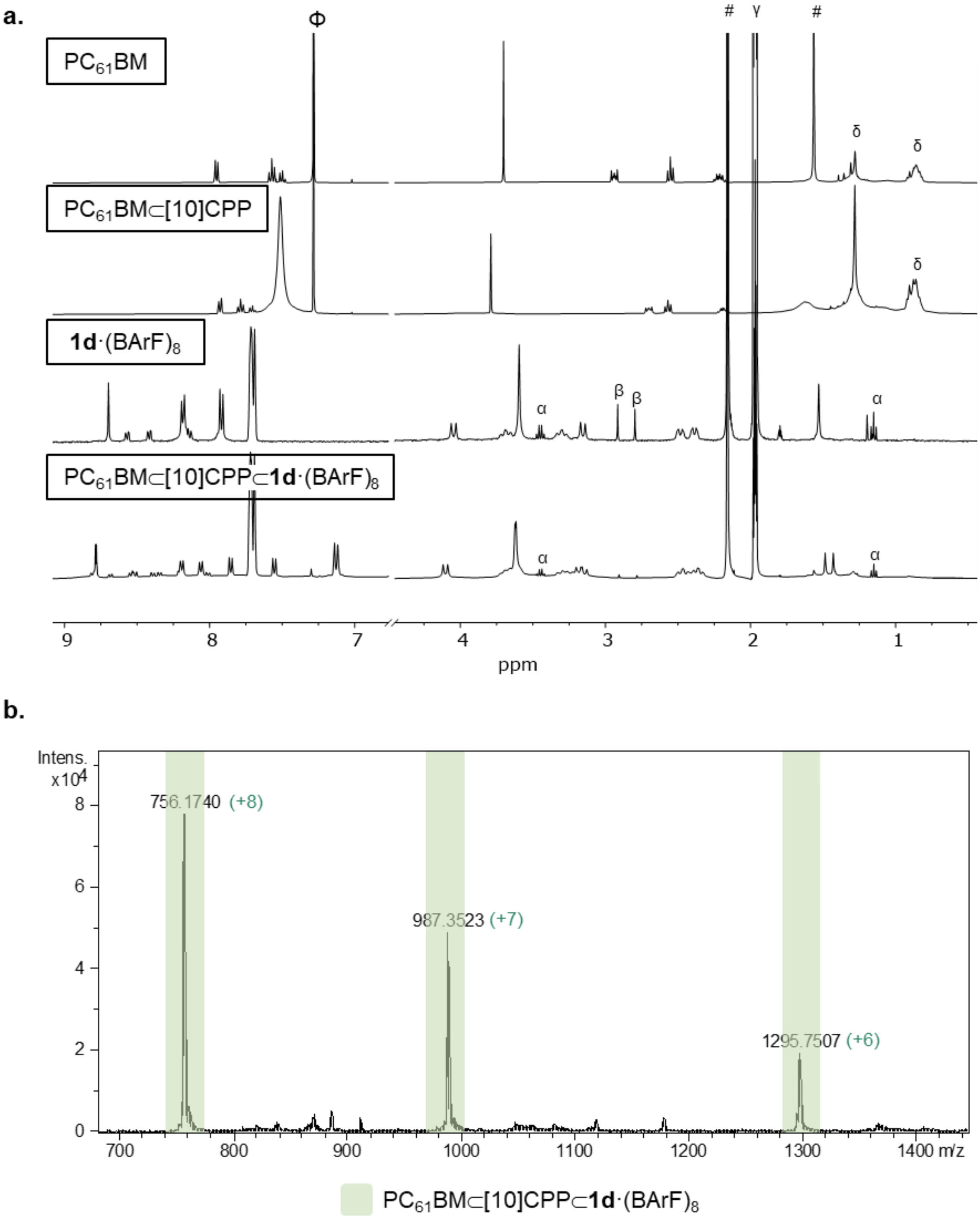

*Figure V.9. a) $^1$H-NMR for PC$_{61}$BM, PC$_{61}$BM⊂[10]CPP, **1d**·(BArF)$_8$ and PC$_{61}$BM⊂[10]CPP⊂**1d**·(BArF)$_8$. Experiments performed in CDCl$_3$ at 298K (400 MHz). Φ: CHCl$_3$, #: H$_2$O, γ: CH$_3$CN, δ: grease, α: diethyl ether, β: DMF. b) HR-ESI-MS analysis of PC$_{61}$BM⊂[10]CPP⊂**1d**·(BArF)$_8$.*

### V.2.2 Synthesis of PCBM-based bis-heteroadducts

Synthesis of PCBM-based bis-heteroadducts was tested using **1b**·(BArF)$_8$ following the same supramolecular mask approach and applying different functionalization reactions.

$PC_{61}BM\subset$**1b**$\cdot(BArF)_8$ was submitted to Prato reaction, a 1,3-dipolar cycloaddition which enables the addition of *N*-methylpyrrolidine rings to fullerenes at high temperatures.[154] After the addition of 3 equivalents of sarcosine and 7.5 equivalents of paraformaldehyde, bis-heteroadduct **12** was detected as the major product (see HR-ESI-MS monitoring in Annex V, Figure S.86). Nevertheless, this reaction was not regioselective because a mixture of intractable several bis-adducts was obtained once the products were released from **1b**$\cdot(BArF)_8$ (Annex V, Figure S.87).

Also, $PC_{61}BM\subset$**1b**$\cdot(BArF)_8$ was submitted to Bingel reaction. After 4.5 hours and 4.25 equivalents of dimethyl bromomalonate and NaH, the corresponding bis-adduct **13** was detected as the major product (see HR-ESI-MS monitoring in Annex V, Figure S.88). Again, this reaction was not regioselective because a mixture of several bis-adducts were obtained once the products were released from **1b**$\cdot(BArF)_8$ and analysed by MALDI-MS, HPLC and UV-vis spectroscopy (Annex V, Figures S.89 and S.90).

At this point, we envisioned that this lack of regioselectivity could be overcome using the abovementioned matryoshka-like complex as template instead of **1b**$\cdot(BArF)_8$, since there is more steric hindrance due to the presence of [10]CPP. In order to explore the steric limitations of $PC_{61}BM\subset[10]CPP\subset$**1d**$\cdot(BArF)_8$, this complex was submitted to a screening of different reactions adding substituent groups with different sizes (Figure V.10).

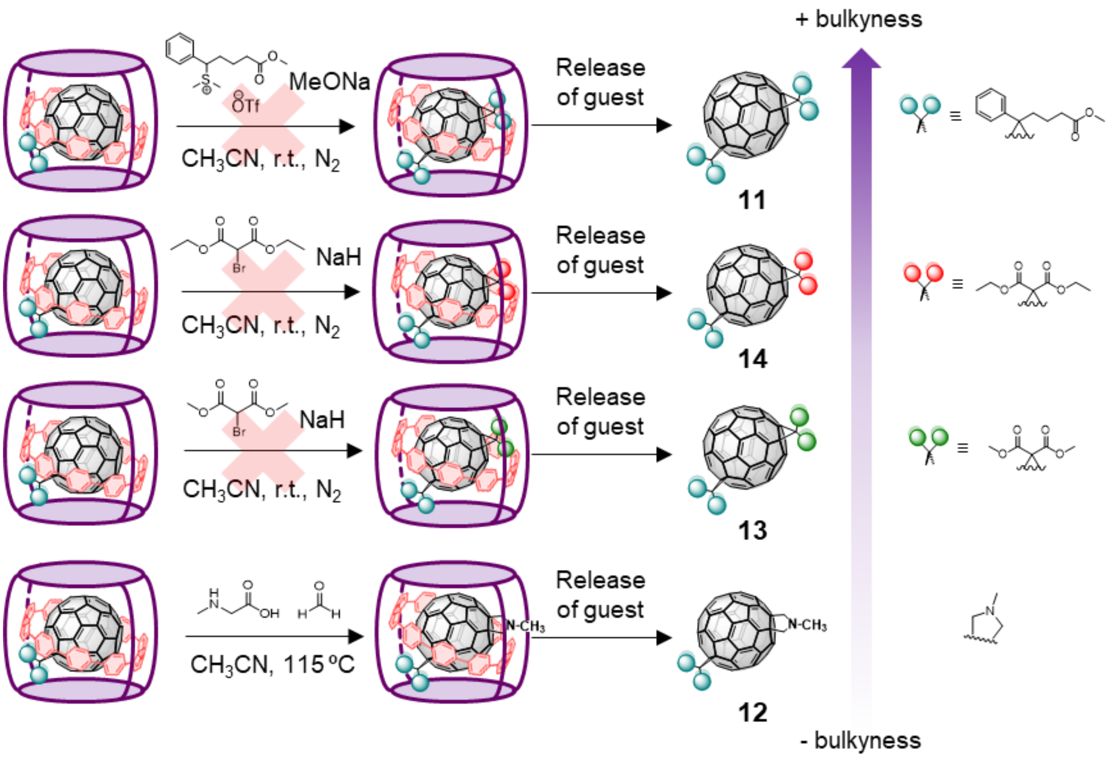

*Figure V.10. Schematic representation of the reactions screening for the synthesis of bis-adducts using the matryoshka supramolecular mask strategy.*

Since the formation of **11**$\subset$[10]CPP$\subset$**1d**·(BArF)$_8$ was not detected by HR-ESI-MS as discussed in *V.2.1 Synthesis of PCBM-based bis-homoadducts*, PC$_{61}$BM$\subset$[10]CPP$\subset$**1d**·(BArF)$_8$ was submitted to Bingel reaction, since it adds smaller substituent groups than PCBM addends. After two days and 9 equivalents of diethyl bromomalonate and base, less than 20% of the encapsulated hetero-bis-adduct **14** was formed (see HR-ESI-MS monitoring in Annex V, Figure S.91). Attempts to improve the yield of the reaction failed because the cage decomposed after the addition of a large excess of diethyl bromomalonate and base, and the outcome reaction could not be analysed.

Then, Bingel reaction was tested on PC$_{61}$BM$\subset$[10]CPP$\subset$**1d**·(BArF)$_8$ using a smaller bromomalonate (dimethyl bromomalonate) to give the bis-heteroadduct **13**, but the reaction didn’t work either. After the addition of a large excess of the corresponding bromomalonate and NaH, the cage decomposed (HR-ESI-MS monitoring in Annex V, Figure S.92).

Following the trend in Figure V.10, PC$_{61}$BM$\subset$[10]CPP$\subset$**1d**·(BArF)$_8$ was submitted to Prato reaction, since this reaction adds smaller functional groups to fullerenes than Bingel cyclopropanation. PC$_{61}$BM$\subset$[10]CPP$\subset$**1d**·(BArF)$_8$ was submitted to a total of 27.5 equivalents of sarcosine and 66 equivalents of formaldehyde at 115ºC (see monitoring at Figure V.11). After 35.5 hours, although nanocapsule was partially decomposed (probably due to the large excess of added precursors) the encapsulated bis-heteroadduct **12** was detected as the main product (44% relative yield among all the encapsulated species) alongside encapsulated PC$_{61}$BM (42.5% PC$_{61}$BM$\subset$[10]CPP$\subset$**1d**·(BArF)$_8$) and tris-adduct (13.5%, tris-PCBM-(Prato)$_2$-C$_{60}$$\subset$[10]CPP$\subset$**1d**·(BArF)$_8$).

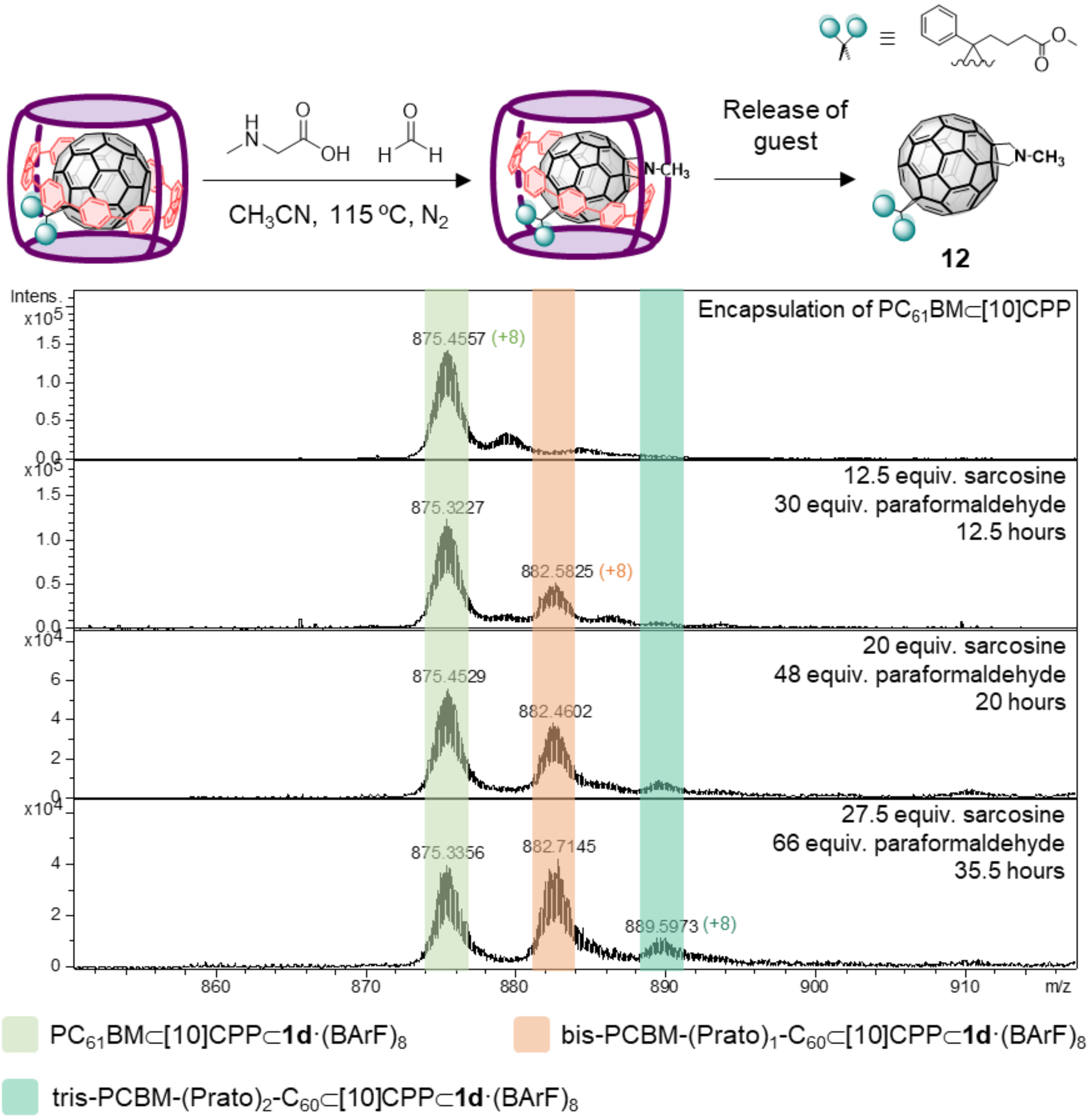

*Figure V.11. HR-ESI-MS monitoring of formation of hetero-bis-adduct **12** through Prato reaction via supramolecular mask strategy.*

**12**⊂[10]CPP was released from **1d**·(BArF)$_8$ with washes of chloroform until the nanocapsule was empty (Annex V, Figure S.93). Then, exchange with 2.5 equivalents of C$_{60}$ was performed to release bis-adducts from **12**⊂[10]CPP. After stirring overnight at room temperature, released derivatives were purified by preparative TLC using toluene as eluent. Two fractions were obtained which corresponded to two bis-adducts, as detected by MALDI-MS (Figure V.12.a). Although these bis-adducts could be analysed by HPLC and UV-vis spectroscopy (Annex V, Figure S.94 and Figure V.12.b), the identity of these compounds could not be assigned by comparison of fingerprint UV-vis spectra since they are not reported in the current literature. Moreover, due to the decomposition of **1d**·(BArF)$_8$ during the reaction, characterization by NMR could not be performed because low yields of these derivatives were obtained. Presumably, the two regioisomers might correspond to *trans*-3-bis-adducts, due to the non-symmetric nature of PCBM addend.

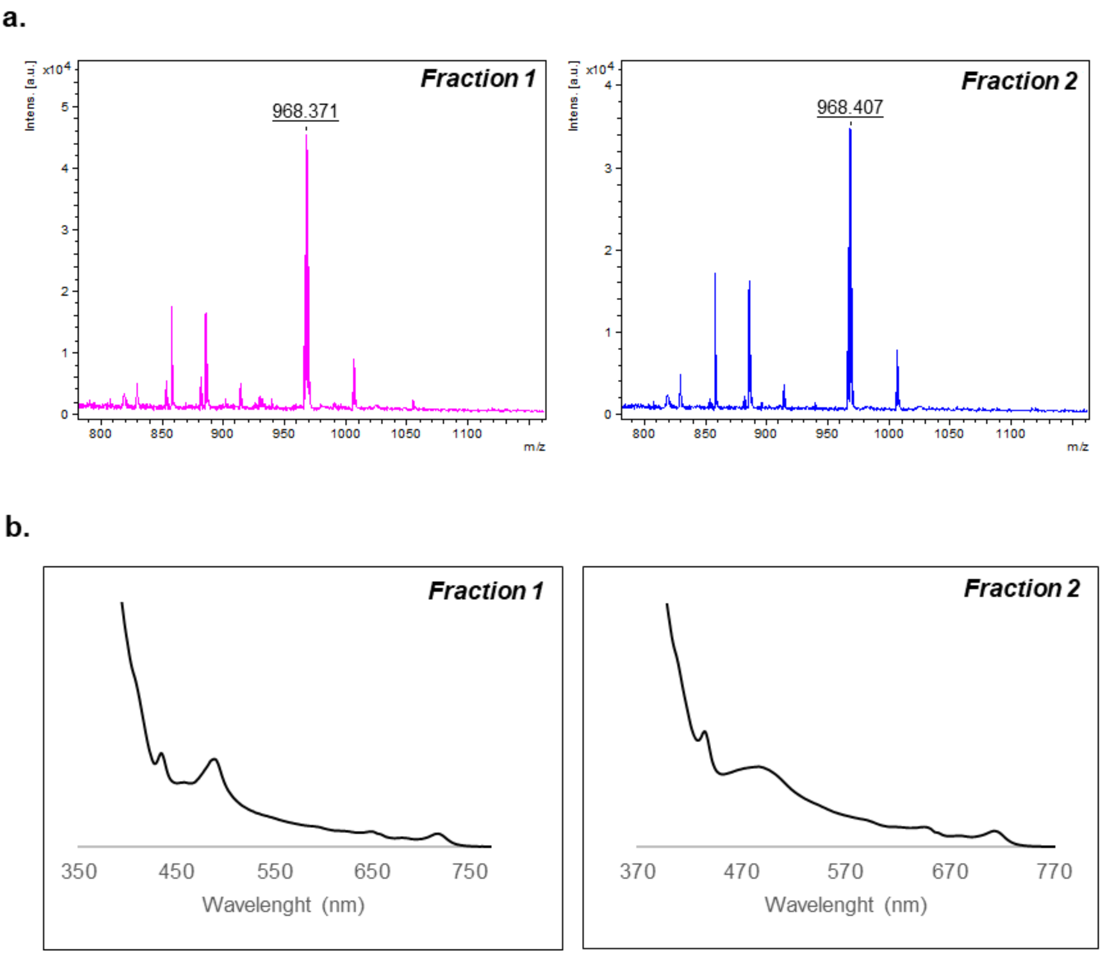

*Figure V.12. a) MALDI-MS analysis of fraction 1 and 2 after TLC preparative of the synthesis of bis-heteroadduct* ***12****. b) UV-vis spectra of fraction 1 and 2 after TLC preparative of the synthesis of bis-heteroadduct* ***12****.*

Finally, **1f**·(BArF)$_8$ nanocapsule was also used for the synthesis of bis-heteroadducts. **1f**·(BArF)$_8$ cage presents a larger cavity than previous ones (distance between zinc porphyrins of 18.4 Å).[31] This nanocapsule was able to form successfully a 1:1:1 ternary complex including PC$_{61}$BM⊂[10]CPP in its cavity in an analogous fashion to PC$_{61}$BM⊂[10]CPP⊂**1d**·(BArF)$_8$ and it was analysed by $^1$H-NMR and HR-ESI-MS (Figure V.13 and Annex V, Figure S.95). Then, Bingel conditions were applied to PC$_{61}$BM⊂[10]CPP⊂**1f**·(BArF)$_8$. After 12 equivalents of diethyl bromomalonate and NaH, only a 20% of bis⊂[10]CPP⊂**1f**·(BArF)$_8$ was formed (HR-ESI-MS monitoring in Annex V, Figure S.96.a). However, it could be released from [10]CPP⊂**1f**·(BArF)$_8$ and analysed. Unfortunately, the reaction was not regioselective since an intractable mixture of bis-adducts was obtained (Annex V, Figure S.96.b).

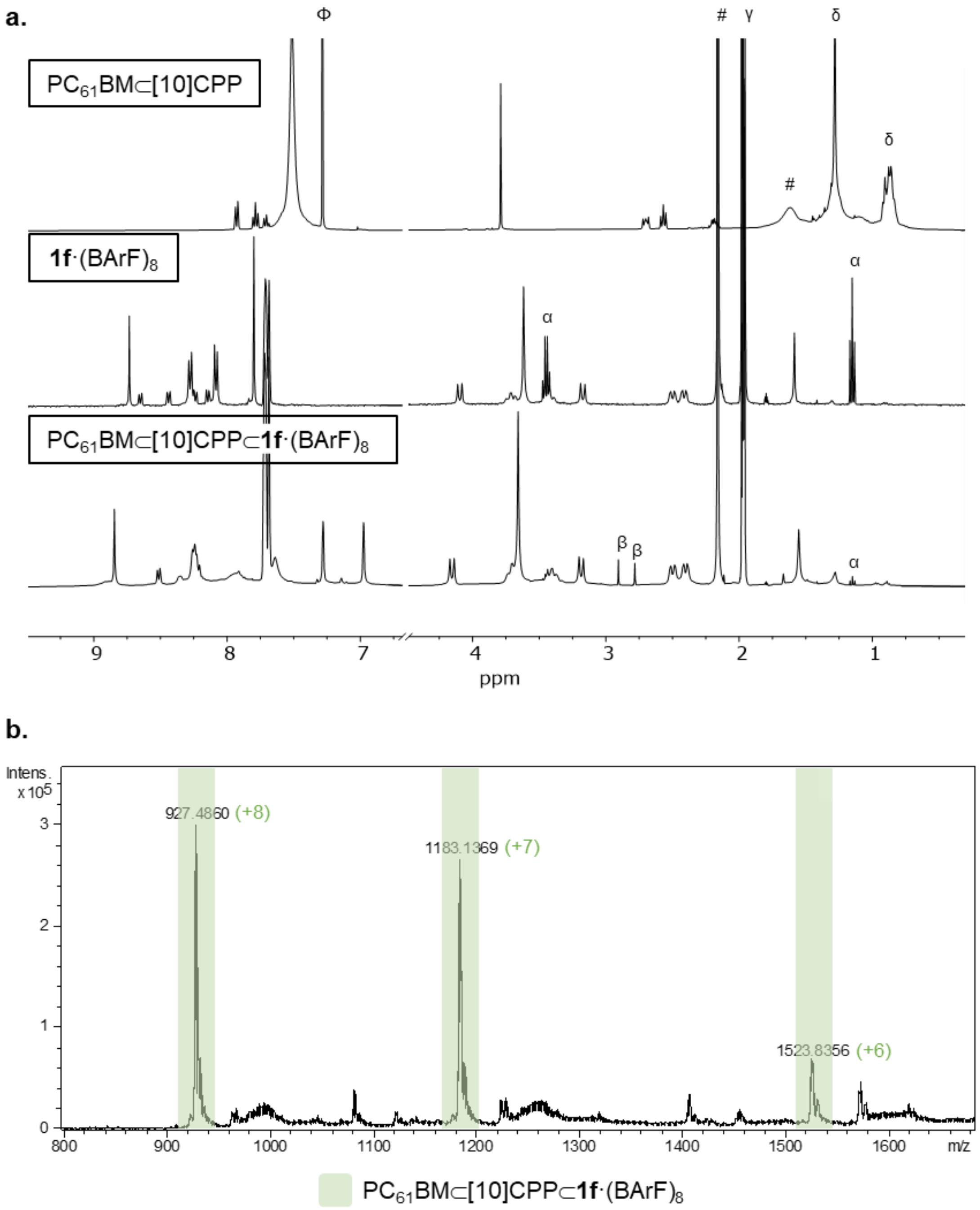

*Figure V.13. a) $^{1}$H-NMR for PC$_{61}$BM⊂[10]CPP, **1f**·(BArF)$_8$ and PC$_{61}$BM⊂[10]CPP⊂**1f**·(BArF)$_8$. Experiments performed in CDCl$_3$ at 298K (400 MHz). Φ: CHCl$_3$, #: H$_2$O, γ: CH$_3$CN, δ: grease, α: diethyl ether, β: DMF. b) HR-ESI-MS analysis of PC$_{61}$BM⊂[10]CPP⊂**1f**·(BArF)$_8$*

# CHAPTER VI. SYNTHESIS OF A FULLERENE-BASED MOLECULAR SHUTTLE VIA SUPRAMOLECULAR MASK STRATEGY

During the last three decades, the scientific community has made a big effort in the design of molecular shuttles.[155] A molecular shuttle can be defined as an artificial nanomachine that undergoes well-defined, large amplitude, dynamics of one mechanically interlocked component with respect to the other.[156] The design of artificial molecular machines is inspired by the insights of biological molecular motors, although there is still a lack of studies regarding the dynamics and mechanistic principles that control the motion of these molecular architectures.[157]

A catenane is a mechanically interlocked molecular architecture that consists of two or more intertwined macrocycles that cannot be separated without breaking covalent bonds. Catenanes have been used to create synthetic rotary motors in which small rings rotate directionally around a larger ring when the latter presents (potential) binding sites that the former can recognize.[158,159]

In this context, last year, Ribas, Delius and coworkers developed a $C_{60}$/[10]CPP-based [2]catenane that featured a *trans*-3-bis-adduct (a fullerene bis-functionalized by tether approach) with a mechanically interlocked [10]CPP ring.[97] This [2]catenane was synthesized using the matryoshka-like system from Ribas, Delius and coworkers (see *I.2.2.2 Supramolecular receptors as functionalization platforms for fullerenes*) which delivered excellent selectivity for *trans*-3 double bond even using unsymmetric bis-bromomalonates. Inspired by this example, the objective of this chapter is to use the supramolecular mask shadow approach to synthesize a $C_{60}$/[10]CPP-based [2]catenane containing two fullerenes (i.e. two degenerated recognition sites for one [10]CPP ring), as depicted in Figure VI.1. Therefore, this mechanically interlocked system will display the dynamic behaviour typically related to a molecular shuttle due to the translational movement of the [10]CPP ring between both stations (fullerene sites).

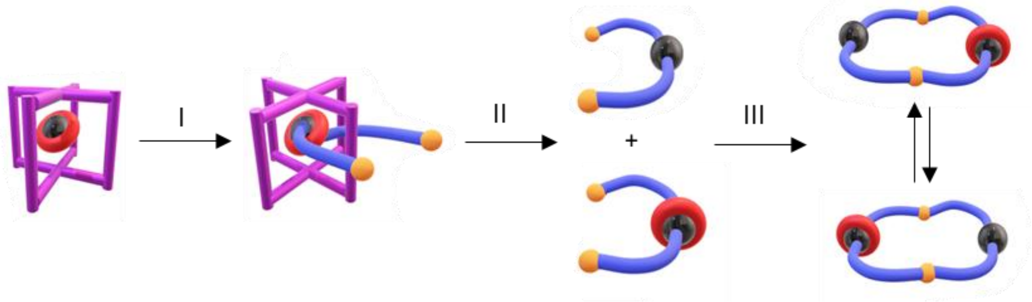

*Figure VI.1. General schematic synthetic route to form a $C_{60}$/[10]CPP-based molecular shuttle. I) Synthesis of bis-adducts via matryoshka supramolecular mask strategy. II) Release of bis-adduct/bis-adduct⊂[10]CPP from matryoshka complex. III) Connection of bis-adducts to form the final [2]catenane.*

## VI.1 First strategy: combination of Bingel reaction and olefin metathesis

The synthetic route to obtain the targeted fullerene-based molecular shuttle started with bis-functionalization of fullerene $C_{60}$ using the matryoshka-like complex from Ribas, Delius and coworkers.[46] The $Pd^{II}$-based nanocapsule (**1d**·(BArF)$_8$ from Chapter IV, Figure IV.1) can host in its cavity a fullerene $C_{60}$ wrapped by a [10]CPP ring and allow the functionalization of the fullerene by Bingel reaction using either symmetric or unsymmetric bromomalonates in an itero-, chemo- and regioselective fashion.

In this context, the unsymmetric bromomalonate used in the first reaction step (Bingel reaction) of the synthetic route presented one aliphatic chain with a terminal alkene. Upon bis-functionalization of $C_{60}$ using this compound, these terminal moieties might undergo an olefin metathesis (2nd step of the synthetic route) in order to join together two bis-adducts (one of them wrapped by a [10]CPP ring) to form the desired [2]catenane bearing two fullerene stations, as depicted in Figure VI.2.

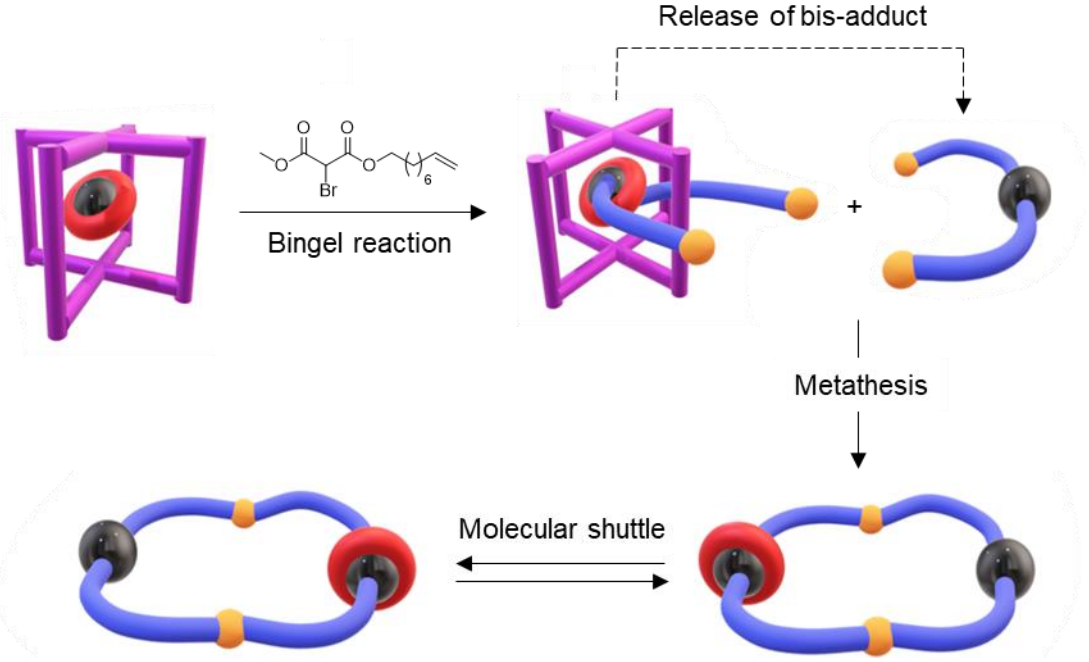

*Figure VI.2. Representative scheme of the 1st synthetic strategy to form the desired fullerene-based molecular shuttle.*

### VI.1.1 Bingel reaction

The ongoing collaboration with Prof. Max von Delius and MSc Fabian Steudel (University of Ulm, Germany) provided us with all the bromomalonate reagents to be used. Bromomalonate **15** was easily synthesized by mixing mono-methylmalonate and the corresponding alcohol with $PBr_3$ and $Br_2$ at 100ºC (see in *Annex Chapter VI. Experimental procedures* for more details and Annex VI, Figure S.97).

Bingel reaction via supramolecular mask strategy was carried out using similar protocols reported in previous works by Ribas, Delius and coworkers.[46] $C_{60}\subset$[10]CPP$\subset$**1d**·(BArF)$_8$ was dissolved in acetonitrile and NaH and the corresponding bromomalonate (**15**) was added and stirred under a $N_2$ atmosphere at room temperature. After 7.5 equivalents of base and bromomalonate **15** and 23 hours of stirring, the corresponding encapsulated bis-adduct was obtained successfully as the main product of the reaction (only traces of encapsulated tris-adduct were detected), as monitored by HR-ESI-MS (Figure VI.3).

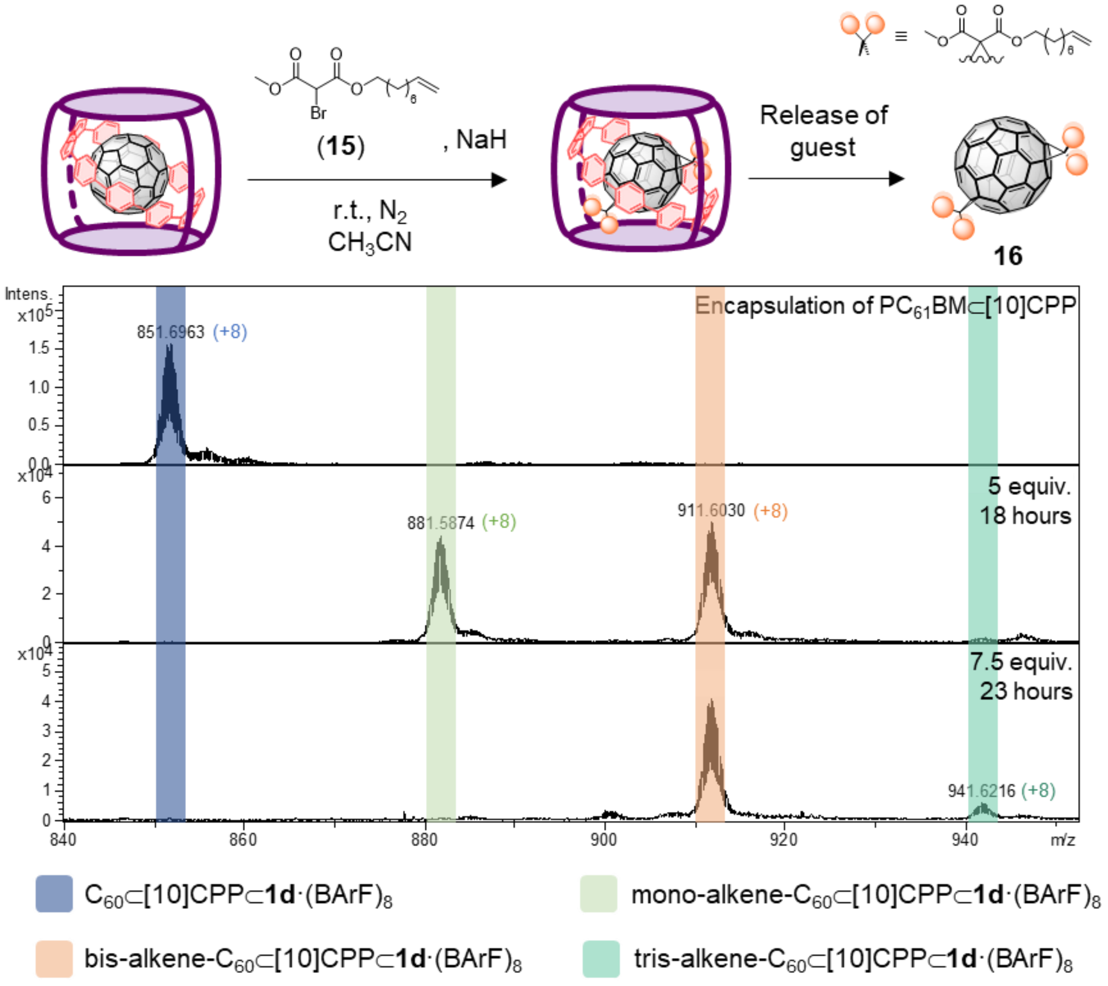

*Figure VI.3. HR-ESI-MS monitoring of the formation of bis-alkene-$C_{60}\subset$[10]CPP$\subset$**1d**·(BArF)$_8$ through Bingel reaction using bromomalonate **15**.*

Bis-adducts were released from bis-alkene-$C_{60}\subset$[10]CPP$\subset$**1d**·(BArF)$_8$ by an exchange with $C_{60}$ in a mixture of acetonitrile and toluene (1:9). Unfortunately, it worked only in small scale (2 mg of **1d**·(BArF)$_8$). Nevertheless, this quantity was enough to characterize the nature of the bis-adduct by MALDI-MS and UV-vis spectroscopy. For our delight, only two fractions were obtained after TLC preparative (Annex VI, Figure S.98) that both corresponded to bis-adducts, confirmed by MALDI-MS (Figure VI.4.a). By comparison of the obtained UV-vis spectra with the reported UV-vis spectra of cyclopropanated bis-adducts in the literature,[81] both bands corresponded to *trans*-3-bis-adducts (**16**), as expected (Figure VI.4.b). Both *trans*-3 isomers come from the non-symmetric nature of the starting bromomalonate.

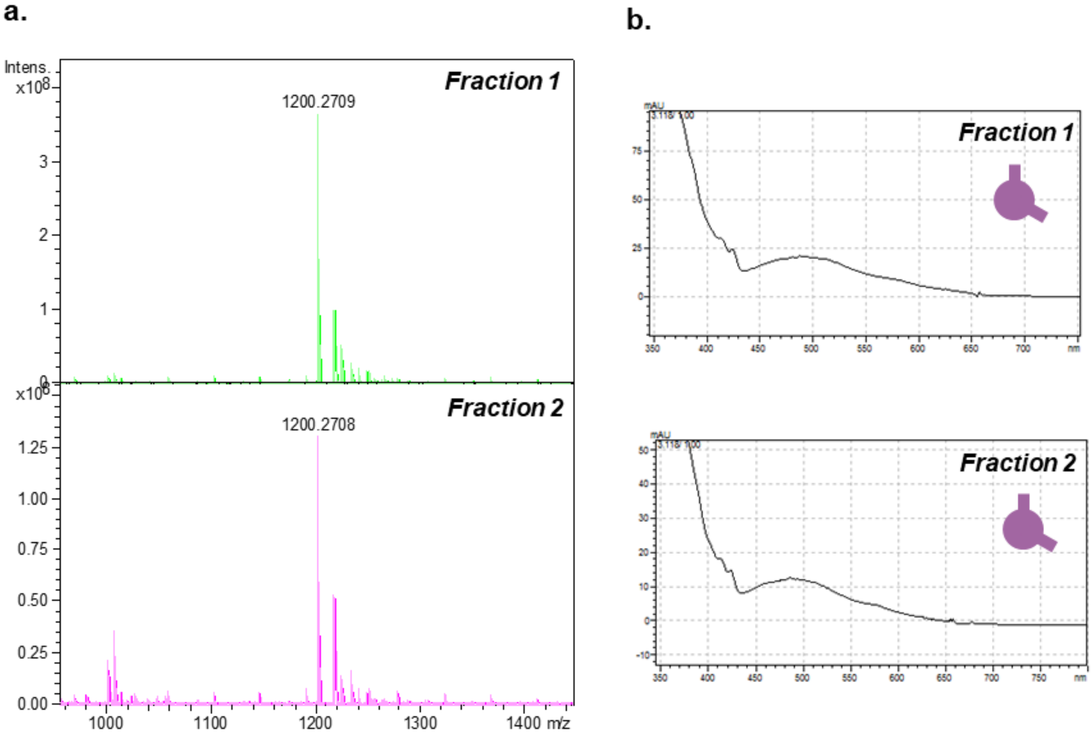

*Figure VI.4. a) MALDI mass spectra of fraction 1 and fraction 2 of **16** obtained from the Bingel reaction using bromomalonate **15**. b) UV-vis spectra of fraction 1 and fraction 2 of **16** obtained from the Bingel reaction using bromomalonate **15**.*

When the exchange was carried out in larger scale (~15 mg of host-guest complex), bis-adducts were released alongside [10]CPP, since only empty nanocapsule was found at the end of the exchange (see mass spectrum in Annex VI, Figure S.99) instead of $C_{60}\subset$[10]CPP$\subset$**1d**·(BArF)$_8$. For this reason, Bingel reaction with **1b**·(BArF)$_8$ nanocapsule instead of the matryoshka system ($C_{60}\subset$[10]CPP$\subset$**1d**·(BArF)$_8$) was also carried out to accumulate bis-adduct without [10]CPP. As can be seen in the HR-ESI-MS monitoring (Figure VI.5.a), the encapsulated bis-adduct was the main product of the reaction. After disassembly of the cage with triflic acid and a straightforward preparative TLC (Annex VI, Figure S.100), *e,e*-bis-adduct (**18**) was the main regioisomer obtained (22% relative yield among all bis-adducts), confirmed by MALDI-MS and UV-vis spectroscopy (Figure VI.5.b and Figure VI.5.c, respectively).

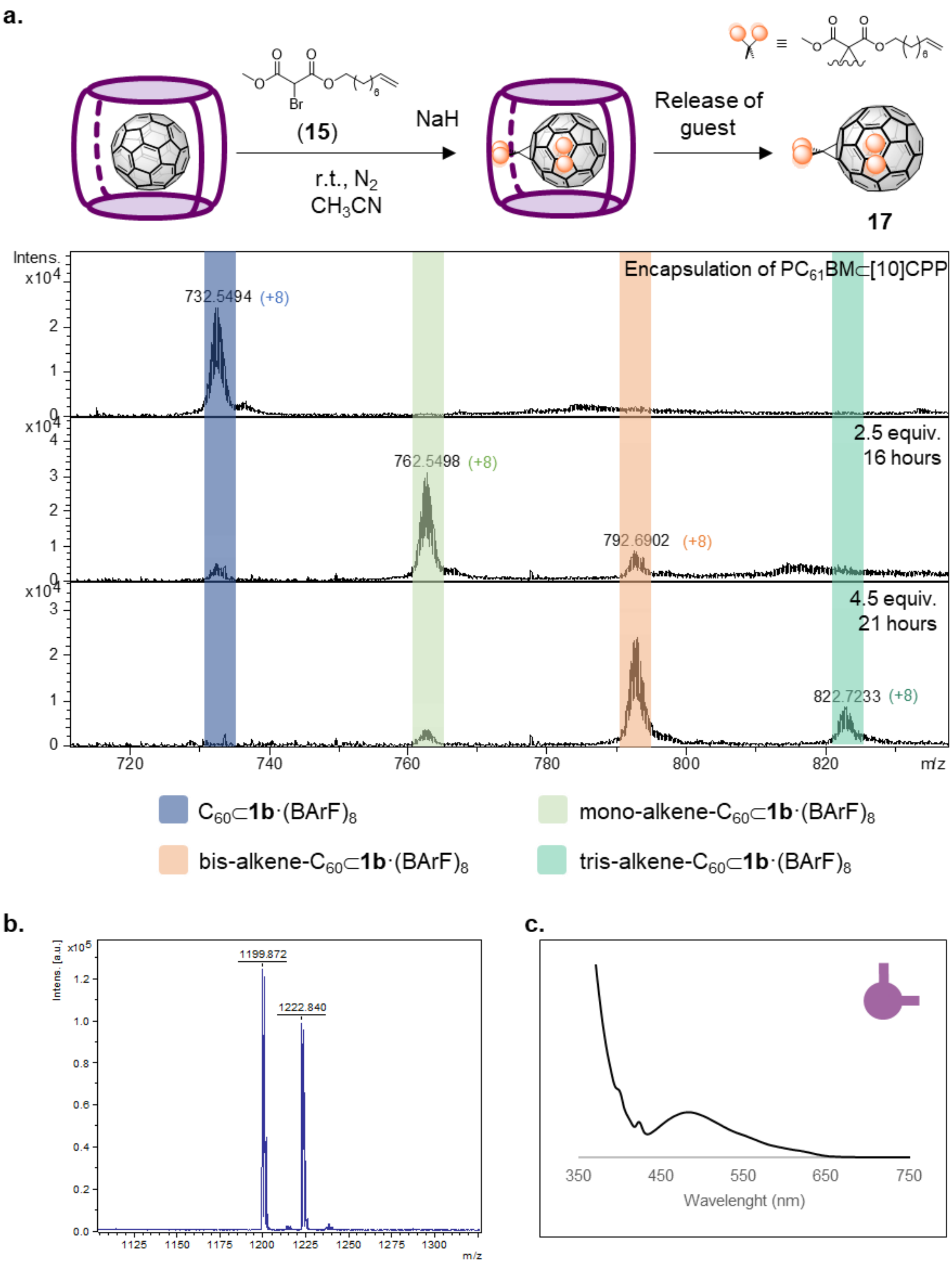

*Figure VI.5. a) HR-ESI-MS monitoring of the formation of bis-alkene-C$_{60}$⊂**1b**·(BArF)$_8$ through Bingel reaction and using bromomalonate **15**. b) MALDI mass spectrum of the main bis-adduct (**17**) obtained from the Bingel reaction using bromomalonate **15**. c) UV-vis spectra of the main regioisomer (i.e. e,e-bis-alkene-C$_{60}$, **17**) from the Bingel reaction using bromomalonate **15**.*

### VI.1.1 Olefin metathesis

Olefin metathesis is a metal-catalysed reaction that entails the redistribution of alkenes by the scission and regeneration of carbon-carbon double bonds.[160] The well-known catalysts used in this reaction are the Grubbs catalysts, a series of homogeneous ruthenium-based carbene complexes that tolerate many functional groups, works under mild conditions and are compatible with a wide range of solvents.[161]

We started with optimization of the temperature, % mol catalyst, concentration and reaction time of olefin metathesis using mono-adducts without the presence of the nanocapsule. Mono-adduct **18** were easily synthesized through a Bingel reaction following a similar protocol reported by Jin, Peng and coworkers[162] using bromomalonate **15** (Figure VI.6.a). It was characterized by $^1$H-NMR (Annex VI, Figure S.101). The vanishing of the acidic proton of the bromomalonate (4.8 ppm) in the $^1$H-NMR spectrum confirmed that the reaction was carried out successfully (Annex VI, Figure S.102). Then, this mono-adduct was used for the optimization of olefin metathesis using Grubbs and Hoveyda-Grubbs catalysts of 2nd generation (Figure VI.6.b) to give compound **19**. All the data collected is summarized in Table VI.1.

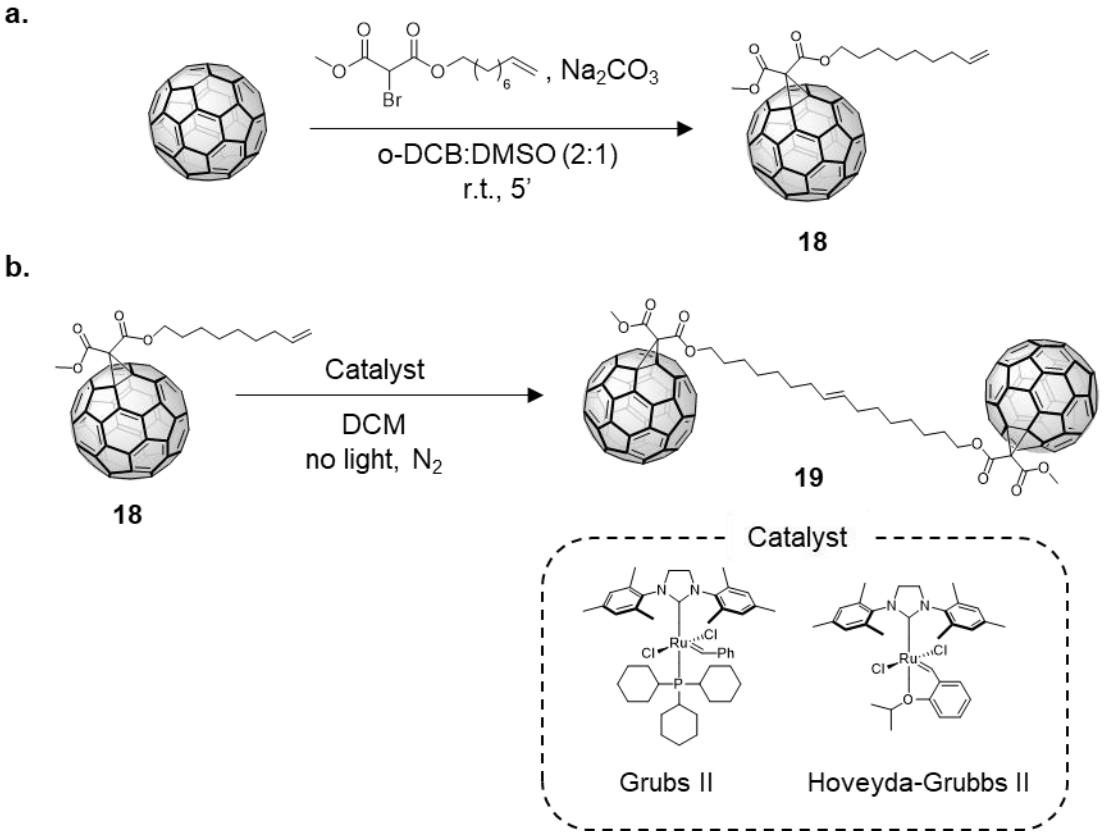

*Figure VI.6. a) Synthesis of mono-adduct **18** through Bingel reaction using similar conditions reported by Jin, Peng and coworkers.[162] b) Olefin metathesis using mono-adduct **18**.*

*Table VI.1. Conditions optimization for the olefin metathesis using mono-adduct **18** without nanocapsule. *Conversion and relative yield calculated by $^1$H-NMR. **All experiments were performed by using Hoveyda-Grubbs II as catalyst, except for experiment 1 and 2, in which Grubbs II catalyst was used.*

| Experiment | Temperature (ºC) | % mol catalyst | Concentration (mM) | Time (days) | Conversion (%)* | Relative yield (%)* | Isolated yield (%) |
|---|---|---|---|---|---|---|---|
| 1** | r.t. | 10+10 | 5 | 1+3 | 67 | 48 | 45 |
| 2** | 40 | | | | >99 | 56 | 21 |
| 3 | r.t. | 10 | 5 | 4 | 40 | 34 | 49 |
| 4 | 40 | 5 | | | 27 | 23 | --- |
| 5 | r.t. | 10 | 10 | 3 | 48 | 46 | 43 |
| 6 | 40 | | | | 50 | 47 | 56 |
| 7 | r.t. | 15 | 10 | 3 | 50 | 46 | 50 |
| 8 | 40 | | | | 55 | 51 | 66 |
| 9 | r.t. | 10+10 | 10 | 3+3 | 65 | 61 | 62 |
| 10 | 40 | | | | >99 | 94 | 85 |

As can be seen in Table VI.1, experiment 10 shows the best conditions of the metathesis starting from mono-adduct **18**. The reaction at 40ºC stirring for 6 days and using Hoveyda-Grubbs catalyst of 2$^{nd}$ generation (20% mol) and a 10 mM concentration of **18** in dichloromethane under N$_2$ atmosphere gave an 85% isolated yield (94% relative yield) with a >99% conversion. As can be seen in the $^1$H-NMR spectrum of the crude reaction of experiment 10, the starting material was totally consumed and a new peak appeared which corresponded to the product **19** (Figure VI.7). The product was characterized by $^1$H-NMR and MALDI-MS (Annex VI, Figure S.103 – S.104, respectively).

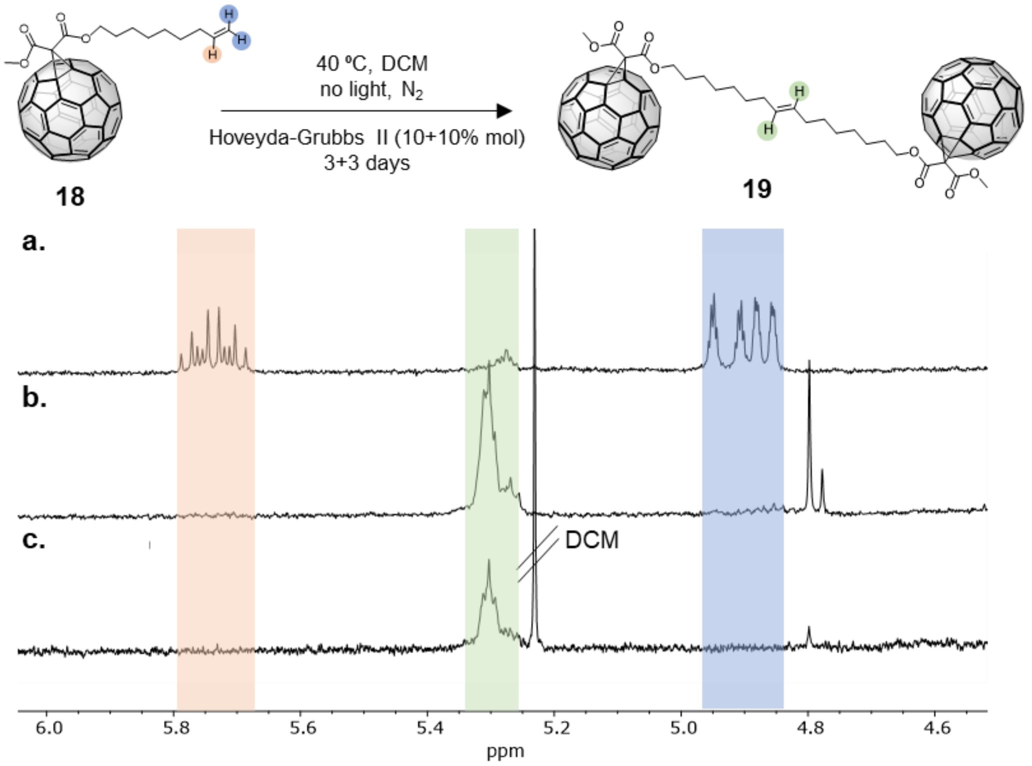

*Figure VI.7. Zoom between 4.6 and 6.0 ppm of $^1$H-NMR spectra of experiment 10 (Table VI.1). a) $^1$H-NMR spectrum of mono-adduct **18** (starting material). b) $^1$H-NMR spectrum of crude reaction after 6 days. c) $^1$H-NMR spectrum of purified product of olefin metathesis (**19**).*

Once the conditions were optimized in DCM, olefin metathesis was tested with encapsulated mono-adducts, since the presence of the nanocapsule might prevent the intramolecular olefin metathesis of bis-adducts.

Since nanocapsules are not totally soluble in dichloromethane in high concentrations, an experiment was performed using mono-adduct **18** dissolved in a mixture of DCM and acetonitrile (9:1) and submitted at conditions of experiment 10 (Table VI.1). After 6 days, the reaction crude was analysed by MALDI-MS and $^1$H-NMR. Only 5% of product **19** was detected in comparison to the starting material (Annex VI, Figure S.105 and S.106), probably due to detrimental coordination of acetonitrile to the catalyst.

In order to replace acetonitrile an avoid its coordination to the catalyst, an experimental test using **18**$\subset$**1b**·(BArF)$_8$ was performed in tetrahydrofuran (THF), in which **1b**·(BArF)$_8$ is also highly soluble. The reaction was successful with non-encapsulated mono-adducts, as monitored by $^1$H-NMR (Annex VI, Figure S.107). However, as can be seen in the HR-ESI-MS monitoring, the reaction didn't proceed at all when **18**$\subset$**1b**·(BArF)$_8$ was used as the starting material in THF (Annex VI, Figure S.108).

Olefin metathesis was tested also using bis-adducts **16**$\subset$[10]CPP and **17** without nanocapsule (*trans*-3-bis-alkene-$C_{60}\subset$[10]CPP and *e,e*-bis-alkene-$C_{60}$) in DCM with the same conditions of experiment 10 (Table VI.1), but the reaction didn't work either (Annex VI, Figure S.109).

Finally, a control experiment was carried out using a non-encapsulated molecule instead of fullerene derivatives to check if the presence of the nanocapsule inhibits the reaction. Two parallel experiments were done using 4-*tert*-butylstyrene, one of them adding a 30% of **1b**·(BArF)$_8$ to the mixture. As can be seen in $^1$H-NMR spectra of the crude reactions (Figure VI.7), after 3 days of stirring, only a 10% of product **21** (peak at 7.09 ppm) was detected when **1b**·(BArF)$_8$ was added, since signals corresponding to 4-*tert*-butylstyrene (5.2 – 5.3, 5.71 – 5.75 and 6.69 – 6.76 ppm) remained in the spectrum (Figure VI.8.a). On the other hand, in the spectrum of the blank experiment (without cage), the signals corresponding to the starting material disappeared completely (Figure VI.8.b). Therefore, we concluded that the presence of the nanocapsule unfortunately inhibits the olefin metathesis and this route is deemed as a dead end.

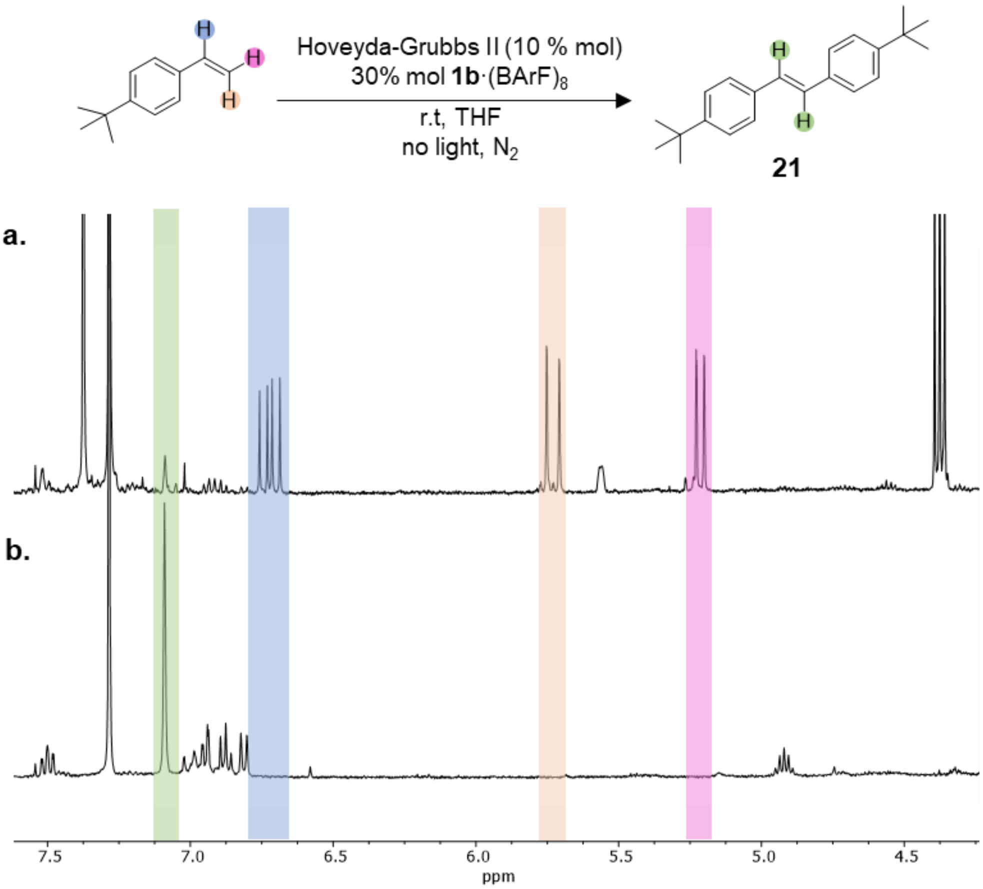

*Figure VI.8. Zoom between 4.5 and 7.5 ppm of $^1$H-NMR spectra of control experiments of olefin metathesis. a) $^1$H-NMR spectrum of experiment with addition of 30% of **1b**·(BArF)$_8$. b) $^1$H-NMR spectrum of the same experiment without the presence of **1b**·(BArF)$_8$.*

## VI.2 Second strategy: combination of Bingel reaction and copper(I)-catalysed azide-alkyne cycloaddition (CuAAC)

A new synthetic route to form the fullerene-based molecular shuttle was proposed after realizing that olefin metathesis was inhibited in the presence of Pd$^{II}$-based nanocapsules: instead of using metathesis reaction to join together both fullerenes, copper(I)-catalysed azide-alkyne cycloaddition (CuAAc) will be employed.

CuAAc transforms organic azides and terminal alkynes into the corresponding 1,4-disubstituted 1,2,3-triazoles through copper(I) active species under mild conditions. CuAAc fulfils the criteria of “click chemistry” defined by Sharpless and coworkers, who defines this concept as “the reaction must be modular, wide in scope, give very high yields, generate only inoffensive byproducts, be stereospecific, with simple reaction conditions and readily available starting materials, use benign solvents and require simple product isolation”.[163]

The catalyst of these 1,3-dipolar cycloadditions is easily prepared by reduction of copper(II) salts, for instance $CuSO_4 \cdot 5H_2O$ with the presence of sodium ascorbate (NaAsc) as the reducing agent at 0.25 – 2 % mol catalyst loading. Also, copper(I) salts might be used directly in the absence of a reducing agent and with the presence of a nitrogen base.[164]

In this context, the synthetic route for the desired [2]catenane is very similar to the previous one from Figure VI.2. First, a Bingel reaction will take place via supramolecular mask strategy using the matryoshka system. However, two different unsymmetrical bromomalonates will be used this time, since two different fullerene derivatives have to be synthesized to carry out the cycloaddition: one featuring a terminal alkyne (**22**) and one with a terminal azide group (**23**). This way, the intramolecular reaction can also be prevented in contrast to metathesis reaction. Once these bis-adducts are synthesized, CuAAc will be carried out to join together both adducts and form the molecular shuttle (Figure VI.9).

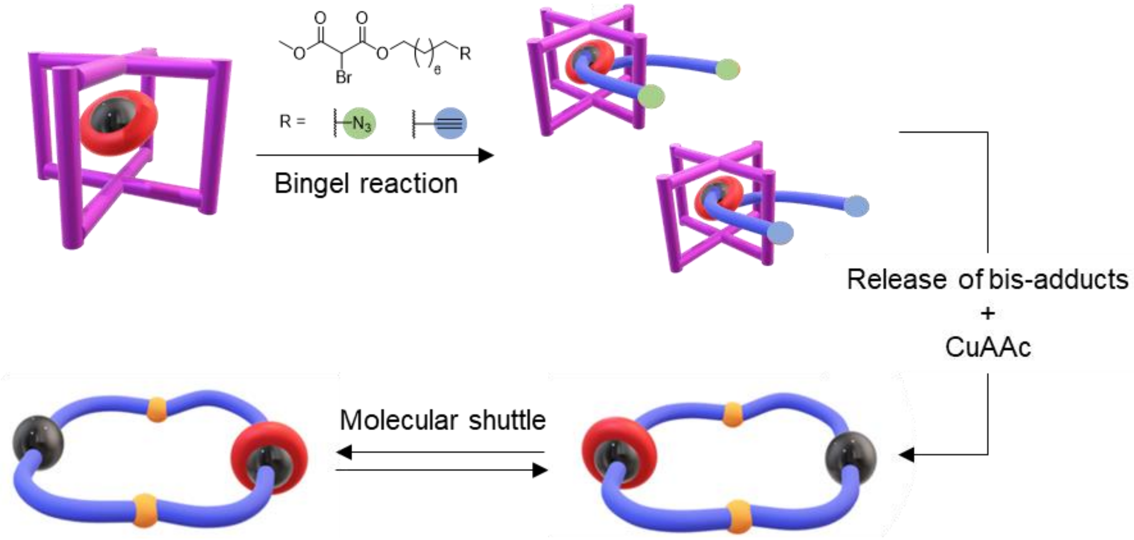

*Figure VI.9. Representative scheme of the 2nd synthetic strategy to form the desired fullerene-based molecular shuttle.*

### *VI.2.1 Bingel reaction*

Bingel reaction via supramolecular mask strategy was carried out using similar conditions as the 1st strategy explained in the previous section. $C_{60}$⊂[10]CPP⊂**1d**·$(BArF)_8$ was dissolved in acetonitrile and NaH and bromomalonate **22** was added and stirred under a $N_2$ atmosphere at room temperature. The encapsulated bis-alkyne-$C_{60}$ was achieved as the main product of the crude reaction, as can be seen in the monitoring by HR-ESI-MS in Figure VI.10. However, after pushing the reaction (long reaction time and addition of a large excess of **22** and NaH) encapsulated mono-adduct was still present in a proportion of 0.8:1 (mono-alkyne-$C_{60}$:bis-alkyne-$C_{60}$, respectively).

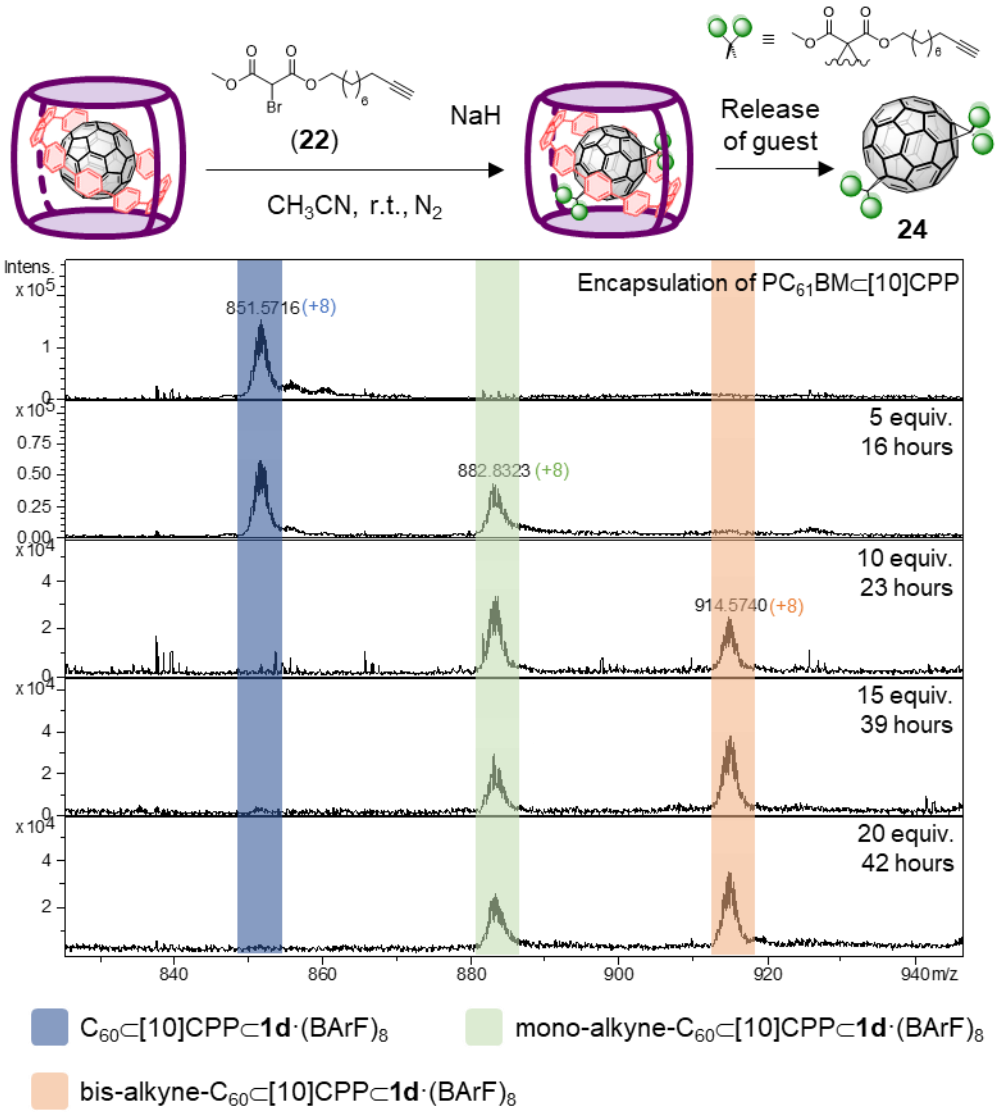

*Figure VI.10. HR-ESI-MS monitoring of the formation of bis-alkyne-$C_{60}$⊂[10]CPP⊂**1d**·(BArF)$_8$ through Bingel reaction using bromomalonate **22**.*

After the exchange with fullerene $C_{60}$, bis-adduct was released from [10]CPP⊂**1d**·(BArF)$_8$ and purified by a preparative TLC. As previously, only two fractions corresponding to bis-adducts were obtained and they were analysed altogether. MALDI-MS and UV-vis spectroscopy confirmed that both fractions are *trans*-3-bis-adducts (**24**), since both peaks of the chromatogram have the same UV-vis pattern and resemble to reported ones[81] (Figure VI.11).

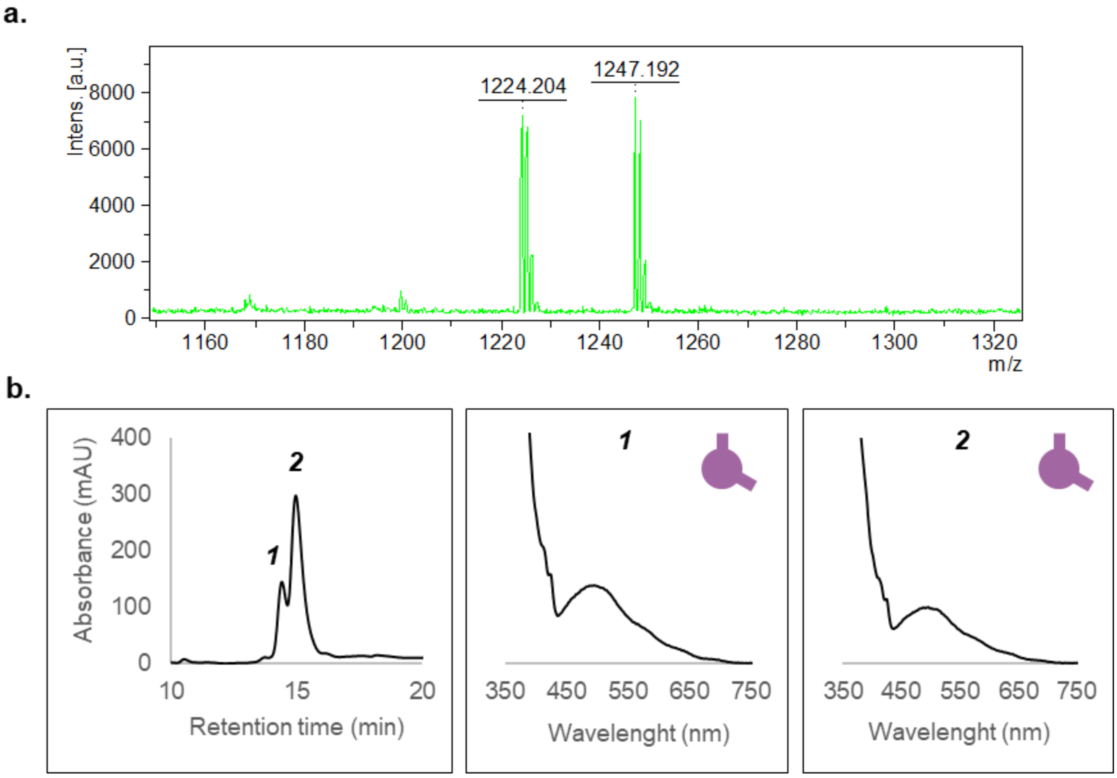

*Figure VI.11. Characterization of bis-adduct **24**. a) MALDI mass spectrum of purified compound **24**. b) HLPC chromatogram (left) of purified compound **24** and UV-vis spectra (middle and right) of each peak of the chromatogram.*

Bingel reaction was carried out also using bromomalonate **23** with the same procedure. After almost 40 hours of reaction and the addition of 25 equivalents of bromomalonate **23** and 13 equivalents of NaH, the encapsulated mono-adduct still was the main product of the crude in a ratio of 2:1 (mono-azide-$C_{60}$:bis-azide-$C_{60}$, respectively). Moreover, **1d**·$(BArF)_8$ started to decompose, as can be seen in the HR-ESI-MS monitoring in Figure VI.12.

The exchange with fullerene $C_{60}$ was carried out. However, after purification of the sample through preparative TLC and analysis by MALDI-MS of the obtained fractions (Annex VI, Figure S.112), none of them corresponded to neither mono-azide-$C_{60}$ nor bis-azide-$C_{60}$, probably due to the azide moieties of the adducts that can undergo further intra- or intermolecular reactivity with fullerene surface.

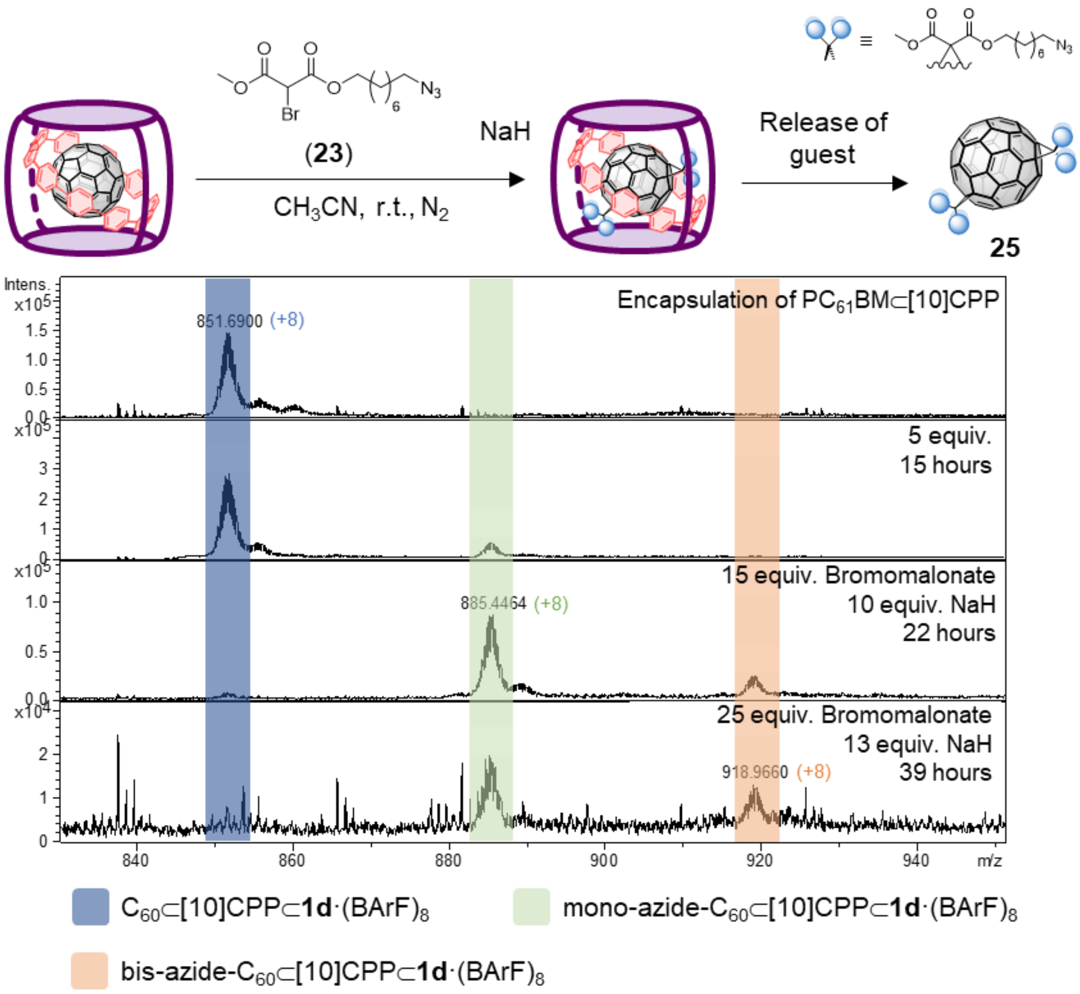

*Figure VI.12. HR-ESI-MS monitoring of the formation of bis-azide-$C_{60}$⊂[10]CPP⊂**1d**·$(BArF)_8$ through Bingel reaction using bromomalonate **23**.*

### *VI.2.2 Copper(I)-catalysed azide-alkyne cycloaddition*

First, CuAAc was carried out using mono-adducts **26** and **27** without being encapsulated in order to find the optimal conditions. Following the same procedures of the 1st strategy, mono-adducts were synthesized successfully (Figure VI.13.a). They were characterized by MALDI-MS and $^1$H-NMR (Annex VI, Figure S.113 – S.117). Then, both mono-adducts were submitted to CuAAc in a proportion of 1:1 using 2 equivalents of $CuSO_4 \cdot 5H_2O$ and 10 equivalents of sodium ascorbate in a mixture of DCM and Milli-Q water (1:1) at 40ºC.[165] The biphasic mixture was stirred vigorously for 18 hours. After this time, the cycloaddition took place as confirmed by MALDI-MS (calculated m/z of product **28**: 1962.277). Nevertheless, some starting mono-adduct **26** (calculated m/z: 972.970) still remained in the crude, while mono-adduct **27** (calculated m/z: 989.138) was totally consumed (Figure VI.13.c)

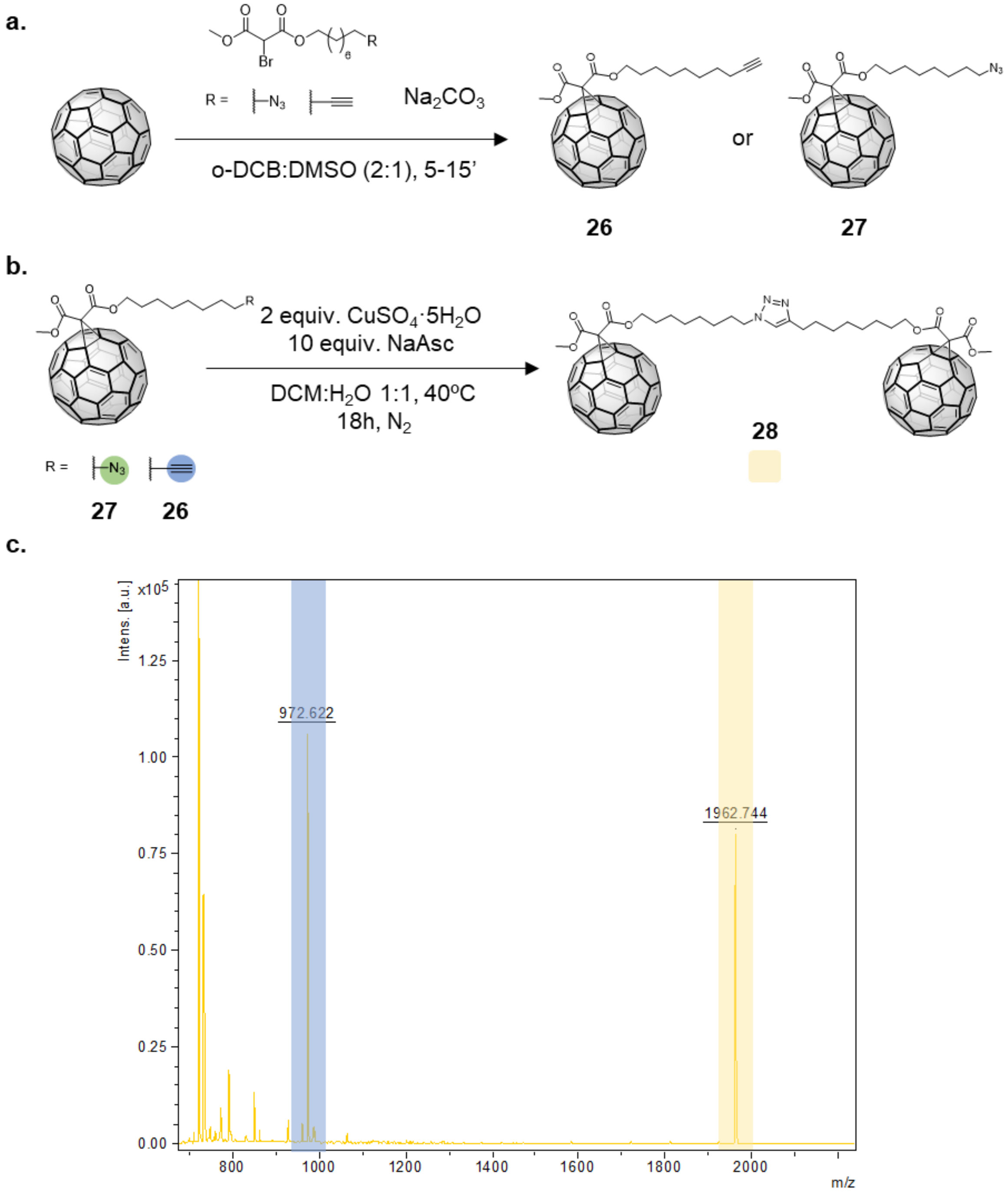

*Figure VI.13. a) Synthesis of mono-adducts **26** and **27** through Bingel reaction using similar conditions reported by Jin, Peng and coworkers.[162] b) Copper(I)-catalysed azide-alkyne cycloaddition using mono-adducts **26** and **27**. c) MALDI mass spectrum of the organic phase of the CuAAc after 18 hours of reaction.*

Once the reaction conditions were stablished for the CuAAc with non-encapsulated mono-adducts **26** and **27**, the reaction was performed using **27**⊂**1b**·$(BArF)_8$ and **26**, since some instability of **27** was observed during its release from the **27**⊂[10]CPP⊂**1d**·$(BArF)_8$, as mentioned before. Nevertheless, the reaction didn't proceed even adding an excess of $CuSO_4\cdot5H_2O$ and NaAsc (see HR-ESI-MS monitoring in Annex VI, Figure S.118).

Finally, a stability test using **27**⊂**1b**·(BArF)$_8$ was carried out to make sure that mono-adduct **27** is stable inside the cage. Once **27** was encapsulated within **1b**·(BArF)$_8$, the complex was dissolved in DCM. Next, Milli-Q water was added (1:1) and it was vigorously stirred for 18 hours at 40ºC. Then, $CuSO_4 \cdot 5H_2O$ and NaAsc was added and it was stirred for 18 hours more. As can be seen in the mass spectra of Figure VI.14, after the first 18 hours, the complex started to decompose considerably. At the end of the reaction, the signal corresponding **27**⊂**1b**·(BArF)$_8$ almost disappeared, meaning that mono-adduct **27** is also unstable inside **1b**·(BArF)$_8$, and therefore, this route is also deemed as a dead end.

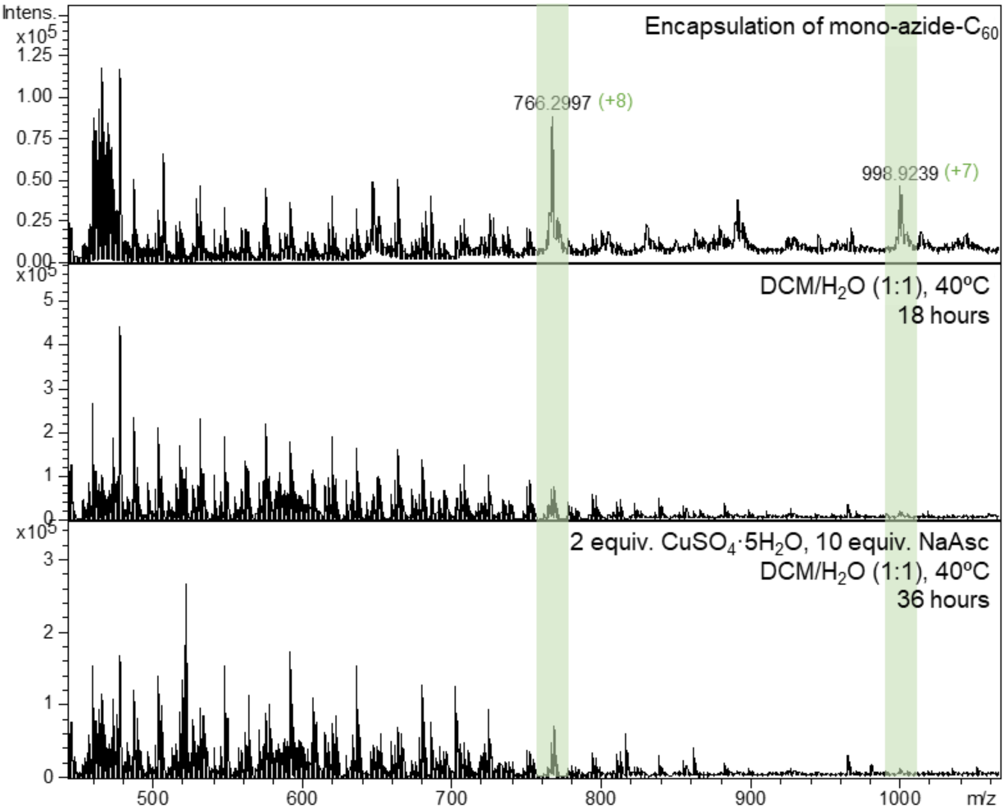

*Figure VI.14. Stability test of **27** inside **1b**·(BArF)$_8$ nanocapsule. HR mass spectra of **27**⊂**1b**·(BArF)$_8$ (top), **27**⊂**1b**·(BArF)$_8$ in a mixture of DCM:$H_2O$ (1:1) at 40ºC after 18 hours stirring (middle) and **27**⊂**1b**·(BArF)$_8$ with the presence of $CuSO_4 \cdot 5H_2O$ and NaAsc after 18 hours more (bottom).*

## VI.3 Third strategy: combination of Bingel and Bingel-Hirsch reaction

A third synthetic route was proposed to form the desired [2]catenane after demonstrating the instability of the previous fullerene derivatives. This time, the second step of the route will be a Bingel-Hirsch reaction.

Bingel-Hirsch reaction is a variant from Bingel reaction, that instead of reacting bromomalonates with fullerene to give methanofullerenes, involves the use of malonates with the presence of $CBr_4$ and diazabicyclo[5.4.0]undec-7-ene (DBU) as base. This way, the bromomalonate is generated *in situ* and, with the presence of a base, it undergoes the corresponding fullerene cyclopropanation.[166]

The 3rd synthetic route starts, as previously, with a Bingel reaction via supramolecular mask approach using the matryoshka system. This time, the bromomalonate used in this cyclopropanation present one alkyl chain with a terminal malonate. Upon bis-functionalization of fullerene $C_{60}$, these terminal malonates might allow to carry out a Bingel-Hirsch reaction with the presence of $CBr_4$ and DBU (2nd step of the route), forming the desired [2]catenane (Figure VI.15). In order to have only one [10]CPP ring, Bingel-Hirsch reaction will be performed using **1b**·(BArF)$_8$ nanocapsule instead the matryoshka system ($C_{60}$⊂[10]CPP⊂**1d**·(BArF)$_8$). In principle, bis-adduct coming from **1b**·(BArF)$_8$ will present a regiochemistry (equatorial) different from that one coming from [10]CPP⊂**1d**·(BArF)$_8$ (*trans*-3). Thus, the molecular shuttle will present two non-degenerated fullerene stations.

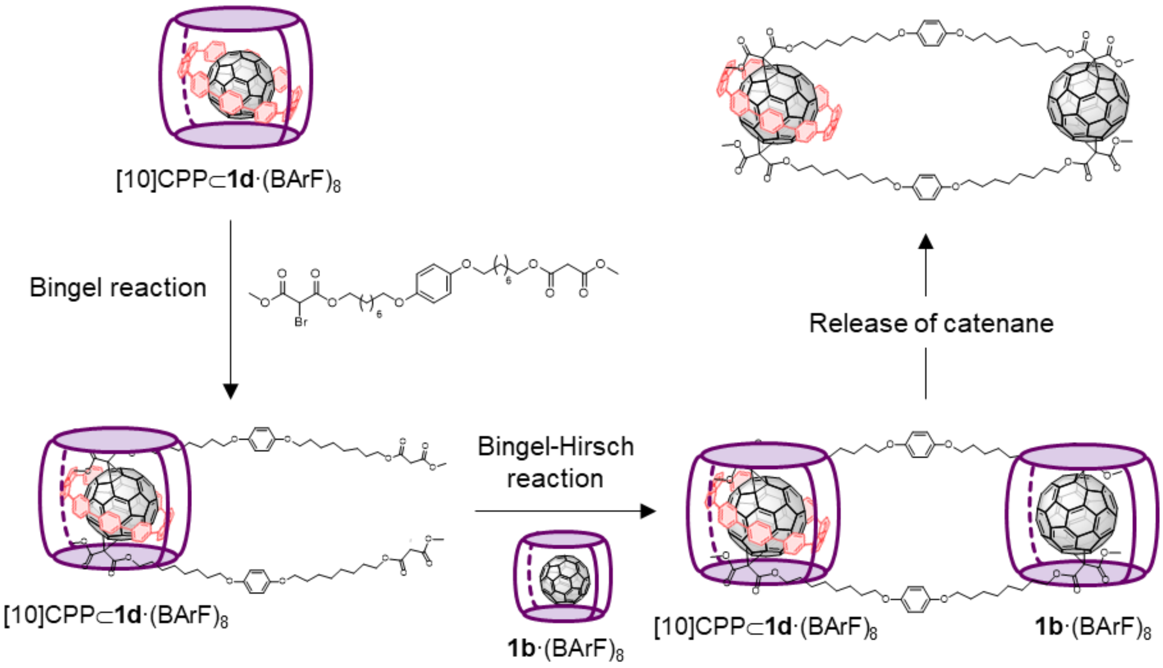

*Figure VI.15. Representative scheme of the 3rd synthetic strategy to form the desired fullerene-based molecular shuttle.*

### *VI.3.1 Bingel reaction*

Bingel reaction via supramolecular mask strategy was carried out using similar conditions as the 1st and 2nd strategies. $C_{60}$⊂[10]CPP⊂**1d**·(BArF)$_8$ was dissolved in acetonitrile and NaH and bromomalonate **29** was added and stirred under a $N_2$

atmosphere at room temperature. As can be seen in the HR-ESI-MS monitoring (Figure VI.16), a set of 2 peaks appeared for the encapsulated mono-adduct and a set of 3 peaks for the encapsulated bis-adduct (**30**⊂[10]CPP⊂**1d**·(BArF)$_8$) due to the free bromide (coming from the Bingel reaction) that attacks the acidic protons of the terminal malonates. Therefore, for mono-malonate-C$_{60}$⊂[10]CPP⊂**1d**·(BArF)$_8$, one peak corresponds to the non-brominated malonate (m/z: 922.3510) and one to the brominated malonate (m/z: 932.3431). For bis-malonate-C$_{60}$⊂[10]CPP⊂**1d**·(BArF)$_8$, one peak corresponds to the non-brominated malonates (m/z: 992.7636), one to the mono-brominated malonate (m/z: 1002.5042) and one to the bis-brominated malonates (m/z: 1012.2527).

Despite pushing the conditions of the Bingel reaction (large excess of bromomalonate **29** and base, 21 and 12 equivalents, respectively), a mixture of encapsulated mono- and bis-adduct was obtained in a proportion of 0.9:1, respectively. Also, nanocapsule **1d**·(BArF)$_8$ started to decompose.

In order to promote the formation of **30**, mono-malonate-C$_{60}$⊂[10]CPP⊂**1d**·(BArF)$_8$ was submitted to Bingel reaction using the same conditions instead of C$_{60}$⊂[10]CPP⊂**1d**·(BArF)$_8$. To do so, first, mono-adduct **31** was synthesized successfully using the reported conditions by Jin, Peng and coworkers.[162] The vanishing of the acidic proton (4.85 ppm) from the bromomalonate **29** of the $^1$H-NMR spectrum and the MALDI mass spectrum confirmed the synthesis of **31** (Annex VI, Figure S.123 – S.125). Then, 1 equivalent of mono-adduct **31** was mixed with 1 equivalent of [10]CPP in order to synthesize **31**⊂[10]CPP. The shift of the protons close to the aromatic ring confirmed the successful formation of the complex (Figure VI.17 and Annex VI, Figure S.126 – 127).

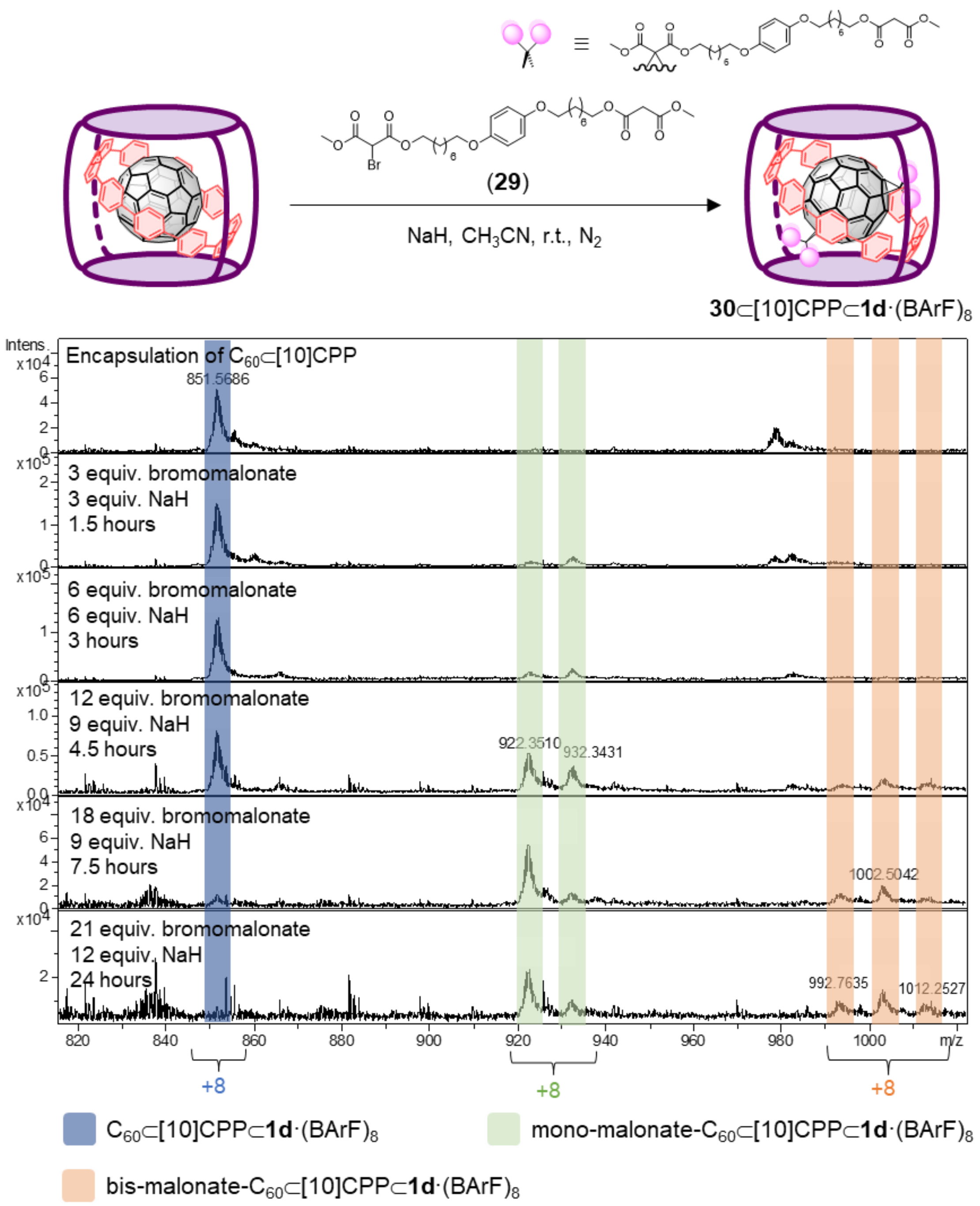

*Figure VI.16. HR-ESI-MS monitoring of the formation of bis-malonate-C$_{60}$⊂[10]CPP⊂**1d**·(BArF)$_8$ through Bingel reaction starting from C$_{60}$⊂[10]CPP⊂**1d**·(BArF)$_8$.*

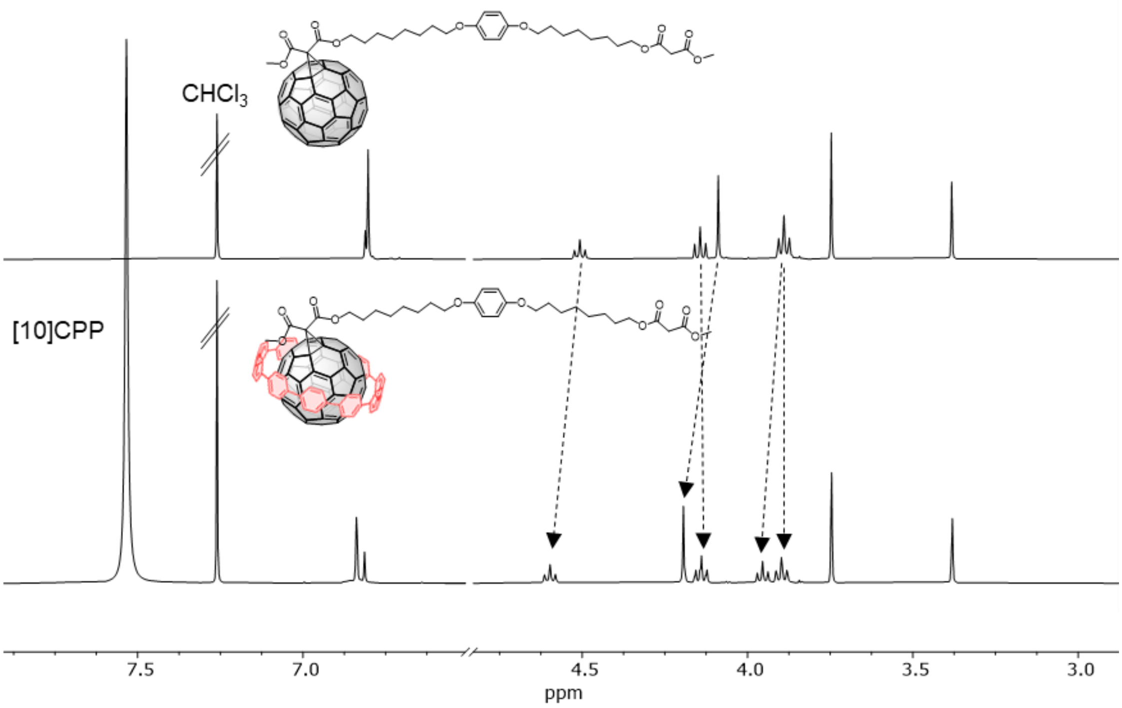

*Figure VI.17. Zoom between 3.0 and 8.0 ppm of $^1$H-NMR spectra of **31** (top) and **31**⊂[10]CPP (bottom). Experiments performed in $CDCl_3$ at 298K (400 MHz).*

Upon successful encapsulation of **31**⊂[10]CPP into **1d**·(BArF)$_8$, Bingel reaction took place using the same conditions as previously. The reaction was stop after only 5 hours and 9 equivalents of bromomalonate **29** and NaH in order to prevent the decomposition of the nanocapsule, as seen in the previous experiment. Even starting with **31**⊂[10]CPP⊂**1d**·(BArF)$_8$, the proportion of encapsulated **31**:**30** derivatives was 1:0.8, respectively (see HR-ESI-MS monitoring in Figure VI.18).

Although **30**⊂[10]CPP⊂**1d**·(BArF)$_8$ was not the main product of the crude, preliminary tests of the second step of the synthetic route (i.e. Bingel-Hirsch reaction) was performed using this proportion of encapsulated species as starting point.

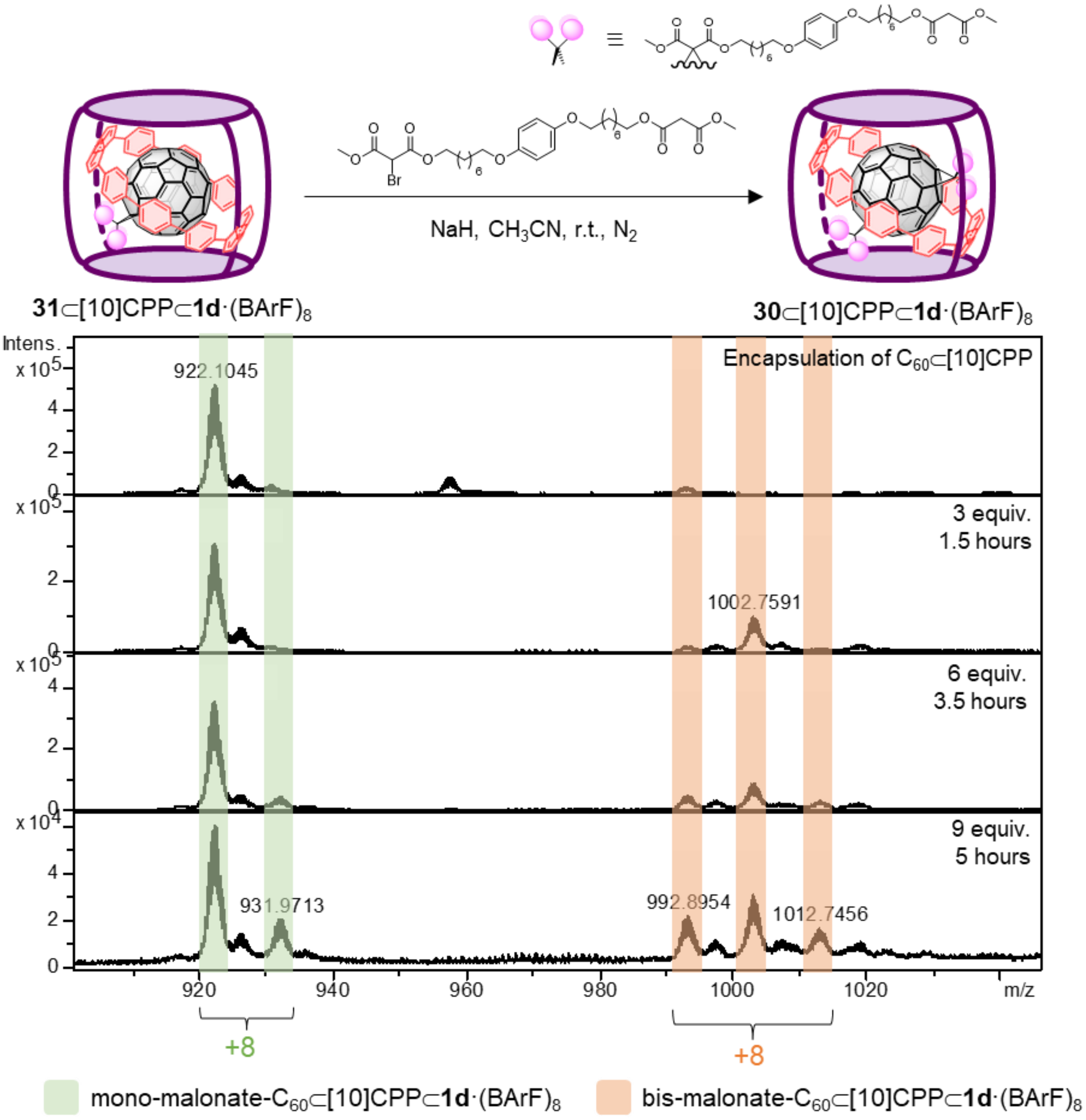

*Figure VI.18. HR-ESI-MS monitoring of the formation of **30**⊂[10]CPP⊂**1d**·(BArF)$_8$ through Bingel reaction starting from **31**⊂[10]CPP⊂**1d**·(BArF)$_8$.*

### *VI.3.2 Bingel-Hirsch reaction*

First of all, a test of the Bingel-Hirsch reaction using $CBr_4$, NaH, diethyl malonate and $C_{60}$⊂**1b**·(BArF)$_8$ was performed to check if the reaction could take place in the presence of **1b**·(BArF)$_8$ nanocapsule. It is worth noting that DBU was replaced by NaH, since in Chapter V it was demonstrated that DBU decomposes the cage. Bingel-Hirsch reaction was carried out following similar procedures of Bingel reaction in the presence of **1b**·(BArF)$_8$ nanocapsule. Successfully, after 5.5 hours and 6 equivalents of $CBr_4$, NaH and diethyl malonate, the corresponding encapsulated bis-adduct **32** (bis-(Bingel-E)-$C_{60}$⊂**1b**·(BArF)$_8$) was detected as the main product of the crude, as monitored by HR-

ESI-MS (Figure VI.19). However, significant peaks of mono- and tris-adducts were detected (mono-(Bingel-E)-$C_{60}\subset$**1b**·(BArF)$_8$ and tris-(Bingel-E)-$C_{60}\subset$**1b**·(BArF)$_8$, respectively).

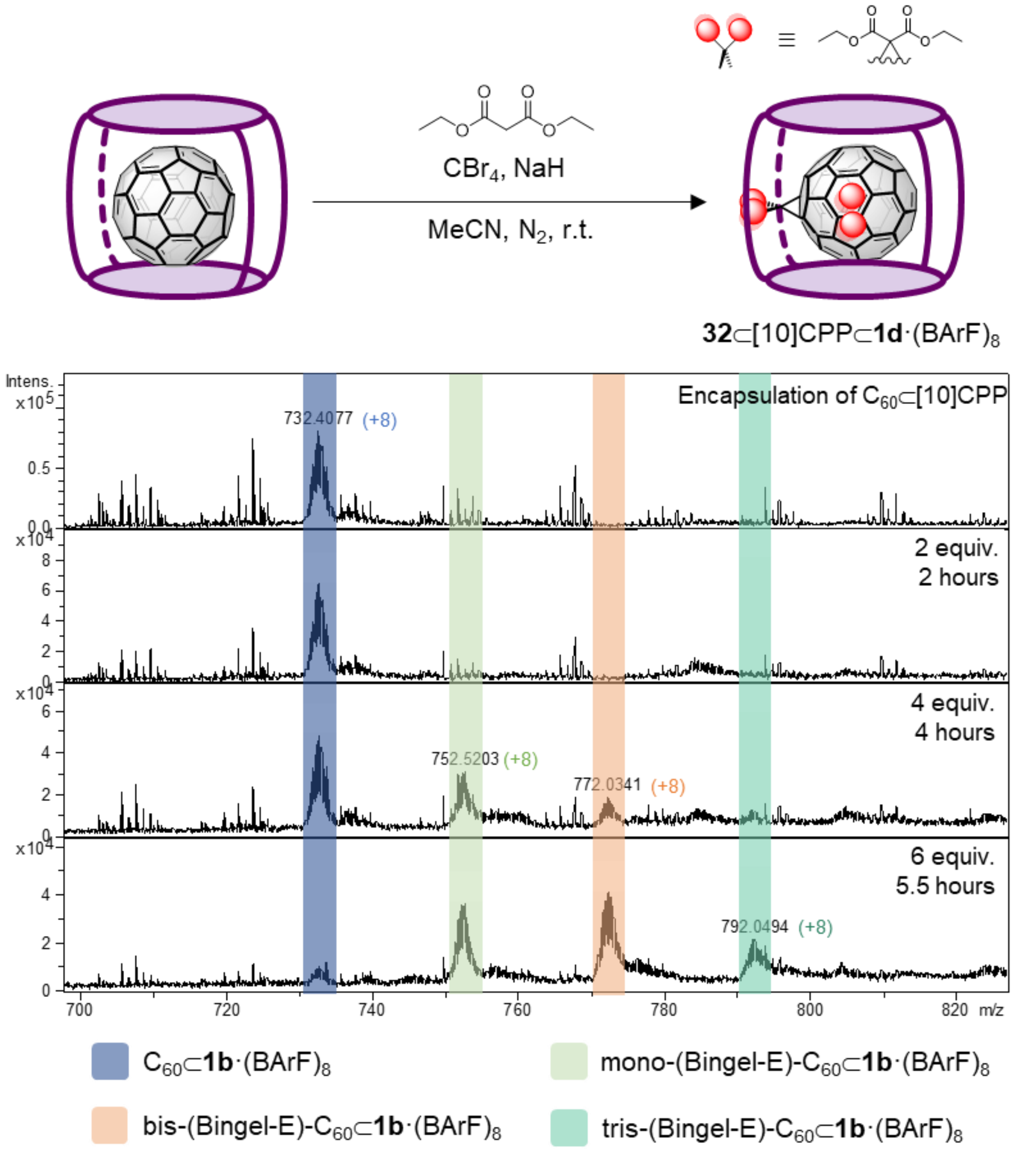

*Figure VI.19. HR-ESI-MS monitoring of the formation of bis-(Bingel-E)-$C_{60}\subset$**1b**·(BArF)$_8$ through Bingel-Hirsch reaction starting from $C_{60}\subset$**1b**·(BArF)$_8$.*

After checking the stability of **1b**·(BArF)$_8$ under Bingel-Hirsch conditions, the 2$^{nd}$ step of the synthetic route took place starting from the crude reaction without further purification of the 1$^{st}$ step (Figure VI.18). The first experiment was carried out working in lower concentrations ($10^{-4}$ M) in order to avoid polymerization and promote the ring-closing reaction between two encapsulated bis-adducts. Nevertheless, after the stepwise addition of the reactants (CBr$_4$, NaH and $C_{60}\subset$**1b**·(BArF)$_8$) in 20 hours, only empty cage (**1b**·(BArF)$_8$ and **1d**·(BArF)$_8$) was detected in the mass spectrum (Annex VI, Figure S.128) after washing the crude with chloroform (otherwise, not a single signal of nanocapsule or host-guest complex was detected).

Another experiment was carried out starting with washes of diethyl ether of the crude reaction of the 1st step in order to remove the excess of bromomalonate **29**. Then, Bingel-Hirsch reaction was performed in the same concentration as Bingel reaction ($10^{-3}$ M) to pursue the formation of the fullerene-based [2]catenane (**33**). After the addition of less equivalents of reagents ($CBr_4$, NaH and $C_{60}\subset$**1b**$\cdot$(BArF)$_8$) in shorter times between additions, the crude reaction was analysed by HR-ESI-MS. This time, washes with chloroform of the crude was not necessary to analyse the sample. As can be seen in the mass spectrum of Figure VI.20, several peaks appeared that corresponds to empty cages (**1b**$\cdot$(BArF)$_8$ and **1d**$\cdot$(BArF)$_8$), to $C_{60}\subset$[10]CPP$\subset$**1d**$\cdot$(BArF)$_8$, to encapsulated mono-adduct **31** in both cages and to **30**$\subset$**1b**$\cdot$(BArF)$_8$. It indicates that all guests ($C_{60}$, mono-adduct **31** and bis-adduct **30**) have been exchanged between both cages, which is detrimental for our strategy.

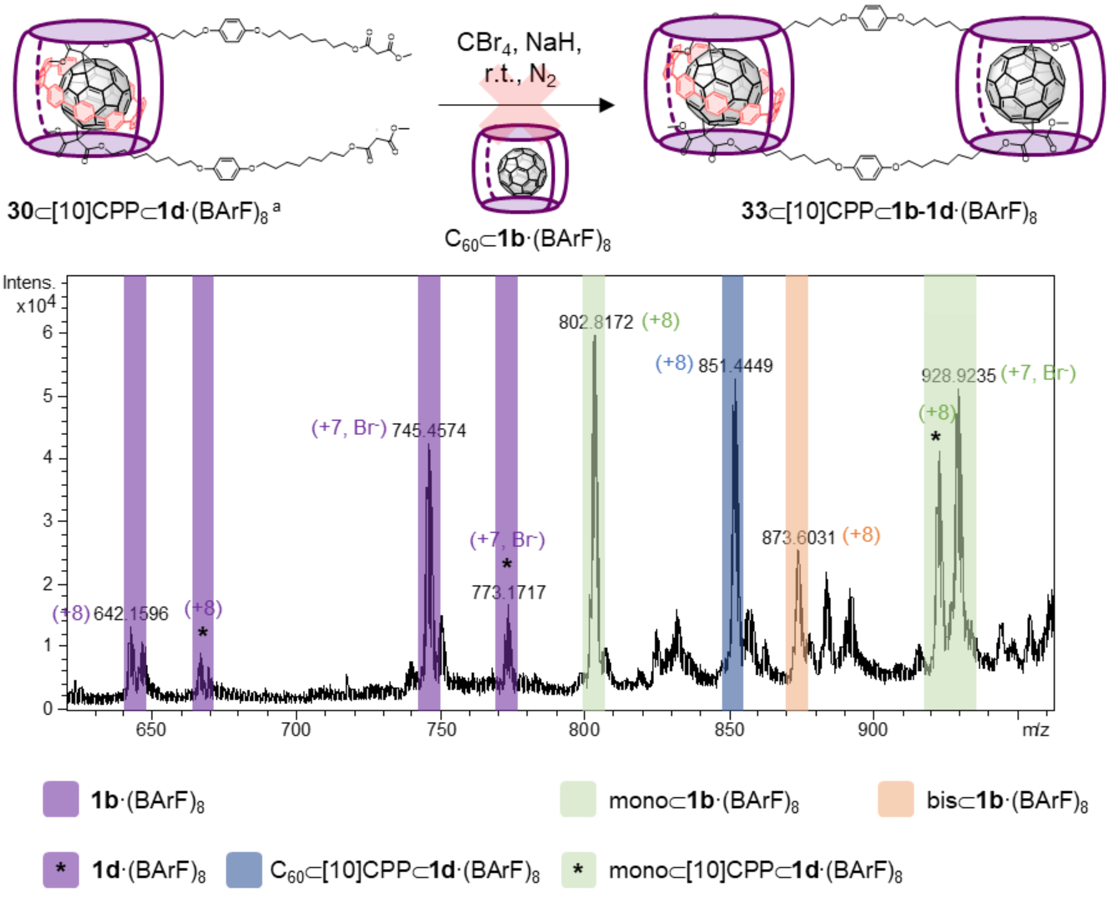

*Figure VI.20. HR mass spectrum of the crude of Bingel-Hirsch reaction (2nd step). Note that some peaks with (+7) charge correspond to nanocapsules with $Br^-$ instead of $BArF^-$ as counterion. $^a$: The starting material was a mixture of encapsulated **31** and **30** (1:0.8, respectively), but only **30**$\subset$[10]CPP$\subset$**1d**$\cdot$(BArF)$_8$ is depicted for clarity.*

In order to increase the success possibilities of this strategy in future work, it is mandatory to increase the relative yield of bis-adduct **30** from the 1st step (Figure VI.18), release it from **30**$\subset$[10]CPP$\subset$**1d**$\cdot$(BArF)$_8$ and purify it, if needed. Subsequently, the Bingel-Hirsch reaction should be performed using the **30**$\subset$[10]CPP (without **1d**·$(BArF)_8$ nanocapsule) acting as the malonate of the reaction and starting from $C_{60}$$\subset$**1b**·$(BArF)_8$. This way, exchange of guests between different cages might be prevented and the [2]catenane might be formed.

# CHAPTER VII. SELECTIVE ENCAPSULATION OF $TB_2@C_{80}^-$ FROM A TERBIUM-BASED EMF EXTRACT USING SUPRAMOLECULAR NANOCAPSULES

As mentioned in section *I.3 Endohedral metallofullerenes*, fullerenes cages are able to encapsulate metallic clusters which would be unstable in its isolated form thanks to the intramolecular charge transfer between the entrapped cluster and the carbon cage. These metal clusters have been recently recognized as single molecule magnets (SMM) with potential applications in spintronics, quantum computing and high-density storage devices.[167] A strategy to improve the performance of SMMs is to increase the single-ion magnetic anisotropy, and this approach is possible to achieve using lanthanide-based EMFs.[105,168] Particularly, dimetallofullerenes (EMFs with a dimetallic dimer in their cavities) offer unprecedented possibilities for a strong exchange coupling.[169–171]

Ribas, Echegoyen and coworkers used a $Cu^{II}$-based prismatic tetragonal nanocapsule (**1c**·$(BArF)_8$ from Chapter IV, Figure IV.1) to selectively encapsulate and purify a dimetallofullerene from an uranium-based EMF extract.[32] As discussed in *I.3.2 Molecular recognition of EMFs using supramolecular platforms*, the nanocapsule was able to discriminate $U_2@C_{80}$-$I_h$ from $Sc_2CU@C_{80}$-$I_h$ due to the internal cluster, since the alignment of the two uranium ions from $U_2@C_{80}$-$I_h$ with both zincs of the porphyrin of the nanocapsule favoured the interaction with the nanocapsule because of the higher negative charge present on carbon atoms closer to the $U^{3+}$.

In this chapter, **1b**·$(BArF)_8$ and **1c**·$(BArF)_8$ (Chapter IV, Figure IV.1) nanocapsules will be used to explore their selectivity towards a fullerene/EMF extract which contains different terbium-based mono- and bimetallic species. This project is in collaboration with Prof. Alexey A. Popov from Leibniz Institute for Solid State and Materials Research, in Dresden (Germany), who provided the starting material.

## VII.1 Prepurification of the EMF extract

The starting material was an EMF extract that contained anionic terbium-based endohedral metallofullerenes, including $Tb@C_{80}^-$, $Tb@C_{82}^-$, $Tb_2@C_{78}^-$ and $Tb_2@C_{80}^-$ (Figure VII.1). In order to stabilize EMFs in the anionic form, tetrabutylammonium perchlorate (TBAP) was added to the extraction process in *N,N*-dimethylformamide (DMF) from the carbon soot to form the corresponding neutral species (tetrabutylammonium acted as the countercation of these anionic EMFs).

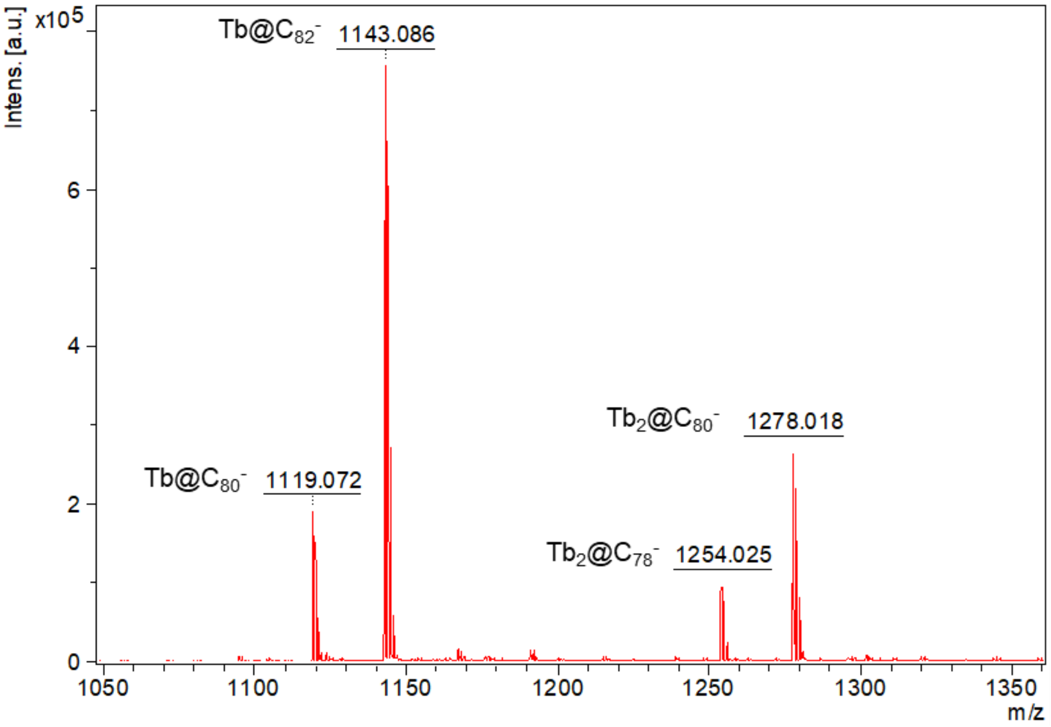

*Figure VII.1. MALDI mass spectrum of anionic EMF-based extract.*

After a few attempts adding directly **1b**·$(BArF)_8$ and **1c**·$(BArF)_8$ nanocapsules to the fullerene/EMF extract dissolved in different solvents (toluene, chloroform and mixtures of them with acetonitrile), the host-guest product could not be isolated, probably due to the presence of perchlorate anion coming from the extraction process of the carbon soot. This anion might exchange with the initial anion of the cage ($BArF^-$) resulting in a highly insoluble nanocapsule that couldn't be neither isolated nor analysed. For this reason, a pre-treatment before adding the nanocapsule was attempted. First, a liquid-solid extraction was carried out to the fullerene/EMF extract with a mixture of $CS_2$ and acetone (4:1) or chloroform since EMFs are highly soluble in these solvents. Then, a preparative TLC with dichloromethane with 8% of methanol was performed. After MALDI-MS analysis of all fractions obtained from the preparative TLC, only 2 fractions contained EMFs (mostly Tb@$C_{82}^-$ and $Tb_2$@$C_{80}^-$). As can be seen in Figure VII.2, the mass spectrum corresponding to the first fraction was much cleaner, so the second fraction was discarded and we focused on the first one. This fraction represented only 0.7% with respect to the initial sample.

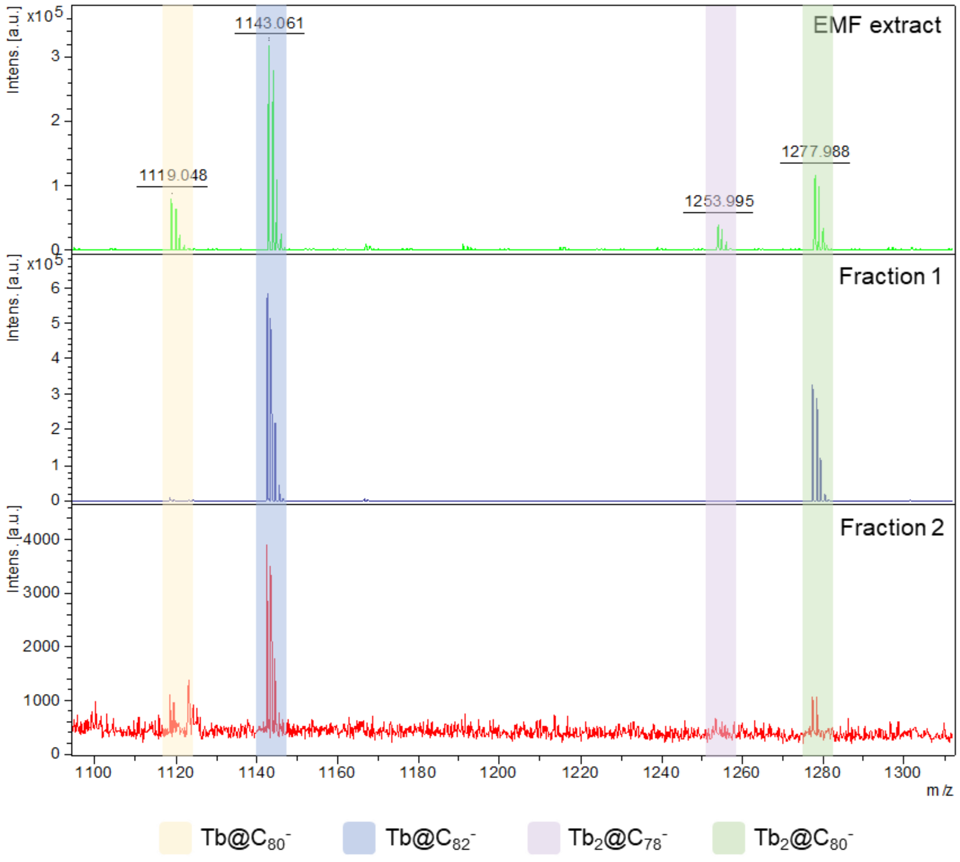

*Figure VII.2. MALDI mass spectra of EMF extract (top) and fractions after preparative TLC with DCM and 8% of methanol (middle and bottom).*

## VII.2 Competition experiments towards the selective encapsulation of $Tb_2@C_{80}^-$

Sequential sub-stoichiometric additions of 0.006 mg (0.5 nmols) of **1b**·$(BArF)_8$ in acetonitrile were performed at room temperature to a solution of terbium-based EMFs (323.2 nmols considering that all EMFs are $Tb_2@C_{82}^-$, fraction 1 of Figure VII.2) in chloroform, which contained majorly a mixture of $Tb@C_{82}^-$ and $Tb_2@C_{80}^-$ in a 1:0.46 ratio, respectively, with traces of $Tb@C_{80}^-$ and $Tb_2@C_{78}^-$. The mixture was stirred for only one minute after each addition and the crude was monitored by MALDI-MS. After some minutes, a precipitate appeared due to the presence of chloroform in the crude in which **1b**·$(BArF)_8$ is insoluble. As can be seen in the MALDI-MS monitoring (Figure VII.3), **1b**·$(BArF)_8$ encapsulated $Tb_2@C_{80}^-$ selectively, since the signal corresponding to $Tb_2@C_{80}^-$ decreases proportionally to the amount of **1b**·$(BArF)_8$ added to the mixture.

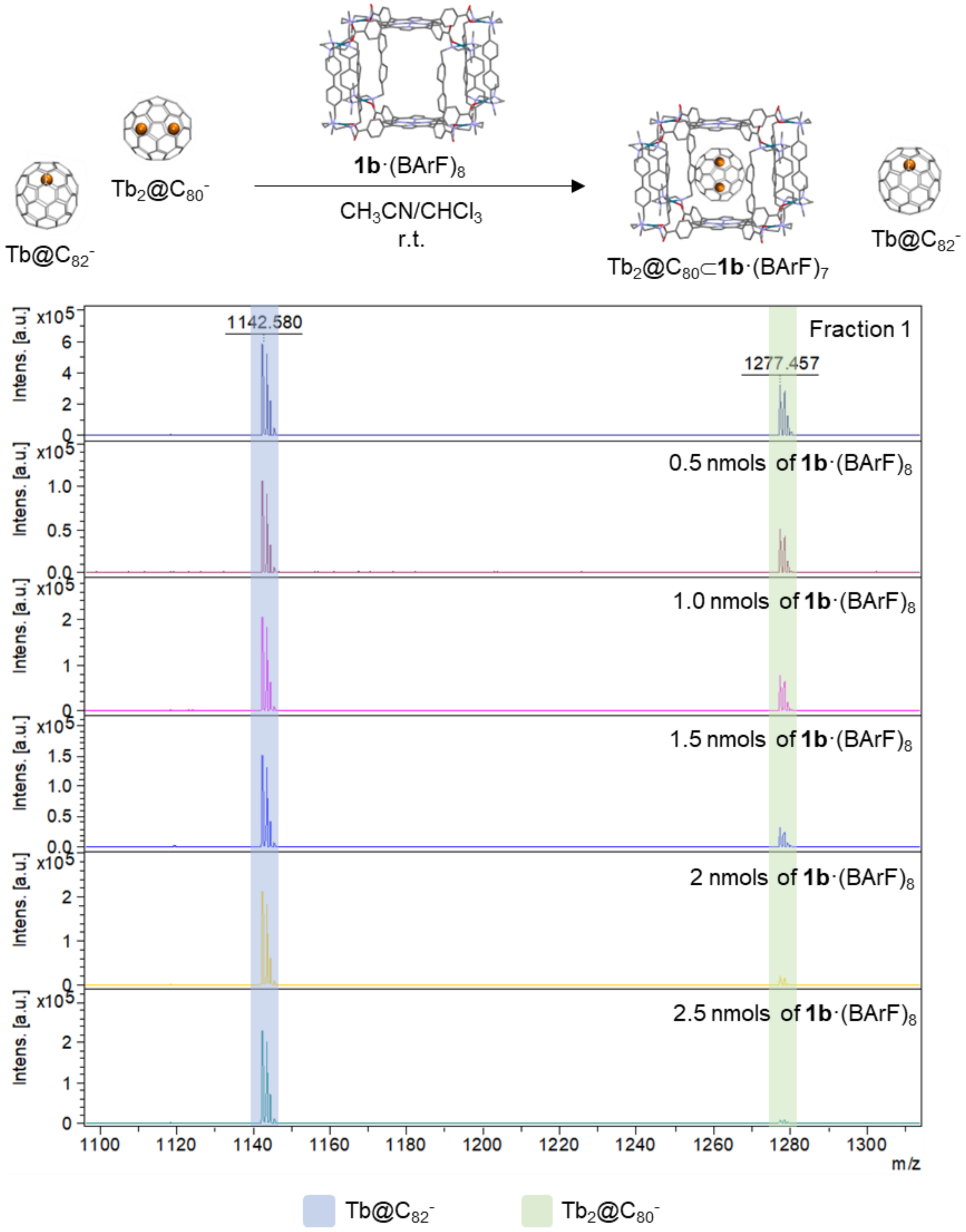

*Figure VII.3. MALDI-MS monitoring of the sequential additions of* ***1b***$\cdot$*(BArF)*$_8$ *to a mixture of mainly* $Tb@C_{82}^-$ *and* $Tb_2@C_{80}^-$*.*

Attempts to scale-up the reaction following the same procedure in order to confirm by HR-ESI-MS that $Tb_2@C_{80}^-$ was the unique encapsulated species failed due to host-guest solubility issues (the host-guest complex didn't precipitate). Moreover, **1b**$\cdot$(BArF)$_8$ appeared almost empty (Annex VII, Figure S.129). For this reason, instead of adding the nanocapsule in solution (dissolved in acetonitrile), it was added in the solid state (a suspension of chloroform) at room temperature and it was stirred for longer times, as reported in previous protocols by Ribas, Echegoyen and coworkers.[32,34,125] This way, the isolation of the host-guest complex would be accomplished easily by a simple filtration. A comparative monitoring was performed using analogous Pd$^{II}$- and Cu$^{II}$-based nanocapsules (i.e. **1b**·(BArF)$_8$ and **1c**·(BArF)$_8$) to study the different selectivity of each nanocapsule towards the terbium-based EMFs, as can be seen in Figure VII.4.

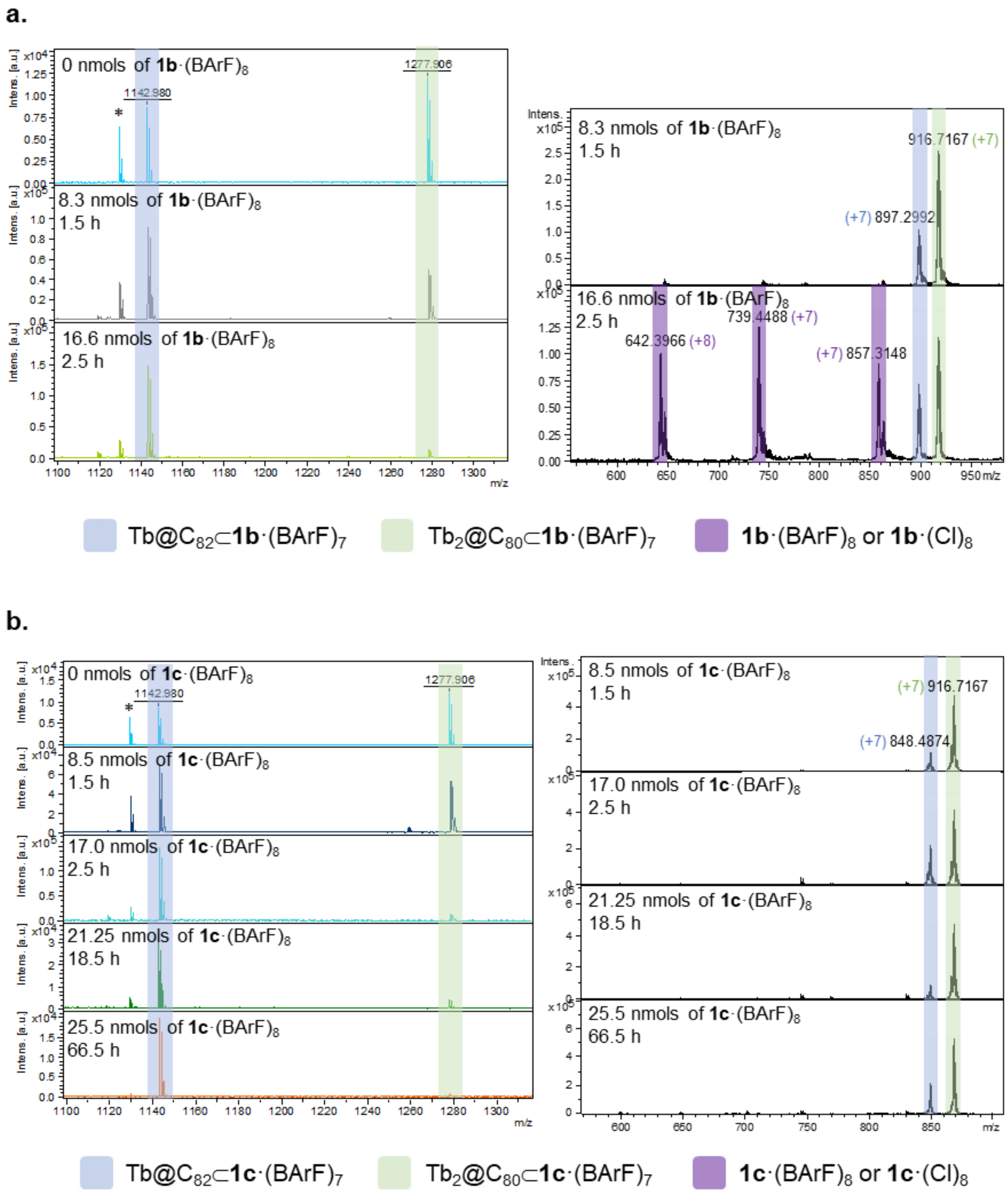

*Figure VII.4. Comparative monitoring for the selective encapsulation of $Tb_2@C_{80}^-$ using analogous a) **1b**·(BArF)$_8$ and b) **1c**·(BArF)$_8$ nanocapsules. Left: MALDI-MS monitoring of the supernatant once solid (host-guest complexes with **1b**·(BArF)$_8$ or **1c**·(BArF)$_8$, respectively) have been filtrated. Right: HR-ESI-MS monitoring of the solid (host-guest complexes with **1b**·(BArF)$_8$ or **1c**·(BArF)$_8$, respectively) after filtration.*

As can be observed in the previous mass spectra, **1c**·(BArF)$_8$ nanocapsule is much more selective towards $Tb_2@C_{80}^-$ than **1b**·(BArF)$_8$. For instance, after the first addition (8.3

nmols of **1b**·(BArF)$_8$ and 8.5 nmols of **1c**·(BArF)$_8$ added in each experiment) a ratio of 0.44:1 of the encapsulated species (Tb@C$_{82}$⊂**1b**·(BArF)$_7$ vs Tb$_2$@C$_{80}$⊂**1b**·(BArF)$_7$, respectively) is observed for the Pd$^{II}$ nanocapsule, while a ratio of 0.22:1 (Tb@C$_{82}$⊂**1c**·(BArF)$_7$ vs Tb$_2$@C$_{80}$⊂**1c**·(BArF)$_7$, respectively) is observed for the Cu$^{II}$ cage. The same tendency is observed in the next addition for both nanocapsules. Moreover, **1b**·(BArF)$_8$ nanocapsule is partially empty at the second addition, in contrast to **1c**·(BArF)$_8$ that is still completely full at the fourth addition. For this reason, Cu$^{II}$-based **1c**·(BArF)$_8$ nanocapsule was selected to carry out the next experiments.

An addition of 8.5 nmols of **1c**·(BArF)$_8$ in the solid state (suspension of the nanocapsule in chloroform) to a mixture of Tb@C$_{82}^-$ and Tb$_2$@C$_{80}^-$ (0.8:1 respectively) in chloroform was carried out. Delightfully, after stirring overnight the suspension at room temperature and a simple filtration of the solid, the formation of the Tb$_2$@C$_{80}$⊂**1c**·(BArF)$_7$ complex was confirmed by HR-ESI-MS in a >99% selectivity (Figure VII.5, note that the monoanionic charge of the EMF guest is accounted and observed in the HR-ESI-MS spectrum as expected).

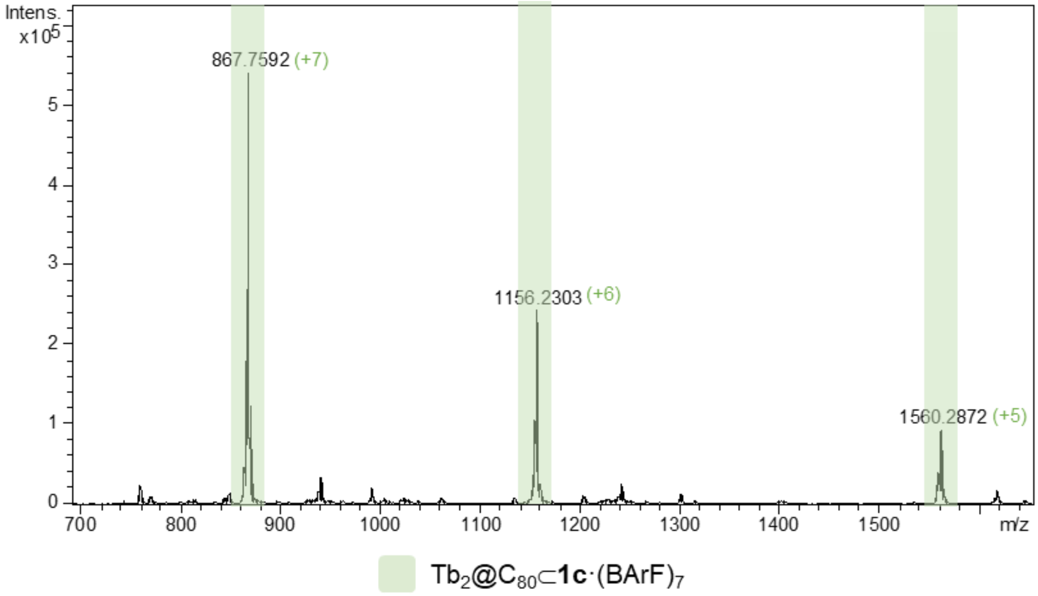

*Figure VII.5. HR mass spectrum of the Tb$_2$@C$_{80}$⊂**1c**·(BArF)$_7$ complex.*

At this point, aiming at continuing the study, another batch of EMF/fullerene extract was received by Prof. Alexey A. Popov. This one was pretreated applying an iodine oxidation after the extraction in DMF with sodium tetrakis[3,5-bis(trifluoromethyl)phenyl]borate (NaBArF) instead of TBAP in order to remove the excess of carbon-based impurities of the extract. Nevertheless, again, an additional preparative TLC was needed using dichloromethane and 8% of methanol as eluent. The purified sample resulted in a 0.5% with respect to the initial sample. After a sub-stoichiometric addition of **1c**·(BArF)$_8$ (34.2

nmols) in the solid state to the purified terbium-based extract in chloroform (821.8 nmols considering that all EMF of the sample are $Tb_2@C_{80}^-$) and stirring for 24 hours the suspension at room temperature, the solid was filtrated and analysed by HR-ESI-MS (Figure VII.6). The mass spectrum indicated that **1c**·$(BArF)_8$ nanocapsule was highly selective towards $Tb_2@C_{80}^-$ (>90%). Nevertheless, a small amount of $Tb@C_{82}\subset$**1c**·$(BArF)_7$ was present and the nanocapsule was not fully filled (35% of empty **1c**·$(BArF)_8$ remained) unlike the results of the previous carbon extract.

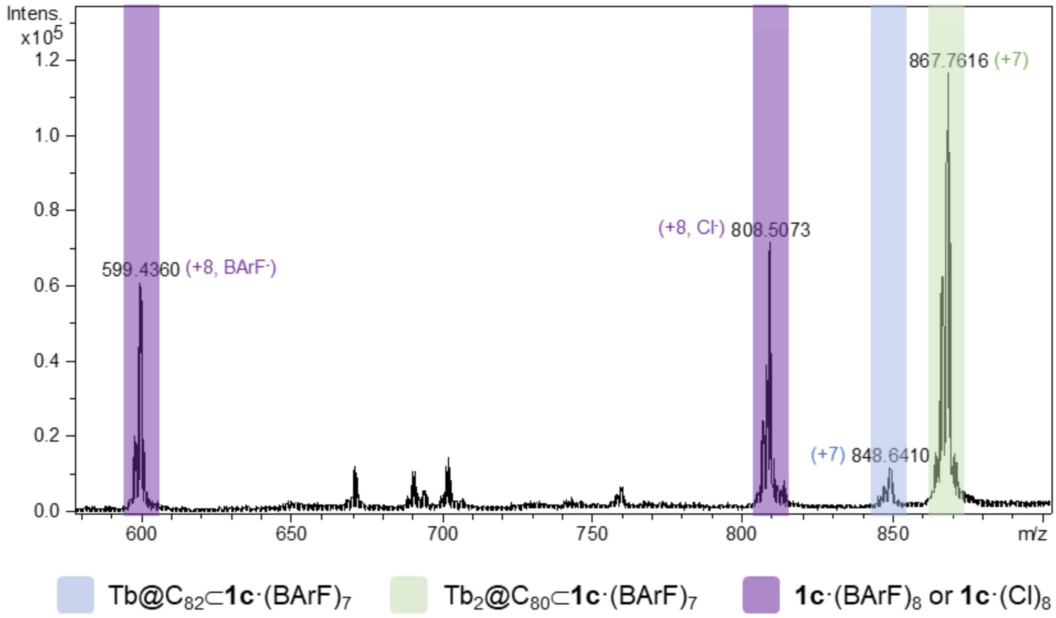

*Figure VII.6. HR mass spectrum of the solid after a sub-stoichiometric addition of **1c**·$(BArF)_8$ to a purified extract of EMF.*

Efforts in reproducing the same results with extended stirring times in order to fill completely the cage using **1c**·$(BArF)_8$ nanocapsule were performed. Unfortunately, after 4 days of stirring, **1c**·$(BArF)_8$ was almost empty with traces of $Tb@C_{82}^-$ and, after 10 days, the nanocapsule was completely empty (Figure VII.7).

At this point, more starting material extracted and treated with TBAP and without the iodine oxidation (the same procedure as the first carbon extract) is needed in order to reproduce the experiment in Figure VII.5 and accumulate $Tb_2@C_{80}\subset$**1c**·$(BArF)_7$ in higher quantities to fully characterize it. Needless to say, this study was extremely challenging due to the sub-milligram quantities of the extract that can be obtained from the arc-discharge furnace.

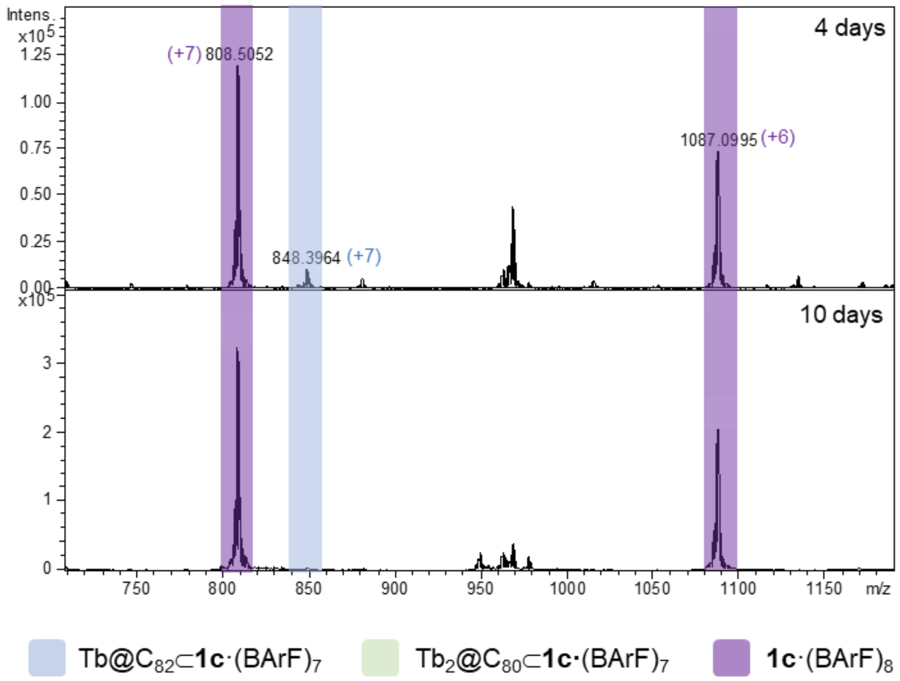

*Figure VII.7. HR-ESI-MS monitoring of the addition **1c**·(BArF)$_8$ nanocapsule in a mixture of Tb@C$_{82}^-$ and Tb$_2$@C$_{80}^-$.*

# CHAPTER VIII. GENERAL CONCLUSIONS

Self-assembled prismatic tetragonal nanocapsules have been used as supramolecular platforms to recognize fullerenes and endohedral metallofullerenes within their inner cavities. These fullerene receptors have turned out to be excellent supramolecular tools to functionalize fullerenes in an itero-, chemo- and regioselective way and to selectively isolate EMFs from fullerene extracts. In this thesis, the scope of functionalization reactions of fullerenes when using supramolecular nanocapsules as templates has been widely extended and also a new bimetallic terbium-based endohedral fullerene has been encapsulated selectively using the same family of nanocapsules.

In Chapter IV, bis-functionalization of fullerene $C_{60}$ has been carried out through Diels-Alder reaction using **1b**·$(BArF)_8$ and **1c**·$(BArF)_8$ nanocapsules as supramolecular shadow masks. Moreover, enlarging the acene (anthracene vs pentacene), the regioselective outcome has been orthogonally switched from equatorial bond (*e,e*-bis-An-$C_{60}$ (**2**)) to *trans*-1 bond (*trans*-1-bis-Pn-$C_{60}$ (**4**)). Computational modeling has shown that the differences in regioselectivity are induced by the different host-guest interactions established between An- and Pn-based mono-adducts with the nanocapsule: mono-Pn-$C_{60}$ can sample only one orientation within the cavity of the nanocapsule (with the pentacene addend vertically aligned), while mono-An-$C_{60}$ spins along its $C_{2v}$ axis and two orientations are indistinctively sampled by the mono-adduct (addend oriented in parallel o perpendicularly to the porphyrin units of the nanocapsule). Furthermore, novel poly-heteroadducts have been synthesized upon submitting encapsulated *e,e*-bis-An-$C_{60}$ (**2**) and mono-Pn-$C_{60}$ (**3**) to Bingel cyclopropanation conditions. Also, bare *e,e*-bis-An-$C_{60}$ (**2**) and *trans*-1-bis-Pn-$C_{60}$ (**4**) have been submitted to exhaustive Bingel conditions to achieve the corresponding *Th*-hexakis-heteroadducts.

In Chapter V, PCBM-based bis-adducts **11** have been synthesized using **1b**·$(BArF)_8$ nanocapsules, semi-stabilized sulfur ylides and milder conditions instead of classical conditions that include the use of diazo compounds and high temperatures, which were detrimental for the nanocapsule. It is worth noting that synthesis of **11** using **1b**·$(BArF)_8$ nanocapsule has enriched the relative yield of equatorial bis-adducts from 26 to 57% in comparison to the non-templated reaction. Also, this strategy allows their formation by an easy, rapid and straightforward methodology in front of the reported multi-stage and multicolumn HPLC process in peak-recycling mode.

Additionally, the synthesis of novel heteroadducts has also been explored using $PC_{61}BM\subset$**1b**·$(BArF)_8$, $PC_{61}BM\subset[10]CPP\subset$**1d**·$(BArF)_8$ and $PC_{61}BM\subset[10]CPP\subset$**1f**·$(BArF)_8$ as starting platforms in combination with Prato or Bingel reactions. Interestingly, only two regioisomers (**12**) were obtained when $PC_{61}BM\subset[10]CPP\subset$**1d**·$(BArF)_8$ was submitted to

Prato cycloaddition. Although these bis-heteroadducts could be analysed by HPLC and UV-vis spectroscopy, there was not enough quantity to analyse them by NMR, so their identity could only be tentatively assigned as *trans*-3 regioisomers.

In Chapter VI, three synthetic routes have been developed pursuing the synthesis of a molecular shuttle based on the $C_{60}$/[10]CPP [2]catenane, featuring two fullerenes as recognition sites for one [10]CPP ring. For the first strategy, the first step was achieved successfully, which focused on the bis-functionalization of $C_{60}$ through Bingel reaction using the matryoshka complex ($C_{60}$⊂[10]CPP⊂**1d**·(BArF)$_8$) and **1b**·(BArF)$_8$ nanocapsule. The obtained *trans*-3-bis-adducts **16** and *e,e*-bis-adduct **17** from the respective systems presented two alkene terminal moieties that were intended to perform an olefin metathesis to join together two bis-adducts (one of them with a [10]CPP ring). Unfortunately, the presence of the nanocapsule inhibited the metathesis reaction and the route was deemed as a dead end.

The second strategy was very similar to the first one: bis-functionalization through Bingel reaction using the matryoshka complex ($C_{60}$⊂[10]CPP⊂**1d**·(BArF)$_8$) have been achieved successfully. This time, *trans*-3-bis-adducts featured terminal alkynes (**26**) and terminal azide groups (**27**) to connect both bis-adducts by a copper(I)-catalysed azide-alkyne cycloaddition. Nevertheless, bis-adduct **27** was highly unstable and the reaction didn't proceed.

Finally, the third strategy started, again, with the bis-functionalization of $C_{60}$ through Bingel reaction using the matryoshka complex ($C_{60}$⊂[10]CPP⊂**1d**·(BArF)$_8$). The synthesis of encapsulated bis-adduct **30**⊂[10]CPP⊂**1d**·(BArF)$_8$ has been obtained in a 50% relative yield in comparison to the corresponding encapsulated mono-adduct. This time, these derivatives featured terminal malonates, intending to carry out a Bingel-Hirsch reaction to close the macrocyclic shuttle. Unfortunately, Bingel-Hirsch reaction has not been achieved successfully. In order to increase the success possibilities of this strategy in future work, *trans*-3-bis-adduct **30** will be released from **30**⊂[10]CPP⊂**1d**·(BArF)$_8$ and Bingel-Hirsch reaction will be performed using **30**⊂[10]CPP as the malonate of the reaction and starting from $C_{60}$⊂**1b**·(BArF)$_8$.

In Chapter VII, the bimetallic monoanionic species $Tb_2@C_{80}^-$ have been encapsulated selectively (>99%) by **1c**·(BArF)$_8$ nanocapsule in small amounts after a straightforward preparative TLC of the EMFs extract. The complex $Tb_2@C_{80}$⊂**1c**·(BArF)$_7$ was characterized by HR-ESI-MS. However, when we wanted to reproduce the same procedure with another batch of starting material, selectivity towards $Tb_2@C_{80}^-$ was lower (90%) and empty nanocapsule remained (35%), probably due to the different pretreatment of the extract. Nevertheless, selective encapsulation of monoanionic EMF derivatives has been demonstrated.

# REFERENCES

1. Lehn, J.-M. Supramolecular Chemistry. *Science*, **1993**, 260, 1762–1763.

2. Diederich, F.; Stang, P. J.; Tykwinski, R. R. *Modern Supramolecular Chemistry*; Wiley-VCH Verlag GmbH & Co.: Weinheim, 2008.

3. Mc Laughlin, C. K.; Hamblin, G. D.; Sleiman, H. F. Supramolecular DNA Assembly. *Chem. Soc. Rev.*, **2011**, 40, 5647–5656.

4. Lewis, J. E. M.; Crowley, J. D. Metallo-Supramolecular Self-Assembly with Reduced-Symmetry Ligands. *ChemPlusChem*, **2020**, 85, 815–827.

5. Furlan, R. L. E.; Otto, S.; Sanders, J. K. M. Supramolecular Templating in Thermodynamically Controlled Synthesis. *Proc. Natl. Acad. Sci.*, **2002**, 99, *8*, 4801–4804.

6. Glink, P. T.; Oliva, A. I.; Fraser Stoddart, J.; White, A. J. P.; Williams, D. J. Template-Directed Synthesis of a [2]Rotaxane by the Clipping under Thermodynamic Control of a Crown Ether like Macrocycle around a Dialkylammonium Ion. *Angew. Chem. Int. Ed.*, **2001**, 40, *10*, 1870–1875.

7. Ibáñez, S.; Peris, E. “Lock and Key” and “Induced-Fit” Host-Guest Models in Two Digold(I)-Based Metallotweezers. *Inorg. Chem.*, **2023**, 62, 1820–1826.

8. Ishiwari, F.; Shoji, Y.; Fukushima, T. Supramolecular Scaffolds Enabling the Controlled Assembly of Functional Molecular Units. *Chem. Sci.*, 2018, *9*, 2028–2041.

9. Yamamoto, K.; Imaoka, T. Precision Synthesis of Subnanoparticles Using Dendrimers as a Superatom Synthesizer. *Acc. Chem. Res.*, **2014**, 47, 1127–1136.

10. Hasobe, T.; Imahori, H.; Kamat, P. V.; Tae, K. A.; Seong, K. K.; Kim, D.; Fujimoto, A.; Hirakawa, T.; Fukuzumi, S. Photovoltaic Cells Using Composite Nanoclusters of Porphyrins and Fullerenes with Gold Nanoparticles. *J. Am. Chem. Soc.*, **2005**, 127, 1216–1228.

11. Liu, J.; He, P.; Yan, J.; Fang, X.; Peng, J.; Liu, K.; Fang, Y. An Organometallic Super-Gelator with Multiple-Stimulus Responsive Properties. *Adv. Mater.*, **2008**, 20, 2508–2511.

12. Hanabusa, K.; Yamada, M.; Kimura, M.; Shirai, H. Prominent Gelation and Chiral Aggregation of Alkylamides Derived from Trans-1,2-Diaminocyclohexane. *Angew. Chem. Int. Ed.*, **1996**, 35, *17*, 1949–1951.

13. Teo, Y. N.; Kool, E. T. DNA-Multichromophore Systems. *Chem. Rev.*, **2012**, 112, 4221–4245.

14. Zheng, Y.; Zhou, H.; Liu, D.; Floudas, G.; Wagner, M.; Koynov, K.; Mezger, M.; Butt, H. J.; Ikeda, T. Supramolecular Thiophene Nanosheets. *Angew. Chem. Int. Ed.*, **2013**, 52, 4845–4848.

15. Shioya, H.; Shoji, Y.; Seiki, N.; Nakano, M.; Fukushima, T.; Iwasa, Y. Raising the Metal-Insulator Transition Temperature of VO2 Thin Films by Surface Adsorption of Organic Polar Molecules. *Appl. Phys. Express*, **2015**, 8, *121101*.

16. Inokuma, Y.; Arai, T.; Fujita, M. Networked Molecular Cages as Crystalline Sponges for Fullerenes and Other Guests. *Nature Chemistry*, **2010**, 2, *9*, 780–783.

17. Schnebeck, R. D.; Freisinger, E.; Glahé, F.; Lippert, B. Molecular Architecture Based on Metal Triangles Derived from 2,2'- Bipyrazine (Bpz) and EnM(II) (M = Pt, Pd). *J. Am. Chem. Soc.*, **2000**, 122, 1381–1390.

18. Lu, J.; Turner, D. R.; Harding, L. P.; Byrne, L. T.; Baker, M. V.; Batten, S. R. Octapi Interactions: Self-Assembly of a Pd-Based [2]Catenane Driven by Eightfold π Interactions. *J. Am. Chem. Soc.*, **2009**, 131, 10372–10373.

19. Krishnaswamy, S.; Prusty, S.; Chartrand, D.; Hanan, G. S.; Chand, D. K. Self-Assembled Molecular Squares as Supramolecular Tectons. *Cryst. Growth Des.*, **2018**, 18, 2016–2030.

20. Kaim, W.; Schwederski, B.; Dogan, A.; Fiedler, J.; Kuehl, C. J.; Stang, P. J. Metalla-Supramolecular Rectangles as Electron Reservoirs for Multielectron Reduction and Oxidation. *Inorg. Chem.*, **2002**, 41, *15*, 4025–4028.

21. Yang, H. B.; Hawkridge, A. M.; Huang, S. D.; Das, N.; Bunge, S. D.; Muddiman, D. C.; Stang, P. J. Coordination-Driven Self-Assembly of Metallodendrimers Possessing Well-Defined and Controllable Cavities as Cores. *J. Am. Chem. Soc.*, **2007**, 129, 2120–2129.

22. Hwang, S. H.; Wang, P.; Moorefield, C. N.; Godínez, L. A.; Manríquez, J.; Bustos, E.; Newkome, G. R. Design, Self-Assembly, and Photophysical Properties of Pentameric Metallomacrocycles: [M5(N-Hexyl[1,2-Bis(2,2′:6′,2″- Terpyridin-4-Yl)]Carbazole)5][M = Fe(II), Ru(II), and Zn(II)]. *Chem. Commun.*, **2005**, 4672–4674.

23. Fujita, M.; Nagao, S.; Ogura, K. Guest-Induced Organization of a Three-Dimensional Palladium (II) Cagelike Comple. A Prototype for “Induced-Fit” Molecular Recognition. *J. Am. Chem. Soc.*, **1995**, 117, 1649–1650.

24. Suzuki, K.; Tominaga, M.; Kawano, M.; Fujita, M. Self-Assembly of an M6L12 Coordination Cube. *Chem. Comm.*, **2009**, 1638–1640.

25. Tominaga, M.; Suzuki, K.; Kawano, M.; Kusukawa, T.; Ozeki, T.; Sakamoto, S.; Yamaguchi, K.; Fujita, M. Finite, Spherical Coordination Networks That Self-Organize from 36 Small Components. *Angew. Chem. Int. Ed.*, **2004**, 43, 5621–5625.

26. Fujita, D.; Ueda, Y.; Sato, S.; Yokoyama, H.; Mizuno, N.; Kumasaka, T.; Fujita, M. Self-Assembly of M30L60 Icosidodecahedron. *Chem*, **2016**, 1, 91–101.

27. Sun, Q.-F.; Iwasa, J.; Ogawa, D.; Ishido, Y.; Sato, S.; Ozeki, T.; Sei, Y.; Yamaguchi, K.; Fujita, M. Self-Assembled M24L48 Polyhedra and Their Sharp Structural Switch upon Subtle Ligand Variation. *Science*, **2010**, 328, 1141–1144.

28. Takezawa, H.; Kanda, T.; Nanjo, H.; Fujita, M. Site-Selective Functionalization of Linear Diterpenoids through U-Shaped Folding in a Confined Artificial Cavity. *J. Am. Chem. Soc.*, **2019**, 141, 5112–5115.

29. Fuertes-Espinosa, C.; García-Simón, C.; Pujals, M.; Garcia-Borràs, M.; Gómez, L.; Parella, T.; Juanhuix, J.; Imaz, I.; Maspoch, D.; Costas, M.; Ribas, X. Supramolecular Fullerene Sponges as Catalytic Masks for Regioselective Functionalization of C60. *Chem*, **2020**, 6, 169–186.

30. Zhang, D.; Ronson, T. K.; Mosquera, J.; Martinez, A.; Nitschke, J. R. Selective Anion Extraction and Recovery Using a FeII4L4 Cage. *Angew. Chem. Int. Ed.*, **2018**, 57, 3717–3721.

31. Ubasart, E.; García-Simón, C.; Pujals, M.; Asad, K.; Chronakis, N.; Parella, T.; Ribas, X. Straightforward Supramolecular Purification of C84 from a Fullerene Extract. *Org. Chem. Front.*, **2021**, 8, 4101–4105.

32. Fuertes-Espinosa, C.; Gómez-Torres, A.; Morales-Martínez, R.; Rodríguez-Fortea, A.; García-Simón, C.; Gándara, F.; Imaz, I.; Juanhuix, J.; Maspoch, D.; Poblet, J. M.; Echegoyen, L.; Ribas, X. Purification of Uranium-Based Endohedral Metallofullerenes (EMFs) by Selective Supramolecular Encapsulation and Release. *Angew. Chem. Int. Ed.*, **2018**, 7, 11294–11299.

33. Fuertes-Espinosa, C.; García-Simón, C.; Castro, E.; Costas, M.; Echegoyen, L.; Ribas, X. A Copper-Based Supramolecular Nanocapsule That Enables Straightforward Purification of Sc3N-Based Endohedral Metallofullerene Soots. *Chem. Eur. J.*, **2017**, 23, 3553–3557.

34. Fuertes-Espinosa, C.; Murillo, J.; Soto, M. E.; Ceron, M. R.; Morales-Martínez, R.; Rodríguez-Fortea, A.; Poblet, J. M.; Echegoyen, L.; Ribas, X. Highly Selective Encapsulation and Purification of U-Based C78-EMFs within a Supramolecular Nanocapsule. *Nanoscale*, **2019**, 11, 23035–23041.

35. García-Simón, C.; Gramage-Doria, R.; Raoufmoghaddam, S.; Parella, T.; Costas, M.; Ribas, X.; Reek, J. N. H. Enantioselective Hydroformylation by a Rh-Catalyst Entrapped in a Supramolecular Metallocage. *J. Am. Chem. Soc.*, **2015**, 137, 2680–2687.

36. Brown, C. J.; Bergman, R. G.; Raymond, K. N. Enantioselective Catalysis of the Aza-Cope Rearrangement by a Chiral Supramolecular Assembly. *J. Am. Chem. Soc.*, **2009**, 131, 17530–17531.

37. Zheng, Y. R.; Suntharalingam, K.; Bruno, P. M.; Lin, W.; Wang, W.; Hemann, M. T.; Lippard, S. J. Mechanistic Studies of the Anticancer Activity of an Octahedral Hexanuclear Pt(II) Cage. *Inorg. Chim. Acta.*, **2016**, 452, 125–129.

38. Therrien, B.; Süss-Fink, G.; Govindaswamy, P.; Renfrew, A. K.; Dyson, P. J. The “Complex-in-a-Complex” Cations [(Acac)2M⊂Ru6-(p-IPrC6H4Me)6(Tpt) 2(Dhbq)3]6+: A Trojan Horse for Cancer Cells. *Angew. Chem. Int. Ed.*, **2008**, 47, 3773–3776.

39. Burke, B. P.; Grantham, W.; Burke, M. J.; Nichol, G. S.; Roberts, D.; Renard, I.; Hargreaves, R.; Cawthorne, C.; Archibald, S. J.; Lusby, P. J. Visualizing Kinetically Robust CoIII4L6 Assemblies in Vivo: SPECT Imaging of the Encapsulated [99m Tc]TcO4- Anion. *J. Am. Chem. Soc.*, **2018**, 140, 16877–16881.

40. Fujita, D.; Suzuki, R.; Fujii, Y.; Yamada, M.; Nakama, T.; Matsugami, A.; Hayashi, F.; Weng, J. K.; Yagi-Utsumi, M.; Fujita, M. Protein Stabilization and Refolding in a Gigantic Self-Assembled Cage. *Chem*, **2021**, 7, 2672–2683.

41. Sudik, A. C.; Millward, A. R.; Ockwig, N. W.; Côté, A. P.; Kim, J.; Yaghi, O. M. Design, Synthesis, Structure, and Gas (N2, Ar, CO2, CH4, and H2) Sorption Properties of Porous Metal-Organic Tetrahedral and Heterocuboidal Polyhedra. *J. Am. Chem. Soc.*, **2005**, 127, 7110–7118.

42. Craig, G. A.; Larpent, P.; Kusaka, S.; Matsuda, R.; Kitagawa, S.; Furukawa, S. Switchable Gate-Opening Effect in Metal-Organic Polyhedra Assemblies through Solution Processing. *Chem. Sci.*, **2018**, 9, 6463–6469.

43. Kim, T. Y.; Vasdev, R. A. S.; Preston, D.; Crowley, J. D. Strategies for Reversible Guest Uptake and Release from Metallosupramolecular Architectures. *Chem. Eur. J.*, **2018**, 24, 14878–14890.

44. Kim, S.-Y.; Jung, I.-S.; Lee, E.; Kim, J.; Sakamoto, S.; Yamaguchi, K.; Kim, K. Macrocycles within Macrocycles: Cyclen, Cyclam, and Their Transition Metal Complexes Rncapsulated in Cucurbit[8]Uril. *Angew. Chem. Int. Ed.*, **2001**, 40, *11*, 2119–2121.

45. Zhang, D.; Ronson, T. K.; Greenfield, J. L.; Brotin, T.; Berthault, P.; Léonce, E.; Zhu, J.-L.; Xu, L.; Nitschke, J. R. Enantiopure [Cs+/Xe⊂Cryptophane]⊂FeII4L4 Hierarchical Superstructures. *J. Am. Chem. Soc.*, **2019**, 141, 8339–8345.

46. Ubasart, E.; Borodin, O.; Fuertes-Espinosa, C.; Xu, Y.; García-Simón, C.; Gómez, L.; Juanhuix, J.; Gándara, F.; Imaz, I.; Maspoch, D.; von Delius, M.; Ribas, X. A Three-Shell Supramolecular Complex Enables the Symmetry-Mismatched Chemo- and Regioselective Bis-Functionalization of C60. *Nat. Chem.*, **2021**, 13, 420–427.

47. Kroto, H. W.; Heath, J. R.; O'Brien, S. C.; Curl, R. F.; Smalley, R. E. C60: Buckminsterfullerene. *Nature*, **1985**, 318, 162–163.

48. The Nobel Prize. The Nobel Prize in Chemistry 1996. Robert F. Curl Jr., Sir Harold Kroto and Richard E. Smalley.

49. Haufler, R. E.; Conceicao, J.; Chibante, L. P. F.; Chai, Y.; Byrne, N. E.; Flanagan, S.; Haley, M. M.; O'Brien, S. C.; Pan, C.; Xiao, Z.; Billups, W. E.; Ciufolini, M. A.; Hauge, R. H.; Margrave, J. L.; Wilson, L. J.; Curl, R. F.; Smalley, R. E. Efficient Production of C60 (Buckminsterfullerene), C60H36, and the Solvated Buckide Ion. *J. Phys. Chem*, **1990**, 94, 8634–8636.

50. Kroto, H. W. The Stability of the Fullerenes Cn, with n = 24, 28, 32, 36, 50, 60 and 70. *Nature*, **1987**, 329, 529–531.

51. Li, H.; Zhang, H. The Isolated-Pentagon Rule and Nice Substructures in Fullerenes. *Ars Mathematica Contemporanea*, **2021**, 15, *2*, 487–497.

52. Tan, Y. Z.; Xie, S. Y.; Huang, R. Bin; Zheng, L. S. The Stabilization of Fused-Pentagon Fullerene Molecules. *Nat. Chem.*, **2009**, 1, 450–460.

53. Fuertes-Espinosa, C.; Pujals, M.; Ribas, X. Supramolecular Purification and Regioselective Functionalization of Fullerenes and Endohedral Metallofullerenes. *Chem*, **2020**, 6, 3219–3262.

54. Young So, H.; Wilkins, C. L. First Observation of Carbon Aggregate Ions >C600+ by Laser Desorption Fourier Transform Mass Spectrometry. *J. Phys. Chem.*, **1989**, 93, 1184–1187.

55. Irle, S.; Zheng, G.; Wang, Z.; Morokuma, K. The C60 Formation Puzzle “Solved”: QM/MD Simulations Reveal the Shrinking Hot Giant Road of the Dynamic Fullerene Self-Assembly Mechanism. *J. Phys. Chem. B*, **2006**, 110, 14531–14545.

56. Koenig, R. M.; Tian, H. R.; Seeler, T. L.; Tepper, K. R.; Franklin, H. M.; Chen, Z. C.; Xie, S. Y.; Stevenson, S. Fullertubes: Cylindrical Carbon with Half-Fullerene End-Caps and Tubular Graphene Belts, Their Chemical Enrichment, Crystallography of Pristine C90-D5h(1) and C100-D5d(1) Fullertubes, and Isolation of C108, C120, C132, and C156 Cages of Unknown Structures. *J. Am. Chem. Soc.*, **2020**, 142, 15614–15623.

57. Fowler, P. W.; Ceulemans, A. Electron Deficiency of the Fullerenes. *J. Phys. Chem.*, **1995**, 99, 508–510.

58. Di Ventra, M.; R. Heflin, J.; Evoy, S. *Introduction to Nanoscale Science and Technology*; Springer US: Boston, 2004.

59. Hemley, R. J.; Chen, L. C.; Mao, H. K.; Bell, P. M.; Shaner, J. W.; Stein-berg, D. J.; Liu, S.; Lu, Y.; Kappes, M. M.; Ibers, J. A. The Structure of the C60 Molecule: X-Ray Crystal Structure Determination of a Twin at 110K. *Science*, **1991**, 254, 408–410.

60. Taylor, R.; Walton, D. R. M. The Chemistry of Fullerenes. *Nature*, **1993**, 363, 685–693.

61. Lenes, M.; Wetzelaer, G. J. A. H.; Kooistra, F. B.; Veenstra, S. C.; Hummelen, J. C.; Blom, P. W. M. Fullerene Bisadducts for Enhanced Open-Circuit Voltages and Efficiencies in Polymer Solar Cells. *Adv. Mater.*, **2008**, 20, 2116–2119.

62. Zhang, F.; Shi, W.; Luo, J.; Pellet, N.; Yi, C.; Li, X.; Zhao, X.; Dennis, T. J. S.; Li, X.; Wang, S.; Xiao, Y.; Zakeeruddin, S. M.; Bi, D.; Grätzel, M. Isomer-Pure Bis-PCBM-Assisted Crystal Engineering of Perovskite Solar Cells Showing Excellent Efficiency and Stability. *Adv. Mater.*, **2017**, 29, *1606806*.

63. Lenes, M.; Shelton, S. W.; Sieval, A. B.; Kronholm, D. F.; Hummelen, J. C.; Blom, P. W. M. Electron Trapping in Higher Adduct Fullerene-Based Solar Cells. *Adv. Func. Mater.*, **2009**, 19, 3002–3007.

64. Felder-Flesch, D.; Guillon, D.; Donnio, B. Fullerene-Containing Liquid Crystals. In *Handbook of Liquid Crystals*; Wiley-VCH Verlag GmbH & Co. KGaA, 2014; pp. 1–45.

65. Lavendomme, R.; Jabin, I. Iteroselectivity, the Missing Sibling of Chemo-, Regio-, and Stereoselectivities. *Cell Rep. Phys. Sci.*, **2022**, 3, *101121*.

66. Campidelli, S.; Vázquez, E.; Milic, D.; Lenoble, J.; Castellanos, C. A.; Sarova, G.; Guldi, D. M.; Deschenaux, R.; Prato, M. Liquid-Crystalline Bisadducts of [60]Fullerene. *J. Org. Chem.*, **2006**, 71, 7603–7610.

67. Yamaguchi, J.; Yaginuma, S.; Haemori, M.; Itaka, K.; Koinuma, H. An In-Situ Fabrication and Characterization System Developed for High Performance Organic Semiconductor Devices. *Jpn. J. Appl. Phys.*, **2005**, 44, 3757–3759.

68. Anthopoulos, T. D.; Singh, B.; Marjanovic, N.; Sariciftci, N. S.; Montaigne Ramil, A.; Sitter, H.; Cölle, M.; De Leeuw, D. M. High Performance N-Channel Organic Field-Effect Transistors and Ring Oscillators Based on C60 Fullerene Films. *Appl. Phys. Lett.*, **2006**, 89, *213504*.

69. Zhang, X.-H.; Domercq, B.; Kippelen, B. High-Performance and Electrically Stable C60 Organic Field-Effect Transistors. *Appl. Phys. Lett.*, **2007**, 91, *092114*.

70. Pan, S.; Pei, Z.; Jing, Z.; Song, J.; Zhang, W.; Zhang, Q.; Sang, S. A Highly Stretchable Strain Sensor Based on CNT/Graphene/Fullerene-SEBS. *RSC Adv.*, **2020**, 10, 11225–11232.

71. Shi, X.; Liu, S.; Sun, Y.; Liang, J.; Chen, Y. Lowering Internal Friction of 0D–1D–2D Ternary Nanocomposite-Based Strain Sensor by Fullerene to Boost the Sensing Performance. *Adv. Funct. Mater.*, **2018**, 28, *1800850*.

72. Keshtkar, S.; Rashidi, A.; Kooti, M.; Askarieh, M.; Pourhashem, S.; Ghasemy, E.; Izadi, N. A Novel Highly Sensitive and Selective H2S Gas Sensor at Low Temperatures Based on SnO2 Quantum Dots-C60 Nanohybrid: Experimental and Theory Study. *Talanta*, **2018**, 188, 531–539.

73. Zhang, L.; Li, T.; Feng, Y. P.; Li, H.; Shen, L. Highly Sensitive and Selective Sensors for CF4 Gas Molecules Based on Two-Node Hollow Fullerene. *Adv. Mater. Interfaces*, **2020**, 7, *2000985*.

74. Shetti, N. P.; Mishra, A.; Basu, S.; Aminabhavi, T. M. Versatile Fullerenes as Sensor Materials. *Mater. Today Chem.*, **2021**, 20, *100454*.

75. Friedman, S. H.; DeCamp, D. L.; Kenyon, G. L.; Sijbesma, R. P.; Srdanov, G.; Wudl, F. Inhibition of the HIV-1 Protease by Fullerene Derivatives: Model Building Studies and Experimental Verification. *J. Am. Chem. Soc.*, **1993**, 115, 6506–6509.

76. Sijbesma, R.; Srdanov, G.; Wudl, F.; Castoro, J. A.; Wilkins, C.; Friedman, S. H.; DeCamp, D. L.; Kenyon, G. L. Synthesis of a Fullerene Derivative for the Inhibition of HIV Enzymes. *J. Am. Chem. Soc.*, **1993**, 115, 6510–6512.

77. Marchesan, S.; Da Ros, T.; Spalluto, G.; Balzarini, J.; Prato, M. Anti-HIV Properties of Cationic Fullerene Derivatives. *Bioorg. Med. Chem. Lett.*, **2005**, 15, 3615–3618.

78. Grebinyk, A.; Grebinyk, S.; Prylutska, S.; Ritter, U.; Matyshevska, O.; Dandekar, T.; Frohme, M. C60 Fullerene Accumulation in Human Leukemic Cells and Perspectives of LED-Mediated Photodynamic Therapy. *Free Radic. Biol. Med.*, **2018**, 124, 319–327.

79. Hsieh, F. Y.; Zhilenkov, A. V.; Voronov, I. I.; Khakina, E. A.; Mischenko, D. V.; Troshin, P. A.; Hsu, S. H. Water-Soluble Fullerene Derivatives as Brain Medicine: Surface Chemistry Determines If They Are Neuroprotective and Antitumor. *ACS Appl. Mater. Interfaces*, **2017**, 9, *13*, 11482–11492.

80. Shi, W.; Hou, X.; Liu, T.; Zhao, X.; Sieval, A. B.; Hummelen, J. C.; Dennis, T. J. S. Purification and Electronic Characterisation of 18 Isomers of the OPV Acceptor Material Bis-[60]PCBM. *Chem. Commun.*, **2017**, 53, 975–978.

81. Liu, T.; Abrahams, I.; Dennis, T. J. S. Structural Identification of 19 Purified Isomers of the OPV Acceptor Material BisPCBM by 13C NMR and UV-Vis Absorption Spectroscopy and High-Performance Liquid Chromatography. *J. Phys. Chem. A*, **2018**, 122, *16*, 4138–4152.

82. Isaacs, L.; Diederich, F.; Haldimann, R. F. Multiple Adducts of C60 by Tether-Directed Remote Functionalization and Synthesis of Soluble Derivatives of New Carbon Allotropes Cn(60+5). *Helv. Chim. Acta*, **1997**, 80, 317–342.

83. Nierengarten, J.-F.; Gramlich, V.; Cardullo, F.; Diederich, F. Regio- and Diastereoselective Bisfunctionalization of C60 and Enantioselective Synthesis of a C60 Derivative with a Chiral Addition Pattern. *Angew. Chem. Int. Ed.*, **1996**, 35, *18*, 2101–2103.

84. Trinh, T. M. N.; Schillinger, F.; Guerra, S.; Meichsner, E.; Nierengarten, I.; Hahn, U.; Holler, M.; Nierengarten, J. F. Regioselective Preparation of Fullerene Bis-Adducts from Cleavable Macrocyclic Bis-Malonates. *Eur. J. Org. Chem.*, **2021**, 2021, 3770–3786.

85. Schwenninger, R.; Müller, T.; Kräutler, B. Concise Route to Symmetric Multiadducts of [60]Fullerene: Preparation of an Equatorial Tetraadduct by Orthogonal Transposition. *J. Am. Chem. Soc.*, **1997**, 119, 9317–9318.

86. Kräutler, B.; Müller, T.; Maynollo, J.; Gruber, K.; Kratky, C.; Ochsenbein, P.; Schwarzenbach, D.; Bürgi, H.-B. A Topochemically Controlled, Regiospecific Fullerene Bisfunctionalization. *Angew. Chem. Int. Ed.*, **1996**, 35, *11*, 1204–1206.

87. Andersson, T.; Nilsson, K.; Sundahl, M.; Westman, G.; Wennerström, O. C60 Embedded in Y-Cyclodextrin: A Water-Soluble Fullerene. *J. Chem. Soc., Chem. Commun.*, **1992**, 604–606.

88. Chen, B.; Holstein, J. J.; Horiuchi, S.; Hiller, W. G.; Clever, G. H. Pd(II) Coordination Sphere Engineering: Pyridine Cages, Quinoline Bowls, and Heteroleptic Pills Binding One or Two Fullerenes. *J. Am. Chem. Soc.*, **2019**, 141, 8907–8913.

89. García-Simón, C.; Garcia-Borràs, M.; Gómez, L.; Parella, T.; Osuna, S.; Juanhuix, J.; Imaz, I.; Maspoch, D.; Costas, M.; Ribas, X. Sponge-like Molecular Cage for Purification of Fullerenes. *Nat. Commun.*, **2014**, 5, *5557*.

90. Xu, Y.; Kaur, R.; Wang, B.; Minameyer, M. B.; Gsänger, S.; Meyer, B.; Drewello, T.; Guldi, D. M.; Von Delius, M. Concave-Convex π-π Template Approach Enables the Synthesis of [10]Cycloparaphenylene-Fullerene [2]Rotaxanes. *J. Am. Chem. Soc.*, **2018**, 140, 13413–13420.

91. Salazar, A.; Labella, J.; Kumar, S.; Torres, T.; de la Torre, G. Acceleration of the Diels-Alder Reaction between 9-Functionalized Anthracenes and C60/C70 in the Cavity of a Water Soluble Subphthalocyanine Cage. *Adv. Synth. Catal.*, **2024**, 366, 1–9.

92. Salazar, A.; Moreno-Simoni, M.; Kumar, S.; Labella, J.; Torres, T.; de la Torre, G. Supramolecular Subphthalocyanine Cage as Catalytic Container for the Functionalization of Fullerenes in Water. *Angew. Chem. Int. Ed.*, **2023**, 62, *e202311255*.

93. Wang, Y.-B.; Lin, Z. Supramolecular Interactions between Fullerenes and Porphyrins. *J. Am. Chem. Soc.*, **2003**, 125, 6072–6073.

94. Brenner, W.; Ronson, T. K.; Nitschke, J. R. Separation and Selective Formation of Fullerene Adducts within an MII8L6 Cage. *J. Am. Chem. Soc.*, **2017**, 139, 75–78.

95. Xu, Y.; Wang, B.; Kaur, R.; Minameyer, M. B.; Bothe, M.; Drewello, T.; Guldi, D. M.; von Delius, M. A Supramolecular [10]CPP Junction Enables Efficient Electron Transfer in Modular Porphyrin-[10]CPP@fullerene Complexes. *Angew. Chem. Int. Ed.*, **2018**, 57, 11549–11553.

96. Hirsch, A.; Lamparth, I.; Karfunkel, H. R. Fullerene Chemistry in Three Dimensions: Isolation of Seven Regioisomeric Bisadducts and chiral Trisadducts of C60 and Di(Ethoxy-Carbonyl)Methylene. *Angew. Chem. Int. Ed. Engl.*, **1994**, 33, *4*, 437–438.

97. Steudel, F. M.; Ubasart, E.; Leanza, L.; Pujals, M.; Parella, T.; Pavan, G. M.; Ribas, X.; von Delius, M. Synthesis of C60/[10]CPP-Catenanes by Regioselective, Nanocapsule-Templated Bingel Bis-Addition. *Angew. Chem. Int. Ed.*, **2023**, e202309393.

98. Leonhardt, V.; Fimmel, S.; Krause, A. M.; Beuerle, F. A Covalent Organic Cage Compound Acting as a Supramolecular Shadow Mask for the Regioselective Functionalization of C60. *Chem. Sci.*, **2020**, 11, 8409–8415.

99. Lu, Z.; Ronson, T. K.; Heard, A. W.; Feldmann, S.; Vanthuyne, N.; Martinez, A.; Nitschke, J. R. Enantioselective Fullerene Functionalization through Stereochemical Information Transfer from a Self-Assembled Cage. *Nat. Chem.*, **2023**, 15, 405–412.

100. Heath, J. R.; O'Brien, S. C.; Zhang, Q.; Liu, Y.; Curl, R. F.; Kroto, H. W.; TIttel, F. K.; Smalley, R. E. Lanthanum Complexes of Spheroidal Carbon Shells. *J. Am. Chem. Soc.*, **1985**, 107, 7779–7780.

101. Chai, Y.; Guo, T.; Jin, C.; Haufler, R. E.; Chibante, L. P. F.; Pure, J.; Wang, L.; Alford, J. M.; Smalley, R. E. Fullerenes with Metals Inside. *J. Phys. Chem.*, **1991**, 95, 7564–7568.

102. Dunsch, L.; Yang, S. Metal Nitride Cluster Fullerenes: Their Current State and Future Prospects. *Small*, **2007**, 3, *8*, 1298–1320.

103. Yang, S.; Liu, F.; Chen, C.; Jiao, M.; Wei, T. Fullerenes Encaging Metal Clusters - Clusterfullerenes. *Chem. Commun.*, **2011**, 47, 11822–11839.

104. Shinohara, H. Endohedral Metallofullerenes. *Rep. Prog. Phys.*, **2000**, 63, 843–892.

105. Popov, A. A.; Yang, S.; Dunsch, L. Endohedral Fullerenes. *Chem. Rev.*, **2013**, 113, 5989–6113.

106. Yang, S.; Wei, T.; Jin, F. When Metal Clusters Meet Carbon Cages: Endohedral Clusterfullerenes. *Chem. Soc. Rev.*, **2017**, 46, 5005–5058.

107. Iezzi, E. B.; Duchamp, J. C.; Fletcher, K. R.; Glass, T. E.; Dorn, H. C. Lutetium-Based Trimetallic Nitride Endohedral Metallofullerenes: New Contrast Agents. *Nano Lett.*, **2002**, 2, *11*, 1187–1190.

108. Shultz, M. D.; Duchamp, J. C.; Wilson, J. D.; Shu, C. Y.; Ge, J.; Zhang, J.; Gibson, H. W.; Fillmore, H. L.; Hirsch, J. I.; Dorn, H. C.; Fatouros, P. P. Encapsulation of a Radiolabeled Cluster inside a Fullerene Cage, 177LuxLu(3- x)N@C80: An Interleukin-13-Conjugated Radiolabeled Metallofullerene Platform. *J. Am. Chem. Soc.*, **2010**, 132, 4980–4981.

109. Shultz, M. D.; Wilson, J. D.; Fuller, C. E.; Zhang, J.; Dorn, H. C.; Fatouros, P. P. Metallofullerene-Based Nanoplatform for Brain Tumor Brachytherapy and Longitudinal Imaging in a Murine Orthotopic Xenograft Model. *Radiology*, **2011**, 261, *1*, 136–143.

110. Chen, C.; Xing, G.; Wang, J.; Zhao, Y.; Li, B.; Tang, J.; Jia, G.; Wang, T.; Sun, J.; Xing, L.; Yuan, H.; Gao, Y.; Meng, H.; Chen, Z.; Zhao, F.; Chai, Z.; Fang, X. Multihydroxylated [Gd@C82(OH)22]n Nanoparticles: Antineoplastic Activity of High Efficiency and Low Toxicity. *Nano Lett.*, **2005**, 5, *10*, 2050–2057.

111. McCluskey, D. M.; Smith, T. N.; Madasu, P. K.; Coumbe, C. E.; MacKey, M. A.; Fulmer, P. A.; Wynne, J. H.; Stevenson, S.; Phillips, J. P. Evidence for Singlet-Oxygen Generation and Biocidal Activity in Photoresponsive Metallic Nitride Fullerene-Polymer Adhesive Films. *ACS Appl. Mater. Interfaces*, **2009**, 1, *4*, 882–887.

112. Ross, R. B.; Cardona, C. M.; Swain, F. B.; Guldi, D. M.; Sankaranarayanan, S. G.; Van Keuren, E.; Holloway, B. C.; Drees, M. Tuning Conversion Efficiency in Metallo Endohedral Fullerene-Based Organic Photovoltaic Devices. *Adv. Funct. Mater.*, **2009**, 19, 2332–2337.

113. Pinzón, J. R.; Plonska-Brzezinska, M. E.; Cardona, C. M.; Athans, A. J.; Gayathri, S. S.; Guldi, D. M.; Herranz, M. Á.; Martín, N.; Torres, T.; Echegoyen, L.

Sc3N@C80-Ferrocene Electron-Donor/Acceptor Conjugates as Promising Materials for Photovoltaic Applications. *Angew. Chem. Int. Ed.*, **2008**, 47, 4173–4176.

114. Miller, B.; Rosamilia, J. M.; Dabbagh, G.; Tycko, R.; Haddon, R. C.; Muller, A. J.; Wilson, W.; Murphy, D. W.; Hebard, A. F. Photoelectrochemical Behavior of C60 Films. *J. Am. Chem. Soc.*, **1991**, 113, 6291–6293.

115. Spree, L.; Popov, A. A. Recent Advances in Single Molecule Magnetism of Dysprosium-Metallofullerenes. *Dalton Trans.*, **2019**, 48, 2861–2871.

116. Yakigaya, K.; Takeda, A.; Yokoyama, Y.; Ito, S.; Miyazaki, T.; Suetsuna, T.; Shimotani, H.; Kakiuchi, T.; Sawa, H.; Takagi, H.; Kitazawa, K.; Dragoe, N. Superconductivity of Doped Ar@C60. *New J. Chem.*, **2007**, 31, 973–979.

117. Stevenson, S.; Mackey, M. A.; Pickens, J. E.; Stuart, M. A.; Confait, B. S.; Phillips, J. P. Selective Complexation and Reactivity of Metallic Nitride and Oxometallic Fullerenes with Lewis Acids and Use as an Effective Purification Method. *Inorg. Chem.*, **2009**, 48, 11685–11690.

118. Akiyama, K.; Hamano, T.; Nakanishi, Y.; Takeuchi, E.; Noda, S.; Wang, Z.; Kubuki, S.; Shinohara, H. Non-HPLC Rapid Separation of Metallofullerenes and Empty Cages with TiCl4 Lewis Acid. *J. Am. Chem. Soc.*, **2012**, 134, 9762–9767.

119. Ge, Z.; Duchamp, J. C.; Cai, T.; Gibson, H. W.; Dorn, H. C. Purification of Endohedral Trimetallic Nitride Fullerenes in a Single, Facile Step. *J. Am. Chem. Soc.*, **2005**, 127, 16292–16298.

120. Stevenson, S.; Mackey, M. A.; Coumbe, C. E.; Phillips, J. P.; Elliott, B.; Echegoyen, L. Rapid Removal of D5h Isomer Using the “Stir and Filter Approach” and Isolation of Large Quantities of Isomerically Pure Sc3N@C80 Metallic Nitride Fullerenes. *J. Am. Chem. Soc.*, **2007**, 129, 6072–6073.

121. Angeli, C. D.; Cai, T.; Duchamp, J. C.; Reid, J. E.; Singer, E. S.; Gibson, H. W.; Dorn, H. C. Purification of Trimetallic Nitride Templated Endohedral Metallofullerenes by a Chemical Reaction of Congeners with Eutectic 9-Methylanthracene. *Chem. Mater.*, **2008**, 20, 4993–4997.

122. Tsuchiya, T.; Sato, K.; Kurihara, H.; Wakahara, T.; Nakahodo, T.; Maeda, Y.; Akasaka, T.; Ohkubo, K.; Fukuzumi, S.; Kato, T.; Mizorogi, N.; Kobayashi, K.; Nagase, S. Host-Guest Complexation of Endohedral Metallofullerene with Azacrown Ether and Its Application. *J. Am. Chem. Soc.*, **2006**, 128, 6699–6703.

123. Tsuchiya, T.; Kurihara, H.; Sato, K.; Wakahara, T.; Akasaka, T.; Shimizu, T.; Kamigata, N.; Mizorogi, N.; Nagase, S. Supramolecular Complexes of La@C82 with Unsaturated Thiacrown Ethers. *Chem. Commun.*, **2006**, 3585–3587.

124. Nakanishi, Y.; Omachi, H.; Matsuura, S.; Miyata, Y.; Kitaura, R.; Segawa, Y.; Itami, K.; Shinohara, H. Size-Selective Complexation and Extraction of Endohedral Metallofullerenes with Cycloparaphenylene. *Angew. Chem. Int. Ed.*, **2014**, 53, 3102–3106.

125. Fuertes-Espinosa, C.; García-Simón, C.; Castro, E.; Costas, M.; Echegoyen, L.; Ribas, X. A Copper-Based Supramolecular Nanocapsule That Enables Straightforward Purification of Sc3N-Based Endohedral Metallofullerene Soots. *Chem. Eur. J.*, **2017**, 23, 3553–3557.

126. Fuertes-Espinosa, C.; Gómez-Torres, A.; Morales-Martínez, R.; Rodríguez-Fortea, A.; García-Simón, C.; Gándara, F.; Imaz, I.; Juanhuix, J.; Maspoch, D.; Poblet, J. M.; Echegoyen, L.; Ribas, X. Purification of Uranium-based Endohedral Metallofullerenes (EMFs) by Selective Supramolecular Encapsulation and Release. *Angew. Chem. Int. Ed.*, **2018**, 57, 11294–11299.

127. Fuertes-Espinosa, C.; Murillo, J.; Soto, M. E.; Ceron, M. R.; Morales-Martínez, R.; Rodríguez-Fortea, A.; Poblet, J. M.; Echegoyen, L.; Ribas, X. Highly Selective Encapsulation and Purification of U-Based C78-EMFs within a Supramolecular Nanocapsule. *Nanoscale*, **2019**, 11, 23035–23041.

128. Salomon-Ferrer, R.; Götz, A. W.; Poole, D.; Le Grand, S.; Walker, R. C. Routine Microsecond Molecular Dynamics Simulations with AMBER on GPUs. Explicit Solvent Particle Mesh Ewald. *J. Chem. Theory Comput.*, **2013**, 9, 3878–3888.

129. AMBER 2016 (University of California, San Francisco, 2016).

130. Wang, J.; Wolf, R. M.; Caldwell, J. W.; Kollman, P. A.; Case, D. A. Development and Testing of a General Amber Force Field. *J. Comput. Chem.*, **2004**, 25, *9*, 1157–1174.

131. Bayly, C. I.; Cieplak, P.; Cornell, W.; Kollman, P. A. A Well-Behaved Electrostatic Potential Based Method Using Charge Restraints for Deriving Atomic Charges: The RESP Model. *J. Phys. Chem.*, **1993**, 97, 10269–10280.

132. Besler, B. H.; Merz Jr., K. M.; Kollman, P. A. Atomic Charges Derived from Semiempirical Methods. *J. Comput. Chem.*, **1990**, 11, 431–439.

133. Singh, U. C.; Kollman, P. A. An Approach to Computing Electrostatic Charges for Molecules. *J. Comput. Chem.*, **1984**, 5, 129–145.

134. Frisch, M. J.; G. W. T.; Schlegel, B.; Scuseria, G. E.; Robb, M. A.; Cheeseman, J. R.; Scalmani, G.; Barone, V.; Petersson, G. A.; Nakatsuji, H.; Li, X.; Caricato, M.; Marenich, A.; Bloino, J.; Janesko, B. G.; Gomperts, R.; Mennucci, B.; Hratchian, H. P.; Ortiz, J. V.; et al. Gaussian 09, Revision A.02, 2009.

135. Li, P.; Merz, K. M. MCPB.Py: A Python Based Metal Center Parameter Builder. *J. Chem. Inf. Model.*, **2016**, 56, 599–604.

136. Maier, J. A.; Martinez, C.; Kasavajhala, K.; Wickstrom, L.; Hauser, K. E.; Simmerling, C. Ff14SB: Improving the Accuracy of Protein Side Chain and Backbone Parameters from Ff99SB. *J. Chem. Theory Comput.*, **2015**, 11, 3696–3713.

137. Darden, T.; York, D.; Pedersen, L. Particle Mesh Ewald: An N·log(N) Method for Ewald Sums in Large Systems. *J. Chem. Phys.*, **1993**, 98, 10089–10092.

138. Chai, J. Da; Head-Gordon, M. Long-Range Corrected Hybrid Density Functionals with Damped Atom-Atom Dispersion Corrections. *Phys. Chem. Chem. Phys.*, **2008**, 10, 6615–6620.

139. García-Simón, C.; Garcia-Borràs, M.; Gómez, L.; Garcia-Bosch, I.; Osuna, S.; Swart, M.; Luis, J. M.; Rovira, C.; Almeida, M.; Imaz, I.; Maspoch, D.; Costas, M.; Ribas, X. Self-Assembled Tetragonal Prismatic Molecular Cage Highly Selective for Anionic π Guests. *Chem. Eur. J.*, **2013**, 19, 1445–1456.

140. García-Simón, C.; Gramage-Doria, R.; Raoufmoghaddam, S.; Parella, T.; Costas, M.; Ribas, X.; Reek, J. N. H. Enantioselective Hydroformylation by a Rh-Catalyst Entrapped in a Supramolecular Metallocage. *J. Am. Chem. Soc.*, **2015**, 137, 2680–2687.

141. Diels, O.; Alder, K. Synthesen in Der Hydroaromatischen Reihe. *Lieb. Ann. Chem*, **1928**, 460, *1*, 98–122.

142. Woodward, R. B.; Katz, T. J. The Mechanism of the Diels-Alder Reaction. *Tetrahedron*, **1959**, 5, 70–89.

143. Jiao, H.-Y.; Li, C.-X.; He, J.-R.; Peng, J.-L.; Jia, P.-K.; Xie, B.-B.; Cui, C.-X. Diels–Alder Cycloadditions of Fullerene: Advances in Mechanistic Theory. *J. Phys. Org. Chem.*, **2023**, e4579.

144. Duarte-Ruiz, A.; Müller, T.; Wurst, K.; Kräutler, B. The Bis-Adducts of the [5,6]-Fullerene C60 and Anthracene. *Tetrahedron*, **2001**, 57, 3709–3714.

145. Tsuda, M.; Ishida, T.; Nogami, T.; Kurono, S.; Ohashi, M. Isolation and Characterization of Diels-Alder Adducts of C60 with Anthracene and Cyclopentadiene. *J. Chem. Soc., Chem. Commun.*, **1993**, *16*, 1296–1298.

146. Hoffman, R.; Woodward, R. B. Selection Rules for Concerted Cycloaddition Reactions. *J. Am. Chem. Soc.*, **1965**, 87, 2046–2048.

147. Seeman, J. I. Woodward-Hoffmann's Stereochemistry of Electrocyclic Reactions. *J. Org. Chem.*, **2015**, 80, 11632–11671.

148. Bingel, C. Cyclopropanierung von Fullerenen. *Chemische Berichte*, **1993**, 126, 1957–1959.

149. J. Janssen, R. A.; Hummelen, J. C.; Wudl, F. Photochemical Fulleroid to Methanofullerene Conversion via the Di-Pi-Methane (Zimmerman) Rearrangement. *J. Am. Chem. Soc*, **1995**, 117, 544–545.

150. Hummelen, J. C.; Knight, B. W.; Lepeq, F.; Wudl, F.; Yao, J.; Wilkins, C. L. Preparation and Characterization of Fulleroid and Methanofullerene Derivatives. *J. Org. Chem.*, **1995**, 60, 532–538.

151. Wang, Y.; Cao, J.; Schuster, D. I.; Wilson, S. R. A Superior Synthesis of [6,6]-Methanofullerenes: The Reaction of Sulfonium Ylides with C60. *Tetrahedron Letters*, **1995**, 36, *38*, 6843–6846.

152. Ito, H.; Kishi, Y.; Nishikawa, Y.; Tada, T.; Ishida, Y.; Saigo, K. A General Method for the Synthesis of 2,2-[60]Fullerenoalkanals: The Reaction of [60]Fullerene with 2-Bromoenol Silyl Ethers. *Synlett*, **2010**, 12, 1811–1814.

153. Ito, T.; Iwai, T.; Matsumoto, F.; Hida, K.; Moriwaki, K.; Takao, Y.; Mizuno, T.; Ohno, T. Facile Synthesis of [6,6]-Phenyl-C61/71-Butyric Acid Methyl Esters via Sulfur Ylides for Bulk-Heterojunction Solar Cell. *Synlett*, **2013**, 24, *15*, 1988–1992.

154. Maggini, M.; Scorrano, G.; Prato, M. Addition of Azomethine Ylides to C60: Synthesis, Characterization, and Functionalization of Fullerene Pyrrolidines. *J. Am. Chem. Soc.*, **1993**, 115, 9798–9799.

155. Ibáñez, S.; Salvà, P.; Dawe, L. N.; Peris, E. V. Guest-shuttling in a Nanosized Metallobox. *Angew. Chem. Int. Ed.*, **2024**, e202318829.

156. Chen, S.; Su, D.; Jia, C.; Li, Y.; Li, X.; Guo, X.; Leigh, D. A.; Zhang, L. Real-Time Observation of the Dynamics of an Individual Rotaxane Molecular Shuttle Using a Single-Molecule Junction. *Chem*, **2022**, 8, 243–252.

157. Delius, M. Von; Leigh, D. A. Walking Molecules. *Chem. Soc. Rev.*, **2011**, 40, 3656–3676.

158. Hernández, J. V.; Kay, E. R.; Leigh, D. A. A Reversible Synthetic Rotary Molecular Motor. *Science*, **2004**, 306, *5701*, 1532–1537.

159. Leigh, D. A.; Wong, J. K. Y.; Dehez, F.; Zerbetto, F. Unidirectional Rotation in a Mechanically Interlocked Molecular Rotor. *Nature*, **2003**, 424, 174–179.

160. Calderon, N.; Chen, H. Y.; Soott, K. W. Olefin Metathesis - A Novel Reaction for Skeletal Transformations of Unsaturated Hydrocarbons. *Tetrahedron*, **1967**, 34, 3327–3329.

161. Trnka, T. M.; Grubbs, Robert. H. The Development of L2X2RU=CHR Olefin Metathesis Catalysts: An Organometallic Success Story. *Acc. Chem. Res.*, **2001**, 34, 18–29.

162. Jin, B.; Shen, J.; Peng, R.; Chen, C.; Zhang, Q.; Wang, X.; Chu, S. DMSO: An Efficient Catalyst for the Cyclopropanation of C60, C70, SWNTs, and Graphene through the Bingel Reaction. *Ind. Eng. Chem. Res.*, **2015**, 54, 2879–2885.

163. Kolb, H. C.; Finn, M. G.; Sharpless, K. B. Click Chemistry: Diverse Chemical Function from a Few Good Reactions. *Angew. Chem. Int. Ed.*, **2001**, 40, 2004–2021.

164. Rostovtsev, V. V.; Green, L. G.; Fokin, V. V.; Sharpless, K. B. A Stepwise Huisgen Cycloaddition Process: Copper(I)-Catalyzed Regioselective “Ligation” of Azides and Terminal Alkynes. *Angew. Chem. Int. Ed.*, **2002**, 41, *14*, 2596–2599.

165. Iehl, J.; Pereira De Freitas, R.; Delavaux-Nicot, B.; Nierengarten, J.-F. Click Chemistry for the Efficient Preparation of Functionalized [60]Fullerene Hexakis-Adducts. *Chem. Commun.*, **2008**, 2450–2452.

166. Camps, X.; Hirsch, A. Efficient Cyclopropanation of C60 Starting from Malonates. *J. Chem. Soc., Perkin Trans. 1*, **1997**, 1595–1596.

167. Liu, F.; Wang, S.; Gao, C.; Deng, Q.; Zhu, X.; Kostanyan, A.; Westerström, R.; Jin, F.; Xie, S.; Popov, A. A.; Greber, T.; Yang, S. Mononuclear Clusterfullerene Single-

Molecule Magnet Containing Strained Fused-Pentagons Stabilized by a Nearly Linear Metal Cyanide Cluster. *Angew. Chem. Int. Ed.*, **2017**, 56, 1830–1834.

168. Spree, L.; Popov, A. A. Recent Advances in Single Molecule Magnetism of Dysprosium-Metallofullerenes. *Dalton Trans.*, **2019**, 48, 2861–2871.

169. Hu, Z.; Dong, B. W.; Liu, Z.; Liu, J. J.; Su, J.; Yu, C.; Xiong, J.; Shi, D. E.; Wang, Y.; Wang, B. W.; Ardavan, A.; Shi, Z.; Jiang, S. Da; Gao, S. Endohedral Metallofullerene as Molecular High Spin Qubit: Diverse Rabi Cycles in Gd2@C79N. *J. Am. Chem. Soc.*, **2018**, 140, 1123–1130.

170. Velkos, G.; Krylov, D. S.; Kirkpatrick, K.; Liu, X.; Spree, L.; Wolter, A. U. B.; Büchner, B.; Dorn, H. C.; Popov, A. A. Giant Exchange Coupling and Field-Induced Slow Relaxation of Magnetization in Gd2@C79N with a Single-Electron Gd-Gd Bond. *Chem. Commun.*, **2018**, 54, 2902–2905.

171. Velkos, G.; Krylov, D. S.; Kirkpatrick, K.; Spree, L.; Dubrovin, V.; Büchner, B.; Avdoshenko, S. M.; Bezmelnitsyn, V.; Davis, S.; Faust, P.; Duchamp, J.; Dorn, H. C.; Popov, A. A. High Blocking Temperature of Magnetization and Giant Coercivity in the Azafullerene Tb2@C79N with a Single-Electron Terbium-Terbium. *Angew. Chem. Int. Ed.*, **2019**, 58, 5951–5956.

# ANNEX

# Annex Chapter IV

## *Annex IV.1 Experimental procedures*

### *Synthesis and characterization of e,e-bis-An-$C_{60}$ (**2**)*

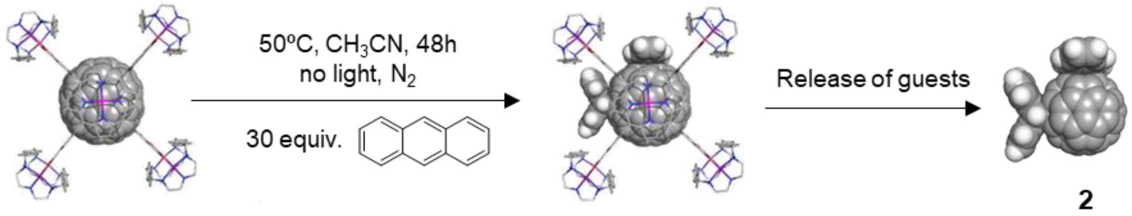

*Scheme S.1. Synthesis of e,e-bis-An-$C_{60}$ (**2**).*

Anthracene (30 equivalents, 12.6 mg, 70.5 µmol) was added to a solution of $C_{60}\subset$**1b**·$(BArF)_8$ (32 mg, 2.35 µmol) in 2.3 ml dry $CH_3CN$ and the reaction was stirred for 48 h at 50ºC under $N_2$. Then, the crude was cool down in the freezer, filtered and the solvent was removed using a $N_2$ flow (without heat). The guests were released from the nanocapsule by suspending the remaining solid with chloroform and sonicating the suspension for 15 minutes. Finally, the suspension was filtered and the products (mono-adduct-$C_{60}$ and *e,e*-bis-adduct-$C_{60}$) were purified through preparative thin layer chromatography using $CS_2$:hexane (3:1) as eluent. It's important to avoid the heat during all the workup to avoid the retro-Diels-Alder and also the promotion of tris-adducts. Yield*: 38%.

*Yield calculated by HPLC using $C_{60}$ as internal standard.

**$^1$H-NMR** (400MHz, $CDCl_3$) δ ppm: 7.65 – 7.30 (16H, m), 5.43 (2H, s), 5.41 (1H, s), 4.76 (1H, s).

**$^{13}$C-NMR** (125.75MHz, $CDCl_3$) δ ppm: 127.0 – 125.4 ($C_{sp2}$-H), 58.8 ($C_{sp3}$-H), 58.3 ($C_{sp3}$-H), 58.1 ($C_{sp3}$-H).

**HR-ESI-MS of 2⊂1b** ($CH_3CN$), m/z: calc. for $[\mathbf{2}\subset\mathbf{1b}]^{8+}$ 776.5537, observed 776.7934; calc. for $[\mathbf{2}\subset\mathbf{1b}\cdot(BArF)]^{7+}$ 1010.7853, observed 1011.3447; calc. for $[\mathbf{2}\subset\mathbf{1b}\cdot(BArF)_2]^{6+}$ 1323.0941, observed 1323.7360.

## *Synthesis and characterization of mono-Pn-$C_{60}$ (**3**)*

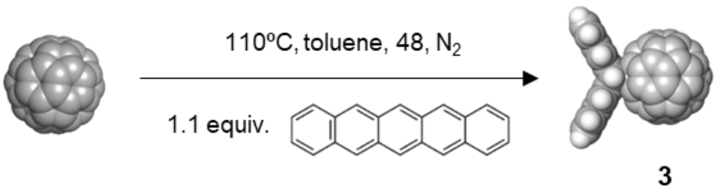

*Scheme S.2. Synthesis of mono-Pn-$C_{60}$ (**3**).*

The synthesis of mono-Pn-$C_{60}$ was carried out with procedures already reported in the literature.[15,16] Fullerene $C_{60}$ (40 mg, 55.5 μmol) and pentacene (1.1 equivalents, 17 mg, 61 μmol) were refluxed under a $N_2$ atmosphere in toluene for 48 hours. Then, the crude reaction was concentrated under vacuum at low temperatures (maximum of 35ºC) and was purified through a chromatographic column using carbon disulfide and hexane (1:1) as eluent. Yield: 32%.

**$^1$H-NMR** (400 MHz, $CDCl_3$) δ ppm: 8.27 (4H, s), 8.04 – 8.01 (4H, m), 7.61 – 7.58 (4H, m), 6.05 (2H, s).

**HR-ESI-MS of 3$\subset$1b** ($CH_3CN$), m/z: calc. for [**3**$\subset$**1b**]$^{8+}$ 767.0498, observed 767.0459; calc. for [**3**$\subset$**1b**·(BArF)]$^{7+}$ 999.9237, observed 1000.2041; calc. for [**3**$\subset$**1b**·$(BArF)_2$]$^{6+}$ 1310.4221, observed 1310.5719.

## *Synthesis and characterization of trans-1-bis-Pn-$C_{60}$ (**4**)*

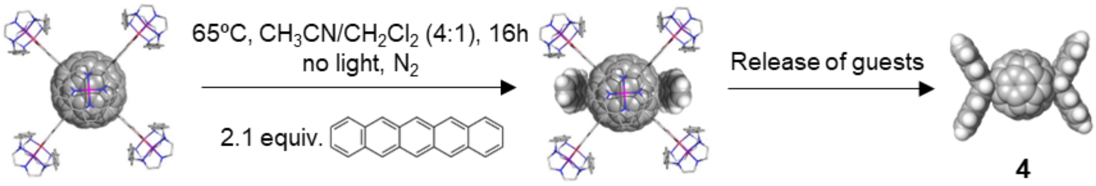

*Scheme S.3. Synthesis of trans-1-bis-Pn-$C_{60}$ (**4**).*

Pentacene (3.4 mg, 12.30 μmol) was added to a solution of $C_{60}$$\subset$**1b**·$(BArF)_8$ (74.3 mg, 5.86 μmol) in 7.25 ml dry $CH_3CN/CH_2Cl_2$ (4:1) and the reaction was stirred for 16 h at 65ºC under a $N_2$ atmosphere. Then, the crude was cool down in the freezer, filtered and trifluoromethanesulfonic acid (20 equivalents) was added and the mixture was stirred for 45 minutes to disassemble the **1b**·$(BArF)_8$ cage and release the products. The solvent was removed using a $N_2$ flow (without heat) and the guests were recovered by suspending the remaining solid with carbon disulfide and sonicating it for 15 minutes. The major product was purified through two preparative TLC. The first one using a mixture of carbon disulfide and hexane (3:1) and then, using a mixture of hexane and dichloromethane (1:1). To avoid the promotion of tris-adducts, it is important to avoid the use of heat. Yield*: 30%.

*Yield calculated by HPLC using $C_{60}$ as internal standard. The HPLC spectrum of the crude mixture (Figure S.14) indicates that the main peak of the bis-adduct region corresponds to **4**, although its insolubility only allows for the isolation of a 30% yield.

**$^1$H-NMR** (400 MHz, $CDCl_3$) δ ppm: 8.35 (8H, s), 8.07 – 8.04 (8H, m), 7.61 – 7.59 (8H, m), 6.32 (4H, s).

**HR-ESI-MS of 4⊂1b** ($CH_3CN$), m/z: calc. for [**4**⊂**1b**]$^{8+}$ 801.5617, observed 802.0615: calc. for [**4**⊂**1b**·(BArF)]$^{7+}$ 1039.3658, observed 1039.9379; calc. for [**4**⊂**1b**·(BArF)$_2$]$^{6+}$ 1356.4379, observed 1357.1041; calc. for [**4**⊂**1b**·(BArF)$_3$]$^{5+}$ 1800.3390, observed 1800.9437.

*Synthesis and characterization of e,e-bis-An-Pn-C$_{60}$ (**5**)*

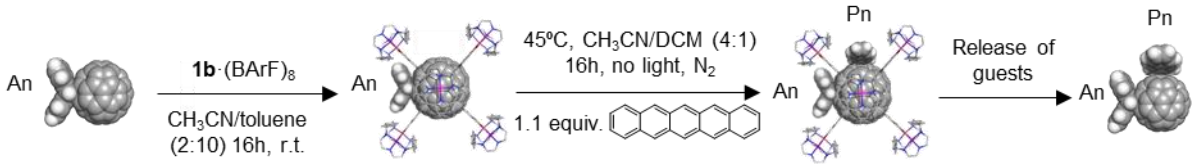

**5**

*Scheme S.4. Synthesis of e,e-bis-An-Pn-C$_{60}$ (**5**).*

Pentacene (1.27 mg, 4.56 μmol) was added to a solution of mono-An-$C_{60}$⊂**1b**·(BArF)$_8$ (50.75 mg, 4.15 μmol) in 4.1 ml dry $CH_3CN/CH_2Cl_2$ (4:1) and the reaction was stirred for 16 h at 45ºC under a $N_2$ atmosphere. Then, the crude was cool down in the freezer, filtered and trifluoromethanesulfonic acid (20 equivalents) was added and the mixture was stirred for 45 minutes to disassemble the **1b**·(BArF)$_8$ cage and release the products. The solvent was removed using a $N_2$ flow (without heat) and the guests were recovered by suspending the remaining solid with carbon disulfide and sonicating it for 15 minutes. The major product was purified through a preparative TLC using a mixture of carbon disulfide and hexane (3:1) as eluent. To avoid the promotion of tris-adducts, it is important to avoid the use of heat. Yield: 16%.

**$^1$H-NMR** (400 MHz, $CDCl_3$) δ ppm: 8.10 (2H, s, $C_{sp2}$-H, Pn addend), 7.95 (2H, s, $C_{sp2}$-H, Pn addend), 7.94 – 7.89 (4H, m, $C_{sp2}$-H), 7.69 – 7.64 (4H, m, $C_{sp2}$-H), 7.55 – 7.50 (6H, m, $C_{sp2}$-H), 7.42 – 7.40 (2H, m, $C_{sp2}$-H), 5.62 (1H, s, $C_{sp3}$-H, Pn addend), 5.45 (2H, s, $C_{sp3}$-H, An addend), 4.98 (1H, s, $C_{sp3}$-H, Pn addend).

**$^{13}$C-NMR** (125.75MHz, $CDCl_3$) δ ppm: 128.0 ($C_{sp2}$-H), 127.9 ($C_{sp2}$-H), 127.0 ($C_{sp2}$-H), 126.9 ($C_{sp2}$-H), 126.0 ($C_{sp2}$-H), 125.7 ($C_{sp2}$-H), 124.2 ($C_{sp2}$-H), 124.2 ($C_{sp2}$-H), 58.6 ($C_{sp3}$-H), 58.3 ($C_{sp3}$-H), 57.8 ($C_{sp3}$-H).

**HR-ESI-MS of 5$\subset$1b** ($CH_3CN$), m/z: calc. for [**5**$\subset$**1b**]$^{8+}$ 789.0577, observed 789.5537: calc. for [**5**$\subset$**1b**·(BArF)]$^{7+}$ 1025.6401, observed 1025.0755; calc. for [**5**$\subset$**1b**·$(BArF)_2$]$^{6+}$ 1339.7660, observed 1340.4194; calc. for [**5**$\subset$**1b**·$(BArF)_3$]$^{5+}$ 1780.3326, observed 1781.1277.

*Synthesis and characterization of e,e-bis-An-e-mono-diethylmalonate-$C_{60}$ (**6**)*

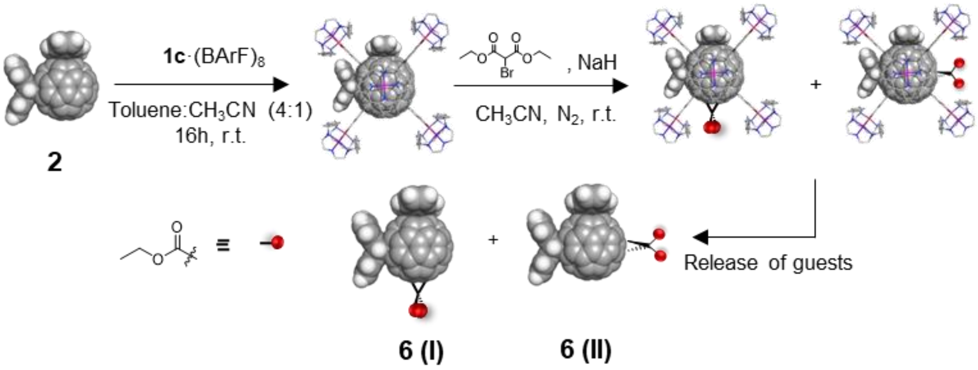

*Scheme S.5. Synthesis of e,e-bis-An-e-mono-diethylmalonate-$C_{60}$ (**6**).*

Two stock solutions of diethyl bromomalonate and sodium hydride in dry acetonitrile were prepared. Then, 5.25 equivalents of diethyl bromomalonate and NaH from these solutions were added to a solution of **2**$\subset$**1c**·$(BArF)_8$ (19 mg, 1.49 µmol) in 1.5 ml of dry acetonitrile at room temperature. After monitoring the reaction by HR-ESI-MS for 9 hours, the solvent was removed under a $N_2$ flow. The guests were released from the nanocapsule by suspending the remaining solid with chloroform (guests in solution and cage in the solid state) and sonicating the suspension for 15 minutes. Finally, the suspension was filtered and the products (both isomers of tris-heteroadducts) were purified through preparative TLC using toluene as eluent. The empty cage was recovered passing acetonitrile through the filter. Yield*: 41%.

*Yield corresponding to **6**(I)+**6**(II) mixture and calculated by HPLC using $C_{60}$ as internal standard.

**Proportion (I:II) is 1:3.7**

**$^1$H-NMR isomer 6(I) minor** (400 MHz, $CDCl_3$) δ ppm: 7.75 – 7.28 (16H, m, $C_{sp2}$-H), 5.61 (1H, s, $C_{sp3}$-H), 5.60 (1H, s, $C_{sp3}$-H), 5.38 (1H, s, $C_{sp3}$-H), 4.89 (1H, s, $C_{sp3}$-H), 4.51 (4H, q, $-CH_2-$), 1.47 (6H, t, $-CH_3$).

**$^{13}$C-NMR isomer 6(I) minor** (125.75 MHz, $CDCl_3$) δ ppm: 126.5 – 118.9 ($C_{sp2}$-H), 63.1 (-$CH_2$-), 58.5 ($C_{sp3}$-H), 58.2 ($C_{sp3}$-H), 58.2 ($C_{sp3}$-H), 58.2 ($C_{sp3}$-H), 29.8 (-$CH_3$).

**$^{1}$H-NMR isomer 6(II) major** (400 MHz, $CDCl_3$) δ ppm: 7.75 – 7.28 (16H, m, $C_{sp2}$-H), 5.50 (1H, s, $C_{sp3}$-H), 5.40 (1H, s, $C_{sp3}$-H), 5.25 (1H, s, $C_{sp3}$-H), 4.82 (1H, s, $C_{sp3}$-H), 4.64 (2H, q, -$CH_2$-), 4.51 (2H, q, -$CH_2$-), 1.58 (3H, t, -$CH_3$), 1.47 (3H, t, -$CH_3$).

**$^{13}$C-NMR isomer 6(II) major** (125.75 MHz, $CDCl_3$) δ ppm: 126.5 – 118.9 ($C_{sp2}$-H), 63.2 (-$CH_2$-), 63.1 (-$CH_2$-), 58.9 ($C_{sp3}$-H), 58.2 ($C_{sp3}$-H), 58.1 ($C_{sp3}$-H), 57.1 ($C_{sp3}$-H), 29.8(-$CH_3$), 27.6 (-$CH_3$).

**HR-ESI-MS of $\mathbf{6\subset1c}$** ($CH_3CN$), m/z: calc. for [$\mathbf{6\subset1c}$]$^{8+}$ 753.4608, observed 753.8423: calc. for [$\mathbf{6\subset1b}\cdot(BArF)_1$]$^{7+}$ 984.3934, observed 984.9783; calc. for [$\mathbf{6\subset1c}\cdot(BArF)_2$]$^{6+}$ 1292.3035, observed 1292.9709.

**MALDI-MS** (DCTB, (+)), m/z: calc. for [**6** - (anthracene)$_2$]$^+$ 878.074, observed 878.079.

*Synthesis and characterization of mono-Pn-e,e-bis-diethylmalonate-$C_{60}$ (**7**)*

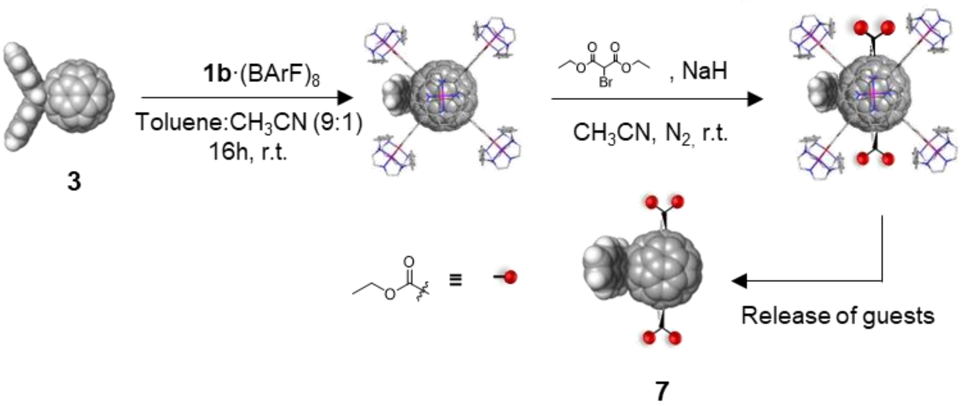

*Scheme S.6. Synthesis of mono-Pn-e,e-bis-diethylmalonate-$C_{60}$ (**7**).*

Two stock solutions of diethyl bromomalonate and sodium hydride in dry acetonitrile were prepared. Then, 2.2 and 2.5 equivalents of diethyl bromomalonate and NaH, respectively, from these solutions were added to a solution of mono-Pn-$C_{60}\subset\mathbf{1b}\cdot(BArF)_8$ (10.2 mg, 0.78 μmol) in 0.8 ml of dry acetonitrile. After monitoring the reaction by HR-ESI-MS for 24 hours, diethyl ether was added to suspend the host-guest complex. Then, the suspension was filtered through Celite® in a pipette. The solid remaining in the filter was washed with chloroform until the filtrate was completely colourless to extract the desired product. A preparative TLC using toluene:ethyl acetate (95:5) was performed in order to eliminate the traces of bis-heteroadduct and the remaining tetrakis-heteroadduct. The empty cage was recovered passing acetonitrile through the filter. Yield*: 63%.

*Yield calculated by HPLC using $C_{60}$ as internal standard.

**$^{1}$H-NMR** (500 MHz, $CDCl_3$) δ ppm: 8.20 (4H, d), 7.99 – 7.97 (4H, m), 7.56 – 7.54 (4H, m), 5.86 (2H, s), 4.51 – 4.43 (8H, m), 1.45 – 1.40 (12H, m).

**$^{13}$C-NMR** (125.75 MHz, $CDCl_3$) δ ppm: 128.2 ($C_{sp2}$-H), 126.1 ($C_{sp2}$-H), 124.1 ($C_{sp2}$-H), 63.5 (-$CH_2$-), 57.7 ($C_{sp3}$-H), 14.1 (-$CH_3$).

**HR-ESI-MS of 7$\subset$1b** ($CH_3CN$), m/z: calc. for [**7**$\subset$**1b**]$^{8+}$ 806.5643, observed 806.6985: calc. for [**7**$\subset$**1b**·$(BArF)_1$]$^{7+}$ 1045.0831, observed 1045.3803; calc. for [**7**$\subset$**1b**·$(BArF)_2$]$^{6+}$ 1363.1082, observed 1363.4505.

**MALDI-MS** (DCTB, (+)), m/z: calc. for [**7** - (pentacene) + $Na^+$]$^+$ 1059.137, observed 1059.204.

*Synthesis and characterization of Th-hexakis-An-$C_{60}$ (**8**)*

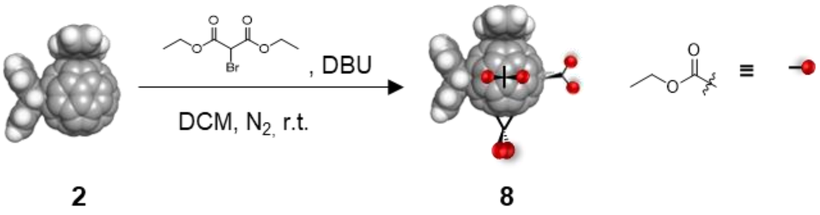

*Scheme S.7. Synthesis of Th-hexakis-An-$C_{60}$ (**8**).*

The synthesis of **8** was carried out with procedures already reported in the literature.[17] Two stock solutions of diethyl bromomalonate and 1,8-diazabicyclo(5.4.0)undec-7-ene (DBU) in dry DCM were prepared. Then, 20 equivalents of these solutions were added to a solution of **2** (0.95 mg, 0.88 μmol) in DCM under a $N_2$ atmosphere at room temperature. After 24 hours, 20 equivalents more of both stock solutions were added. After 24 hours more, the solvent was removed with a $N_2$ flow and the crude reaction was purified through a preparative TLC to remove the excess of diethyl bromomalonate and DBU. Yield*: 12.5%.

*Yield calculated by $^{1}$H-NMR using mesitylene-$D_{12}$ as internal standard.

**$^{1}$H-NMR** (500 MHz, $CDCl_3$) δ ppm**:** 7.56 – 7.14 (16H, m), 5.03 (2H, s), 5.00 (1H, s), 4.54 (1H, s), 4.43 – 4.24 (16H, m), 1.35 – 1.29 (24H, m).

**$^{13}$C-NMR** (125.75 MHz, $CDCl_3$) δ ppm: 126.3 – 124.4 ($C_{sp2}$-H), 62.4 (-$CH_2$-), 62.3 (-$CH_2$-), 58.6 ($C_{sp3}$-H), 58.5 ($C_{sp3}$-H), 58.6 ($C_{sp3}$-H), 15.2 (-$CH_3$), 14.1 (-$CH_3$).

**MALDI-MS** (DCTB, (+)), m/z: calc. for [**8** - (anthracene)$_2$]$^+$ 1352.294, observed 1351.454; calc. for [**8** - (anthracene)$_2$ + Na$^+$]$^+$ 1375.284, observed 1375.346.

*Synthesis and characterization of trans-1-bis-Pn-e,e,e,e-tetrakis-diethylmalonate-$C_{60}$ (**9**)*

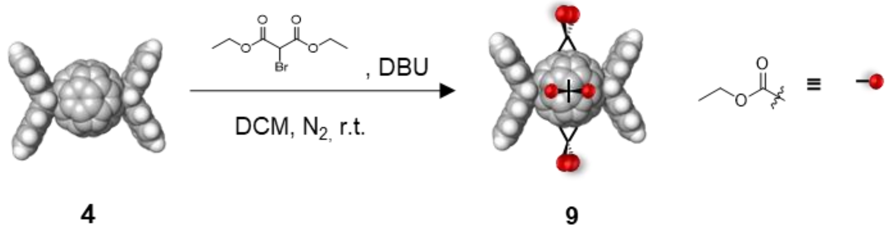

*Scheme S.8. Synthesis of trans-1-bis-Pn-e,e,e,e-tetrakis-diethylmalonate-$C_{60}$ (**9**).*

The synthesis of **9** was carried out with analogue procedures already reported in the literature.[17] Two stock solutions of diethyl bromomalonate and DBU in dry DCM were prepared. Then, 20 equivalents of these solutions were added to a solution of **4** (2 mg, 1.6 µmol) in DCM under a $N_2$ atmosphere at room temperature. After 24 hours, 20 equivalents more of both stock solutions were added. After 24 hours more, the solvent was removed with a $N_2$ flow and the crude reaction was purified through a preparative TLC to remove the excess of diethyl bromomalonate and DBU. The precise yield could not be calculated due to the small quantities used and the low solubility of the pure initial reactant.

**$^1$H-NMR** (400 MHz, $CDCl_3$) δ ppm: 7.94 (8H, s), 7.86 (8H, m), 7.48 (8H, m), 5.43 (4H, s), 4.44 (8H, q, J = 7 Hz), 4.12 (8H, q, J = 7 Hz), 1.45 (12H, t, J = 7 Hz), 1.23 (12H, t, J = 7 Hz).

**$^{13}$C-NMR** (125.75 MHz, $CDCl_3$) δ ppm: 127.7 ($C_{sp2}$-H), 125.7 ($C_{sp2}$-H), 123.6 ($C_{sp2}$-H), 62.5 (-$CH_2$-), 62.1 (-$CH_2$-), 57.6 ($C_{sp3}$-H), 14.6 (-$CH_3$), 13.9 (-$CH_3$).

**MALDI-MS** (DCTB, (+)), m/z: calc. for [**9** - (pentacene)$_2$ + Na$^+$]$^+$ 1375.284, observed 1374.513.

## *Annex IV.2 Supplemental tables*

*Table S.1. Conditions optimization for the formation of e,e-bis-An-$C_{60}$. [a]: Ratio calculated by HR-ESI-MS before releasing derivatives from the nanocapsule. [b] Ratio calculated by HPLC after releasing derivatives from the nanocapsule (tris-adducts were formed during workup).*

| Entry | Equiv. of anthracene | T (°C) | Time (h) | Mono:bis (MS)[a] | Mono:bis:tris (HPLC)[b] |
|---|---|---|---|---|---|
| **1** | 30 | 60 | 24 | 1:1.5 | 1:1.2:0.7 |
| **2** | 30 | 50 | 24 | 1:1.6 | --- |
| **3** | 30 | 50 | 48 | 1:2.2 | 1:2.3:1.3 |
| **4** | 7 | 50 | 48 | 1:0.6 | --- |
| **5** | 7 | 50 | 72 | 1:0.8 | 1:0.8:0.2 |
| **6** | 30 | 40 | 24 | 1:1 | --- |
| **7** | 30 | 40 | 48 | 1:2.7 | 1:2.3:1.2 |
| **8** | 30 | 40 | 72 | 1:2.4 | 1:2.1:1.1 |
| **9** | 50 | 40 | 48 | 1:2.4 | --- |
| **10** | 50 | 40 | 72 | 1:3.9 | 1:2.8:1.5 |
| **11** | 30 | 65 | 16 | 1:0.8 | 1:1.8:0.7 |

*Table S.2. Calculated reaction energies for the formation of the different bis-adducts (e,e-bis-An-$C_{60}$, trans-1-bis-An-$C_{60}$, e,e-bis-Pn-$C_{60}$, trans-1-bis-Pn-$C_{60}$). Energies are given in kcal/mol. E: electronic energies, G: Gibbs free energies.*

| | ΔE (kcal/mol) | ΔG (kcal/mol) |
|---|---|---|
| *e,e*-bis-An-$C_{60}$ | **-31.1** | **-13.1** |
| *trans*-1-bis-An-$C_{60}$ | -29.5 | -11.7 |
| | | |
| *e,e*-bis-Pn-$C_{60}$ | -46.5 | -28.6 |
| *trans*-1-bis-Pn-$C_{60}$ | **-44.5** | **-26.7** |

## *Annex IV.3 Supplemental figures*

### *Annex IV.3.1 HR-ESI-MS and NMR spectra*

### *Characterization of e,e-bis-An-$C_{60}$⊂**1b**·$(BArF)_8$ and e,e-bis-An-$C_{60}$ (**2**)*

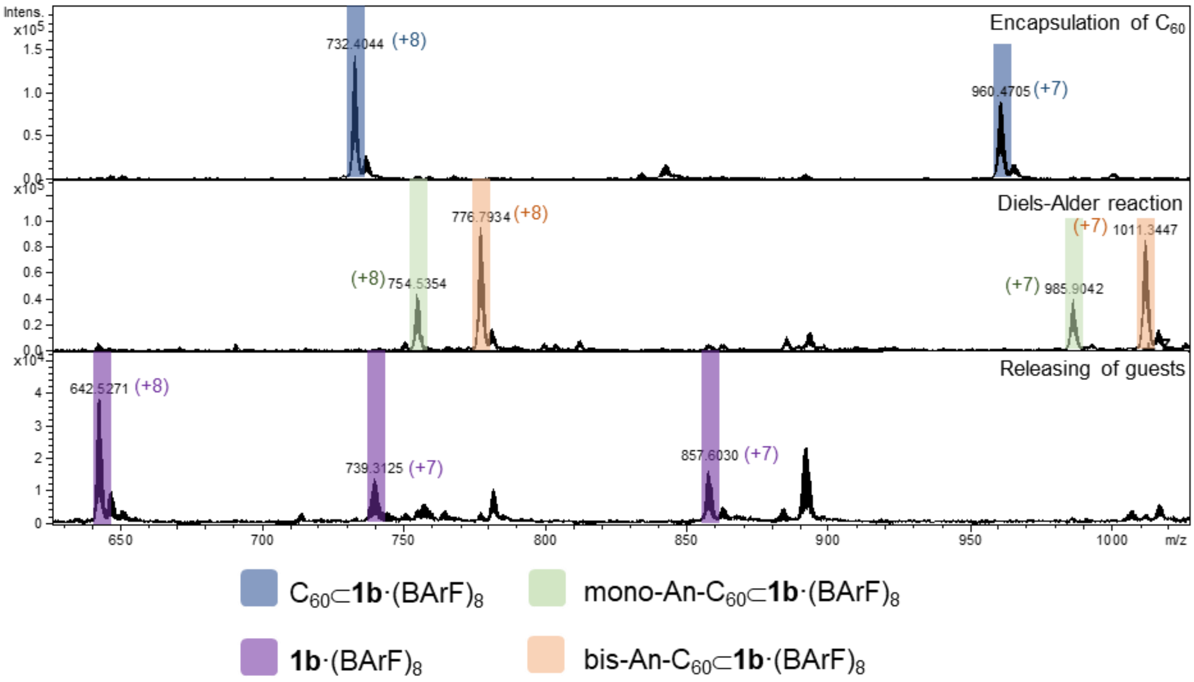

*Figure S.1. HR-ESI-MS monitoring of the synthesis of e,e-bis-An-$C_{60}$⊂**1b**·$(BArF)_8$ and releasing of bis-adduct by sonication with $CHCl_3$.*

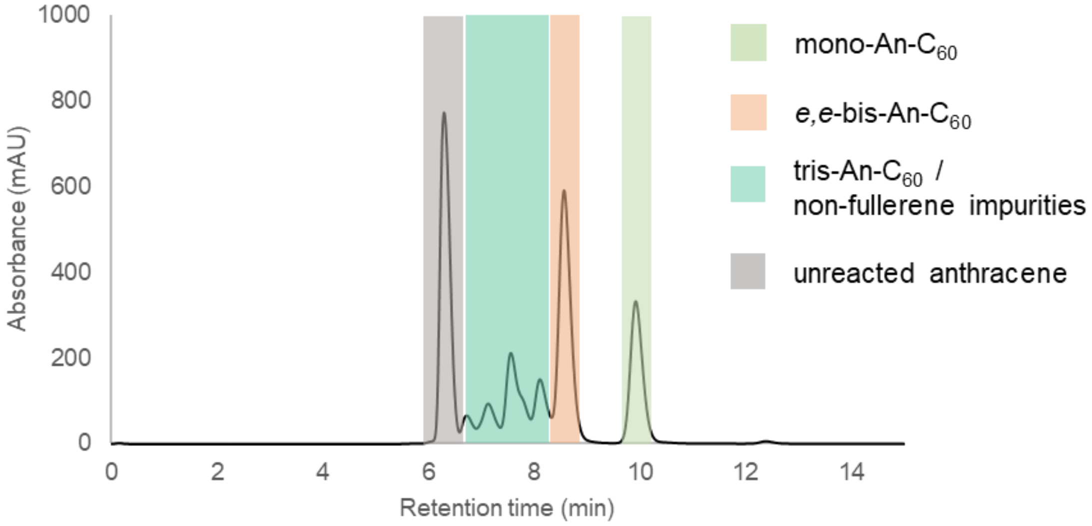

*Figure S.2. HPLC analysis of the reaction crude after releasing of the product for the formation of e,e-bis-An-$C_{60}$ (**2**).*

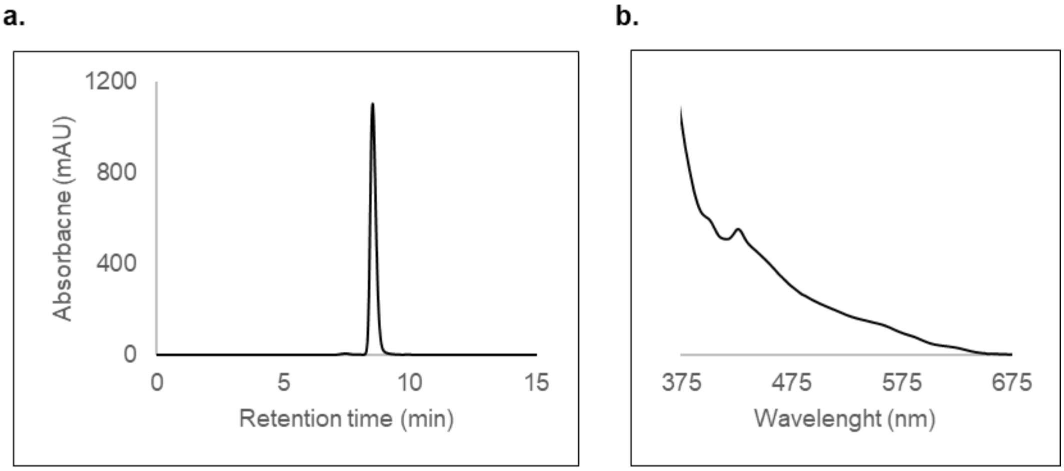

*Figure S.3. Characterization of e,e-bis-An-$C_{60}$ (**2**). a) HPLC analysis of purified e,e-bis-An-$C_{60}$ (**2**).$R_t$=8.603 min, b) UV-vis spectrum of e,e-bis-An-$C_{60}$ (**2**).*

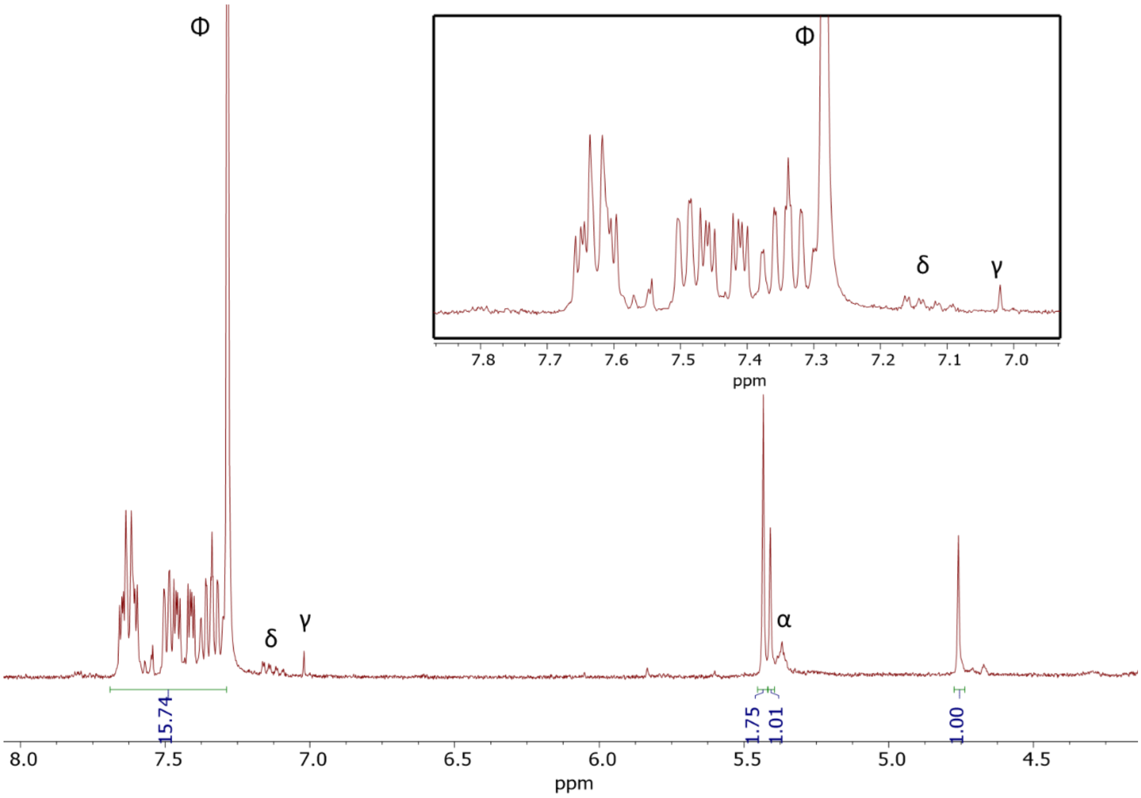

*Figure S.4. $^1$H-NMR spectrum of e,e-bis-An-$C_{60}$ (**2**). Experiment performed in $CDCl_3$ at 298K (400 MHz). φ: chloroform, γ: chloroform's satellites, δ: impurities of the purification solvent ($CS_2$), α: TLC-silica impurities.*

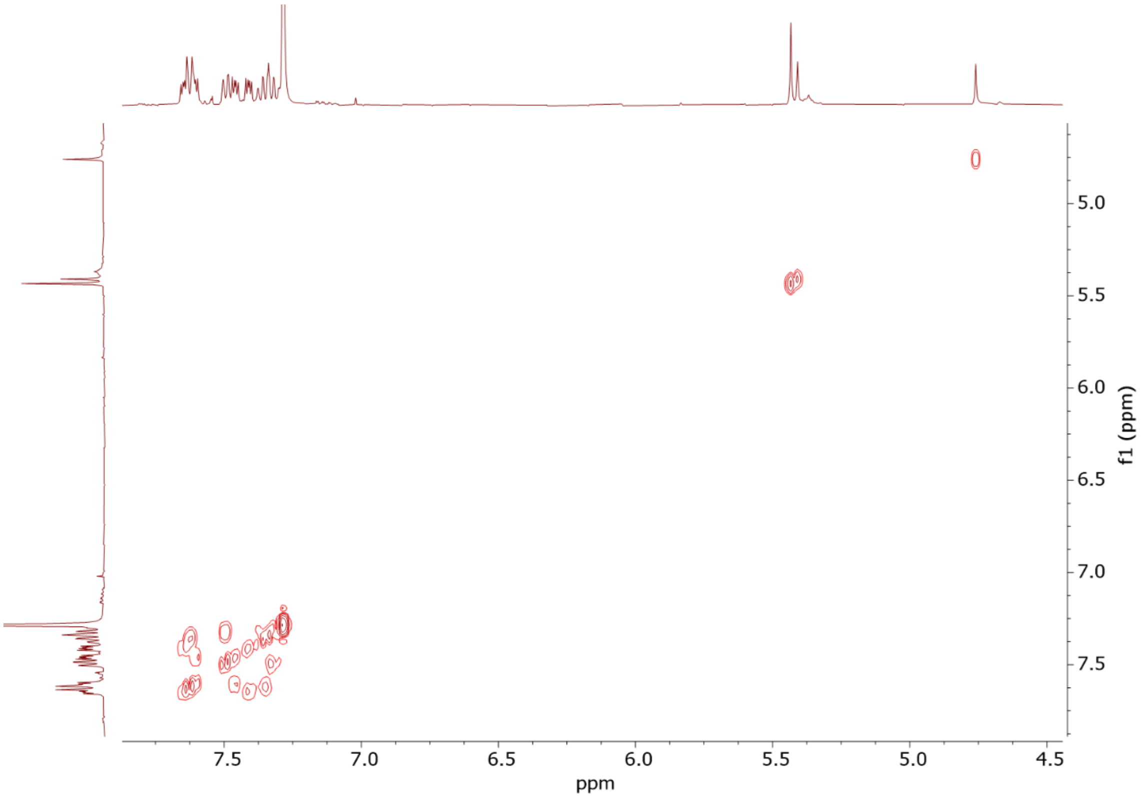

*Figure S.5. 2D COSY spectrum of e,e-bis-An-$C_{60}$ (**2**). Experiment performed in $CDCl_3$ at 298K (400 MHz).*

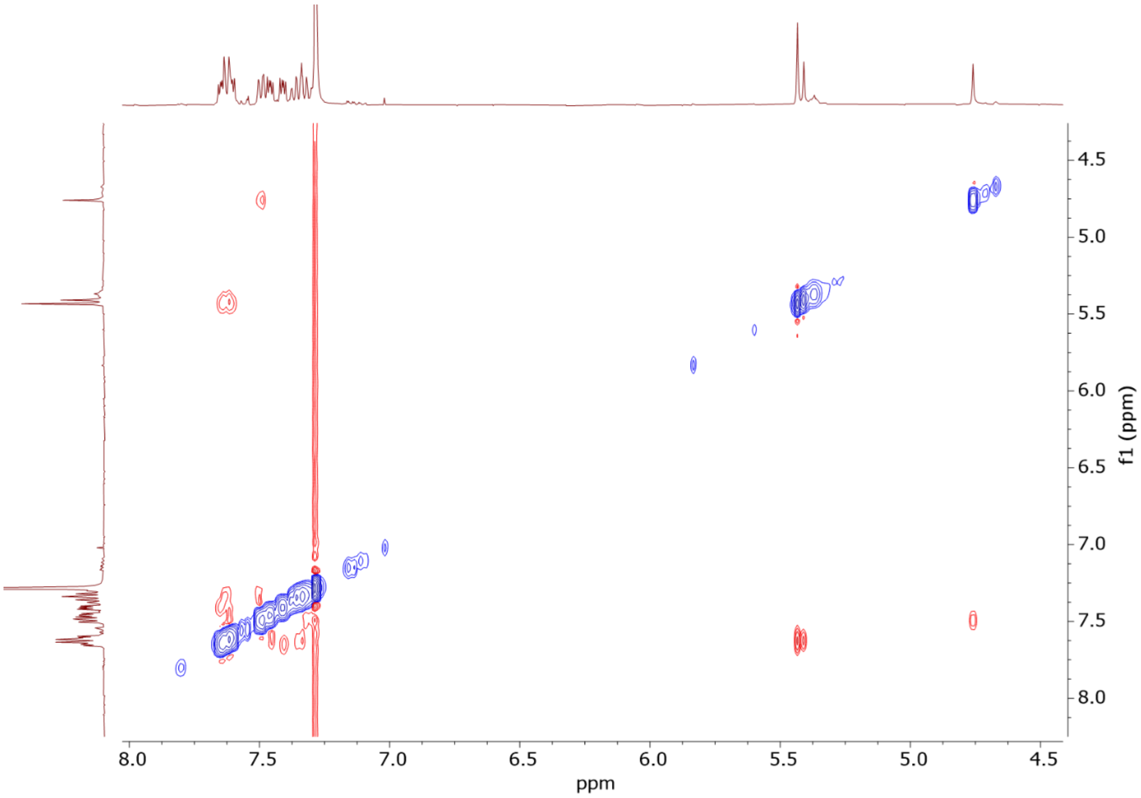

*Figure S.6. 2D NOESY spectrum of e,e-bis-An-$C_{60}$ (**2**). Experiment performed in $CDCl_3$ at 298K (400 MHz).*

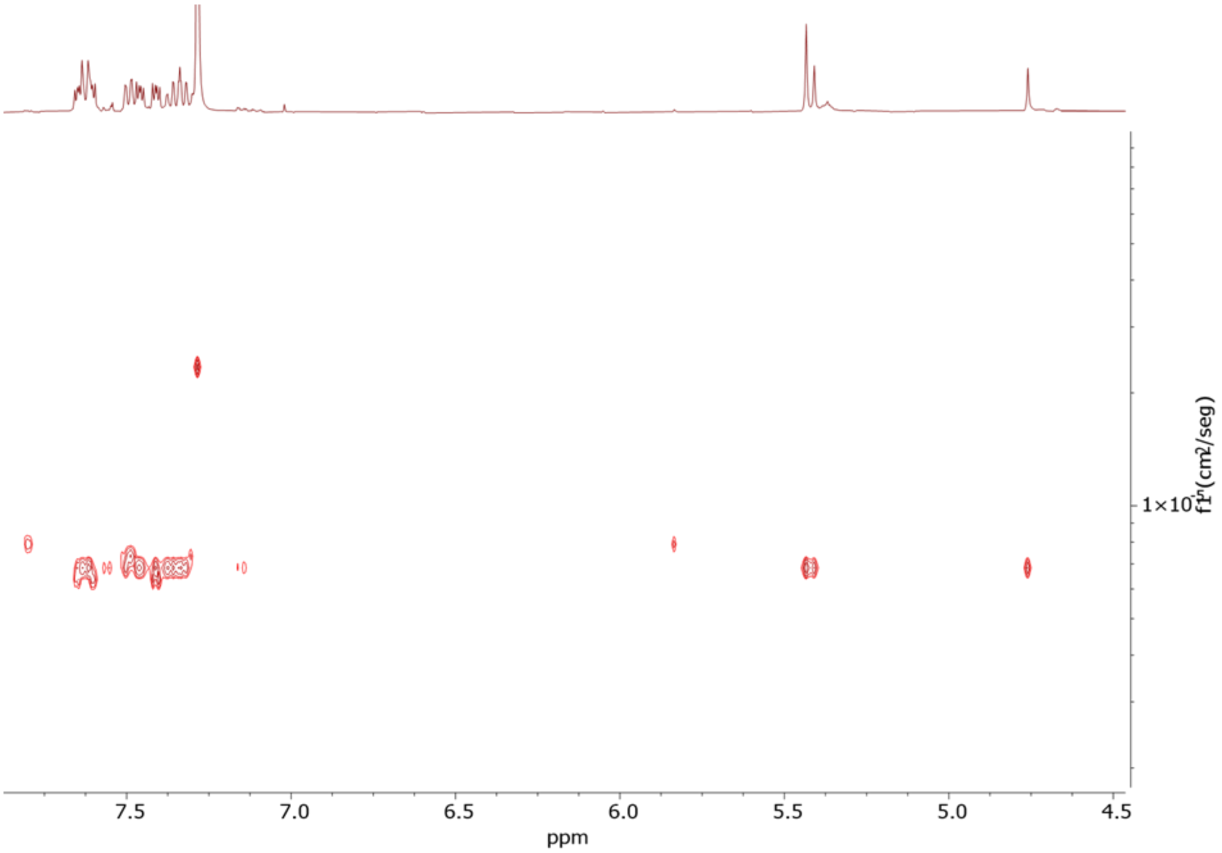

*Figure S.7. DOSY representation of e,e-bis-An-$C_{60}$ (**2**). Experiment performed in $CDCl_3$ at 298K (500 MHz).*

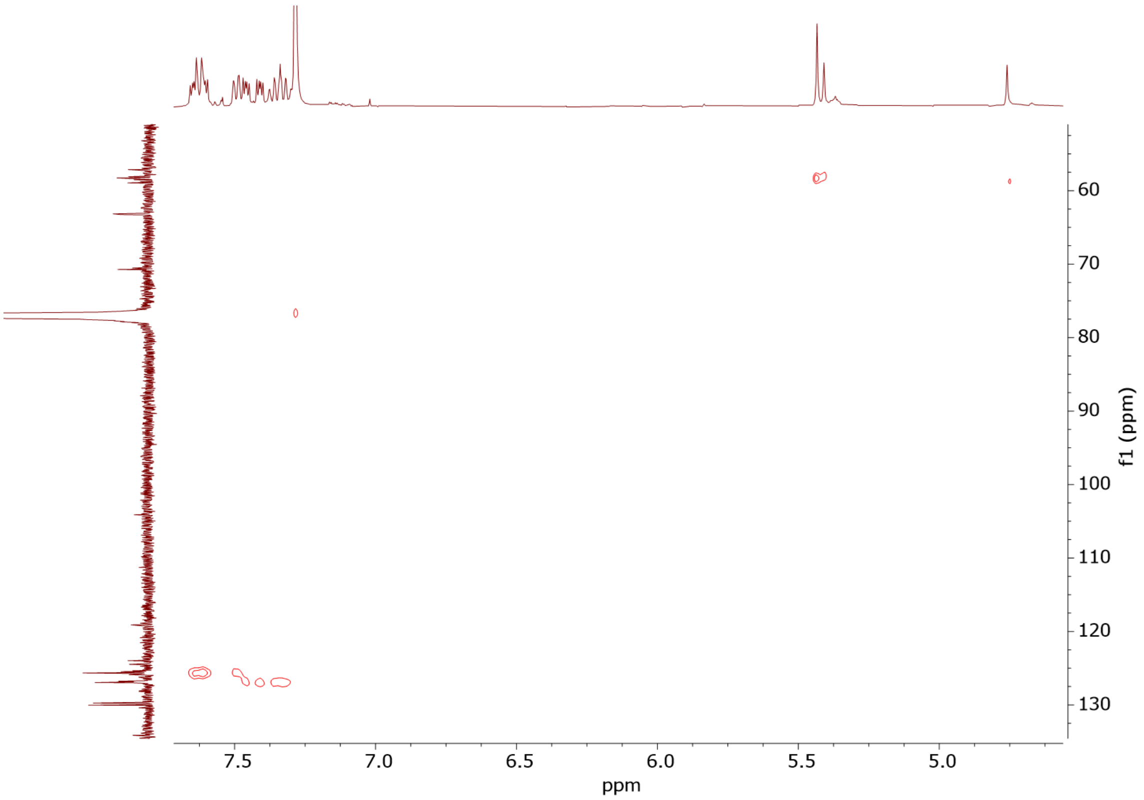

*Figure S.8. 2D HSQC spectrum of e,e-bis-An-$C_{60}$ (**2**). Experiment performed in $CDCl_3$ at 298K (400 MHz).*

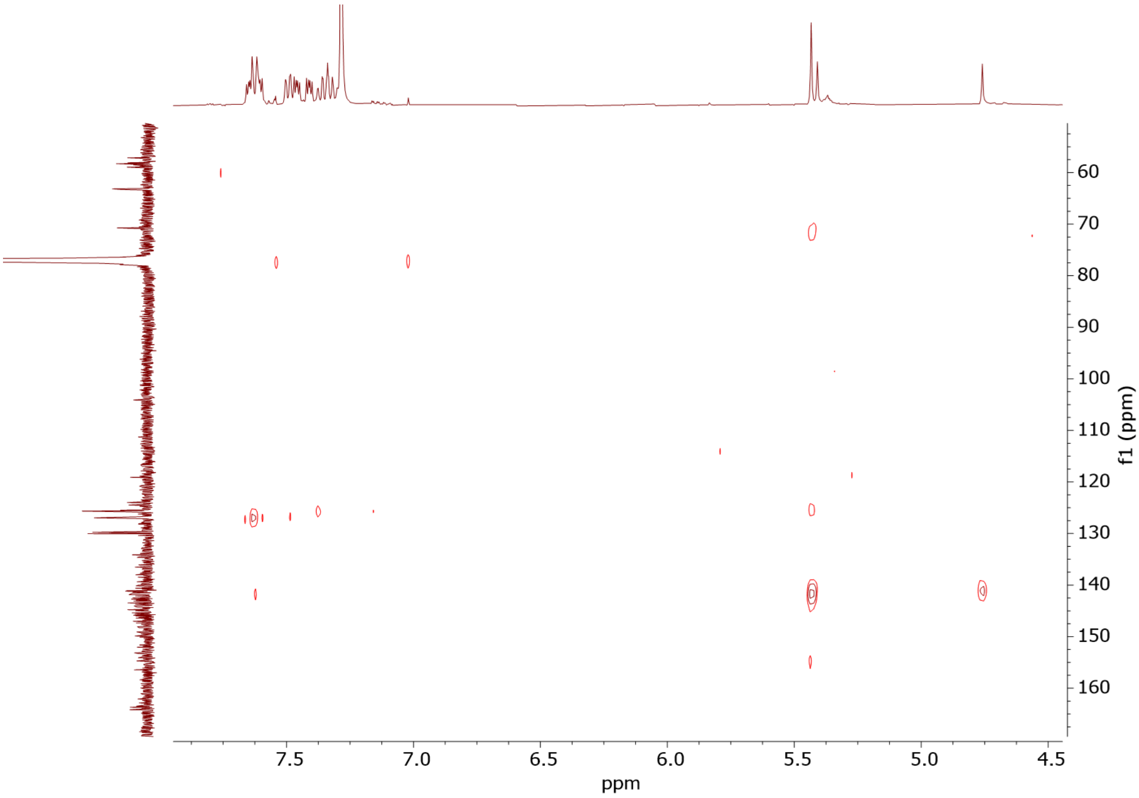

*Figure S.9. 2D HMBC spectrum of e,e-bis-An-$C_{60}$ (**2**). Experiment performed in $CDCl_3$ at 298K (400 MHz).*

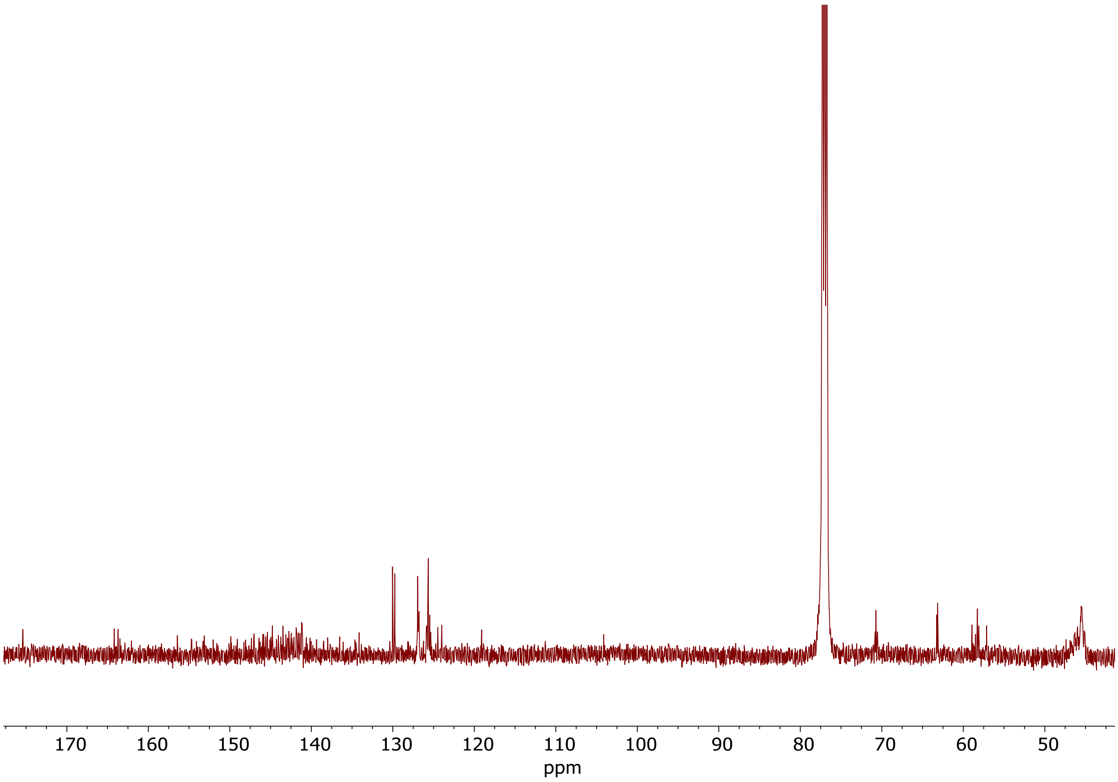

*Figure S.10. $^{13}$C-NMR spectrum of e,e-bis-An-$C_{60}$ (**2**). Experiment performed in $CDCl_3$ at 298K (125.75 MHz). Number of scans of 22828, a recycle delay of 2 s and the overall experimental time was 19h 42 min.*

### *Characterization of mono-Pn-$C_{60}$⊂**1b**·$(BArF)_8$ and mono-Pn-$C_{60}$ (**3**)*

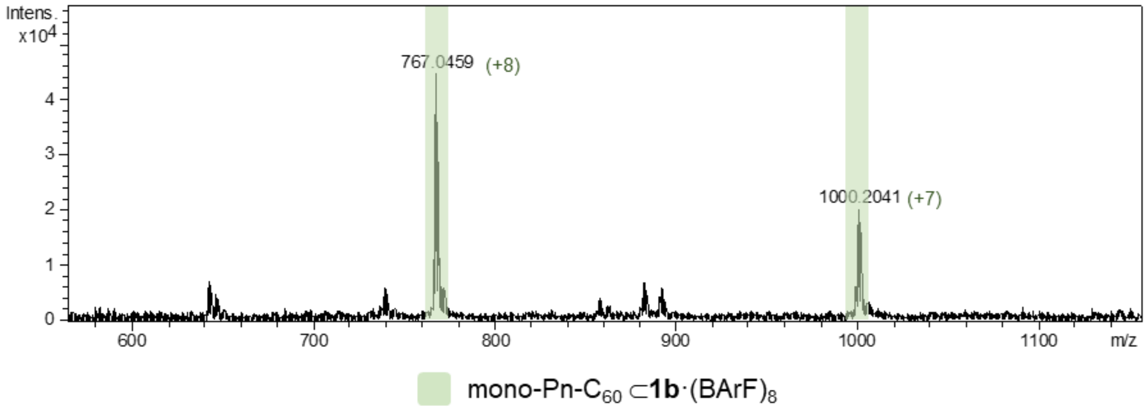

*Figure S.11. HR-ESI-MS of mono-Pn-$C_{60}$⊂**1b**·$(BArF)_8$.*

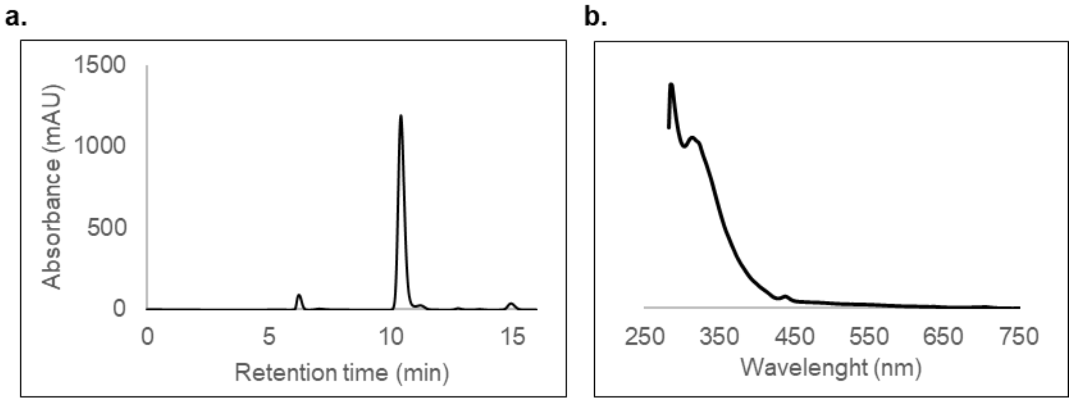

*Figure S.12. Characterization of mono-Pn-$C_{60}$ (**3**). a) HPLC analysis of purified mono-Pn-$C_{60}$ (**3**). $R_t$=10.326 min, b) UV-vis spectrum of mono-Pn-$C_{60}$.*

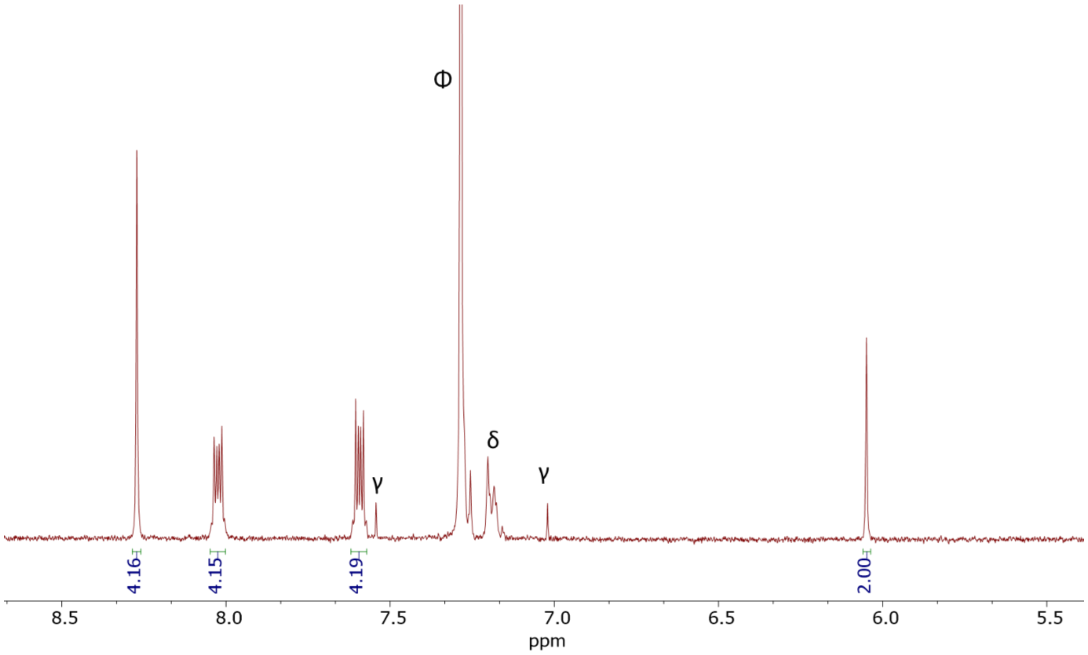

*Figure S.13. $^1$H-NMR spectrum of mono-Pn-$C_{60}$ (**3**). Experiment performed in $CDCl_3$ at 298K (400 MHz). γ: chloroform's satellites, φ: chloroform.*

## *Characterization of trans-1-bis-Pn-$C_{60}$⊂**1b**·$(BArF)_8$ and trans-1-bis-Pn-$C_{60}$ (**4**)*

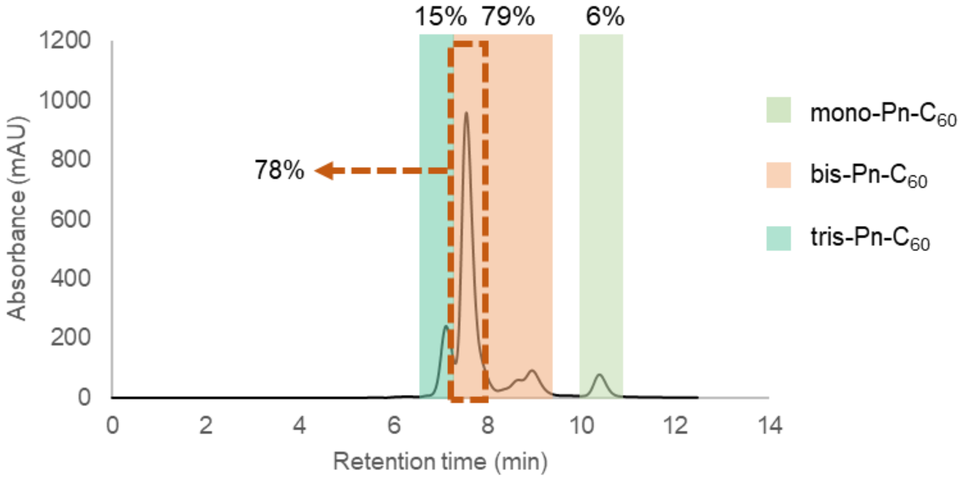

*Figure S.14. HPLC analysis of the reaction crude after disassembly of the nanocapsule for the formation of bis-Pn-$C_{60}$. Peak corresponding to trans-1-bis-Pn-$C_{60}$ (**4**) in the dotted orange box.*

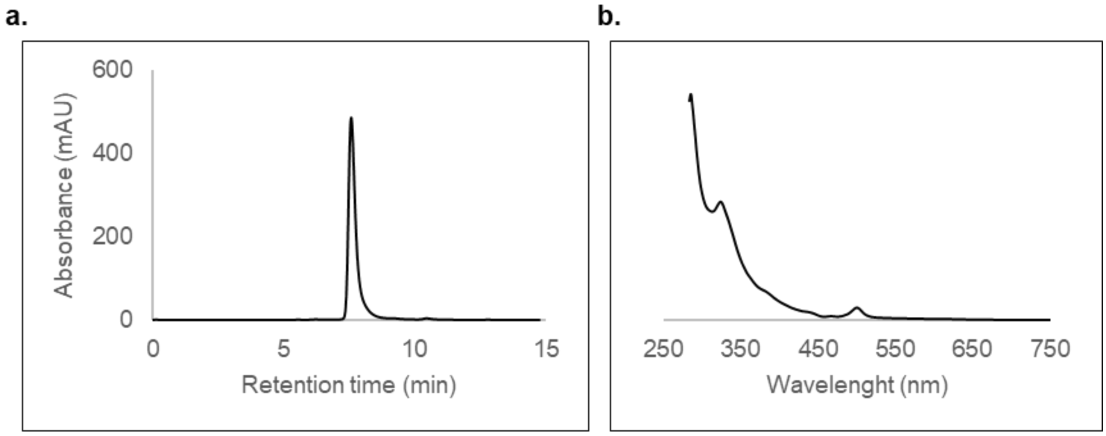

*Figure S.15. a) HPLC analysis of purified trans-1-bis-Pn-C$_{60}$ (**4**). R$_t$=7.576 min, b) UV-vis spectrum of pure trans-1-bis-Pn-C$_{60}$ (**4**).*

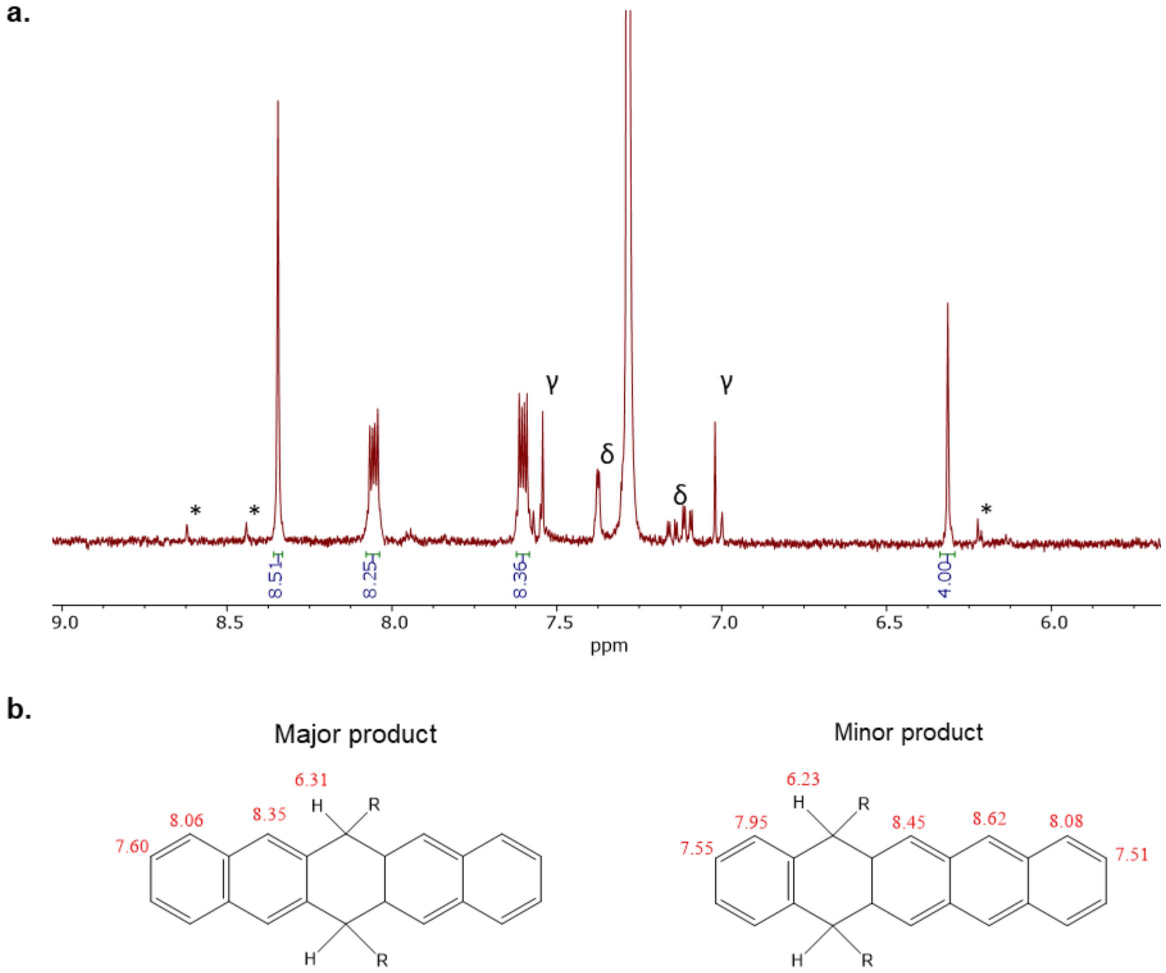

*Figure S.16. $^1$H-NMR spectra of trans-1-bis-Pn-C$_{60}$. a) $^1$H-NMR spectrum of trans-1-bis-Pn-C$_{60}$ (**4**). Experiment performed in CDCl$_3$ at 298K (400 MHz). γ: chloroform's satellites, φ: chloroform, δ: impurities of the purification solvent (CS$_2$) *minor product due to isomerization of pentacene-based addends. b) $^1$H-NMR prediction of isomers due to the isomerization of pentacene addends, both being trans-1-bis-adducts. 'R' = fullerene core.*

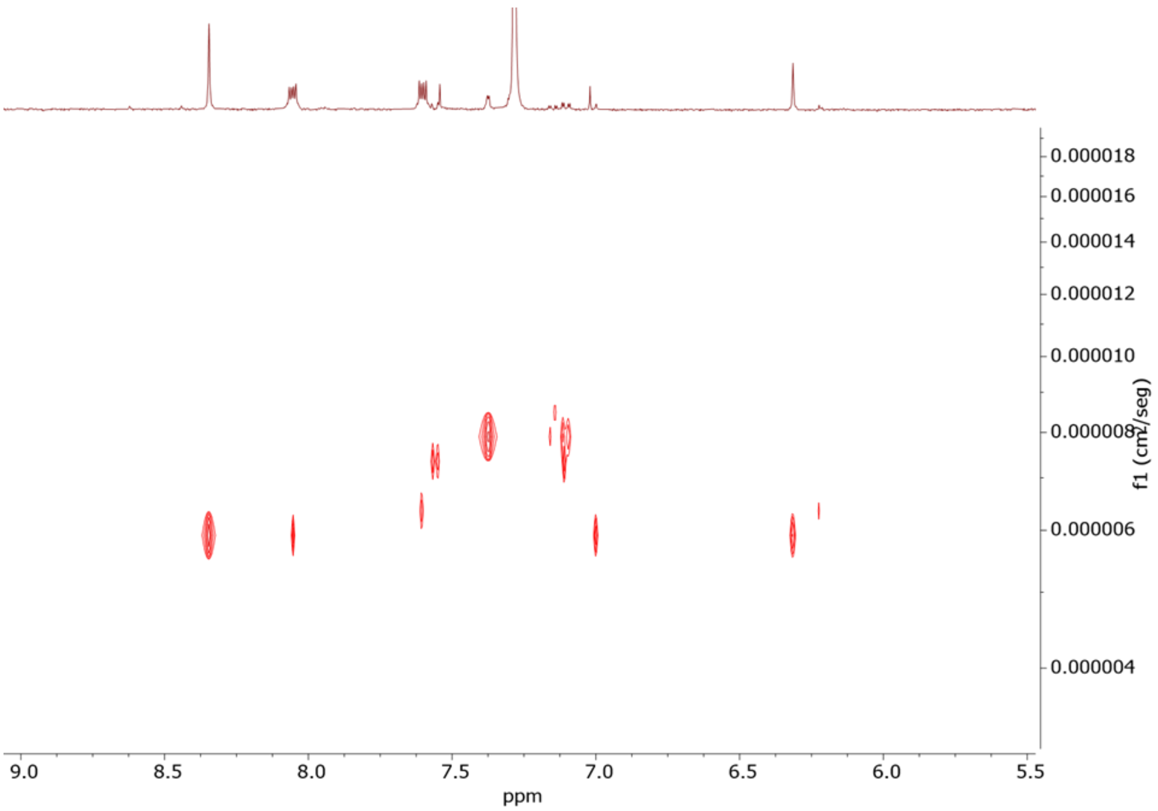

*Figure S.17. DOSY representation of trans-1-bis-Pn-$C_{60}$ (**4**). Experiment performed in $CDCl_3$ at 298K (500 MHz).*

## *Characterization of e,e-bis-An-Pn-$C_{60}\subset$**1b**$\cdot$(BArF)$_8$ and e,e-bis-An-Pn-$C_{60}$ (**5**)*

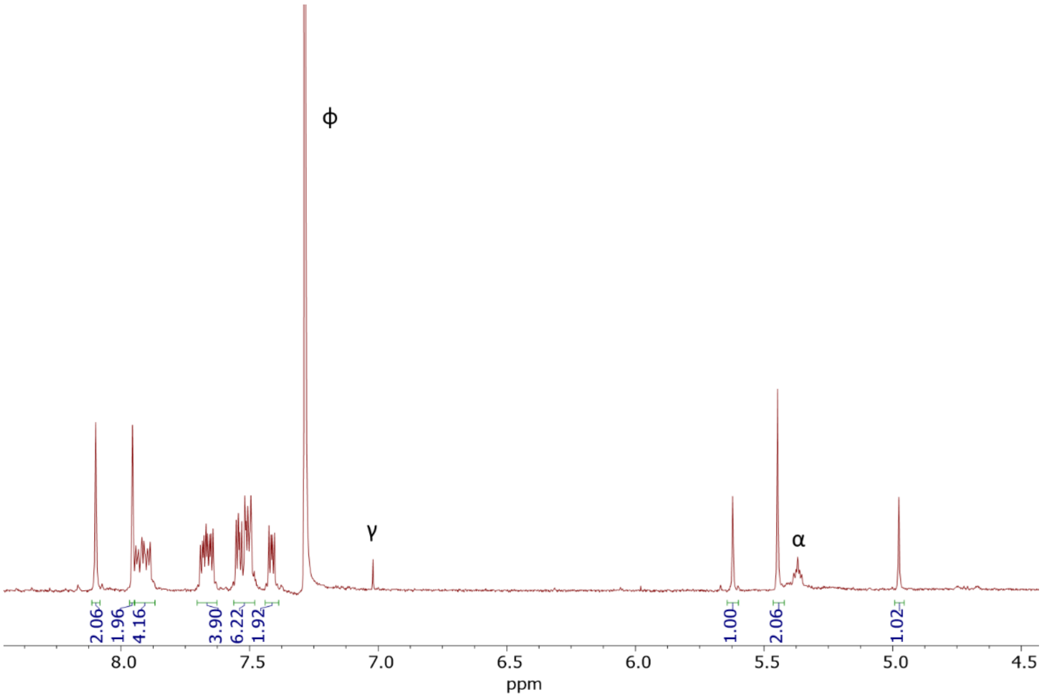

*Figure S.18. $^1$H-NMR spectrum of e,e-bis-An-Pn-$C_{60}$ (**5**). Experiment performed in $CDCl_3$ at 298K (400 MHz). γ: chloroform's satellites, φ: chloroform, $\alpha$: TLC-silica impurities.*

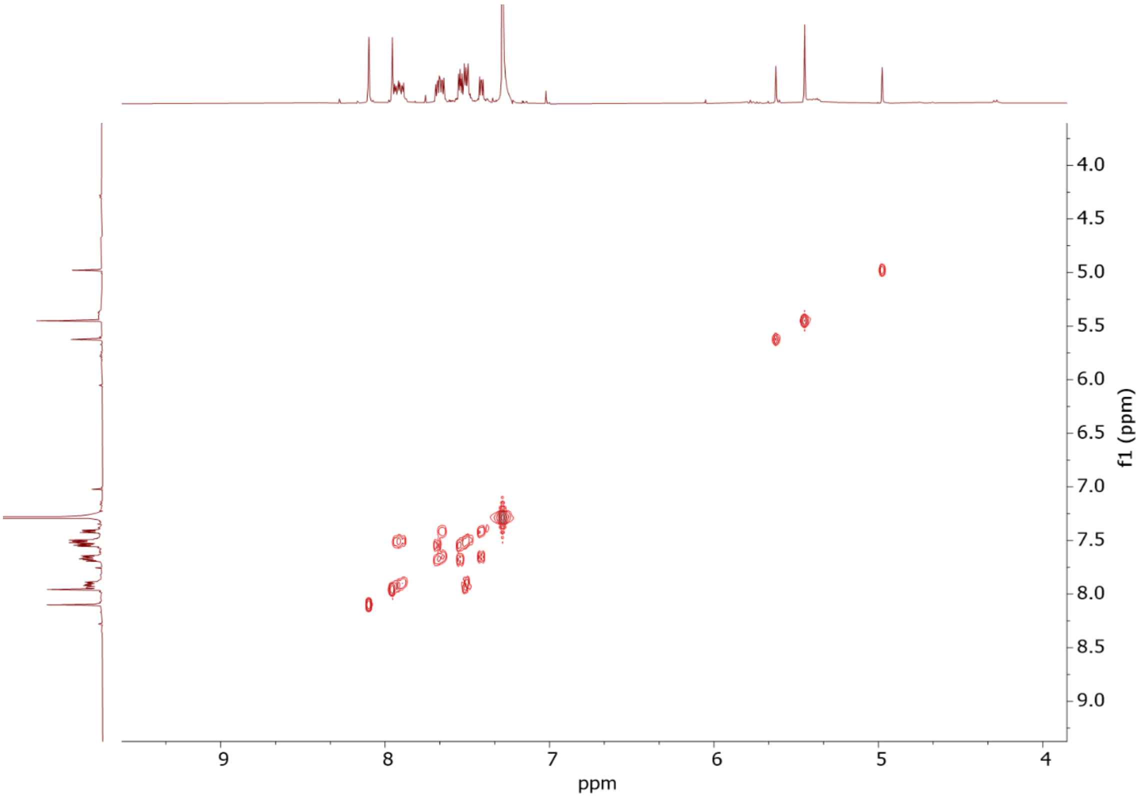

*Figure S.19. 2D COSY spectrum of e,e-bis-An-Pn-$C_{60}$ (**5**). Experiment performed in $CDCl_3$ at 298K (400 MHz).*

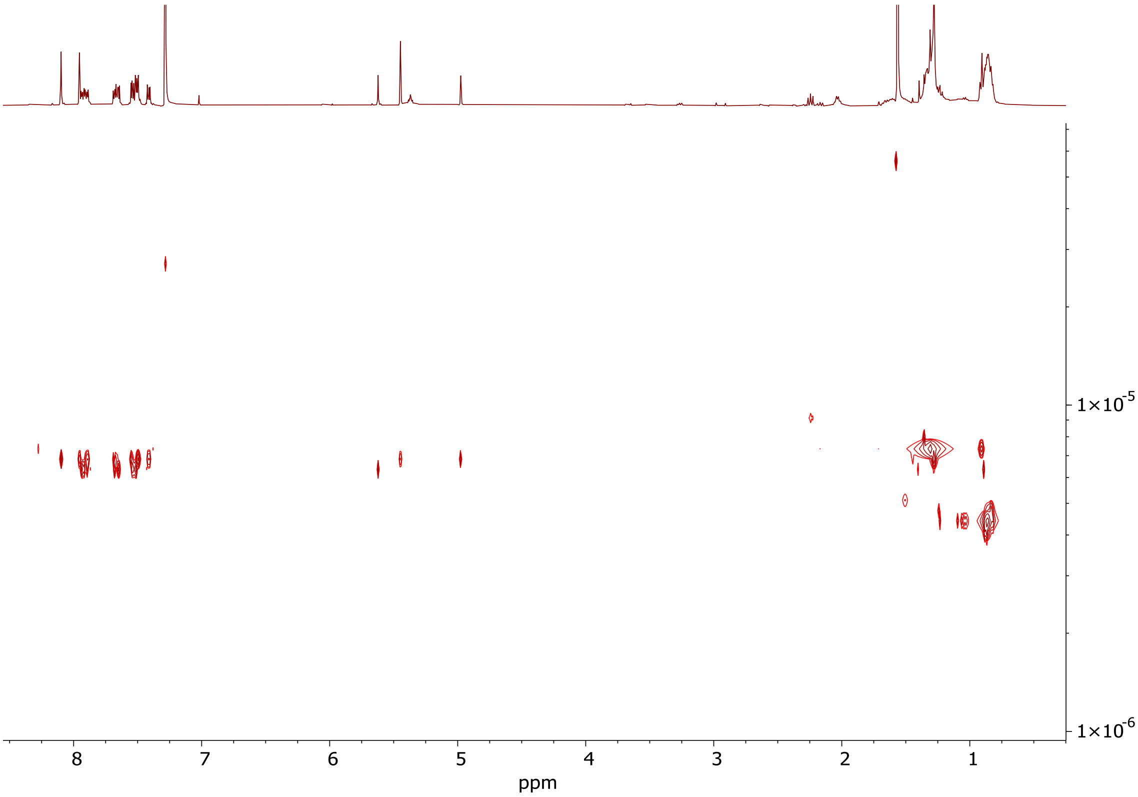

*Figure S.20. DOSY representation e,e-bis-An-Pn-$C_{60}$ (**5**). Experiment performed in $CDCl_3$ at 298K (500 MHz).*

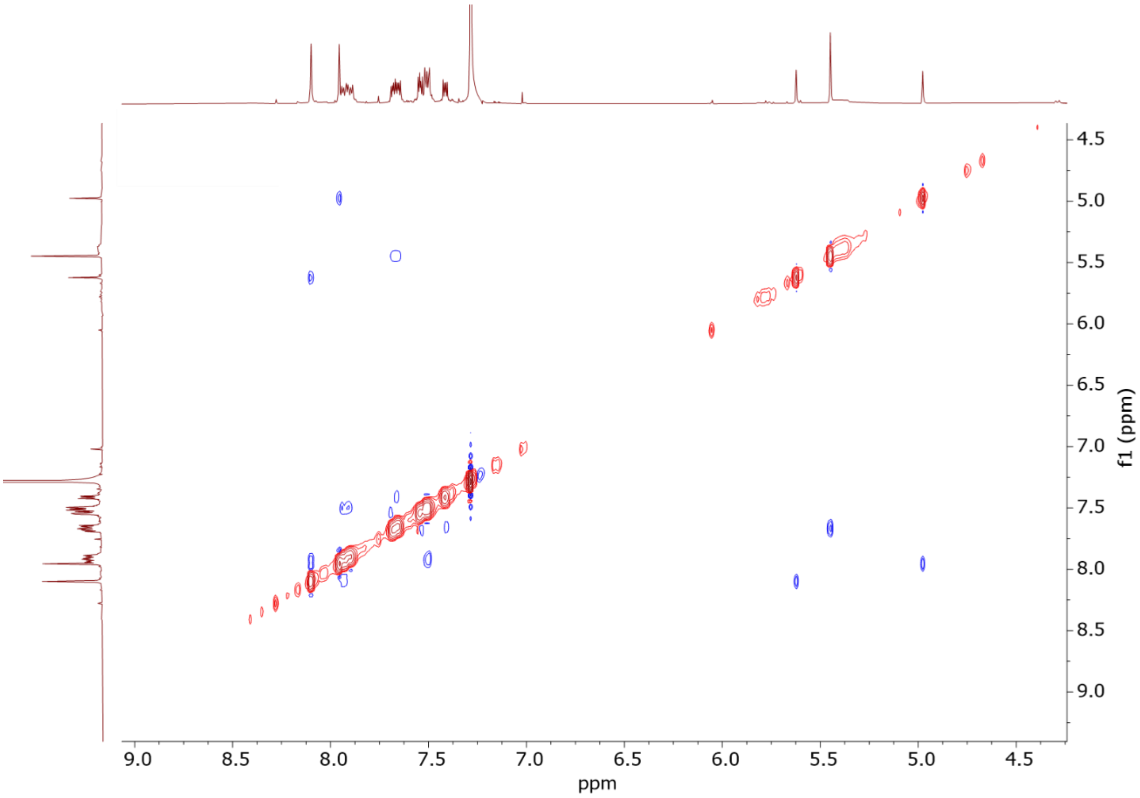

*Figure S.21. 2D NOESY spectrum of e,e-bis-An-Pn-C$_{60}$ (**5**). Experiment performed in CDCl$_3$ at 298K (400 MHz).*

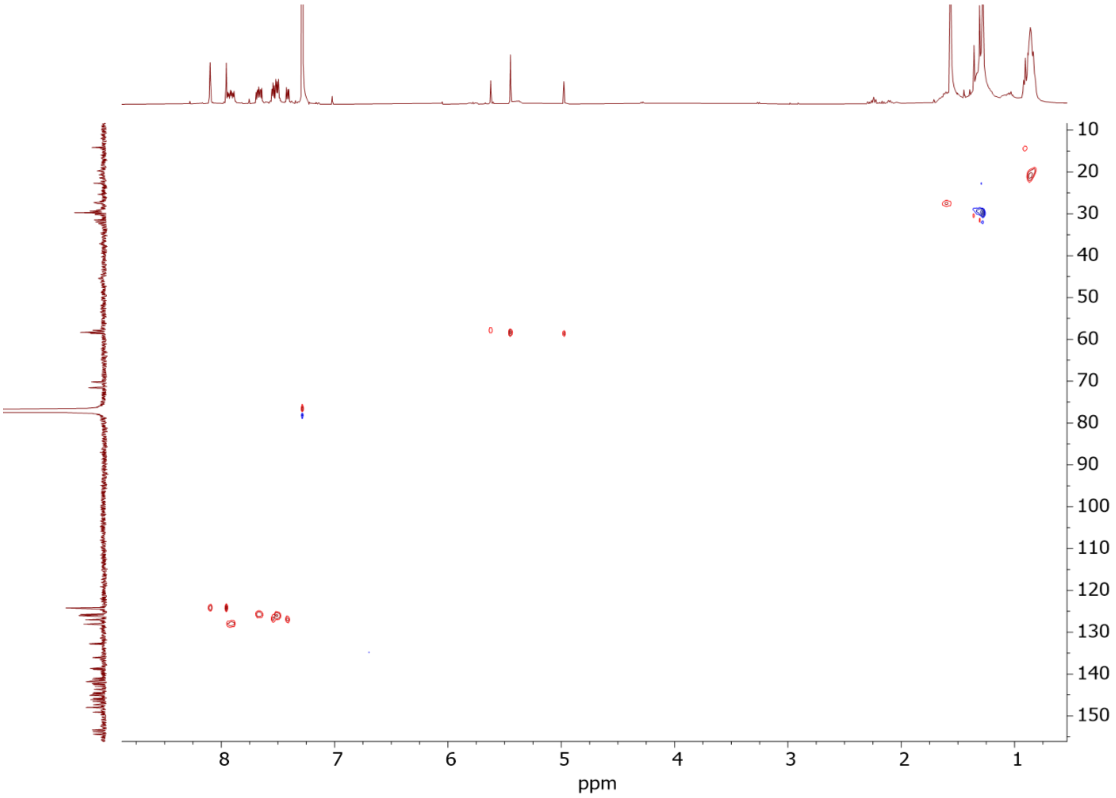

*Figure S.22. 2D HSQC spectrum of e,e-bis-An-Pn-C$_{60}$ (**5**). Experiment performed in CDCl$_3$ at 298K (400 MHz).*

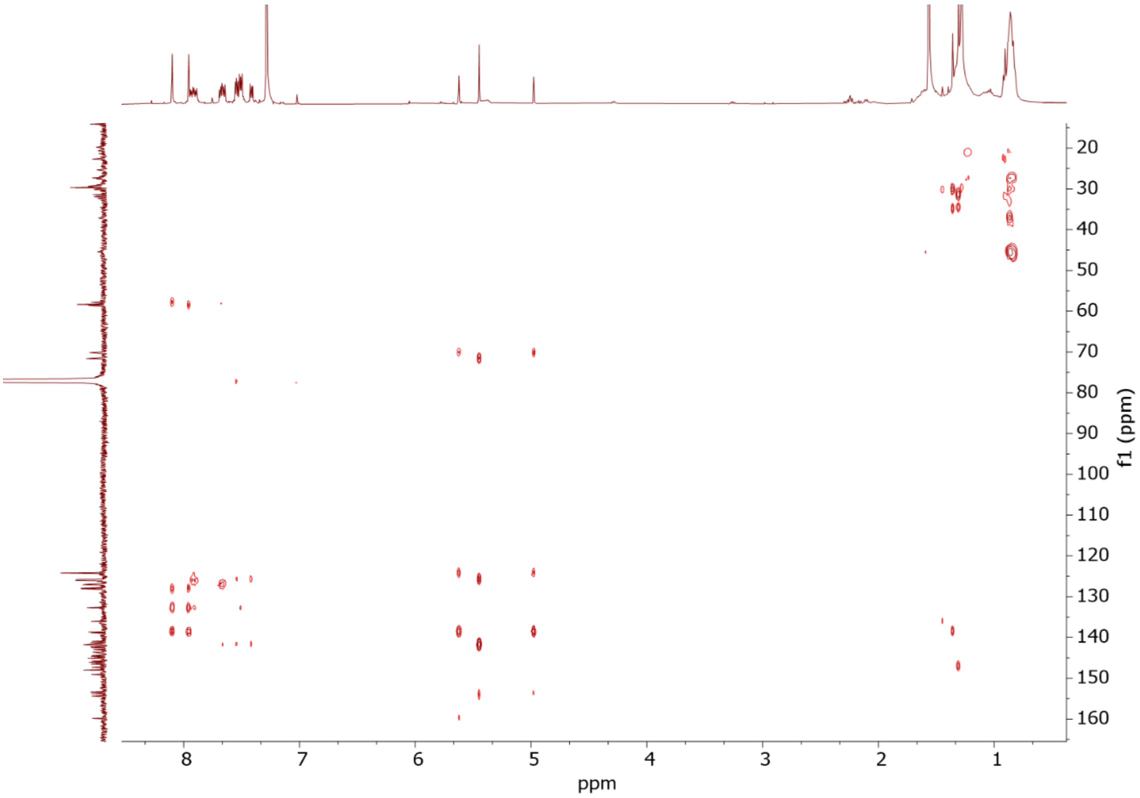

*Figure S.23. 2D HMBC spectrum of e,e-bis-An-Pn-$C_{60}$ (**5**). Experiment performed in $CDCl_3$ at 298K (400 MHz).*

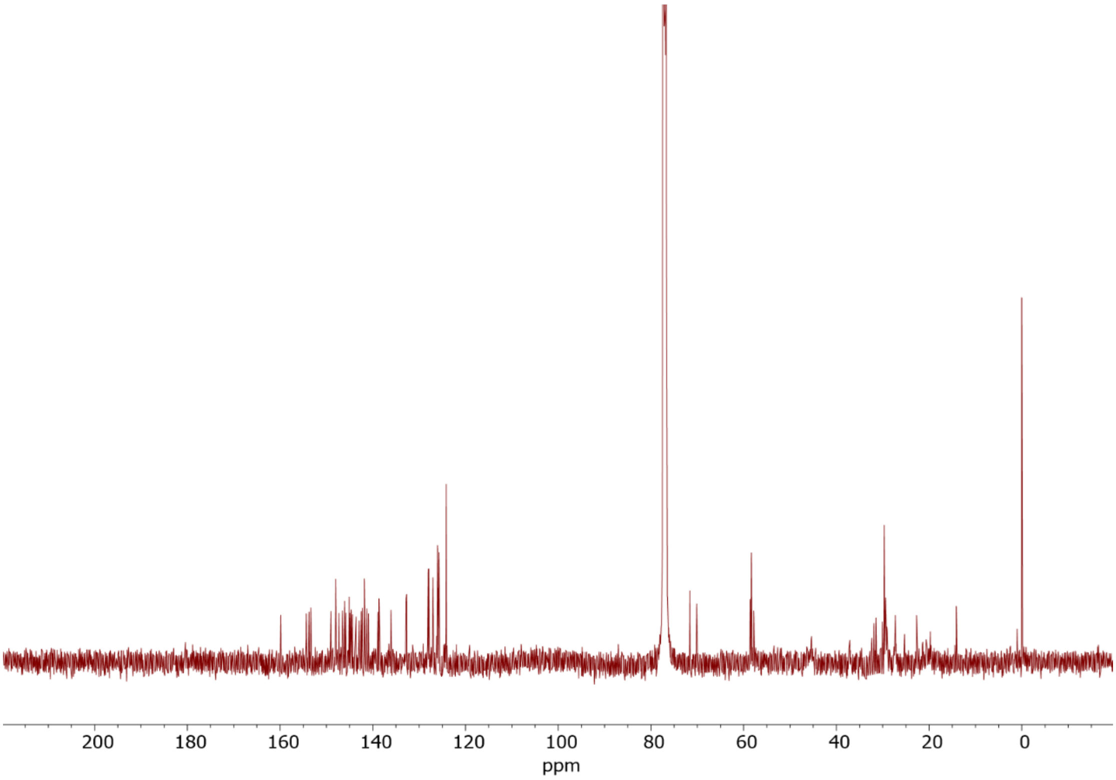

*Figure S.24. $^{13}$C-NMR spectrum of e,e-bis-An-Pn-$C_{60}$ (**5**). Experiment performed in $CDCl_3$ at 298K (125.75 MHz). Number of scans of 32768 and the overall experimental time was 38h.*

### *Characterization of e,e-bis-An-mono-diethylmalonate-$C_{60}$⊂**1c**·$(BArF)_8$ and e,e-bis-An-mono-diethylmalonate-$C_{60}$ (**6**)*

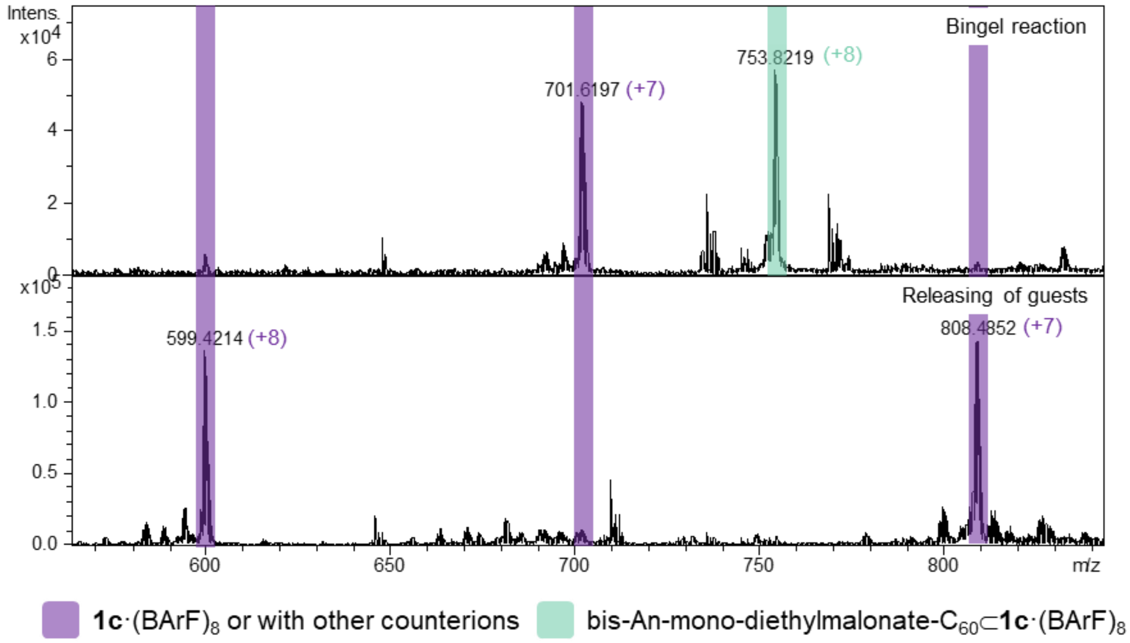

*Figure S.25. HR-ESI-MS monitoring of bis-An-e-mono-diethylmalonate-$C_{60}$ releasing from **1c**·$(BArF)_8$ by sonication of the host-guest complex with chloroform.*

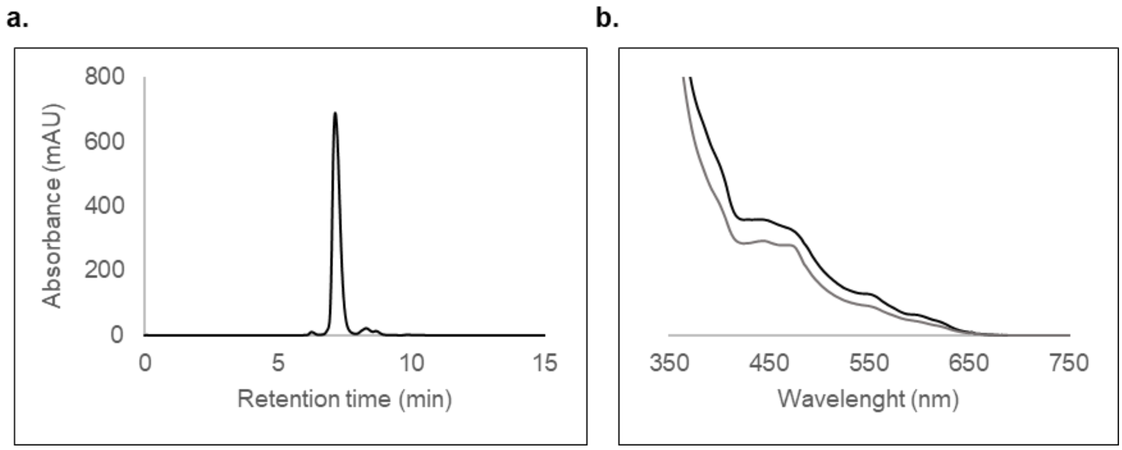

*Figure S.26. a) HPLC analysis of purified e,e-bis-An-e-mono-diethylmalonate-$C_{60}$ (mixture of **6**(I) and **6**(II) isomers). $R_t$=7.133 min, b) UV-vis spectra of e,e-bis-anthracene-e-mono-diethylmalonate-$C_{60}$ at the beginning (6.758 min) and at the end (7.542 min) of the chromatogram peak, indicating the presence of at least two isomers.*

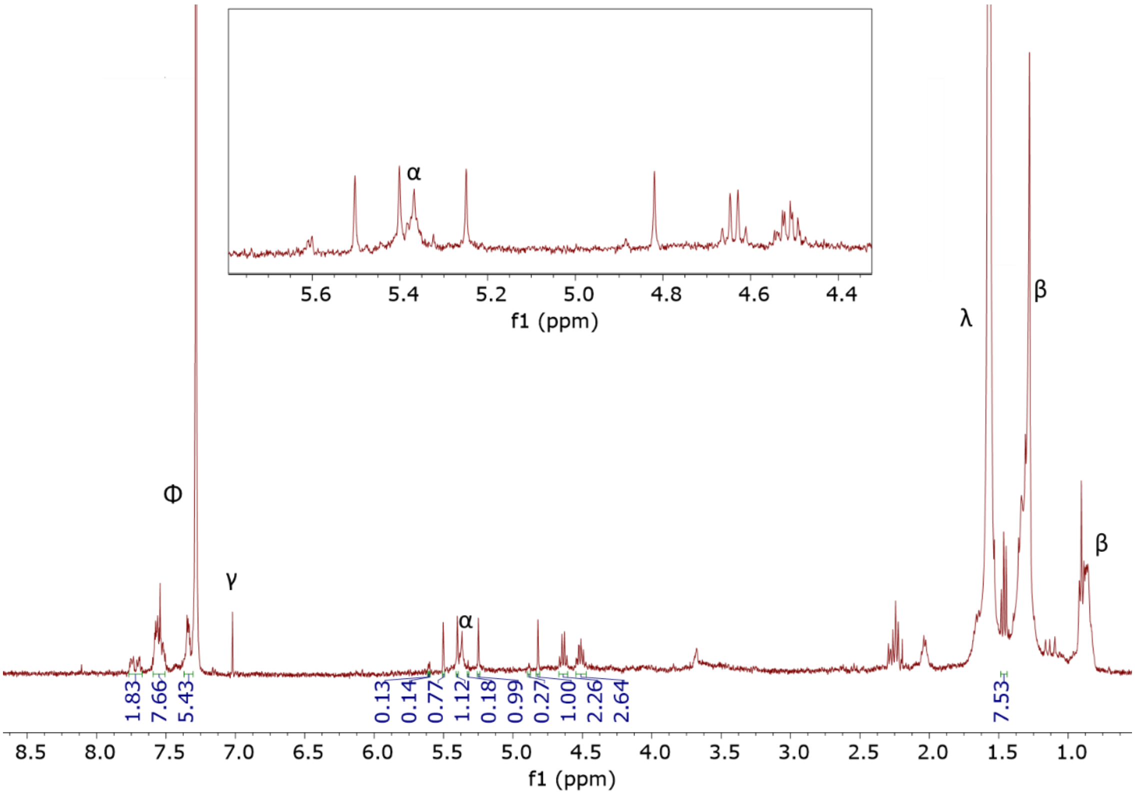

*Figure S.27. $^1$H-NMR spectrum of e,e-bis-An-e-mono-diethylmalonate-$C_{60}$ (mixture of **6**(I) and **6** (II) isomers). Experiment performed in $CDCl_3$ at 298K (400 MHz). φ: chloroform, γ: chloroform's satellites, α: TLC-silica impurities, λ: $H_2O$, β: grease.*

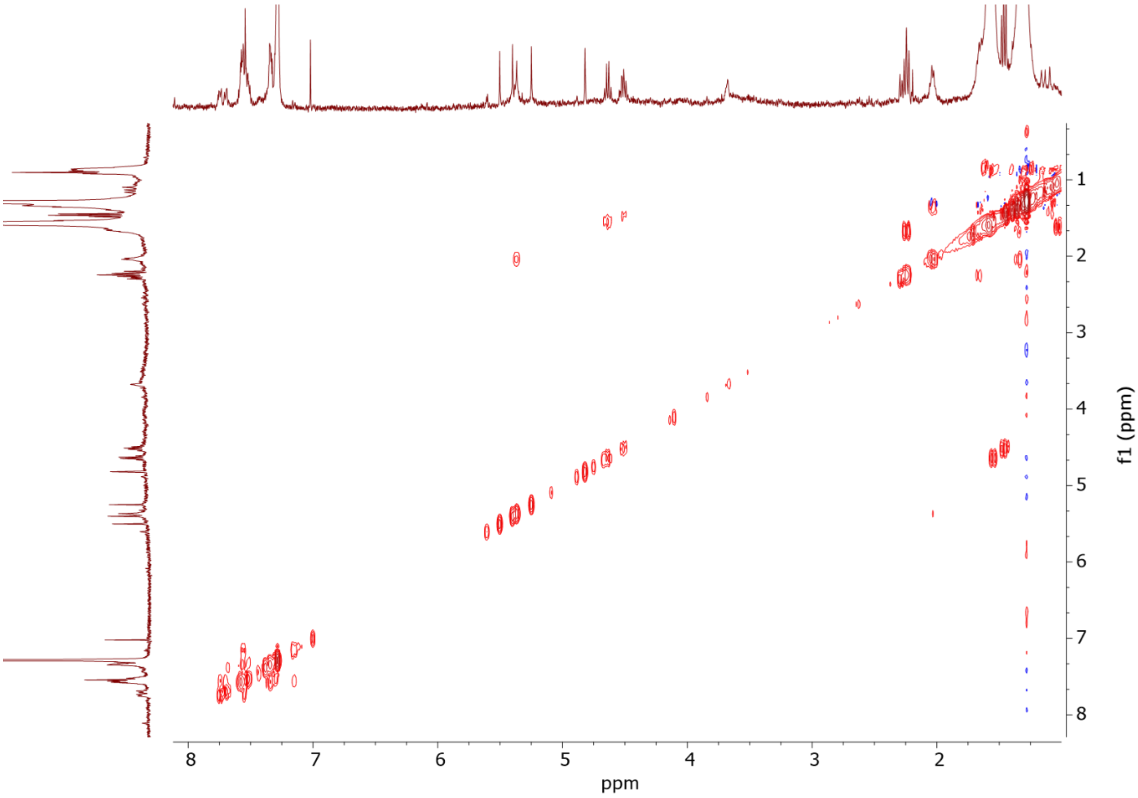

*Figure S.28. 2D COSY spectrum of e,e-bis-An-e-mono-diethylmalonate-$C_{60}$ (mixture of **6**(I) and **6**(II) isomers). Experiment performed in $CDCl_3$ at 298K (400 MHz).*

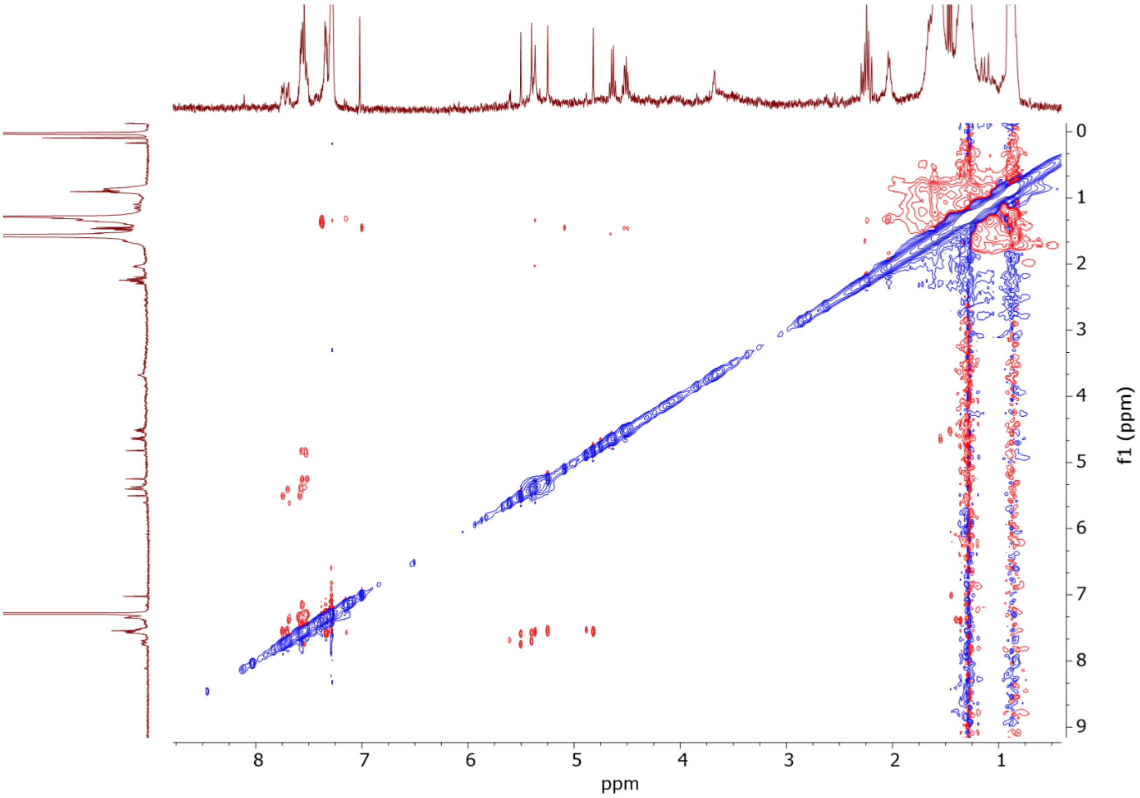

*Figure S.29. 2D ROESY spectrum of e,e-bis-An-e-mono-diethylmalonate-C$_{60}$ (mixture of **6**(I) and **6**(II) isomers). Experiment performed in CDCl$_3$ at 298K (500 MHz).*

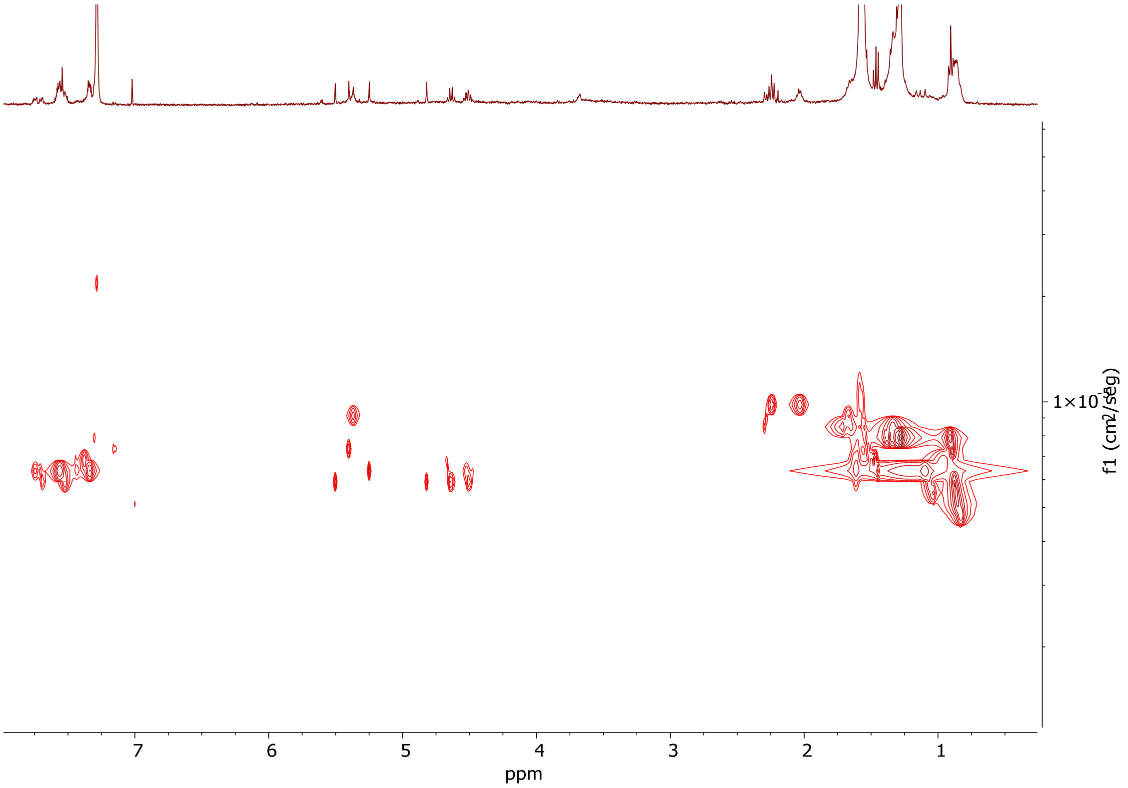

*Figure S.30. DOSY representation of e,e-bis-An-e-mono-diethylmalonate-C$_{60}$ (mixture of **6**(I) and **6**(II) isomers). Experiment performed in CDCl$_3$ at 298K (500 MHz).*

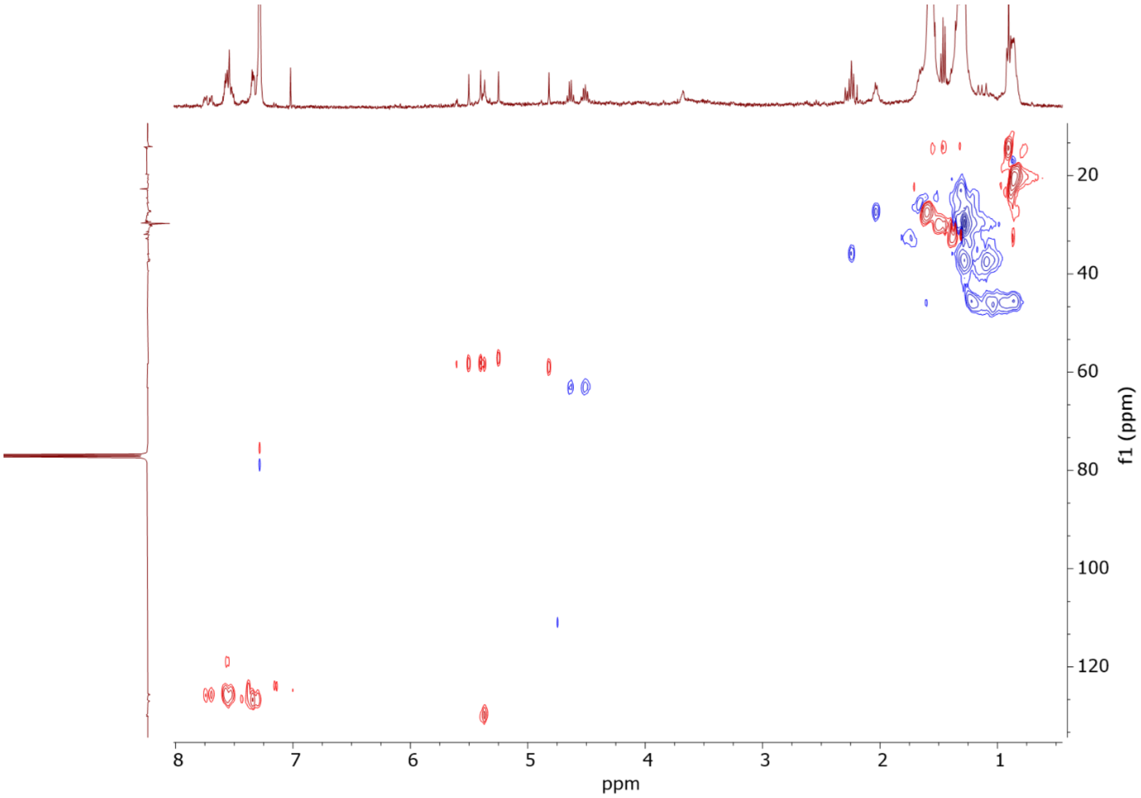

*Figure S.31. 2D multiplicity-edited HSQC spectrum of e,e-bis-An-e-mono-diethylmalonate-$C_{60}$ (mixture of **6**(I) and **6**(II) isomers). Experiment performed in $CDCl_3$ at 298K (500 MHz).*

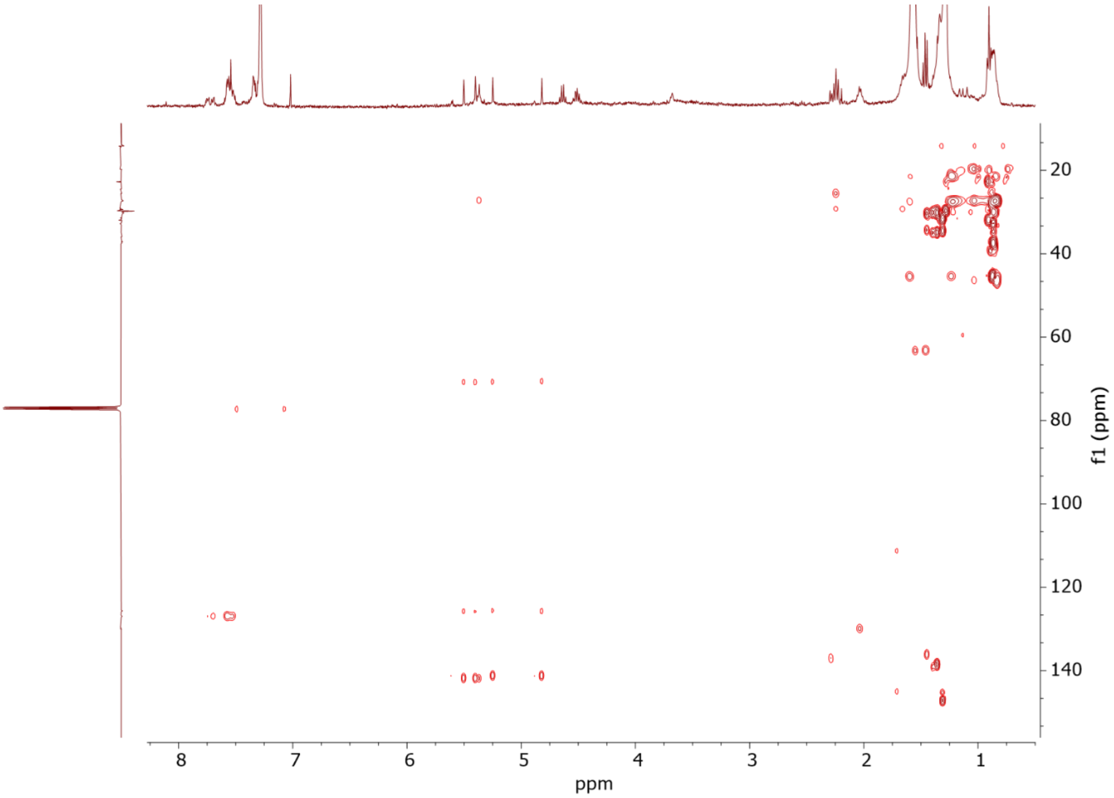

*Figure S.32. 2D HMBC spectrum e,e-bis-An-e-mono-diethylmalonate-$C_{60}$ (mixture of **6**(I) and **6**(II) isomers). Experiment performed in $CDCl_3$ at 298K (500 MHz).*

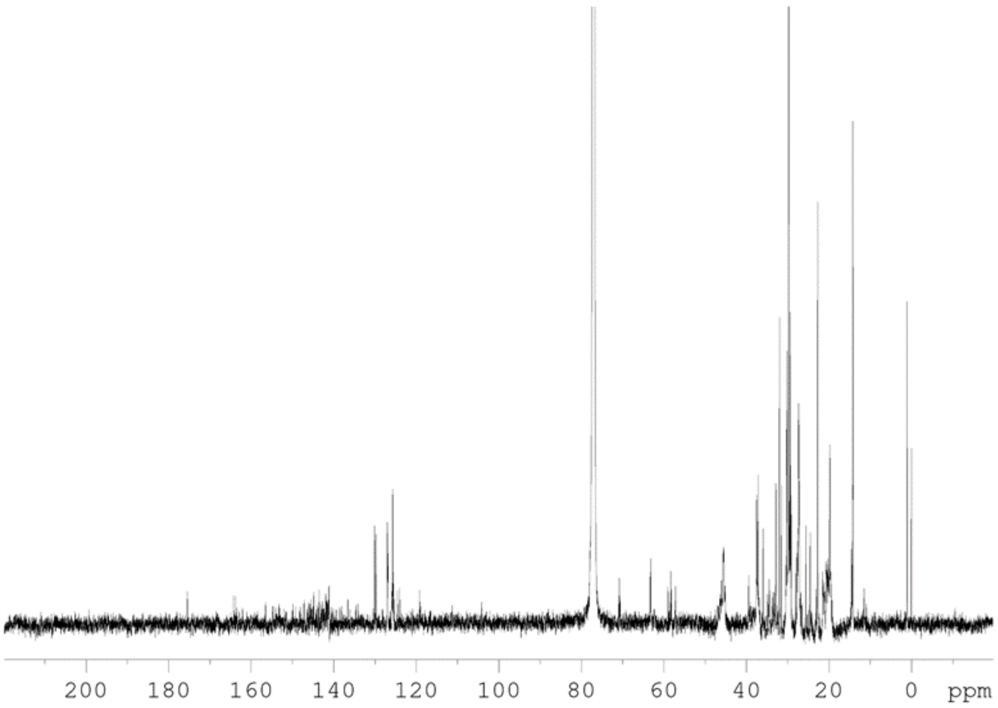

*Figure S.33. $^{13}$C-NMR spectrum of e,e-bis-An-e-mono-diethylmalonate-$C_{60}$ (mixture of **6**(I) and **6**(II) isomers). Experiment performed in $CDCl_3$ at 298K (125.75 MHz). Number of scans of 22828, a recycle delay of 2 s and the overall experimental time was 19h 42 min.*

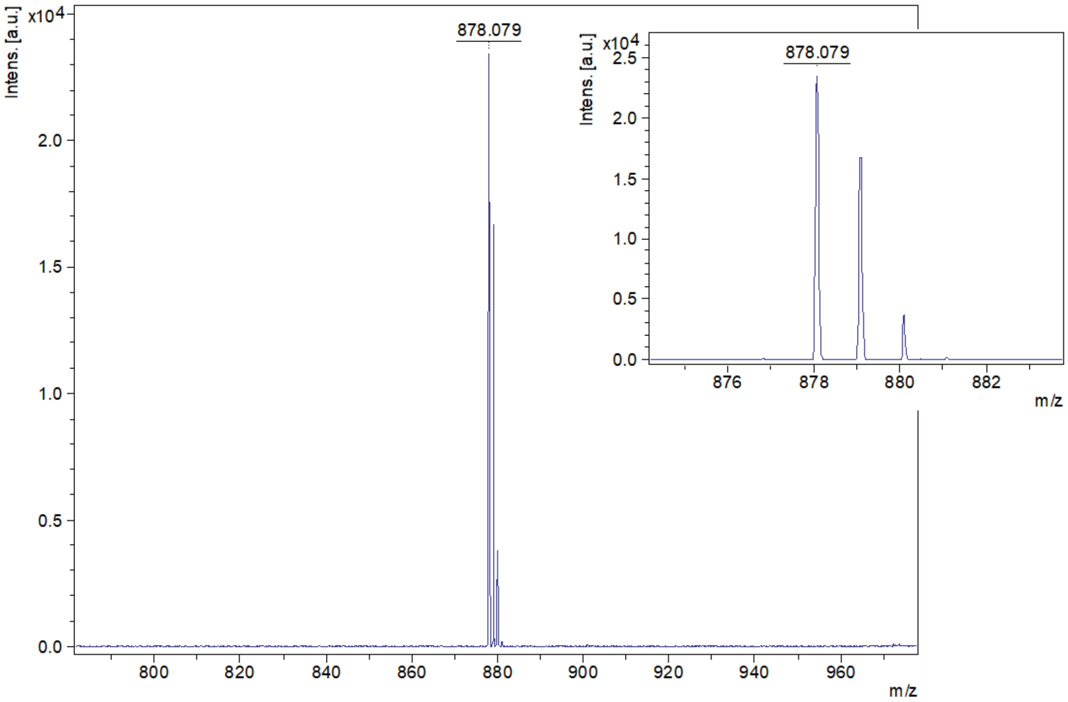

*Figure S.34. MALDI-MS of e,e-bis-An-e-mono-diethylmalonate-$C_{60}$ (**6**). The peak (m/z=878.079) corresponds to the mono-diethylmalonate-adduct analogue due to the laser of the instrument which promotes the Retro-Diels-Alder of the anthracene addends.*

### *Characterization of mono-Pn-trans-1-bis-diethylmalonate-$C_{60}\subset$**1b**·(BArF)$_8$ and mono-Pn-trans-1-bis-diethylmalonate-$C_{60}$ (**7**)*

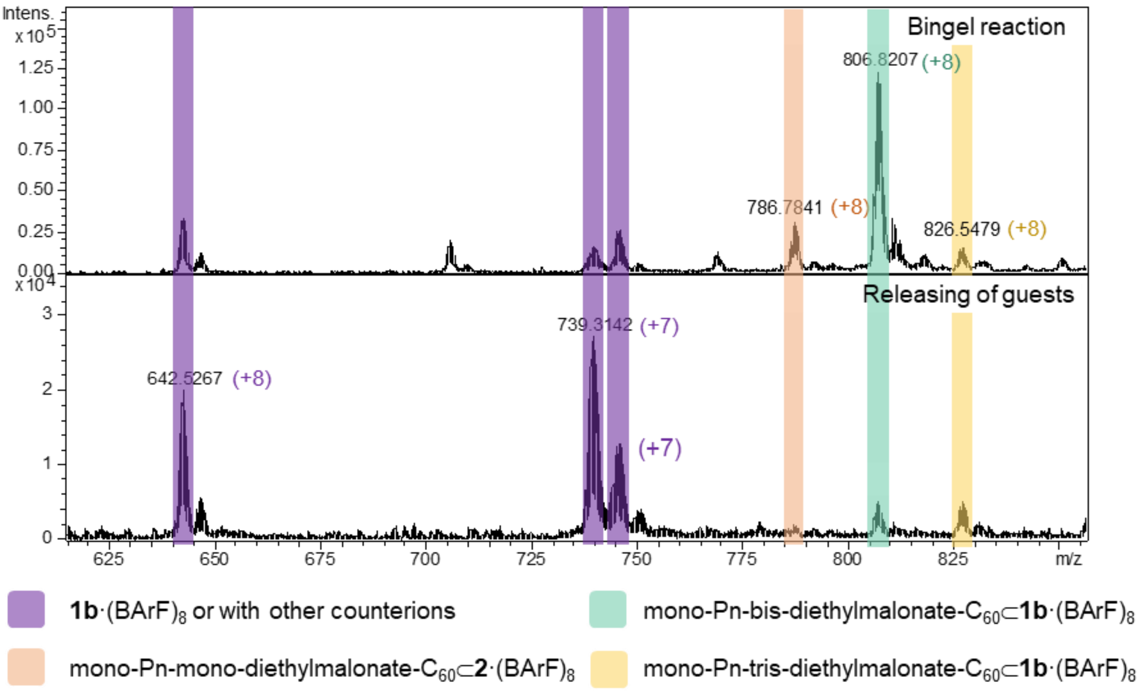

*Figure S.35. HR-ESI-MS monitoring of mono-Pn-bis-diethylmalonate-$C_{60}$ releasing from **1b** ·(BArF)$_8$ by solvent washing of the host-guest solid with chloroform.*

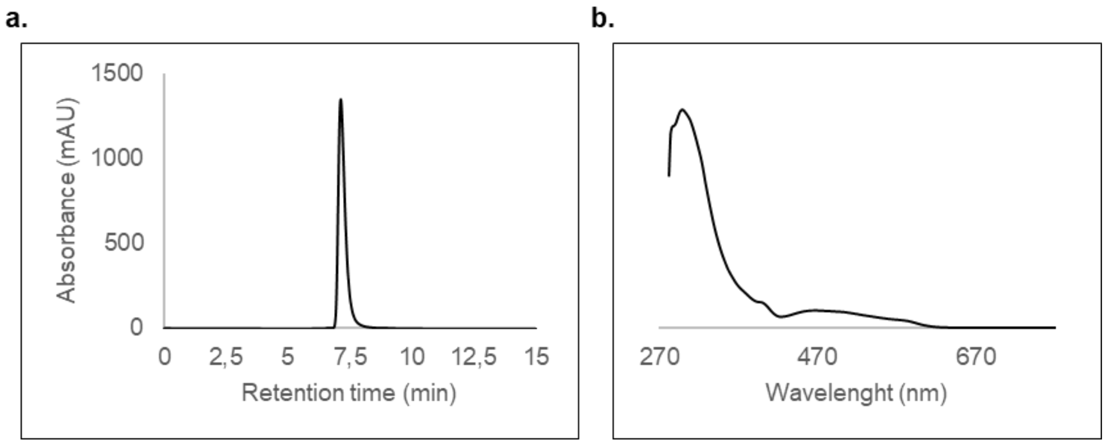

*Figure S.36. a) HPLC analysis of purified e-mono-Pn-trans-1-bis-diethylmalonate-$C_{60}$ (**7**). $R_t$=7.125 min, b) UV-vis spectrum of pure e-mono-Pn-trans-1-bis-diethylmalonate-$C_{60}$ (**7**).*

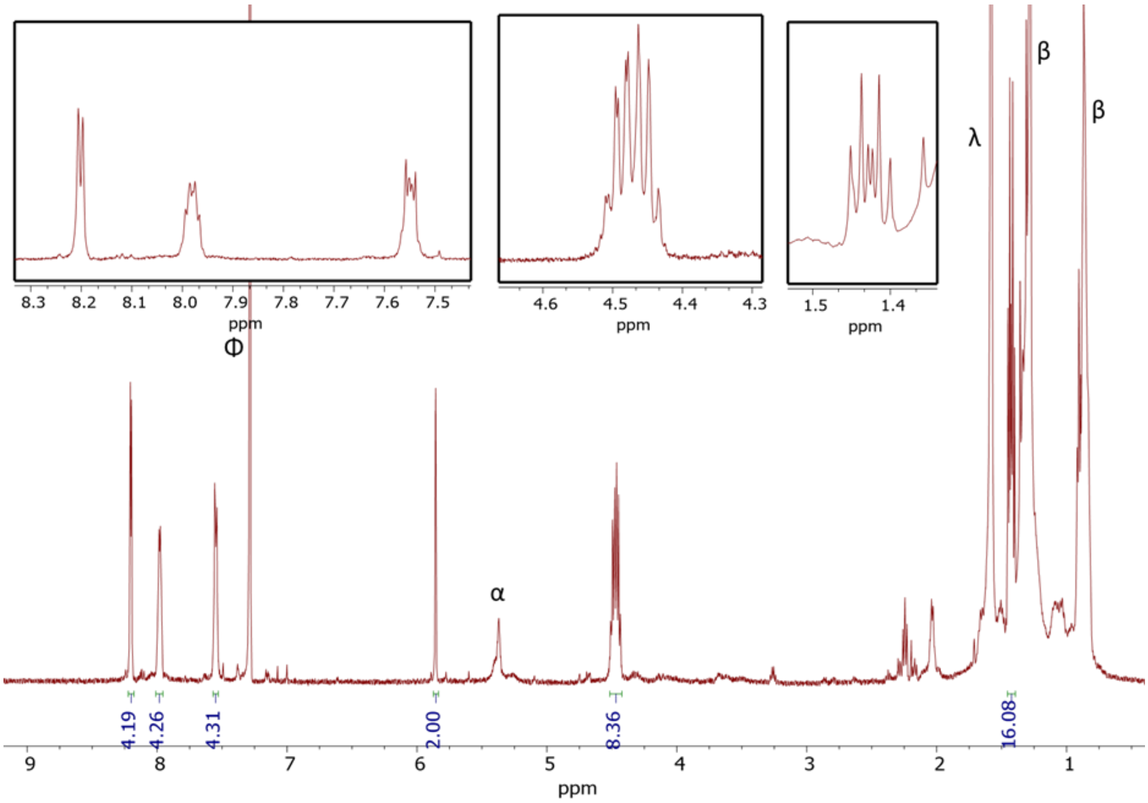

*Figure S.37. $^1$H-NMR spectrum of e-mono-Pn-trans-1-bis-diethylmalonate-C$_{60}$ (**7**). Experiment performed in CDCl$_3$ at 298K (500 MHz). φ: chloroform, α: TLC-silica impurities, λ: H$_2$O, β: grease*

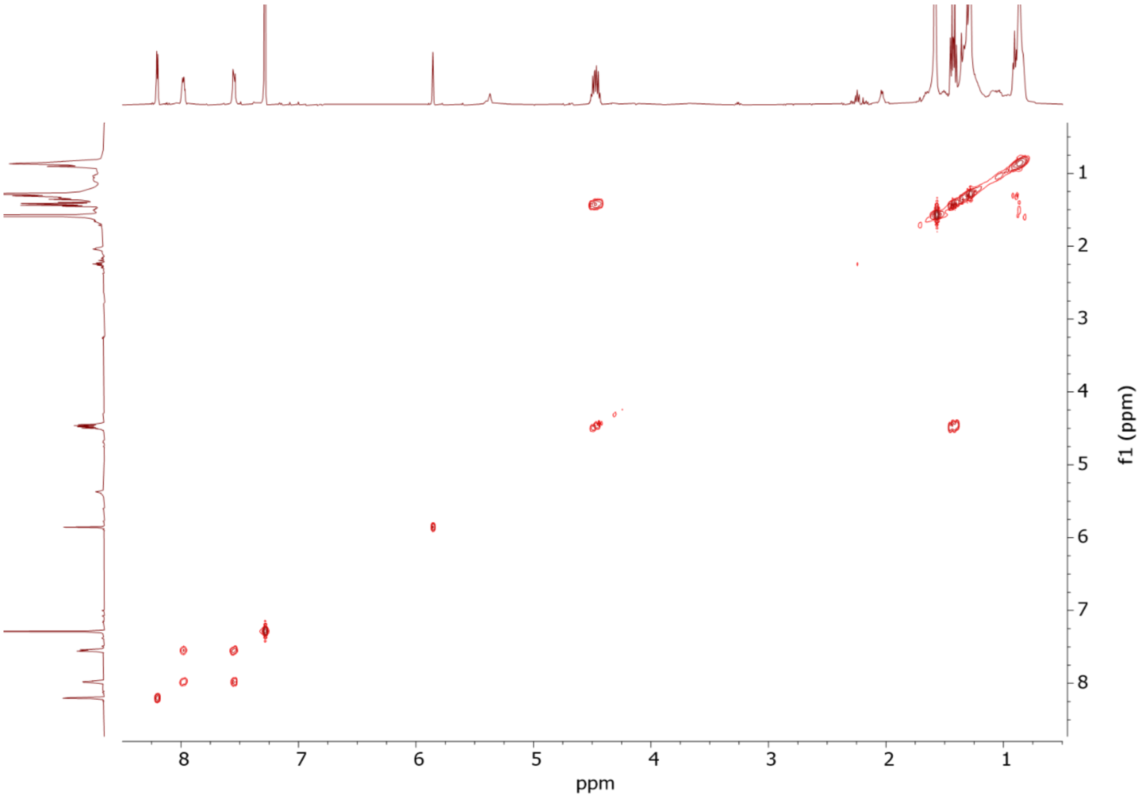

*Figure S. 38. 2D COSY spectrum of e-mono-Pn-trans-1-bis-diethylmalonate-C$_{60}$ (**7**). Experiment performed in CDCl$_3$ at 298K (500 MHz).*

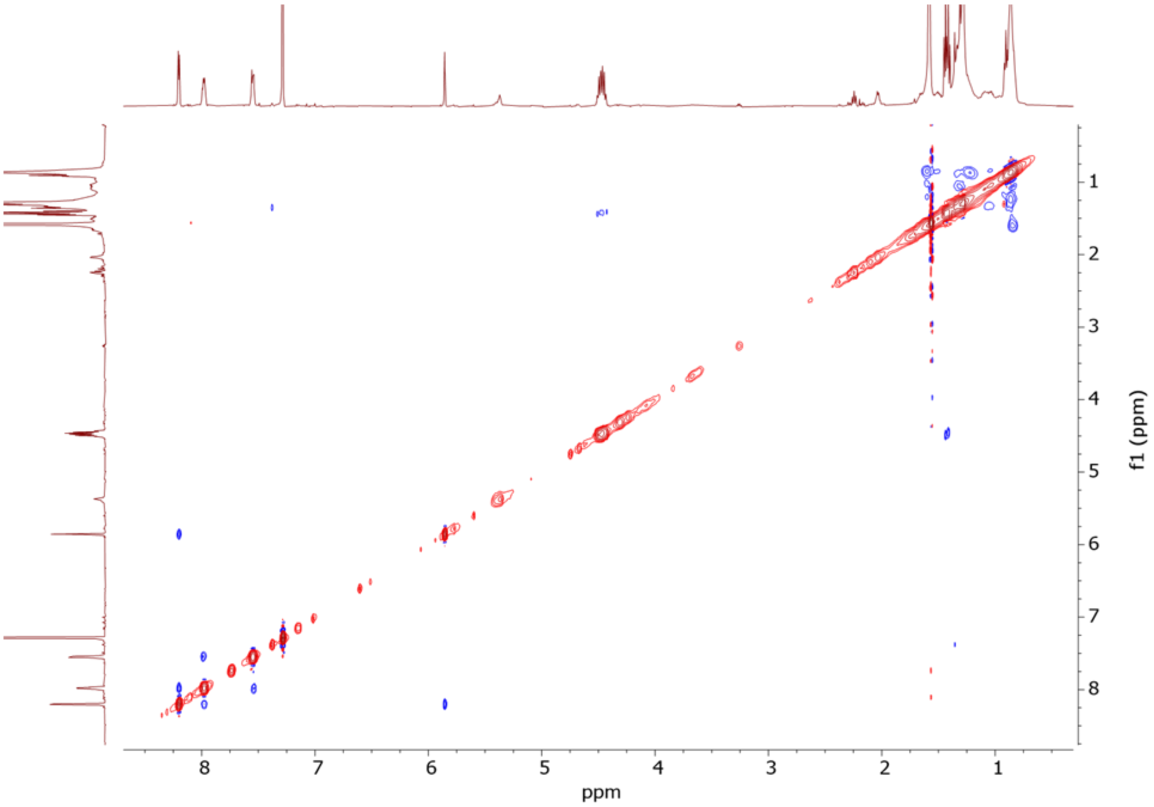

*Figure S.39. 2D ROESY spectrum of e-mono-Pn-trans-1-bis-diethylmalonate-C$_{60}$ (**7**). Experiment performed in CDCl$_3$ at 298K (500 MHz).*

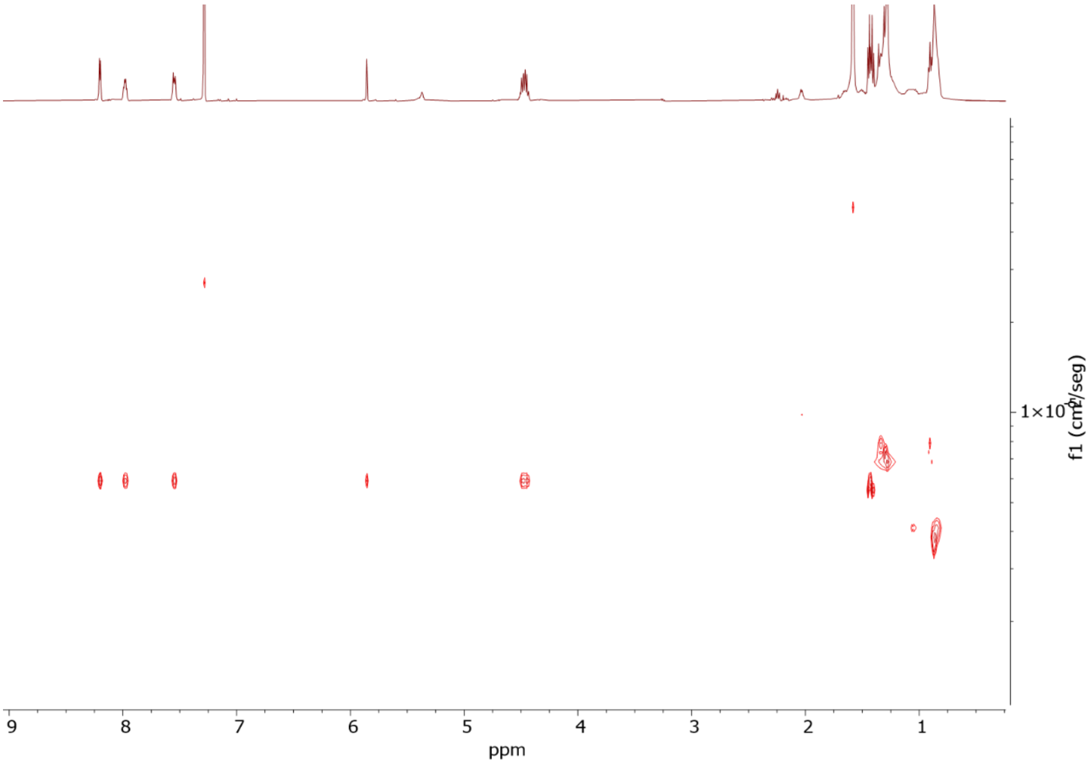

*Figure S.40. DOSY representation of e-mono-Pn-trans-1-bis-diethylmalonate-C$_{60}$ (**7**). Experiment performed in CDCl$_3$ at 298K (500 MHz).*

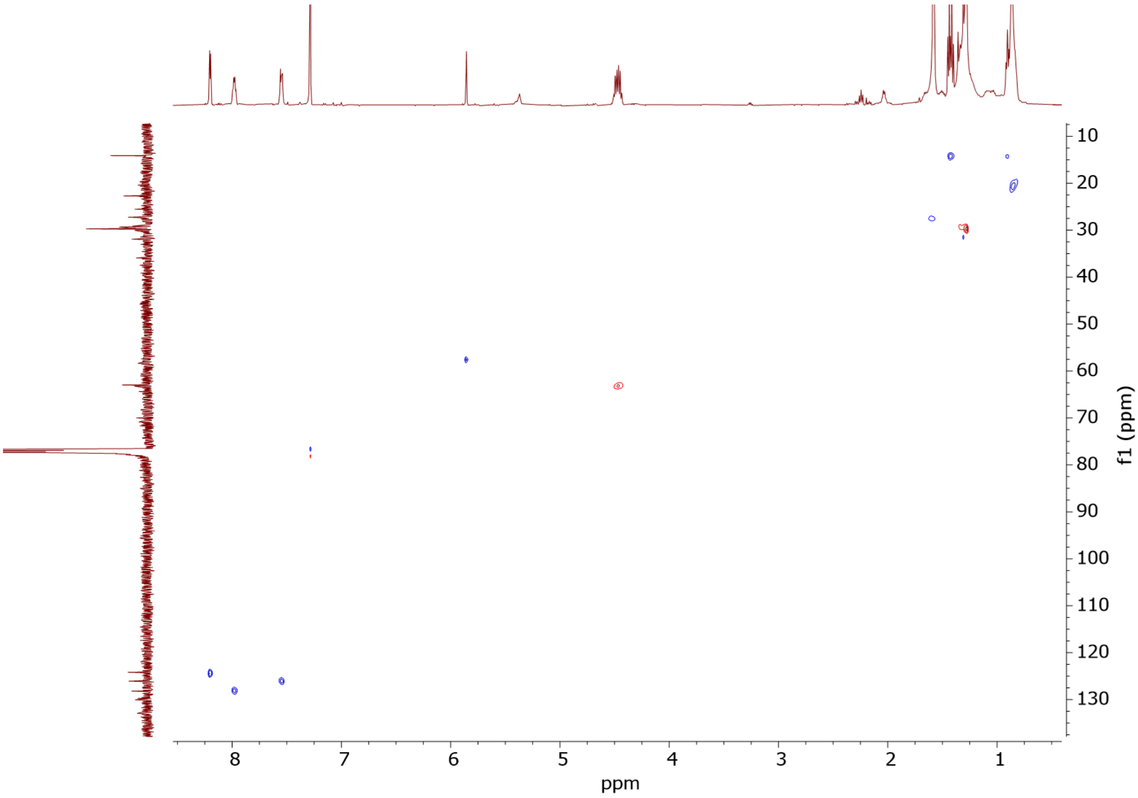

*Figure S.41. 2D multiplicity-edited HSQC spectrum of e-mono-Pn-trans-1-bis-diethylmalonate-$C_{60}$ (**7**). Experiment performed in $CDCl_3$ at 298K (600 MHz).*

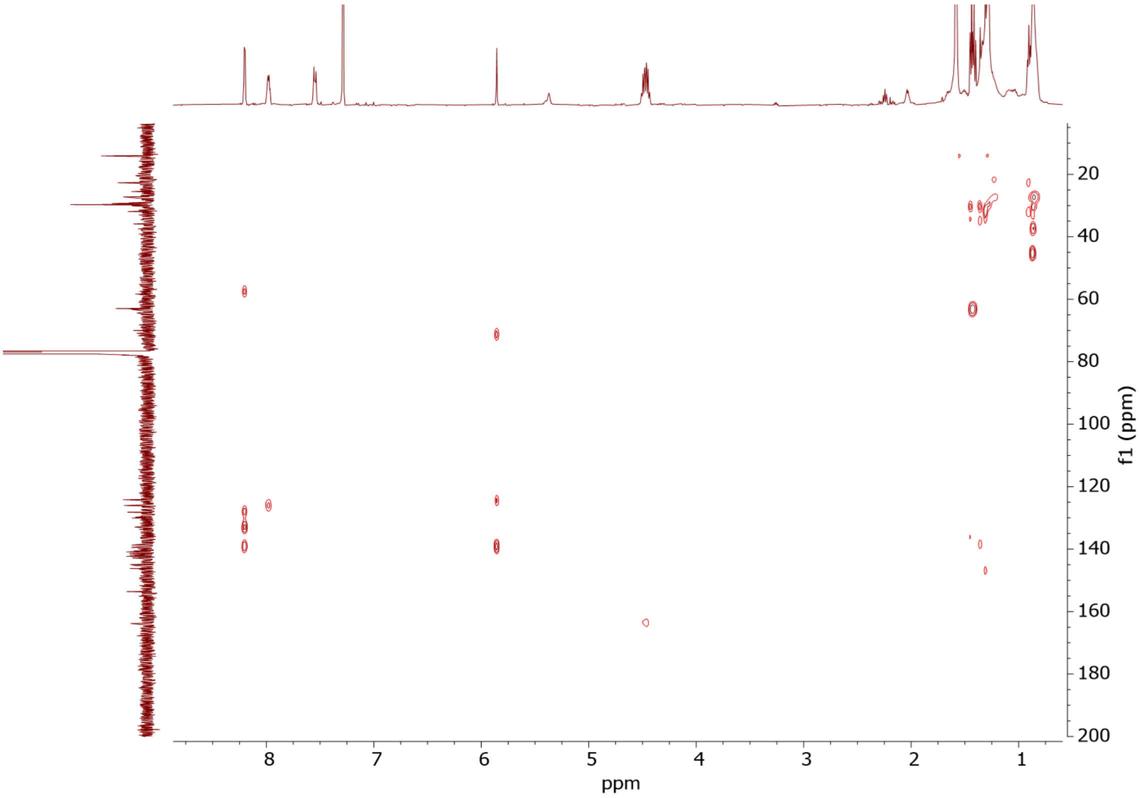

*Figure S.42. 2D HMBC spectrum of e-mono-Pn-trans-1-bis-diethylmalonate-$C_{60}$ (**7**). Experiment performed in $CDCl_3$ at 298K (600 MHz).*

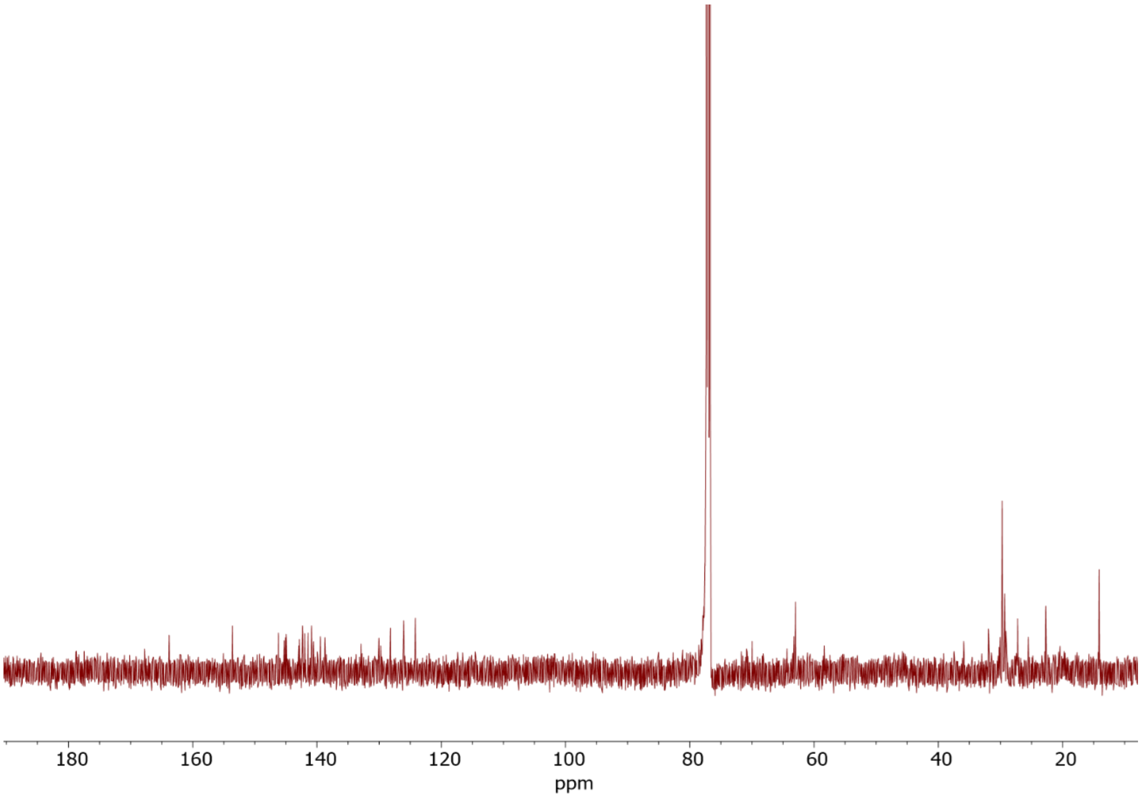

*Figure S.43. $^{13}$C-NMR spectrum of e-mono-Pn-trans-1-bis-diethylmalonate-$C_{60}$ (**7**). Experiment performed in $CDCl_3$ at 298K (125.75 MHz). Number of scans of 40960, a recycle delay of 1 s and the overall experimental time was 24h 26 min.*

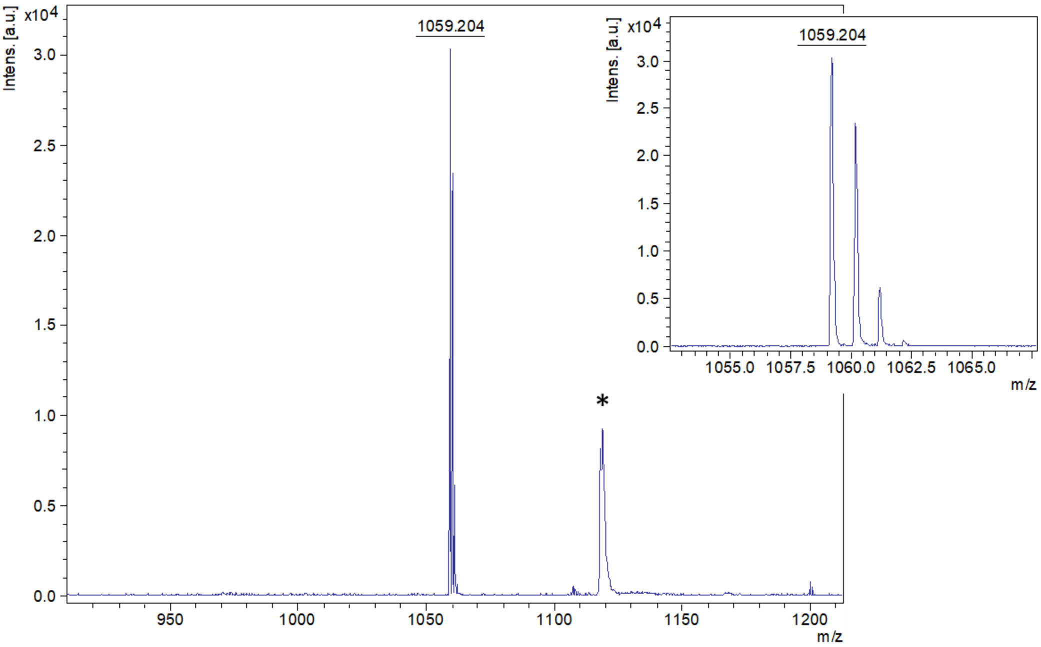

*Figure S. 44. MALDI-MS of e-mono-Pn-trans-1-bis-diethylmalonate-$C_{60}$ (**7**). The major peak (m/z=1059.204) corresponds to the trans-1-bis-diethylmalonate-$C_{60}$ analogue plus $Na^+$ due to the laser of the instrument which promotes the Retro-Diels-Alder of the pentacene addends. *The peak at m/z=1118.073 correspond to impurity which doesn't present a fullerene pattern.*

### *Characterization of bis-An-based hetero-hexakis-$C_{60}$ (**8**)*

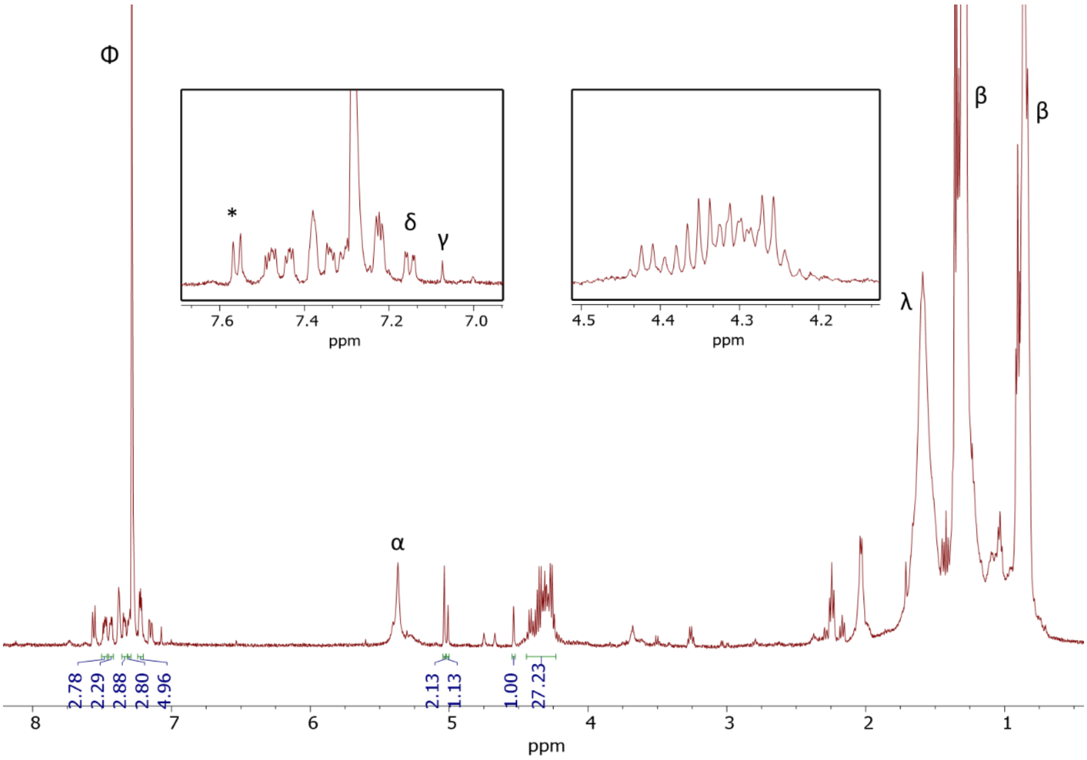

*Figure S.45. $^1$H-NMR spectrum of bis-An-based hetero-hexakis-$C_{60}$ (**8**). Experiment performed in $CDCl_3$ at 298K (500 MHz). φ: chloroform, γ: chloroform's satellites, δ: impurities of the purification solvent ($CS_2$), α: TLC-silica impurities, λ: $H_2O$, β: grease.*

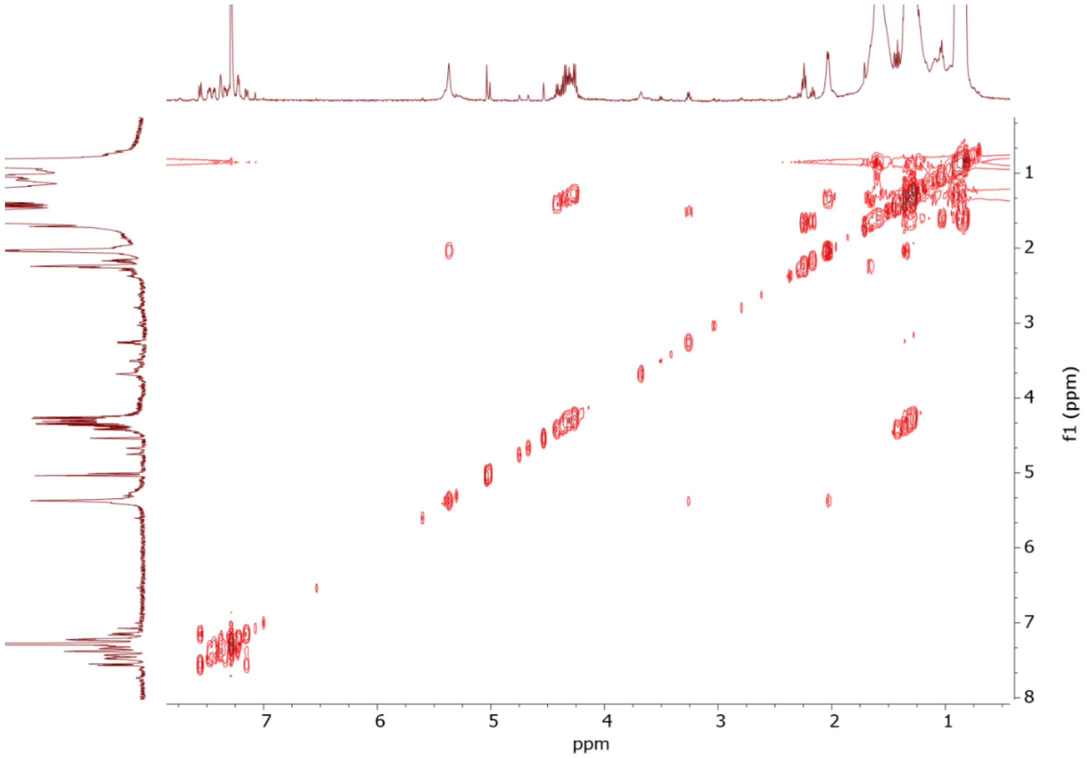

*Figure S.46. 2D COSY spectrum of bis-An-based hetero-hexakis-$C_{60}$ (**8**). Experiment performed in $CDCl_3$ at 298K (500 MHz).*

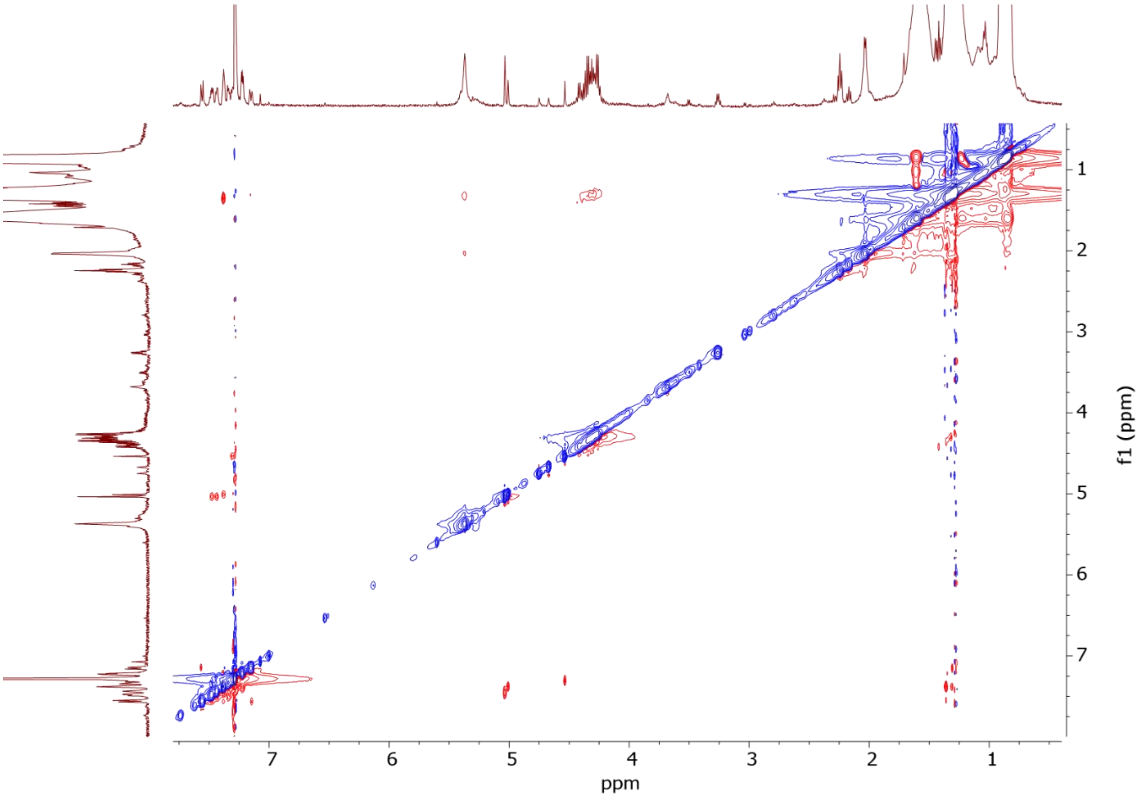

*Figure S.47. 2D ROESY spectrum of bis-An-based hetero-hexakis-$C_{60}$ (**8**). Experiment performed in $CDCl_3$ at 298K (500 MHz).*

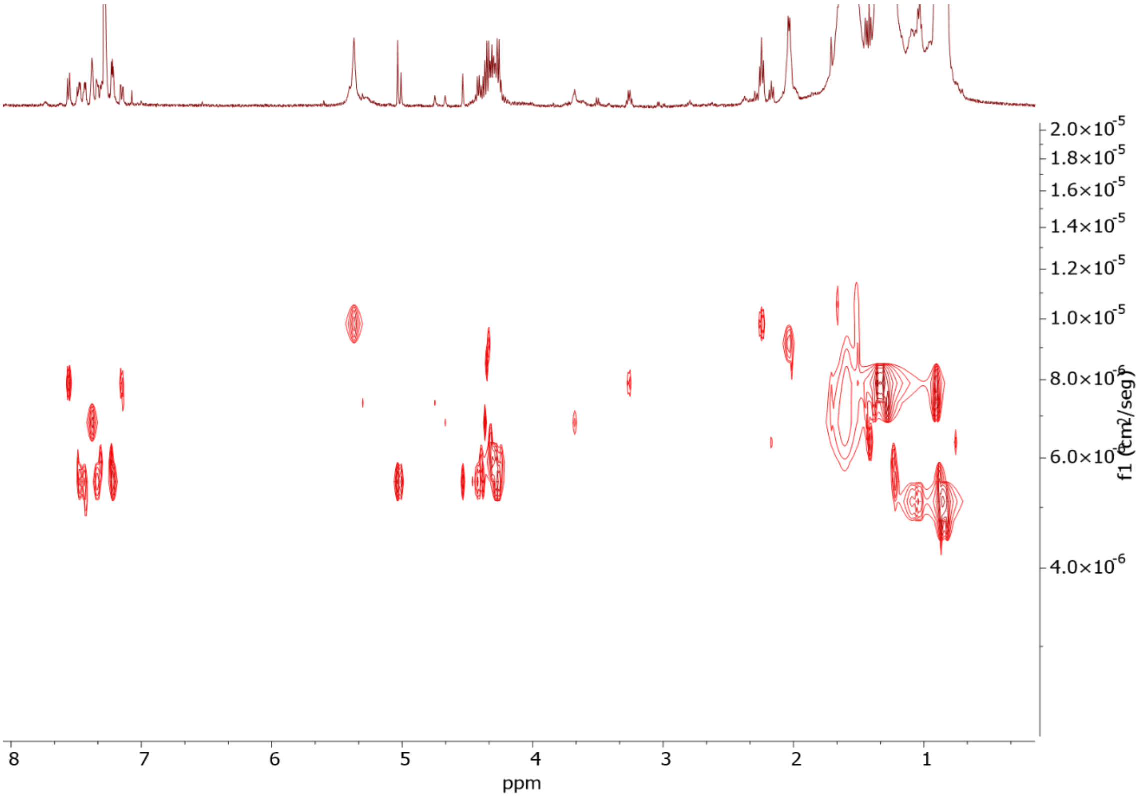

*Figure S.48. DOSY representation of bis-An-based hetero-hexakis-$C_{60}$ (**8**). Experiment performed in $CDCl_3$ at 298K (500 MHz).*

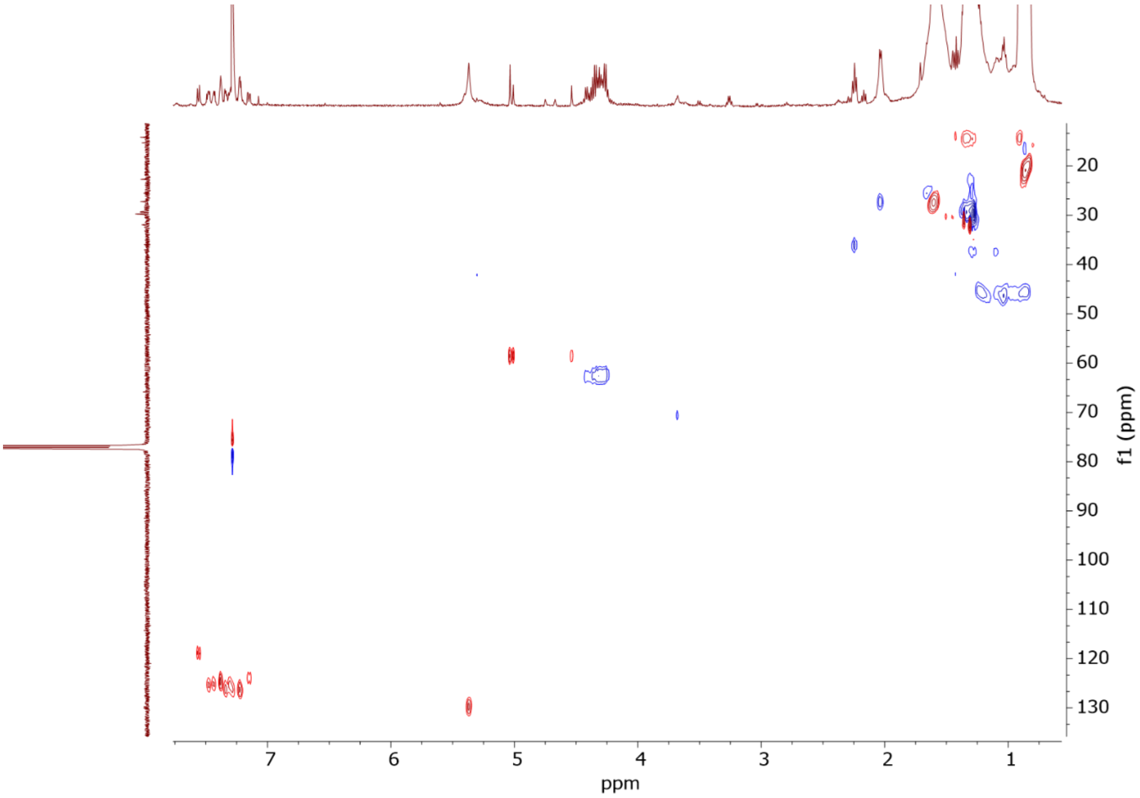

*Figure S.49. 2D multiplicity-edited HSQC spectrum of bis-An-based hetero-hexakis-$C_{60}$ (**8**). Experiment performed in $CDCl_3$ at 298K (500 MHz).*

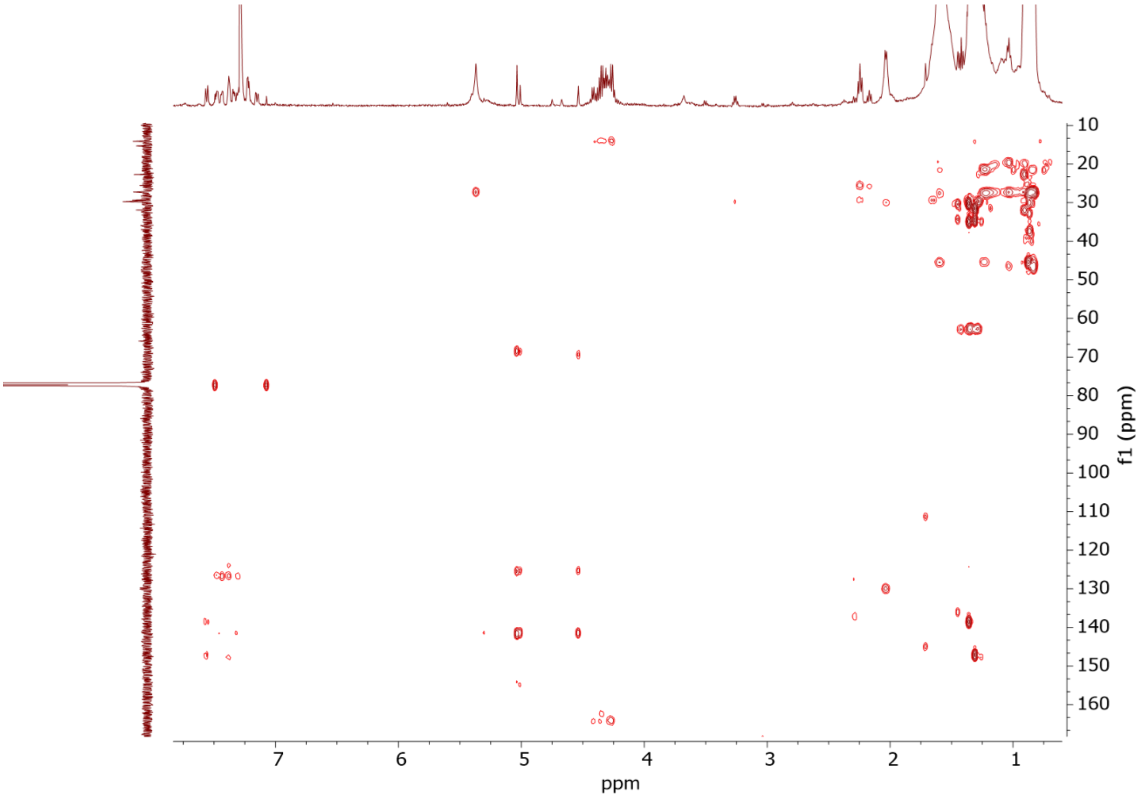

*Figure S.50. 2D HMBC spectrum of bis-An-based hetero-hexakis-$C_{60}$ (**8**). Experiment performed in $CDCl_3$ at 298K (500 MHz).*

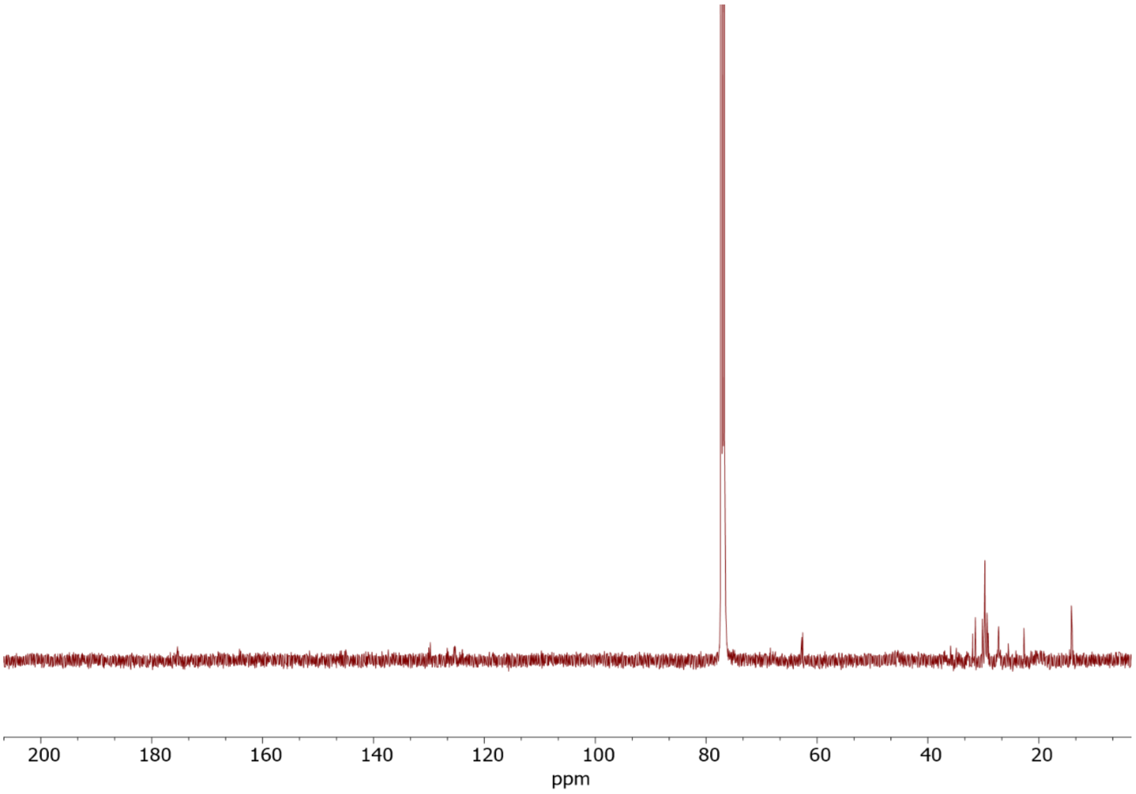

*Figure S.51. $^{13}$C-NMR spectrum of bis-An-based hetero-hexakis-C$_{60}$ (**8**). Experiment performed in CDCl$_3$ at 298K (125.75 MHz). Number of scans of 16384, a recycle delay of 3 s and the overall experimental time was 18h 52 min.*

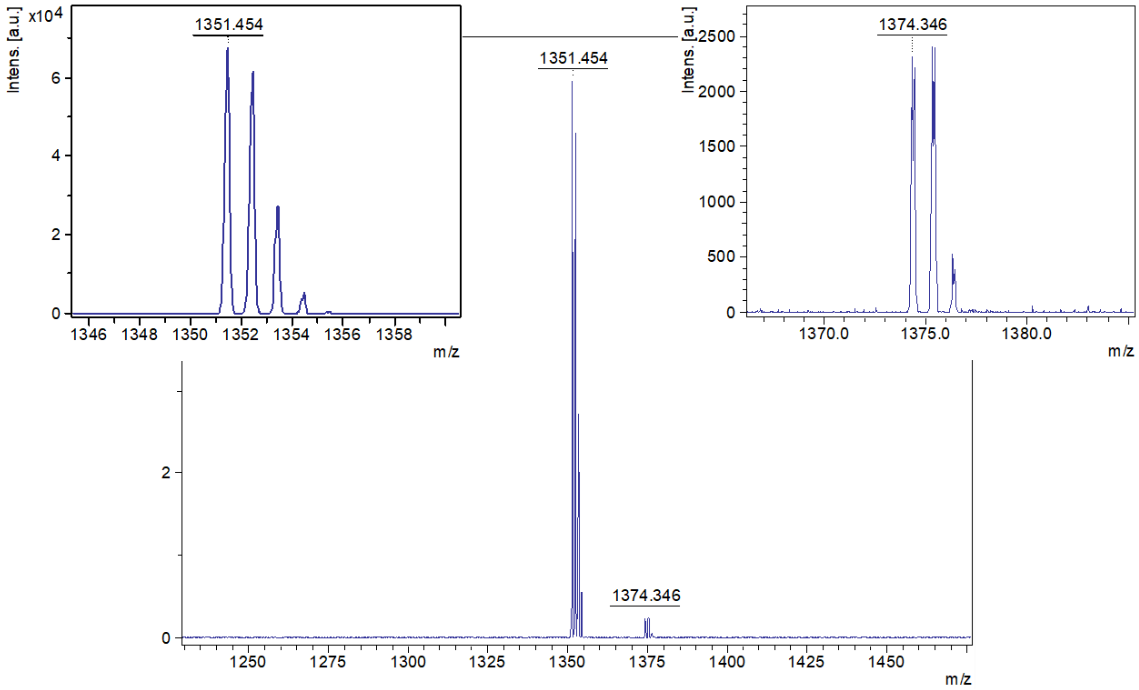

*Figure S.52. MALDI-MS of bis-An-based hetero-hexakis-C$_{60}$ (**8**). The main peak (m/z=1351.454) corresponds to the tetrakis-adduct analogue due to the laser of the instrument which promotes the Retro-Diels-Alder of the two anthracene addends. The little peak (m/z=1374.346) correspond to the same compound + Na$^+$.*

Characterization of trans-1-bis-Pn-e,e,e,e-tetrakis-diethylmalonate-$C_{60}$ (**9**)

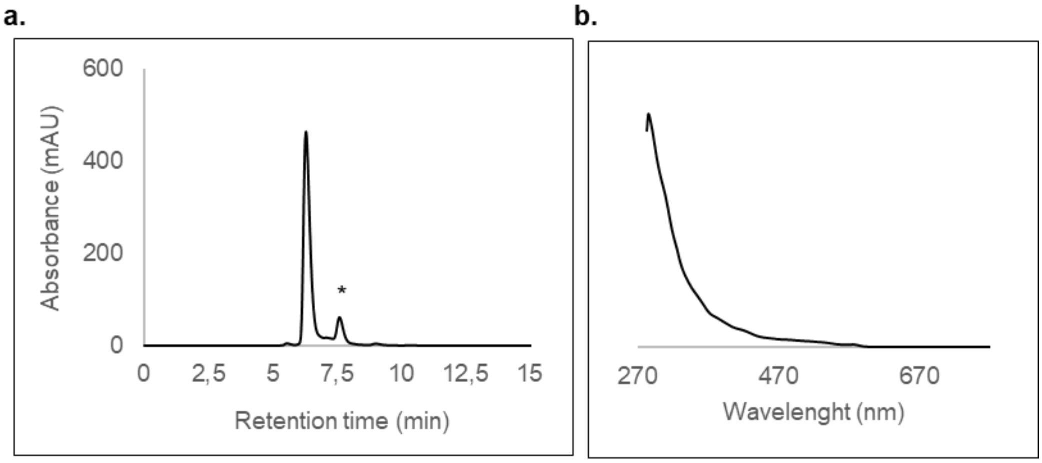

*Figure S.53. a) HPLC analysis of trans-1-bis-Pn-e,e,e,e-tetrakis-diethylmalonate-$C_{60}$ (**9**). Rt=6.288 min. *: unreacted trans-1-bis-pentacene-$C_{60}$, b) UV-vis spectrum of trans-1-bis-Pn-e,e,e,e-tetrakis-diethylmalonate-$C_{60}$.*

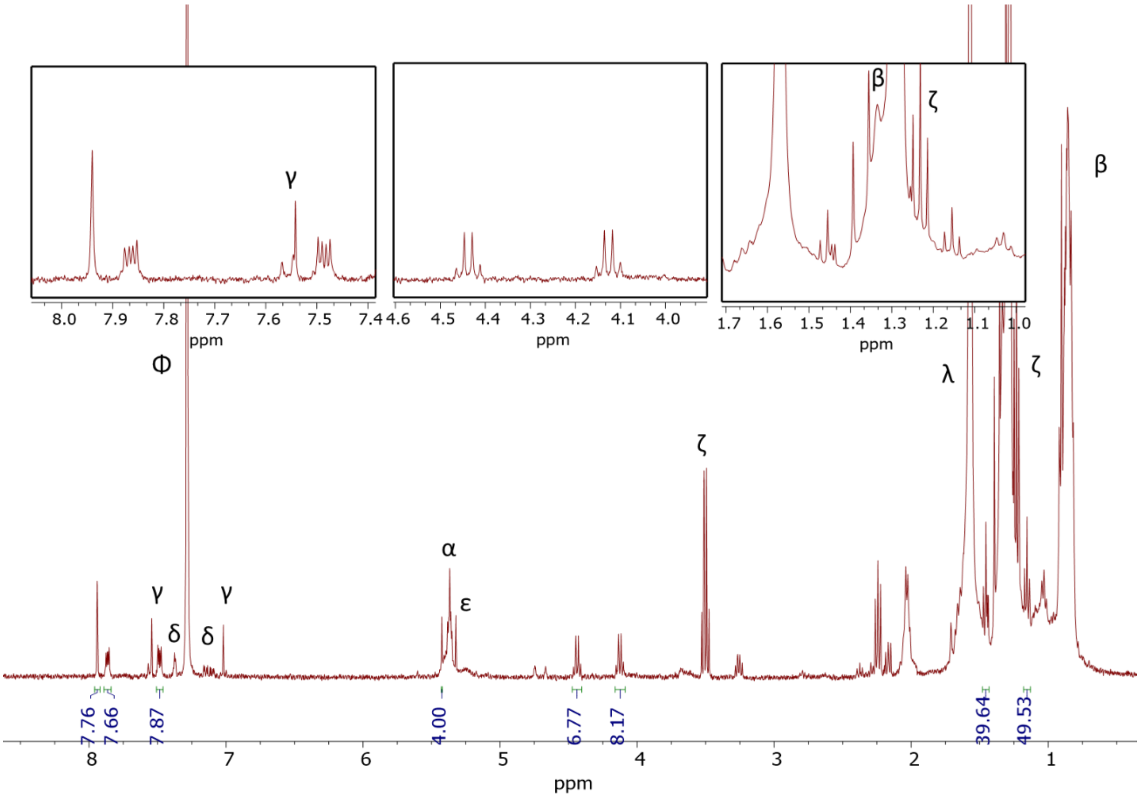

*Figure S.54. $^1$H-NMR spectrum of trans-1-bis-Pn-e,e,e,e-tetrakis-diethylmalonate-$C_{60}$ (**9**). Experiment performed in $CDCl_3$ at 298K (500 MHz). φ: chloroform, γ: chloroform's satellites, δ: impurities of the purification solvent ($CS_2$), α: TLC-silica impurities, ε: dichloromethane, ζ: diethyl ether, λ: $H_2O$, β: grease.*

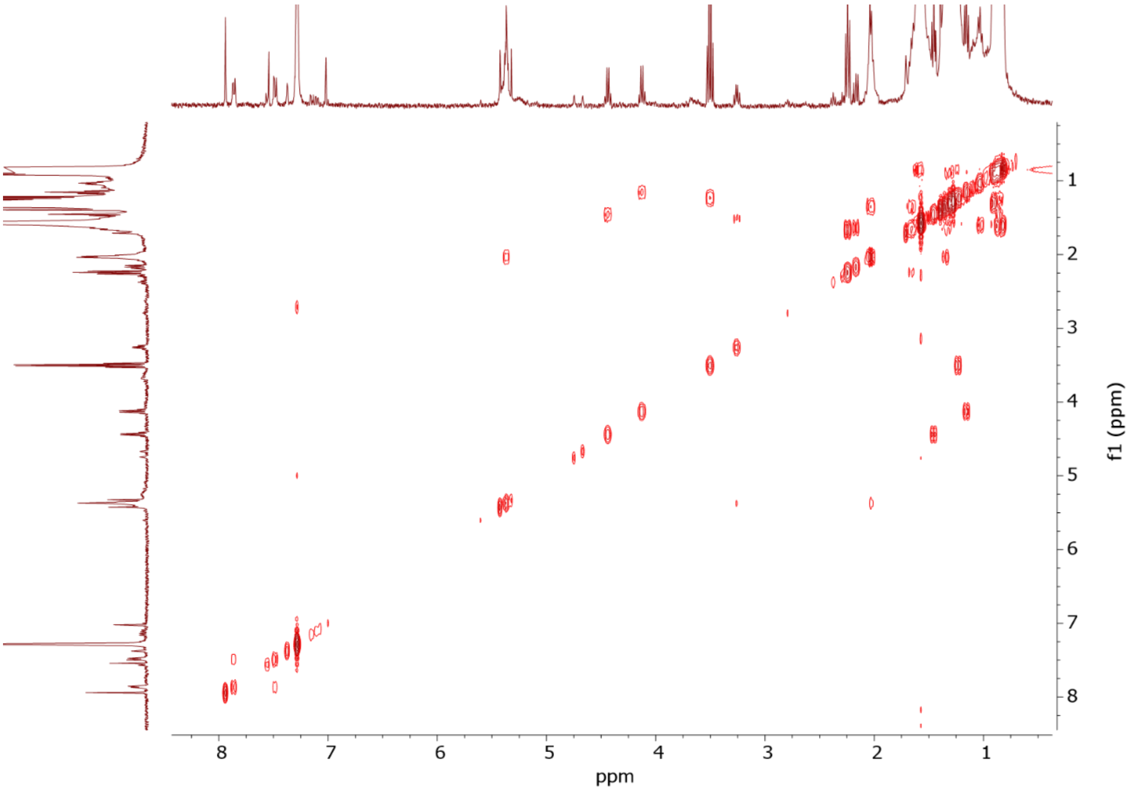

*Figure S.55. 2D COSY spectrum of trans-1-bis-Pn-e,e,e,e-tetrakis-diethylmalonate-$C_{60}$ (**9**). Experiment performed in $CDCl_3$ at 298K (500 MHz).*

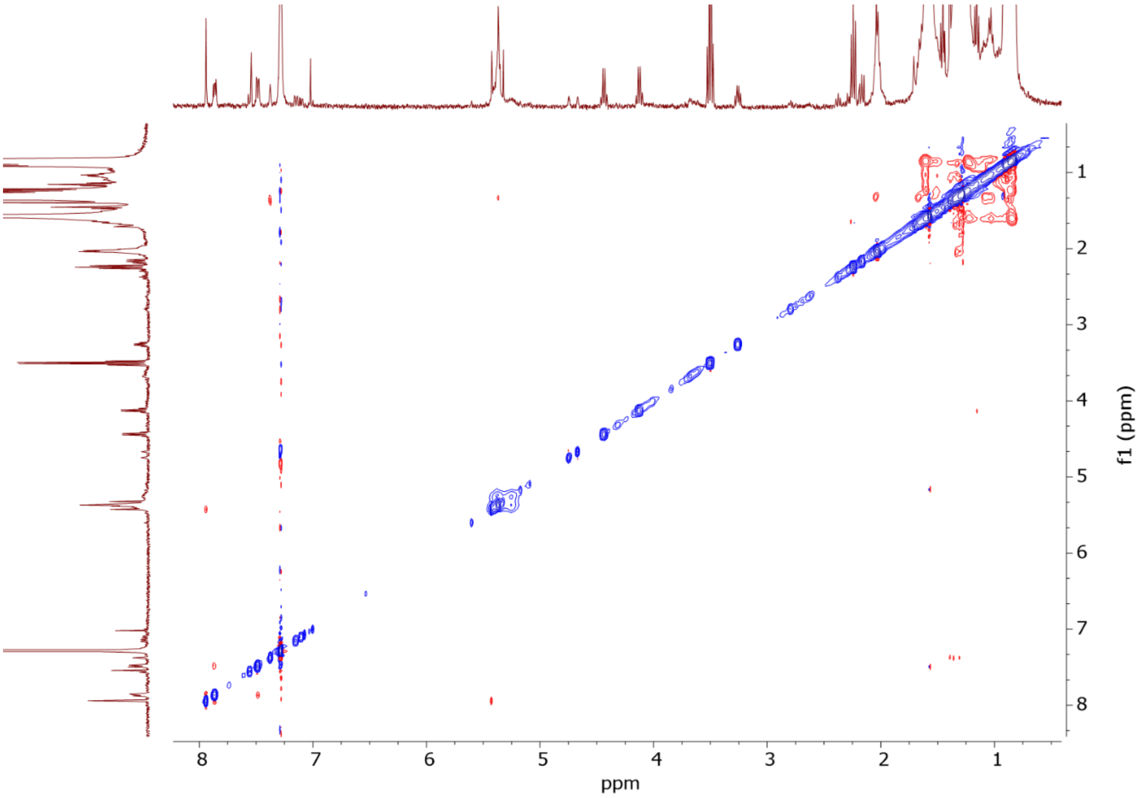

*Figure S.56. 2D ROESY spectrum of trans-1-bis-Pn-e,e,e,e-tetrakis-diethylmalonate-$C_{60}$ (**9**). Experiment performed in $CDCl_3$ at 298K (500 MHz).*

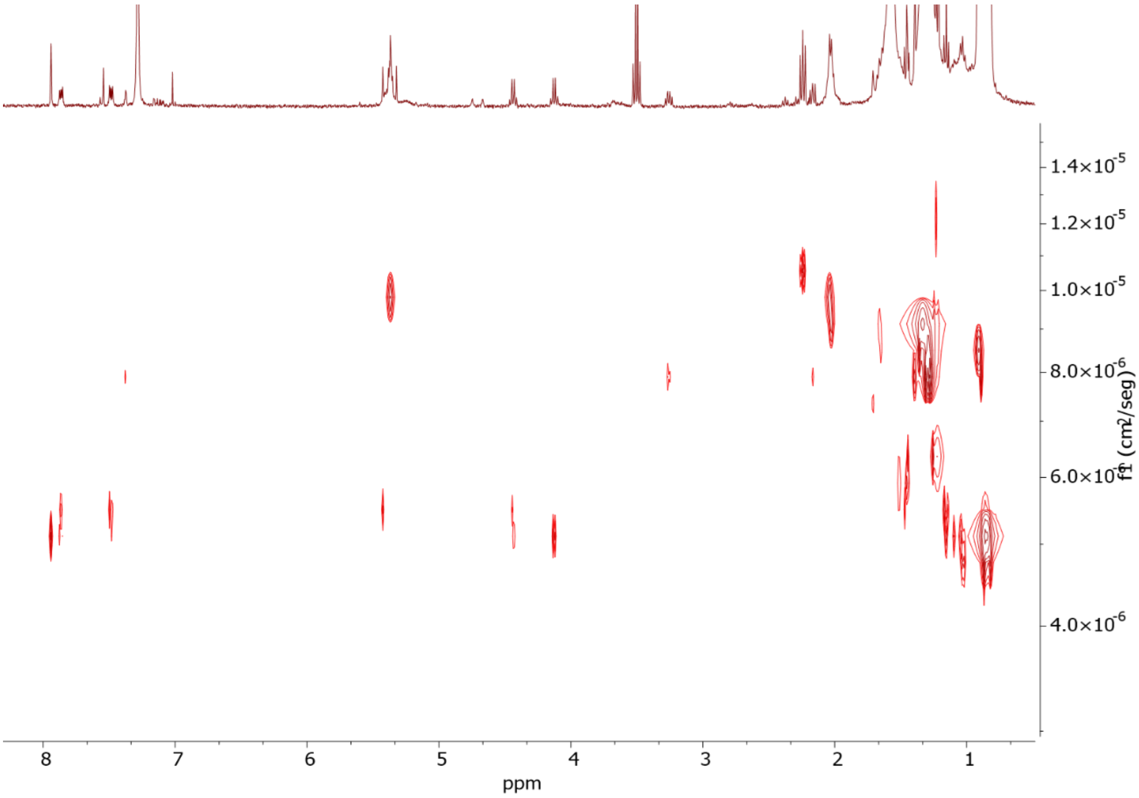

*Figure S.57. DOSY spectrum of trans-1-bis-Pn-e,e,e,e-tetrakis-diethylmalonate-$C_{60}$ (**9**). Experiment performed in $CDCl_3$ at 298K (500 MHz).*

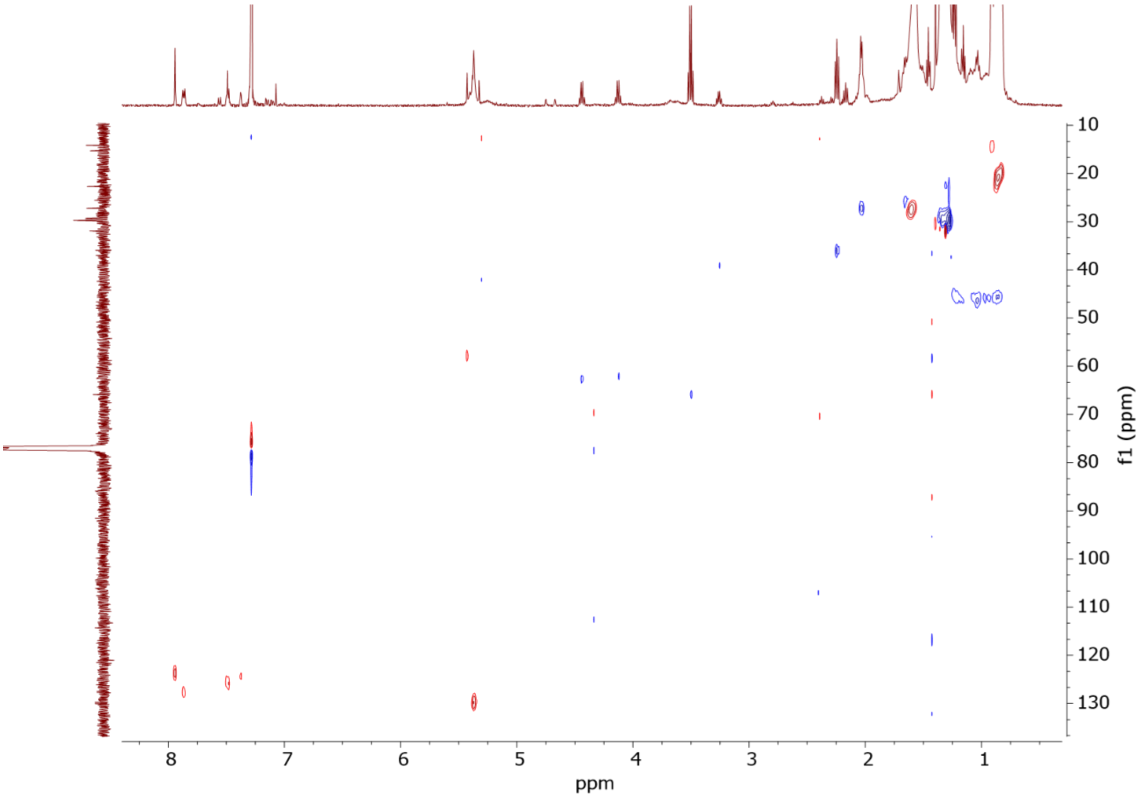

*Figure S.58. 2D multiplicity-edited HSQC spectrum of trans-1-bis-Pn-e,e,e,e-tetrakis-diethylmalonate-$C_{60}$ (**9**). Experiment performed in $CDCl_3$ at 298K (500 MHz).*

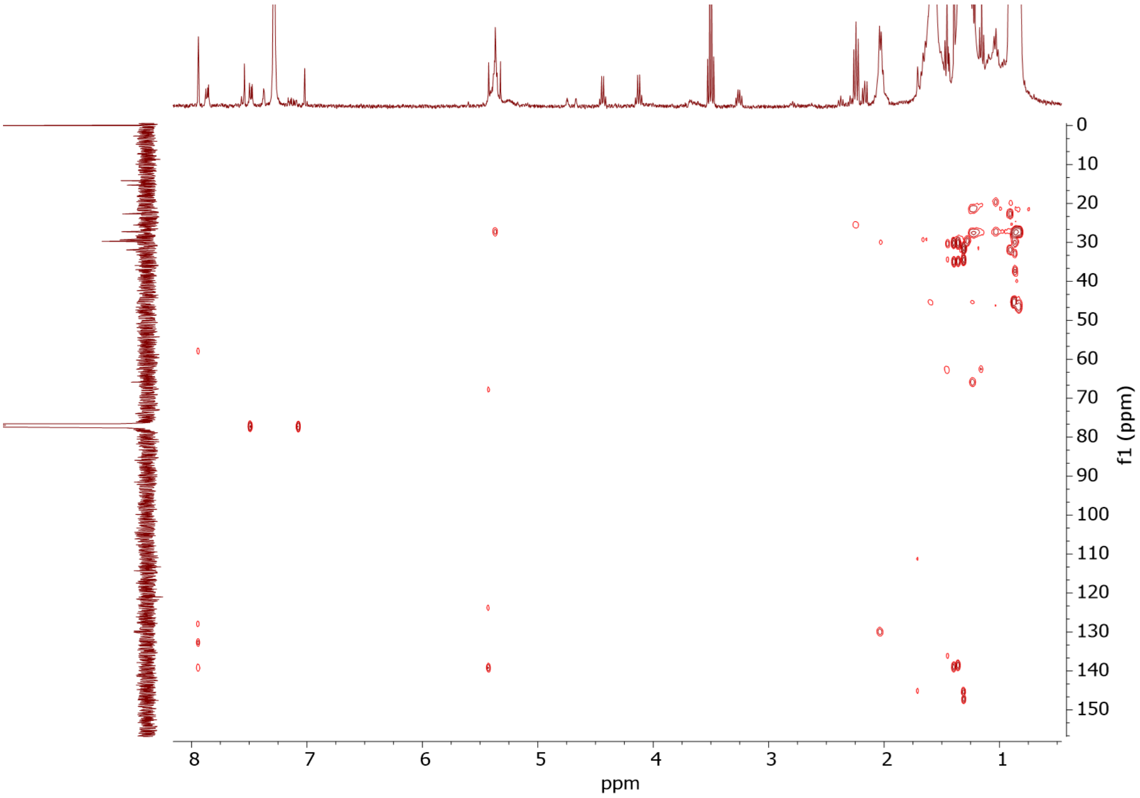

*Figure S.59. 2D HMBC spectrum of trans-1-bis-Pn-e,e,e,e-tetrakis-diethylmalonate-$C_{60}$ (**9**). Experiment performed in $CDCl_3$ at 298K (500 MHz).*

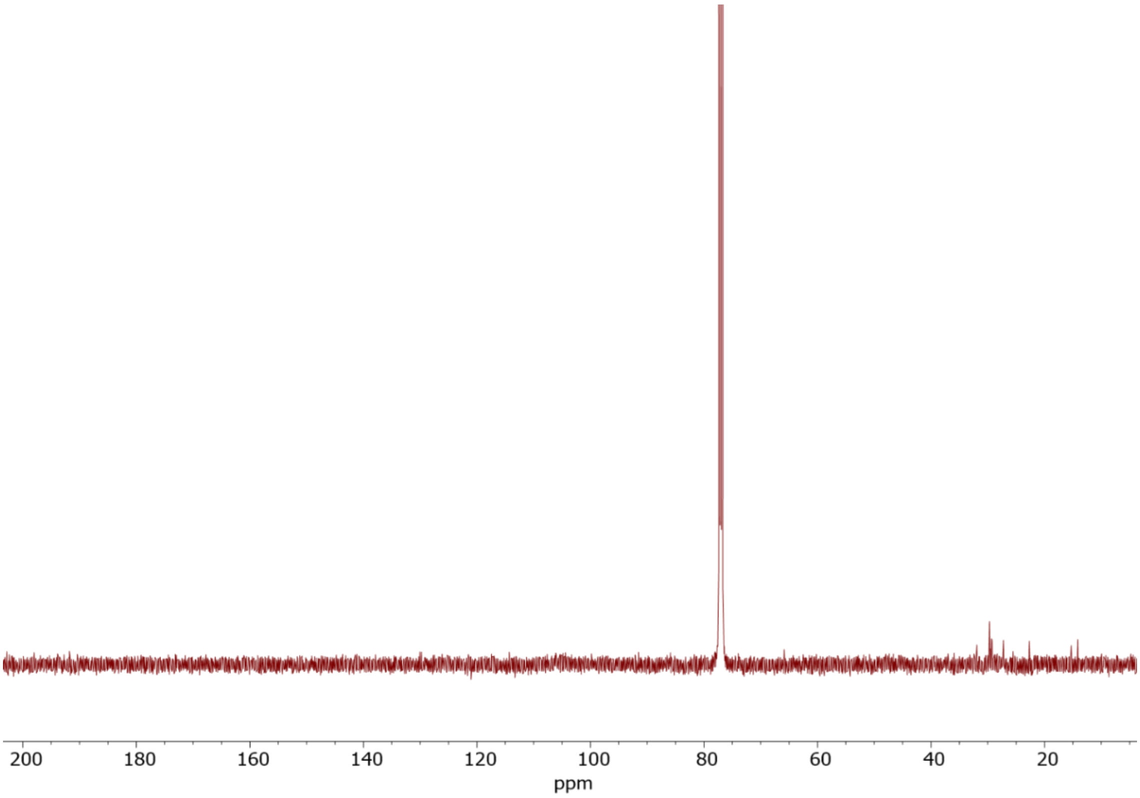

*Figure S.60. $^{13}$C-NMR spectrum of trans-1-bis-Pn-e,e,e,e-tetrakis-diethylmalonate-$C_{60}$ (**9**). Experiment performed in $CDCl_3$ at 298K (125.75 MHz). Number of scans of 12000, a recycle delay of 3 s and the overall experimental time was 13h 49 min.*

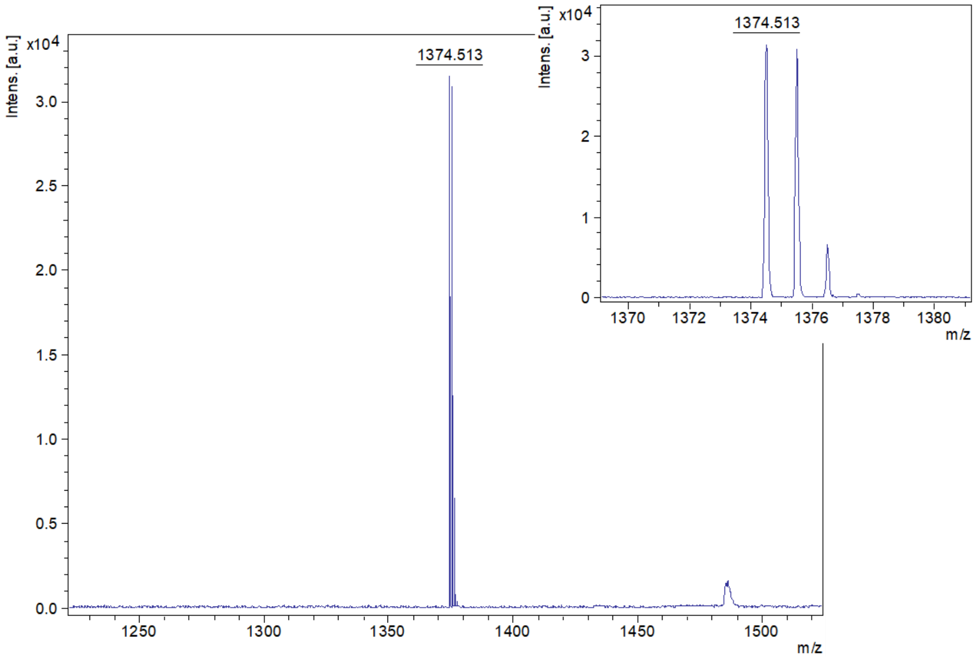

*Figure S.61. MALDI-MS of trans-1-bis-Pn-e,e,e,e-tetrakis-diethylmalonate-$C_{60}$ (**9**). The peak (m/z=1374.513) corresponds to the e,e,e,e-tetrakis-adduct analogue plus $Na^+$ due to the laser of the instrument which promotes the Retro-Diels-Alder of the two pentacene addends.*

| | Adduct | Molecular weight (g/mol) | Diffusion coefficient ($m^2/s$) | Hydrodynamic radius (m) |
|---|---|---|---|---|
| e,e-bis-anthracene-$C_{60}$ | **2** | 1077,128 | 7,24436E-10 | 5,55904E-10 |
| mono-pentacene-$C_{60}$ | **3** | 999,014 | 7,87046E-10 | 5,11681E-10 |
| trans-1-bis-pentacene-$C_{60}$ | **4** | 1277,368 | 6,35331E-10 | 6,33869E-10 |
| e,e-bis-anthracene-pentacene-$C_{60}$ | **5** | 1173,248 | 6,80769E-10 | 5,91561E-10 |
| e,e-bis-anthracene-mono-diethylmalonate-$C_{60}$ | **6** | 1235,297 | 6,60693E-10 | 6,09536E-10 |
| e-mono-pentacene-trans-1-bis-diethylmalonate-$C_{60}$ | **7** | 1315,352 | 6,09537E-10 | 6,60693E-10 |
| e,e-bis-anthracene-tetrakis-diethylmalonate-$C_{60}$ | **8** | 2026,142 | 5,74116E-10 | 7,01455E-10 |
| trans-1-bis-pentacene-e,e,e,e-tetrakis-diethylmalonate-$C_{60}$ | **9** | 2226,382 | 5,44503E-10 | 7,39605E-10 |

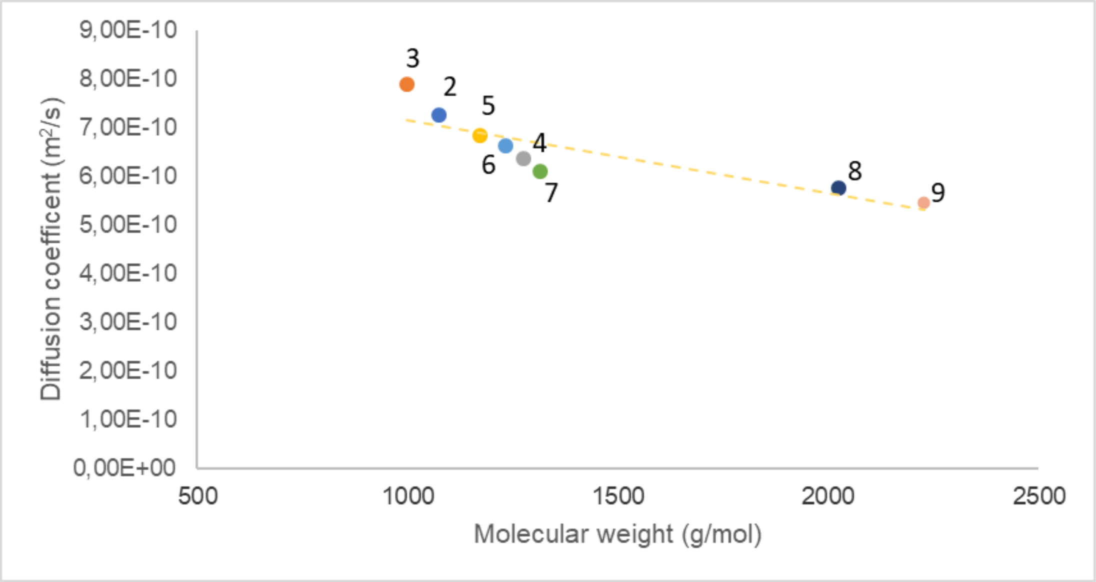

*Figure S.62. Diffusion coefficients of fullerene adducts **2**, **3**, **4**, **5**, **6**, **7**, **8** and **9**. At the top, graphical correlation between DOSY NMR diffusion coefficients and molecular weight of each adduct (500 MHz, 298 K, $CDCl_3$). At the bottom, experimental diffusion coefficients and hydrodynamic radius values calculated from Stokes-Einstein equation for each of the adducts.*

## *Annex IV.3.2 Analysis of molecular dynamic simulations*

### *MD simulations of mono-An-$C_{60}$⊂**1b**·$(Cl)_8$ host-guest system*

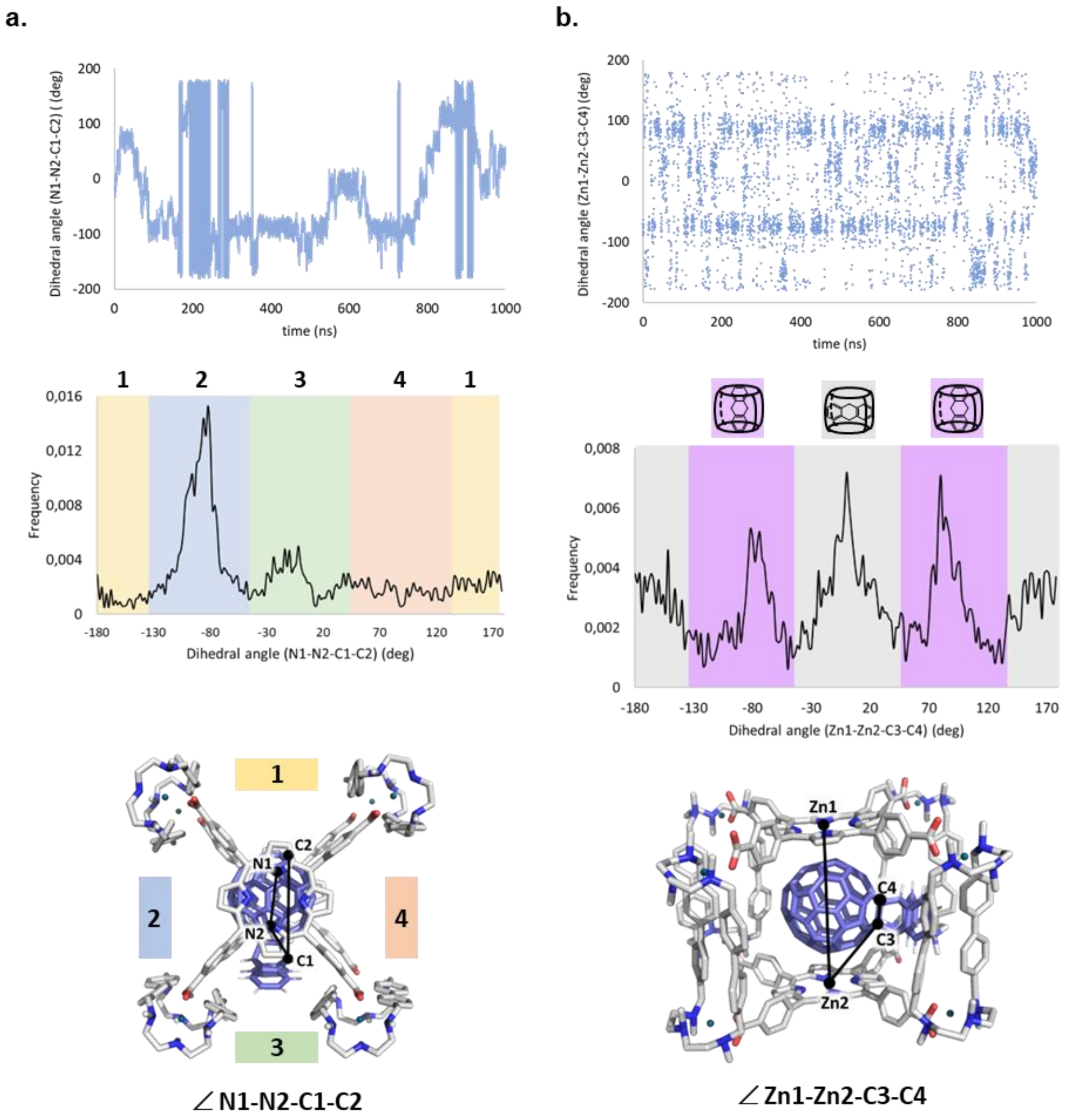

*Figure S.63. Conformational analysis of mono-An-$C_{60}$⊂**1b**·$(Cl)_8$ host-guest complex from 1000 ns MD trajectories in explicit $CH_3CN$. Replica 1. a) ∠N1-N2-C1-C2 dihedral angle measured along the MD trajectory (top plot). ∠N1-N2-C1-C2 angle describes the relative rotation of the encapsulated mono-An-$C_{60}$ with respect to the nanocapsule. Different nanocapsule windows (labelled as 1, 2, 3, and 4 in the figure on the bottom) are visited by the addend along the trajectory, which is described by the different values explored by dihedral angle during the simulation time. Histogram plot (frequency vs. angle value, center plot) describes that all windows are visited during the trajectory. b) ∠Zn1-Zn2-C3-C4 dihedral angle measured along the MD trajectory (top plot). ∠Zn1-Zn2-C3-C4 angle describes the relative orientation of the addend with respect to the porphyrins of the capsule. Ranges of ∠Zn1-Zn2-C3-C4 values highlighted in purple in the histogram plot (center plot) indicate that the addend is oriented perpendicularly with respect to the porphyrins, while range of values highlighted in grey indicate that it is oriented parallelly with respect to the porphyrins.*

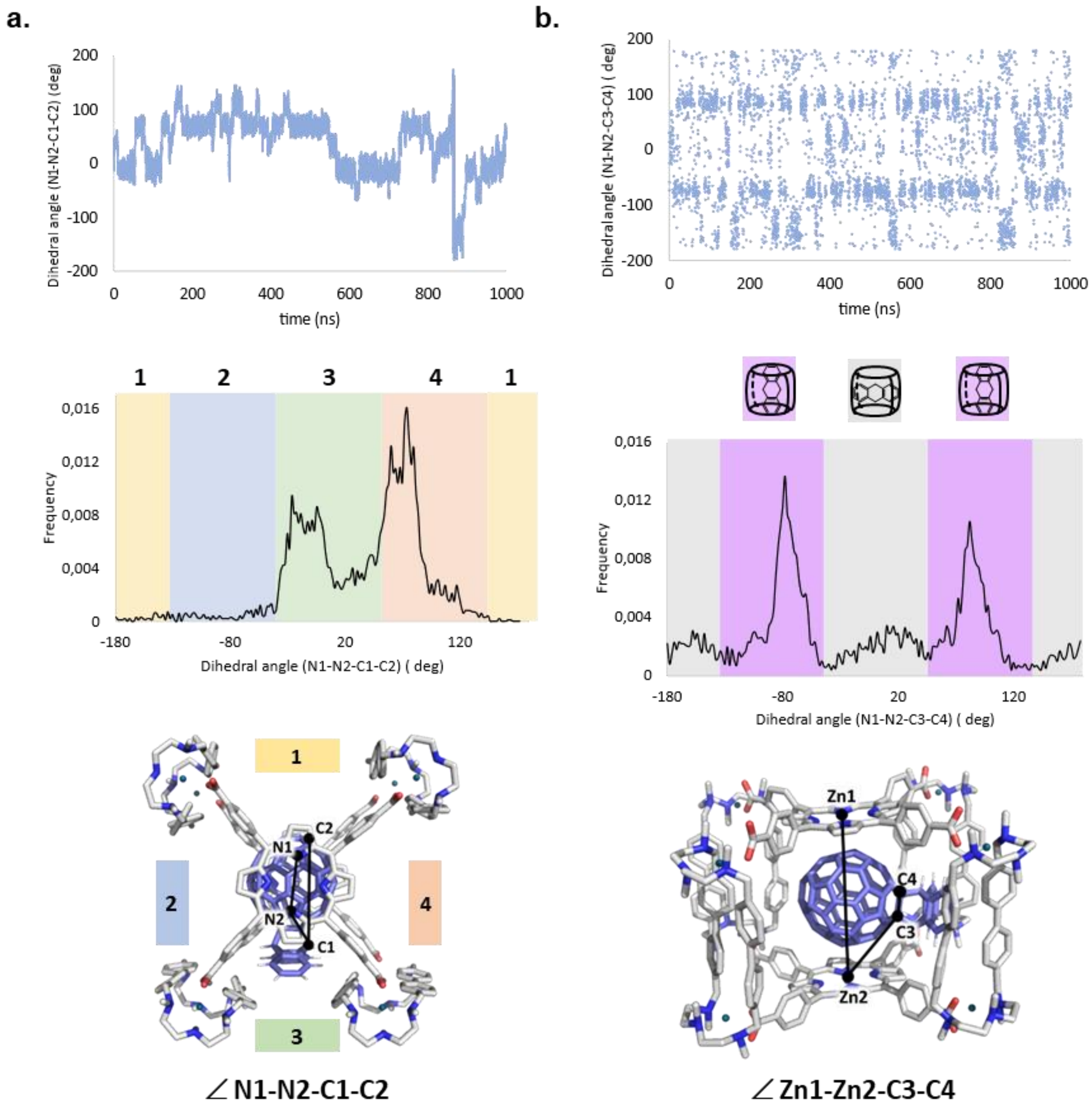

*Figure S.64. Conformational analysis of mono-An-C$_{60}$⊂**1b**·(Cl)$_8$ host-guest complex from 1000 ns MD trajectories in explicit CH$_3$CN. Replica 2. a) ∠N1-N2-C1-C2 dihedral angle measured along the MD trajectory (top plot). ∠N1-N2-C1-C2 angle describes the relative rotation of the encapsulated mono-An-C$_{60}$ with respect to the nanocapsule. Different nanocapsule windows (labelled as 1, 2, 3, and 4 in the figure on the bottom) are visited by the addend along the trajectory, which is described by the different values explored by dihedral angle during the simulation time. Histogram plot (frequency vs. angle value, center plot) describes that all windows are visited during the trajectory. b) ∠Zn1-Zn2-C3-C4 dihedral angle measured along the MD trajectory (top plot). ∠Zn1-Zn2-C3-C4 angle describes the relative orientation of the addend with respect to the porphyrins of the capsule. Ranges of ∠Zn1-Zn2-C3-C4 values highlighted in purple in the histogram plot (center plot) indicate that the addend is oriented perpendicularly with respect to the porphyrins, while range of values highlighted in grey indicate that it is oriented parallelly with respect to the porphyrins.*

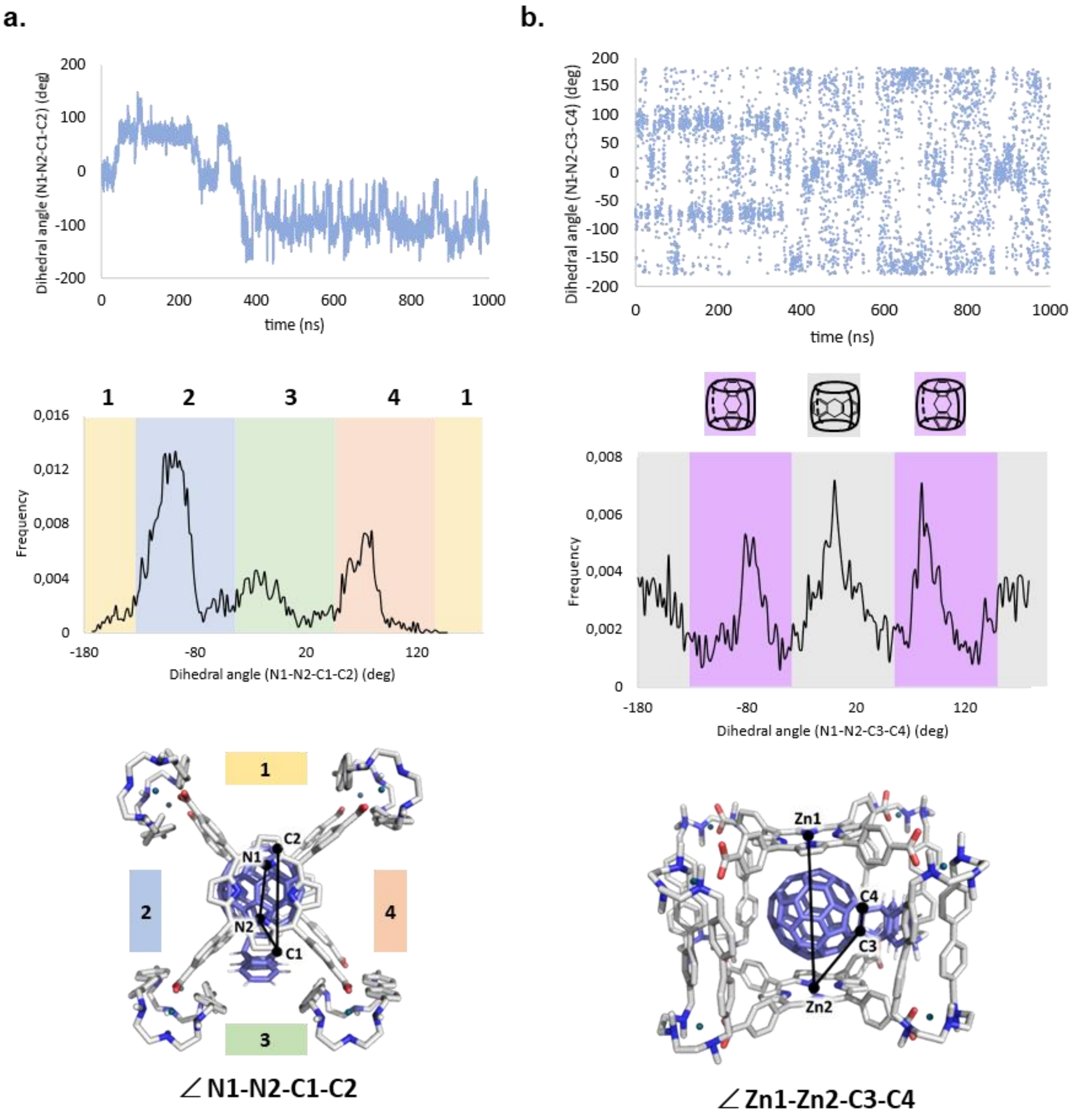

*Figure S.65. Conformational analysis of mono-An-$C_{60}$⊂**1b**·$(Cl)_8$ host-guest complex from 1000 ns MD trajectories in explicit $CH_3CN$. Replica 3. a) ∠N1-N2-C1-C2 dihedral angle measured along the MD trajectory (top plot). ∠N1-N2-C1-C2 angle describes the relative rotation of the encapsulated mono-An-$C_{60}$ with respect to the nanocapsule. Different nanocapsule windows (labelled as 1, 2, 3, and 4 in the figure on the bottom) are visited by the addend along the trajectory, which is described by the different values explored by dihedral angle during the simulation time. Histogram plot (frequency vs. angle value, center plot) describes that all windows are visited during the trajectory. b) ∠Zn1-Zn2-C3-C4 dihedral angle measured along the MD trajectory (top plot). ∠Zn1-Zn2-C3-C4 angle describes the relative orientation of the addend with respect to the porphyrins of the capsule. Ranges of ∠Zn1-Zn2-C3-C4 values highlighted in purple in the histogram plot (center plot) indicate that the addend is oriented perpendicularly with respect to the porphyrins, while range of values highlighted in grey indicate that it is oriented parallelly with respect to the porphyrins.*

## *MD simulations of e,e-bis-An-$C_{60}\subset$**1b**$\cdot(Cl)_8$ host-guest system*

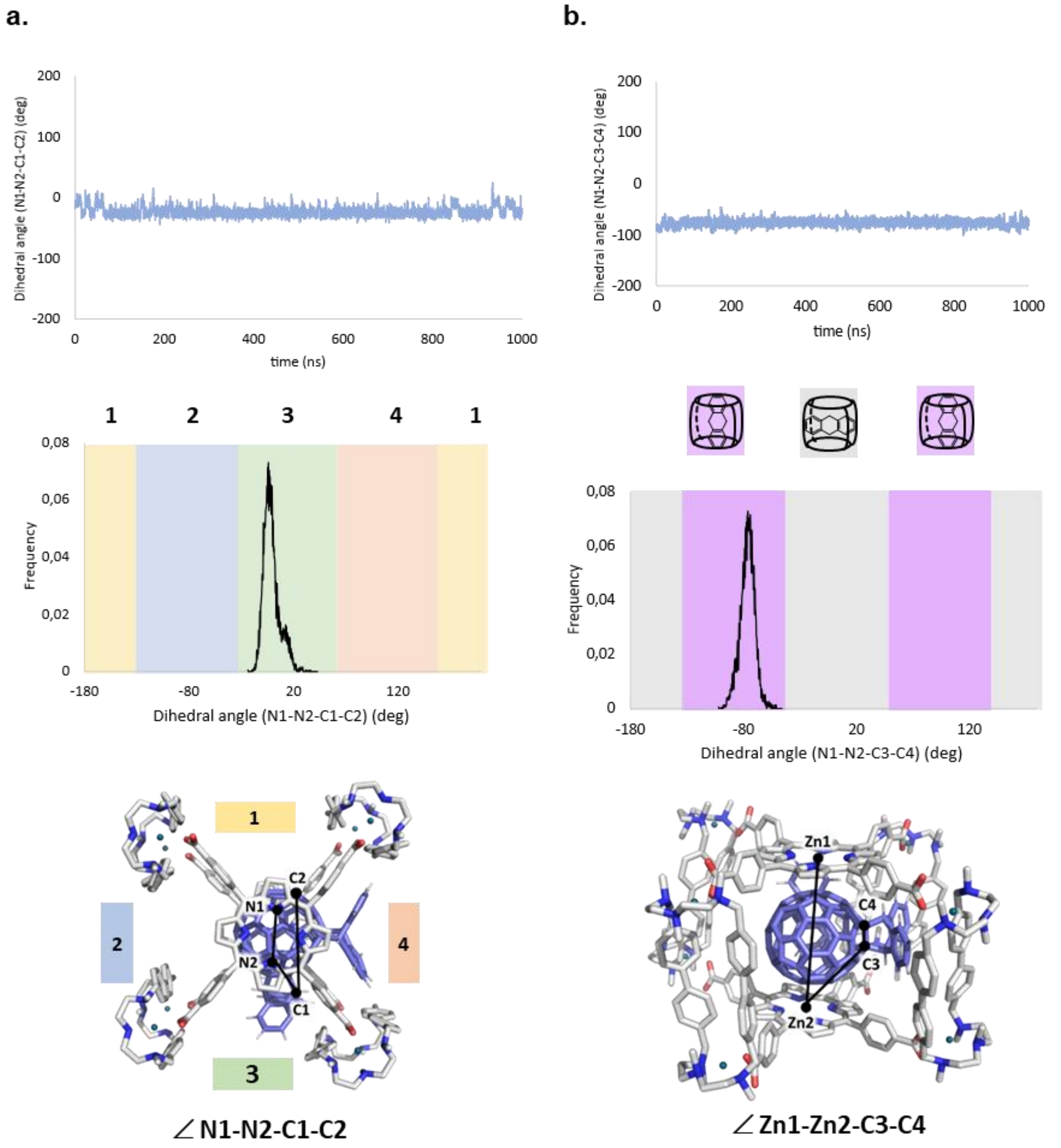

*Figure S.66. Conformational analysis of e,e-bis-An-$C_{60}\subset$**1b**$\cdot(Cl)_8$ host-guest complex from 1000 ns of MD trajectories in explicit $CH_3CN$. Replica 1. a) ∠N1-N2-C1-C2 dihedral angle measured along the MD trajectory (top plot). ∠N1-N2-C1-C2 angle describes the relative rotation of the encapsulated e,e-bis-An-$C_{60}$ with respect to the nanocapsule. Different nanocapsule windows (labelled as 1, 2, 3, and 4 in the figure on the bottom) are visited by the addend along the trajectory, which is described by the different values explored by dihedral angle during the simulation time. Histogram plot (frequency vs. angle value, center plot) describes that windows are visited during the trajectory. b) ∠Zn1-Zn2-C3-C4 dihedral angle measured along the MD trajectory (top plot). ∠Zn1-Zn2-C3-C4 angle describes the relative orientation of the addend with respect to the porphyrins of the capsule. Ranges of ∠Zn1-Zn2-C3-C4 values highlighted in purple in the histogram plot (center plot) indicate that the addend is oriented perpendicularly with respect to the porphyrins, while range of values highlighted in grey indicate that it is oriented parallelly with respect to the porphyrins.*

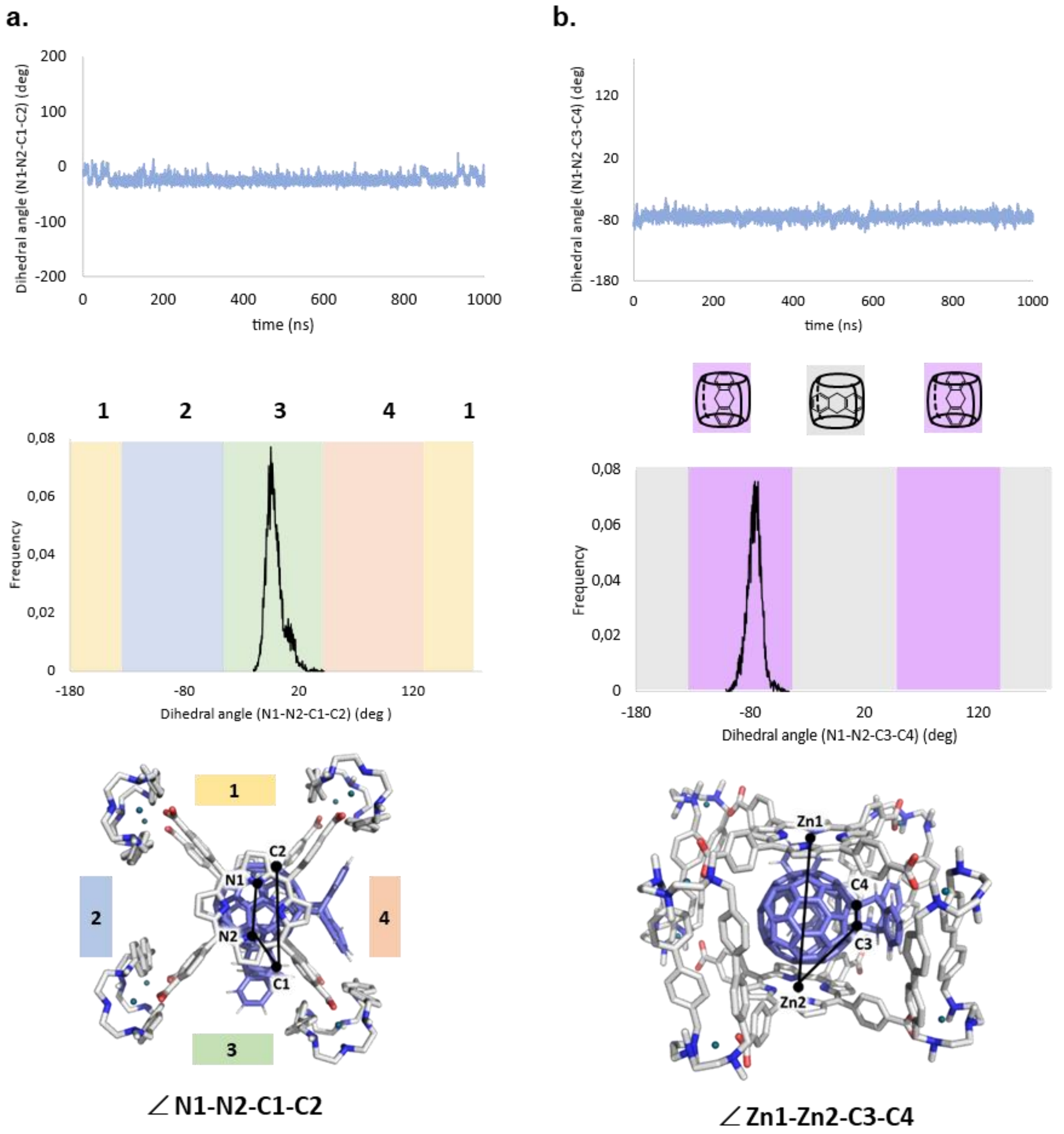

*Figure S.67. Conformational analysis of e,e-bis-An-$C_{60}\subset$**1b**$\cdot(Cl)_8$ host-guest complex from 1000 ns of MD trajectories in explicit $CH_3CN$. Replica 2. a) ∠N1-N2-C1-C2 dihedral angle measured along the MD trajectory (top plot). ∠N1-N2-C1-C2 angle describes the relative rotation of the encapsulated e,e-bis-An-$C_{60}$ with respect to the nanocapsule. Different nanocapsule windows (labelled as 1, 2, 3, and 4 in the figure on the bottom) are visited by the addend along the trajectory, which is described by the different values explored by dihedral angle during the simulation time. Histogram plot (frequency vs. angle value, center plot) describes that windows are visited during the trajectory. b) ∠Zn1-Zn2-C3-C4 dihedral angle measured along the MD trajectory (top plot). ∠Zn1-Zn2-C3-C4 angle describes the relative orientation of the addend with respect to the porphyrins of the capsule. Ranges of ∠Zn1-Zn2-C3-C4 values highlighted in purple in the histogram plot (center plot) indicate that the addend is oriented perpendicularly with respect to the porphyrins, while range of values highlighted in grey indicate that it is oriented parallelly with respect to the porphyrins.*

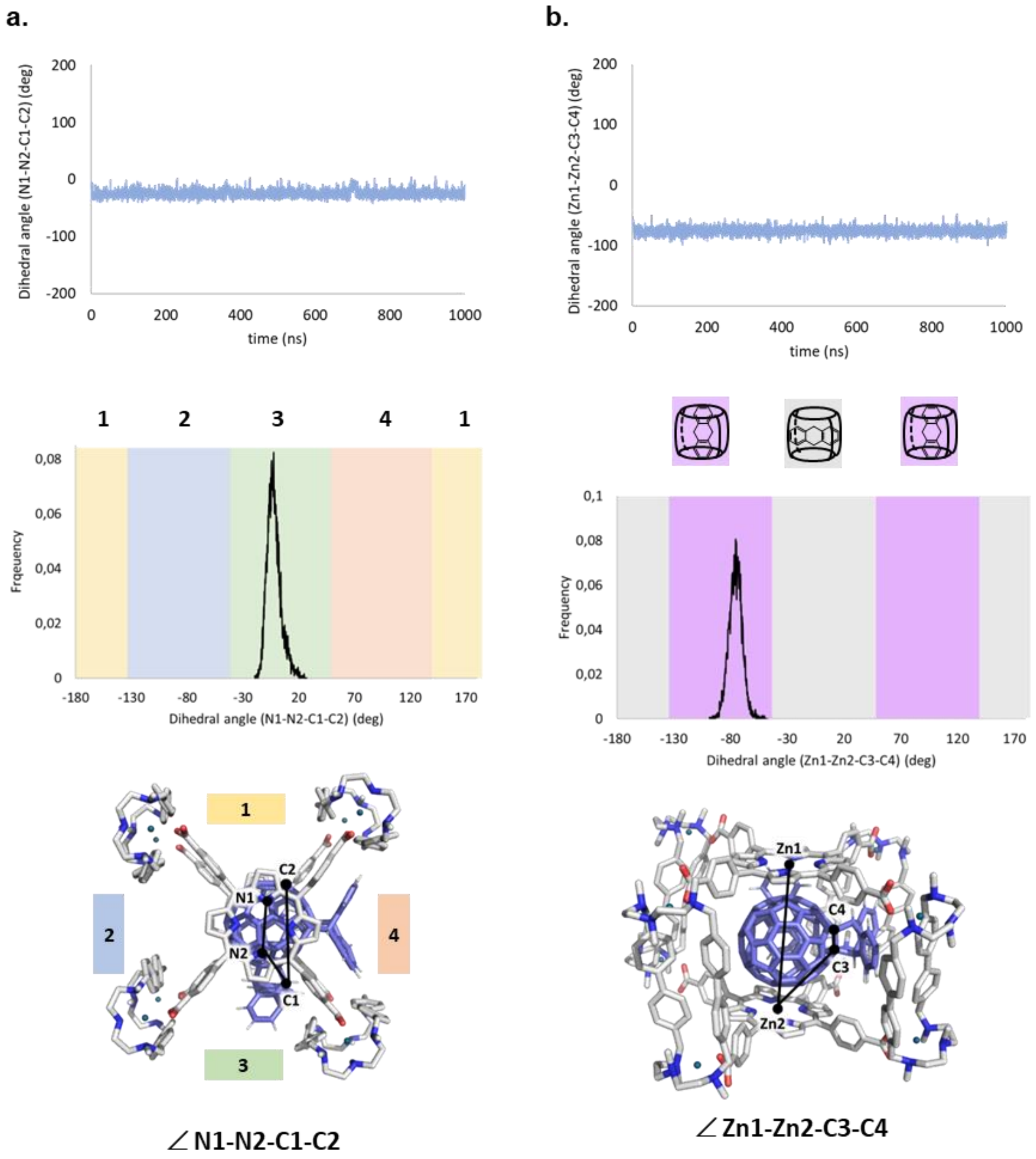

*Figure S.68. Conformational analysis of e,e-bis-An-C$_{60}$⊂**1b**·(Cl)$_8$ host-guest complex from 1000 ns of MD trajectories in explicit CH$_3$CN. Replica 3. a) ∠N1-N2-C1-C2 dihedral angle measured along the MD trajectory (top plot). ∠N1-N2-C1-C2 angle describes the relative rotation of the encapsulated e,e-bis-An-C$_{60}$ with respect to the nanocapsule. Different nanocapsule windows (labelled as 1, 2, 3, and 4 in the figure on the bottom) are visited by the addend along the trajectory, which is described by the different values explored by dihedral angle during the simulation time. Histogram plot (frequency vs. angle value, center plot) describes that windows are visited during the trajectory. b) ∠Zn1-Zn2-C3-C4 dihedral angle measured along the MD trajectory (top plot). ∠Zn1-Zn2-C3-C4 angle describes the relative orientation of the addend with respect to the porphyrins of the capsule. Ranges of ∠Zn1-Zn2-C3-C4 values highlighted in purple in the histogram plot (center plot) indicate that the addend is oriented perpendicularly with respect to the porphyrins, while range of values highlighted in grey indicate that it is oriented parallelly with respect to the porphyrins.*

## *MD simulations of mono-Pn-$C_{60}$⊂**1b**·$(Cl)_8$ host-guest system*

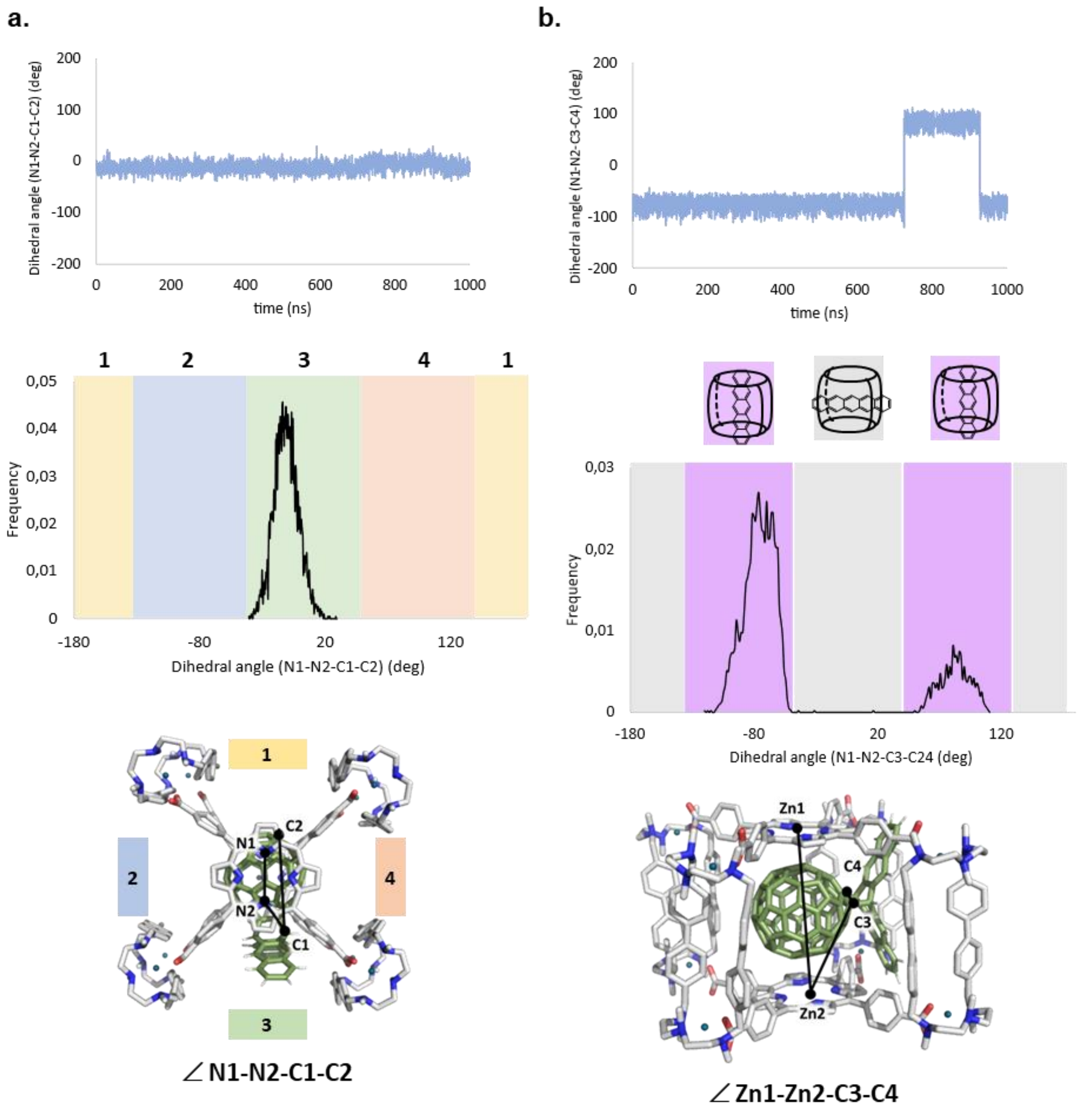

*Figure S.69. Conformational analysis of mono-Pn-$C_{60}$⊂**1b**·$(Cl)_8$ host-guest complex from 1000 ns of MD trajectories in explicit $CH_3CN$. Replica 1. a) ∠N1-N2-C1-C2 dihedral angle measured along the MD trajectory (top plot). ∠N1-N2-C1-C2 angle describes the relative rotation of the encapsulated mono-Pn-$C_{60}$ with respect to the nanocapsule. Different nanocapsule windows (labelled as 1, 2, 3, and 4 in the figure on the bottom) are visited by the addend along the trajectory, which is described by the different values explored by dihedral angle during the simulation time. Histogram plot (frequency vs. angle value, center plot) describes that windows are visited during the trajectory. b) ∠Zn1-Zn2-C3-C4 dihedral angle measured along the MD trajectory (top plot). ∠Zn1-Zn2-C3-C4 angle describes the relative orientation of the addend with respect to the porphyrins of the capsule. Ranges of ∠Zn1-Zn2-C3-C4 values highlighted in purple in the histogram plot (center plot) indicate that the addend is oriented perpendicularly with respect to the porphyrins, while range of values highlighted in grey indicate that it is oriented parallelly with respect to the porphyrins.*

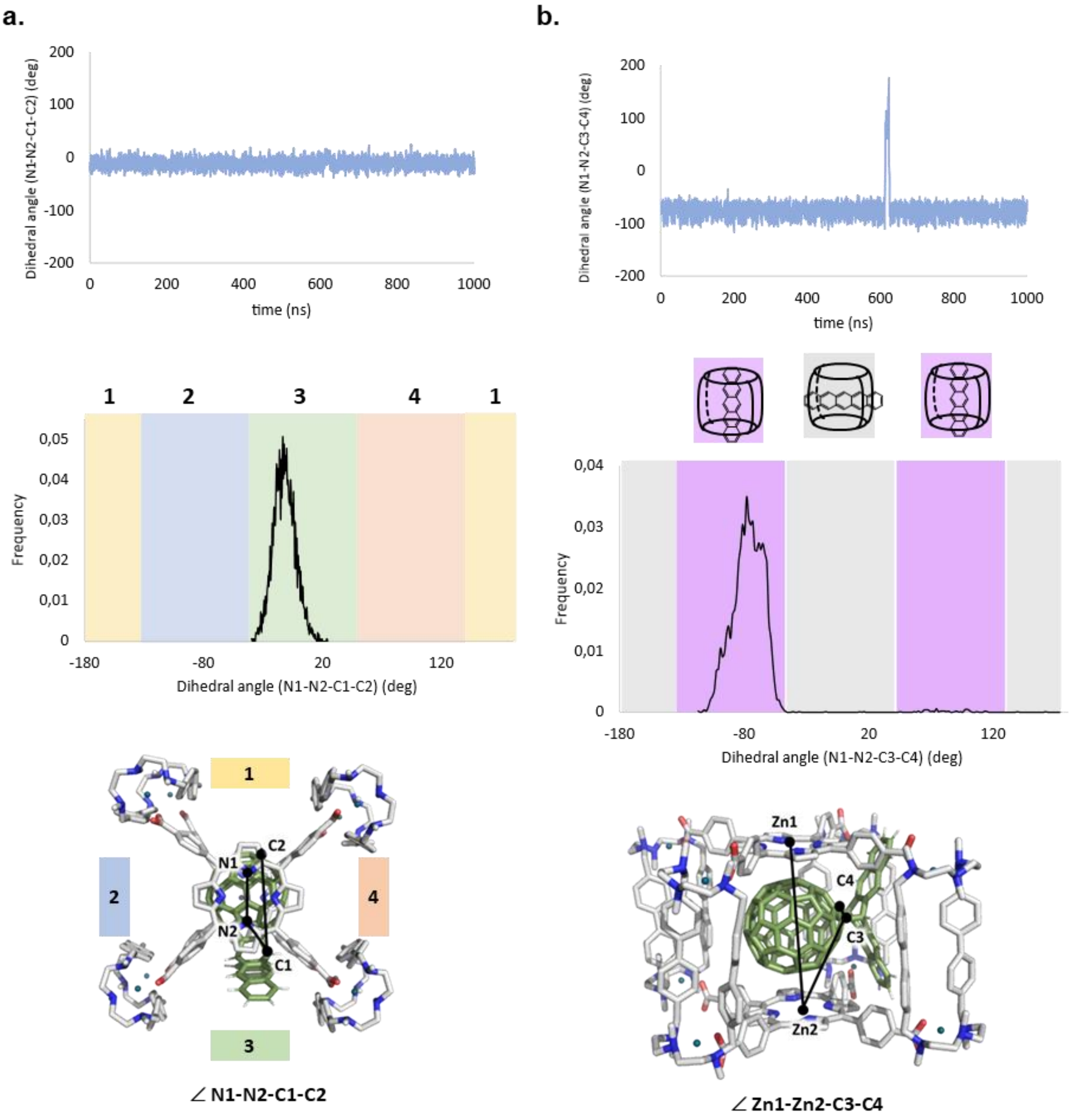

*Figure S.70. Conformational analysis of mono-Pn-$C_{60}$⊂**1b**·$(Cl)_8$ host-guest complex from 1000 ns of MD trajectories in explicit $CH_3CN$. Replica 2. a) ∠N1-N2-C1-C2 dihedral angle measured along the MD trajectory (top plot). ∠N1-N2-C1-C2 angle describes the relative rotation of the encapsulated mono-Pn-$C_{60}$ with respect to the nanocapsule. Different nanocapsule windows (labelled as 1, 2, 3, and 4 in the figure on the bottom) are visited by the addend along the trajectory, which is described by the different values explored by dihedral angle during the simulation time. Histogram plot (frequency vs. angle value, center plot) describes that windows are visited during the trajectory. b) ∠Zn1-Zn2-C3-C4 dihedral angle measured along the MD trajectory (top plot). ∠Zn1-Zn2-C3-C4 angle describes the relative orientation of the addend with respect to the porphyrins of the capsule. Ranges of ∠Zn1-Zn2-C3-C4 values highlighted in purple in the histogram plot (center plot) indicate that the addend is oriented perpendicularly with respect to the porphyrins, while range of values highlighted in grey indicate that it is oriented parallelly with respect to the porphyrins.*

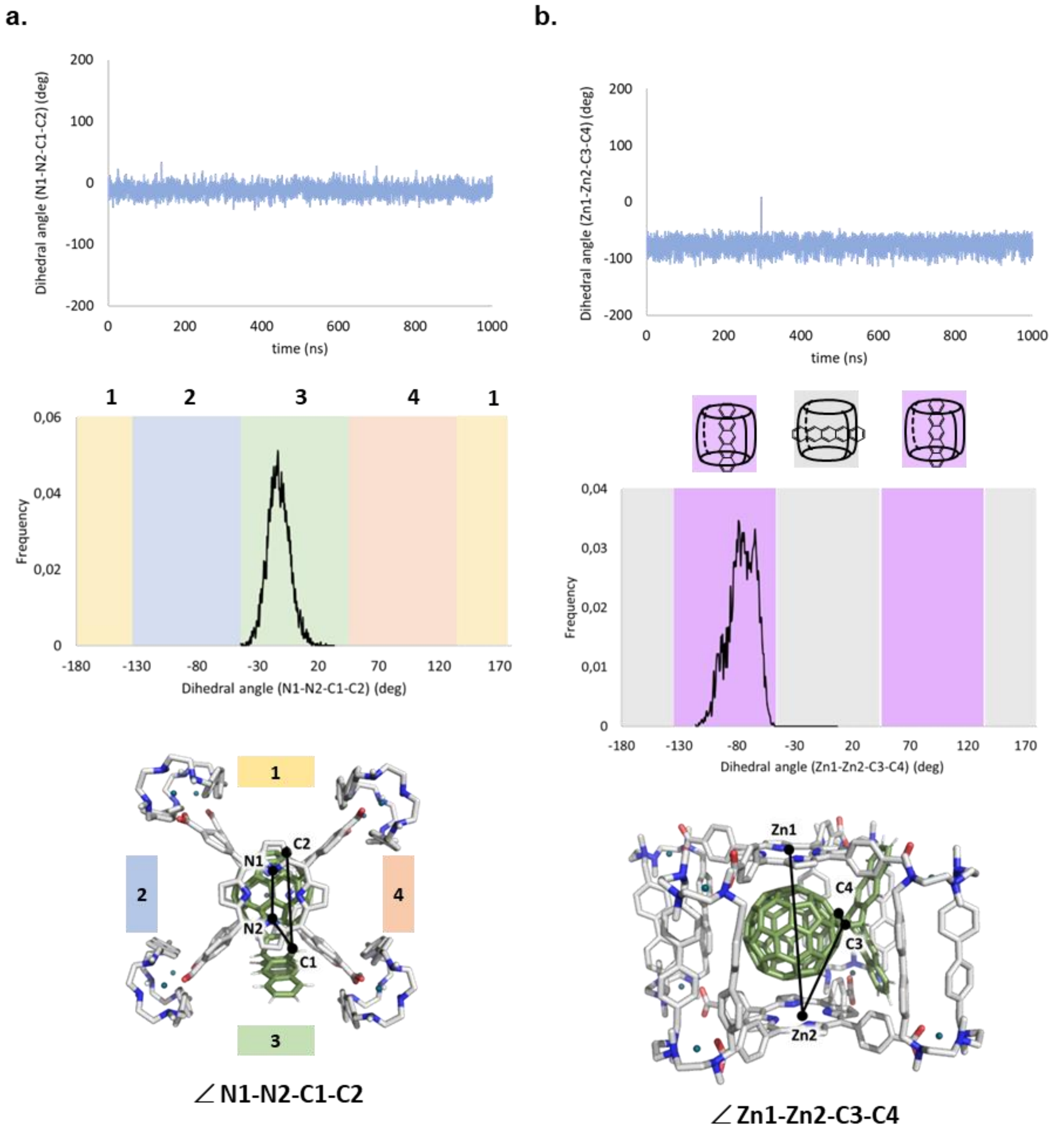

*Figure S.71. Conformational analysis of mono-Pn-$C_{60}$⊂**1b**·$(Cl)_8$ host-guest complex from 1000 ns of MD trajectories in explicit $CH_3CN$. Replica 3. a) ∠N1-N2-C1-C2 dihedral angle measured along the MD trajectory (top plot). ∠N1-N2-C1-C2 angle describes the relative rotation of the encapsulated mono-Pn-$C_{60}$ with respect to the nanocapsule. Different nanocapsule windows (labelled as 1, 2, 3, and 4 in the figure on the bottom) are visited by the addend along the trajectory, which is described by the different values explored by dihedral angle during the simulation time. Histogram plot (frequency vs. angle value, center plot) describes that windows are visited during the trajectory. b) ∠Zn1-Zn2-C3-C4 dihedral angle measured along the MD trajectory (top plot). ∠Zn1-Zn2-C3-C4 angle describes the relative orientation of the addend with respect to the porphyrins of the capsule. Ranges of ∠Zn1-Zn2-C3-C4 values highlighted in purple in the histogram plot (center plot) indicate that the addend is oriented perpendicularly with respect to the porphyrins, while range of values highlighted in grey indicate that it is oriented parallelly with respect to the porphyrins.*

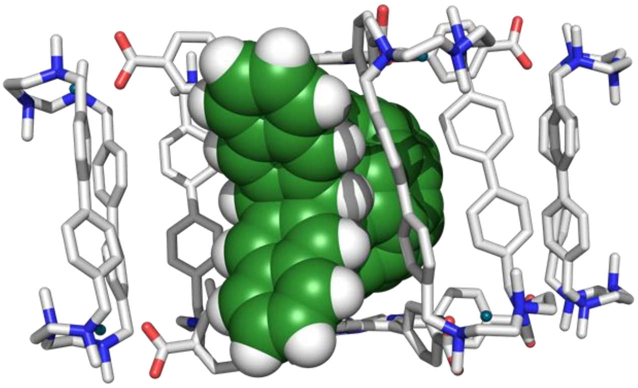

*Figure S.72. Selected snapshot from mono-Pn-$C_{60}\subset$**1b**$\cdot(Cl)_8$ MD simulation, showing that pentacene moiety stands out of the nanocapsule.*

## *MD simulations of trans-1-bis-Pn-$C_{60}\subset$**1b**$\cdot(Cl)_8$ host-guest system*

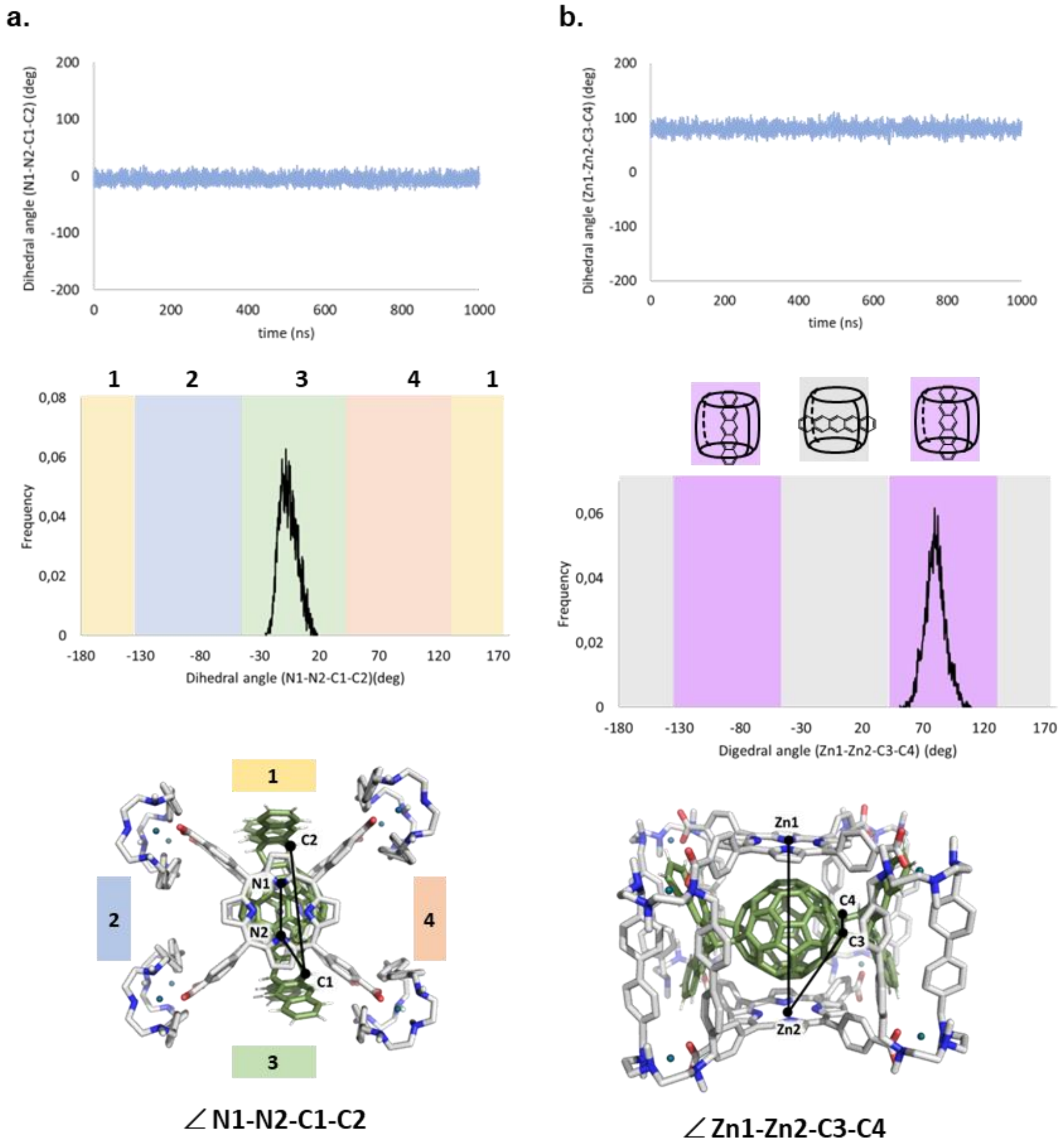

*Figure S.73. Conformational analysis of trans-1-bis-Pn-$C_{60}\subset$**1b**$\cdot(Cl)_8$ host-guest complex from 1000 ns of MD trajectories in explicit $CH_3CN$. Replica 1. a) ∠N1-N2-C1-C2 dihedral angle measured along the MD trajectory (top plot). ∠N1-N2-C1-C2 angle describes the relative rotation of the encapsulated trans-1-bis-Pn-$C_{60}$ with respect to the nanocapsule. Different nanocapsule windows (labelled as 1, 2, 3, and 4 in the figure on the bottom) are visited by the addend along the trajectory, which is described by the different values explored by dihedral angle during the simulation time. Histogram plot (frequency vs. angle value, center plot) describes that windows are visited during the trajectory. b) ∠Zn1-Zn2-C3-C4 dihedral angle measured along the MD trajectory (top plot). ∠Zn1-Zn2-C3-C4 angle describes the relative orientation of the addend with respect to the porphyrins of the capsule. Ranges of ∠Zn1-Zn2-C3-C4 values highlighted in purple in the histogram plot (center plot) indicate that the addend is oriented perpendicularly with respect to the porphyrins, while range of values highlighted in grey indicate that it is oriented parallelly with respect to the porphyrins.*

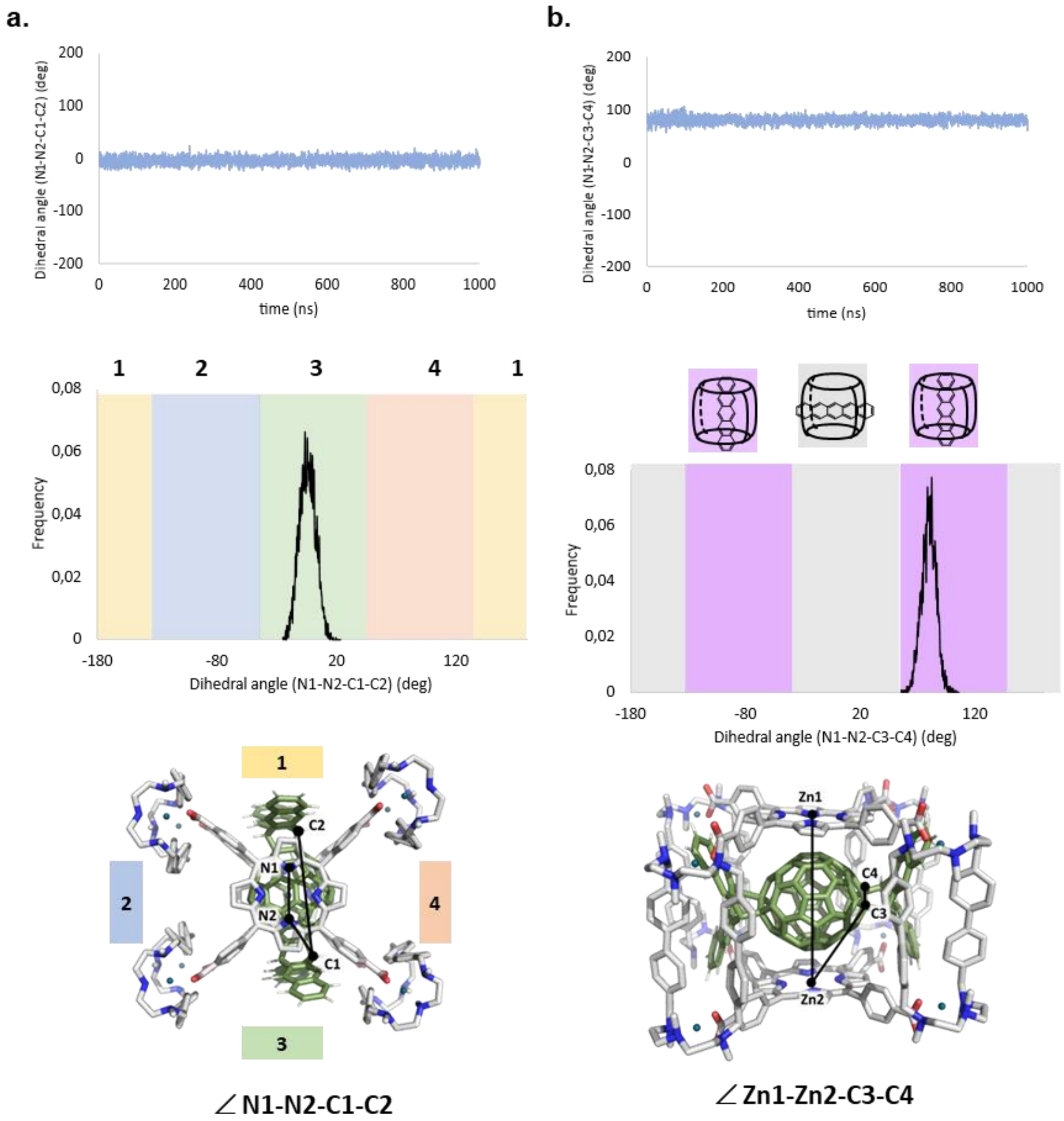

*Figure S.74. Conformational analysis of trans-1-bis-Pn-C$_{60}$⊂**1b**·(Cl)$_8$ host-guest complex from 1000 ns of MD trajectories in explicit CH$_3$CN. Replica 2. a) ∠N1-N2-C1-C2 dihedral angle measured along the MD trajectory (top plot). ∠N1-N2-C1-C2 angle describes the relative rotation of the encapsulated trans-1-bis-Pn-C$_{60}$ with respect to the nanocapsule. Different nanocapsule windows (labelled as 1, 2, 3, and 4 in the figure on the bottom) are visited by the addend along the trajectory, which is described by the different values explored by dihedral angle during the simulation time. Histogram plot (frequency vs. angle value, center plot) describes that windows are visited during the trajectory. b) ∠Zn1-Zn2-C3-C4 dihedral angle measured along the MD trajectory (top plot). ∠Zn1-Zn2-C3-C4 angle describes the relative orientation of the addend with respect to the porphyrins of the capsule. Ranges of ∠Zn1-Zn2-C3-C4 values highlighted in purple in the histogram plot (center plot) indicate that the addend is oriented perpendicularly with respect to the porphyrins, while range of values highlighted in grey indicate that it is oriented parallelly with respect to the porphyrins.*

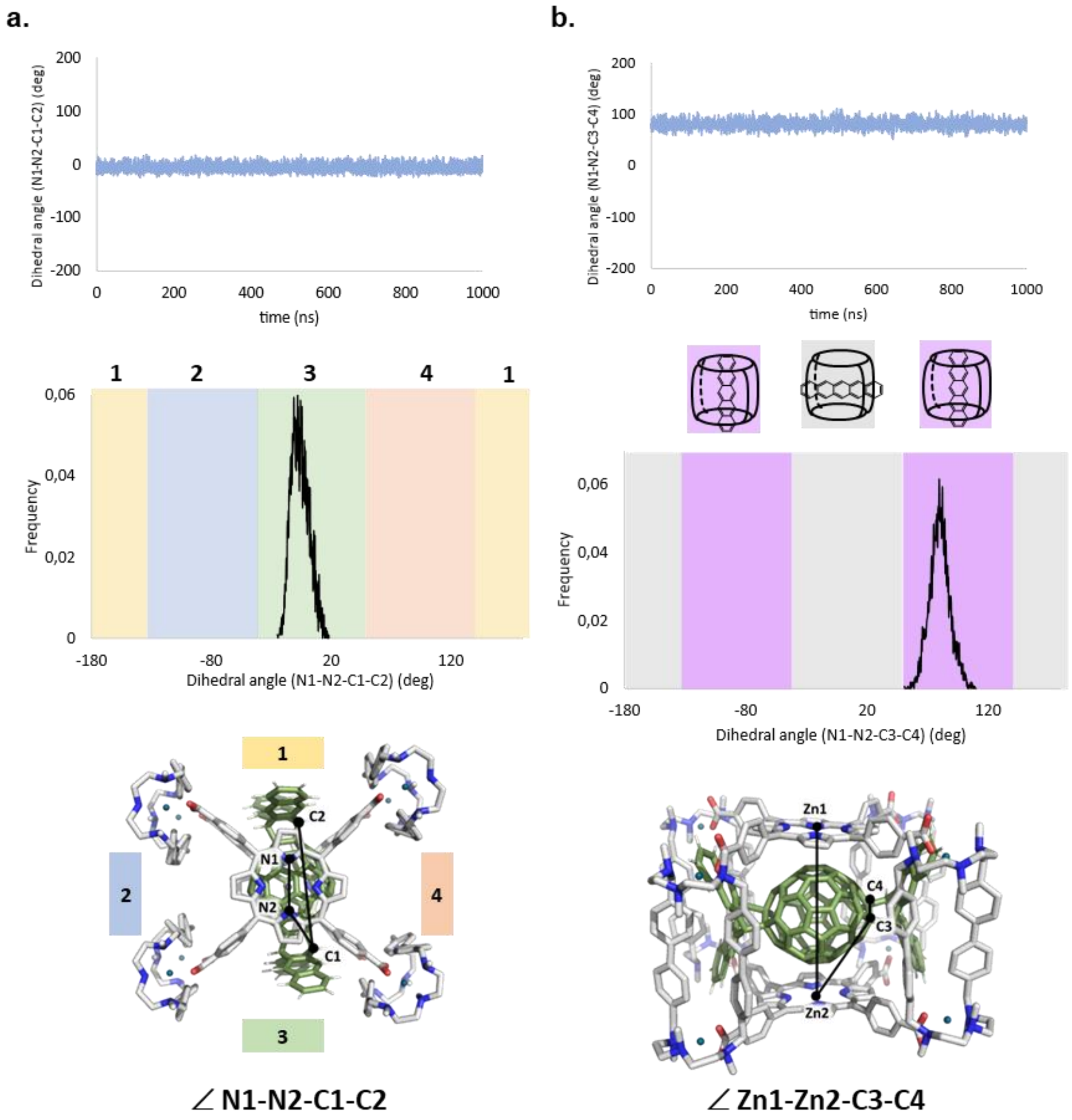

*Figure S.75. Conformational analysis of trans-1-bis-Pn-$C_{60}$⊂**1b**·$(Cl)_8$ host-guest complex from 1000 ns of MD trajectories in explicit $CH_3CN$. Replica 3. a) ∠N1-N2-C1-C2 dihedral angle measured along the MD trajectory (top plot). ∠N1-N2-C1-C2 angle describes the relative rotation of the encapsulated trans-1-bis-Pn-$C_{60}$ with respect to the nanocapsule. Different nanocapsule windows (labelled as 1, 2, 3, and 4 in the figure on the bottom) are visited by the addend along the trajectory, which is described by the different values explored by dihedral angle during the simulation time. Histogram plot (frequency vs. angle value, center plot) describes that windows are visited during the trajectory. b) ∠Zn1-Zn2-C3-C4 dihedral angle measured along the MD trajectory (top plot). ∠Zn1-Zn2-C3-C4 angle describes the relative orientation of the addend with respect to the porphyrins of the capsule. Ranges of ∠Zn1-Zn2-C3-C4 values highlighted in purple in the histogram plot (center plot) indicate that the addend is oriented perpendicularly with respect to the porphyrins, while range of values highlighted in grey indicate that it is oriented parallelly with respect to the porphyrins.*

## *Annex IV.3.3 Analysis of frontier molecular orbitals*

### *FMOs of mono-An-$C_{60}$ (**2**)*

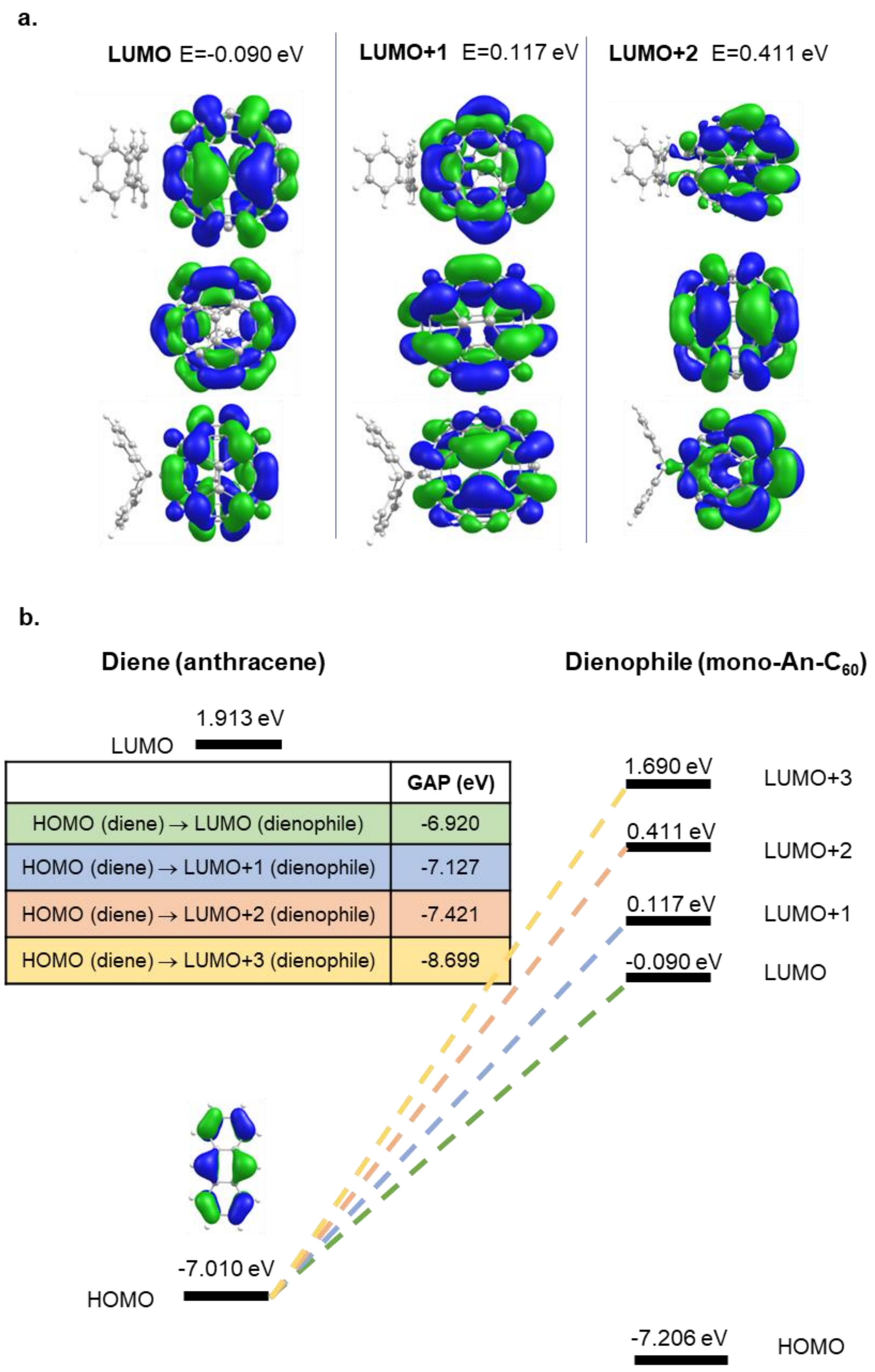

| | **GAP (eV)** |
|---|---|
| HOMO (diene) → LUMO (dienophile) | -6.920 |
| HOMO (diene) → LUMO+1 (dienophile) | -7.127 |
| HOMO (diene) → LUMO+2 (dienophile) | -7.421 |
| HOMO (diene) → LUMO+3 (dienophile) | -8.699 |

*Figure S.76. a) Representation of low-lying LUMO (LUMO, LUMO+1, LUMO+2 and LUMO+3) of mono-An-$C_{60}$. Each orbital is shown from three different perspectives. Orbital energies are given in eV. b) Molecular orbital diagram for the calculated FMOs of anthracene and mono-An-$C_{60}$. Orbital energies are given in eV.*

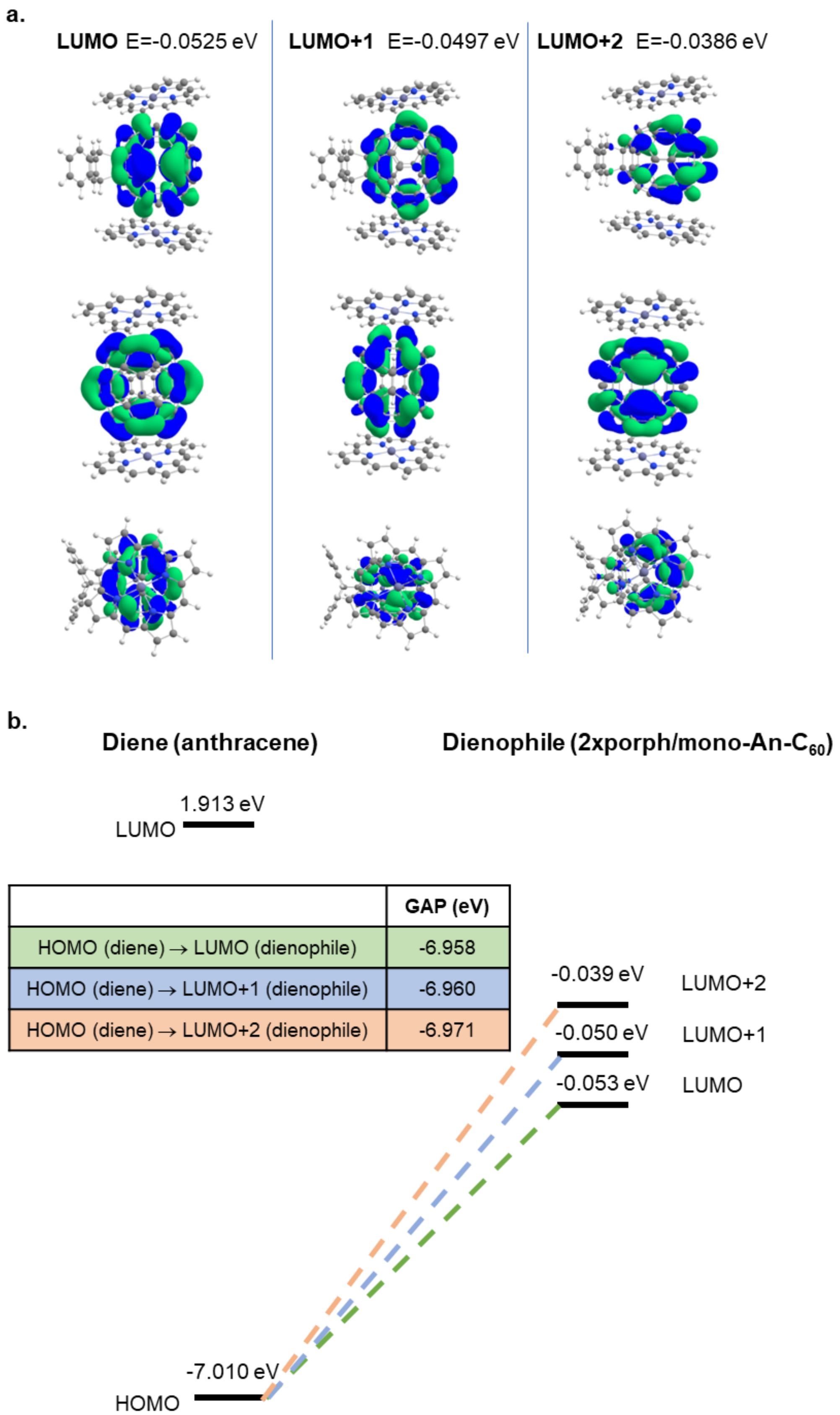

| | GAP (eV) |
|---|---|
| HOMO (diene) → LUMO (dienophile) | -6.958 |
| HOMO (diene) → LUMO+1 (dienophile) | -6.960 |
| HOMO (diene) → LUMO+2 (dienophile) | -6.971 |

*Figure S.77. a) Representation of low-lying LUMO (LUMO, LUMO+1 and LUMO+2) of 2xporph/mono-An-$C_{60}$ complex. Each orbital is shown from three different perspectives. Orbital energies are given in eV. b) Molecular orbital diagram for the calculated FMOs of anthracene and 2xporph/mono-An-$C_{60}$. Orbital energies are given in eV.*

*FMOs of mono-Pn-$C_{60}$ (**4**)*

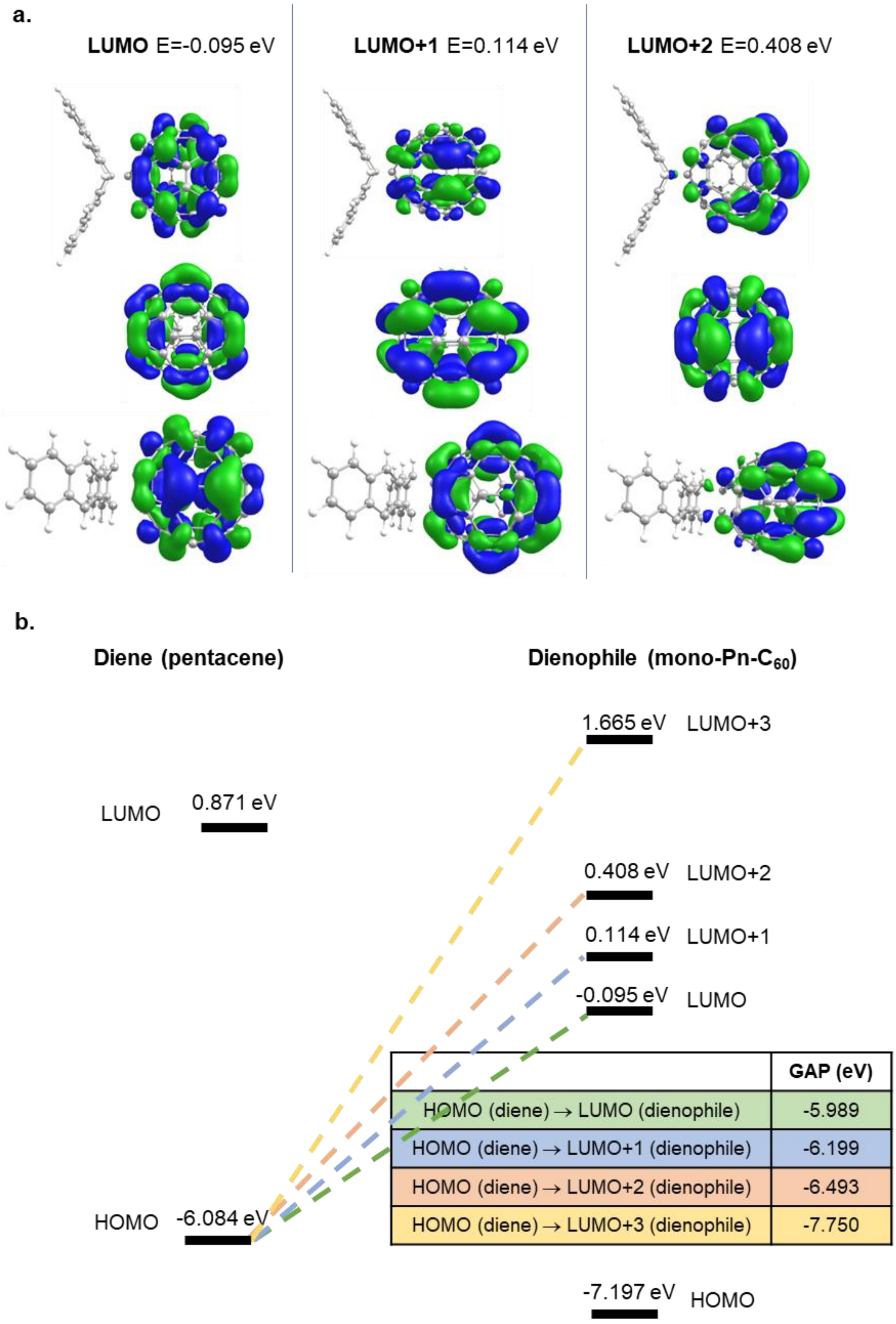

| | GAP (eV) |
|---|---|
| HOMO (diene) → LUMO (dienophile) | -5.989 |
| HOMO (diene) → LUMO+1 (dienophile) | -6.199 |
| HOMO (diene) → LUMO+2 (dienophile) | -6.493 |
| HOMO (diene) → LUMO+3 (dienophile) | -7.750 |

*Figure S.78. a) Representation of low-lying LUMO (LUMO, LUMO+1, LUMO+2 and LUMO+3) of mono-Pn-$C_{60}$ complex. Each orbital is shown from three different perspectives. Orbital energies are given in eV. b) Molecular orbital diagram for the calculated FMOs of anthracene and mono-Pn-$C_{60}$. Orbital energies are given in eV.*

# Annex Chapter V

## Annex V.1 Experimental procedures

### Annex V.1.1 Synthesis of PCBM-based bis-homoadducts

*Synthesis and characterization of dimethyl(5-methoxy-5-oxo-1-phenylpentyl)sulfonium triflate (**10**)*

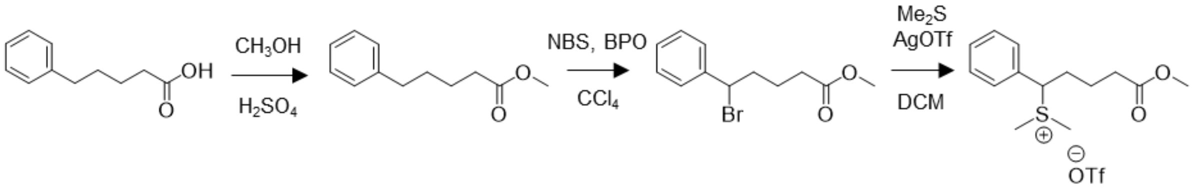

**10.1** **10.2** **10**

*Scheme S.9. Synthesis of dimethyl(5-methoxy-5-oxo-1-phenylpentyl)sulfonium triflate (**10**)*

Synthesis of **10.1**:

2.57 g (14.4 mmol) of 5-phenylvaleric acid were dissolved in 9.5 ml of methanol and 0.475 ml (8.9 mmol) of $H_2SO_4$ was added to the solution. The mixture was stirred at 65ºC for 3 hours. Then, the solvent was evaporated under reduced pressure and 30 ml of distilled $H_2O$ was added. A solution of 30 ml of 10% $Na_2CO_{3(aq)}$ was added. Extractions with ethyl acetate were performed and the combined organic phases were washed with brine. Yield: 88%

**$^1$H-NMR** (400 MHz, $CDCl_3$) δ ppm: 7.29 – 7.26 (m, 2H, $H_{aryl}$), 7.19 – 7.16 (m, 3H, $H_{aryl}$), 3.66 (s, 3H, -O-$CH_3$), 2.63 (t, $J$ = 7.1 Hz, 2H, Ph-$CH_2$-), 2.34 (t, $J$ = 7.1 Hz, 2H, $CH_2$-COO-), 1.73 – 1.59 (m, 4H, -$CH_2$-).

Synthesis of **10.2**:

2.45 mg (12.7 mmol) of compound **10.1** was dissolved in 130 ml of $CCl_4$. 2.36 g (13 mmol) of *N*-bromosuccinimide (NBS) and 36.6 mg (1% mol regarding NBS) of BPO (benzoyl peroxide) were added and the mixture was stirred at 80ºC for 2 hours. Then, the mixture was filtered to remove the remaining solid and the solvent of the filtrate was evaporated under reduced pressure. The compound was purified through a column chromatography (hexane:ethyl acetate 3:1). Yield: 35%

**$^1$H-NMR** (400 MHz, $CDCl_3$) δ ppm: 7.41 – 7.27 (m, 5H, $H_{aryl}$), 4.95 (t, $J$ = 6.8 Hz, 1H, Ph-CHBr-), 3.66 (s, 3H, -O-$CH_3$), 2.35 (t, $J$ = 7.4 Hz, 2H, -$CH_2$-COO-), 2.33 – 2.25 (m, 1H, -

$CH_2$-), 2.23 – 2.13 (m, 1H, -$CH_2$-), 1.91 – 1.77 (m, 1H, -$CH_2$-), 1.71 – 1.59 (m, 1H, -$CH_2$-).

Synthesis of **10**:

1.19 g (4.4 mmol) of compound **10.2** was dissolved in 4.4 ml of DCM and 0.971 ml (13.1 mmol) of dimethyl sulfide ($Me_2S$) was added. The mixture was stirred for 10 min at 0ºC. Then, 1.13 g (4.4 mmol) of silver trifluoromethanesulfonate (AgOTf) were added and the mixture was stirred for 30 min at 0ºC. Then, it was stirred at room temperature for 2 hours. The solvent of the crude was evaporated under reduced pressure and it was purified through a column chromatography with hexane:ethyl acetate 3:1 to elute the remaining starting material and then DCM with 10% of methanol to elute the product. Finally, the product was diluted in 10 ml of acetonitrile and it was washed with 30 ml of hexane. Yield: 62%

**$^1$H-NMR** (400 MHz, $CDCl_3$) δ ppm: 7.55 – 7.40 (m, 5H, $H_{aryl}$), 5.01 (t, *J* = 7.7 Hz, 1H, Ph-C*H*-$SMe_2$), 3.64 (s, 3H, -O-$CH_3$), 3.05 (s, 3H, -S-$CH_3$), 2.65 (s, 3H, -S-$CH_3$), 2.38 (t, *J* = 6.8 Hz, 2H, -$CH_2$-COO-), 2.30 – 2.20 (m, 2H, -$CH_2$-), 1.74 – 1.55 (m, 2H, -$CH_2$-).

*Synthesis and characterization of bis-homoadduct (**11**)*

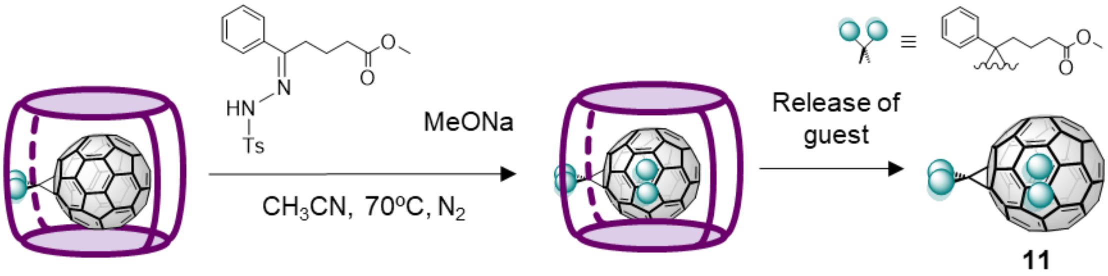

*Scheme S.10. Synthesis of PCBM-based bis-homoadduct (**11**) using diazo compounds.*

Two stock solutions of 4-benzoylbutyrate-*p*-tosylhydrazone and sodium methoxide in dry acetonitrile were prepared. Then, 1 equivalent of tosylhydrazone and MeONa from these solutions were added sequentially to a solution of $PC_{61}BM\subset$**1b**·$(BArF)_8$ (30.31 mg, 2.52 µmol) in 2.52 ml of dry acetonitrile ($10^{-3}$ M) at 70ºC. After monitoring the reaction by HR-ESI-MS for 16 hours, the crude with was filtered and the solvent was removed under a $N_2$ flow. The guests were released from the nanocapsule by decomposition with the addition of 20 equivalents of triflic acid in acetonitrile. After 1 hour of stirring, the solvent was removed under reduced pressure and extractions with toluene were performed.

After release of the derivatives from **1b**·(BArF)$_8$, they were stirred in 2 ml of toluene at 115ºC for 24 hours.

**HR-ESI-MS** of **11**$\subset$**1b**·(BArF)$_8$ ($CH_3CN$), m/z: calc. for [**11**$\subset$**1b**]$^{8+}$ 779.5590, observed 779.9248; calc. for [**11**$\subset$**1b**·(BArF)]$^{7+}$ 1014.2199, observed 1014.6363 calc. for [**11**$\subset$**1b**·(BArF)$_2$]$^{6+}$ 1327.1011, observed 1327.5836.

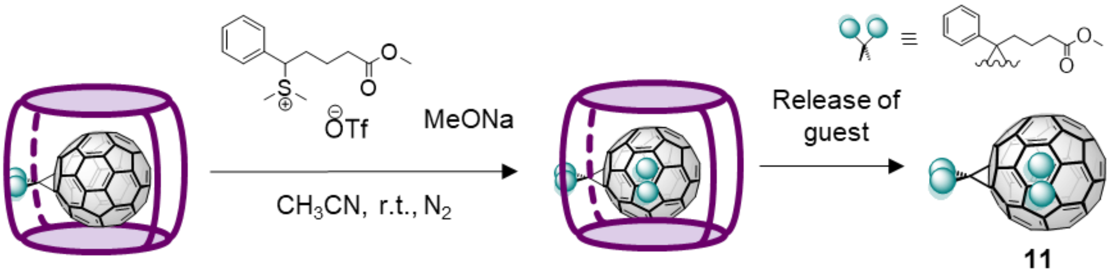

*Scheme S.11. Synthesis of PCBM-based bis-homoadduct (**11**) using semi-stabilized sulfur ylides (**10**).*

Two stock solutions of dimethyl(5-methoxy-5-oxo-1-phenylpentyl)sulfonium triflate **10** and sodium methoxide in dry acetonitrile were prepared. Then, 2.5 equivalents of **10** and MeONa from these solutions were added sequentially to a solution of PC$_{61}$BM$\subset$**1b**·(BArF)$_8$ (6.05 mg, 0.502 μmol) in 0.507 ml of dry acetonitrile ($10^{-3}$ M) at room temperature. After monitoring the reaction by HR-ESI-MS for 18.5 hours, the crude was filtered and the solvent was removed under a $N_2$ flow. The guests were released from the nanocapsule by decomposition with the addition of 20 equivalents of triflic acid in acetonitrile. Then, the solvent was removed under reduced pressure and extractions with toluene were performed. Finally, products (mainly bis-adducts) were purified through preparative TLC using a mixture of toluene and ethyl acetate (95:5) as eluent. Yield*: 36.4%.

*Yield calculated by HPLC using $C_{60}$ as internal standard

**HR-ESI-MS** of **11**$\subset$**1b**·(BArF)$_8$ ($CH_3CN$), m/z: calc. for [**11**$\subset$**1b**]$^{8+}$ 779.5590, observed 779.9387; calc. for [**11**$\subset$**1b**·(BArF)]$^{7+}$ 1014.2199, observed 1014.7963 calc. for [**11**$\subset$**1b**·(BArF)$_2$]$^{6+}$ 1327.1011, observed 1327.5994.

**MALDI-MS** (DCTB, (+)), m/z: calc. for [**11**]$^+$ 1100.199, observed 1099.639.

### *Synthesis and characterization of the complex $PC_{61}BM\subset[10]CPP\subset\mathbf{1d}\cdot(BArF)_8$*

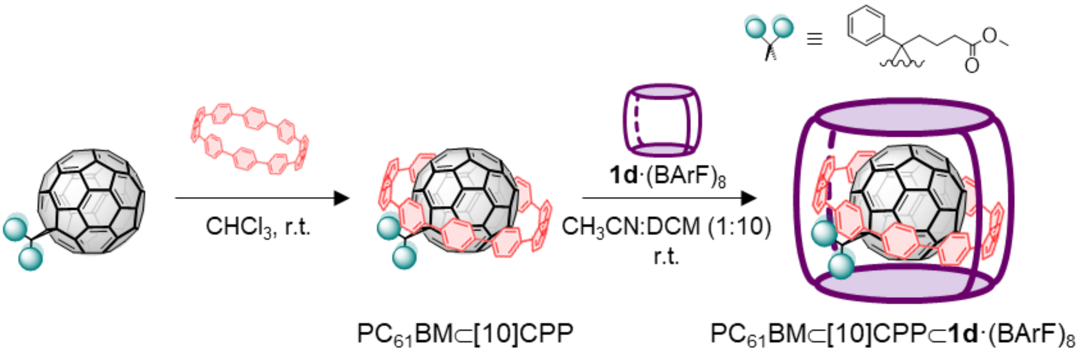

*Scheme S.12. Synthesis of $PC_{61}BM\subset[10]CPP\subset\mathbf{1d}\cdot(BArF)_8$.*

A solution of 7.5 mg of $PC_{61}BM$ in 10 ml $CHCl_3$ was added to a solution of 6.3 mg (1 equivalent) of [10]CPP in 4 ml $CHCl_3$ and it was stirring for 3 hours at room temperature to form $PC_{61}BM\subset[10]CPP$. The solvent was evaporated under reduced pressure.

To form $PC_{61}BM\subset[10]CPP\subset\mathbf{1d}\cdot(BArF)_8$, 2 equivalents of $PC_{61}BM\subset[10]CPP$ (1.53 mg) were dissolved in 10 ml of dichloromethane and were added to 1 equivalent (5.6 mg) of $\mathbf{1d}\cdot(BArF)_8$ in 1 ml of acetonitrile and it was stirring overnight at room temperature. Then, the solvent was evaporated under reduced pressure and the crude was redissolved in acetonitrile and filtered to remove the excess of $PC_{61}BM\subset[10]CPP$. Finally, washes with pentane and diethyl ether of the final solid were carried out.

**$^1$H-NMR** of $PC_{61}BM\subset[10]CPP$ (400 MHz, $CDCl_3$) δ ppm: 7.94 – 7.87 (m, 2H, $H_{aryl}$), 7.76 (t, $J$ = 7.5 Hz, 2H, $H_{aryl}$), 7.68 (t, $J$ = 7.4 Hz, 1H, $H_{aryl}$), 7.49 (s, 40H, [10]CPP), 3.77 (s, 3H, $-CH_3$), 2.72 – 2.63 (m, 2H, $-C_q-CH_2-$), 2.54 (t, $J$ = 7.7 Hz, 2H, $-CH_2-COO-$), 2.21 – 2.12 (m, 2H, $-CH_2-$).

**$^1$H-NMR** of $PC_{61}BM\subset[10]CPP\subset\mathbf{1d}\cdot(BArF)_8$ (400 MHz, $CDCl_3$) δ ppm: 8.82 (d, 4H, arom-porph) 8.78 (d, $J$ = 2.8 Hz, 16H, pyrrole ring), 8.68 (d, $J$ = 7.8 Hz, 4H, arom-porph), 8.58 – 8.48 (m, 8H, arom-porph), 8.39 (d, $J$ = 7.8 Hz, 4H, arom-porph), 8.34 (d, $J$ = 8.1 Hz, 4H, arom-porph), 8.22 (d, 4H, arom-porph), 8.19 (d, $J$ = 7.5 Hz, 16H, arom-clip), 8.06 (d, $J$ = 8.0 Hz, 16H, arom-clip), 8.01 (d, $J$ = 7.8 Hz, 4H), 7.85 (d, $J$ = 8.0 Hz, 16H), 7.75 – 7.67 (m, 96H, $BArF^-$), 7.55 (d, $J$ = 8.1 Hz, 16H, arom-clip), 7.13 (d, $J$ = 10.4 Hz, 40H, [10]CPP), 4.10 (d, $J$ = 12.8 Hz, 16H, $-CH_2-$), 3.67 (m, 16H, $-CH_2-$), 3.62 (d, $J$ = 3.4 Hz, 48H, $-N-CH_3$), 3.33 – 3.22 (m, 16H, $-CH_2-$), 3.19 (d, $J$ = 12.8 Hz, 8H, $-CH_2-$), 3.14 (d, $J$ = 12.9 Hz, 8H, $-CH_2-$), 2.47 (t, $J$ = 13.7 Hz, 16H, $-CH_2-$), 2.36 (t, $J$ = 11.8 Hz, 16H, $-CH_2-$), 1.49 (s, 12H, $-N-CH_3$), 1.43 (s, 12H, $-N-CH_3$).

**HR-ESI-MS** of $PC_{61}BM\subset[10]CPP\subset\mathbf{1d}\cdot(BArF)_8$ ($CH_3CN$), m/z: calc. for $[PC_{61}BM\subset[10]CPP\subset\mathbf{1d}]^{8+}$ 875.0879, observed 875.4578; calc. for

[PC$_{61}$BM⊂[10]CPP⊂**1d**·(BArF)]$^{7+}$ 1123.3958, observed 1123.5333; calc. for [PC$_{61}$BM⊂[10]CPP⊂**1d**·(BArF)$_2$]$^{6+}$ 1454.6397, observed 1454.7929.

*Synthesis of the complex **11**⊂[10]CPP⊂**1d**·(BArF)$_8$*

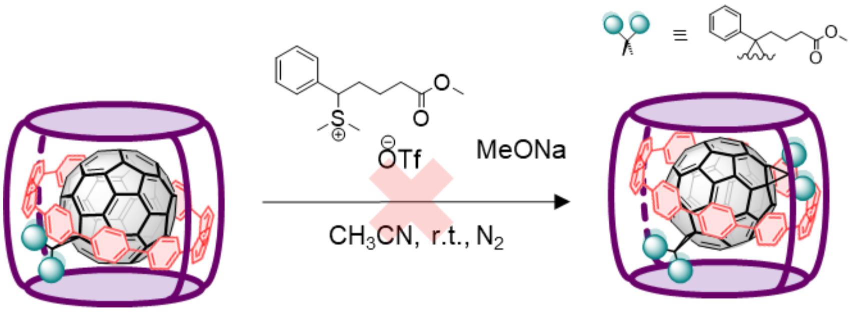

**11**⊂[10]CPP⊂**1d**·(BArF)$_8$

*Scheme S.13. Synthesis of **11**⊂[10]CPP⊂**1d**·(BArF)$_8$.*

Two stock solutions of dimethyl(5-methoxy-5-oxo-1-phenylpentyl)sulfonium triflate **10** and sodium methoxide in dry acetonitrile were prepared. Then, 15 equivalents of diethyl bromomalonate and NaH from these solutions were added sequentially to a solution of PC$_{61}$BM⊂[10]CPP⊂**1d**·(BArF)$_8$ (4.2 mg, 0.34 μmol) in 0.343 ml of dry acetonitrile ($10^{-3}$ M) at room temperature. After monitoring the reaction by HR-ESI-MS for 23 hours, the crude was filtered and the solvent was removed under a $N_2$ flow.

## *Annex V.1.2 Synthesis of PCBM-based bis-heteroadducts*

### *Synthesis and characterization of bis-heteroadduct (**12**)*

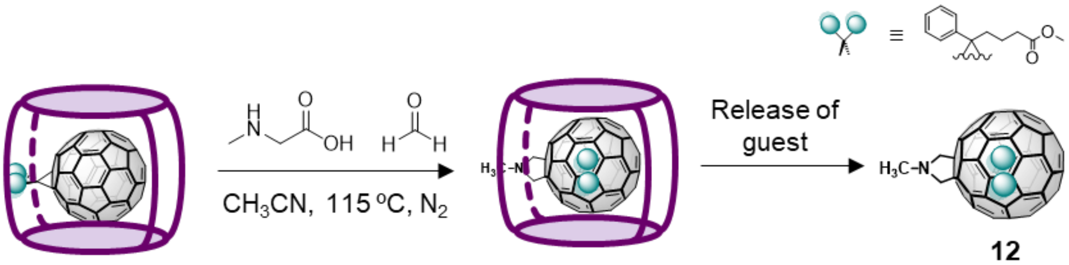

**12**

*Scheme S.14. Synthesis of bis-heteroadduct (**12**) through Prato reaction.*

Two stock solutions of sarcosine and paraformaldehyde in Milli-Q water were prepared. Then, 3 equivalents of sarcosine and 7.5 equivalents of paraformaldehyde from these solutions were added sequentially to a solution of PC$_{61}$BM⊂**1b**·(BArF)$_8$ (9.18 mg, 0.76 μmol) in 6.68 ml of acetonitrile ($1.14 \cdot 10^{-4}$ M) at 115ºC. After monitoring the reaction by HR-ESI-MS for 4 hours, the crude was filtered and the solvent was removed under a $N_2$

flow. The guests were released from the nanocapsule by extractions with chloroform. Finally, products (mainly bis-adducts) were purified through preparative TLC using a mixture of toluene and ethyl acetate (95:5) as eluent.

**HR-ESI-MS** of **12**$\subset$**1b**·(BArF)$_8$ (CH$_3$CN), m/z: calc. for [**12**$\subset$**1b**]$^{8+}$ 763.0557, observed 763.5476; calc. for [**12**$\subset$**1b**·(BArF)]$^{7+}$ 995.5019, observed 995.7784; calc. for [**12**$\subset$**1b**·(BArF)$_2$]$^{6+}$ 1305.2634, observed 1305.2610.

**MALDI-MS** (DCTB, (+)), m/z: calc. for [**12**]$^+$ 967.157, observed 968.624.

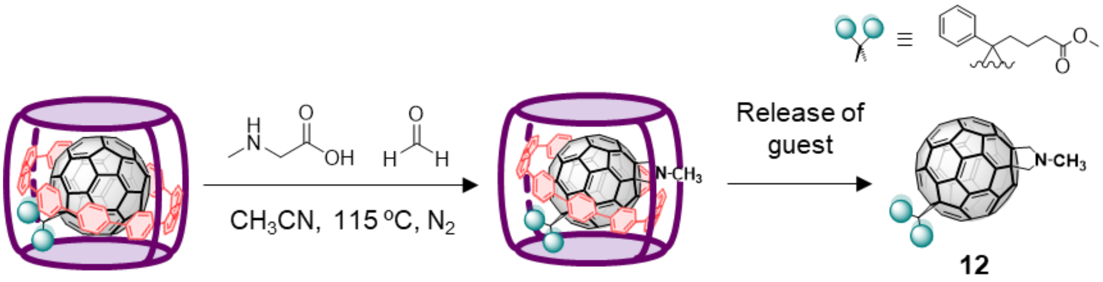

*Scheme S.15. Synthesis of bis-heteroadduct (**12**).*

Two stock solutions of sarcosine and paraformaldehyde in Milli-Q water were prepared. Then, 27.5 equivalents of sarcosine and 66 equivalents of paraformaldehyde from these solutions were added sequentially to a solution of PC$_{61}$BM$\subset$[10]CPP$\subset$**1d**·(BArF)$_8$ (8.36 mg, 0.68 µmol) in 5.99 ml of acetonitrile (1.14·10$^{-3}$ M) at 115ºC. After monitoring the reaction by HR-ESI-MS for 35.5 hours, the crude was filtered and the solvent was removed under a N$_2$ flow. **12**$\subset$[10]CPP was released from **1d**·(BArF)$_8$ with extractions of chloroform until the nanocapsule was empty. Then, exchange with 2.5 equivalents of C$_{60}$ was performed to release bis-adducts from [10]CPP in 4 ml of chloroform. After stirring overnight at room temperature, solvent was removed under reduced pressure and **12** was extracted with toluene. Derivatives were isolated by a preparative TLC using toluene as eluent.

**HR-ESI-MS** of **12**$\subset$[10]CPP$\subset$**1d**·(BArF)$_8$ (CH$_3$CN), m/z: calc. for [**12**$\subset$[10]CPP$\subset$**1d**]$^{8+}$ 882.2202, observed 882.4664; calc. for [**12**$\subset$[10]CPP$\subset$**1d**·(BArF)]$^{7+}$ 1131.5469, observed 1131.8244; calc. for [**12**$\subset$[10]CPP$\subset$**1d**·(BArF)$_2$]$^{6+}$ 1464.1494, observed 1464.1405.

**MALDI-MS** (DCTB, (+)), m/z: calc. for [**12**]$^+$ 967.157, observed 968.371.

### *Synthesis and characterization of bis-heteroadduct (**13**)*

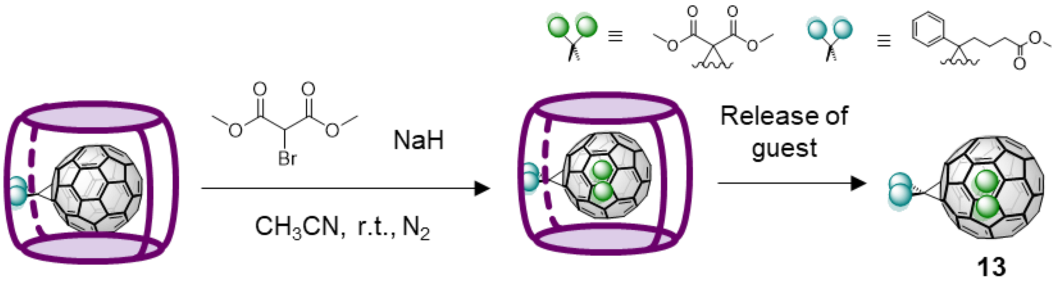

*Scheme S.16. Synthesis of bis-heteroadduct (**13**).*

Two stock solutions of dimethyl bromomalonate and sodium hydride in dry acetonitrile were prepared. Then, 4.25 equivalents of dimethyl bromomalonate and NaH from these solutions were added sequentially to a solution of PC$_{61}$BM⊂**1b**·(BArF)$_8$ (5.9 mg, 0.49 μmol) in 0.5 ml of dry acetonitrile ($10^{-3}$ M) at room temperature. After monitoring the reaction by HR-ESI-MS for 4.5 hours, the crude was filtered and the solvent was removed under a $N_2$ flow. The guests were released from the nanocapsule by decomposition with the addition of 20 equivalents of triflic acid in acetonitrile. Then, the solvent was removed under reduced pressure and extractions with toluene were performed. Finally, products (mainly bis-adducts) were purified through preparative TLC using a mixture of toluene and ethyl acetate (95:5) as eluent.

**HR-ESI-MS** of **13**⊂**1b**·(BArF)$_8$ ($CH_3CN$), m/z: calc. for [**13**⊂**1b**]$^{8+}$ 772.3018, observed 772.4155; calc. for [**13**⊂**1b**·(BArF)]$^{7+}$ 1005.9260, observed 1006.0534; calc. for [**12**⊂**1b**·(BArF)$_2$]$^{6+}$ 1317.4249, observed 1317.5638.

**MALDI-MS** (DCTB, (+)), m/z: calc. for [**13**]$^+$ 1040.126, observed 1040.171; calc. for [**13** + Na$^+$]$^+$ 1063.116, observed 1063.157.

### *Synthesis of the complex **13**⊂[10]CPP⊂**1d**·(BArF)$_8$*

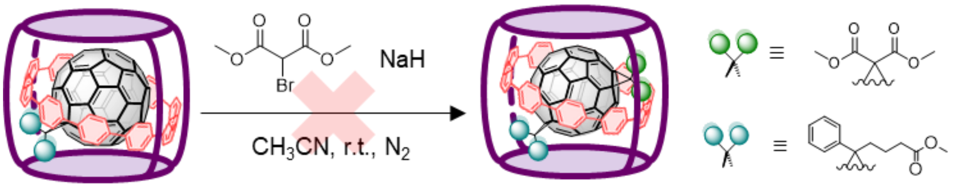

**13**⊂[10]CPP⊂**1d**·(BArF)$_8$

*Scheme S.17. Synthesis of **13**⊂[10]CPP⊂**1d**·(BArF)$_8$.*

Two stock solutions of dimethyl bromomalonate and sodium hydride in dry acetonitrile were prepared. Then, 9 equivalents of diethyl bromomalonate and NaH from these solutions were added sequentially to a solution of PC$_{61}$BM⊂[10]CPP⊂**1d**·(BArF)$_8$ (5.2 mg, 0.37 µmol) in 0.372 ml of dry acetonitrile (10$^{-3}$ M) at room temperature. After monitoring the reaction by HR-ESI-MS for 30 hours, the crude was filtered and the solvent was removed under a N$_2$ flow.

### *Synthesis and characterization of the complex **14**⊂[10]CPP⊂**1d**·(BArF)$_8$*

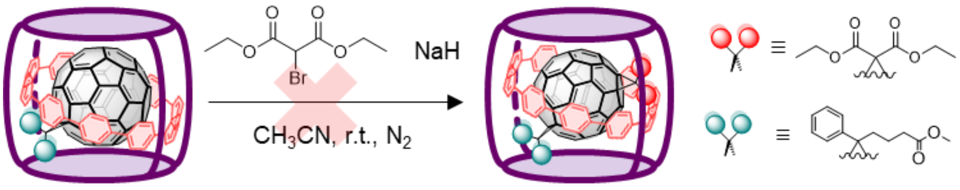

**14**⊂[10]CPP⊂**1d**·(BArF)$_8$

*Scheme S.18. Synthesis of **14**⊂[10]CPP⊂**1d**·(BArF)$_8$.*

Two stock solutions of diethyl bromomalonate and sodium hydride in dry acetonitrile were prepared. Then, 9 equivalents of diethyl bromomalonate and NaH from these solutions were added sequentially to a solution of PC$_{61}$BM⊂[10]CPP⊂**1d**·(BArF)$_8$ (5.2 mg, 0.37 µmol) in 0.372 ml of dry acetonitrile (10$^{-3}$ M) at room temperature. After monitoring the reaction by HR-ESI-MS for 44 hours, the crude was filtered and the solvent was removed under a N$_2$ flow.

**HR-ESI-MS** of **14**⊂[10]CPP⊂**1d**·(BArF)$_8$ ($CH_3CN$), m/z: calc. for [**14**⊂[10]CPP⊂**1d**]$^{8+}$ 894.8452, observed 895.4577; calc. for [**14**⊂[10]CPP⊂**1d**·(BArF)]$^{7+}$ 1146.1184, observed 1146.2618.

### *Synthesis and characterization of the complex PC$_{61}$BM⊂[10]CPP⊂**1f**·(BArF)$_8$*

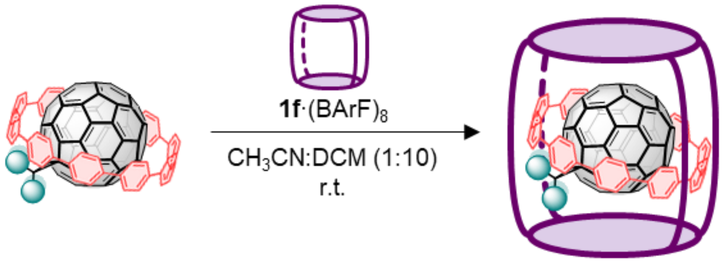

PC$_{61}$BM⊂[10]CPP⊂**1f**·(BArF)$_8$

*Scheme S.19. Synthesis of PC$_{61}$BM⊂[10]CPP⊂**1f**·(BArF)$_8$.*

2 equivalents of PC$_{61}$BM⊂[10]CPP in 10 ml dichloromethane were added to 1 equivalent (9.24 mg) of **1f**·(BArF)$_8$ in 1 ml of acetonitrile and it was stirring overnight at room

temperature. Then, the solvent was evaporated under reduced pressure and the crude was redissolved in acetonitrile and filtered to remove the excess of $PC_{61}BM\subset[10]CPP$. Finally, washes with pentane and diethyl ether of the final solid were carried out.

**$^1$H-NMR** (400 MHz, $CDCl_3$) δ ppm: 8.91 (broad s, 8H, arom-porph), 8.85 (s, 16H, pyrrole ring), 8.52 (d, *J* = 7.4 Hz, 8H, arom-porph), 8.36 (d, 8H, arom-porph), 8.30 – 8.17 (m, 32H, arom-porhp and arom-clip), 8.05 – 7.83 (m, 24H, arom-porh), 7.76 – 7.67 (m, 96H, $BArF^-$), 7.64 (broad s, 16H, arom-clip), 7.28 (s, 20H, [10]CPP), 6.98 (s, 20H, [10]CPP), 4.16 (d, *J* = 12.7 Hz, 16H, $-CH_2-$), 3.74 – 3.69 (m, 16H, $-CH_2-$), 3.66 (s, 48H, $-N-CH_3$), 3.50 – 3.34 (m, 16H, $-CH_2-$), 3.19 (d, *J* = 12.8 Hz, 16H, $-CH_2-$), 2.50 (d, *J* = 13.5 Hz, 16H, $-CH_2-$), 2.40 (d, *J* = 12.7 Hz, 16H, $-CH_2-$), 1.55 (s, 24H, $-N-CH_3$).

**HR-ESI-MS** of $PC_{61}BM\subset[10]CPP\subset$**1f**$\cdot(BArF)_8$ ($CH_3CN$), m/z: calc. for $[PC_{61}BM\subset[10]CPP\subset\mathbf{1f}]^{8+}$ 927.2444, observed 927.4856; calc. for $[PC_{61}BM\subset[10]CPP\subset\mathbf{1f}\cdot(BArF)]^{7+}$ 1183.0032, observed 1183.2788; calc. for $[PC_{61}BM\subset[10]CPP\subset\mathbf{1f}\cdot(BArF)_2]^{6+}$ 1524.0149, observed 1524.3388.

*Synthesis and characterization of bis-heteroadduct (**14**)*

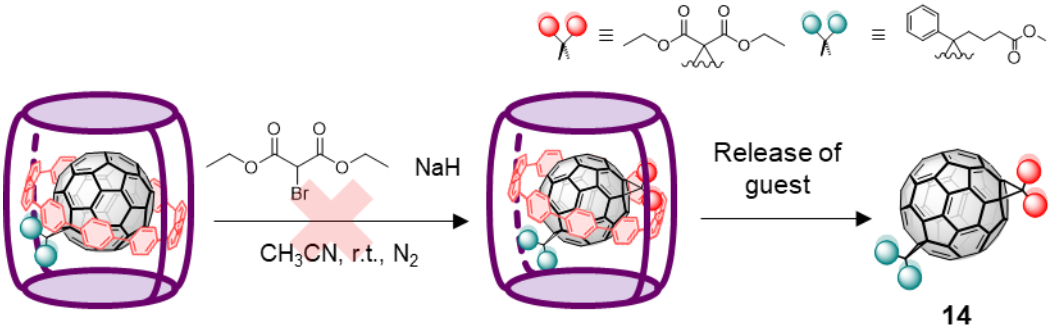

*Scheme S.20. Synthesis of bis-heteroadduct (**14**).*

Two stock solutions of diethyl bromomalonate and sodium hydride in dry acetonitrile were prepared. Then, 12 equivalents of diethyl bromomalonate and NaH from these solutions were added sequentially to a solution of $PC_{61}BM\subset[10]CPP\subset$**1f**$\cdot(BArF)_8$ (5.1 mg, 0.40 µmol) in 0.40 ml of dry acetonitrile ($10^{-3}$ M) at room temperature. After monitoring the reaction by HR-ESI-MS for 28 hours, the crude was filtered and the solvent was removed under a $N_2$ flow. Then, exchange with 5 equivalents of $C_{60}$ was performed to release bis-adducts from $[10]CPP\subset$**1f**$\cdot(BArF)_8$ in a mixture of toluene:acetonitrile (9:2). After stirring overnight at room temperature, solvent was removed under reduced pressure and **14** was extracted with toluene. Derivatives were isolated by preparative TLC using toluene as eluent.

**HR-ESI-MS** of **14**⊂[10]CPP⊂**1f**·(BArF)$_8$ ($CH_3CN$), m/z: calc. for [**14**⊂[10]CPP⊂**1f**]$^{8+}$ 947.0017 observed 946.9849; calc. for [**14**⊂[10]CPP⊂**1f**·(BArF)]$^{7+}$ 1205.5829, observed 1205.8399.

## *Annex V.2 Linear calibration for quantitative HPLC analysis*

For the quantitative determination of yields by HPLC, $C_{60}$ was used as internal standard. Due to the different extinction coefficients of bis-adducts and $C_{60}$, a correction factor was determined by measuring peak area *vs* concentration plots for $C_{60}$ and for bis-adduct. To do so, five solutions of bis-adduct of 0.56, 0.28, 0.14, 0.07, 0.035 μmol concentration and four solutions of $C_{60}$ of 0.117, 0.058, 0.029 and 0.015 μmol concentration were eluted over a Buckyprep-D column at a flow rate of 0.5 mL/min of toluene at 22°C. The integrals (320 nm) respectively were plotted against the concentration. The correction factor "*f*" was determined by comparison of the linear slope "*a"* of both plots obtained from linear regression. This correction factor was used to calculate the HPLC yields for all regioisomers under the reasonable assumption that their extinction coefficients are nearly identical.

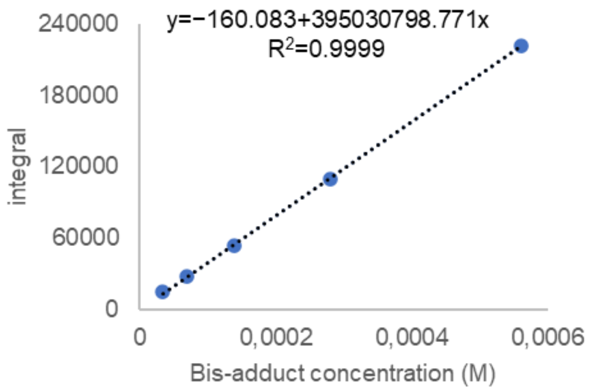

Peak area vs concentration plot of PCBM-based bis-adduct. α=395030798.771

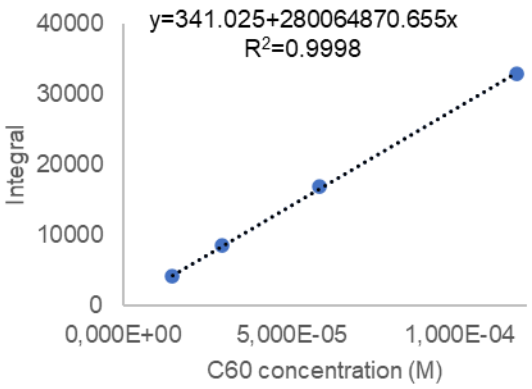

Peak area vs concentration plot of $C_{60}$. α=280064870.655

$$f = \alpha_{bis}/\alpha_{C60} = 1.41$$

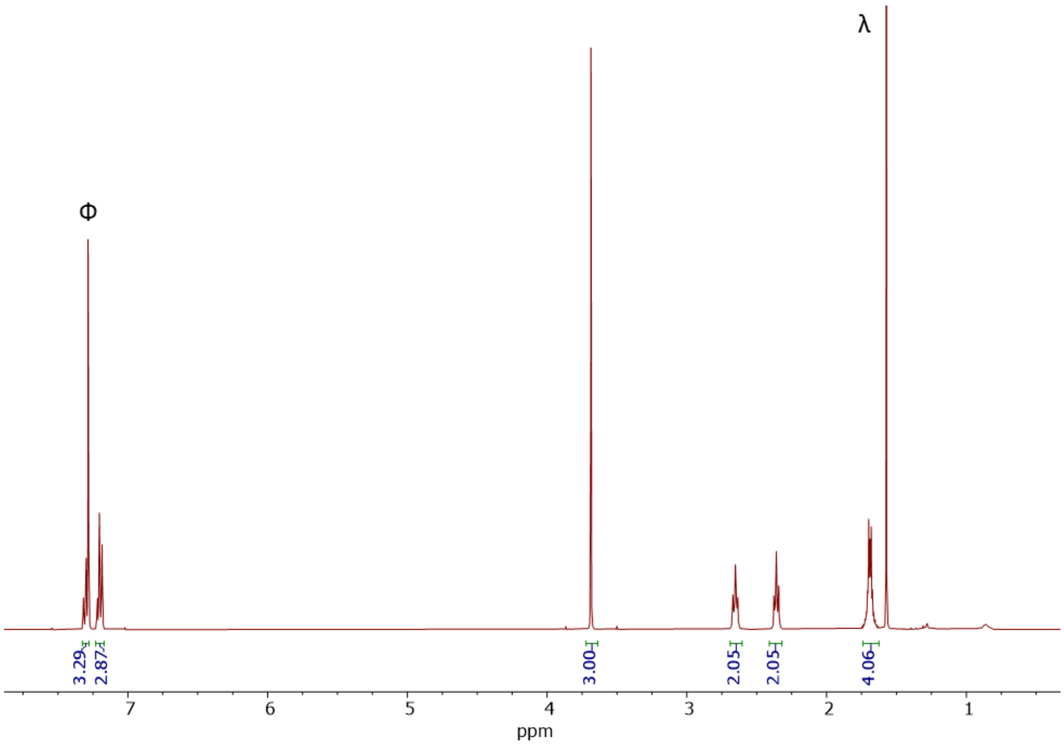

*Figure S.79. $^1$H-NMR spectrum of compound **10.1** for the synthesis of dimethyl(5-methoxy-5-oxo-1-phenylpentyl)sulfonium triflate (**10**). Experiment performed in $CDCl_3$ at 298K (400 MHz). Φ: chloroform, λ: $H_2O$.*

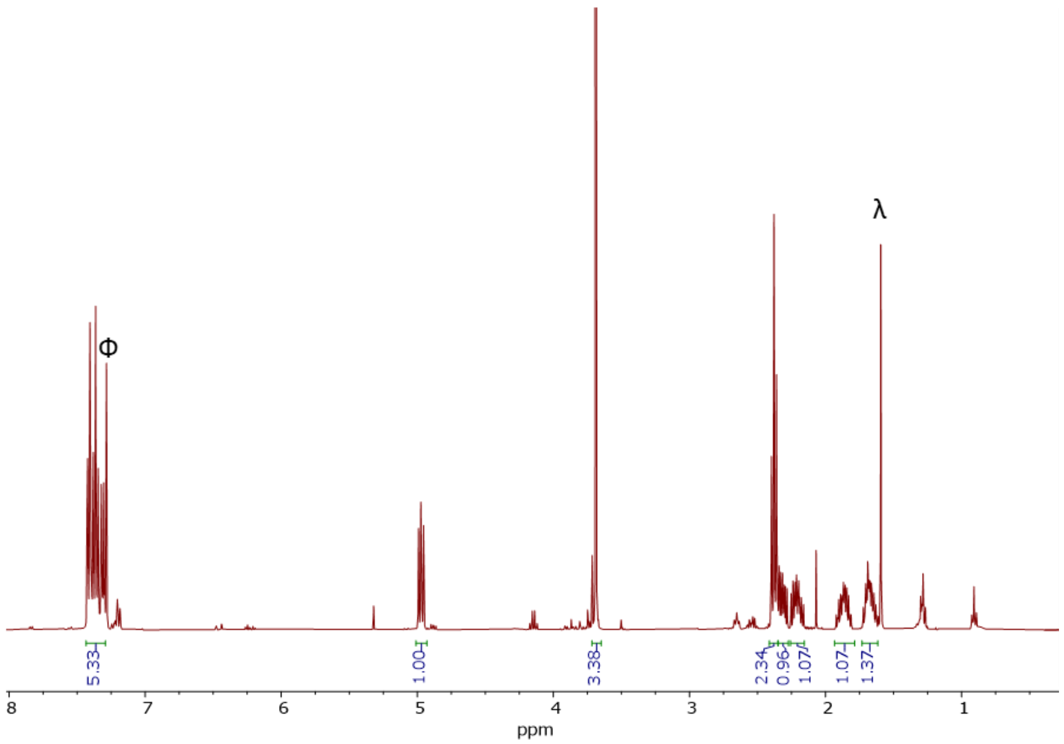

*Figure S.80. $^1$H-NMR spectrum of compound **10.2** for the synthesis of dimethyl(5-methoxy-5-oxo-1-phenylpentyl)sulfonium triflate (**10**). Experiment performed in $CDCl_3$ at 298K (400 MHz). Φ: chloroform, λ: $H_2O$.*

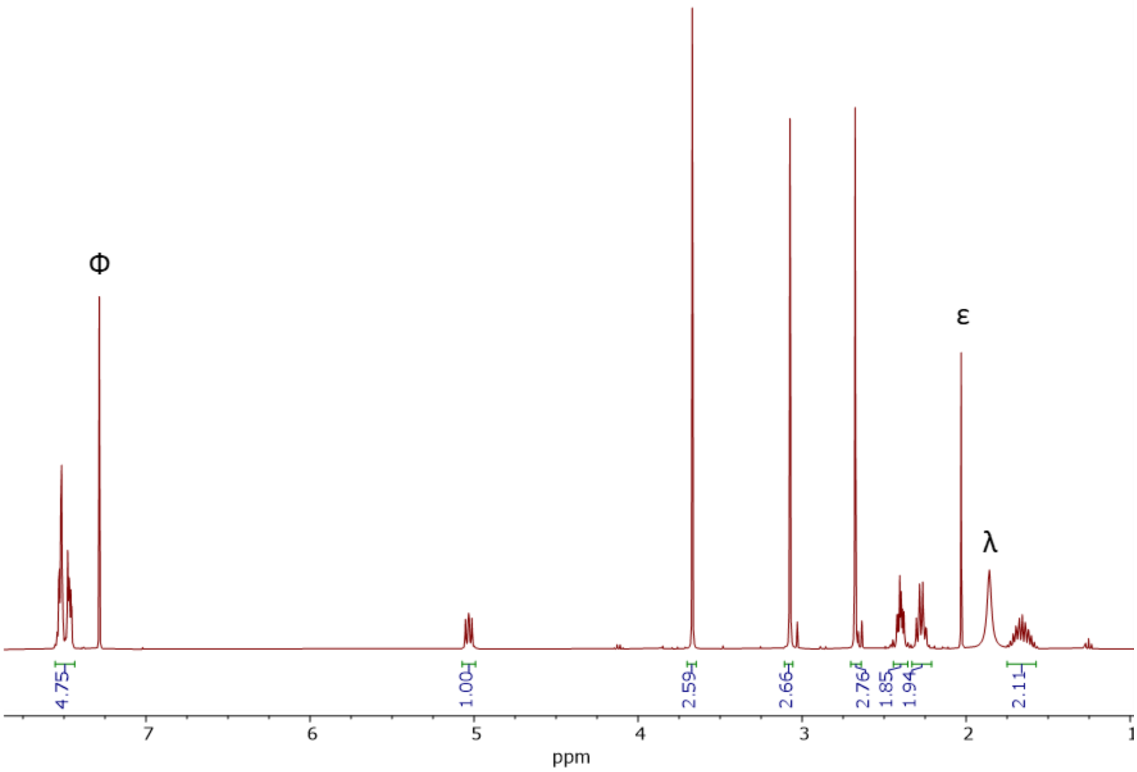

*Figure S.81. $^1$H-NMR spectrum of dimethyl(5-methoxy-5-oxo-1-phenylpentyl)sulfonium triflate (**10**). Experiment performed in $CDCl_3$ at 298K (400 MHz). Φ: chloroform, ε; acetone, λ: $H_2O$.*

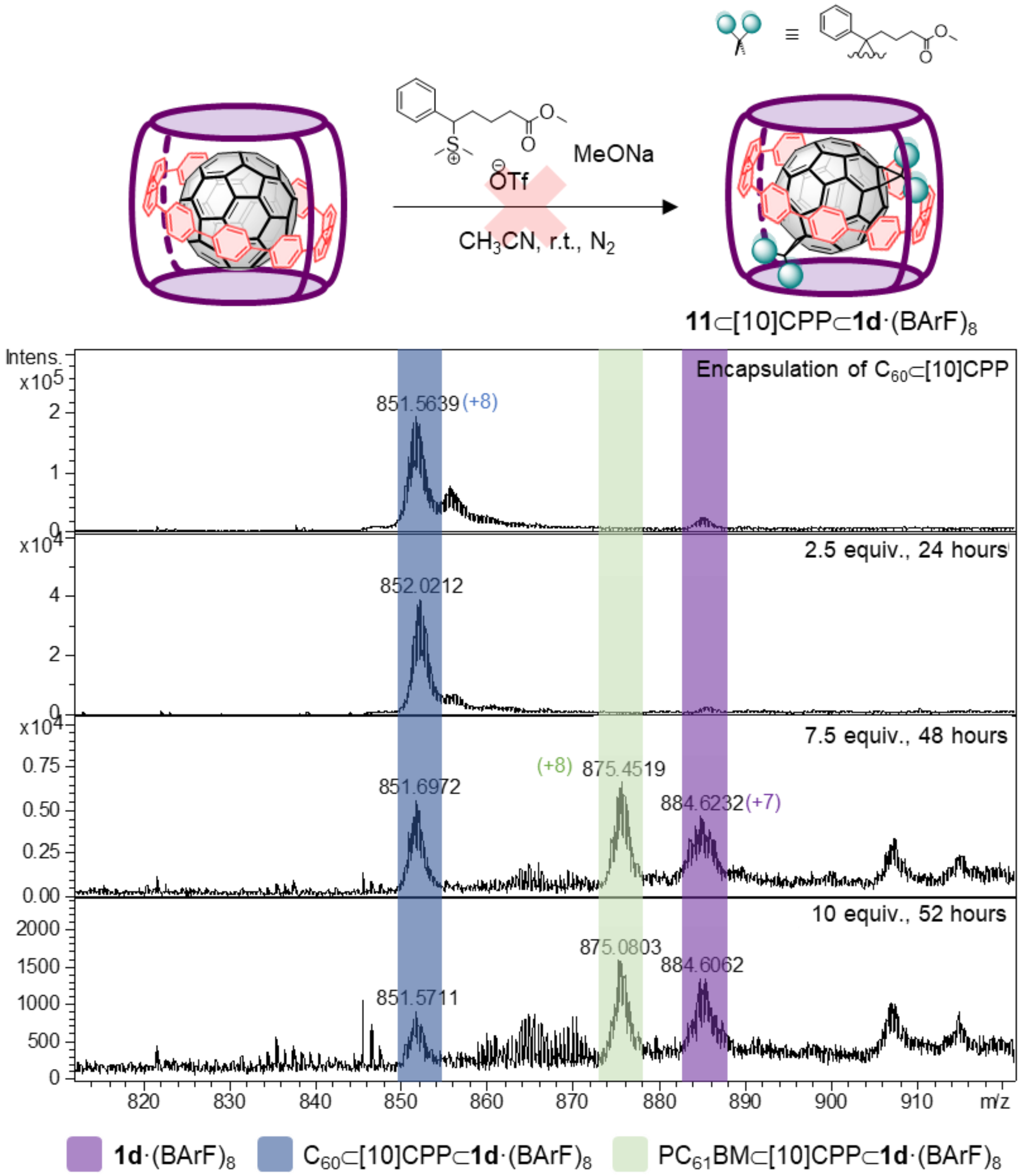

*Figure S.82. HR-ESI-MS monitoring for the synthesis of* ***11***$\subset$*[10]CPP*$\subset$***1d***$\cdot(BArF)_8$ *using sulfonium salt* ***10*** *and starting from* $C_{60}\subset$*[10]CPP*$\subset$***1d***$\cdot(BArF)_8$.

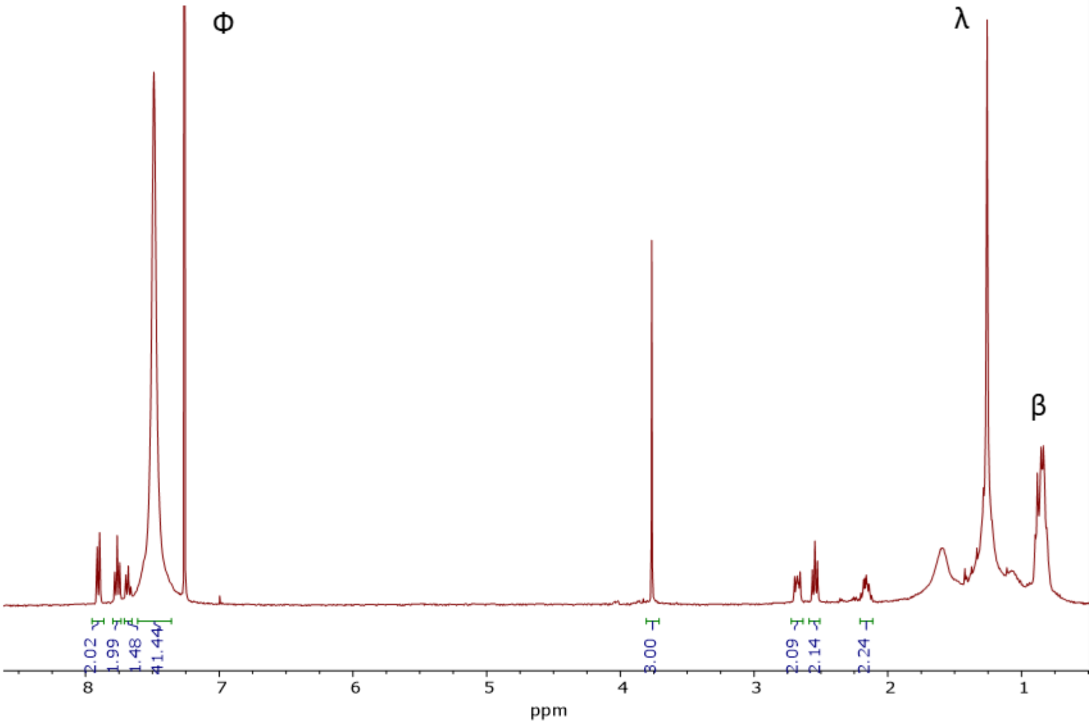

*Figure S.83. $^1$H-NMR spectrum of PC$_{61}$BM$\subset$[10]CPP. Experiment performed in CDCl$_3$ at 298K (400 MHz). Φ: chloroform, λ: H$_2$O, β: grease.*

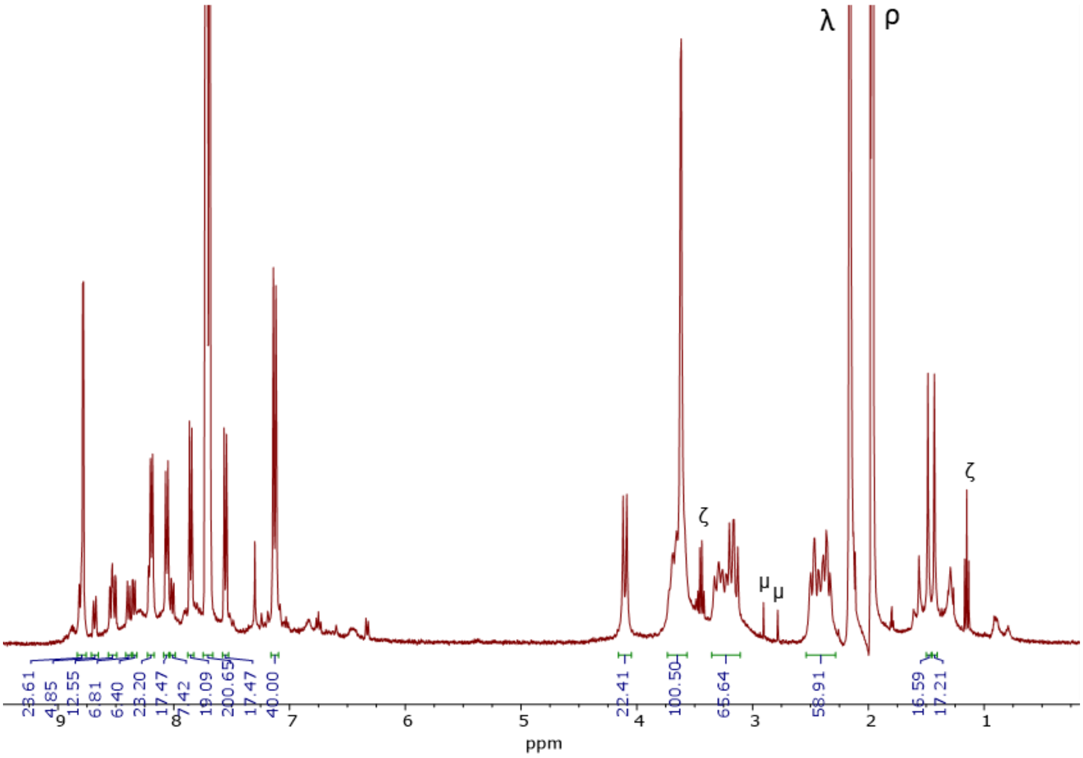

*Figure S.84. $^1$H-NMR spectrum of PC$_{61}$BM$\subset$[10]CPP$\subset$**1d**·(BArF)$_8$. Experiment performed in CDCl$_3$ at 298K (400 MHz). ζ: diethyl ether, μ: DMF, λ: H$_2$O, ρ: CH$_3$CN*

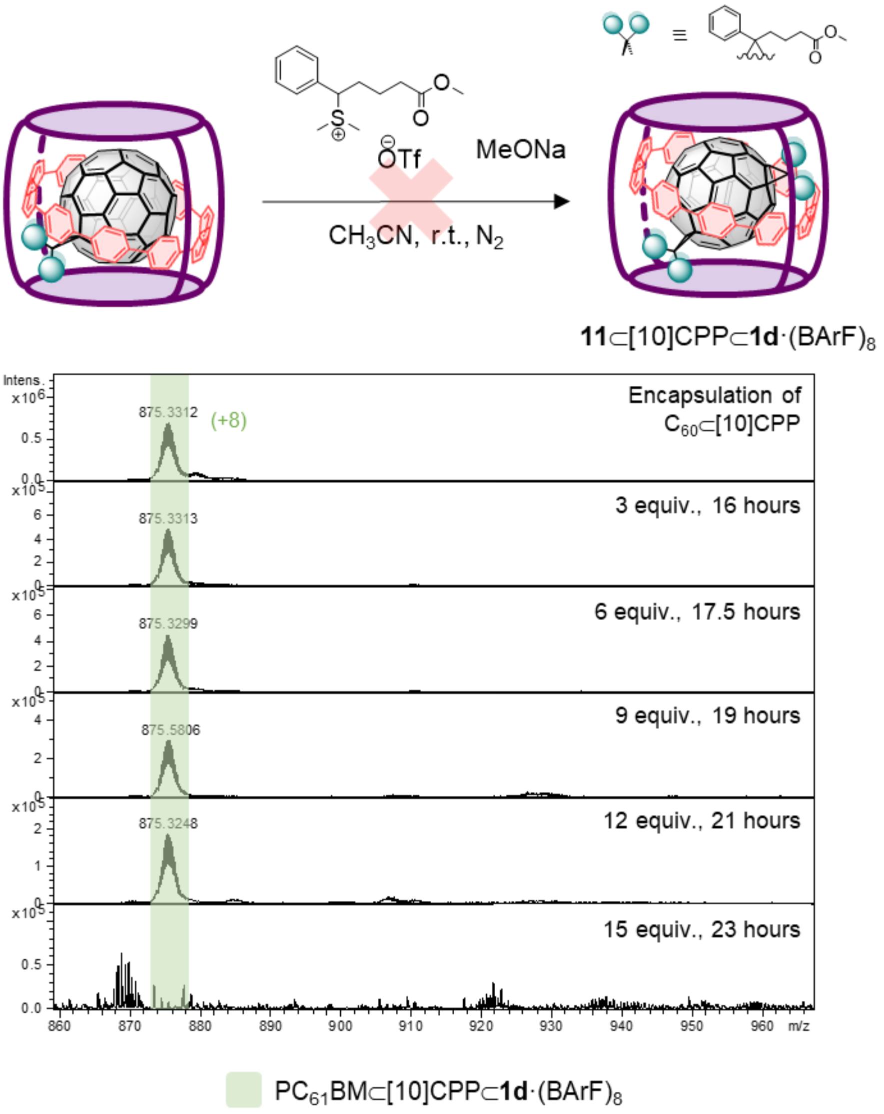

*Figure S.85. HR-ESI-MS monitoring for the synthesis of **11**⊂[10]CPP⊂**1d**·(BArF)$_8$ using sulfonium salt **10** and starting from PC$_{61}$BM⊂[10]CPP⊂**1d**·(BArF)$_8$.*

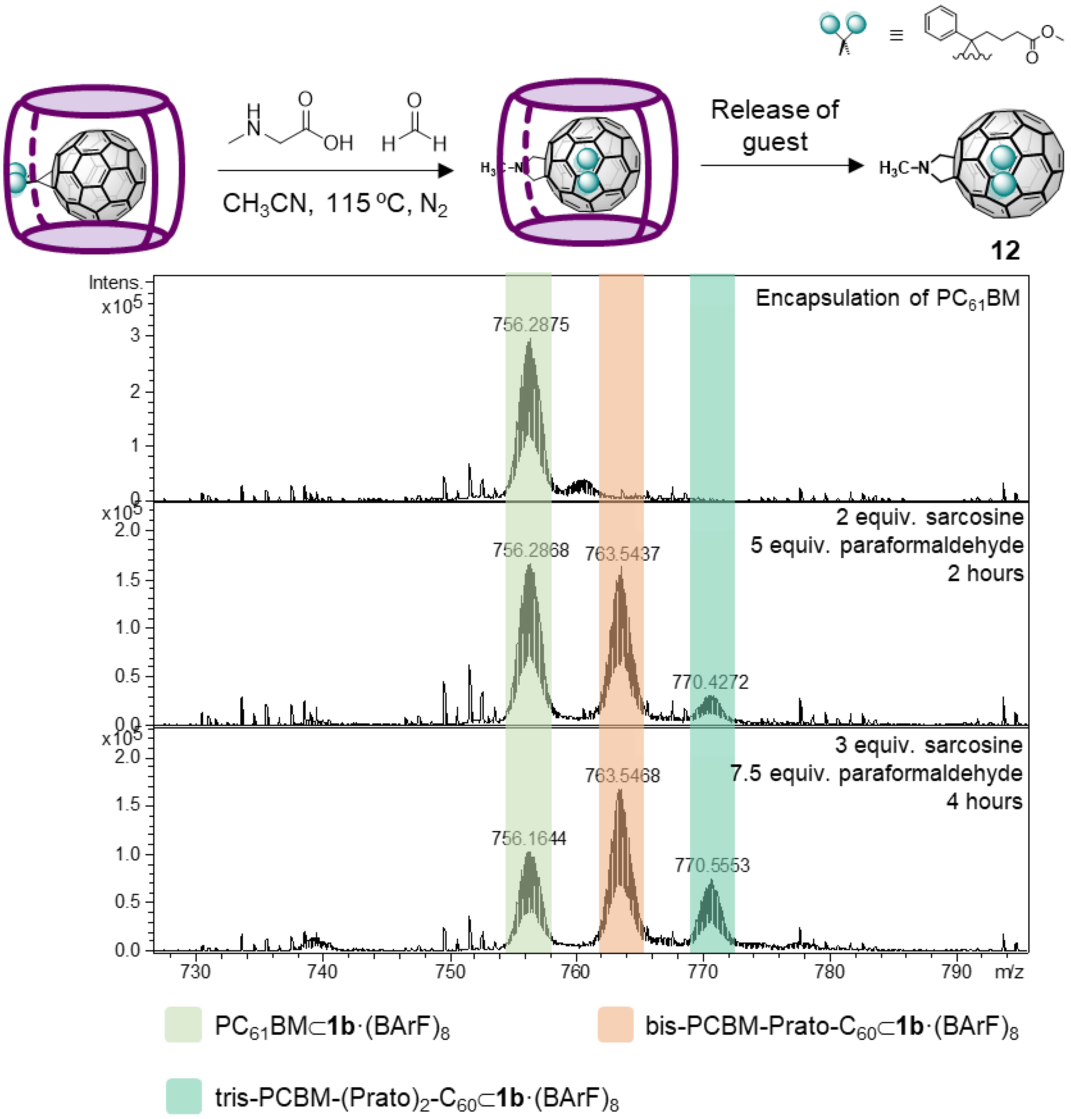

*Figure S.86. HR-ESI-MS monitoring for the synthesis of bis-heteroadducts* ***12*** *through Prato reaction starting from PC$_{61}$BM⊂**1b**·(BArF)$_8$.*

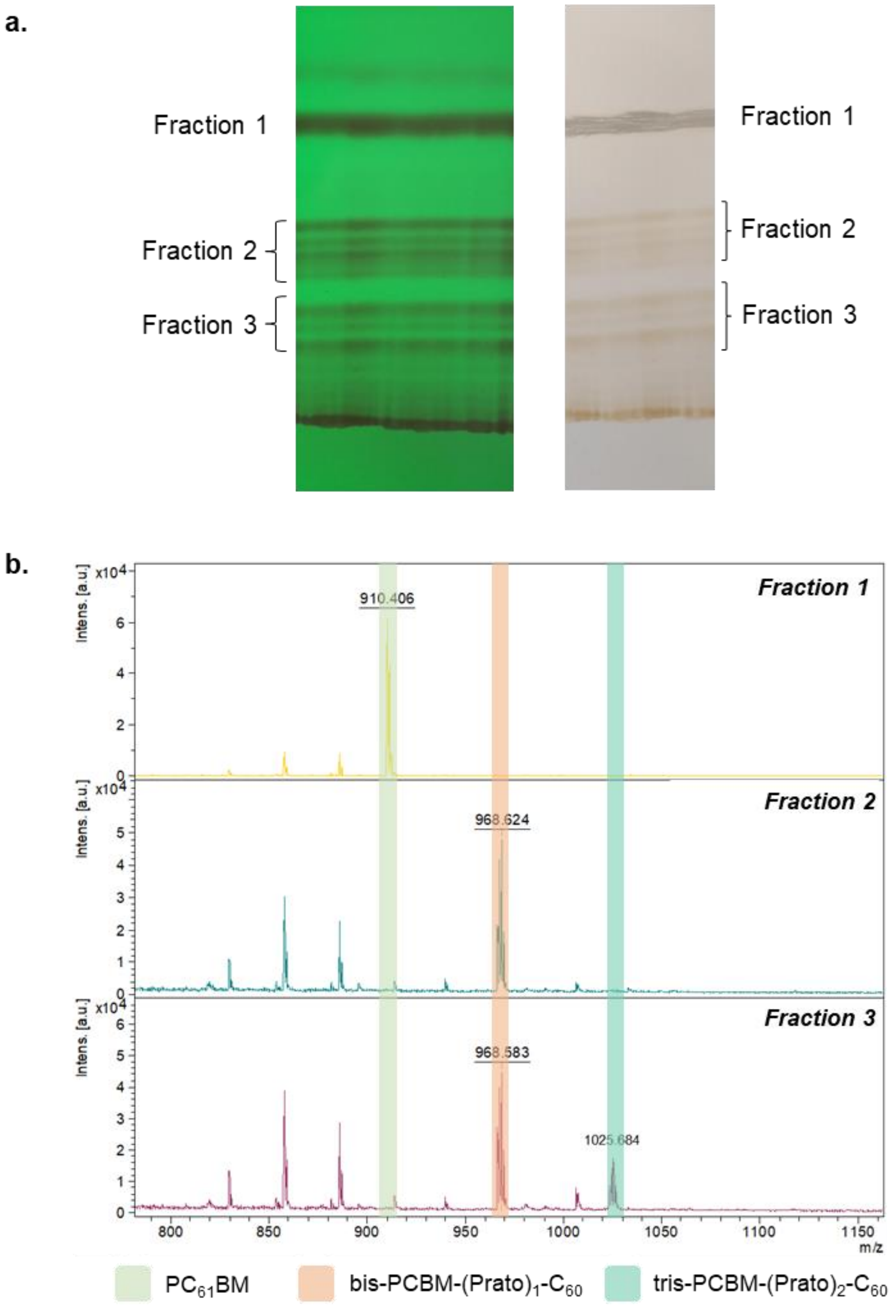

*Figure S.87. a) TLC preparative for the purification of bis-heteroadducts* ***12*** *after Prato reaction starting from* $PC_{61}BM\subset$***1b****·(BArF)*$_8$*. b) MALDI-MS analysis for bis-heteroadducts* ***12*** *after Prato reaction starting from* $PC_{61}BM\subset$***1b****·(BArF)*$_8$*.*

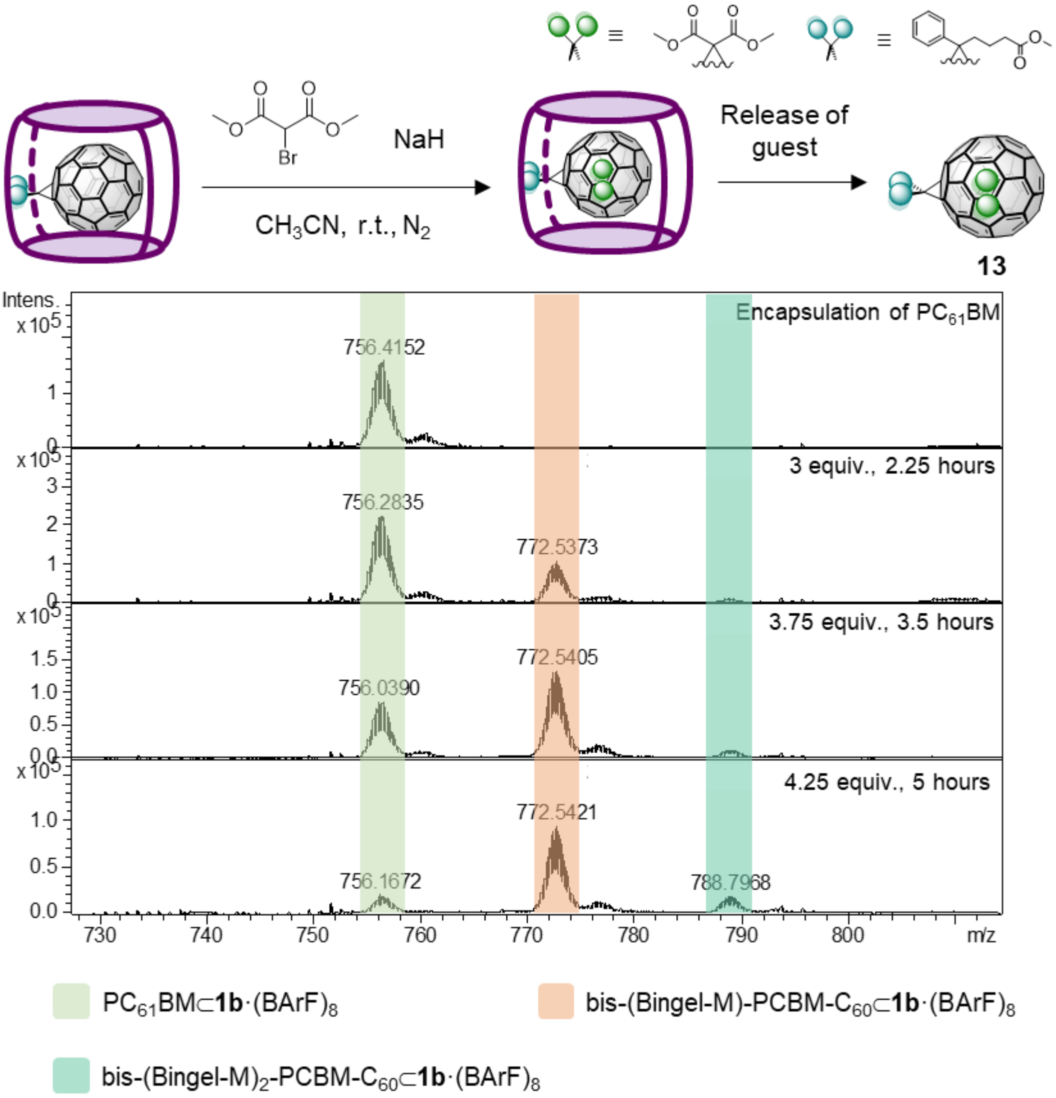

*Figure S.88. HR-ESI-MS monitoring for the synthesis of bis-heteroadducts **13** through Bingel reaction (with dimethyl bromomalonate) starting from PC$_{61}$BM⊂**1b**·(BArF)$_8$.*

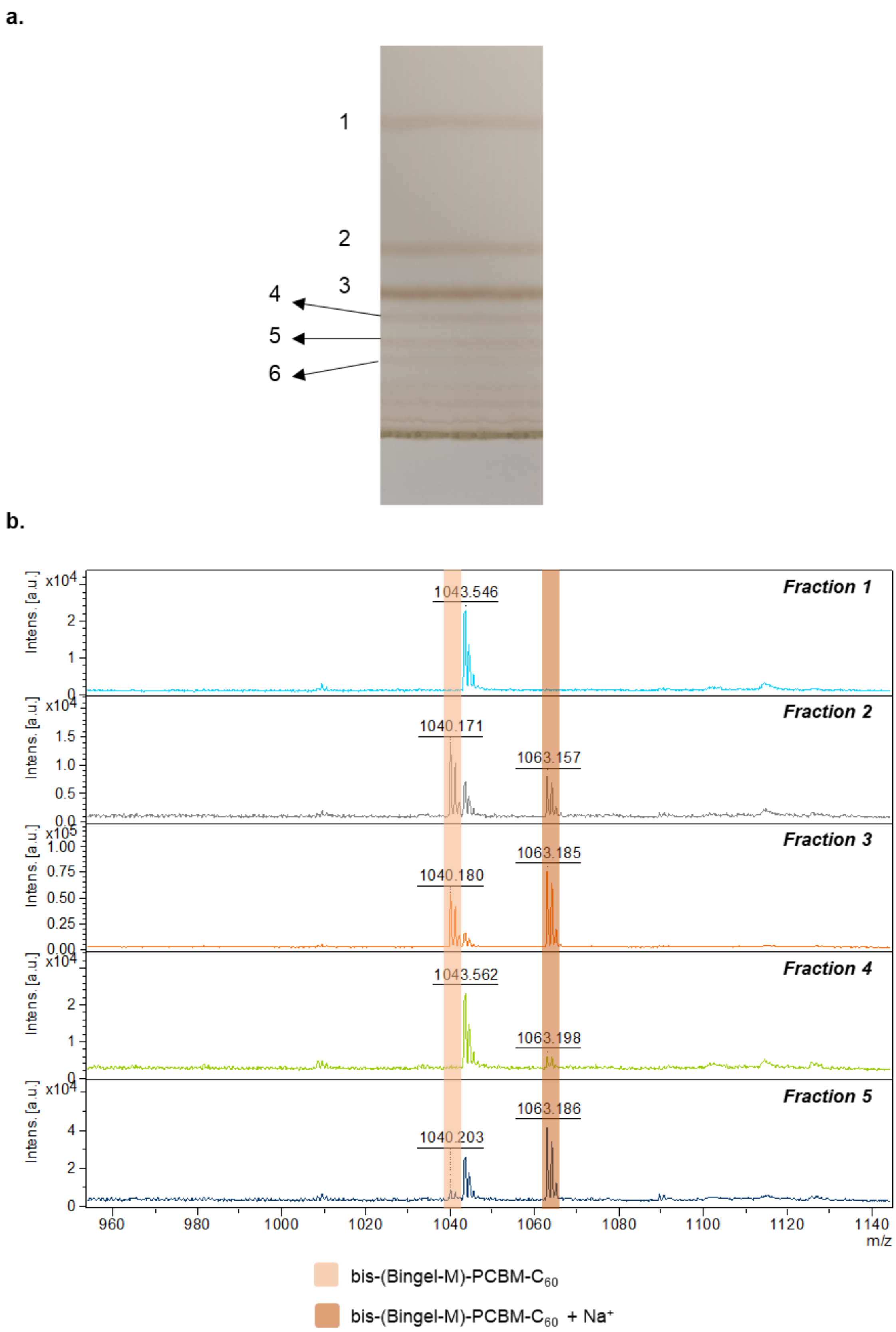

*Figure S.89. a) TLC preparative for the purification of bis-heteroadducts **13** after Bingel reaction (with dimethyl bromomalonate) starting from PC$_{61}$BM$\subset$**1b**·(BArF)$_8$. b) MALDI-MS analysis of bis-heteroadducts **13** after Bingel reaction (with dimethyl bromomalonate) starting from PC$_{61}$BM$\subset$**1b**·(BArF)$_8$.*

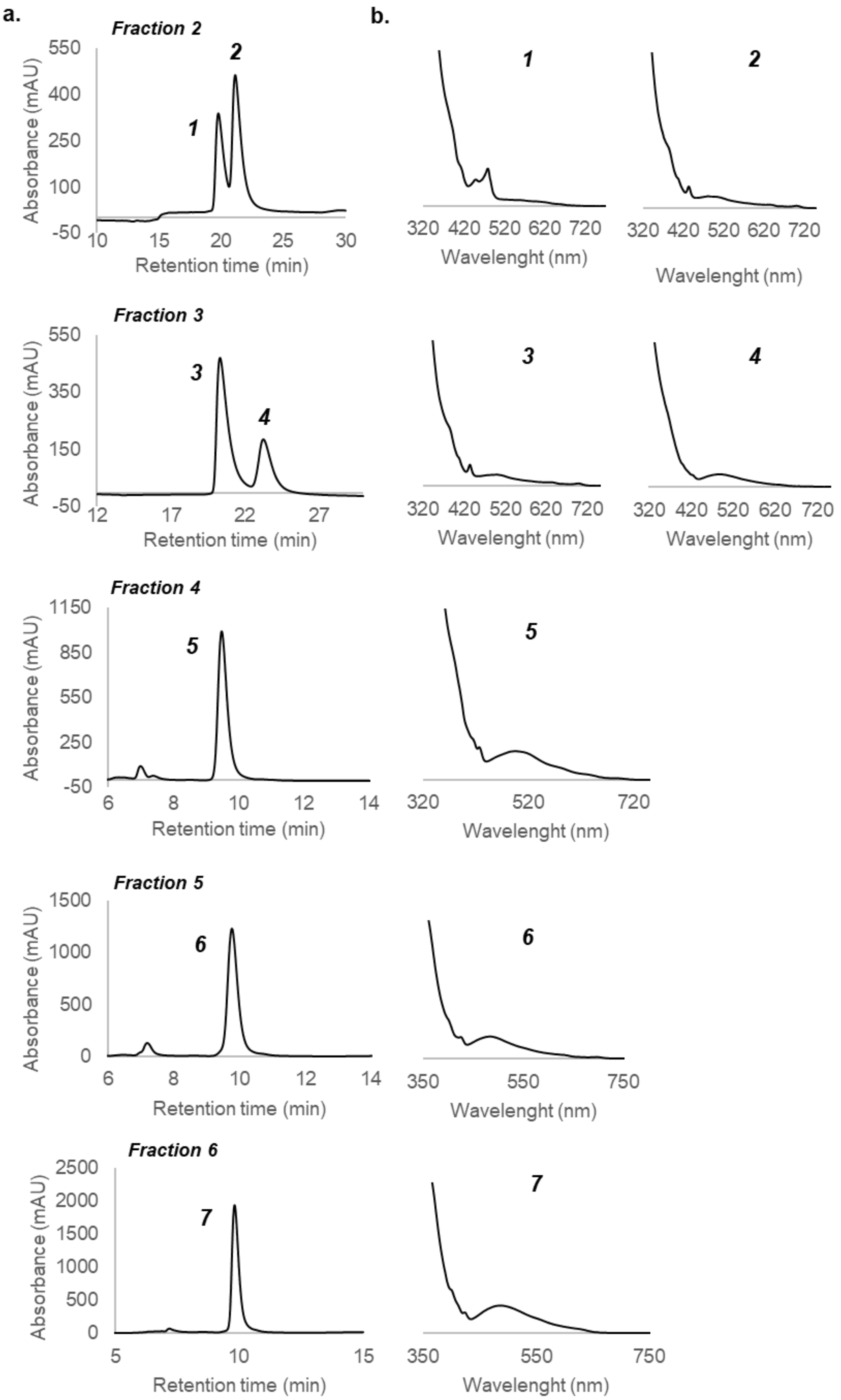

*Figure S.90. a) HPLC analysis of hetero-bis-adducts **13** after Bingel reaction (with dimethyl bromomalonate) starting from $PC_{61}BM\subset$**1b**$\cdot(BArF)_8$. b) UV-vis spectra of each peak from previous HPLC chromatograms.*

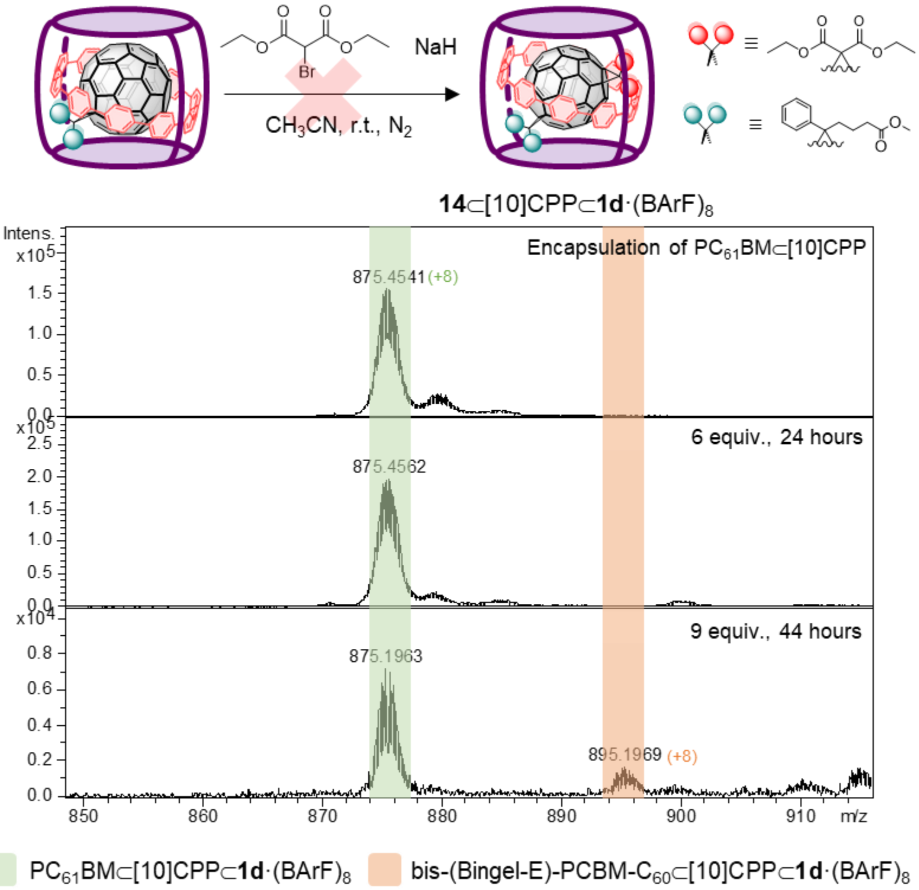

*Figure S.91. HR-ESI-MS monitoring for the synthesis of bis-heteroadducts* ***14*** *through Bingel reaction (with diethyl bromomalonate) starting from PC$_{61}$BM⊂[10]CPP⊂**1d**·(BArF)$_8$.*

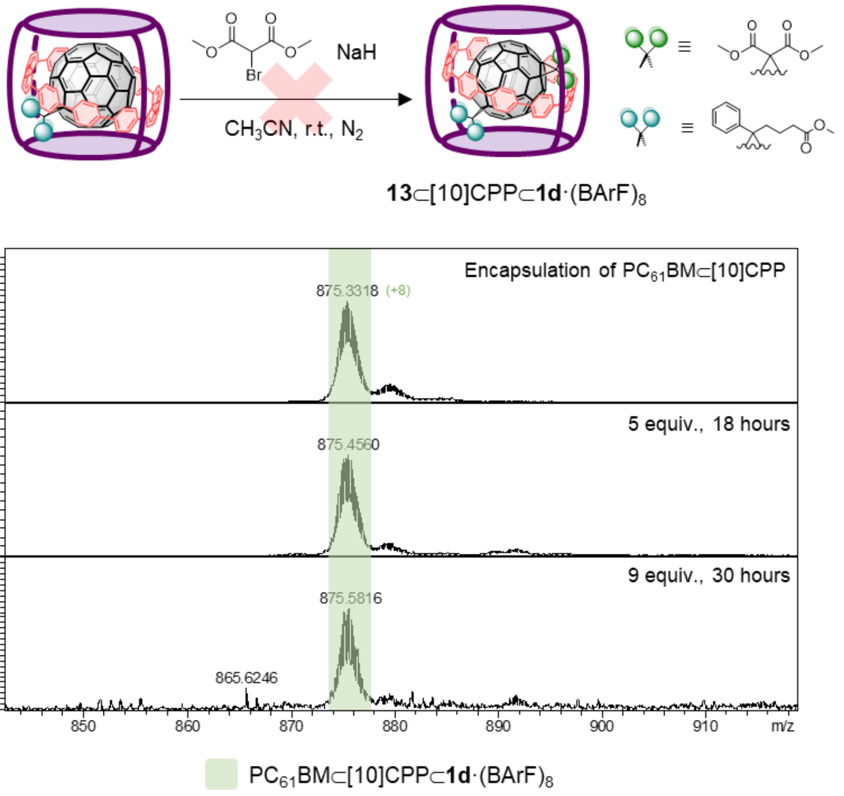

*Figure S.92. HR-ESI-MS monitoring for the synthesis of bis-heteroadducts* ***13*** *through Bingel reaction (with dimethyl bromomalonate) starting from PC$_{61}$BM⊂[10]CPP⊂**1d**·(BArF)$_8$.*

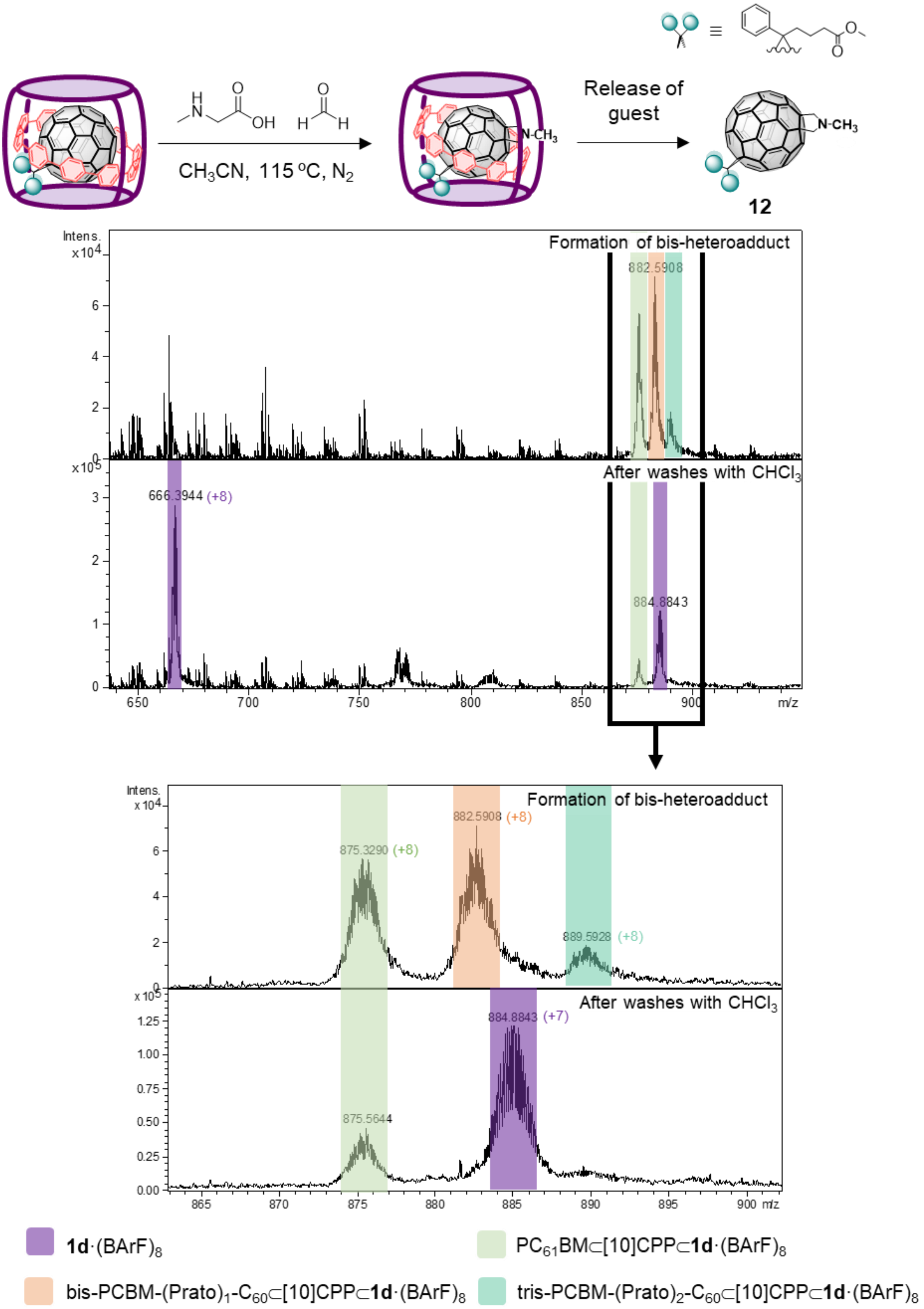

*Figure S.93. HR-ESI mass spectrum of the release of bis-heteroadduct **12** after Prato reaction starting from PC$_{61}$BM⊂[10]CPP⊂**1d**·(BArF)$_8$.*

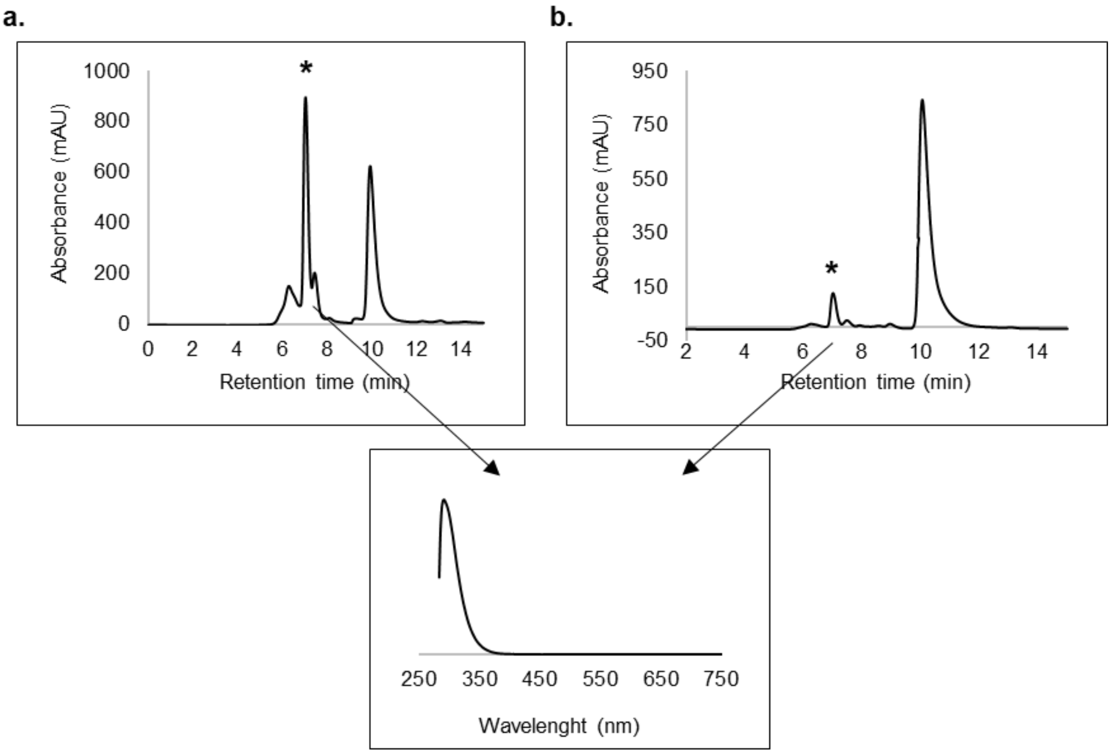

*Figure S.94. HPLC chromatograms of a) fraction 1 and b) fraction 2 after TLC preparative of the synthesis of hetero-bis-adduct **12** through Prato reaction starting from $PC_{61}BM\subset[10]CPP\subset$**1d**$\cdot(BArF)_8$. * Non-fullerene impurity - the corresponding UV-vis spectrum doesn't present a pattern related to fullerenes*

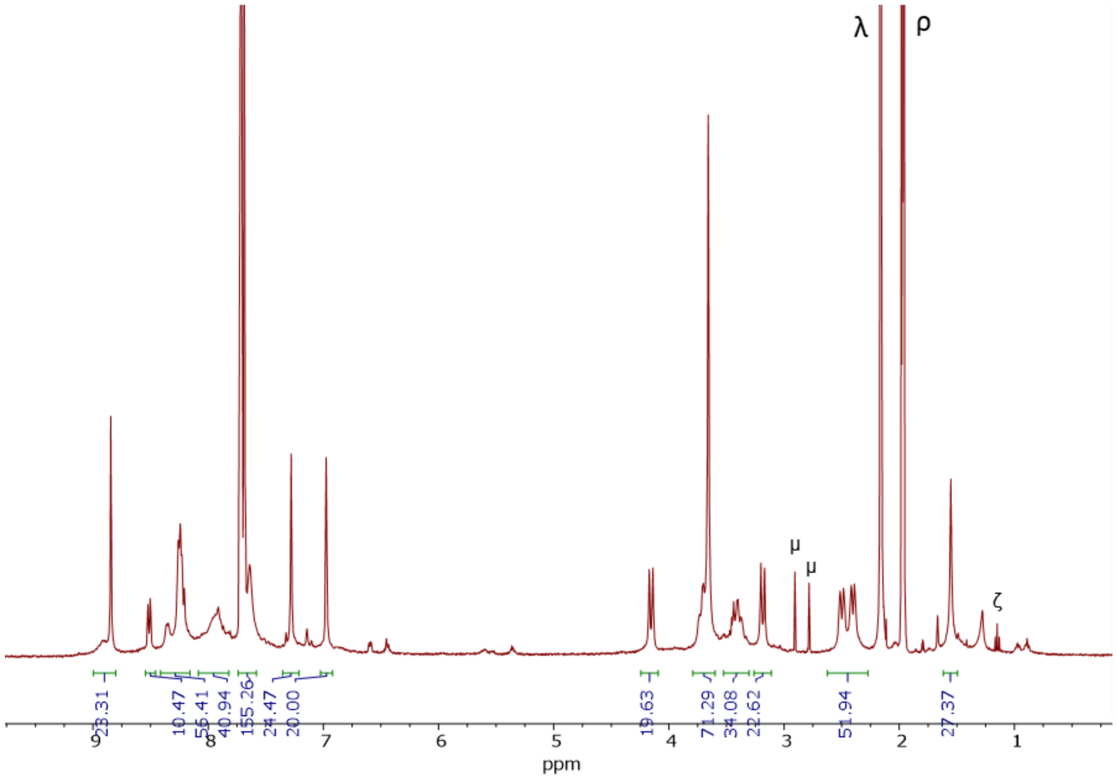

*Figure S.95. $^1$H-NMR spectrum of $PC_{61}BM\subset[10]CPP\subset$**1f**$\cdot(BArF)_8$. Experiment performed in $CDCl_3$ at 298K (400 MHz). μ: DMF, λ: $H_2O$, ρ: $CH_3CN$. ζ: diethyl ether,*

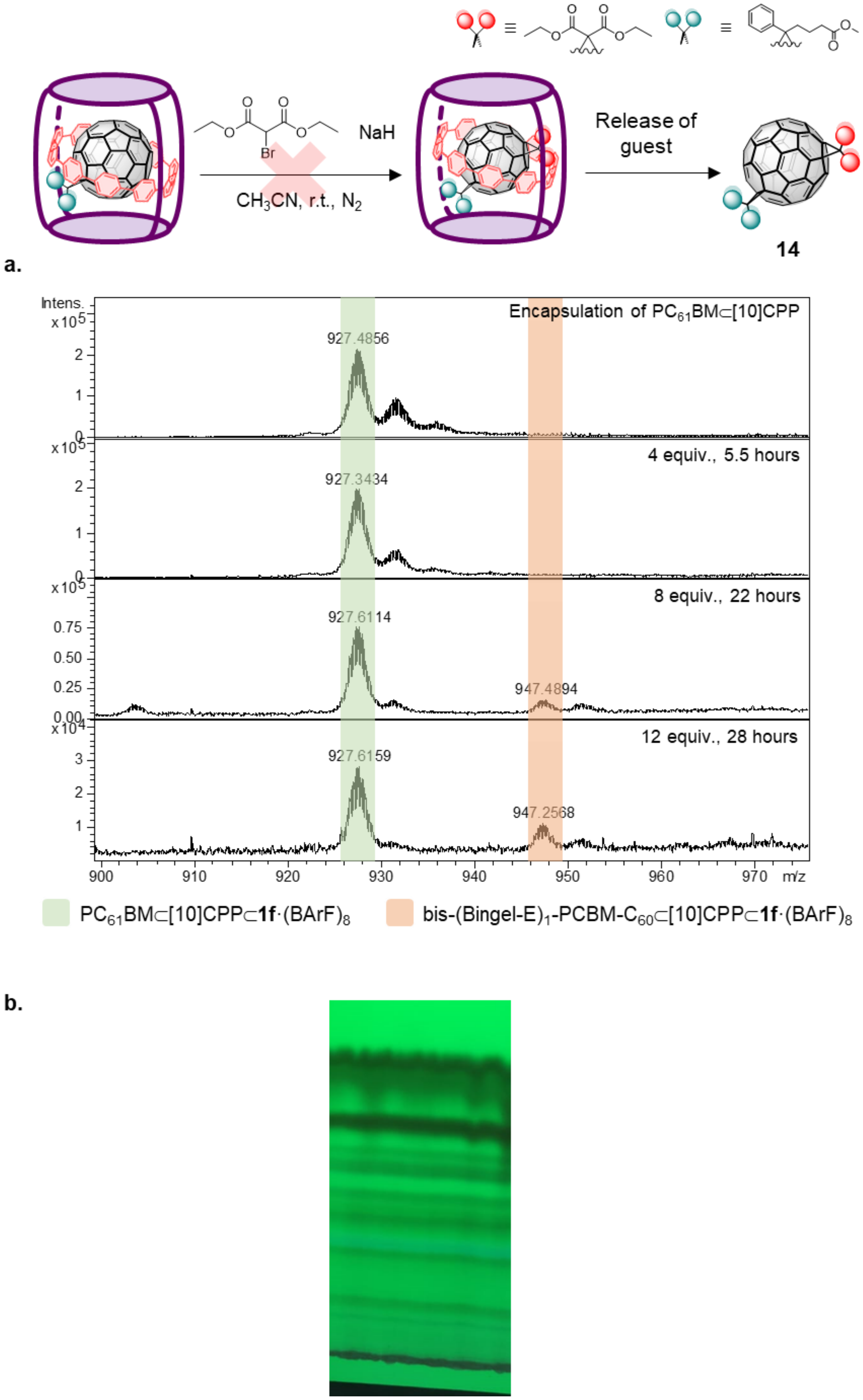

*Figure S.96. a) HR-ESI-MS monitoring for the synthesis of hetero-bis-adducts* ***14*** *through Bingel reaction (with diethyl bromomalonate) starting from* $PC_{61}BM\subset[10]CPP\subset$***1f***$\cdot(BArF)_8$*. b) TLC preparative for the purification of hetero-bis-adducts* ***14*** *after Bingel reaction (with diethyl bromomalonate) starting from* $PC_{61}BM\subset[10]CPP\subset$***1f***$\cdot(BArF)_8$*.*

# Annex Chapter VI

## *Annex VI.1 Experimental procedures*

### *Annex VI.1.1 1st strategy: olefin metathesis*

*Synthesis and characterization of bromomalonate **15** (by Prof. Max von Delius and MSc Fabian Steudel)*

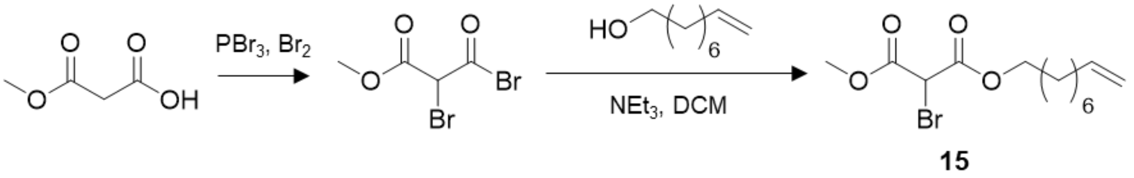

*Scheme S.21. Synthesis of bromomalonate **15**.*

$Br_2$ (5.0 mmol, 2.6 equiv.) was added to a mixture of mono-methyl malonate (1.9 mmol, 1.0 equiv.) and $PBr_3$ (77 mmol, 0.40 equiv.) and stirred for 4 h at 100 °C. The excess of bromine was removed under reduced pressure. The crude reaction was taken up with 2.0 mL DCM and added to a mixture of triethylamine (2.0 mmol, 1.0 equiv.) and 8-nonel-1-ol (0.75 mmol, 0.40 equiv.) dissolved in 48 mL DCM. The reaction was stirred for 1 h at 0 °C. Then, the reaction crude was first washed with 20 mL aqueous $Na_2S_2O_3$-Solution, then extracted twice with 20 mL DCM and washed with 20 mL $NaCl_{aq}$. The product was purified via flash column chromatography using a mixture of petroleum ether and ethyl acetate (19:1). Yield: 45%

**$^1$H-NMR** (400 MHz, $CDCl_3$) δ ppm: 5.80 (qt, *J* = 6.69 Hz, *J* = 10.25 Hz, 1H, -CH=), 5.01 – 4.91 (m, 2H, $=CH_2$), 4.84 (s, 1H, $H_{Malonate}$), 4.22 (t, *J* = 6.70 Hz, 2H, $-O-CH_2-$), 3.84 (s, 3H, $-CH_3$), 2.04 (qt, *J* = 1.52 Hz, *J* = 6.84 Hz, 2H, $-CH_2-$), 1.71 – 1.63 (m, 2H, $-CH_2-$), 1.41 – 1.27 (m, 8H, $-CH_2-$).

*Synthesis and characterization of trans-3-bis-alkene-$C_{60}$ (**16**)*

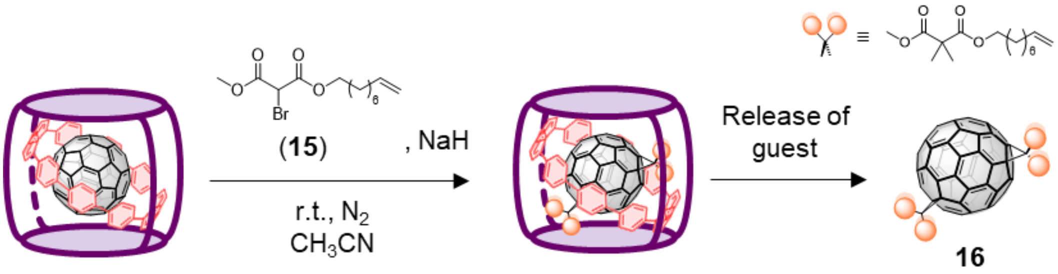

*Scheme S.22. Synthesis of trans-3-bis-alkene-$C_{60}$ (**16**).*

Two stock solutions of the corresponding bromomalonate and sodium hydride in dry acetonitrile were prepared. Then, 7.5 equivalents of bromomalonate **15** and NaH from these solutions were added sequentially to a solution of $C_{60}\subset$[10]CPP$\subset$**1d**·(BArF)$_8$ (8.3 mg, 0.68 µmol) in 0.7 ml of dry acetonitrile ($10^{-3}$ M) at room temperature. After monitoring the reaction by HR-ESI-MS for 23 hours, the crude was filtered and the solvent was removed under a $N_2$ flow. Exchange with 5 equivalents of $C_{60}$ was performed to release bis-adducts from [10]CPP in 1.5 ml of a mixture or acetonitrile and toluene (1:9). After stirring overnight at room temperature, solvent was removed under reduced pressure and **15** was extracted with toluene. Derivatives were isolated by a preparative TLC using toluene as eluent.

**HR-ESI-MS** of **16**$\subset$[10]CPP$\subset$**1d**·(BArF)$_8$ ($CH_3CN$), m/z: calc. for [**16**$\subset$[10]CPP$\subset$**1d**]$^{8+}$ 911.6166, observed 911.6019; calc. for [**16**$\subset$[10]CPP$\subset$**1d**·(BArF)]$^{7+}$ 1165.2800, observed 1165.2686; calc. for [**16**$\subset$[10]CPP$\subset$**1d**·(BArF)$_2$]$^{6+}$ 1503.3379, observed 1503.3269.

**MALDI-MS** (DCTB, (+)), m/z: calc. for [**16**]$^+$ 1200.272, observed 1200.271.

### *Synthesis and characterization of e,e-bis-alkene-$C_{60}$ (**17**)*

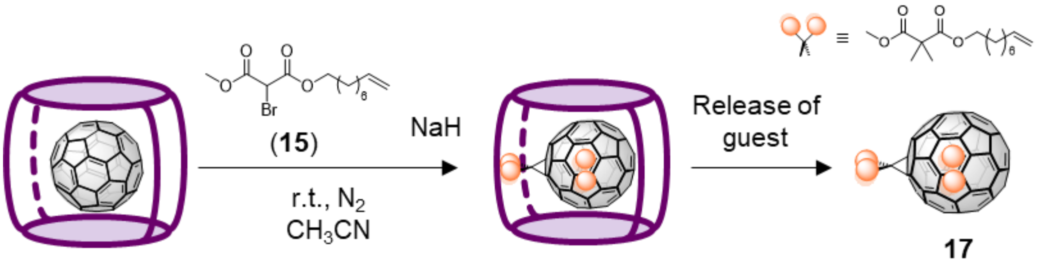

*Scheme S.23. Synthesis of e,e-bis-alkene-$C_{60}$ (**17**).*

Two stock solutions of the corresponding bromomalonate and sodium hydride in dry acetonitrile were prepared. Then, 4.5 equivalents of bromomalonate **15** and NaH from these solutions were added sequentially to a solution of $C_{60}\subset$**1b**·(BArF)$_8$ (42.7 mg, 3.5 µmol) in 3.5 ml of dry acetonitrile ($10^{-3}$ M) at room temperature. After monitoring the reaction by HR-ESI-MS for 21 hours, the crude was filtered and the solvent was removed under a $N_2$ flow. The guests were released from the nanocapsule by decomposition with the addition of 20 equivalents of triflic acid in acetonitrile. Then, the solvent was removed under reduced pressure and extractions with toluene were performed. Derivatives were isolated by a preparative TLC using toluene as eluent.

**HR-ESI-MS** of **17**$\subset$**1b**·(BArF)$_8$ (CH$_3$CN), m/z: calc. for [**17**$\subset$**1b**]$^{8+}$ 792.5721, observed 792.4514; calc. for [**17**$\subset$**1b**·(BArF)]$^{7+}$ 1029.0920, observed 1029.2383; calc. for [**17**$\subset$**1b**·(BArF)$_2$]$^{6+}$ 1344.4519, observed 1344.4606.

**MALDI-MS** (DCTB, (+)), m/z: calc. for [**17**]$^+$ 1200.272, observed 1199.872; calc. for [**17** + Na$^+$]$^+$ 1223.262, observed 1222.840.

*Synthesis and characterization of mono-alkene-C$_{60}$ (**18**)*

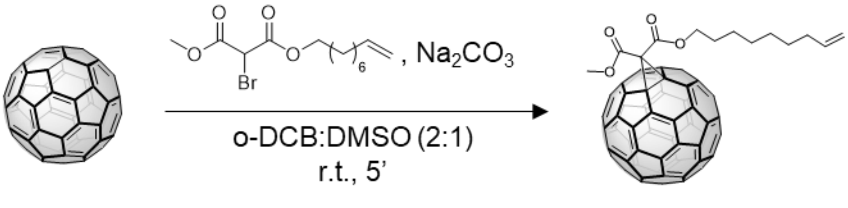

**18**

*Scheme S.24. Synthesis of mono-alkene-C$_{60}$ (**18**).*

A solution of C$_{60}$ (40 mg) was prepared in 3 ml of *o*-DCB. Then, 26.8 mg of bromomalonate **15** (1.5 equivalents) were added. A suspension of Na$_2$CO$_3$ (47 mg, 8 equivalents) in 1.5 ml of DMSO was prepared. The first solution was added to the second solution and it was stirred for 5 minutes. The mixture was added directly to a column to stop the reaction and to separate **18** from C$_{60}$ and other derivatives via flash column chromatography. First, hexane was used to elute the remaining C$_{60}$ and then hexane:ethyl acetate (20:1) was used to elute **18**.

Yield: 51%

**$^1$H-NMR** (400 MHz, CDCl$_3$) δ ppm: 5.80 (qt, *J* = 10.2, 6.7 Hz, 1H, -CH=), 5.05 – 4.50 (m, 2H, =CH$_2$), 4.50 (t, *J* = 6.5 Hz, 2H, -O-CH$_2$-), 4.11 (s, 3H, -CH$_3$), 2.06 (qt, *J* = 1.5 Hz, $_3J$ = 6.8 Hz, 2H, -CH$_2$-), 1.88 – 1.81 (m, 2H, -CH$_2$-), 1.51 – 1.18 (m, 8H, -CH$_2$-).

*Olefin metathesis using mono-adduct **18** without nanocapsule*

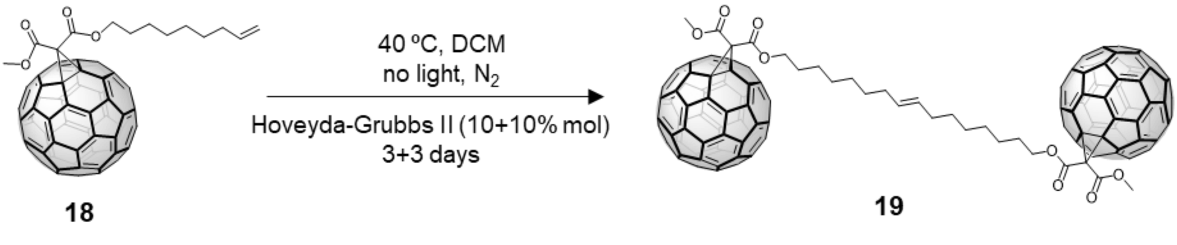

*Scheme S.25. Olefin metathesis using mono-adduct **18** to give product **1** in DCM.*

To a solution of mono-adduct **18** (5.45 mg, 5.64 μmols) in dichloromethane, 10% mol of Hoveyda-Grubbs II (M720) catalyst was added from a stock solution in DCM. The reaction was stirred under a $N_2$ atmosphere for 3 days at 40ºC. Then, a 10% mol more of the same catalyst was added and it was stirred for 3 days more. The reaction was prevented from light. The solvent was evaporated under reduced pressure and a column chromatography was carried out to purify **19** using first a mixture of petroleum ether and ethyl acetate (9:1) to elute the remaining reactants and byproducts and, then, dichloromethane to elute **19**.

**$^1$H-NMR** (400 MHz, $CDCl_3$) δ ppm: 5.31 – 5.29 (m, 2H, -C*H*=C*H*-), 4.43 (t, $J$ = 6.5 Hz, 4H, -O-$CH_2$-), 4.02 (s, 6H, -$CH_3$), 1.80 – 1.73 (m, $J$ = 6.6 Hz, 4H, -$CH_2$-), 1.41 – 1.16 (m, 20H, -$CH_2$-).

**MALDI-MS** (DCTB, (+)), m/z: calc. for [**19**]$^+$ 1893.244, observed 1893.246.

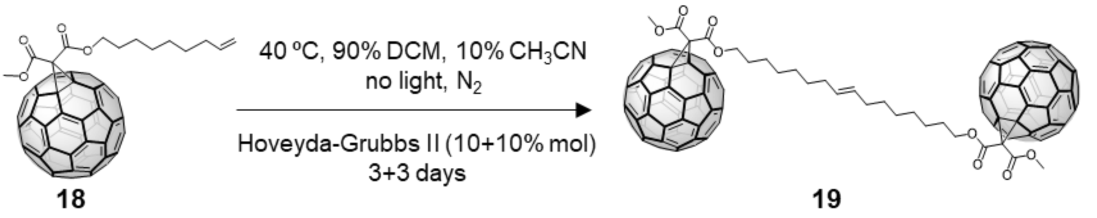

*Scheme S.26. Olefin metathesis using mono-adduct **18** to give product **19** in DCM:$CH_3CN$ 9:1.*

To a solution of mono-adduct **18** (4.6 mg, 4.8 μmols) in 0.97 ml of a mixture of DCM:$CH_3CN$ (9:1), 10% mol of Hoveyda-Grubbs II (M720) catalyst was added from a stock solution in DCM. The reaction was stirred under a $N_2$ atmosphere for 3 days at 40ºC. Then, a 10% mol more of the same catalyst was added and it was stirred for 3 days more. The reaction was prevented from light. The solvent was evaporated under reduced pressure.

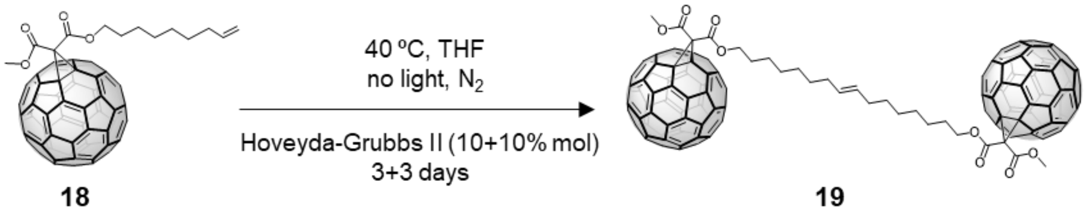

*Scheme S.27. Olefin metathesis using mono-adduct **18** to give product **19** in THF.*

To a solution of mono-adduct **18** (4.9 mg, 5.1 μmols) in tetrahydrofuran. 10% mol of Hoveyda-Grubbs II (M720) catalyst was added from a stock solution in DCM. The reaction was stirred under a $N_2$ atmosphere for 3 days at 40ºC. Then, a 10% mol more of the same catalyst was added and it was stirred for 3 days more. The reaction was prevented from light. The solvent was evaporated under reduced pressure.

### *Olefin metathesis using **18⊂1b**·(BArF)$_8$ complex*

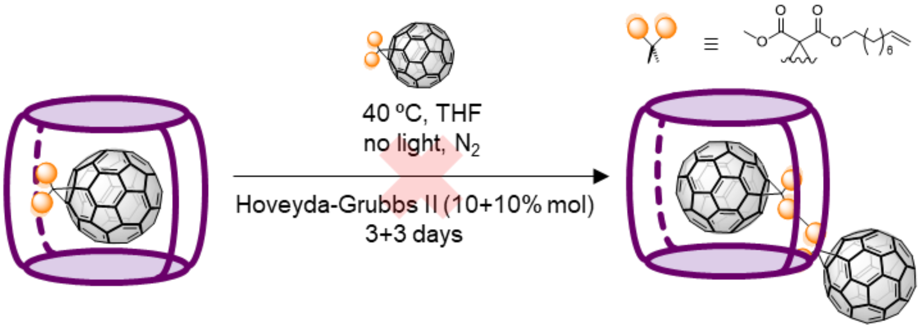

**18⊂1b**·(BArF)$_8$ **19⊂1b**·(BArF)$_8$

*Scheme S.28. Olefin metathesis using **18⊂1b**·(BArF)$_8$ to achieve **19⊂1b**·(BArF)$_8$.*

A solution of **18⊂1b**·(BArF)$_8$ (5.54 mg, 0.46 µmols) in 0.3 ml of dry acetonitrile was prepared in a concentration of $1.5\cdot10^{-3}$ M. Stock solutions of Hoveyda-Grubbs (II) (M720) catalyst and **18** in THF were also prepared. 10% mol catalyst and 1 equivalent of **18** was added to **18⊂1d**·(BArF)$_8$ and it was stirred for 3 days at 40ºC. Then, 10% mol more of catalyst and 3 equivalents more of **18** were added again to the mixture and it was stirred 3 days more at the same temperature. Then, the crude was filtered and the solvent was evaporated under reduced pressure.

### *Synthesis [2]catenane (**20**) through olefin metathesis*

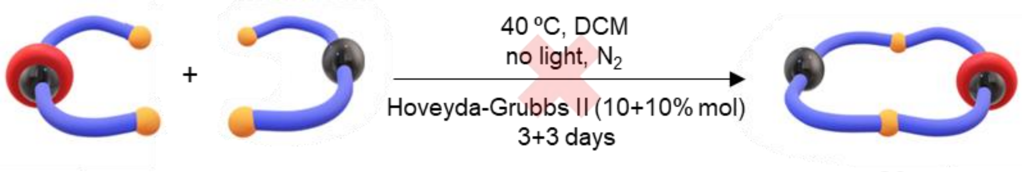

**16⊂**[10]CPP **17** **20**

*Scheme S.29. Synthesis [2]catenane (**20**) through olefin metathesis.*

1.1 mg (0.55 µmols) of *trans*-3-bis-alkene-$C_{60}$⊂[10]CPP were mixed with 1.1 mg (0.91µmols) of *e,e*-bis-alkene-$C_{60}$ in 1.46 ml of DCM ($10^{-3}$ M). Then, a stock solution of Hoveyda-Grubbs II (M720) catalyst was prepared and 10% mol was added to the mixture under $N_2$ atmosphere and at 40ºC and it was stirred for 3 days. Then, 10% mol more of catalyst was added and it was stirred for 3 days more. The solvent was evaporated under reduced pressure.

*Control experiment of olefin metathesis using 4-tert-butylstyrene*

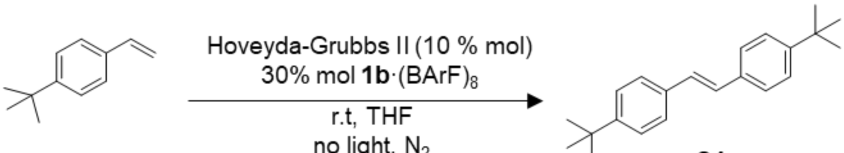

**21**

*Scheme S.30. Control experiment of olefin metathesis using 4-tert-butylstyrene and 30% mol of* ***1b****·(BArF)$_8$ nanocapsule.*

1.1 µl of 4-*tert*-butylsteryne was dissolved in 4 ml of THF and it was divided into two vials (1.53 mmol). A stock solution of Hoveyda-Grubbs II (M720) catalyst was prepared in THF. In the first vial, 10% mol of catalyst and 11.8 mg (30% mol) of **1b**·(BArF)$_8$ were added and the reaction was stirred at room temperature for 3 days. In the second vial, only 10% mol of catalyst was added and it was stirred at the same conditions. After 3 days, the solvent was evaporated under reduced pressure.

### *Annex VI.1.2 2nd strategy: CuAAc*

*Synthesis and characterization of bromomalonate* ***22*** *(by Prof. Max von Delius and MSc Fabian Steudel)*

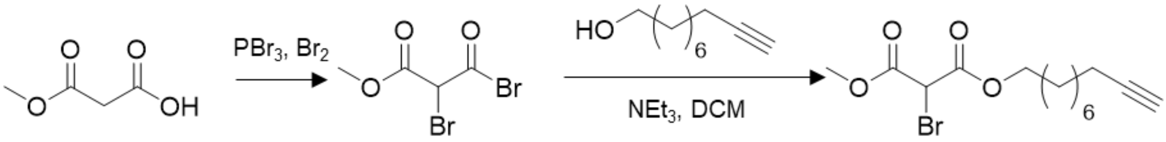

**22**

*Scheme S.31. Synthesis of bromomalonate* ***22****.*

In a heat-dried Schlenk flask a mixture of methyl hydrogen malonate (0.35 mL, 0.39 g, 3.1 mmol, 4.6 equiv.) and phosphorous tribromide (0.12 mL, 0.34 g, 1.3 mmol, 1.9 equiv.) was heated to 100 °C under argon atmosphere. Bromine (0.40 mL, 1.2 g, 7.8 mmol, 11 equiv.) was added dropwise, and the reaction mixture was stirred at 100 °C for 4 h. Excess bromine and hydrogen bromide was removed under reduced pressure. The reaction mixture was diluted with anhydrous THF (1 mL) and was added dropwise to a solution of 9-decyn-1-ol (0.12 mL, 0.10 g, 0.67 mmol, 1.0 equiv.) and triethylamine (0.30 mL, 0.22 g, 2.2 mmol, 3.2 equiv.) in anhydrous THF (12 mL). The reaction mixture was stirred for 1 h at 0 °C and subsequently quenched by addition of saturated aqueous thiosulfate solution (10 mL). Water was added and the aqueous phase was extracted with DCM (3 x 30 mL). The combined organic phases were dried over magnesium sulphate, filtered and evaporated. The compound was purified by flash column chromatography (petroleum ether/ethyl acetate 93:7). Yield: 69%

**$^1$H-NMR** (400 MHz, $CDCl_3$) δ ppm: 4.84 (s, 1H, $H_{Malonate}$), 4.22 (t, *J* = 6.69 Hz, 2H, -O-C*H*$_2$-), 3.83 (s, 3H, -O-$CH_3$), 2.17 (td, *J* = 6.99 Hz, *J* = 2.63 Hz, 2H, -$CH_2$-C≡C-), 1.93 (t, *J* = 2.66 Hz, 1H, -C≡C-*H*), 1.70 – 1.63 (m, 2H, -$CH_2$-), 1.55 – 1.48 (m, 2H, -$CH_2$-), 1.42 – 1.28 (m, 8H, -$CH_2$-).

*Synthesis and characterization of bromomalonate* ***23*** *(by Prof. Max von Delius and MSc Fabian Steudel)*

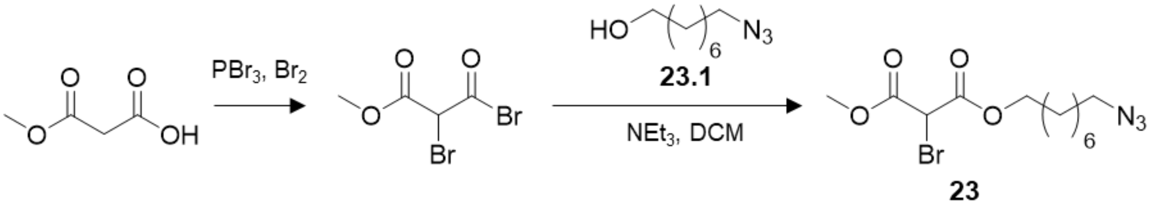

*Scheme S.32. Synthesis of bromomalonate* ***23****.*

Synthesis of **23.1**:

To a solution of 8-bromooctan-1-ol (0.20 mL, 0.24 g, 1.1 mmol, 1.0 equiv.) in DMF (4 mL) was added sodium azide (0.20 g, 3.1 mmol, 2.7 equiv.) at 0 °C. The reaction mixture was slowly heated to 85 °C and stirred at this temperature for 21 h. The reaction mixture was poured into ice-water (30 mL) and extracted with ethyl acetate (3 x 30 mL). The combined organic phases were dried over magnesium sulfate. Yield: 88%

**$^1$H-NMR** (400 MHz, $CDCl_3$) δ ppm: 3.63 (t, *J* = 6.61 Hz, 2H, -O-$CH_2$-), 3.25 (t, *J* = 6.95 Hz, 2H, $N_3$-$CH_2$-), 1.63 – 1.53 (m, 4H, -$CH_2$-), 1.40 – 1.30 (m, 8H, -$CH_2$-).

Synthesis of **23**:

In a heat-dried Schlenk flask a mixture of methyl hydrogen malonate (0.35 mL, 0.39 g, 3.1 mmol, 4.0 equiv.) and phosporous tribromide (0.12 mL, 0.34 g, 1.3 mmol, 1.6 equiv.) was heated to 100 °C under argon atmosphere. Bromine (0.42 mL, 1.3 g, 8.2 mmol, 10 equiv.) was added dropwise, and the reaction mixture was stirred at 100 °C for 4 h. Excess bromine and hydrogen bromide was removed under reduced pressure. The reaction mixture was diluted with anhydrous DCM (1 mL) and was added dropwise to a solution of 8-azidooctan-1-ol **23.1** (0.13 g, 0.78 mmol, 1.0 equiv.) and triethylamine (0.30 mL, 0.22 g, 2.2 mmol, 2.8 equiv.) in anhydrous DCM (6.5 mL). The reaction mixture was stirred for 1 h at 0 °C and subsequently quenched by addition of saturated aqueous thiosulfate solution (10 mL). Water was added and the aqueous phase was extracted with DCM (3 x 30 mL). The combined organic phases were dried over magnesium sulfate, filtered and evaporated. The compound was purified by flash column chromatography (petroleum ether:ethyl acetate 19:1). Yield: 30%

**$^1$H-NMR** (400 MHz, $CDCl_3$) δ ppm: 4.85 (s, 1H, $H_{Malonate}$), 4.23 (t, *J* = 6.69 Hz, 2H, -O-$CH_2$-), 3.84 (s, 3H, -O-$CH_3$), 3.28 (t, *J* = 6.42 Hz, 2H, $N_3$-$CH_2$-), 1.71 – 1.64 (m, 2H, -$CH_2$-), 1.63 – 1.58 (m, 2H, -$CH_2$-), 1.40 – 1.28 (m, 8H, -$CH_2$-).

### *Synthesis and characterization of trans-3-bis-alkyne-$C_{60}$ (**24**)*

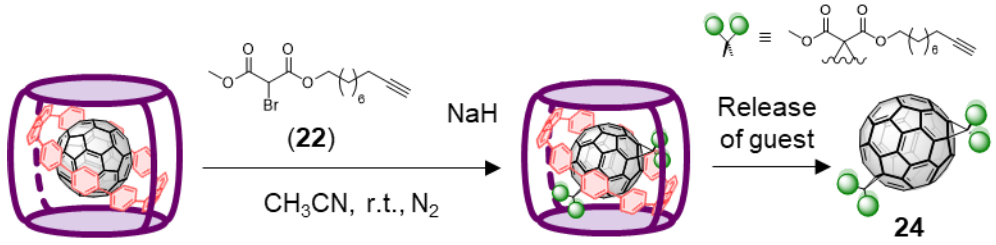

*Scheme S.33. Synthesis of trans-3-bis-alkyne-$C_{60}$ (**24**).*

Two stock solutions of the corresponding bromomalonate and sodium hydride in dry acetonitrile were prepared. Then, 20 equivalents of bromomalonate **22** and NaH from these solutions were added sequentially to a solution of $C_{60}$⊂[10]CPP⊂**1d**·(BArF)$_8$ (9.7 mg, 0.79 μmol) in 0.8 ml of dry acetonitrile ($10^{-3}$ M) at room temperature. After monitoring the reaction by HR-ESI-MS for 42 hours, the crude was filtered and the solvent was removed under a $N_2$ flow. Exchange with 5 equivalents of $C_{60}$ was performed to release bis-adducts from [10]CPP in 3 ml of a mixture or acetonitrile and toluene (1:9). After stirring overnight at room temperature, solvent was removed under reduced pressure and **24** was extracted with toluene. Derivatives were isolated by a preparative TLC using toluene as eluent.

**HR-ESI-MS** of **24**⊂[10]CPP⊂**1d**·(BArF)$_8$ ($CH_3CN$), m/z: calc. for [**24**⊂[10]CPP⊂**1d**]$^{8+}$ 914.6116, observed 914.8477; calc. for [**24**⊂[10]CPP⊂**1d**·(BArF)]$^{7+}$ 1168.7086, observed 1168.5534; calc. for [**24**⊂[10]CPP⊂**1d**·(BArF)$_2$]$^{6+}$ 1507.3379, observed 1507.1639.

**MALDI-MS** (DCTB, (+)), m/z: calc. for [**24**]$^+$ 1222.257, observed 1224.204; calc. for [**24**+$Na^+$]$^+$ 1245.246, observed 1247.192.

### *Synthesis and characterization of bis-azide-$C_{60}$ (**25**)*

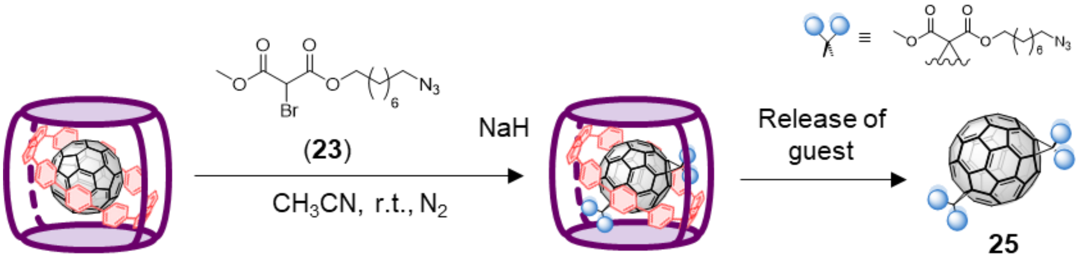

*Scheme S.34. Synthesis of bis-azide-$C_{60}$ (**25**).*

Two stock solutions of the corresponding bromomalonate and sodium hydride in dry acetonitrile were prepared. Then, 25 equivalents of bromomalonate **23** and 13 equivalents of NaH from these solutions were added sequentially to a solution of $C_{60}$⊂[10]CPP⊂**1d**·$(BArF)_8$ (6.3 mg, 0.51 μmol) in 0.5 ml of dry acetonitrile ($10^{-3}$ M) at room temperature. After monitoring the reaction by HR-ESI-MS for 39 hours, the crude was filtered and the solvent was removed under a $N_2$ flow. Exchange with 5 equivalents of $C_{60}$ was performed to release bis-adducts from [10]CPP in 3 ml of a mixture or acetonitrile and toluene (1:9). After stirring overnight at room temperature, solvent was removed under reduced pressure and **25** was extracted by extractions with toluene. Derivatives were isolated by a preparative TLC using toluene as eluent.

**HR-ESI-MS** of **25**⊂[10]CPP⊂**1d**·$(BArF)_8$ ($CH_3CN$), m/z: calc. for [**25**⊂[10]CPP⊂**1d**]$^{8+}$ 918.8619, observed 918.7317.

### *Synthesis and characterization of mono-alkyne-$C_{60}$ (**26**)*

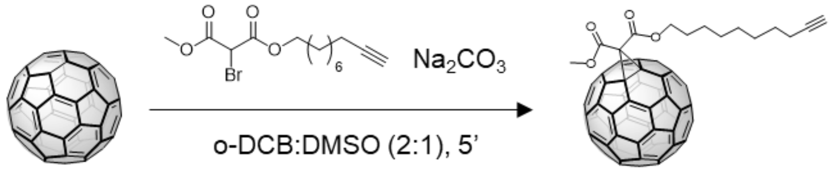

**26**

*Scheme S.35. Synthesis of mono-alkyne-$C_{60}$ (**26**).*

A solution of $C_{60}$ (40 mg) was prepared in 3 ml of o-DCB. Then, 27.7 mg of the bromomalonate **22** (1.5 equivalents) were added. A suspension of $Na_2CO_3$ (47 mg, 8 equivalents) in 1.5 ml of DMSO was prepared. The first solution was added to the second solution and it was stirred for 5 minutes. The mixture was added directly to a column to stop the reaction and to separate **26** from $C_{60}$ and other derivatives via column chromatography. First, hexane was used to elute the remaining $C_{60}$ and then hexane:ethyl acetate (20:1) was used to elute **26**. Yield: 58%

**$^1$H-NMR** (400 MHz, $CDCl_3$) δ ppm: 4.50 (t, *J* = 6.5 Hz, 2H, -O-$CH_2$-), 4.10 (s, 3H, -O-$CH_3$), 2.19 (td, *J* = 7.0, 2.6 Hz, 2H, -$CH_2$-C≡C-), 1.94 (t, *J* = 2.6 Hz, 1H, -C≡C-H), 1.88-1.81 (m, 1H, 2H, -$CH_2$-), 1.53-1.33 (m, 10H).

**MALDI-MS** (DCTB, (+)), m/z: calc. for [**26**]$^+$ 972.136, observed 971.958.

*Synthesis and characterization of mono-azide-$C_{60}$ (**27**)*

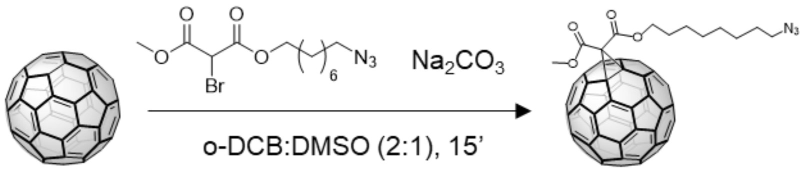

**27**

*Scheme S.36. Synthesis of mono-azide-$C_{60}$ (**27**).*

A solution of $C_{60}$ (40 mg) was prepared in 3 ml of o-DCB. Then, 29.2 mg of the bromomalonate **23** (1.5 equivalents) were added. A suspension of $Na_2CO_3$ (47 mg, 8 equivalents) in 1.5 ml of DMSO was prepared. The first solution was added to the second solution and it was stirred for 5 minutes. The mixture was added directly to a column to stop the reaction and to separate **27** from $C_{60}$ and other derivatives via column chromatography. First, hexane was used to elute the remaining $C_{60}$ and then hexane:ethyl acetate (20:1) was used to elute **27**. Yield: 47%

**$^1$H-NMR** (400 MHz, $CDCl_3$) δ ppm: 4.51 (t, *J* = 6.5 Hz, 2H, -O-$CH_2$-), 4.10 (s, 3H, -O-$CH_3$), 3.26 (t, *J* = 6.9 Hz, 2H, $N_3$-$CH_2$-), 1.88 – 1.81 (m, 2H, -$CH_2$-), 1.63 – 1.57 (m, 2H, -$CH_2$-), 1.44 – 1.36 (s, 8H, -$CH_2$-).

**MALDI-MS** (DCTB, (+)), m/z: calc. for [**27**]$^+$ 989.138, observed 989.446

*CuAAc using mono-adducts **26** and **27** (without nanocapsule)*

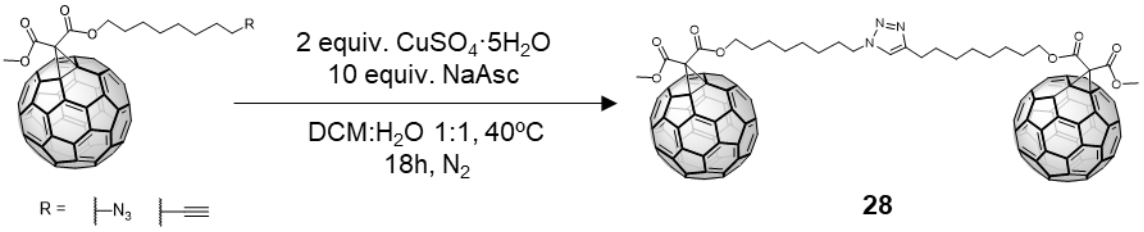

**28**

**27** **26**

*Scheme S.37. CuAAc using mono-adducts **26** and **27** without nanocapsule.*

1.83 mg (1.85 µmol) of mono-adduct **27** and 2.16 mg (2.22 µmol) of mono-adduct **26** were dissolved in 2 ml of DCM. Another solution of 0.92 mg (2 equivalents) of $CuSO_4·5H_2O$ was prepared in Milli-Q water and 3.67 mg (10 equivalents) of NaAsc was added under $N_2$ atmosphere. Organic phase was poured into the aqueous phase and the mixture was vigorously stirred overnight at 40ºC under $N_2$ atmosphere. When both phases were separated, organic phase was extracted and the solvent was evaporated under reduced pressure.

**MALDI-MS** (DCTB, (+)), m/z: calc. for [**28**]$^+$ 1962.277, observed 1962.744

### *CuAAc using **27**⊂**1b**·(BArF)$_8$ and mono-adduct **26***

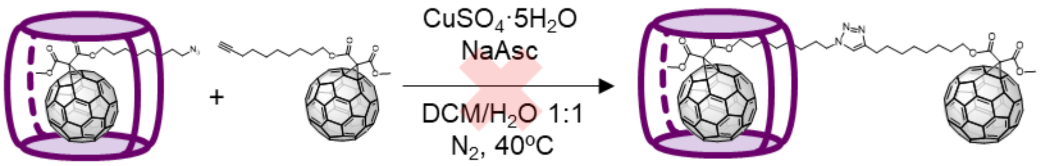

**27**⊂**1b**·(BArF)$_8$ **26** **28**⊂**1b**·(BArF)$_8$

*Scheme S.38. CuAAc using **27**⊂**1b**·(BArF)$_8$ and mono-adduct **26** to give **28**⊂**1b**·(BArF)$_8$.*

A solution of **27**⊂**1b**·(BArF)$_8$ (8.65 mg, 0.66 µmols, 1 equivalent) and 0.77 mg of **26** (0.79 µmols, 1.2 equivalents) in 2 ml of DCM were prepared. Stock solutions of $CuSO_4·5H_2O$ (7.61 mg / 2ml) and sodium ascorbate (12.94 mg / 2ml) in Milli-Q water were also prepared. Then, 2 equivalents of $CuSO_4·5H_2O$ and 10 equivalents of NaAsc were dissolved in 2 ml of Milli-Q water under a $N_2$ atmosphere. This aqueous phase was added to the organic phase and it was vigorously stirred 16 hours at 40ºC under a $N_2$ atmosphere. 2 equivalents of $CuSO_4·5H_2O$ and 10 equivalents of NaAsc were added again to the crude and it was stirred for 17 hours more. When both phases were separated, organic phase was extracted and the solvent was evaporated under reduced pressure.

### *Stability test of **27**⊂**1b**·(BArF)$_8$*

A solution of **27**⊂**1b**·(BArF)$_8$ (4.75 mg, 0.37 µmols) in 2 ml of DCM was prepared under N2 atmosphere. 2 ml of Milli-Q water was added and the mixture was vigorously stirred for 18 hours at 40ºC. After this time, 2 equivalents of $CuSO_4·5H_2O$ and 10 equivalents of NaAsc were added from stock solutions in Milli-Q water (7.61 mg / 2ml and 12.94 mg / 2m, respectively) and the mixture was stirred for 18 hours more. When both phases were separated, organic phase was extracted and the solvent was evaporated under reduced pressure.

### *Annex VI.1.3 3rd strategy: Bingel-Hirsch reaction*

*Synthesis and characterization of bromomalonate* ***29*** *(by Prof. Max von Delius and MSc Fabian Steudel)*

Synthesis of **29.1**

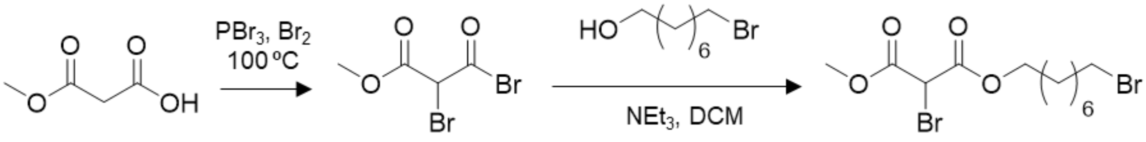

**29.1**

*Scheme S.39. Synthesis of bromomalonate* ***29.1*** *for the synthesis of bromomalonate* ***29****.*

In a heat-dried Schlenk flask a mixture of methyl hydrogen malonate (0.35 mL, 0.39 g, 3.1 mmol, 4.6 equiv.) and phosphorous tribromide (0.12 mL, 0.34 g, 1.3 mmol, 1.9 equiv.) was heated to 100 °C under argon atmosphere. Bromine (0.40 mL, 1.2 g, 7.8 mmol, 12 equiv.) was added dropwise, and the reaction mixture was stirred at 100 °C for 4 h. Excess bromine and hydrogen bromide was removed under reduced pressure. The reaction mixture was diluted with anhydrous THF (1 mL) and was added dropwise to a solution of 8-bromooctan-1-ol (95 µL, 0.14 g, 0.67 mmol, 1.0 equiv.) and triethylamine (0.30 mL, 0.22 g, 2.2 mmol, 3.2 equiv.) in anhydrous THF (12 mL). The reaction mixture was stirred for 1 h at 0 °C and subsequently quenched by addition of saturated aqueous thiosulfate solution (10 mL). Water was added and the aqueous phase was extracted with DCM (6 x 30 mL). The combined organic phases were dried over magnesium sulfate, filtered and evaporated. The compound was purified by flash column chromatography (petroleum ether/ethyl acetate 93:7). Yield: 62%

**$^1$H-NMR** (400 MHz, $CDCl_3$) δ ppm: 4.85 (s, 1H, $H_{Malonate}$), 4.22 (t, *J* = 6.63 Hz, 2H, $-O-CH_2-$), 3.84 (s, 3H, $-O-CH_3$), 3.40 (t, *J* = 6.82 Hz, 2H, $Br-CH_2-$), 1.89 – 1.81 (m, 2H, $-CH_2-$), 1.71 – 1.64 (m, 2H, $-CH_2-$), 1.47 – 1.29 (m, 6H, $-CH_2-$).

Synthesis of **29.2**

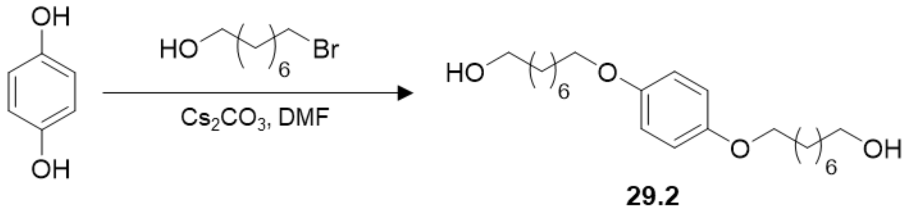

**29.2**

*Scheme S.40. Synthesis of compound **29.2** for the synthesis of bromomalonate **29**.*

In a 100 mL pressure flask a solution of hydroquinone (1.0 g, 9.1 mmol, 1.0 equiv.) in DMF (100 mL) was degassed with argon for 10 min and cesium carbonate (16 g, 50 mmol, 2.6 equiv.) was added. The resulting orange solution was stirred and degassed for ten more minutes under inert atmosphere before dropwise addition of 8-bromooctan-1-ol (4.3 g, 3.5 mL, 19 mmol, 2.1 equiv.). The reaction mixture was stirred at 120 °C for 22 h before the reaction was cooled to room temperature and poured into stirred 1N HCl (700 mL) solution. A colourless precipitate was filtered off, dried under vacuum, and recrystallized from DCM at -32 °C. Yield: 83%

**$^1$H-NMR** (400 MHz, CDCl$_3$) δ ppm: 6.81 (s, 4H, H$_{aryl}$), 3.89 (t, *J* = 6.6 Hz, 4H, -C*H*$_2$-O-Ph-), 3.64 (t, *J* = 6.6 Hz, 4H, -C*H*$_2$-OH), 1.75 (dq, *J* = 7.9, 6.6 Hz, 4H, -CH$_2$-), 1.61 – 1.53 (m, 4H, -CH$_2$-), 1.49 – 1.40 (m, 4H, -CH$_2$-), 1.36 (m, 12H, -CH$_2$-).

Synthesis of **29.3**

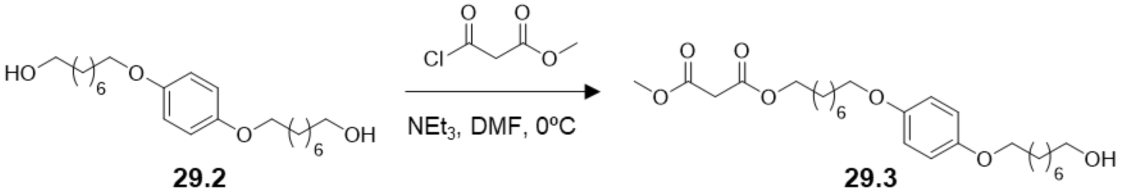

**29.2** **29.3**

*Scheme S.41. Synthesis of malonate **29.3** for the synthesis of bromomalonate **29**.*

To a solution of **29.2** (1.5 g, 4.1 mmol, 1.0 equiv.) and triethylamine (2.5 g, 3.5 mL, 25 mmol, 4.3 equiv.) in DMF (50 mL) was added methyl malonyl chloride (0.79 g, 0.62 mL, 5.8 mmol, 1.4 equiv.) at 0 °C and the reaction was stirred under inert atmosphere for 16 h. The reaction was quenched by addition of water (50 mL) and 2N HCl (10 mL). The aqueous phase was extracted with DCM (4 x 100 mL) and the combined organic phases were dried over magnesium sulphate, filtered and evaporated. The pure compound was obtained after purification with flash column chromatography (petroleum ether/acetone 3:1). Yield: 19%

**$^1$H-NMR** (400 MHz, $CDCl_3$) δ ppm: 6.80 (s, 4H, $H_{Aryl}$), 4.13 (t, $J$ = 6.7 Hz, 2H, -C$H_2$OOC-), 3.88 (t, $J$ = 6.5 Hz, 4H, -$CH_2$-Ph-), 3.73 (s, 3H, -$CH_3$), 3.62 (t, $J$ = 6.6 Hz, 2H, -C$H_2$-OH), 3.37 (s, 2H, $H_{Malonate}$), 1.77 – 1.69 (m, 4H, -$CH_2$-), 1.68 – 1.60 (m, 2H, -$CH_2$-), 1.56 – 1.52 (m, 4H, -$CH_2$-), 1.45 – 1.41 (m, 4H, -$CH_2$-), 1.37 – 1.29 (m, 10H, -$CH_2$-).

Synthesis of bromomalonate **29**

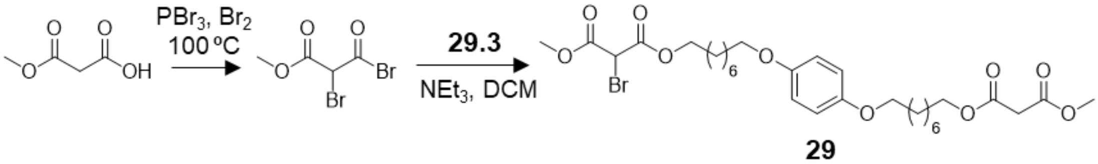

**29**

*Scheme S.42. Synthesis of bromomalonate **29**.*

In an oven-dried Schlenk-tube, phosphorus tribromide (18 µL, 51 mg, 0.19 mmol, 1.64 equiv.) was added to methyl hydrogen malonate (53 µL, 60 mg, 0.47 mmol, 4.0 equiv.). Bromine (55 µL, 0.17 g, 1.1 mmol, 9.2 equiv.) was added dropwise at r.t. and the reaction mixture was stirred at 100 °C for 4 h. After the reaction mixture has cooled down, excess bromine and hydrogen bromide were removed at reduced pressure. The mixture was dissolved in anhydrous THF (1 mL) and was added dropwise to a solution of **29.3** (54 mg, 0.12 mmol, 1.00 eq.) and triethylamine (50 µL, 36 mg, 0.36 mmol, 3.1 equiv.) in anhydrous THF (6 mL) at 0 °C. The reaction mixture was stirred at 0 °C for 1 h and subsequently quenched with an aqueous thiosulfate solution (10 mL). The aqueous phase was extracted with DCM (3 x 20 mL) and the combined organic phases were dried over magnesium sulphate, filtered and evaporated under reduced pressure. After flash column chromatography (petroleum ether/acetone 85:15). Yield: 59%

**$^1$H-NMR** (400 MHz, $CDCl_3$) δ ppm: 6.81 (s, 4H, $H_{Aryl}$), 4.85 (s, 1H, $H_{Bromomalonate}$), 4.23 (t, $J$ = 6.6 Hz, 2H, -C$H_2$OOCCBrH-), 4.14 (t, $J$ = 6.7 Hz, 2H, -C$H_2$OOC$CH_2$-), 3.89 (t, $J$ = 6.5 Hz, 4H, -C$H_2$-Ph-), 3.83 (s, 3H, -CBrHCOOC$H_3$), 3.75 (s, 3H, -$CH_2$COOC$H_3$), 3.38 (s, 2H, $H_{Malonate}$), 1.80 – 1.59 (m, 8H, -$CH_2$-), 1.51 – 1.31 (m, 16H, -$CH_2$-).

### *Synthesis and characterization of **30**⊂[10]CPP⊂**1d**·(BArF)$_8$*

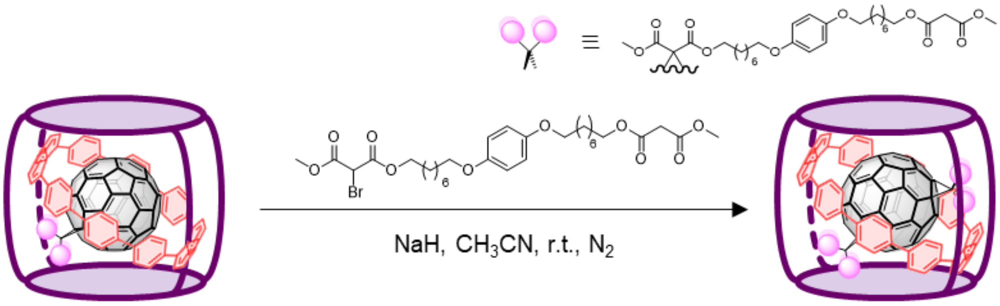

**31**⊂[10]CPP⊂**1d**·(BArF)$_8$

**30**⊂[10]CPP⊂**1d**·(BArF)$_8$

*Scheme S.43. Synthesis of **30**⊂[10]CPP⊂**1d**·(BArF)$_8$.*

Two stock solutions of the corresponding bromomalonate and sodium hydride in dry acetonitrile were prepared. Then, 9 equivalents of bromomalonate **29** and NaH from these solutions were added sequentially to a solution of mono-malonate-C$_{60}$⊂[10]CPP⊂**1d**·(BArF)$_8$ (3.2 mg, 0.25 µmol) in 0.20 ml of dry acetonitrile ($1.3 \cdot 10^{-3}$ M) at room temperature. After monitoring the reaction by HR-ESI-MS for 5 hours, the crude was filtered and the solvent was removed under a N$_2$ flow. The remaining solid was washed with diethyl ether.

**HR-ESI-MS** of **30**⊂[10]CPP⊂**1d**·(BArF)$_8$ (CH$_3$CN), m/z: calc. for [**30**⊂[10]CPP⊂**1d**]$^{8+}$ 992.7761, observed 992.8939; calc. for [**30**-Br⊂[10]CPP⊂**1d**]$^{8+}$ 1002.8832, observed 1012.7508; calc. for [**30**-Br$_2$⊂[10]CPP⊂**1d**]$^{8+}$ 1012.7554, observed 1012.7508; calc. for [**30**⊂[10]CPP⊂**1d**·(BArF)]$^{7+}$ 1257.8966, observed 1256.2903; calc. for [**30**-Br⊂[10]CPP⊂**1d**·(BArF)]$^{7+}$ 1269.3133, observed 1269.4485; calc. for [**30**-Br$_2$⊂[10]CPP⊂**1d**·(BArF)]$^{7+}$ 1280.7301, observed 1281.0071.

### *Synthesis and characterization of mono-adduct **31***

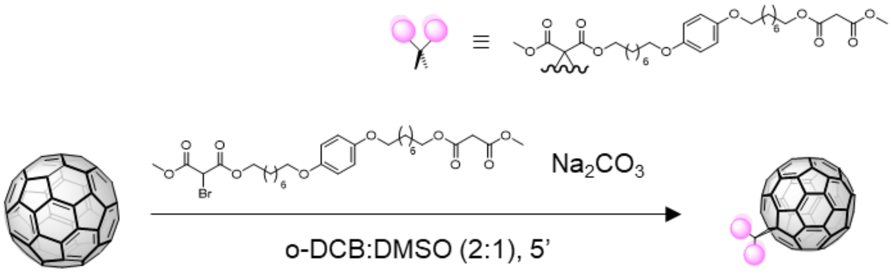

**31**

*Scheme S.44. Synthesis of mono-adduct **31**.*

A solution of C$_{60}$ (5.7 mg) was prepared in 2 ml of *o*-DCB. Then, 5.1 mg of the bromomalonate **29** (1 equivalents) were added. A suspension of Na$_2$CO$_3$ (4.2 mg, 5 equivalents) in 1 ml of DMSO was prepared. The first solution was added to the second solution and it was stirred for 5 minutes. The mixture was added directly to a column to stop the reaction and was purified via column chromatography. First, hexane was used to elute the remaining C$_{60}$ and then hexane:ethyl acetate (20:1) was used to elute **31**. Yield: 56%

$^1$**H-NMR** (400 MHz, CDCl$_3$) δ ppm: 6.80 (s, 4H, H$_{Aryl}$), 4.51 (t, *J* = 6.4 Hz, 2H, -C*H*$_2$-OOCCBrH-), 4.14 (t, *J* = 6.7 Hz, 2H, -C*H*$_2$-OOC-CH$_2$-), 4.09 (s, 3H, -CBrHCOOC*H*$_3$), 3.89 (t, *J* = 6.5 Hz, 4H, -C*H*$_2$-Ph-), 3.75 (s, 3H, -CH$_2$COO-C*H*$_3$), 3.38 (s, 2H, H$_{Malonate}$), 1.90 – 1.60 (m, 8H, -CH$_2$-), 1.52 – 1.27 (m, 16H, -CH$_2$-).

**MALDI-MS** (DCTB, (+)), m/z: calc. for [**31**]$^+$ 1284.309, observed 1284.811; calc. for [**31**+Na$^+$]$^+$ 1307.299, observed 1307.925.

*Synthesis and characterization of* ***31***⊂[10]CPP

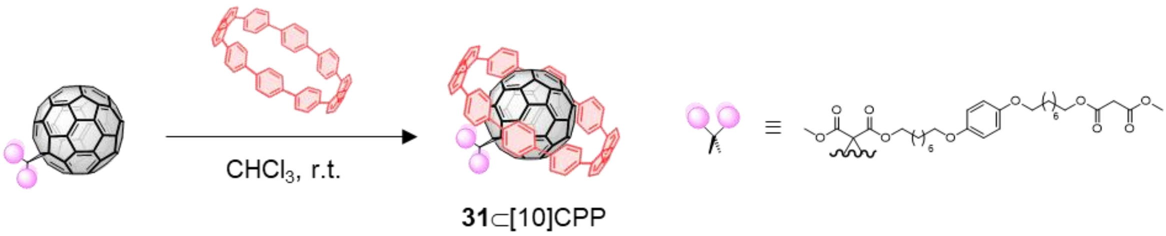

*Scheme S.45. Synthesis of* ***31***⊂*[10]CPP complex*

A solution of 5.9 mg of mono-adduct **31** in 5 ml CHCl$_3$ was added to a solution of 3.3 mg (1 equivalent) of [10]CPP in 5 ml CHCl$_3$ and it was stirred for 3 hours at room temperature to form **31**⊂[10]CPP. The solvent was evaporated under reduced pressure. Yield: 95%

$^1$**H-NMR** (400 MHz, CDCl$_3$) δ ppm: 7.53 (s, 40H, [10]CPP), 6.87 – 6.77 (m, 4H, H$_{Aryl}$), 4.60 (t, *J* = 6.6 Hz, 2H, -C*H*$_2$OOC-CBrH-), 4.19 (s, 3H, -CBrH-COO-C*H*$_3$), 4.14 (t, *J* = 6.7, 2H, -C*H*$_2$-OOC-CH$_2$-), 3.95 (t, *J* = 6.5 Hz, 1H, -C*H*$_2$-Ph-), 3.90 (t, *J* = 6.6 Hz, 1H, -C*H*$_2$-Ph-), 3.75 (s, 3H, -CH$_2$COO-C*H*$_3$), 3.38 (s, 2H, H$_{Malonate}$), 2.01 – 1.94 (m, 2H, -CH$_2$-), 1.87 – 1.80 (m, 2H, -CH$_2$-), 1.79 – 1.71 (m, 2H, -CH$_2$-), 1.68 – 1.39 (m, 18H, -CH$_2$-).

*Blank Bingel-Hirsch reaction using **1b**·(BArF)$_8$ nanocapsule*

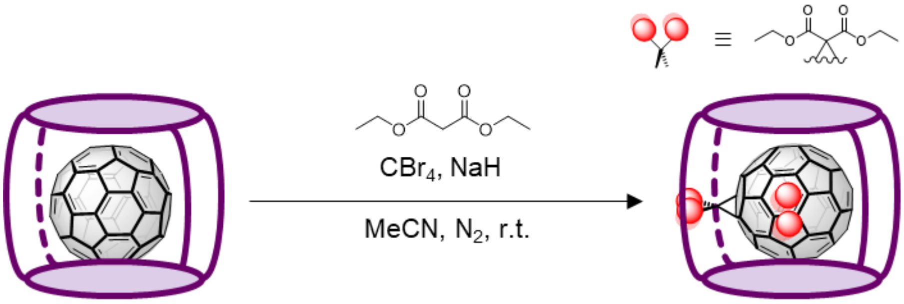

**32**$\subset$[10]CPP$\subset$**1d**·(BArF)$_8$

*Scheme S.46. Blank Bingel-Hirsch reaction using **1b**·(BArF)$_8$ nanocapsule.*

Three stock solutions of the corresponding bromomalonate, sodium hydride and CBr$_4$ in dry acetonitrile were prepared. Then, 6 equivalents of diethyl bromomalonate**,** NaH and CBr$_4$ from these solutions were added sequentially to a solution of C$_{60}$$\subset$**1b**·(BArF)$_8$ (6.7 mg, 0.55 μmol) in 0.55 ml of dry acetonitrile ($10^{-3}$ M) at room temperature. After monitoring the reaction by HR-ESI-MS for 5.5 hours, the crude was filtered and the solvent was removed under a N$_2$ flow.

**HR-ESI-MS** of **32**$\subset$[10]CPP$\subset$**1d**·(BArF)$_8$ (CH$_3$CN), m/z: calc. for [**32**$\subset$**1b**]$^{8+}$ 772.0525, observed 771.9195; calc. for [**32**$\subset$**1b**·(BArF)]$^{7+}$ 1005.6410, observed 1005.6343; calc. for [**32**$\subset$**1b**·(BArF)$_2$]$^{6+}$ 1317.0924, observed 1316.9405.

*Bingel-Hirsch reaction starting from encapsulated **31** and **30** by [10]CPP$\subset$**1d**·(BArF)$_8$*

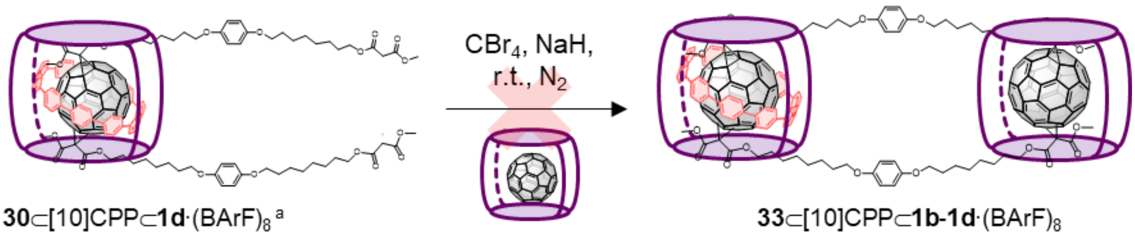

**30**$\subset$[10]CPP$\subset$**1d**·(BArF)$_8$ $^a$

C$_{60}$$\subset$**1b**·(BArF)$_8$

**33**$\subset$[10]CPP$\subset$**1b-1d**·(BArF)$_8$

*Scheme S.47. Bingel-Hirsch reaction starting from encapsulated **31** and **30** (1:08) by [10]CPP$\subset$**1d**·(BArF)$_8$. $^a$: only **30**$\subset$[10]CPP$\subset$**1d**·(BArF)$_8$ is depicted for clarity.*

Three stock solutions of CBr$_4$, NaH and C$_{60}$$\subset$**1b**·(BArF)$_8$ in dry acetonitrile were prepared. Then, 1.5 equivalents of CBr$_4$, 0.75 equivalents of NaH and 1 equivalent of C$_{60}$$\subset$**1b**·(BArF)$_8$ from these solutions were added sequentially to a solution of **31**$\subset$[10]CPP$\subset$**1d**·(BArF)$_8$ and **30**$\subset$[10]CPP$\subset$**1d**·(BArF)$_8$ (1:08, respectively) (0.26 μmol) in 0.26 ml of dry acetonitrile ($10^{-3}$ M) at room temperature. After monitoring the reaction by HR-ESI-MS for 4 hours, the crude was filtered and the solvent was removed under a $N_2$ flow.

## *Annex VI.2 Supplemental figures*

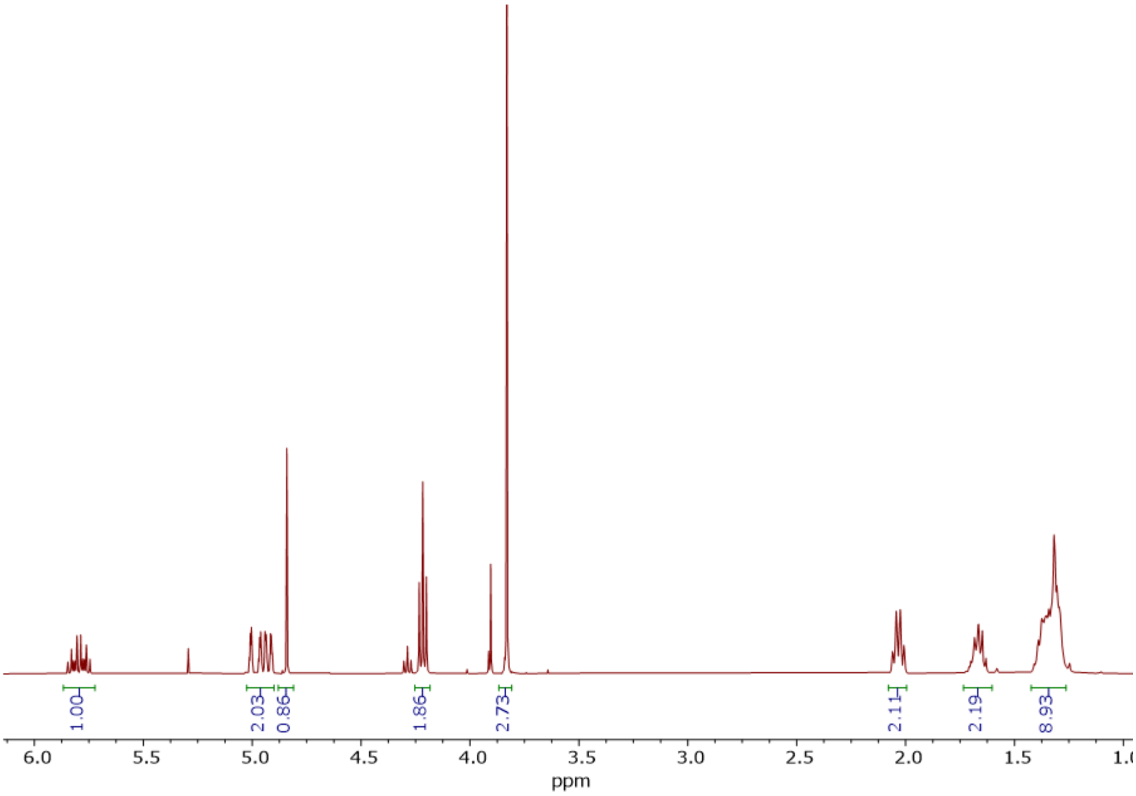

*Figure S.97. $^1$H-NMR spectrum of bromomalonate **15**. Experiment performed in $CDCl_3$ at 298K (400 MHz).*

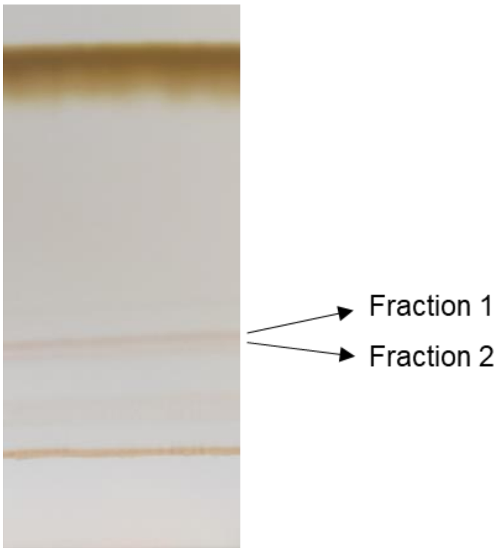

*Figure S.98. TLC preparative of the purification of bis-adducts after Bingel reaction using the vinyl-containing bromomalonate and starting from $C_{60}$⊂[10]CPP⊂**1d**·$(BArF)_8$.*

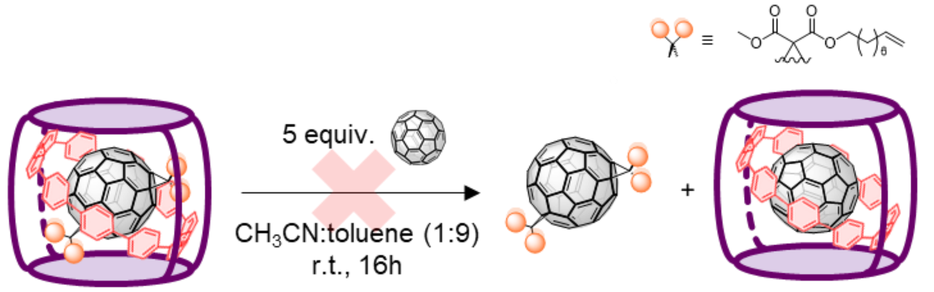

**15**⊂[10]CPP⊂**1d**·(BArF)$_8$ **15** C$_{60}$⊂[10]CPP⊂**1d**·(BArF)$_8$

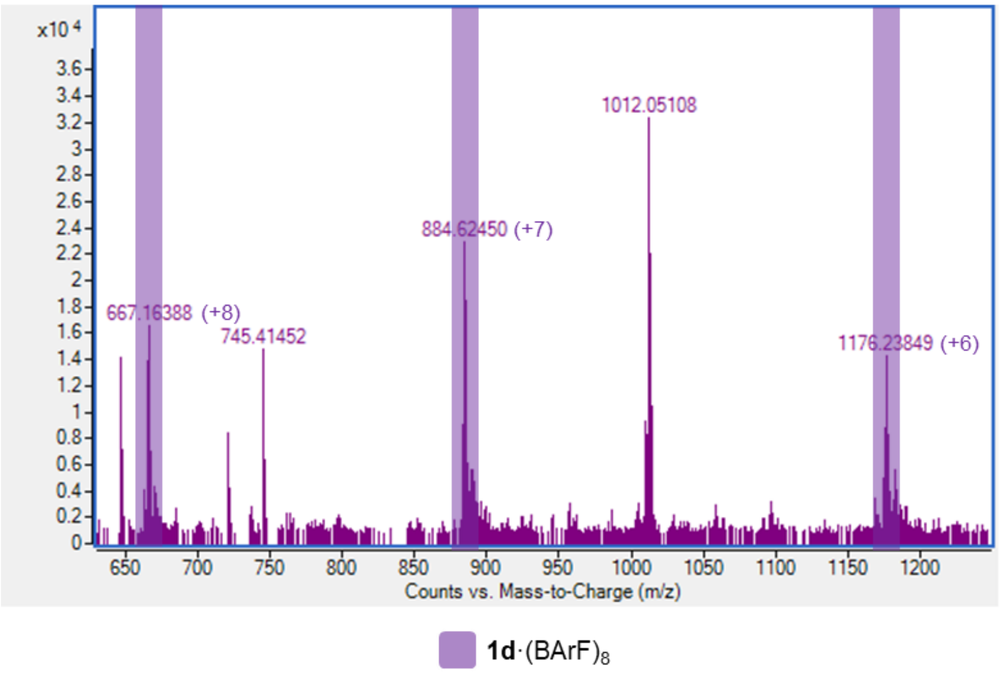

*Figure S.99. HR-ESI mass spectrum after the exchange with C$_{60}$ from the Bingel reaction using bromomalonate **15**.*

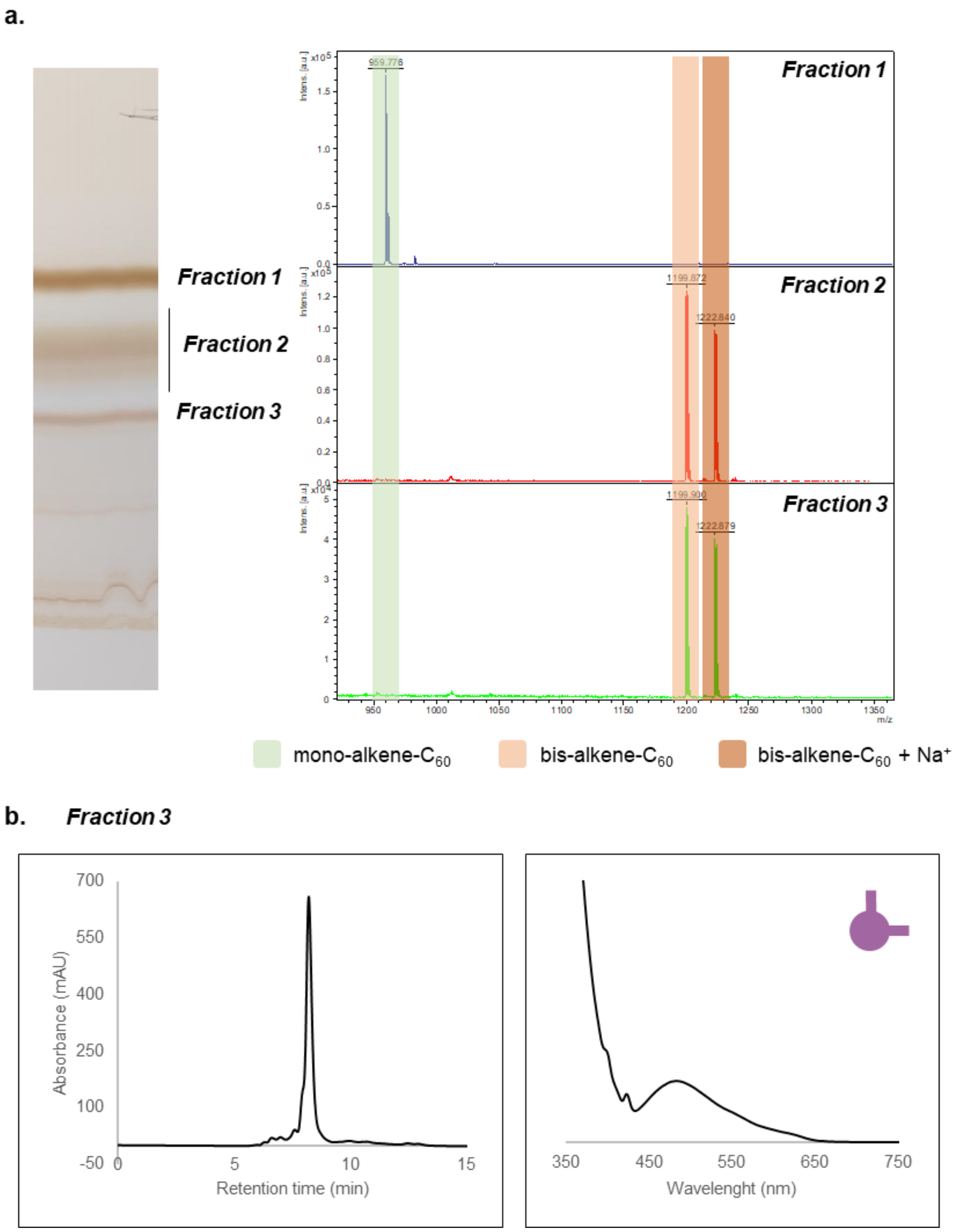

*Figure S.100. a) Preparative TLC of the purification of bis-adducts **17** after Bingel reaction using bromomalonate **15**. b) HPLC analysis of e,e-bis-adduct **17** and UV-vis spectrum of the corresponding peak.*

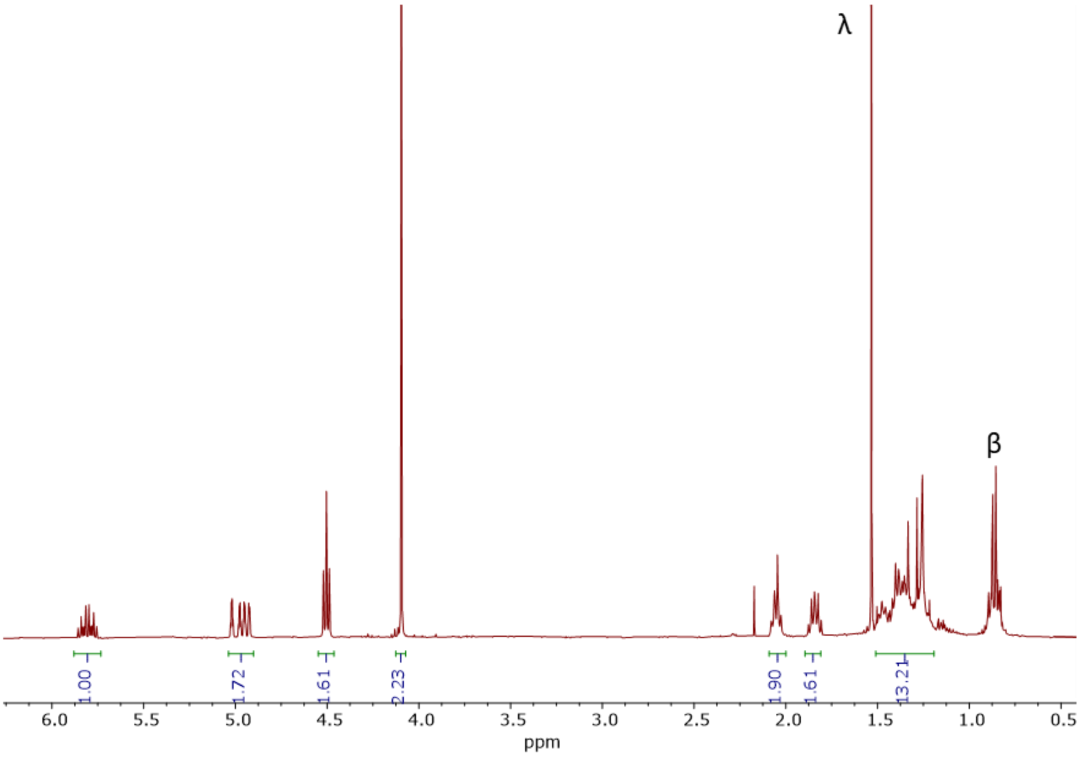

*Figure S.101. $^1$H-NMR spectrum of mono-adduct* ***18****. Experiment performed in $CDCl_3$ at 298K (400 MHz). λ: $H_2O$, β: grease.*

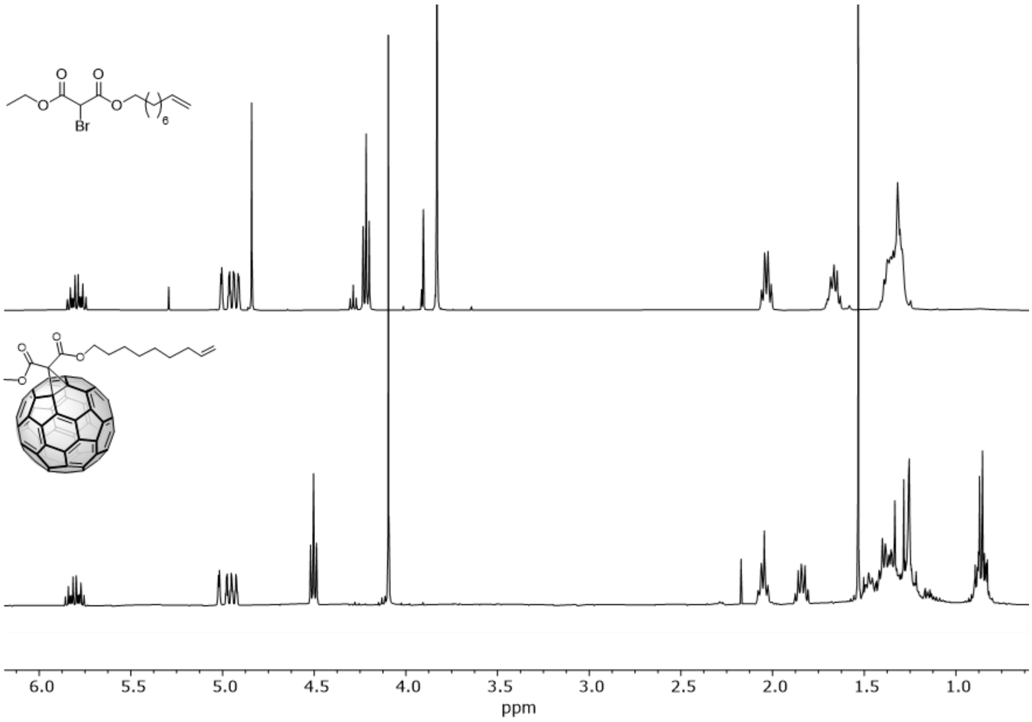

*Figure S.102. Top: $^1$H-NMR spectrum of bromomalonate* ***15****. Bottom: $^1$H-NMR spectrum of mono-adduct* ***18****. Experiments performed in $CDCl_3$ at 298K (400 MHz).*

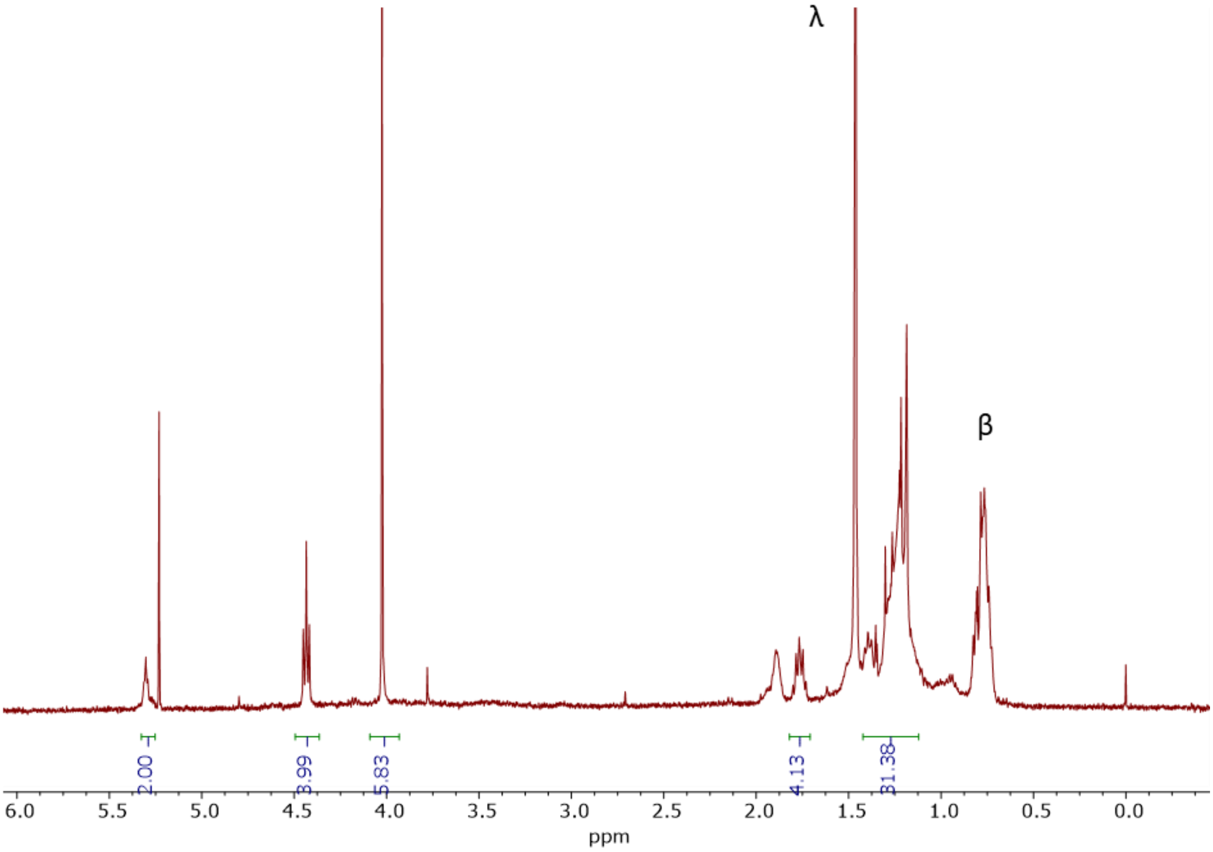

*Figure S.103. ${}^1$H-NMR spectrum of olefin metathesis product (**19**) using mono-adduct **18**. Experiment performed in $CDCl_3$ at 298K (400 MHz). λ: $H_2O$, β: grease.*

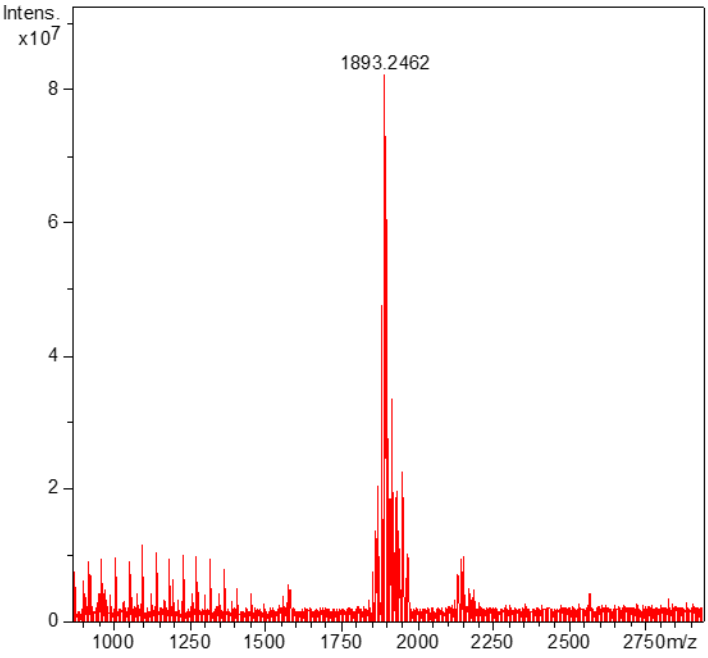

*Figure S.104. MALDI mass spectrum of olefin metathesis product (**19**) using mono-adduct **18**.*

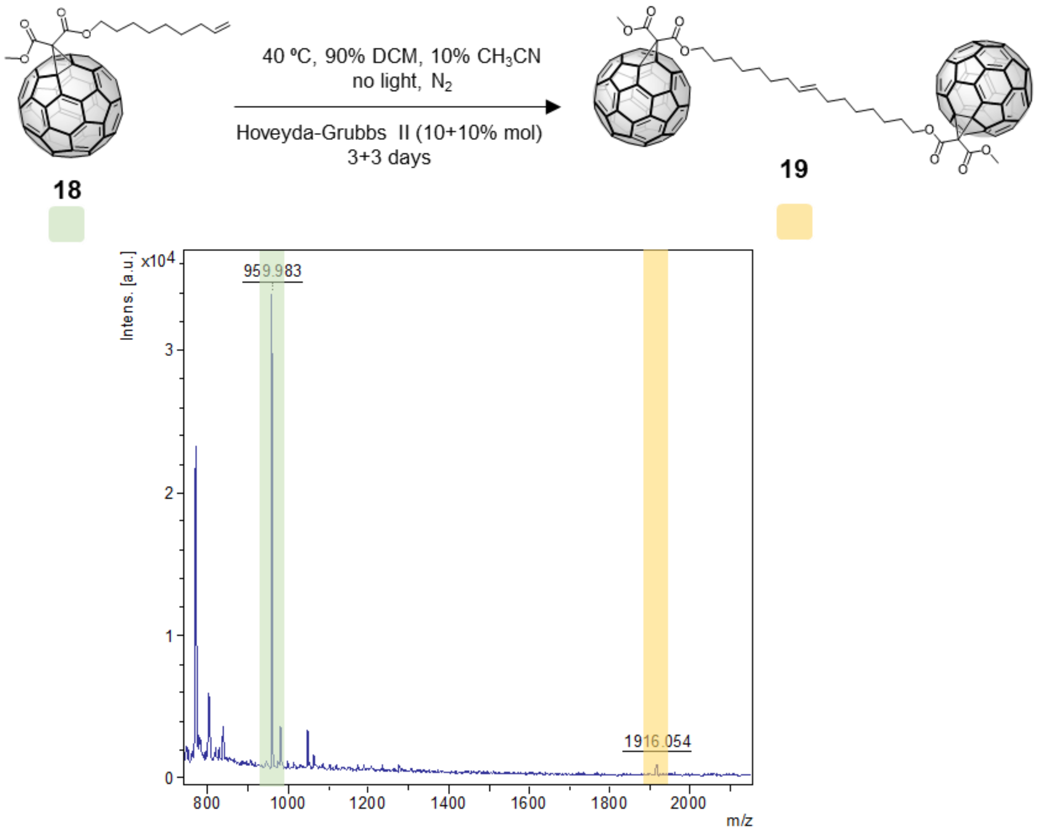

*Figure S.105. MALDI mass spectrum of the crude reaction after 6 days of olefin metathesis starting from mono-adduct **18** using a mixture of dichloromethane and acetonitrile (9:1).*

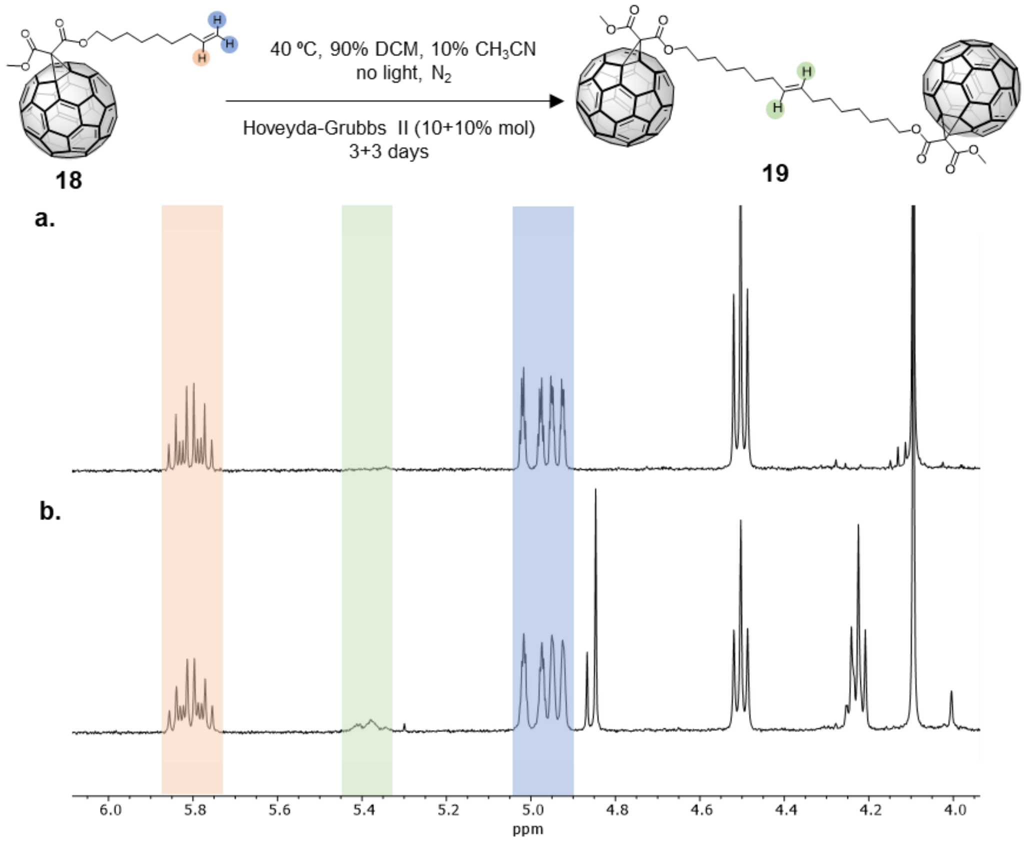

*Figure S.106. a) $^1$H-NMR spectrum of mono-adduct **18** (starting material). b) $^1$H-NMR spectrum of the crude reaction after 6 days of olefin metathesis starting from **18** in a mixture of dichloromethane and acetonitrile (9:1).*

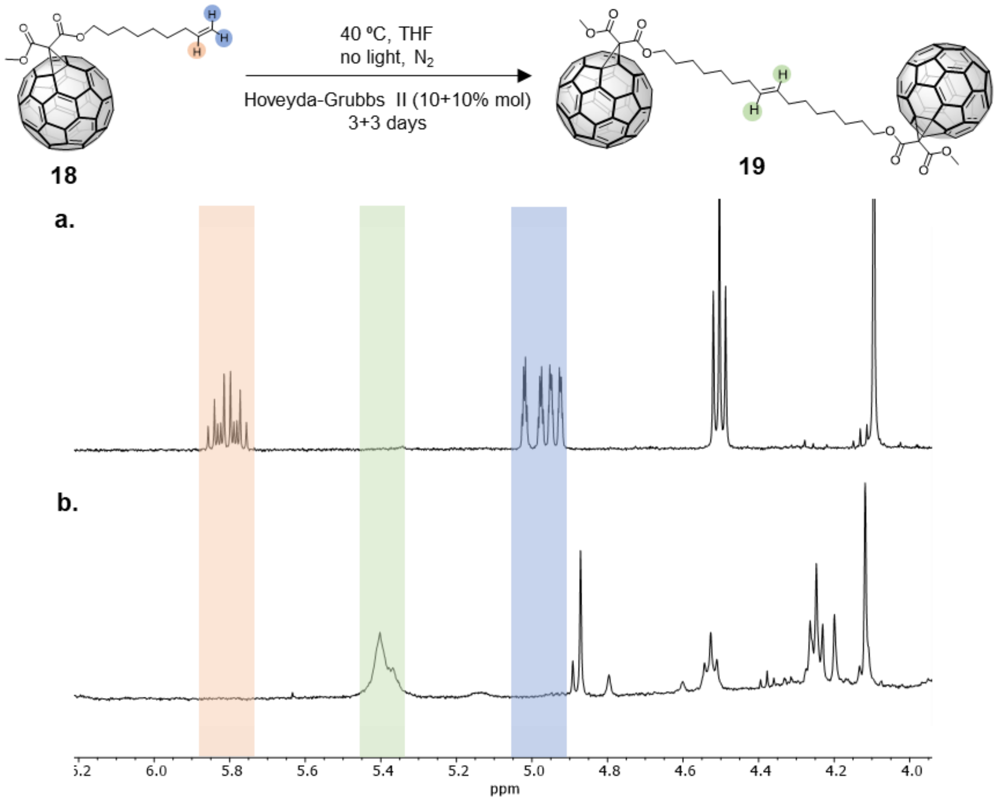

*Figure S.107. a) $^1$H-NMR spectrum of **18** (starting material). b) $^1$H-NMR spectrum of the crude reaction after 6 days of olefin metathesis starting from **18** in THF.*

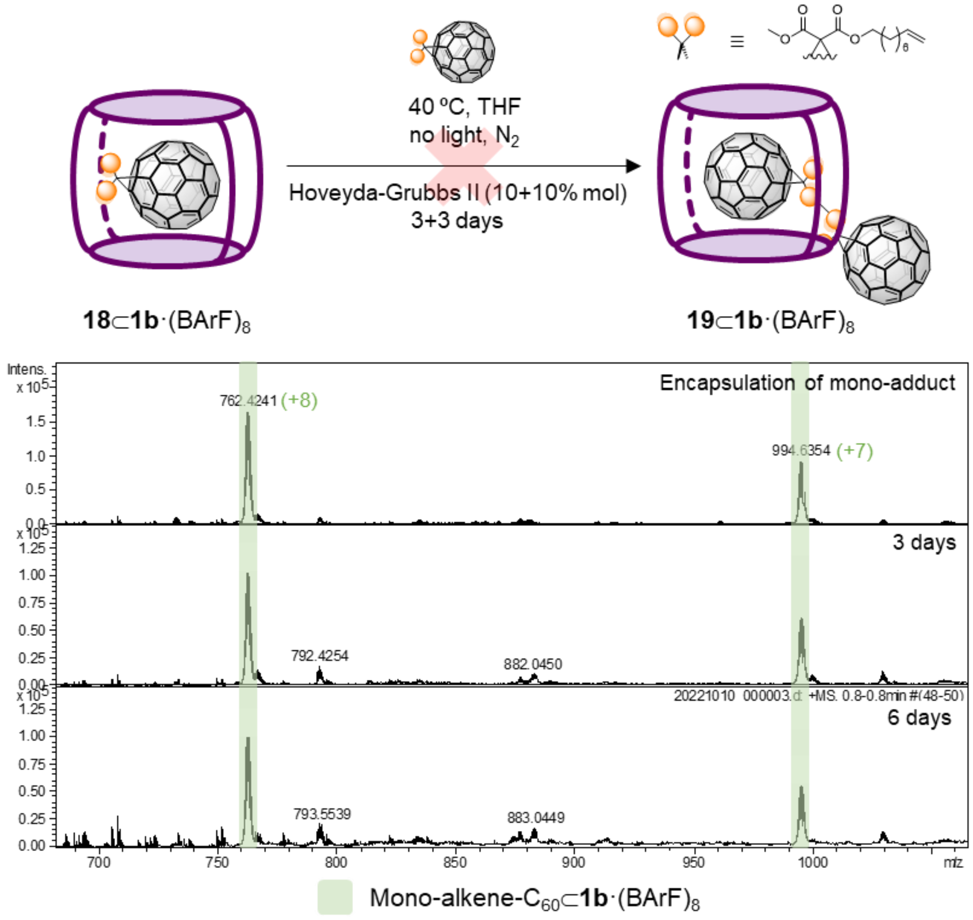

*Figure S.108. HR-ESI-MS monitoring of olefin metathesis starting from **18⊂1b**·(BArF)₈ in THF.*

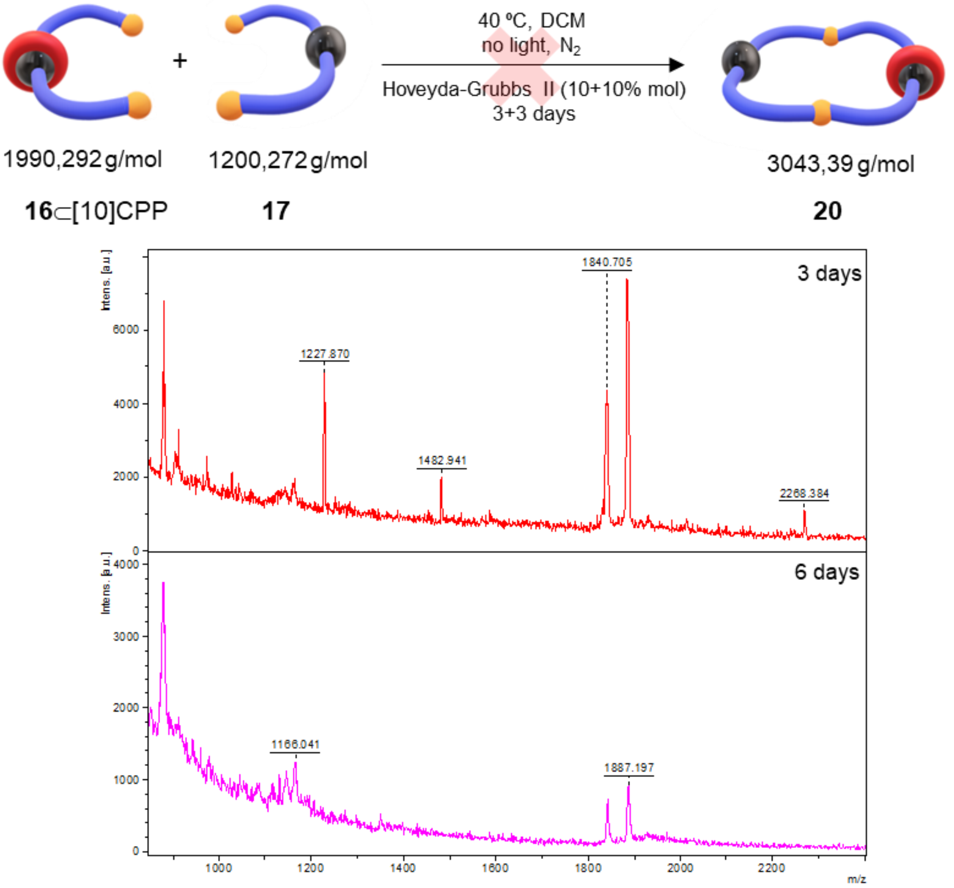

*Figure S.109. MALDI-MS monitoring of olefin metathesis starting from bis-adducts **16**⊂[10]CPP and **17**.*

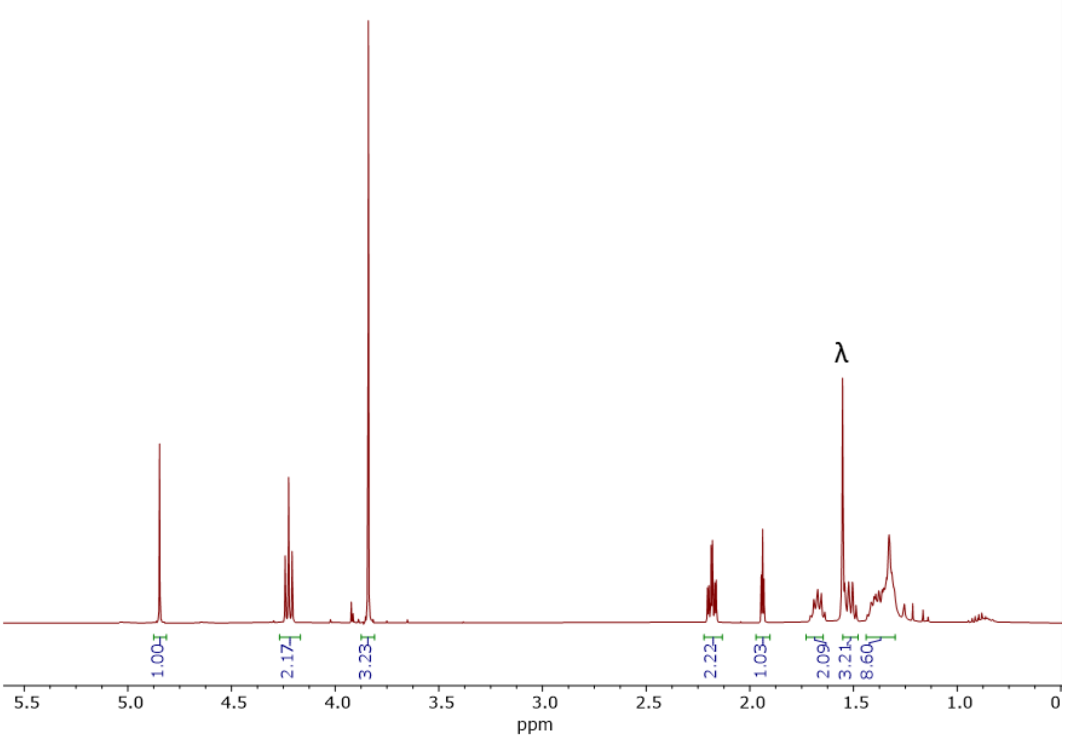

*Figure S.110. $^1$H-NMR spectrum of bromomalonate **22**. Experiment performed in $CDCl_3$ at 298K (400 MHz). λ: $H_2O$*

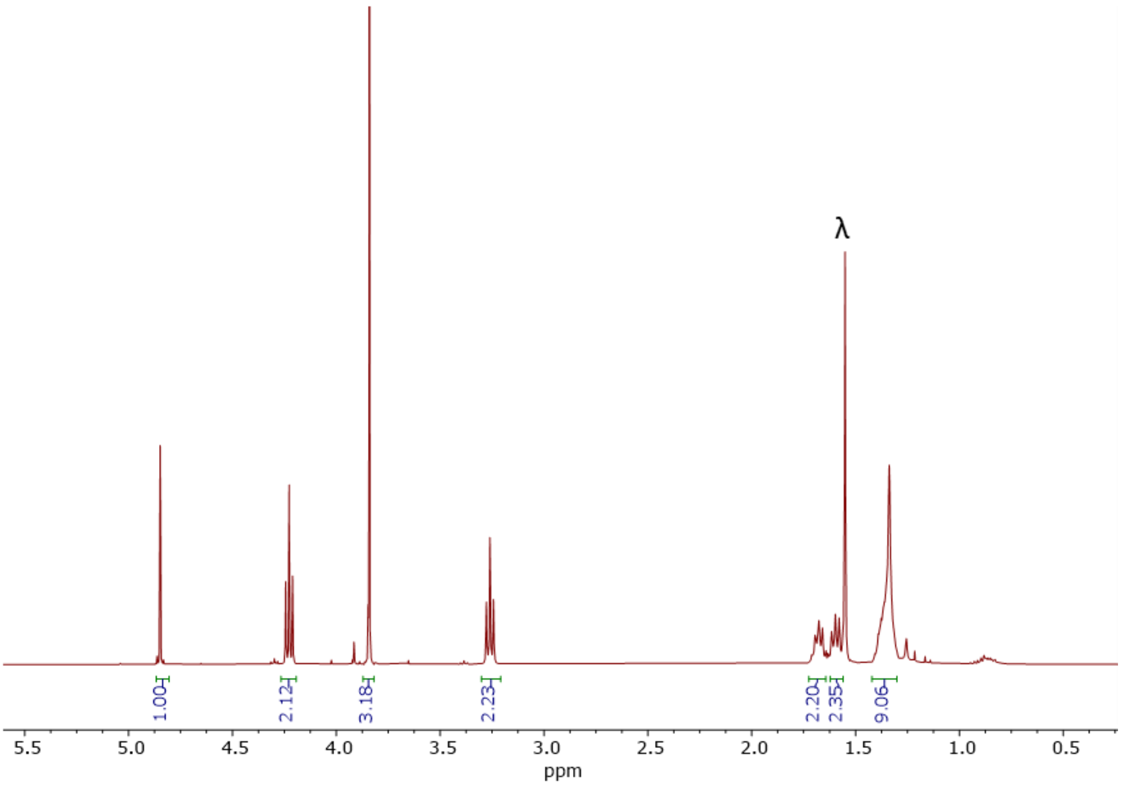

*Figure S.111. $^1$H-NMR spectrum of bromomalonate **23**. Experiment performed in $CDCl_3$ at 298K (400 MHz). λ: $H_2O$*

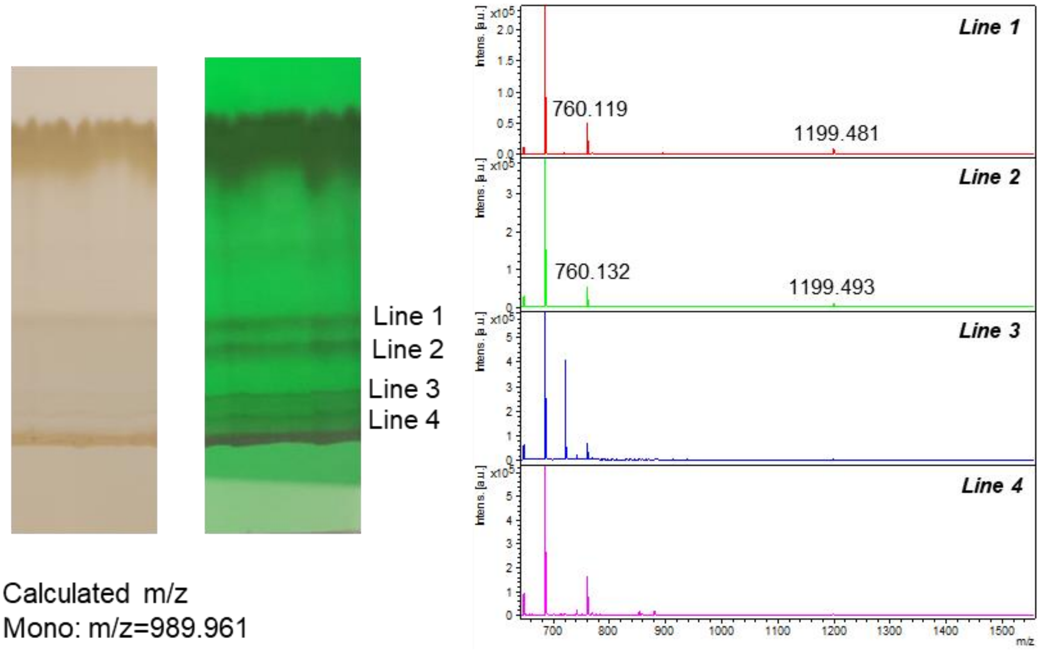

Calculated m/z
Mono: m/z=989.961
Bis: m/z=1259.262

*Figure S.112. MALDI mass spectra of fractions collected after preparative TLC after releasing **25** from **25**⊂[10]CPP⊂**1d**·(BArF)$_8$.*

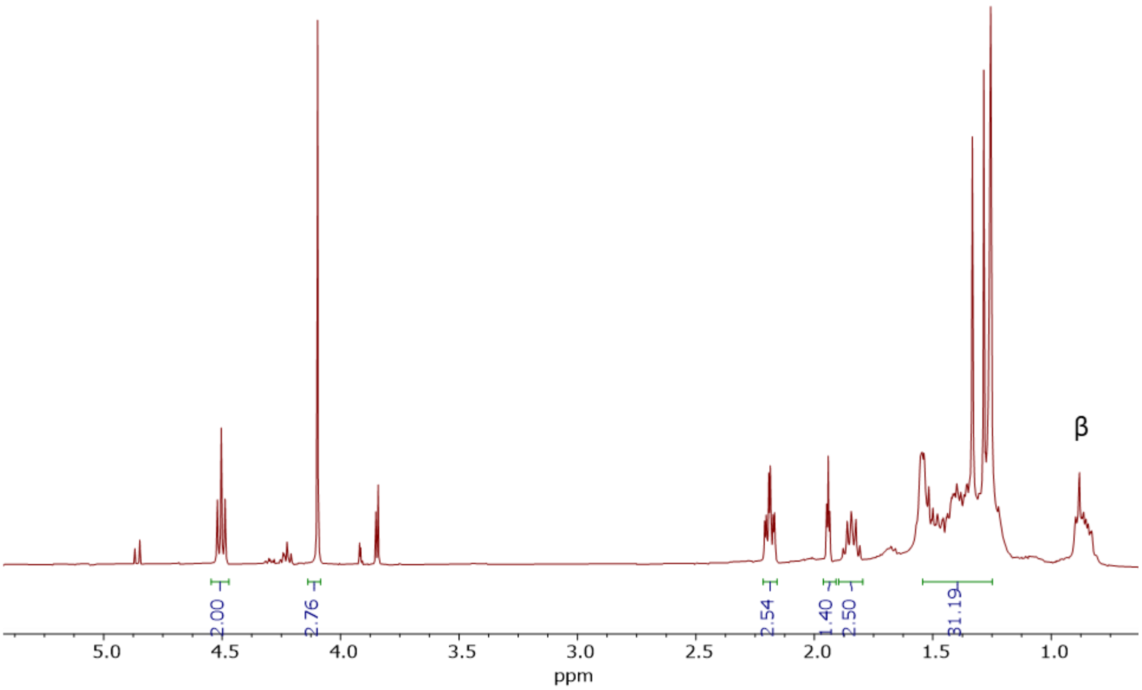

*Figure S.113. $^1$H-NMR spectrum of mono-adduct **26**. Experiment performed in $CDCl_3$ at 298K (400 MHz). β: grease*

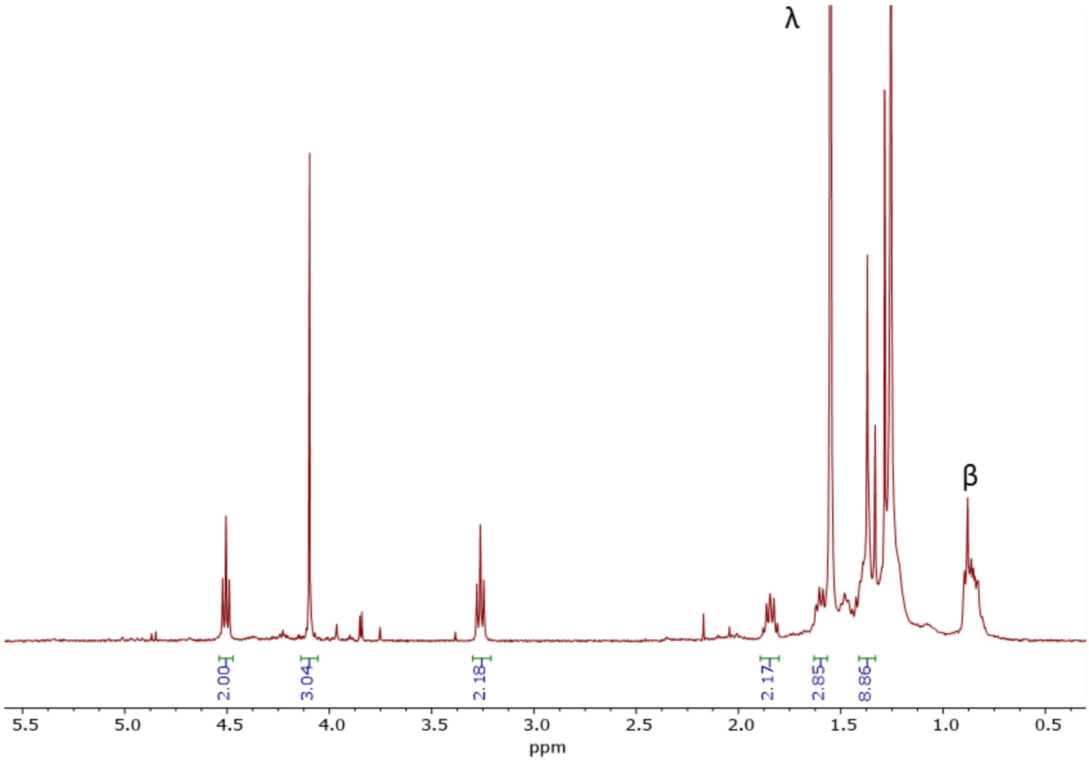

*Figure S.114. $^1$H-NMR spectrum of mono-adduct **27**. Experiment performed in $CDCl_3$ at 298K (400 MHz). λ: $H_2O$, β: grease*

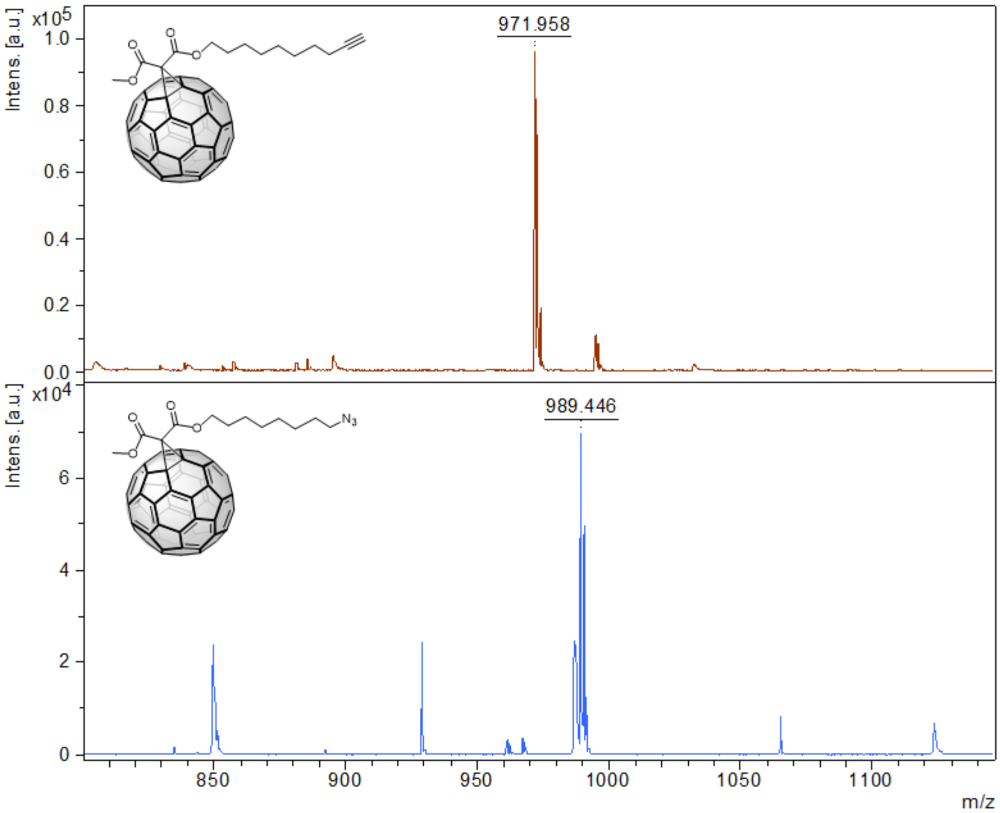

*Figure S.115. MALDI mass spectra of mono-adduct* ***26*** *(top) and mono-adduct* ***27*** *(bottom).*

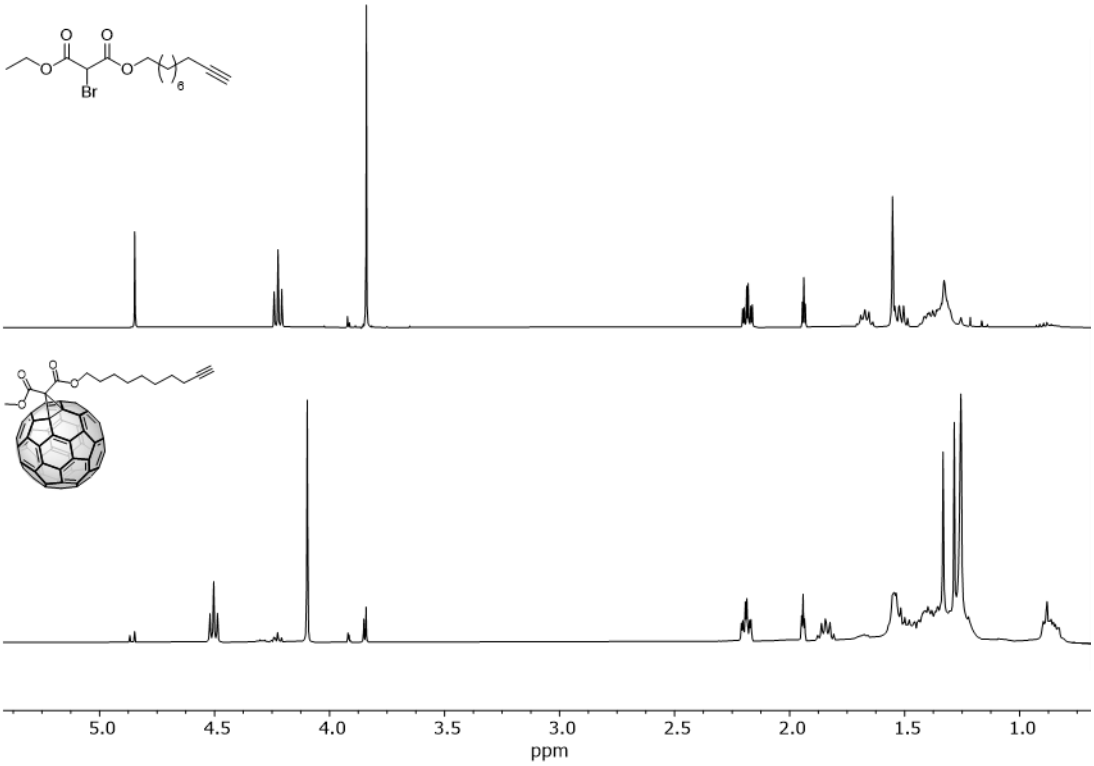

*Figure S.116. Top: $^1$H-NMR spectrum of the bromomalonate* ***22****. Bottom: $^1$H-NMR spectrum of the mono-adduct* ***26****.*

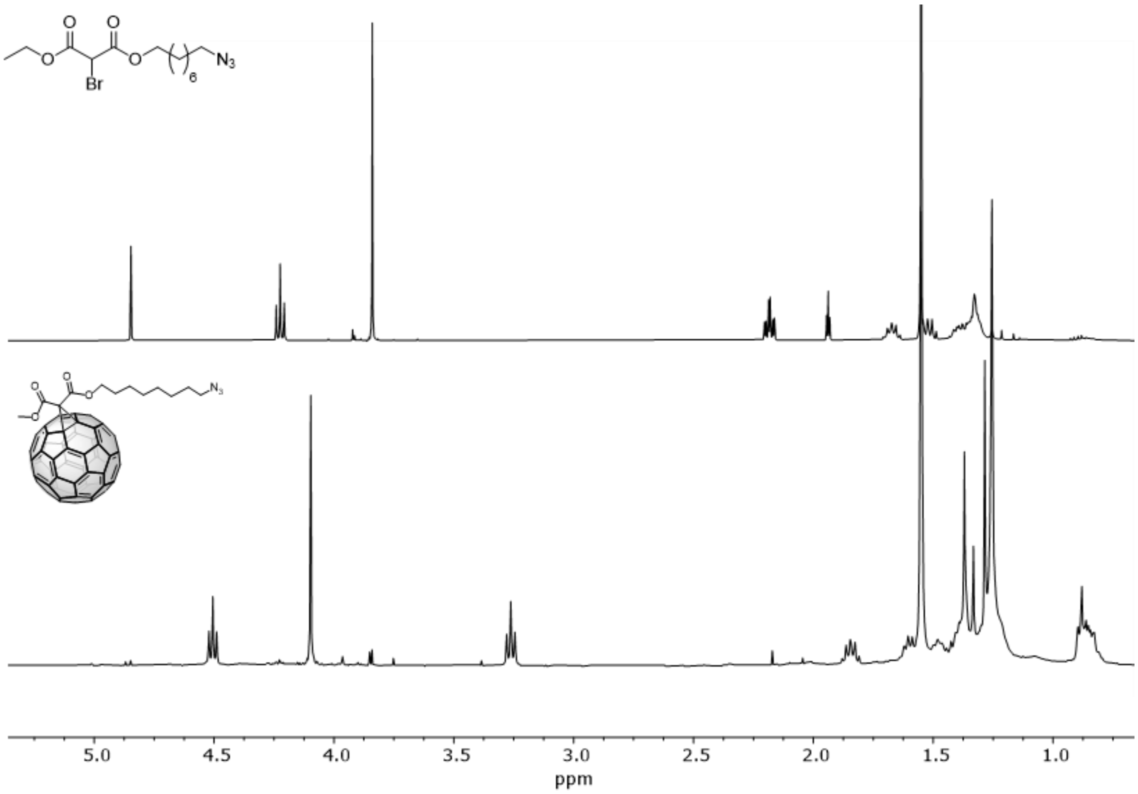

*Figure S.117. Top: $^1$H-NMR spectrum of bromomalonate **23**. Bottom: $^1$H-NMR spectrum of mono-adduct **27**.*

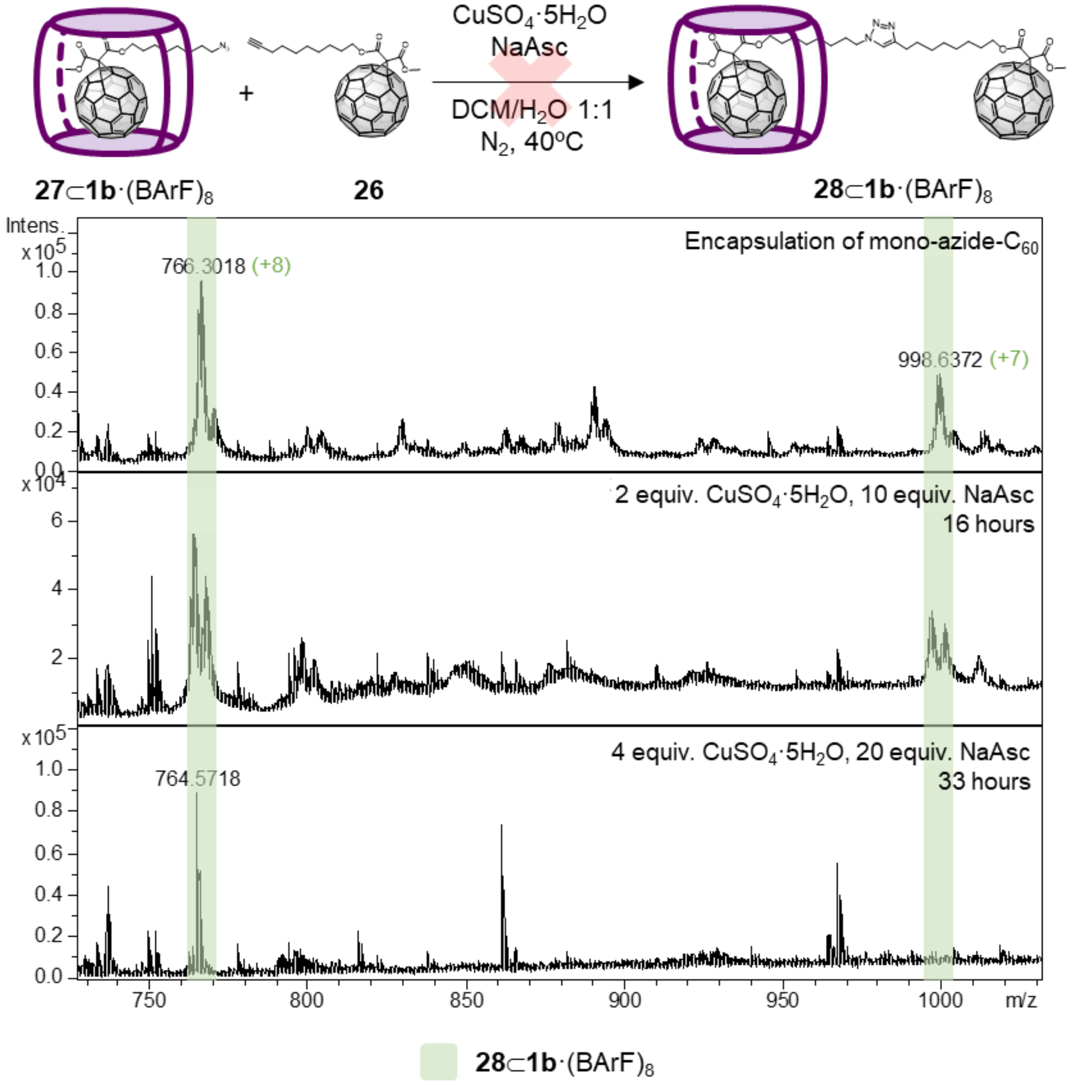

*Figure S.118. HR-ESI-MS monitoring of CuAAC starting from **27⊂1b**·(BArF)$_8$ and **26**.*

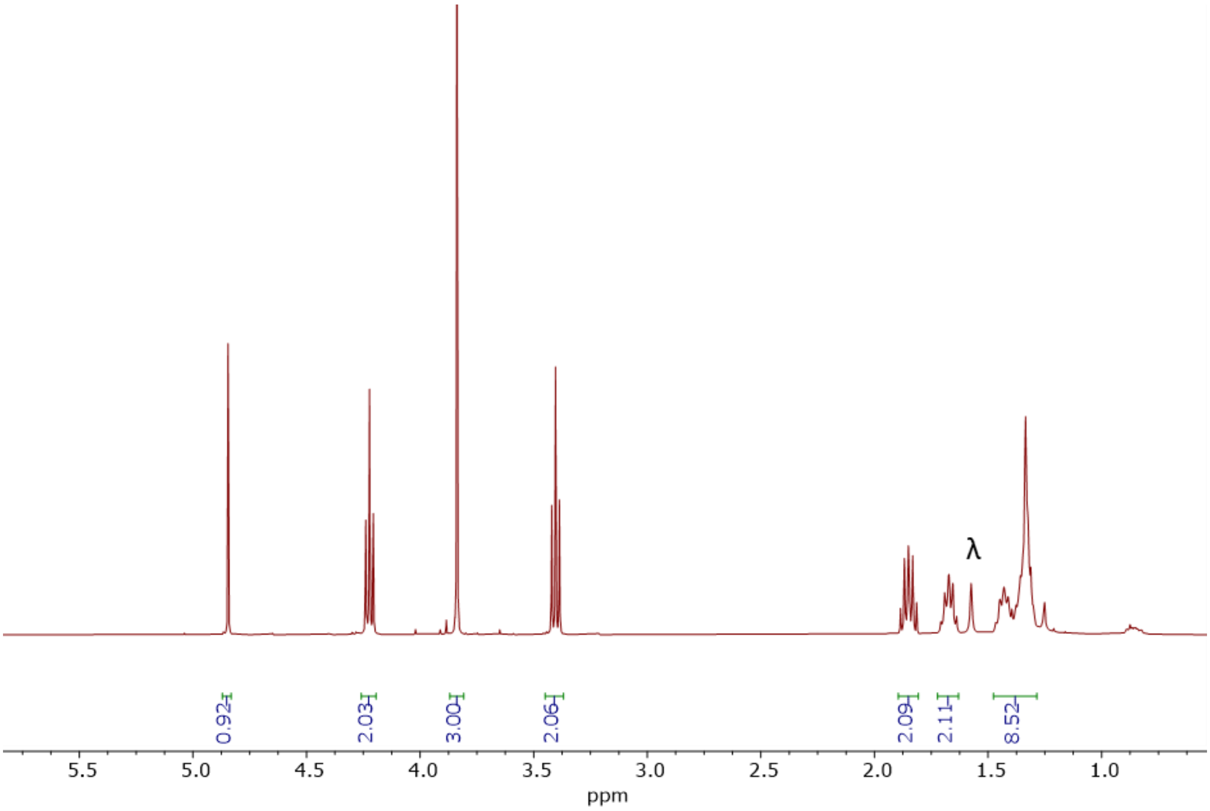

*Figure S.119. $^1$H-NMR spectrum of compound **29.1**. Experiment performed in $CDCl_3$ at 298K (400 MHz). λ: $H_2O$.*

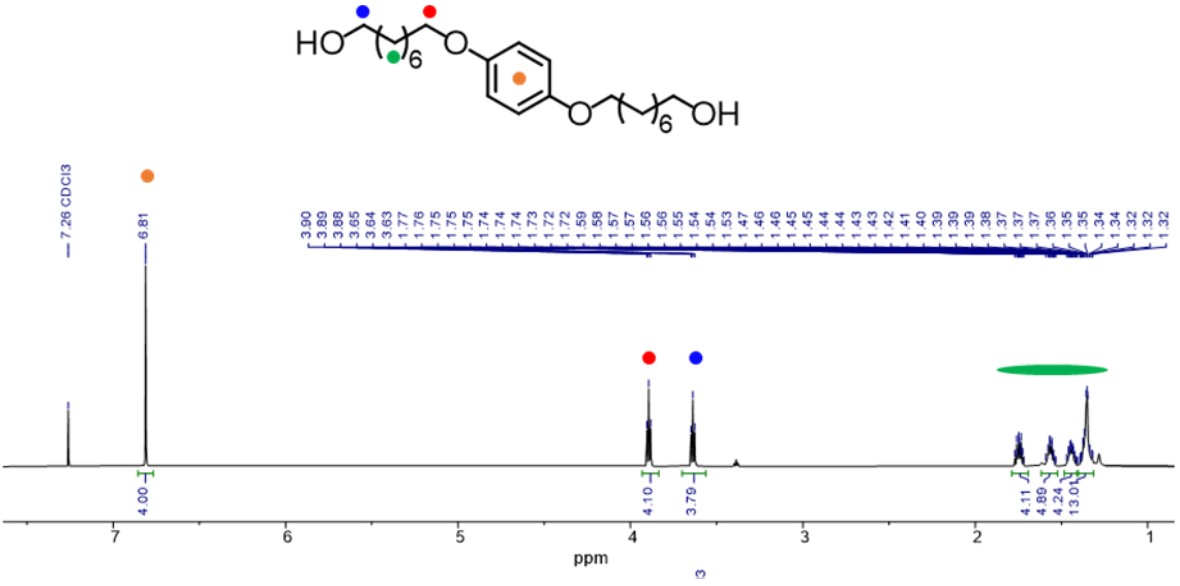

*Figure S. 120. $^1$H-NMR spectrum of compound **29.2**. Experiment performed in $CDCl_3$ at 298K (400 MHz).*

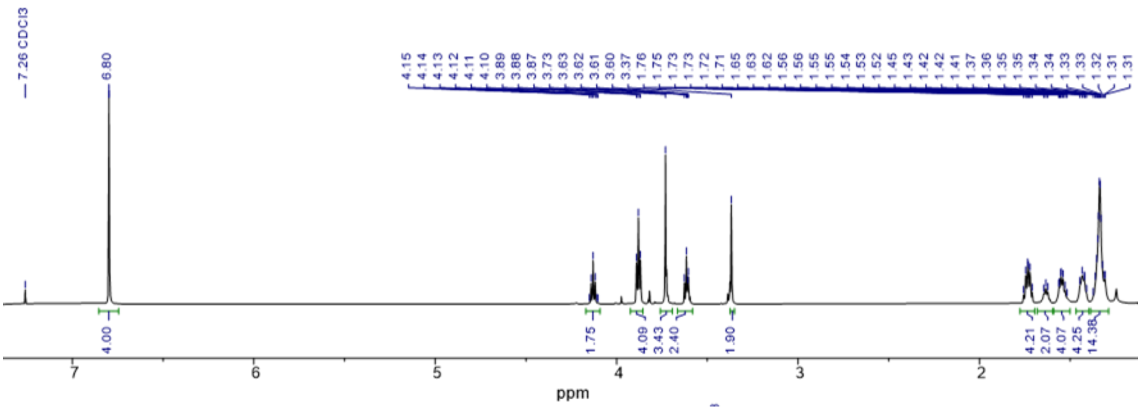

*Figure S.121. $^1$H-NMR spectrum of compound* ***29.3****. Experiment performed in $CDCl_3$ at 298K (400 MHz).*

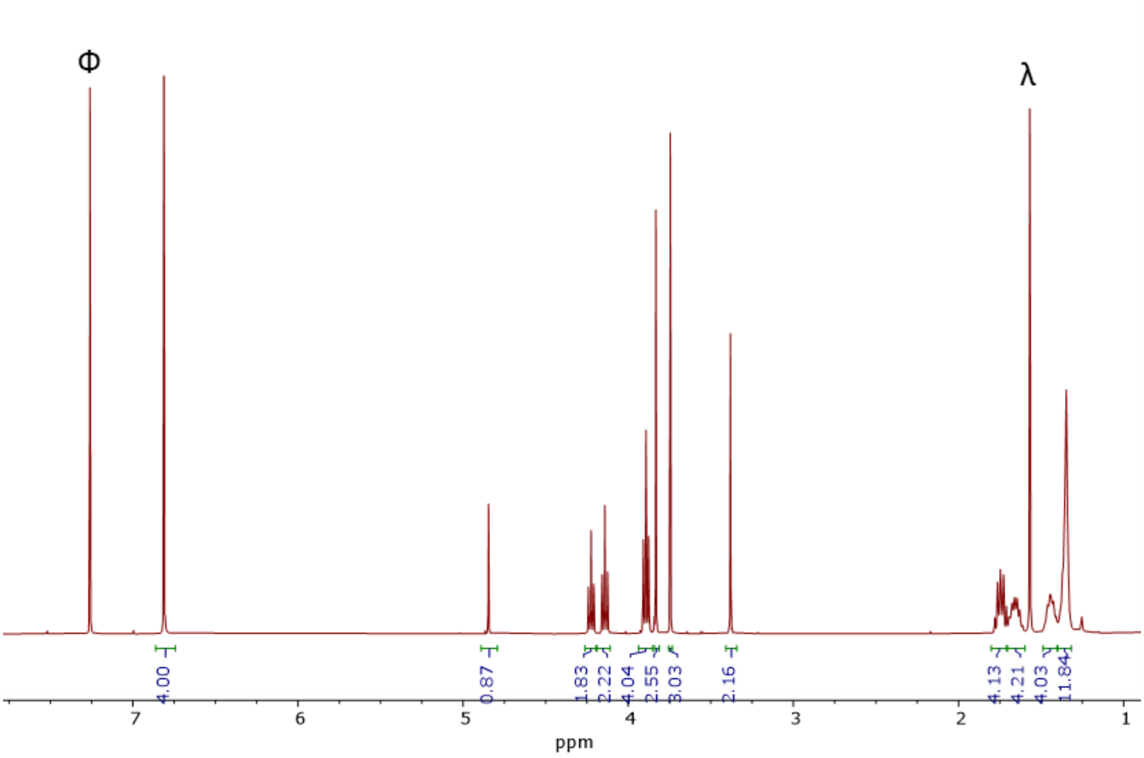

*Figure S.122. $^1$H-NMR spectrum of bromomalonate* ***29****. Experiment performed in $CDCl_3$ at 298K (400 MHz). Φ: $CHCl_3$, λ: $H_2O$*

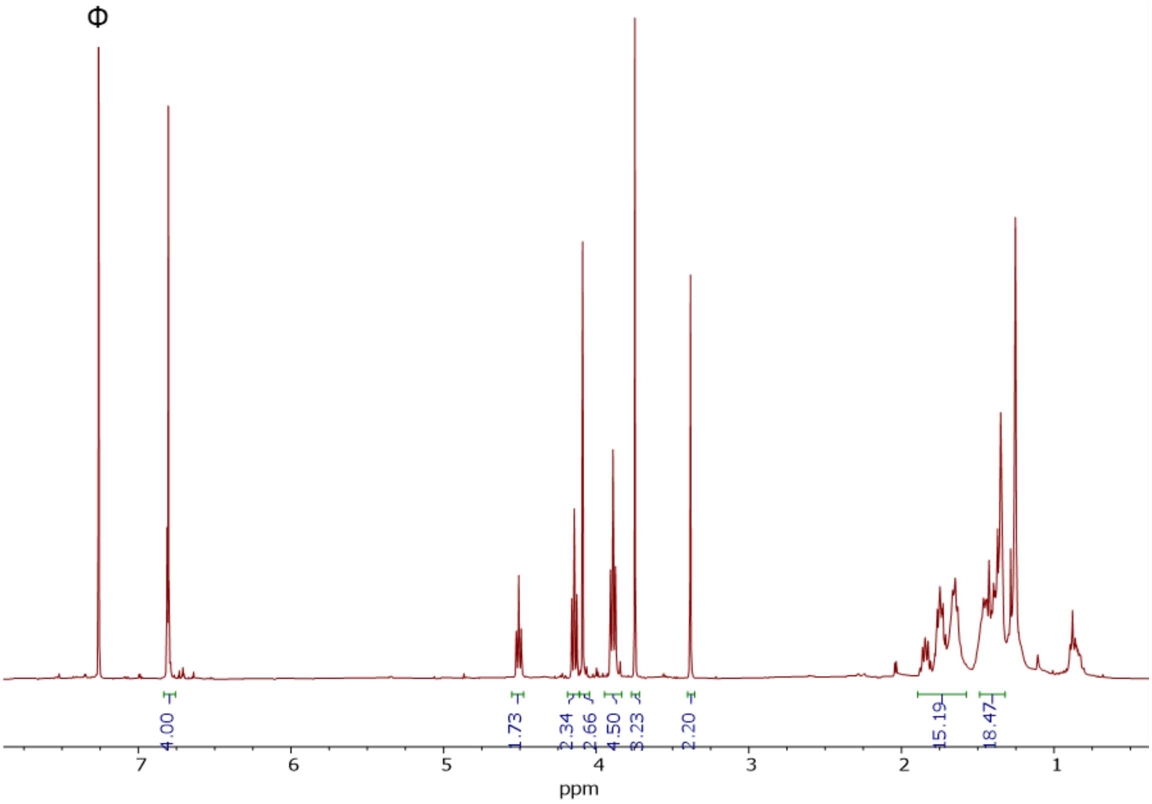

*Figure S.123. ¹H-NMR spectrum of mono-adduct **31**. Experiment performed in CDCl₃ at 298K (400 MHz). Φ: CHCl₃.*

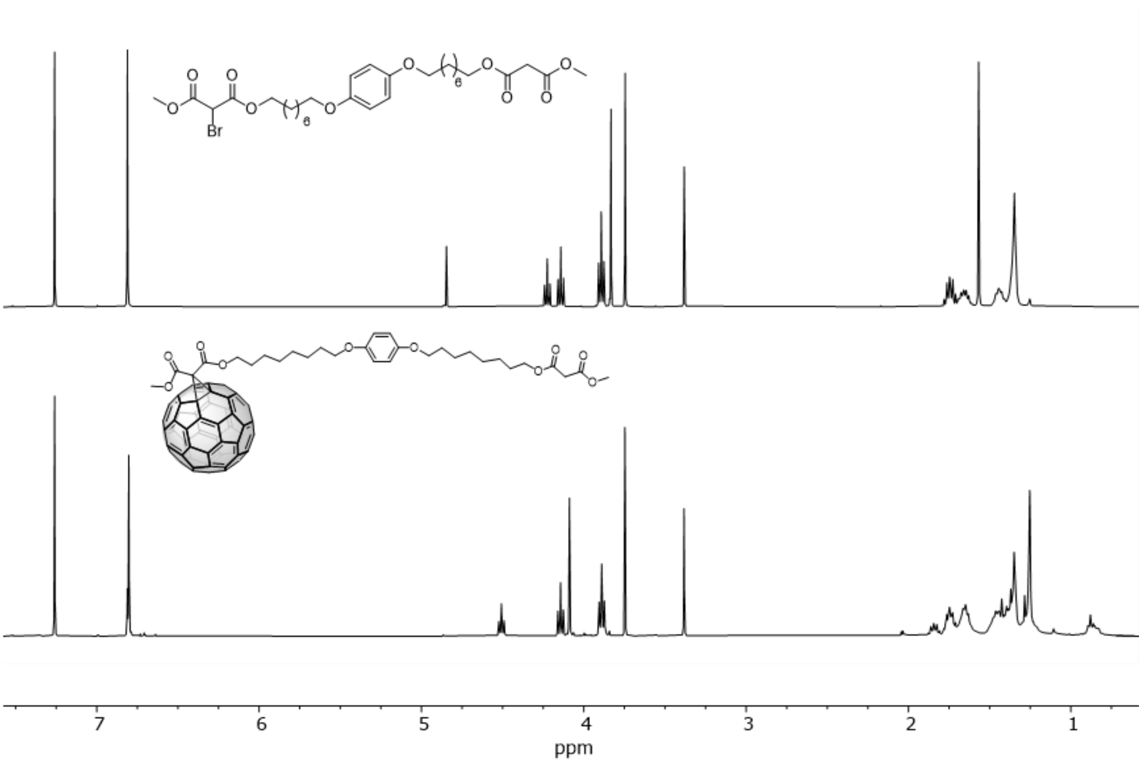

*Figure S.124. Top: ¹H-NMR spectrum of the bromomalonate **29**. Bottom: ¹H-NMR spectrum of mono-adduct **31**.*

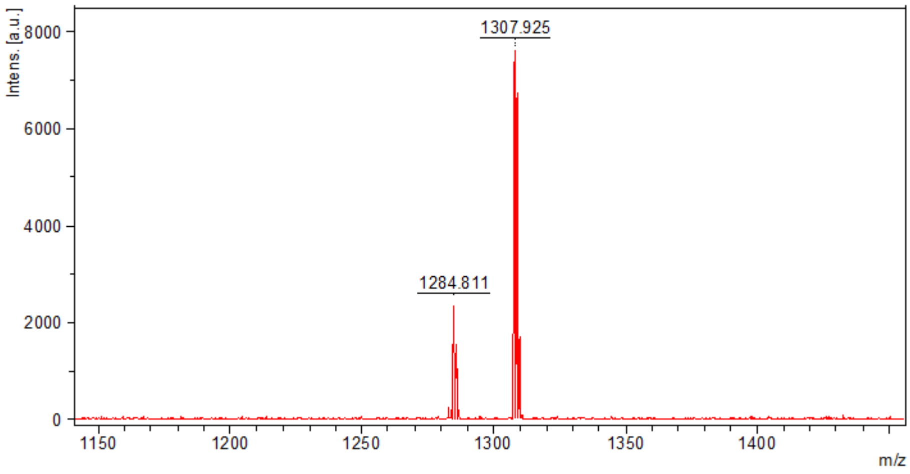

*Figure S.125. MALDI mass spectra of mono-adduct* ***31****. Peaks corresponding to [****31****]$^+$ (m/z=1284.811) and [****31****+Na$^+$]$^+$ (m/z=1307.925).*

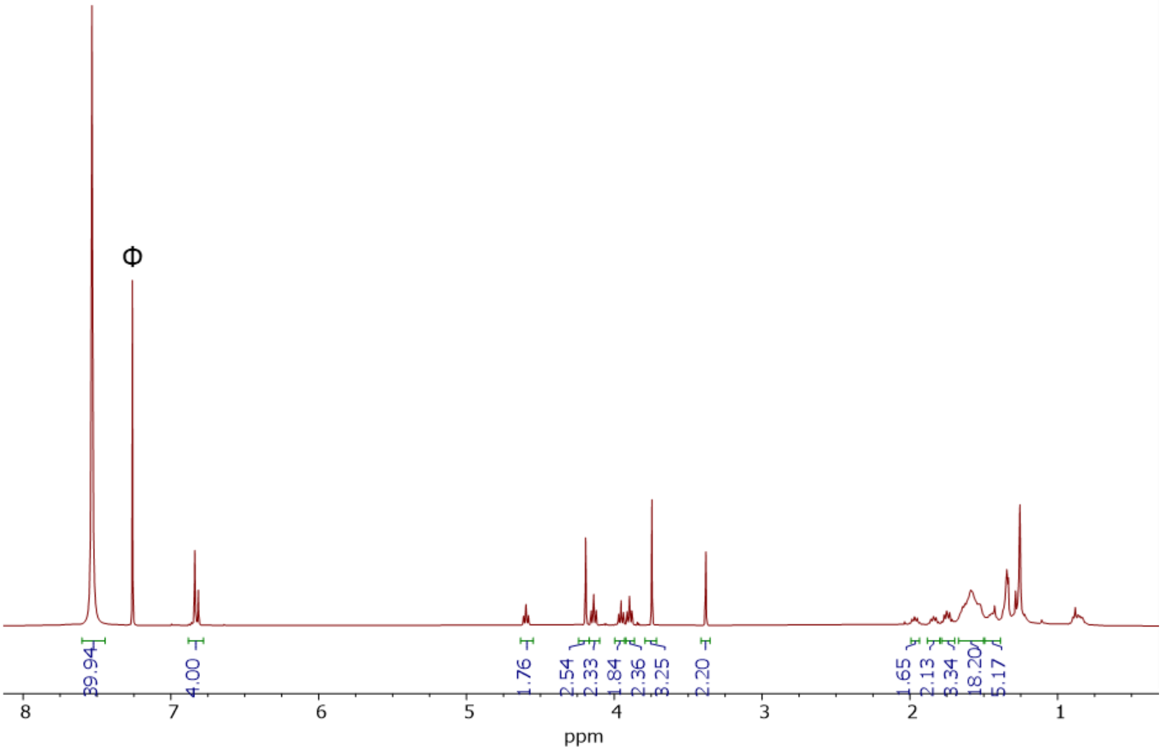

*Figure S.126. $^1$H-NMR spectrum of complex* ***31****⊂[10]CPP. Experiment performed in $CDCl_3$ at 298K (400 MHz). Φ: $CHCl_3$.*

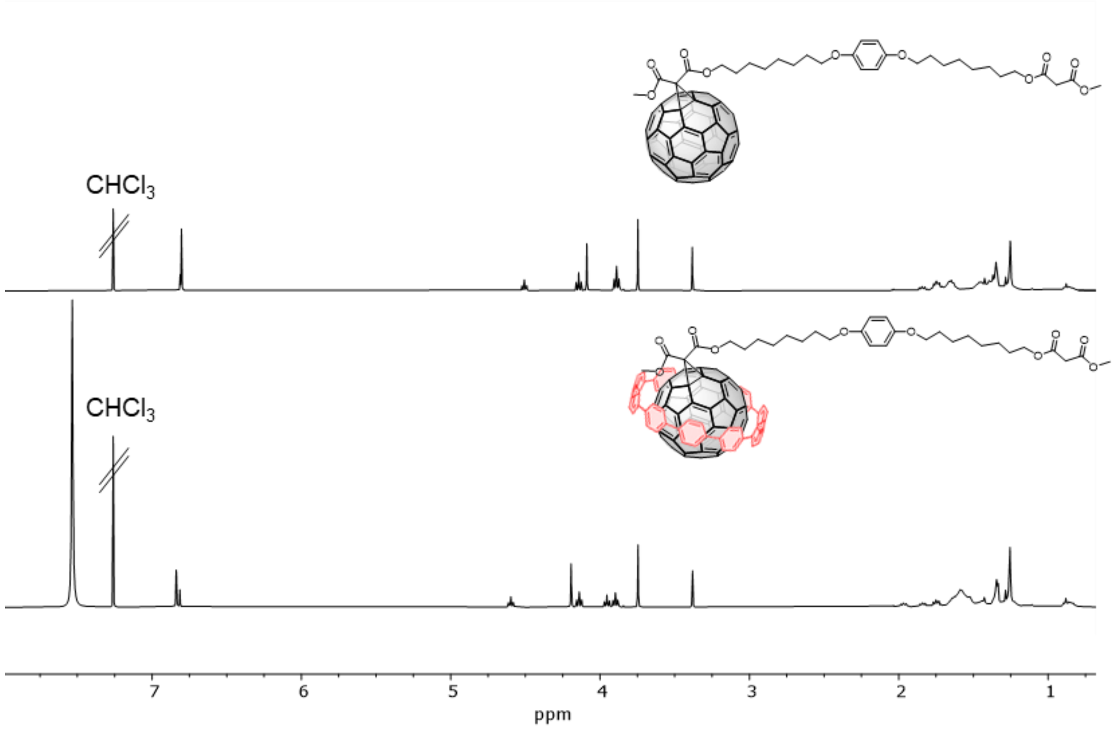

*Figure S.127. Top: $^1$H-NMR spectrum of mono-adduct **31**. Bottom: $^1$H-NMR spectrum of **31**⊂[10]CPP.*

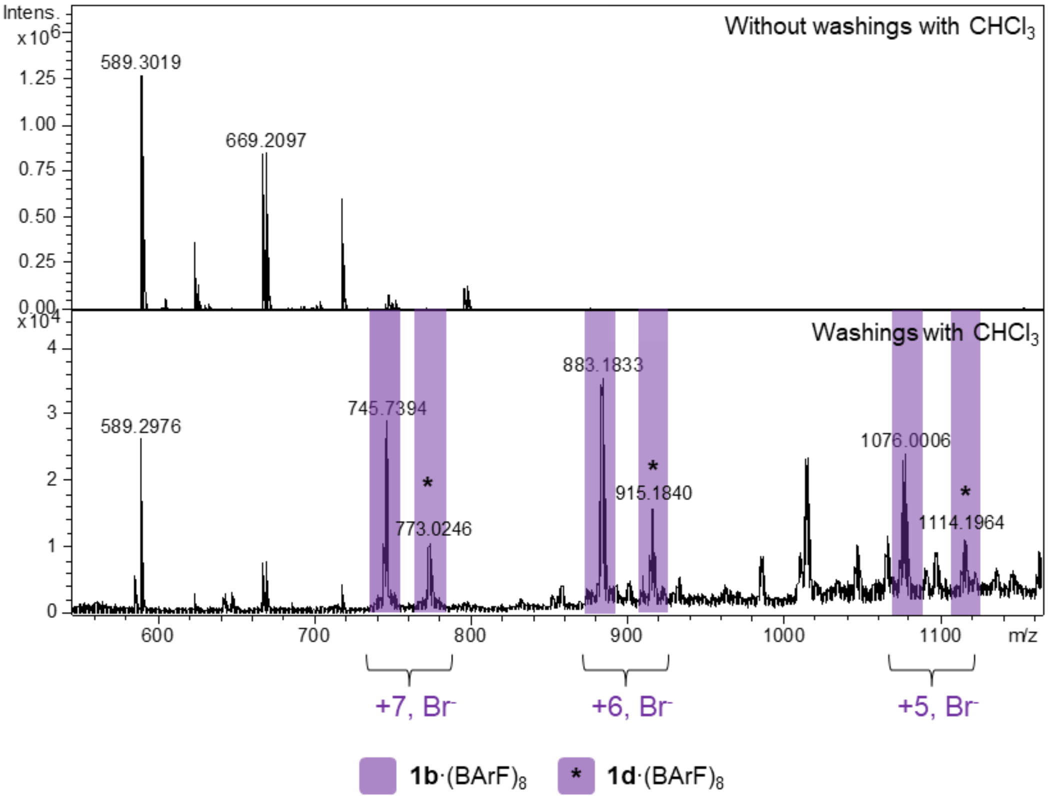

*Figure S.128. HR mass spectra of the crude reaction of Bingel-Hirsch reaction without washes of CHCl$_3$ (top) and with washes of CHCl$_3$ (bottom). Note that peaks with (+7) charge correspond to nanocapsules with Br$^-$ instead of BArF$^-$ as counterion.*

# Annex Chapter VII

## *Annex VII.1 Experimental procedures*

### *Competition experiment between Tb@$C_{82}^-$ and $Tb_2$@$C_{80}^-$ species using **1b**·(BArF)$_8$ nanocapsule (small scale)*

0.7 mg (323.3 nmols considering that all EMFs are $Tb_2$@$C_{80}^-$) of fraction 1 (Figure VII.2) were dissolved in 1 ml of $CHCl_3$. Also, a stock solution of **1b**·$(BArF)_8$ in $CH_3CN$ (2 mg/ml) was prepared. Additions of 3 µl (0.5 nmols) of **1b**·$(BArF)_8$ solution to the EMFs solution were performed. After each addition, the mixture was stirred for 1 minute and it was analysed directly by MALDI-MS.

### *Competition experiment between Tb@$C_{82}^-$ and $Tb_2$@$C_{80}^-$ species using **1b**·(BArF)$_8$ and **1c**·(BArF)$_8$ nanocapsule (bigger scale)*

A sample of 3 mg of purified EMFs extract was divided into two samples, one for each experiment. EMFs were dissolved in 1 ml of $CHCl_3$. A stock suspension of **1b**·$(BArF)_8$ and **1c**·$(BArF)_8$ in $CHCl_3$ (1 mg/ml) were prepared.

Experiment with **1b**·$(BArF)_8$: two additions of 100 µl each (8.3 nmols each addition) of **1b**·$(BArF)_8$ were performed to the solution of EMFs (692.5 nmols). Stirring times were 1-1.5 hours at room temperature. After each addition, the solid was filtrated with Celite© and recovered with $CH_3CN$. The supernatant was monitored by MALDI-MS and the solid was monitored by HR-ESI-MS.

Experiment with **1c**·$(BArF)_8$: four additions of 50-100 µl each (4.25-8.5 nmols each addition) of **1c**·$(BArF)_8$ were performed to the other solution of EMFs (692.5 nmols). Stirring times were 1-1.5h for the first and second additions and 16-48 hours for the third and fourth additions at room temperature. After each addition, the solid was filtrated with Celite © and recovered with $CH_3CN$. The supernatant was monitored by MALDI-MS and the solid was monitored by HR-ESI-MS.

### *Selective encapsulation of $Tb_2$@$C_{80}^-$ from a mixture of Tb@$C_{82}^-$ and $Tb_2$@$C_{80}^-$ using **1c**·(BArF)$_8$ nanocapsule*

0.75 mg (346.3 nmols considering that all EMFs are $Tb_2$@$C_{80}^-$) of a purified EMF extract was dissolved in 1 ml of $CHCl_3$. Also, a stock suspension of **1c**·$(BArF)_8$ in $CHCl_3$ (1 mg/ml) was prepared. One addition of 100 µl (8.5 nmols) of **1c**·(BArF)$_8$ was performed at room temperature and the suspension was stirred overnight (18 hours). Then, the suspension was filtrated with Celite© and the solid was recovered with $CH_3CN$.

**HR-ESI-MS** of $Tb_2@C_{80}\subset$**1c**·(BArF)$_7$ ($CH_3CN$), m/z: calc. for [$Tb_2@C_{80}\subset$**1c**]$^{7+}$ 867.7649, observed 867.7597; calc. for [$Tb_2@C_{80}\subset$**1c**·(BArF)]$^{6+}$ 1156.2369, observed 1156.2314; calc. for [$Tb_2@C_{80}\subset$**1c**·(BArF)$_2$]$^{5+}$ 1560.2978, observed 1560.2868.

### *Annex VII.2 Supplemental figures*

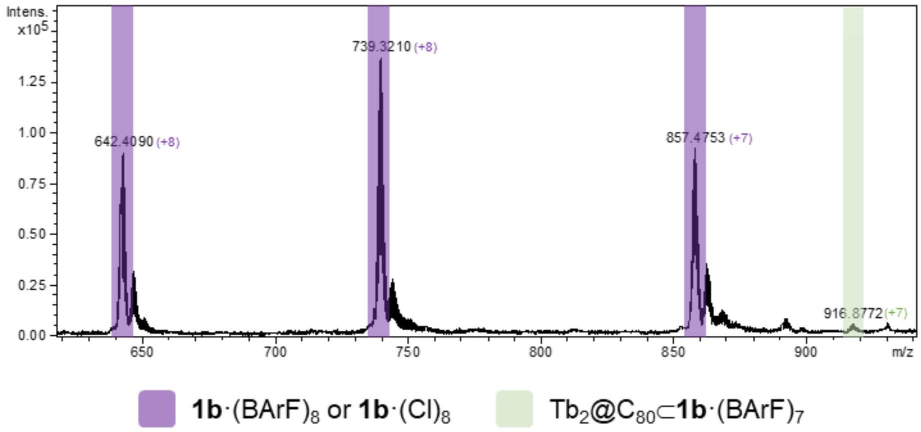

*Figure S.129. HR mass spectrum of the solid obtained after competitive experiments between $Tb@C_{82}^-$ and $Tb_2@C_{80}^-$, adding **1b**·(BArF)$_8$ in solution.*